Transactions of the ASME, Journal of Heat Transfer (ISSN 0022-1481) is published monthly by The American Society of Mechanical Engineers, Three Park Avenue, New York, NY 10016. Periodicals postage paid at New York, NY and additional mailing offices. POSTMASTER: Send address changes to Transactions of the ASME, Journal of Heat Transfer, c/o THE AMERICAN SOCIETY OF MECHANICAL ENGINEERS, 22 Law Drive, Box 2300, Fairfield, NJ 07007-2300. **CHANGES OF ADDRESS** must be received at Society headquarters seven weeks before they are to be effective. Please send old label and new address. **STATEMENT from By-Laws.** The Society shall not be responsible for statements or opinions advanced in papers or ... printed in its publications (B7.1, Para. 3).

Journal of Heat Transfer

Published Monthly by ASME

VOLUME 132 • NUMBER 10 • OCTOBER 2010

EDITORIAL

RESEARCH PAPERS

Conduction

Evaporation, Boiling, and Condensation

Forced Convection

Heat Exchangers

Melting and Solidification

Micro/Nanoscale Heat Transfer

(**Contents continued on inside back cover**)

This journal is printed on acid-free paper, which exceeds the ANSI Z39.48-1992 specification for permanence of paper and library materials. ♾™
♻ 85% recycled content, including 10% post-consumer fibers.

Journal of Heat Transfer Volume 132, Number 10 OCTOBER 2010

TECHNICAL BRIEFS

The ASME Journal of Heat Transfer is abstracted and indexed in the following:

Applied Science and Technology Index, Chemical Abstracts, Chemical Engineering and Biotechnology Abstracts (Electronic equivalent of Process and Chemical Engineering), Civil Engineering Abstracts, Compendex (The electronic equivalent of Engineering Index), Corrosion Abstracts, Current Contents, E & P Health, Safety, and Environment, Ei EncompassLit, Engineered Materials Abstracts, Engineering Index, Enviroline (The electronic equivalent of Environment Abstracts), Environment Abstracts, Environmental Engineering Abstracts, Environmental Science and Pollution Management, Fluidex, Fuel and Energy Abstracts, Index to Scientific Reviews, INSPEC, International Building Services Abstracts, Mechanical & Transportation Engineering Abstracts, Mechanical Engineering Abstracts, METADEX (The electronic equivalent of Metals Abstracts and Alloys Index), Petroleum Abstracts, Process and Chemical Engineering, Referativnyi Zhurnal, Science Citation Index, SciSearch (The electronic equivalent of Science Citation Index), Theoretical Chemical Engineering

Journal of Heat Transfer

Editorial

Editor's Farewell Note

It has been an honor and a privilege for me to serve as the Editor for the *ASME Journal of Heat Transfer* over the last five years. Though it has been challenging and time consuming, I have felt fortunate in following in the footsteps of the previous Editors, who are among the leading figures in the heat transfer community. The journal has grown substantially over the past decade, going from quarterly publication to monthly and becoming one of the largest and best known journals published by ASME. It has also become a preeminent venue for publication in the field of heat transfer, with a considerable international presence. This is seen in more than 60% of the submissions coming from abroad and the large number of Associate Editors from outside the USA.

The journal has a very strong reputation for high quality papers in a wide variety of areas in which heat transfer plays a dominant role. Uniformity of standards is ensured by the Associate Editors, who are assigned papers on the basis of their expertise rather than the country in which they are located. It has been a pleasure to work with some of the most active and dedicated researchers in the field as Associate Editors. They have worked hard to uphold the prestige of the journal by interacting with experts in different areas as reviewers. It is largely because of their effort that the journal has grown in stature in recent years. In 2008, the impact factor of the journal stood at 1.421, with a 5-year impact factor of 1.634 and a half life of greater than 10. Though the impact factor has fluctuated through the years, it cannot be denied that the journal, with an acceptance rate of around 35%, is a widely respected publication, which presents the best in traditional and emerging areas in the field of heat transfer.

The journal has also focused on the publication of a number of special volumes in areas like micro/nanoscale heat transfer, materials processing, bio heat transfer, computational heat transfer, microchannels, and boiling, in order to present the state of the art in these important areas and indicate current trends and future needs. These volumes have also expanded the reach of the journal by bringing in researchers from outside the heat transfer community. The Editorial Board has always felt that heat transfer arises in many important areas of thermal sciences, such as energy, environment, manufacturing, bio systems, and nanomaterials, that are often not considered as part of heat transfer. It has thus been our effort to bring researchers and engineers interested in such fields to the journal, both as contributors and as readers.

Because of the importance of heat transfer in practical and industrial processes and systems, the Editorial Board developed plans for a new journal, which would focus on thermal sciences and bridge the gap between long-term fundamental research and practical use of this information. These efforts resulted in the *ASME Journal of Thermal Science and Engineering Applications*. Though I served as the proposer and then briefly as Editor of this journal, it is now a well-established independent journal which attracts applied papers in different areas of thermal science and engineering. It is expected and hoped that this journal will play an important role in attracting industrial researchers and engineers to thermal science and engineering and provide impetus to applied research in this field.

My assistant, Shefali Patel, has been instrumental in the success of the journal through her constant and careful monitoring of the papers, correspondence with authors, Associate Editors and ASME staff, preparation of the reports on the journal, and taking care of many other routine and non-routine matters, such as selection of best reviewers, maintenance of reviewer lists and appointment of Associate Editors. I am greatly indebted to her for her dedicated and outstanding service to the journal. I am also grateful for the excellent support provided by ASME publication staff, particularly Philip DiVietro, Colin McAteer, Judith Sierant, and Beth Darchi. They were always willing to help if problems or urgent issues arose. I could always turn to them for their guidance and support for new ideas and plans for the journal. Certainly, the expansion of the journal, development of the new journal, publication of a wide variety of special volumes, and improvements in the web system would not have been possible without their support and encouragement. I would also like to thank the Executive Committee of the Heat Transfer Division for their continuous support and guidance and the previous Editor, Vijay Dhir, for his initial guidance to get me started. I learned a lot about the journal from Ray Viskanta and Jack Howell, with whom I served as Associate Editor, and this experience has been valuable in my service as editor.

On October 1, 2010, Professor Terry Simon of the University of Minnesota will take over as the Editor. Terry has served in the past as an Associate Editor of JHT and is an active researcher and member of the heat transfer community. I am fully confident that Terry, along with the dedicated group of Associate Editors, will continue to uphold the excellent reputation and prestige of the Journal.

Best wishes to all our readers and contributors.

Yogesh Jaluria
Editor
2005–2010

Entropy Generation in Thin Films Evaluated From Phonon Radiative Transport

T. J. Bright

Z. M. Zhang[1]
e-mail: zhuomin.zhang@me.gatech.edu

George W. Woodruff School of Mechanical Engineering,
Georgia Institute of Technology,
Atlanta, GA 30332

One of the approaches for micro/nanoscale heat transfer in semiconductors and dielectric materials is to use the Boltzmann transport equation, which reduces to the equation of phonon radiative transfer under the relaxation time approximation. Transfer and generation of entropy are processes inherently associated with thermal energy transport, yet little has been done to analyze entropy generation in solids at length scales comparable with or smaller than the mean free path of heat carriers. This work extends the concept of radiation entropy in a participating medium to phonon radiation, thus, providing a method to evaluate entropy generation at both large and small length scales. The conventional formula for entropy generation in heat diffusion can be derived under the local equilibrium assumption. Furthermore, the phonon brightness temperature is introduced to describe the nature of nonequilibrium heat conduction. A diamond film is used as a numerical example to illustrate the distribution of entropy generation at the walls and inside the film at low temperatures. A fundamental knowledge of the entropy generation processes provides a thermodynamic understanding of heat transport in solid microstructures; this is particularly important for the performance evaluation of thermal systems and microdevices. [DOI: 10.1115/1.4001913]

Keywords: conduction, entropy, phonon radiative transfer, thermodynamics, thin film

1 Introduction

As electronic and thermal devices continue to decrease in size, energy dissipation, or heat generation becomes more spatially concentrated. Device reliability is affected by the peak temperature of operation. Thermal transport in small structures exhibits different behavior that conventional models do not adequately describe [1]. Such small structures, specifically thin dielectric films, are usually present in microelectronic circuits and energy conversion devices where heat is generated [2]. The heat flux and temperature distribution become important design considerations. Furthermore, in order to improve the thermodynamic performance of a device or system, sources of entropy generation should be eliminated or minimized.

Phonon transport in crystalline insulators and semiconductors has been extensively investigated. Casimir [3] used phonon radiation to study thermal transport in crystals at low temperatures when the mean free path is larger than the crystal dimensions and in the case when internal scattering is negligible. This regime is often called the Casimir limit at low temperatures when the energy transfer by elastic waves is governed by the T^4-law just like the Stefan–Boltzmann law of thermal radiation. Little [4] considered the reflection and transmission coefficients of phonon radiation at the interface of dissimilar materials to derive the acoustic mismatch model for thermal boundary resistance. Callaway [5] modeled the lattice thermal conductivity based on the Boltzmann transport equation (BTE), considering different scattering mechanisms. More recently, phonon radiation and BTE have been extensively studied by many groups [6–16]. Modeling phonon transport allows engineers to estimate peak temperatures and heat fluxes for maximum performance.

The BTE reduces to the equation of phonon radiative transport (EPRT) [8], under the relaxation time approximation, which is valid when the distribution function is not too far from equilibrium such that the collision term can be approximated as linear. The EPRT utilizes similarities between the phonon and the photon to take advantage of a large body of research previously done on thermal radiation and to apply it to the conduction of heat via phonons in an electrically nonconducting medium. The EPRT does not contain a term similar to the in- and out-scattering of photons (or simply photon scattering) and hence is relatively easier to solve.

Despite numerous studies on the phonon radiative transfer, there seems to be a lack of research dealing with the entropy generation associated with phonon radiation. Second law analysis can offer a thermodynamic understanding of the irreversible process during nonequilibrium heat transfer. This can help improve the thermodynamic efficiency and performance of energy conversion and generation systems. For this reason, second law analysis has been extensively studied in conventional thermal systems involving conduction, fluid flow, and thermal radiation transfer [17–19]. The study of entropy generation in microfluidics has become an active area of research [18,20]. While entropy generation associated with heat diffusion is well known [17], the conventional control volume analysis is only for large scales when diffusion is the dominant process of heat conduction. The entropy of radiation has been used to derive Planck's law of thermal radiation and can model the entropy generation in radiative transfer both at the boundaries and in participating medium [21–23]. The knowledge of entropy transfer and generation processes in phonon radiation helps understand the irreversibility associated with lattice conduction from the microscale to the macroscale.

As an initial step in second law analysis of phonon heat conduction, the present work develops a model for entropy analysis based on the BTE under the relaxation time approximation and steady-state conditions. The 1D phonon radiative transport between two constant-temperature thermal reservoirs (black walls), as illustrated in Fig. 1, is considered to develop fundamental arguments that could be extended to multiple dimensions. The boundaries or surfaces of the medium are treated as infinite thermal reservoirs and are referred to throughout this work as walls

[1]Corresponding author.

Contributed by the Heat Transfer Division of ASME for publication in the JOURNAL OF HEAT TRANSFER. Manuscript received June 5, 2009; final manuscript received April 5, 2010; published online July 27, 2010. Assoc. Editor: Kenneth Goodson.

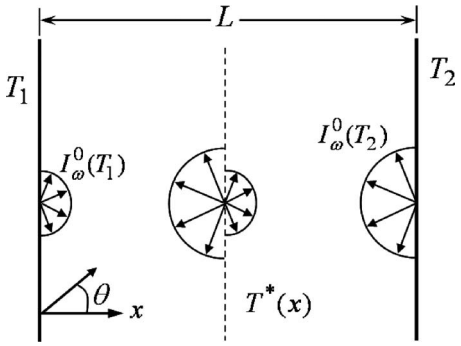

Fig. 1 Schematic showing directional intensity distribution at a single frequency inside a medium between two black walls at temperatures T_1 and T_2. The intensity at a vertical plane inside of the medium (dashed line) is shown qualitatively for $T_2 > T_1$ in the acoustically thin limit. Each wall acts as a thermal reservoir, thus, heat is transported as a radiation process inside the medium.

due to the arbitrary choice of vertical orientation. It extends the analogy between photons and phonons to understand the process of entropy generation at different length scales. Furthermore, a phonon brightness temperature, which is independent of frequency and direction, is defined to depict the nonequilibrium nature of microscale heat conduction.

2 Phonon Radiative Transfer

The 1D BTE under the relaxation time approximation can be expresses as follows [1,8,24]:

$$\frac{\partial f}{\partial t} + v_x \frac{\partial f}{\partial x} = \frac{f_0 - f}{\tau} \tag{1}$$

by neglecting the acceleration term. Here, v_x is the x-component of the velocity, f is the actual distribution function (in terms of frequency) and is usually anisotropic at a given x and t, f_0 is the equilibrium distribution function, and τ is the relaxation time that is in general a function of frequency and phonon velocity. For phonons, the equilibrium distribution function is given by the Bose–Einstein statistics that is a function of temperature and frequency but not the direction (i.e., isotropic).

Based on the energy flux, the phonon intensity can be defined that is consistent with the intensity as defined in the case of thermal radiation. The intensity of a phonon gas in a given direction at a single frequency is [1]

$$I_\omega(\omega, \theta, \phi) = \sum_P v_g \hbar \omega f D(\omega) \tag{2}$$

where $\hbar$ is Planck's constant divided by 2π, the density of states $D(\omega)$ is defined such that $D(\omega)d\omega$ represents the number of vibration modes between ω and $\omega + d\omega$ per unit volume per unit solid angle, and $v_{g,p}$ is the group velocity in the direction defined by the zenith angle θ and azimuthal angle ϕ. Since the energy of a single phonon is $\hbar\omega$, Eq. (2) represents the rate of heat transfer per unit projected area, per solid angle, and per unit frequency interval, just as in the case of photon radiation. Based on this definition of phonon intensity, the heat flux in the x direction can be evaluated from the phonon intensity. For 1D heat transfer in the x direction, the phonon intensity can be assumed to be independent of azimuthal angle, giving

$$q_x'' = \int_0^\infty q_\omega'' d\omega = 2\pi \int_0^\infty \int_{-1}^1 I_\omega(\omega, \mu) \mu d\mu d\omega \tag{3}$$

where $\mu = \cos(\theta)$ is the direction cosine relative to the x direction (see Fig. 1) and q_ω'' is the spectral heat flux. The phonon equilibrium intensity can be derived from the Bose–Einstein distribution function [1]. Assume that the phonon dispersion is linear and an average acoustic speed (i.e., the sound velocity) v_a can be used for all three polarizations. Then, the (isotropic) equilibrium intensity becomes

$$I_\omega^0(\omega, T) = \frac{3\hbar\omega^3}{8\pi^3 v_a^2 (e^{\hbar\omega/k_B T} - 1)} \tag{4}$$

Note that emission of phonons from a black wall has the intensity equal to the equilibrium intensity defined by Eq. (4). Substituting Eq. (2) into Eq. (1) and noting that $v_x = v_a \cos\theta$, one obtains the EPRT at a steady state [8]

$$\mu \frac{dI_\omega}{dx} = \frac{I_\omega^0(\omega, T^*) - I_\omega}{v_a \tau} \tag{5}$$

Equation (5) resembles the radiative transfer equation (RTE) for electromagnetic radiation in an absorbing and emitting medium with no scattering. Under the relaxation time approximation, scattering of phonons by crystalline defects and other phonons is analogous to the emission and absorption processes in the conventional RTE. The actual phonon scattering processes may involve the reservoir modes (optical phonons), scattering on defects, and the three-phonon scattering (acoustic phonons) that can result in the creation or annihilation of phonons [1,24]. Unlike RTE for a gas medium, $T^*(x)$ in Eq. (5) is an *effective* temperature of the medium. Rigorously speaking, a thermodynamic temperature cannot be defined in the medium unless the thickness of the film L is much greater than the phonon mean free path $\Lambda = v_a \tau$. The Knudsen number given by $\mathrm{Kn} = \Lambda / L$ is a parameter that characterizes the acoustic thickness of the medium. A large Kn implies the acoustically thin limit known as Casimir's limit [3], whereas a very small Kn implies the diffusion limit where Fourier's law can be applied. Only in the acoustically thick limit, the effective temperature $T^*(x)$ converges to the local equilibrium temperature in the conventional sense. A further assumption is made such that the relaxation time is independent of the frequency, i.e., the gray-medium assumption since the inverse of the mean free path is analogous to the absorption coefficient in photon radiative transfer.

Radiative equilibrium is the condition [25,26]

$$\nabla \cdot \mathbf{q}'' = 0 \tag{6}$$

which corresponds to the case where there are no sources or sinks in the medium. In the case of steady-state conduction, Eq. (6) holds for phonon transport. For the 1D case, it implies that

$$\frac{\partial q_x''}{\partial x} = 2\pi \int_0^\infty \int_{-1}^1 \frac{\partial I_\omega(\omega, \mu)}{\partial x} \mu d\mu d\omega = 0 \tag{7}$$

Integrating Eq. (5) over the frequency and direction cosine and applying Eq. (7), one obtains the following relation for a gray medium (i.e., the relaxation time is independent of frequency):

$$\int_0^{\omega_D} I_\omega^0 d\omega = \frac{1}{2} \int_0^{\omega_D} \int_{-1}^1 I_\omega d\mu d\omega \tag{8}$$

where the upper limit is replaced by the Debye cut-off frequency ω_D, which is related to the Debye temperature by $\Theta_D = \hbar\omega_D / k_B$ [1,24]. While Eq. (6) is applicable to steady states only, it was shown that Eq. (8) is also applicable to transient EPRT [9]. Furthermore, when the medium temperature is much lower than Θ_D, the total equilibrium intensity can be expressed as

$$I^0(T) = \int_0^{\omega_D} I_\omega^0 d\omega \approx \frac{\sigma_{SB}' T^4}{\pi} \tag{9}$$

where $\sigma_{SB}' = \pi^2 k_B^4 / 40\hbar^3 v_a^2$ is the Stefan–Boltzmann constant for phonons [1,8]. Using the total intensity defined as $I = \int_0^{\omega_D} I_\omega d\omega$, Eq. (8) can be simplified to the following:

$$I^0 = \frac{1}{2}\int_{-1}^{1} I d\mu \tag{10}$$

Hence, for a gray medium, one can integrate Eq. (5) over all frequencies and substitute Eq. (10) for $I^0(T^*)$ to obtain

$$\mu\frac{\partial I}{\partial x} = \frac{1}{\Lambda}\left(\frac{1}{2}\int_{-1}^{1} I d\mu - I\right) \tag{11}$$

When the boundary conditions are prescribed, Eq. (11) can be solved for I using standard techniques for radiative transfer analysis, such as the discrete ordinates method and the Monte Carlo method [25,26]. Once I is found, I^0 can be calculated from Eq. (10) and then the effective temperature $T^*(x)$ throughout the medium can be determined using Eq. (9) from I^0. For black walls, the local intensities toward the right and left hemispheres can be expressed, respectively, as follows [1]:

$$I_\omega^+(x,\omega,\mu) = I_\omega^0(\omega,T_1)\exp\left(-\frac{x}{\Lambda\mu}\right) + \int_0^x I_\omega^0(\omega,T^*(\xi))\exp\left(-\frac{x-\xi}{\Lambda\mu}\right)\frac{d\xi}{\Lambda\mu}, \quad \text{for } \mu > 0 \tag{12a}$$

$$I_\omega^-(x,\omega,\mu) = I_\omega^0(\omega,T_2)\exp\left(\frac{L-x}{\Lambda\mu}\right) - \int_x^L I_\omega^0(\omega,T^*(\xi))\exp\left(\frac{x-\xi}{\Lambda\mu}\right)\frac{d\xi}{\Lambda\mu}, \quad \text{for } \mu < 0 \tag{12b}$$

3 The Criteria of Local Equilibrium

In some early studies [8,9], a more restrictive assumption was used such that phonon radiative equilibrium exists at every frequency so that

$$I_\omega^0 = \frac{1}{2}\int_{-1}^{1} I_\omega d\mu \tag{13}$$

which is equivalent of saying that

$$\frac{\partial q_\omega''}{\partial x} = 2\pi\int_{-1}^{1}\frac{\partial I_\omega(\omega,\mu)}{\partial x}\mu d\mu = 0 \tag{14}$$

From the derivation in the preceding section, Eqs. (13) and (14) are not needed in order to solve EPRT. Even for a gray medium, Eqs. (13) and (14) are not satisfied unless the medium is acoustically thick. Zhang [1] mentioned that Eq. (13) is equivalent to the local equilibrium assumption but without any proof. In the following, the local equilibrium conditions are discussed and shown to be consistent with Eq. (13) or (14).

Under the relaxation time approximation, the local equilibrium assumption states that

$$\frac{\partial f}{\partial x} = \frac{\partial f_0}{\partial x} = \frac{\partial f_0}{\partial T}\frac{dT}{dx} \quad \text{or} \quad \frac{\partial I_\omega}{\partial x} = \frac{\partial I_\omega^0}{\partial x} = \frac{\partial I_\omega^0}{\partial T}\frac{dT}{dx} \tag{15}$$

To the first-order approximation, the intensity can be expressed as follows [23,24]:

$$I_\omega \approx I_\omega^0 - \mu\Lambda\frac{\partial I_\omega^0}{\partial T}\frac{\partial T}{\partial x} \tag{16}$$

where T is used instead of T^* to signify that local equilibrium has been established. For Eq. (16) to be a good approximation, the implicit assumptions are $\mathrm{Kn} \ll 1$, i.e., the medium is acoustically thick and, in addition $\partial T/\partial x \ll T/\Lambda$, which requires that the temperature of the medium should not change abruptly over a mean free path (Λ). Under these assumptions, the Fourier law can be derived such that

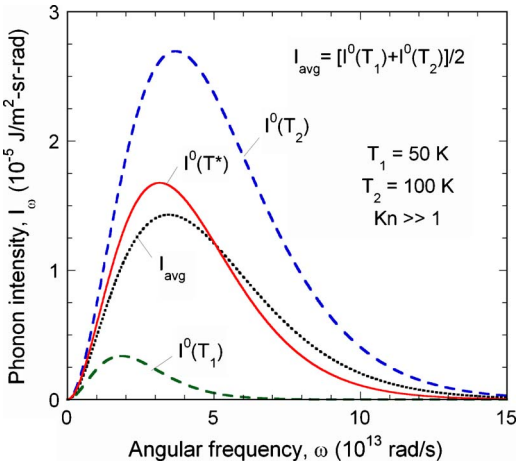

Fig. 2 Phonon intensity at different frequencies corresponding to two black walls at temperatures T_1=50 K and T_2=100 K in the ballistic limit. The equilibrium temperature of the medium is denoted by T^* (which is 85.4 K in this case) and I_{avg} is the average intensity of the two wall distributions.

$$q_x'' = -k\frac{dT}{dx} = -\frac{dT}{dx}\int_0^{\omega_D}\frac{4\pi}{3}\Lambda\frac{\partial I_\omega^0}{\partial T}d\omega \tag{17}$$

where the thermal conductivity k is given by the frequency integral. It should be noted that the assertion that the hyperbolic heat equation can be derived from BTE or EPRT by keeping the transient term in Eq. (1), is misleading as pointed out by the present authors recently [27].

If both sides of Eq. (16) are integrated over the direction cosine, the result will be the same as Eq. (13), suggesting that local equilibrium is a sufficient condition of Eq. (13). Furthermore, using Eq. (12), the spatial derivative of q_ω'' can be expressed as [1]

$$\frac{\partial q_\omega''}{\partial x} = \frac{4\pi}{\Lambda}I_\omega^0(\omega,T^*(x)) - \frac{2\pi}{\Lambda}\int_0^L I_\omega^0(\omega,T^*(\xi))E_1\left(\frac{|x-\xi|}{\Lambda}\right)\frac{d\xi}{\Lambda} - \frac{2\pi}{\Lambda}I_\omega^0(\omega,T_1)E_2\left(\frac{x}{\Lambda}\right) - \frac{2\pi}{\Lambda}I_\omega^0(\omega,T_2)E_2\left(\frac{L-x}{\Lambda}\right) \tag{18}$$

where $E_m(x) = \int_0^1 \mu^{m-2}e^{-x/\mu}d\mu$ is the mth exponential integral. The last two terms on the right-hand side of Eq. (18) originated from the wall emission. It can be seen that, in general, $\partial q_\omega''/\partial x \neq 0$ unless $L \gg \Lambda$ and x is not too close to the wall, i.e., in the acoustically thick limit. Therefore, Eq. (13) or (14) can be viewed as the local equilibrium condition that should not be imposed in solving EPRT for thin films.

Consider a thin film in Casimir's limit where ballistic phonon transport dominates between two black walls. One may view phonon radiation as being emitted from two black walls with no scattering and little absorption/emission inside of the medium. Figure 2 shows the equilibrium intensity distributions evaluated at the wall temperatures along with the exact equilibrium intensity distribution $I_\omega^0(\omega,T^*)$ evaluated using the effective temperature $T^* \approx 85.4$ K inside the medium. The average speed of sound is taken as that of diamond, i.e., $v_a = 12288$ m/s [8]. At low temperatures, the dispersion relation of diamond is essentially linear [28], thus, the proceeding analysis and approximations are reasonable. The intensity integration over the direction cosine is the same as the algebraic average $I_{avg}(\omega)$ of the intensities of the two walls. The two curves do not overlap except at a single finite frequency. In

general, $I_\omega^0(T^*) > I_{\text{avg}}$ at lower frequencies and $I_\omega^0(T^*) < I_{\text{avg}}$ at higher frequencies. If $I_{\text{avg}}(\omega)$ were taken as the equilibrium distribution, a frequency-dependent effective temperature would be obtained. It is worth noting that the results presented in Refs. [8,9] are correct, despite of the excessive assumption in the form of Eq. (13) made in those studies.

4 Phonon Radiative Entropy and Brightness Temperature

When comparing photon and phonon radiation, it is important to keep in mind the physical differences between the two processes. Phonon emission and absorption should not be interpreted literally as in thermal radiation when the radiative energy is released and absorbed by the medium at its local (equilibrium) temperature. Rather, they are associated with the complex phonon scattering mechanisms as mentioned previously. In EPRT, the phonon radiation process is analogous to photon radiation with absorption and emission but without scattering, as prescribed by Eq. (5). As suggested by Prasher [29], a phonon scattering phase function may be introduced to derive a more general EPRT that includes the in-scattering term just like the conventional RTE for thermal radiation. For anisotropic scattering, however, the generalized EPRT reduces to Eq. (5).

Despite the differences, it is convenient to think of phonon radiation as also having a local medium, which emits phonons according to the equilibrium distribution at the effective temperature (T^*). Under the relaxation time approximation, the distribution function is not too far from equilibrium and the medium temperature is thus obtained by the equilibrium intensity (I^0). Furthermore, such a medium can also absorb phonon radiation. While the total emitted and absorbed energy must be the same, as required by the radiative equilibrium condition, the absorbed and emitted energy in any particular frequency are in general not equal to each other, unless Eq. (14) is satisfied. One should keep in mind that in actuality all phonons are governed by the nonequilibrium distribution function (f) or intensity (I_ω) that is determined by solving the BTE or EPRT. While the state-of-the-art understanding of phonon transport in nanostructures is based on molecular dynamics simulation, anharmonic lattice dynamics, as well as the solution of BTE that involves nonlinear dispersion relations [16,30,31], the preceding analysis captures the basic transport process under conditions that are not too far away from equilibrium and helps establish a simple model for entropy analysis to be described in the following. This entropy model may be extended in the future to the study of transient and multidimensional processes, as well as those far from equilibrium and involving nonlinear dispersion relations.

The process of entropy generation due to phonon transport is caused largely by the redistribution of the phonon radiative intensity over the spectrum. If a medium is at a constant temperature (no heat transfer), then phonon transport still takes place but the phonon "emission" and "absorption" both correspond to the equilibrium distribution. This results in no entropy generation since the phonon intensity cannot be redistributed across the spectrum. If there is a temperature gradient in the medium (i.e., temperature difference between the two walls), phonons emitted from one side will have a different intensity spectrum than those from the other. Temperature gradients result in a gradual spectral shift of the phonon intensity, toward longer wavelength in the direction of decreasing temperature, across the medium.

The entropy of thermal radiation has been extensively studied [21–23]. It is convenient in the analysis of radiative entropy generation to introduce a frequency-dependent temperature, known as the brightness temperature, and an entropy intensity, which is analogous to radiation intensity but in terms of the flow of entropy rather than energy. The brightness temperature is the temperature of an equilibrium distribution, which has the same intensity as the nonequilibrium distribution at a given frequency in a given direction. The inverse of the brightness temperature can be found by [1]

$$\frac{1}{T_\omega(\omega,\theta)} = \frac{k_{\text{B}}}{\hbar\omega}\ln\left(\frac{1+x}{x}\right) \tag{19}$$

where $x = 8\pi^3 v_{\text{a}}^2 I_\omega/(\beta\hbar\omega^3)$ and β is the number of phonon modes that is taken to be 3 (two transverse and one lateral mode) in the present study. The entropy intensity is defined based on the phonon radiation intensity as [1,23]

$$L_\omega = \frac{\beta k_{\text{B}}\omega^2}{8\pi^3 v_{\text{a}}^2}[(1+x)\ln(1+x) - x\ln(x)] \tag{20}$$

Furthermore, the phonon entropy intensity and the brightness temperature are related by the definition of thermodynamic temperature as follows:

$$\frac{1}{T_\omega(\omega,\theta)} = \left(\frac{\partial L_\omega}{\partial I_\omega}\right)_\omega \tag{21}$$

The 1D entropy generation rate per unit volume in radiation transfer in a participating medium is given by [22,23],

$$s'''_{\text{gen}} = 2\pi\int_0^\infty\int_{-1}^1 \frac{I_\omega^0 - I_\omega}{\Lambda}\left(\frac{1}{T_\omega} - \frac{1}{T^*}\right)d\mu d\omega \tag{22}$$

which can be used to evaluate the entropy generation in the medium for phonon radiation. Due to the temperature jump at the boundaries, there will also be entropy generation at the wall, which can be written as [1,22,23]

$$s''_{\text{gen,w}} = 2\pi\int_0^{\omega_{\text{D}}}\int_0^1 \left[\frac{I_{\text{in},\omega} - I_{\text{out},\omega}}{T_{\text{w}}} - (L_{\text{in},\omega} - L_{\text{out},\omega})\right]\mu d\mu d\omega \tag{23}$$

where T_{w} is the wall temperature and, for the right wall, μ should be replaced by $-\mu$ to make it positive. The term with $(I_{\text{in},\omega} - I_{\text{out},\omega})/T_{\text{w}}$ is net heat flux from the medium to the wall by phonon radiation and the term with $(L_{\text{in},\omega} - L_{\text{out},\omega})$ is the net entropy flux from the medium to the wall. Note that the entropy generation inside of the wall in a real system may depend on the acoustical properties of the boundaries and may not be well described by a black wall model. In the present study, only the entropy generation between the walls and the medium and inside the medium are considered since each wall is assumed to be at a uniform temperature (i.e., as a thermal reservoir).

Under the local equilibrium assumption, $T^*(x)$ in Eq. (22) can be replaced by $T(x)$ and one can use the first-order expansion to approximate T_ω in the following:

$$T_\omega(I_\omega) \approx T(I_\omega^0) + \frac{\partial T}{\partial I_\omega^0}(I_\omega - I_\omega^0) \tag{24}$$

In writing Eq. (24), the local equilibrium condition given of Eq. (15) was used. Substituting Eqs. (16) and (24) into Eq. (22) and under the assumption that $\partial T/\partial x \ll T/L$, one obtains

$$s'''_{\text{gen}} = -\left(\frac{1}{T}\frac{dT}{dx}\right)^2\int_0^\infty \Lambda\frac{4\pi}{3}\frac{dI_\omega^0}{dx}d\omega \tag{25}$$

Compared with Eq. (17) for the heat flux in the diffusion limit, Eq. (25) can be expressed as

$$s'''_{\text{gen}} = \frac{q''_x \nabla T}{T^2} \tag{26}$$

which is the classical expression of entropy generation during heat conduction [17] as well as thermal radiation in the optically thick limit [19].

Equations (22) and (23) are general case of entropy generation and can be evaluated after the EPRT solution is obtained and the intensity is known. The total entropy generation due to heat transfer across the film under the radiation model can be found by adding the wall entropy generation and the generation inside of the medium. Under the local equilibrium assumption, the entropy generation due to phonon radiation can be approximated with the entropy generation model derived based on heat diffusion from control volume analysis. Liu and Chu [32] studied entropy generation using numerical techniques to solve the radiative transfer equation and showed that a medium must be optically thick for the diffusion model to correctly predict the entropy generation.

5 Results and Discussion

The techniques for solving the radiative transfer equation in a participating medium are numerous [25,26]. In the present study, the discrete ordinates method is employed except when the Kn is very small. For a 1D thin medium a solution with 16 discrete directions is used with weights and abscissas corresponding to the standard Gaussian quadrature technique. The temperature solution is obtained directly using linear algebra techniques to get an exact solution to the system of equations. For $\mathrm{Kn} \leq 0.001$, the system of equations given by the discrete ordinates becomes very inefficient and time consuming to solve exactly due to the need for higher numerical precision. A diffusion approximation [33] is used instead to solve the temperature distribution inside of the medium, coupled with the jump boundary condition at the walls, in order to satisfy the condition of a continuous heat flux at the wall and throughout the medium. The jump boundary condition can be expressed as [25,33]

$$\pi I^0(T_1) - \pi I^0(T^*(0)) = \left(\frac{1}{\varepsilon_1} - \frac{1}{2}\right) q_x'' \tag{27a}$$

$$\pi I^0(T^*(L)) - \pi I^0(T_2) = \left(\frac{1}{\varepsilon_2} - \frac{1}{2}\right) q_x'' \tag{27b}$$

where ε_1 and ε_2 are the emissivities of the walls and both are equal to 1 (blackbody). Equations (27*a*) and (27*b*) can be iteratively solved with the Rosseland diffusion equation [25]

$$q_x'' = -\frac{16\Lambda}{3}\sigma_{\mathrm{SB}}' T^3 \frac{dT}{dx} \tag{28}$$

when Kn is extremely small. To the first-order approximation, Eqs. (27) and (28) can give a T^4 temperature distribution inside the medium with a temperature jump at each boundary. The application of Eq. (28) implies that the thermal conductivity is proportional to T^3. This is reasonable since at low temperatures, phonon specific heat is proportional to T^3 and the scattering rate is governed by defect scattering that is independent of temperature.

Figure 3 shows several solutions for the effective temperature inside of a medium for different Kn plotted in terms of the dimensionless position $\xi = x/L$. Solutions of the EPRT using the discrete ordinates method (exact) are compared with the diffusion approximation with temperature jump at the boundaries. When $\mathrm{Kn} = 0.001$, the two methods give essentially the same results. As Kn increases, deviation becomes larger, suggesting that the diffusion approximation is not applicable.

The spectral intensity can be calculated for different Kn based on the exact solution. For diamond, the relaxation time is independent of temperature at low temperatures and the mean free path is calculated to be $\Lambda = 1.343$ μm from Ref. [8]. The Debye temperature of diamond of 1860 K is much higher than the temperatures considered here. The average speed of sound is $v_a = 12288$ m/s as mentioned before. These parameters are used to obtain all the numerical results in the following.

The intensity distribution is shown in Fig. 4 for $\mathrm{Kn} = 1$ with $T_1 = 10$ K and $T_2 = 50$ K at three locations inside the medium and two frequencies. Since the mean free path is equal to the film thickness, approximately 37% of the phonon radiation will be preserved from one wall to the other in the direction normal to the walls. The calculated temperatures in the medium are $T^*(\xi=0) = 36.6$ K, $T^*(\xi=0.5) = 42.1$ K, and $T^*(\xi=1) = 46.0$ K. There is a larger temperature jump near the lower-temperature wall. Note that the phonon intensity for $\mu > 0$ in Fig. 4(*a*) is very small but not zero. The dotted circles represent the phonon equilibrium intensity (or emitted intensity) $I_\omega^0(T^*)$, which is isotropic and increases from the left to the right. It should be noted that the change of $I_\omega^0(T^*)$ is more prominent at higher frequencies than at lower frequencies. This is because the distribution function is more sensitive to temperature change at higher frequencies. The dashed curve is the actual intensity $I_\omega(\xi)$, which is always larger in the left hemisphere than in the right hemisphere since $T_2 > T_1$ and heat transfer is from right to the left. Note that $I_\omega(\xi=0)$ for $\cos\theta > 0$ is the emitted intensity from the left wall and $I_\omega(\xi=1)$ for $\cos\theta < 0$ is the emitted intensity from the right wall. It is interesting to compare the area inside the $I_\omega(\xi)$ and $I_\omega^0(T^*)$ curve. At high frequencies, $\int_{-1}^{1} I_\omega^0(T^*) d\mu < \int_{-1}^{1} I_\omega d\mu$ so the area surrounded by $I_\omega(\xi)$ is bigger as can be seen from the upper three figures. At lower frequencies, the opposite is true as can be seen from the lower figures in Fig. 4. Clearly, Eq. (13) is not satisfied for $\mathrm{Kn} = 1$ since the condition of local equilibrium is not met.

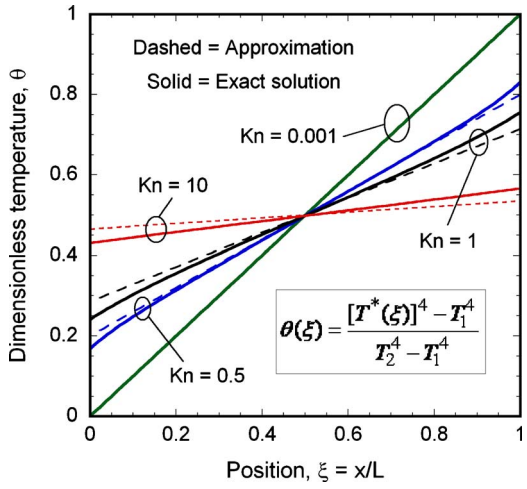

Fig. 3 Temperature distribution inside of medium between two black walls as given by the EPRT (solid) and the diffusion approximation (dashed) for various Kn.

In Fig. 5, the intensity distribution at the center of the medium for different Kn is plotted at a single frequency for $T_1 = 10$ K and $T_2 = 50$ K. Note that the phonon intensity for $\mu > 0$ in Fig. 5(*a*) is nonzero but much smaller than that for $\mu < 0$. As the thickness of the medium increases, the nonequilibrium and equilibrium distributions appear to overlap in all directions, suggesting that the classical definition of temperature in heat conduction becomes reasonable in the diffusion limit. However, a small difference between the two distributions is always present since $I_\omega(\xi)$ must be anisotropic for the heat transfer to occur. Although the difference between $I_\omega(\xi)$ and $I_\omega^0(T^*)$ may be very small at the same location, integration over all frequencies can yield a significant amount of heat transfer in the diffusion limit. Both Figs. 4 and 5 reveal some properties unique to the 1D heat transfer problem. For instance, the symmetry over the horizontal line is due to the fact that the transport properties are independent of ϕ. At the same location and frequency, $I_\omega(180 \text{ deg})$ is the largest and $I_\omega(0 \text{ deg})$ is the smallest. The actual medium thickness is defined according to $L/\cos\theta$. Hence, in the x direction, the effect of ballistic transport is the strongest. The curves of $I_\omega(\xi)$ and $I_\omega^0(T^*)$ cross over each

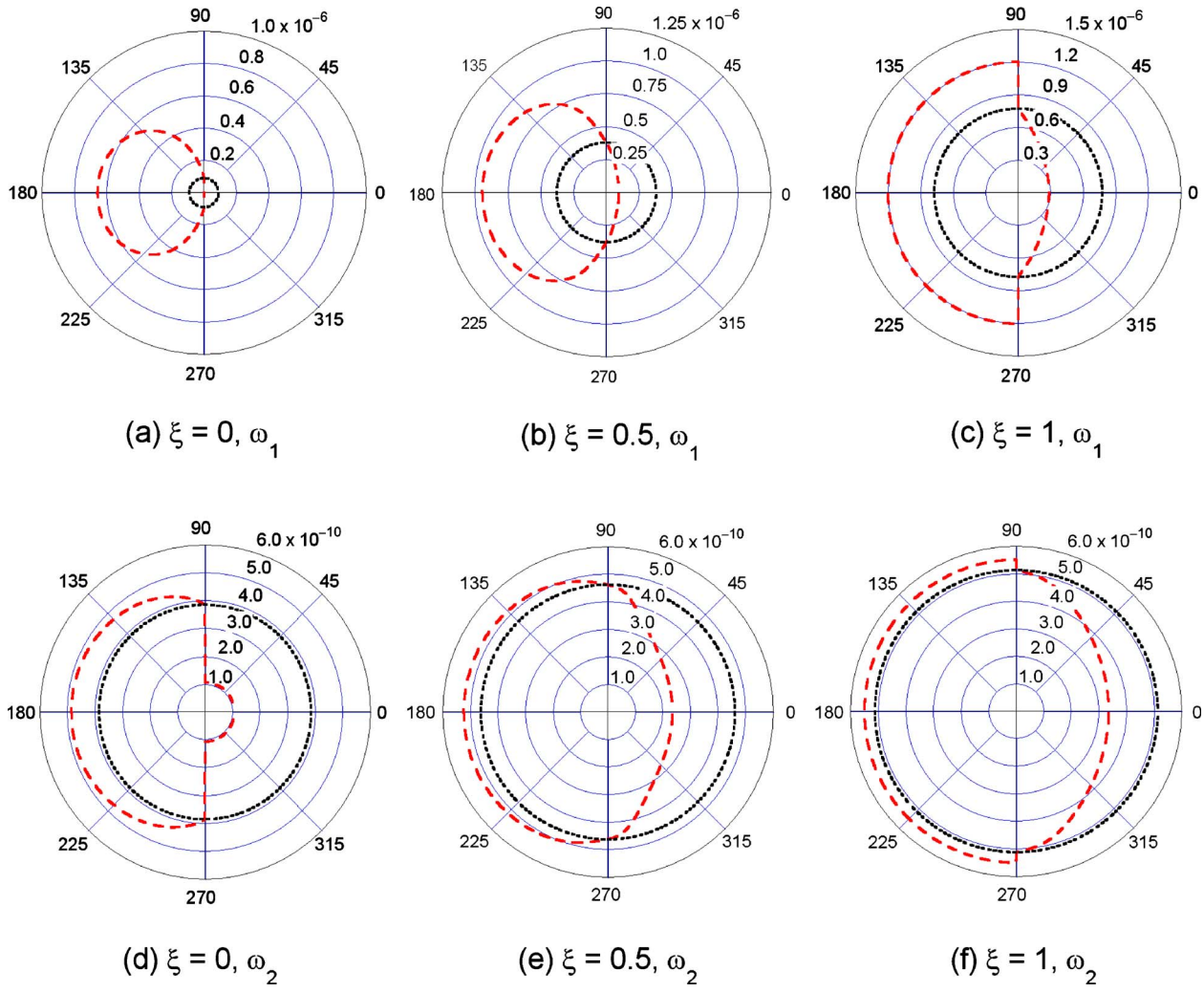

Fig. 4 Phonon intensity I_ω (red dashed) and $I^0_\omega(T^*)$ (black dotted) distributions inside a medium with Kn=1 when T_1=10 K and T_2=50 K, at three different locations and two different frequencies, i.e., $\omega_1=4\times10^{13}$ rad/s and $\omega_2=1\times10^{11}$ rad/s. The unit of intensity is J/(m^2 sr rad).

other at θ=90 deg and at θ=270 deg (i.e., when μ=0). In essence, the medium along the vertical direction is infinitely thick (i.e., diffusion limit).

Figure 6 shows the brightness temperature at the center of the medium at two different frequencies under the same conditions as in Fig. 5. The higher-frequency curve always bounds the lower-frequency curve for the same Kn. The difference in the brightness temperature at different frequencies is the largest in the direction θ=0. For smaller Kn as shown in Fig. 6(*c*), the brightness temperature converges to the medium temperature at every frequency and the curves almost overlap to a circle. It should be emphasized that these curves cannot be perfect circles for heat transfer to occur.

Figure 7 plots the phonon brightness temperature as a function of frequency for Kn=1 at the center of the medium with several direction cosine values. The other parameters are the same as in Fig. 6. At any given frequency, the brightness temperature increases as θ varies from 0 deg to 180 deg (μ=1 to −1). When μ=0, the brightness temperature is not a function of frequency and is equal to the effective medium temperature of the medium T^*. Furthermore, at any given μ that is not equal to zero, the brightness temperature increases with increasing frequency. The increase in brightness temperature with frequency is consistent with the plot shown in Fig. 2. As seen from Fig. 2, the higher the frequency the larger the relative difference between the average local intensity I_{avg} and the equilibrium intensity I^0_ω. At lower frequencies, I_{avg} becomes smaller than I^0_ω. From thermodynamic point of view, this suggests that more phonons at higher frequencies are absorbed than emitted while at the same time more phonons at lower frequencies are emitted than absorbed. The absorption of higher-frequency phonons and emission of lower-frequency phonons is an irreversible process that is associated with entropy generation. Recall that the phonon absorption and emission processes are associated with the complex scattering mechanisms. It should be noted that, for gray medium, the absorption coefficient (which is inverse of the mean free path) is independent of frequency. Since the intensity is calculated from Eq. (12), the coupled absorption and emission processes result in the brightness temperatures at lower frequencies being closer to the medium temperature when $\mu<0$. On the other hand, for $\mu>0$, the brightness temperatures at higher frequencies are closer to the medium temperature. Since the effective thickness is $L/|\mu|$, in the direction normal to the wall, the effect of frequency on the brightness temperature is expected to be the largest. However, the variation of brightness temperature for $\mu<0$ is not as large as for $\mu>0$. It turns out that the lower-temperature side has a more prominent impact on the brightness temperature distribution, especially when μ=1.

In classical heat conduction, entropy flux can be expressed as

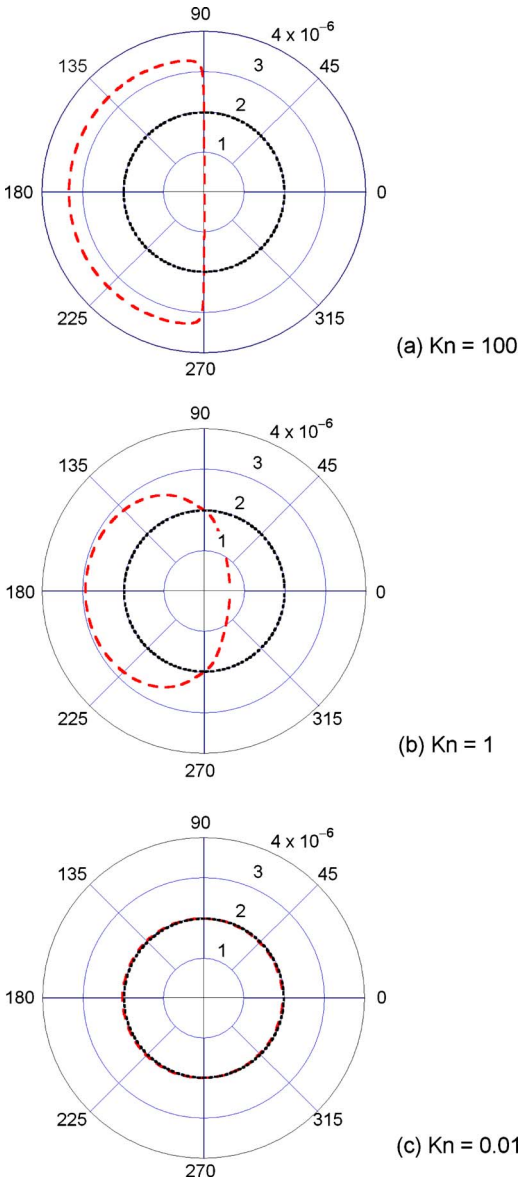

Fig. 5 Phonon intensity I_ω (red dashed) and $I^0_\omega(T^*)$ (black dotted) distributions at the center of the medium: (*a*) Kn=100, (*b*) Kn=1, and (*c*) Kn=0.01. The unit of intensity is J/(m^2 sr rad), the wall temperatures are T_1=10 K and T_2=50 K, and the angular frequency is set to ω=1.7×10^{13} rad/s.

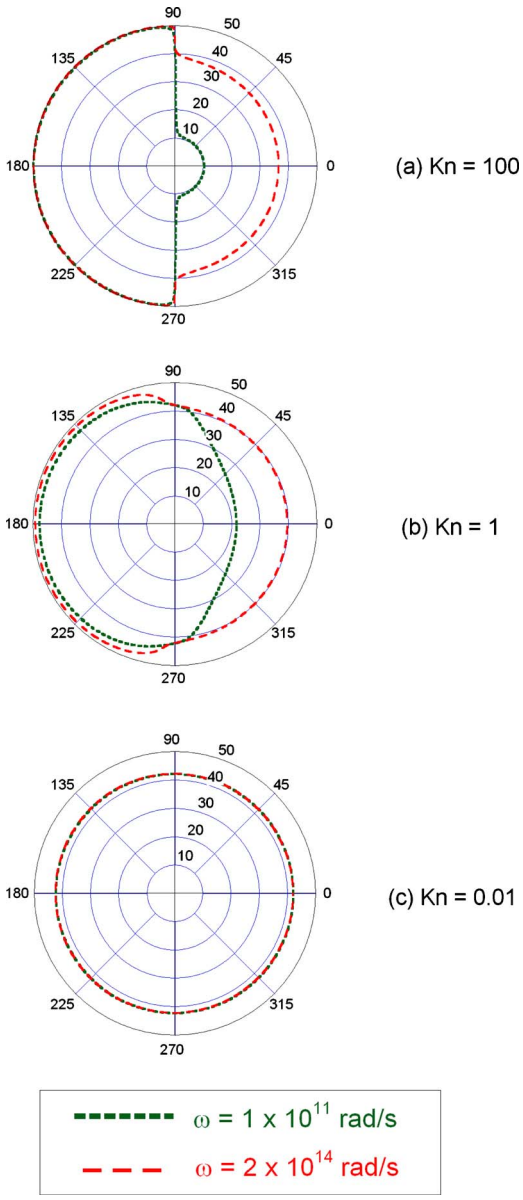

Fig. 6 Polar plots of the brightness temperature $T_\omega(\omega,\theta)$ at two frequencies, at the center of the medium, for (*a*) Kn=100, (*b*) Kn=1, and (*c*) Kn=0.01. The wall temperatures are T_1=10 K and T_2=50 K.

$$s''_x(x) = \frac{q''_x}{T^*(x)} \tag{29}$$

which is not applicable inside the medium under the radiation model unless the medium is acoustically thick. From the entropy intensity evaluated from Eq. (20), the entropy flux inside the medium can be expressed as

$$s''_x(x) = 2\pi \int_0^{\omega_D} \int_{-1}^{1} L_\omega(\omega,\mu)\mu d\mu d\omega \tag{30}$$

The total entropy generation rate per unit area over the thickness L for heat conduction between two thermal reservoirs at T_1 and T_2 is

$$s''_{tot} = q''_x\left(\frac{1}{T_1} - \frac{1}{T_2}\right) \tag{31}$$

which is applicable for all thicknesses. Figure 8 shows the normalized entropy flux calculated from Eq. (30) for T_1=10 K and T_2=50 K. At the walls, $s''_{w1}=q''_x/T_1$ and $s''_{w2}=q''_x/T_2$. The increase in the entropy flux from right to left is caused by irreversibility inside the medium due to phonon radiative transfer. In fact, the integration of Eq. (22) from x_1 to x_2 is the same as the subtraction of the entropy flux, Eq. (30) at these two locations. Furthermore, there is an entropy flux jump at the wall that represents the entropy generation by the wall as predicted by Eq. (23). The entropy generation is more significant toward lower temperatures. Furthermore, the entropy generation at the lower-temperature wall is much greater than at the higher-temperature wall. Even with Kn =0.001 when the distance is 1000 times the mean free path, the entropy generation at the left wall is nearly 10% compared with the overall entropy generation.

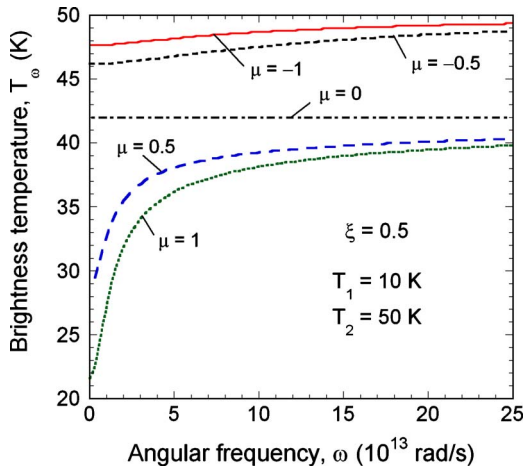

Fig. 7 Brightness temperature for different direction cosine in center of medium with Kn=1 as a function of frequency

Table 1 compares the entropy generation for different Kn at the walls and inside the medium. If the classical expression, Eq. (26), is used to calculate the medium entropy generation, there will be a large error when Kn is large. Even when Kn is relatively small, e.g., Kn=0.1, the difference can be as large as 15%. Note that one could simply use the entropy flux, Eq. (29), to calculate the conduction entropy generation inside the medium by

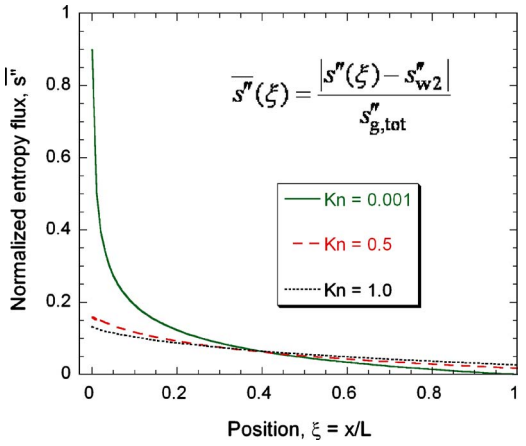

Fig. 8 Normalized entropy flux at different locations across the medium for different Kn. Note the jump at the walls corresponding to wall entropy generation.

$$s''_{gen,m} = q''_x \left[\frac{1}{T^*(0)} - \frac{1}{T^*(L)} \right] \tag{32}$$

It is difficult to generalize the results presented in the table to different wall temperatures as they are presented as dimensional values. However, the same general trend is expected regardless of the wall temperatures. The general trend is a decrease in the difference between the radiation model and the conduction model as thickness of the medium is increased. Increasing medium thickness also results in the majority of entropy generation occurring inside of the medium and a decrease in the relative contribution of wall entropy generation. For all numerical integrations, a convergence criterion was used such that the relative difference between two iterations $\varepsilon_{rel} \leq 10^{-5}$ by mesh refinement. In the case of very small Kn (less than 0.001), the numerical calculation is based on the diffusion model with jump boundary conditions. In addition, the heat flux decreases as the thickness increases, thus, reducing the numerical accuracy. Hence, the differences between the diffusion model and the radiation model in bottom two rows in Table 1 are presumably due to numerical error.

6 Conclusions

Entropy transfer and generation in heat conduction are studied based on phonon radiation. An analytical expression of entropy generation inside of a medium is presented according to the phonon radiative entropy and brightness temperature, a concept that has been used for a long time in electromagnetic thermal radiation. Furthermore, the entropy generation mechanism during phonon transport is elucidated as due to the "absorption" of high frequency phonons and "emission" of lower-frequency phonons, arising from the actual phonon scattering processes. Numerical results show that the relative disagreement between the exact solution based on phonon radiation and the diffusion approximation for entropy generation inside the medium can be as high as 15% for Knudsen number as small as 0.1. Even when Kn=0.001, the entropy generation at the lower-temperature wall can account for 10% of the overall entropy generation. This work also offers insight on the local equilibrium conditions and the proper definition of phonon radiative equilibrium. The fundamental understanding gained in the present study will benefit the thermodynamic analysis of phonon transport in microscale energy conversion devices.

Acknowledgment

The authors wish to thank the support of the National Science Foundation (Grant No. CBET-0828701) and Mr. Soumyadipta Basu for valuable discussions.

Nomenclature

D_P = density of state, s/(rad sr m^3)
f = phonon distribution function, s/(rad sr m^3)

Table 1 Calculated entropy generation rate per unit area (W/K m^2) between two black walls at temperatures T_1=10 K and T_2=50 K for various Kn for diamond. The relative difference in the medium entropy generation between the diffusion model and the radiation model is compared. The percentage of entropy generation by the walls is also shown.

Kn	Medium (radiation)	Left wall	Right wall	Percentage of walls (%)	Total	Medium (diffusion)	Relative difference (%)
1000	1.612×10^{4}	2.320×10^{7}	2.036×10^{6}	99.98	2.524×10^{7}	6.754×10^{3}	58
100	1.177×10^{5}	2.297×10^{7}	1.934×10^{6}	99.50	2.503×10^{7}	6.496×10^{4}	45
10	6.285×10^{5}	2.109×10^{7}	1.415×10^{6}	97.26	2.314×10^{7}	4.695×10^{5}	25
1	1.491×10^{6}	1.211×10^{7}	3.511×10^{5}	89.33	1.395×10^{7}	1.230×10^{6}	17
0.1	8.723×10^{5}	2.080×10^{6}	1.188×10^{4}	70.58	2.964×10^{6}	7.447×10^{5}	15
0.01	2.037×10^{5}	1.272×10^{5}	1.416×10^{2}	38.46	3.311×10^{5}	1.933×10^{5}	5.1
0.001	3.015×10^{4}	3.389×10^{3}	1.443×10^{0}	10.11	3.354×10^{4}	3.013×10^{4}	0.07
0.0001	3.323×10^{3}	4.359×10^{1}	1.445×10^{-2}	1.30	3.367×10^{3}	3.315×10^{3}	0.26
0.00001	3.365×10^{2}	4.501×10^{-1}	1.444×10^{-4}	0.13	3.369×10^{2}	3.351×10^{2}	0.40

f_0 = equilibrium distribution function, $s/(\text{rad sr m}^3)$
$\hbar$ = Planck's constant divided by 2π
I_ω = spectral intensity of phonon radiation, $J/(m^2 \text{ rad sr})$
I = total intensity, $W/(m^2 \text{ sr})$
I^0_ω = equilibrium spectral intensity, $J/(m^2 \text{ rad sr})$
k = thermal conductivity, $W/(m \text{ K})$
k_B = Boltzmann constant
L = distance between walls, m
L_ω = entropy intensity, $J/(K \text{ m}^2 \text{ rad sr})$
$\mathbf{q}''$ = heat flux vector, W/m^2
q''_x = heat flux in the x direction, W/m^2
q''_ω = spectral heat flux, $J/(\text{rad m}^2)$
s'''_{gen} = volumetric entropy generation, $W/(K \text{ m}^3)$
$s''_{gen,w}$ = entropy generation at the wall per unit area, $W/(K \text{ m}^2)$
s''_{tot} = combined wall and medium entropy generation per unit area, $W/(K \text{ m}^2)$
T = temperature, K
T^* = effective temperature of medium, K
T_ω = brightness temperature, K
v_a = speed of sound, m/s
v_p or v_g = phase or group velocity, m/s
x = coordinate, m

Greek Symbols

Θ_D = Debye temperature, K
θ = polar angle, deg
ξ = dimensionless position, x/L
Λ = mean free path, m
ϕ = azimuthal angle, deg
μ = direction cosine
σ'_{SB} = phonon Stefan–Boltzmann constant
τ = relaxation time, s
ω = angular frequency, rad/s
ω_D = Debye cut-off frequency, rad/s

Subscripts

1 or 2 = left or right wall
m = medium
w = wall

References

[1] Zhang, Z. M., 2007, *Nano/Microscale Heat Transfer*, McGraw-Hill, New York.
[2] Cahill, D. G., Ford, W. K., Goodson, K. E., Mahan, G. D., Majumdar, A., Maris, H. J., Merlin, R., and Phillpot, S. R., 2003, "Nanoscale Thermal Transport," J. Appl. Phys., **93**, pp. 793–818.
[3] Casimir, H. B. G., 1938, "Note on the Conduction of Heat in Crystals," Physica, **5**, pp. 495–500.
[4] Little, W. A., 1959, "The Transport of Heat Between Dissimilar Solids at Low Temperatures," Can. J. Phys., **37**, pp. 334–349.
[5] Callaway, J., 1959, "Model for Lattice Thermal Conductivity at Low Temperatures," Phys. Rev., **113**, pp. 1046–1051.
[6] Mahan, G. D., and Claro, F., 1988, "Nonlocal Theory of Thermal Conductivity," Phys. Rev. B, **38**, pp. 1963–1969.
[7] Klitsner, T., Vancleve, J. E., Fischer, H. E., and Pohl, R. O., 1988, "Phonon Radiative Heat Transfer and Surface Scattering," Phys. Rev. B, **38**, pp. 7576–7594.
[8] Majumdar, A., 1993, "Microscale Heat Conduction in Dielectric Thin Films," ASME J. Heat Transfer, **115**, pp. 7–16.
[9] Joshi, A. A., and Majumdar, A., 1993, "Transient Ballistic and Diffusive Phonon Heat Transport in Thin Films," J. Appl. Phys., **74**, pp. 31–39.
[10] Peterson, R. B., 1994, "Direct Simulation of Phonon-Mediated Heat Transfer in a Debye Crystal," ASME J. Heat Transfer, **116**, pp. 815–822.
[11] Mazumder, S., and Majumdar, A., 2001, "Monte Carlo Study of Phonon Transport in Solid Thin Films Including Dispersion and Polarization," ASME J. Heat Transfer, **123**, pp. 749–759.
[12] Sverdrup, P. G., Ju, Y. S., and Goodson, K. E., 2001, "Sub-Continuum Simulations of Heat Conduction in Silicon-on-Insulator Transistors," ASME J. Heat Transfer, **123**, pp. 130–137.
[13] Chen, G., 2002, "Ballistic-Diffusive Equations for Transient Heat Conduction From Nano to Macroscales," ASME J. Heat Transfer, **124**, pp. 320–328.
[14] Murthy, J. Y., and Mathur, S. R., 2003, "An Improved Computational Procedure for Sub-Micron Heat Conduction," ASME J. Heat Transfer, **125**, pp. 904–910.
[15] Sinha, S., Pop, E., Dutton, R. W., and Goodson, K. E., 2006, "Non-Equilibrium Phonon Distributions in Sub-100 nm Silicon Transistors," ASME J. Heat Transfer, **128**, pp. 638–647.
[16] Escobar, R. A., and Amon, C. H., 2008, "Thin Film Phonon Heat Conduction by the Dispersion Lattice Boltzmann Method," ASME J. Heat Transfer, **130**, p. 092402.
[17] Bejan, A., Tsatsaronis, G., and Moran, M., 1996, *Thermal Design and Optimization*, Wiley, New York.
[18] Naterer, G. F., and Camberos, J. A., 2008, *Entropy Based Design and Analysis of Fluids Engineering Systems*, CRC/Taylor&Francis, Boca Raton, FL.
[19] Arpaci, V. S., 1987, "Radiative Entropy Production—Lost Heat Into Entropy," Int. J. Heat Mass Transfer, **30**, pp. 2115–2123.
[20] Hooman, K., 2007, "Entropy Generation for Microscale Forced Convection: Effects of Different Thermal Boundary Conditions, Velocity Slip, Temperature Jump, Viscous Dissipation, and Duct Geometry," Int. Commun. Heat Mass Transfer, **34**, pp. 945–957.
[21] Planck, M., 1959, *The Theory of Heat Radiation*, Dover, New York.
[22] Caldas, M., and Semiao, V., 2005, "Entropy Generation Through Radiative Transfer in Participating Media: Analysis and Numerical Computation," J. Quant. Spectrosc. Radiat. Transf., **96**, pp. 423–437.
[23] Zhang, Z. M., and Basu, S., 2007, "Entropy Flow and Generation in Radiative Transfer Between Surfaces," Int. J. Heat Mass Transfer, **50**, pp. 702–712.
[24] Kittel, C., 2004, *Introduction to Solid State Physics*, 8th ed., Wiley, New York.
[25] Siegel, R., and Howell, J. R., 2002, *Thermal Radiation Heat Transfer*, 4th ed., Taylor & Francis, New York.
[26] Modest, M. F., 2003, *Radiative Heat Transfer*, 2nd ed., Academic, San Diego.
[27] Bright, T. J., and Zhang, Z. M., 2009, "Common Misperceptions of the Hyperbolic Heat Equation," J. Thermophys. Heat Transfer, **23**, pp. 601–607.
[28] Warren, J. L., Yarnell, J. L., Dolling, G., and Cowley, R. A., 1967, "Lattice Dynamics of Diamond," Phys. Rev., **158**, pp. 805–808.
[29] Prasher, R., 2003, "Phonon Transport in Anisotropic Scattering Particulate Media," ASME J. Heat Transfer, **125**, pp. 1156–1162.
[30] McGaughey, A. J. H., and Kaviany, M., 2006, "Phonon Transport in Molecular Dynamics Simulations: Formulation and Thermal Conductivity Prediction," Adv. Heat Transfer, **39**, pp. 169–255.
[31] Turney, J. E., Landry, E. S., McGaughey, A. J. H., and Amon, C. H., 2009, "Predicting Phonon Properties and Thermal Conductivity From Anharmonic Lattice Dynamics Calculations and Molecular Dynamics Simulations," Phys. Rev. B, **79**, p. 064301.
[32] Liu, L. H., and Chu, S. X., 2006, "On the Entropy Generation Formula of Radiation Heat Transfer Processes," ASME J. Heat Transfer, **128**, pp. 504–506.
[33] Deissler, R. G., 1964, "Diffusion Approximation for Thermal Radiation in Gases With Jump Boundary Condition," ASME J. Heat Transfer, **86**, pp. 240–246.

Optimal Thin-Film Topology Design for Specified Temperature Profiles in Resistive Heaters

François Mathieu-Potvin

Louis Gosselin[1]
e-mail: louis.gosselin@gmc.ulaval.ca

Département de Génie Mécanique,
Université Laval,
Québec City, QC, G1V 0A6, Canada

In this paper, we optimized the topology of a thin-film resistive heater as well as the electrical potential of the electrodes on the boundaries. The objective was to minimize the difference between the actual and prescribed temperature profiles. The thin-film thickness was represented by 100 design variables, and the electrical potential at each electrode were also design variables. The topology optimization problem (inverse problem) has been solved with two methods, i.e., with a genetic algorithm (GA) and with a conjugate gradient method using adjoint and sensitivity problems (CGA). The genetic algorithm used here was modified in order to prevent nonconvergence due to the nonuniqueness of topology representation. The conjugate gradient method used in inverse conduction was extended to cope with our electrothermal problem. The GA and CGA methods started with random topologies and random electrical potential values at electrodes. Both the CGA and GA succeeded in finding optimal thin-film thickness distributions and electrode potential values, even with 100 topology design variables. For most cases, the maximum discrepancy between the optimized and prescribed temperature profiles was under 0.5°C, relative to temperature profiles of the order of 70°C. The CGA method was faster to converge, but was more complex to implement and sometimes led to local minima. The GA was easier to implement and was more unlikely to lead to a local minimum, but was much slower to converge. [DOI: 10.1115/1.4001935]

Keywords: inverse conduction, thin-film, topology optimization, uniform temperature, resistive heater, conjugate gradient, genetic algorithm

1 Introduction

One of the main challenges in the domain of heat transfer is to optimize the heat flux distribution and the temperature field in a system. This holds true in several applications, where one wants to minimize entropy generation, minimize global cost, minimize thermal resistance, etc. [1]. In line with this challenge, an interesting problem arises with thin-film used as resistive heaters. Thin-film resistive heaters are used, for example, in tunable Bragg gratings/optical fibers [2–5]; the temperature is adjusted by Joule heating in the film so as to tune the optical properties, which are functions of the temperature. Other applications of thin-film microheaters include various sensors and microboilers (see, e.g., Refs. [6,7]). In Ref. [8], a finite element model predicts the thermal field of a microheater. An analytical thermal model of thin-film resistive heater has been proposed by Kozlov [9] but applies only to the geometry considered. In addition to applying the appropriate control on these films (i.e., optimizing the potential applied at the electrodes), the topology (shape, geometry) of the film is to be designed (i.e., optimized) to reach a desired heat-generation field or a desired temperature profile. This topology optimization problem is an inverse problem.

To solve the problem described above, we have to find the thin-film distribution whose temperature profile corresponds to the desired one. We propose two algorithms that gradually change the film topology until an acceptable temperature profile is achieved. Up to now, topological optimizations have shown to be effective in performing specific thermal objectives. In Refs. [10,11], the shape of a medium is allowed to morph toward an optimal geometry in order to reach the desired outer surface temperature. In Ref. [12], minimal hot-spot temperature is achieved with an evolutionary algorithm by gradually morphing the topology of a domain made of two different materials. Heat conductive elements can be progressively removed for optimizing heat flux [13,14] and for reducing the temperature [15]. In Ref. [16], holes are gradually inserted through a material in the context of a steady-state heat conduction problem. Heat evacuation is maximized by locally varying thermal conductivity within a heat-generating body in Refs. [17,18]. Shape and topology optimization for thermal management has also attracted interest in microelectromechanical systems. Reference [19] suggests a multiple material topology optimization to achieve an electrothermal-compliant device to accomplish maximal local displacement. In Ref. [20], a topological optimization is performed in order to obtain specific thermoelastic properties profile in a domain. Time-dependent nonuniform temperature distribution of compliant mechanisms are obtained in Ref. [21] by topology optimization using a sensitivity analysis.

2 Objectives of the Paper

The typical geometry of the system considered here is shown in Fig. 1. It consists in a rectangular glass plate on which a thin film of chromium is deposited. The thermal properties of these materials are presented in Table 1, along with the geometrical features considered. An electrical current circulates in the film between electrodes, leading to heat generation (Joule heating) within the film. The thickness of the film can be adjusted by successive depositions. In any case, it is much smaller than that of the glass. Heat travels by conduction in the *x-y* plane and escapes from the top and bottom surfaces due to convection and radiation. The objective of the system is to provide a specified temperature profile within the dashed surface in Fig. 1.

In this paper we aim at minimizing the discrepancy between a

[1]Corresponding author.

Contributed by the Heat Transfer Division of ASME for publication in the JOURNAL OF HEAT TRANSFER. Manuscript received October 2, 2008; final manuscript received November 11, 2009; published online August 18, 2010. Assoc. Editor: Ben Q. Li.

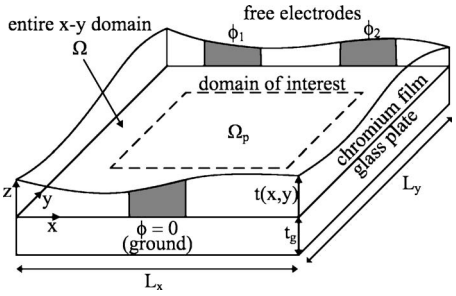

Fig. 1 The geometrical features of the resistive heating system

prescribed temperature profile in the glass $\theta_p(x,y)$ and the actual temperature profile $\theta(x,y)$. We characterized this deviation by the following objective function that is to be minimized:

$$F_\theta = \int_{\Omega_p}\int (\theta(x,y) - \theta_p(x,y))^2 dxdy \tag{1}$$

where $\theta = T - T_\infty$. Since the region for which the temperature is prescribed does not necessarily correspond to the whole domain, the integral of Eq. (1) is performed only in the subregion Ω_p of interest (see Fig. 1). In our work, this domain of interest lies between x_L (left boundary) and x_R (right boundary) for the abscissas, and y_B (bottom boundary) and y_T (top boundary) for the ordinates. In the other regions of the system (i.e., outside Ω_p), the temperature profile can take any value. The design variables available for minimizing F_θ are first the potential values ϕ_i for each free electrode. Furthermore, the topology of the chromium film (i.e., distribution of chromium thickness) can be varied. Modifying these parameters will affect the local heat generation, leading to different temperature profiles.

Two different strategies for the optimization of the topology of chromium will be benchmarked and compared in this paper. The first one is the conjugate gradient with adjoint problem (CGA). In view of the large number of design variable used in this paper, this technique distinguishes from other gradient based methods because it alleviates the need for the computation of the sensitivity matrix [22]. Typically, CGA has the advantage to yield fast results. However, it could converge to local minima. The second optimization technique that we use in this paper is the genetic algorithm (GA). Despite the existence of other evolutionary optimizers (e.g., Particle Swarm, Predator-Prey), we chose to use GA because this method has attracted more and more attention in heat transfer [23]. Typically, this technique is robust, easy to implement, and leads to global extremum, but it has the disadvantage to require a large number of objective function evaluations, which is numerically costly.

3 Temperature Profile Calculation

In general, the 3D conduction equation could be solved for determining the temperature profile in the entire structure in Fig. 1. Here, we rely on a simplified 2D model. A z-averaged temperature profile in the x-y plane will be estimated in the glass plate. The chromium layer will be disregarded for the temperature calculation because its thickness is much smaller than that of glass. This simplified model, similar to the one presented in Ref. [9], follows from the following observations:

(i) The temperature is essentially z-independent in the chromium layer. Furthermore, the x-y plane thermal resistance of the chromium film is large compared with the other thermal resistances involved in the problem due to its nanoscaled thickness. For instance, the glass-to-chromium x-y plane conduction resistance ratio is at most of the order of 10^{-2}. In fact, because film in-plane effective conductivity decreases as the film thickness decreases [9], this thermal resistance ratio represents an upper bound value. Therefore, the presence of the chromium film will be accounted for via a heat flux boundary condition for the temperature calculation. How to evaluate this heat flux is the object of Sec. 4.

(ii) In the glass plate, the thermal conduction resistance associated with conduction in the z-direction is of the order of 6×10^{-4} m^2 K W^{-1}, and the resistance associated with convection scales as $1/h \sim 10^{-1}$ m^2 K W^{-1}. Therefore, in the glass layer, the z-variations in the temperature are small compared with the glass-to-air temperature difference. Therefore, z-variations in the temperature profile will be neglected.

Table 1 Thermal properties and geometrical parameters

k_g	1.1 W m^{-1} K^{-1}
k_c	67 W m^{-1} K^{-1}
h_{top}	10 W m^{-2} K^{-1}
h_{bottom}	5 W m^{-2} K^{-1}
t_g	1 mm
t_c	0.1 μm
σ_c	7.741×10^6 Ω m
L_x	0.1 m
L_y	0.1 m

A heat loss term with a global heat transfer coefficient U is introduced in the conduction equation for taking into account the heat leaks from the top and bottom. This modified conduction equation is used for determining the temperature profile in the domain in Fig. 1

$$\frac{\partial^2\theta}{\partial x^2} + \frac{\partial^2\theta}{\partial y^2} + \frac{q''(x,y) - U\theta}{t_g k_g} = 0 \quad \text{in } \Omega \tag{2}$$

where t_g is the glass layer thickness, Ω is the entire domain, and U is the global heat loss coefficient accounting for losses from the top and bottom

$$U = h_{\text{top}} + h_{\text{bottom}} \tag{3}$$

The heat transfer coefficients h_{top} and h_{bottom} account for both convection and radiation. We assumed $U = 15$ W/m^2 K, which corresponds to a typical natural convection condition. Other values could be considered in the future. The heat flux $q''(x,y)$ comes from the local Joule heating in the chromium film. Adiabatic boundary conditions are applied on every side faces of Ω. This means that the only escape route for heat is via the top or bottom.

4 Calculation of the Heat Flux

The heat generation in the chromium layer depends on the film thickness topology, as well as on the voltage applied on the electrodes. We define the local film thickness as $t(x,y) = n(x,y) \times t_c$, where t_c is the typical thickness of a single chromium film (see Table 1) and $n(x,y)$ is the local number of deposition. To evaluate the heat flux $q''(x,y)$ generated by the chromium film, one solves the electrical potential equation in the area of Fig. 1 filled with chromium

$$\frac{\partial}{\partial x}\left(n(x,y)t_c\sigma_c\frac{\partial\phi}{\partial x}\right) + \frac{\partial}{\partial y}\left(n(x,y)t_c\sigma_c\frac{\partial\phi}{\partial y}\right) = 0 \tag{4}$$

where σ_c is the chromium electrical conductivity. We neglected the z-variation in the potential in the thickness of the film, and we assumed that the electrical conductivity of glass is nil. The local generation of heat in the chromium thin-film follows from

$$q'''(x,y) = \frac{\|\boldsymbol{j}\|^2}{\sigma_c} \tag{5}$$

where the current density is given by

$$\boldsymbol{j} = -\sigma_c \nabla \phi \tag{6}$$

The local volumetric heat generation in the film (Eq. (5)) is related to the heat flux applied on the glass plate by

$$q''(x,y) = q'''(x,y) \times t(x,y) \tag{7}$$

No-current flow boundary conditions are applied everywhere on the Ω domain, except at the electrode positions where potentials ϕ_i are specified. Since only potential differences matter here, one or more electrodes may be set to ground (zero potential). The potentials at the other electrodes are adapted (i.e., optimized) to match the prescribed temperature distribution as will be described later

5 Numerical Model and Validation

A finite volume code is implemented for solving Eqs. (2) and (4). As both equations are similar, the approach for solving these equations is the same. The domain is discretized with quadrilateral cells, and Eqs. (2) and (4) are integrated on the resulting control volumes. Harmonic means are considered for determining the equivalent properties at the faces of the control volumes. The resulting set of algebraic equations is solved line-by-line with a TDMA procedure in MATLAB. For a given material distribution, convergence of $\phi(x,y)$ is declared when

$$\frac{\max(|\phi^{it-1}(x,y) - \phi^{it}(x,y)|)}{\max(|\phi^{it-1}(x,y)|)} < 10^{-7} \tag{8}$$

The same convergence criteria is applied for $\theta(x,y)$. More stringent convergence criteria were tested and did not change significantly the temperature and potential profiles. In order to validate the code, we compared several results with those obtained with the commercial software [24]. Results showed temperature and potential value differences smaller than 0.1% in all cases, which validates our finite volume code.

Mesh independence was tested exhaustively. The temperature profile θ and potential field ϕ were calculated for a given mesh density. Then, the mesh density was doubled until further grid doubling resulted in a variation in θ smaller than 0.05%. For most calculations, a grid of 160×160 was shown to be sufficient for mesh independence.

6 Optimization Procedure

Sections 3–5 described how to calculate the potential and temperature profiles required for estimating the objective function F_θ (Eq. (1)) when the design variables (i.e., film topology $n(x,y)$ and applied voltages ϕ_i on electrodes) are given. Here, we present the optimization procedure that has been used to minimize F_θ.

The first thing to note is that specifying the required temperature profile $\theta_p(x,y)$ yields directly the required heat flux $q''_p(x,y)$. This is because when $\theta_p(x,y)$ is known, the second derivatives of θ_p are also known in Eq. (2). Therefore, the required heat flux to achieve θ_p can be deduced from Eq. (2). The problem of minimizing F_θ can be translated into the problem of minimizing F_q

$$F_q = \int_{\Omega_p} \int (q''(x,y) - q''_p(x,y))^2 dxdy \tag{9}$$

The advantage of this formulation is that now only Eq. (4) needs to be solved in the optimization process.

There are two types of design variables in this problem. The first is the potentials ϕ_i at the electrodes, and the second is the chromium thickness topology itself, specified here by $n(x,y)$. The optimization approaches for determining ϕ_i and $n(x,y)$ are different; hence, there are two optimization levels. An "outer" algorithm optimizes the topology, while an "inner" algorithm optimizes the electrode potentials for each individual topology used in the outer algorithm. The problem of optimizing the topology (outer optimization algorithm) is an inverse design problem, which we solved by two different methods (i.e., GA and CGA), the efficiency of which will be compared later.

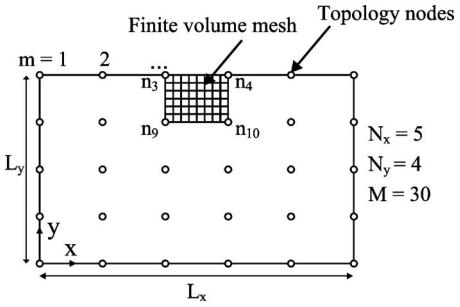

Fig. 2 Example of topology mesh and finite volume mesh

Finally, note that for a given design, the temperature profile $\theta(x,y)$ may remain unchanged if the topology $n(x,y)$ is multiplying by a factor f while the free-electrode potentials ϕ_i are divided by a factor $f^{1/2}$. This property will be used later in the text.

6.1 Determination of the Optimal Potential. The adjustment of the electrode potentials to minimize F_θ or F_q for a fixed film topology can be performed quite straightforwardly thanks to the properties of bilinear functions, as described in Ref. [25]. As this boundary control problem has been described in details in Ref. [25], we only recall here the main ideas leading to its solution. Since the heat generation is quadratic in ϕ, the heat-generation field can be expressed as a combination of "fundamental" fields and of bilinear functions. Therefore, it is not necessary to recalculate the heat generation every time the potential at the electrodes are changed during the optimization process. This allows for a quick identification of the electrode potentials ϕ_i that minimize F_θ or F_q with a typical steepest descent method.

6.2 Representation of a Topology. A strategy has been adopted to model a continuous chromium thickness distribution. First, the domain is divided in N_x sections along the x-axis and in N_y sections along the y-axis, so that the domain looks like a checkerboard (see Fig. 2). This is the topology mesh and it is coarser than the finite volume mesh. At each topology nodes (identified by indices $m=1,2,\ldots,M$), the $n(x_m,y_m)$ values (noted n_m for compactness) are defined as design variables. Then, within each rectangular subsection, $n(x,y)$ is completely determined by a two-dimensional Lagrange interpolation [26] using the four surrounding n_m values. For example, in Fig. 2, the spatial variation in $n(x,y)$ in the rectangular section delimited by nodes $m=\{3,4,9,10\}$ is determined by Lagrange interpolations using the specified values n_3, n_4, n_9, and n_{10}, and so on for the rest of the domain. Note that for a $N_x \times N_y$ topology mesh, there are $M=(N_x+1)\times(N_y+1)$ topology nodes. With the Lagrange linear interpolants, one can express the topology of the entire domain Ω as

$$n(x,y) = \sum_m n_m \Psi_m(x,y) \tag{10}$$

where $\Psi_m(x,y)$ is the $n(x,y)$ field when n_m is set to 1 and the rest of the design variables are set to 0.

6.3 Topology Determination by GAs. One of the two approaches that we considered for solving the inverse conduction problem and determine the topology is GAs. We determined the optimal topology (optimal film thickness at topological nodes, see Sec. 6.2) by minimizing F_q (Eq. (9)). The design variables are represented by real numbers and their admissible range is n_m

$\in [0.01,1]$ for $m=1,2,\ldots,M$. The GA starts by generating randomly a population of 50 designs. For each, the performance is evaluated (Eq. (9)), which requires solving Eq. (4). Note that the potential values ϕ_i at the free electrodes are optimized straightforwardly for each individual (see Sec. 6.1) so that potentials are not included formally as design variables for the GA. Then, individuals are selected and matched by couples for crossovers, with larger probabilities of being selected for the best designs.

Just before crossovers, for each couple, the topology of one of the two individual (say individual "*a*") is scaled relative to the other (say individual "*b*"). That is, its design variables $n_{a,m}$ are multiplied by a factor f that minimized the squared difference of topology between individuals a and b

$$f = \frac{\int_\Omega \int n_a(x,y) \times n_b(x,y) dxdy}{\int_\Omega \int n_a(x,y)^2 dxdy} \tag{11}$$

This strategy is used to prevent the crossover of similar individual represented by the thickness of different orders of magnitude (see the equivalence property stated at the beginning of Sec. 6). Note that this artificial change in topology before crossover preserves the fitness-values F_θ and F_q of the concerned individuals because the electrodes potentials ϕ_i may be multiplied by $f^{-1/2}$ at the same time.

Mutation is applied on the offspring (rate=0.03), and a new generation of designs is created from the offspring and from the seven best designs of the initial population, which are ensured to propagate (elitism). The process is repeated until the decrease in the objective function is smaller than 1% for 100 successive generations or when an individual has reached an accuracy of 0.5°C (i.e., the maximal temperature difference between the actual and prescribed fields is less than 0.5°C). This temperature verification requires solving Eq. (2), and it is performed only for the best individual of each generation. The abovementioned steps are illustrated in Fig. 3. Note that the GA being a heuristic process, different runs with the same settings might lead to different results.

6.4 Topology Determination by the CGA. The second approach on which we relied to determine the optimal topology is the conjugate gradient method with adjoint problem (CGA). The idea is to calculate the gradient of the objective function F_q with regard to the M design variables n_m, and then to change these design variables using previous gradient directions, similar to the steepest descent method. These two steps are repeated until a minimum is found. Note that the use of finite differences or sensibility analysis for the calculation of the gradient would require as many numerical simulations as there are design variables (M design variables), which would be time-consuming. However, we rely on an adjoint problem that allows to calculate the gradient components with only one numerical simulation [22]. The adjoint problem is defined by differential equations where the dependant variable is a Lagrange multiplier field $\lambda(x,y)$. In this paper, we developed a CGA adapted to our multifields problem. The main steps of the CGA are summarized in Fig. 4, and the mathematical development are given in the Appendix. It is worth to note that the gradient calculated with the help of the efficient Lagrangian multiplier method has been compared several times with the finite difference gradient (numerically costly). They have shown to corroborate with very high accuracy.

7 Optimization of Topology and Potential With One Free Electrode

To assess the efficiency of the two topology optimization methods (inverse problems) proposed in this paper (i.e., CGA and GA), three prescribed temperature profiles were considered, and are

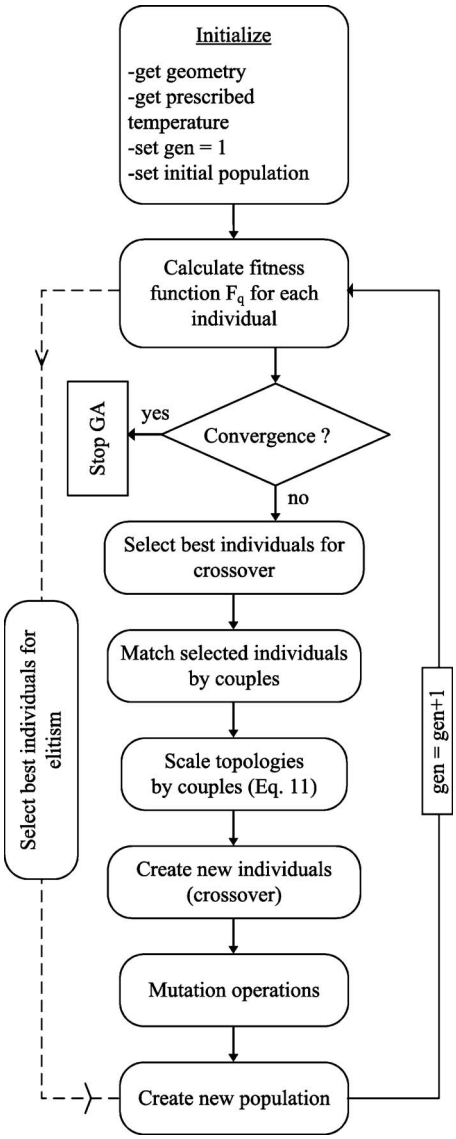

Fig. 3 The main steps of the genetic algorithm method

shown in the left-hand side in Fig. 5. These temperature profiles come from predefined topologies $n(x,y)$ and electrodes potentials values ϕ_i (see right-hand side in Fig. 5). Hence, we know that a solution exists for these three inverse problems. Note that for these three cases, Ω_p is the entire domain. To begin, we considered topologies with only two electrodes (thick black lines in the figures), one set to the ground and the other for which the potential is optimized as explored in Ref. [25]. There are $M=81$ nodes (design variables) to describe the topology. The position of the nodes is illustrated by white circles in the figures. The first prescribed topology (Fig. 5(*b*)) is a film with uniform thickness, i.e., $n_m=1$ for all m. The corresponding temperature profile (Fig. 5(*a*)) is also uniform, and the electrode potential was adjusted in order to reach a temperature of 70°C. The second prescribed topology (Fig. 5(*d*)) looks like a uniform topology with two symmetric holes, and n_m values lie between 0.43 and 1. The electrode potential was adjusted arbitrarily to achieve a temperature profile of the order of 70°C (Fig. 5(*c*)). Observe from this example that a temperature profile does not necessarily look like the thin-film topology. The third prescribed topology (Fig. 5(*f*)) is a diagonal pathway between the two electrodes, and n_m values lie between 0.01 and 1. The electrode potential was adjusted arbitrarily to achieve a

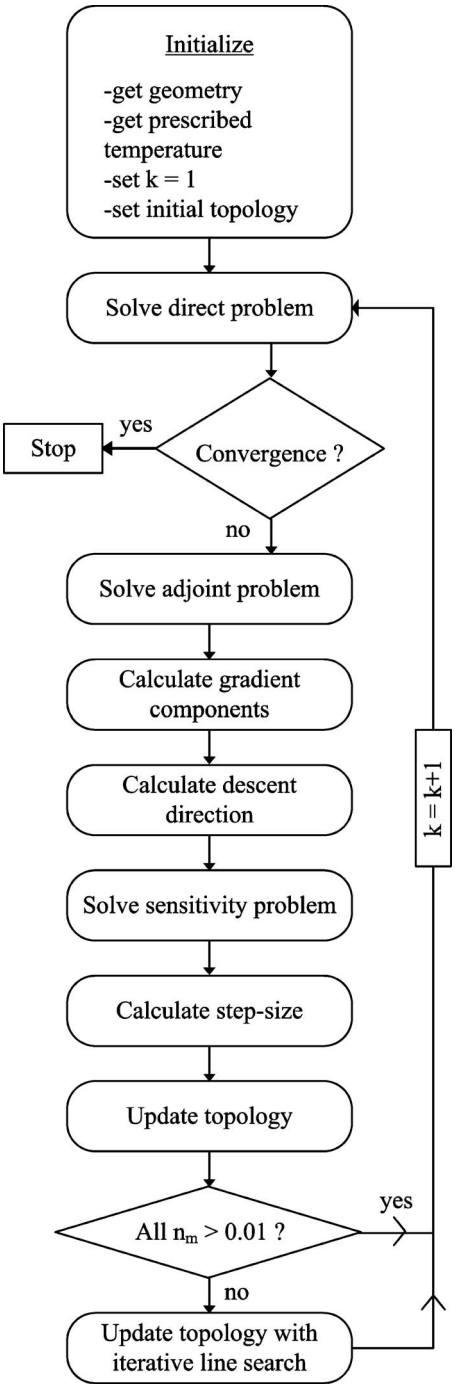

Fig. 4 The main steps of the conjugate gradient method with adjoint problem

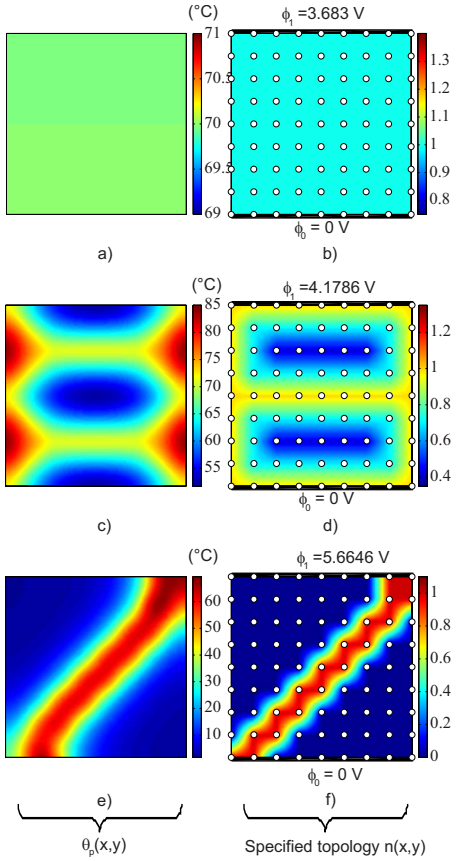

Fig. 5 Prescribed temperature profiles and their known topologies with one free electrode

temperature profile of the order of 70°C (Fig. 5(*e*)). The three prescribed profiles in Fig. 5 will be used as a benchmark for the CGA and GA.

In the right-hand side in Fig. 6, we present the optimized topology obtained with the CGA (as described in Sec. 6 and Appendix) using the prescribed temperature fields $\theta_p(x,y)$ previously shown in Fig. 5. These optimized topologies are scaled against the prescribed topologies to facilitate the comparison between them. Also, the temperature discrepancy between the optimized and prescribed temperature are shown in the left-hand side in Fig. 6. For the three problems, the initial guess was a random topology, i.e., the initial n_m values were chosen randomly, so that no bias is introduced in the optimization process. In Fig. 6(*b*), we see that the optimized topology related to the prescribed uniform temperature field (see (Fig. 5(*a*)) is relatively different from the known topology shown in Fig. 5(*b*). Nonetheless, the resulting temperature discrepancy in Fig. 6(*a*) are less than 0.5°C. In Fig. 6(*d*), we see that the CGA was successful in finding the overall topology (two holes) related to the prescribed temperature field in Fig. 5(*c*). Refining further the topology was not necessary to reach a maximum temperature discrepancy of 0.5°C (see Fig. 6(*c*)). In Fig. 6(*f*), we see that the CGA found a topology in good agreement with the specified topology (Fig. 5(*f*)). A maximum discrepancy of 1.22°C between the optimized and prescribed temperature is observed in Fig. 6(*e*). In fact, the CGA failed to reach a precision of 0.5°C because it fell in a local minimum during the optimization process. For the three cases mentioned above, the optimized potential values are in good agreement compared with the specified ones (less than 0.5% of discrepancy).

In Fig. 7, we present the optimized topology and the temperature discrepancy obtained with the GA (as described in Sec. 6), again using the prescribed temperature fields shown in Fig. 5. Recall that the initial populations were random so that no bias is introduced in the optimization process. In Fig. 7(*a*), we see that the GA was successful in achieving temperature discrepancy smaller than 0.5°C for the uniform temperature case. Nonetheless, the optimized topology (Fig. 7(*b*)) is relatively different from the known topology, as with the CGA. In Fig. 7(*d*), the GA found the correct overall pattern of topology (two holes) related to the prescribed temperature field of Fig. 5(*c*). Moreover, it resulted in a maximum temperature discrepancy of 0.5°C (Fig. 7(*c*)). In Fig. 7(*f*), we see that the GA found a topology in good agreement with the specified diagonal topology from Fig. 5(*f*). Also, contrary to the CGA, the GA was successful in finding a temperature discrepancy smaller than 0.5°C. In fact, GAs are not as likely to fall in

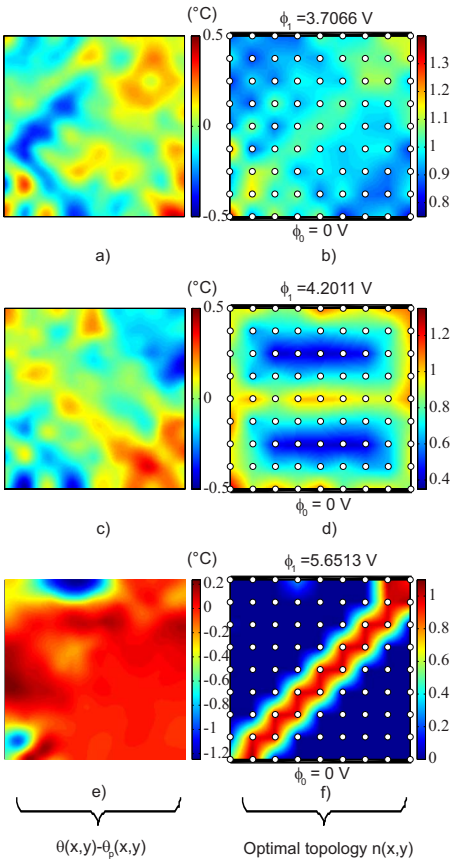

Fig. 6 Optimized topologies with the CGA method for one free electrode

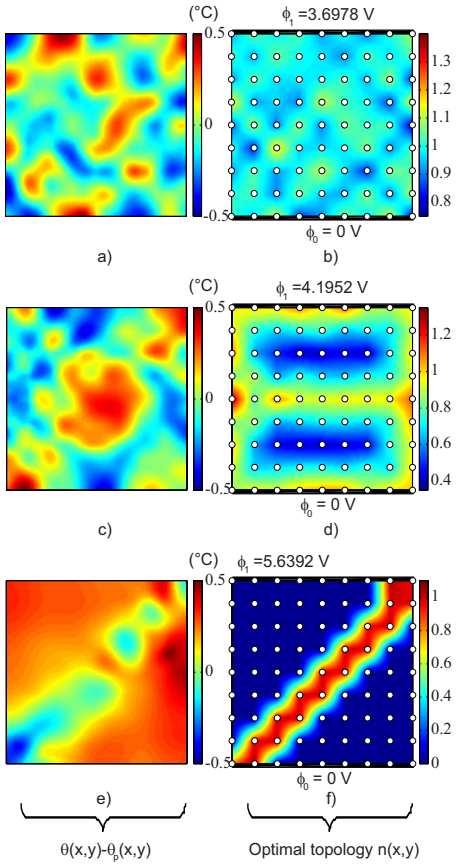

Fig. 7 Optimized topologies with the GA method for one free electrode

local minimum because of their probabilistic approach. For the three cases mentioned above, the optimized electrode potentials corresponded to the prescribed ones with high accuracy (discrepancy smaller than 1%).

In Table 2, we present the numerical cost of each problem for both the CGA and GA in terms of number of numerical simulations. For the GA, this is simply the number of topology tested during all the generations. For the CGA, the total numbers of numerical simulations is the sum of the direct problem simulations, adjoint problem simulations, sensitivity simulations, and iterative line search simulations during each iteration (see Fig. 4 and Appendix for details). We also present the number of iterations for the CGA (N_{it}) and the number of generations for the GA (N_{gen}). For the prescribed temperature of Figs. 5(*a*), 5(*c*), and 5(*e*), the CGA supplants the GA in terms of number of numerical simulations (the GA is 6.42 to 470.26 times slower than the CGA, depending on the problem). Note that for the prescribed temperature in Fig. 5(*e*), the CGA's number of iterations increases drastically (4213 simulations). This is because for this specific case, the CGA "hits" the topology constraint (i.e., $n_m > 0.01$) during the optimization process; hence, the step-size at each iteration is found iteratively instead of analytically (see Appendix), which requires many more numerical simulations. Nonetheless, for this prescribed temperature, the GA algorithm requires still more numerical simulations (4213 against 27054 simulations).

To summarize this section, we could conclude that gradient based algorithms (here represented by CGA) are well suited for topology multiphysics problem. It converged extremely fast to a minimum, despite the large number of design variables. However, we observed that it may fall in a local minima. On the other hand, the GA showed robustness in finding global minima. In Sec. 8, we verify how these algorithms behave when many electrodes potential are to be optimized on the boundary of the domain.

8 Optimal Topology With Many Electrodes

We present in Fig. 8(*a*) a prescribed temperature resulting from a known topology shown in Fig. 8(*b*). This topology is made of two distinct pathways, and the potentials at the electrodes were arbitrarily chosen so that the temperature profile be of the order of 30 °C. Here, the zone of interest Ω_p is different from the entire domain Ω, so that the complete mathematical development performed in the Appendix may be used. There are 100 topology points ($M=100$ design variables) to describe the topology. Their positions are illustrated by white circles in the figures.

The topology shown in Fig. 8(*b*) has a special feature. The fact that the two electrical pathways are distinct (disconnected) implies that the potential values of the electrodes in the upper side will not influence the electrical field in the lower side pathway, and vice-versa. Hence, the ground value of the potential for the electrode in the upper side could be arbitrarily different from the ground value of the potential for the electrodes in the lower side. In view of this fact, we chose not to set any electrode to a ground value, and the potentials at the four electrodes are considered as design variables.

Based on the result of Sec. 7 (the CGA algorithm is better than the GA in terms of optimization time), we used only the CGA in this section. We started the CGA with a random topology. The optimized topology is shown in Fig. 8(*d*). The CGA found an overall topology pattern very similar to the original one. Visible differences compared with the original topology are found on each side of the two film pathway (Fig. 8(*d*)). In fact, the CGA finished his optimization process in a local minimum. In Fig. 8(*c*), we see that the discrepancies between optimal and specified temperature are small in the center (minimum value of 0.11 °C) but increase

Table 2 Optimization data for each approach

	CGA			GA		
θ_p	θ_{opt}	N_{it}	N_{simul}	θ_{opt}	N_{gen}	N_{simul}
Fig. 5(*a*)	Fig. 6(*a*)	11	44	Fig. 7(*a*)	465	20045
Fig. 5(*c*)	Fig. 6(*c*)	19	76	Fig. 7(*c*)	830	35740
Fig. 5(*e*)	Fig. 6(*e*)	320	4213	Fig. 7(*e*)	628	27054
Fig. 8(*a*)	Fig. 8(*c*)	198	1627			

near the boundary of the zone of interest (up to 14.82°C). For the optimal electrodes potentials values, we must focus our attention on the difference of potential values for each pair of electrodes, because none of them was set to ground in this optimization. The discrepancies are of the order of 8% (5.36 V and 5.32 V compared with 4.95 V), and these are due to the error on the optimal topology. The total number of simulations is shown in Table 2, and the CGA stopped when the objective function did not diminished, i.e., after 198 iterations.

9 Conclusions

In this paper, we optimized the topology of a thin-film resistive heater and the electrical potential on the boundaries. The objective was to minimize the difference between the required and the actual temperature profiles. The topology optimization problem (inverse problem) has been solved with two methods, i.e., with a genetic algorithm and with a conjugate gradient method using adjoint and sensitivity problems. Overall, both methods led to excellent and similar results. The CGA method was faster to converge, but was more complex to implement and sometimes led to local minima. The GA was easier to implement and was more unlikely to lead to a local minima, but was much slower to converge.

Further work could combine the best features of the CGA and of the GA using a hybrid optimization algorithm or other optimization approaches. The model could also be refined by including 3D and transient effects. The effect of the heat loss coefficient may be investigated. Another optimization opportunity is the positions of the electrodes that could be varied to improve further the results. The electrical potential could also vary continuously along electrodes [27].

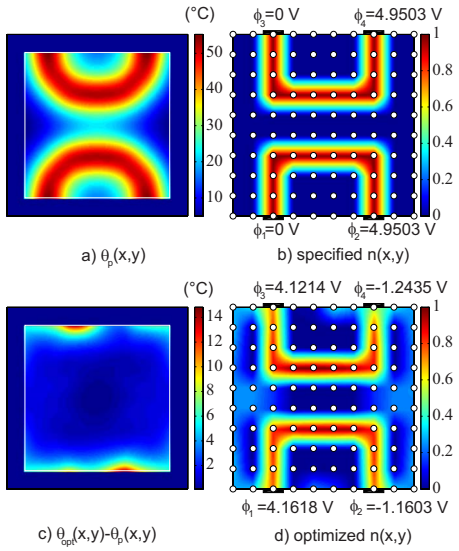

Fig. 8 Optimized topology and potentials with the CGA method for four electrodes

Finally, it is worth to note that the ideas developed in this paper could be extended to other topological problems governed by similar equations. For example, one could design the permeability distribution of a porous medium [28–30] and choose the pressure on the boundaries to achieve a certain distribution of local mass flow or cooling rate, which would be useful in design problems related to irrigation, cooling of electronic, etc.

Acknowledgment

The work L.G. was supported by the Fonds québécois de recherche sur la nature et les technologies (FQRNT) of the Province of Québec, via the New Researchers Start-Up Program. F. Mathieu-Potvin's work was supported by the FQRNT of the Province of Québec and the Natural Sciences and Engineering Research Council of Canada (NSERC).

Nomenclature

F_θ = objective function on specified temperature (K^2 m^2)
F_q = objective function on specified heat flux (W^2 m^{-4} m^2)
f = scaling topology factor
H = height (m)
h = heat transfer coefficient (W m^{-2} K^{-1})
j = current density (A m^{-2})
k = thermal conductivity (W m^{-1} K^{-1})
L = length (m)
M = number of topology nodes
m = topology node index
N_{gen} = number of generations in the genetic algorithm
N_{it} = number of iterations in the conjugate gradient algorithm
N_{simul} = number of simulations
N_x, N_y = number of topology sections
n = number of film depositions
q'' = heat flux (W m^{-2})
q''' = volumetric heat generation in thin film (W m^{-3})
s = normal coordinate at boundary (m)
T = temperature (K)
T_∞ = ambient temperature, (K)
t = thickness (m)
U = global heat transfer coefficient (W m^{-2} K^{-1})
x,y,z = Cartesian coordinates (m)

Greek Symbols

δ = delta Dirac function
θ = temperature difference (K)
σ = electrical conductivity (A m^{-1} V^{-1})
ϕ = electrical potential (V)
Ψ_m = *x-y* field associated with node *m*
Ω = entire domain
Ω_p = prescribed temperature domain

Subscripts

a,b = indices of scaled individuals before crossover

B = bottom boundary of the prescribed zone
T = top boundary of the prescribed zone
L = left boundary of the prescribed zone
m = node index
R = right boundary of the prescribed zone
c = chromium layer (film)
g = glass layer (substrate)
i = electrode index
p = prescribed

Superscripts

k = CGA iteration
it = numerical iteration

Appendix: Equations of the CGA Approach

The superscript k designates the iteration in the conjugate gradient method.

1. Prescribed heat flux from prescribed temperature

$$q_p'' = -t_g k_g\left(\frac{\partial^2\theta_p}{\partial x^2}+\frac{\partial^2\theta_p}{\partial y^2}\right)+U\theta_p \tag{A1}$$

2. Direct problem

$$\frac{\partial}{\partial x}\left(n^k t_c\sigma_c\frac{\partial\phi^k}{\partial x}\right)+\frac{\partial}{\partial y}\left(n^k t_c\sigma_c\frac{\partial\phi^k}{\partial y}\right)=0$$

$$n^k t_c\sigma_c\frac{\partial\phi^k}{\partial s}=0 \quad \text{at nonelectrode boundaries}$$

$$\phi_0=0 \quad \text{at ground-electrode boundaries}$$

$$\phi^k=\phi_i^k \quad \text{at free-electrode boundaries}$$

(Optimized for each topology, see Sec. 6.3) (A2)

3. Adjoint problem

$$\frac{\partial}{\partial x}\left(n^k\frac{\partial\lambda^k}{\partial x}\right)+\frac{\partial}{\partial y}\left(n^k\frac{\partial\lambda^k}{\partial x}\right)=0 \quad \text{in } \Omega\setminus\Omega_p \tag{A3}$$

and

$$\begin{aligned}\frac{\partial}{\partial x}\left(n^k\frac{\partial\lambda^k}{\partial x}\right)+\frac{\partial}{\partial y}\left(n^k\frac{\partial\lambda^k}{\partial x}\right)&=-\frac{\partial}{\partial x}\left(4(q_P''-q''^k)n^k\sigma_f t_f\frac{\partial\phi^k}{\partial x}\right)\\&-\frac{\partial}{\partial y}\left(4(q_P''-q''^k)n^k\sigma_f t_f\frac{\partial\phi^k}{\partial y}\right)\\&+4(q_P''-q''^k)n^k\sigma_f t_f\frac{\partial\phi^k}{\partial y}\delta(y-y_T)\\&-4(q_P''-q''^k)n^k\sigma_f t_f\frac{\partial\phi^k}{\partial y}\delta(y-y_B)\\&+4(q_P''-q''^k)n^k\sigma_f t_f\frac{\partial\phi^k}{\partial x}\delta(x-x_R)\\&-4(q_P''-q''^k)n^k\sigma_f t_f\frac{\partial\phi^k}{\partial x}\delta(x-x_L) \quad \text{in } \Omega_P\end{aligned} \tag{A4}$$

The boundary conditions are

$$\lambda^k=0 \quad \text{at electrode boundaries}$$

$$n^k\frac{\partial\lambda^k}{\partial s}=0 \quad \text{elsewhere}$$

4. Gradient components

$$\begin{aligned}\frac{\partial F_q^k}{\partial n_m}=&\int_{\Omega_p}\int\Psi_m\left(-2(q_p''^k-q''^k)\sigma_f t_f\left(\left(\frac{\partial\phi^k}{\partial x}\right)^2+\left(\frac{\partial\phi^k}{\partial y}\right)^2\right)\right)dxdy+\int_\Omega\int\Psi_m\left(\delta(y-L_y)\lambda^k\frac{\partial\phi^k}{\partial y}\right.\\&\left.-\delta(y)\lambda^k\frac{\partial\phi^k}{\partial y}\right)dxdy+\int_\Omega\int\Psi_m\left(-\frac{\partial\phi^k}{\partial x}\frac{\partial\lambda^k}{\partial x}\right.\\&\left.-\frac{\partial\phi^k}{\partial y}\frac{\partial\lambda^k}{\partial y}\right)dxdy\end{aligned} \tag{A5}$$

for $m=1,2,\ldots,M$

5. Descent direction

$$\mathbf{d}^k=\nabla F_q^k+\gamma^k\mathbf{d}^{k-1} \tag{A6}$$

$$\gamma^k=\frac{\int_\Omega\int\nabla F_q^k\cdot(\nabla F_q^k-\nabla F_q^{k-1})dxdy}{\int_\Omega\int\nabla F_q^{k-1}\cdot\nabla F_q^{k-1}dxdy} \quad \text{(Polak – Ribiere)} \tag{A7}$$

For the first iteration ($k=1$), the direction is set equal to the gradient ($\gamma^1=0$), which correspond to the steepest descent method.

6. Step-size

The optimal step-size β^k is found by minimizing F_q in the marching direction $\mathbf{d}^k$

$$\min F_q(\beta^k)=\min\int_\Omega\int(q_p''^k-(q''^k+\beta^k\Delta q''^k))^2dxdy \tag{A8}$$

where $\Delta q''^k$ is the directional derivative of the heat flux field q''^k resulting from a change in the M design variables. The minimization of Eq. (A8) is solved by equaling the derivative of $F_q(\beta^k)$ to zero, which leads to

$$\beta^k=\frac{\int_\Omega\int(q_p''^k-q)\Delta q^k dxdy}{\int_\Omega\int\Delta q''^k\Delta q''^k dxdy} \tag{A9}$$

7. Sensitivity problem

The directional derivative $\Delta q''^k$ in Eq. (A9) is obtained using the limiting process on Eq. (7):

$$\Delta q''^k=\sigma_c t_c\left\{2n^k\left(\frac{\partial\phi^k}{\partial x}\frac{\partial\Delta\phi^k}{\partial x}+\frac{\partial\phi^k}{\partial y}\frac{\partial\Delta\phi^k}{\partial y}\right)+\Delta n^k\left(\left(\frac{\partial\phi^k}{\partial x}\right)^2+\left(\frac{\partial\phi^k}{\partial y}\right)^2\right)\right\} \tag{A10}$$

The directional derivative $\Delta\phi^k$ of the potential fields that appears in Eq. (A10) is obtained using the limiting process on Eq. (4)

$$\begin{aligned}\frac{\partial}{\partial x}\left(n^k\frac{\partial\Delta\phi^k}{\partial x}\right)+\frac{\partial}{\partial y}\left(n^k\frac{\partial\Delta\phi^k}{\partial y}\right)=&-\frac{\partial}{\partial x}\left(\Delta n^k\frac{\partial\phi^k}{\partial x}\right)\\&-\frac{\partial}{\partial y}\left(\Delta n^k\frac{\partial\Delta\phi^k}{\partial y}\right)\end{aligned}$$

$$\Delta\phi^k=0 \quad \text{at electrode boundaries}$$

$$n\frac{\partial \Delta \phi^k}{\partial s} = 0 \quad \text{elsewhere on boundaries} \tag{A11}$$

The change in the topological field Δn^k results from a change Δn_m^k of the M design variables n_m^k. The change in the topological values is stated to be equal to the descent direction

$$\Delta n_m^k = d_m^k \quad \text{for } m = 1,2,\ldots,M \tag{A12}$$

and Δn^k in Eq. (A11) is defined as (from Eq. (10))

$$\Delta n^k(x,y) = \sum_{m=1}^{M} \Delta n_m^k \Psi_m(x,y) \tag{A13}$$

8. Topology update

   Once β^k and d_m^k are found, the topology is updated

$$n_m^{k+1} = n_m^k - \beta^k d_m^k \quad \text{for } m = 1,2,\ldots,M \tag{A14}$$

9. Constraint verification

   If at least one of the component n_m^{k+1} is lower than 0.01 (design constraint), the step-size β^k is considered inaccurate (to prevent negative thickness). A line-search along the direction $\boldsymbol{d}^k$ is then performed numerically (interior-reflective Newton algorithm in MATLAB) to find the optimal β^k (minimal $F_q(\beta^k)$). Each component n_m^{k+1} that would fall under 0.01 are kept at 0.01. Once the optimal β^k is found, Eq. (A14) is used again while respecting the constraint, i.e., keeping n_m^{k+1} values over 0.01. Finally, the iteration is updated, $k=k+1$.

10. Stoping criterion

    The algorithm continues until discrepancy between the actual and prescribed temperature fields is less than 0.5 °C, or when there is a stagnation of the objective function.

References

[1] Bejan, A., and Lorente, S., 2006, "Constructal Theory of Generation of Configuration in Nature and Engineering," J. Appl. Phys., **100**(4), p. 041301.

[2] Steinvurzel, P., MacHarrie, R. A., Baldwin, K. W., Van Hise, C. W., Eggleton, B. J., and Rogers, J. A., 2005, "Optimization of Distributed Resistive Metal Film Heaters in Thermally Tunable Dispersion Compensators for High-Bit-Rate Communication Systems," Appl. Opt., **44**(14), pp. 2782–2791.

[3] Kalli, K., Dobb, H. L., Webb, D. J., Carroll, K., Komodromos, M., Themistos, C., Peng, G. D., Fang, Q., and Boyd, I. W., 2007, "Electrically Tunable Bragg Gratings in Single-Mode Polymer Optical Fiber," Opt. Lett., **32**(3), pp. 214–216.

[4] Salamon, T. R., Rogers, J. A., and Eggleton, B. J., 2001, "Analysis of Heat Flow in Optical Fiber Devices That Use Microfabricated Thin Film Heaters," Sens. Actuators, A, **95**(1), pp. 8–16.

[5] Rogers, J. A., Eggleton, B. J., Pedrazzani, J. R., and Strasser, T. A., 1999, "Distributed On-Fiber Thin Film Heaters for Bragg Gratings With Adjustable Chirp," Appl. Phys. Lett., **74**(21), pp. 3131–3133.

[6] Baroncini, M., Placidi, P., Cardinali, G. C., and Scorzoni, A., 2004, "Thermal Characterization of a Microheater for Micromachined Gas Sensors," Sens. Actuators, A, **115**(1), pp. 8–14.

[7] Deng, P. G., Lee, Y. K., and Cheng, P., 2006, "An Experimental Study of Heater Size Effect on Micro Bubble Generation," Int. J. Heat Mass Transfer, **49**(15–16), pp. 2535–2544.

[8] Zhang, K. L., Chou, S. K., and Ang, S. S., 2007, "Fabrication, Modeling and Testing of a Thin Film Au/Ti Microheater," Int. J. Therm. Sci., **46**(6), pp. 580–588.

[9] Kozlov, A. G., 2006, "Analytical Modelling of Temperature Distribution in Resistive Thin-Film Thermal Sensors," Int. J. Therm. Sci., **45**(1), pp. 41–50.

[10] Cheng, C.-H., Lin, H.-H., and Aung, W., 2003, "Optimal Shape Design for Packaging Containing Heating Elements by Inverse Heat Transfer Method," Heat Mass Transfer, **39**(8–9), pp. 687–692.

[11] Park, C. W., and Yoo, Y. M., 1988, "Shape Design Sensitivity Analysis of a Two-Dimensional Heat Transfer System Using the Boundary Element Method," Comput. Struct., **28**(4), pp. 543–550.

[12] Mathieu-Potvin, F., and Gosselin, L., 2006, "Optimal Conduction Pathways for Cooling a Heat Generating Body: A Comparison Exercise," Int. J. Heat Mass Transfer, **50**(15–16), pp. 2996–3006.

[13] Li, Q., Steven, G. P., Querin, O. M., and Xie, Y. M., 1999, "Shape and Topology Design for Heat Conduction by Evolutionary Structural Optimization," Int. J. Heat Mass Transfer, **42**(17), pp. 3361–3371.

[14] Steven, G. P., Li, Q., and Xie, Y. M., 2000, "Evolutionary Topology and Shape Design for General Physical Field Problem," Comput. Mech., **26**(2), pp. 129–139.

[15] Li, Q., Steven, G. P., Xie, Y. M., and Querin, O. M., 2004, "Evolutionary Topology Optimization for Temperature Reduction of Heat Conducting Fields," Int. J. Heat Mass Transfer, **47**(23), pp. 5071–5083.

[16] Novotny, A. A., Feijóo, R. A., Taroco, E., and Padra, C., 2003, "Topological Sensitivity Analysis," Comput. Methods Appl. Mech. Eng., **192**(7–8), pp. 803–829.

[17] Gersborg-Hansen, A., Bendsøe, M. P., and Sigmund, O., 2006, "Topology Optimization of Heat Conduction Problems Using the Finite Volume Method," Struct. Multidiscip. Optim., **31**(4), pp. 251–259.

[18] Wang, A.-H., Liang, X.-G., and Ren, J.-X., 2006, "Constructal Enhancement of Heat Conduction With Phase Change," Int. J. Thermophys., **27**(1), pp. 126–138.

[19] Yin, L., and Ananthasuresh, G. K., 2002, "A Novel Topology Design Scheme for the Multi-Physics Problems of Electro-Thermally Actuated Compliant Micromechanisms," Sens. Actuators, A, **97–98**(1), pp. 599–609.

[20] Nelli Silva, E. C., Nishiwaki, S., Ono Fonseca, J. S., and Kikuchi, N., 1999, "Optimization Methods Applied to Material and Flextensional Actuator Design Using the Homogenization Method," Comput. Methods Appl. Mech. Eng., **172**(1–4), pp. 241–271.

[21] Li, Y., Saitou, K., and Kikuchi, N., 2004, "Topology Optimization of Thermally Actuated Compliant Mechanisms Considering Time-Transient Effect," Finite Elem. Anal. Design, **40**(11), pp. 1317–1331.

[22] Ozisik, M. N., and Orlande, H. R. B., 2000, *Inverse Heat Transfer*, Taylor & Francis, New York.

[23] Gosselin, L., Tye-Gingras, M., and Mathieu-Potvin, F., 2009, "Review of Genetic Algorithms Utilization in Heat Transfer Problems," Int. J. Heat Mass Transfer, **52**(9–10), pp. 2169–2188.

[24] 1998, FLUENT User's Guide, www.fluent.com

[25] Mathieu-Potvin, F., and Gosselin, L., 2009, "Bilinearization Approach for Diffusion Problems Involving the Calculation of Second-Law Fields," Numer. Heat Transfer, Part B, **55**(6), pp. 457–479.

[26] Reddy, J. N., 2006, *An Introduction to the Finite Element Method*, 3rd ed., McGraw-Hill, New York, Chap. 8.

[27] Colaço, M. J., Dulikravich, G. S., and Martin, T. J., 2004, "Optimization of Wall Electrodes for Electro-Hydrodynamic Control of Natural Convection During Solidification," Mater. Manuf. Processes, **19**(4), pp. 719–736.

[28] Tye-Gingras, M., and Gosselin, L., 2008, "Thermal Resistance Minimization of a Fin-and-Porous Medium Heat Sink With Evolutionary Algorithms," Numer. Heat Transfer, **54**(4), pp. 349–366.

[29] Leblond, G., and Gosselin, L., 2008, "Effect of Non-Local Equilibrium on Minimal Thermal Resistance Porous Layered Systems," Int. J. Heat Fluid Flow, **29**(1), pp. 281–291.

[30] Wildi-Tremblay, P., and Gosselin, L., 2007, "Layered Porous Media Architecture for Maximal Cooling," Int. J. Heat Mass Transfer, **50**(3–4), pp. 464–478.

Revisit of Laminar Film Condensation Boundary Layer Theory for Solution of Mixed Convection Condensation With or Without Noncondensables

Y. Liao
Laboratory for Thermal-Hydraulics,
Paul Scherrer Institute,
5232 Villigen PSI, Switzerland
e-mail: yehong.liao@psi.ch

This work presents a unique and unified formulation to solve the laminar film condensation two-phase boundary layer equations for the free, mixed, and forced convection regimes in the absence or presence of noncondensables. This solution explores the vast space of mixed convection across the four cornerstones of laminar film condensation boundary layer theory, two established by Koh for pure vapor condensation in the free or forced convection regimes and the other two established by Sparrow corresponding to condensation with noncondensables. This formulation solves the space of mixed convection completely with Koh and Sparrow's solutions shown to be merely four specific cases of the current solution. [DOI: 10.1115/1.4001929]

Keywords: mixed convection, film condensation, noncondensables

1 A Revisit of Laminar Film Condensation Boundary Layer Theory

The laminar film condensation boundary layer theory was established to study pure vapor condensation in the free convection regime by Sparrow and Gregg [1] and Koh et al. [2] and in the forced convection regime by Koh [3]. The theory was further extended to analyze condensation in the presence of noncondensable gases by Sparrow in the free convection regime [4] and the forced convection regime [5]. These pioneering studies set up the four cornerstones supporting the mixed convection space for laminar film condensation in the absence or presence of noncondensables. A recent review by Tamm et al. [6] describes in detail the assumptions used in the similarity solution of the laminar film condensation boundary layer equations. Though major advancement has been made in the past to partially fill the vacancy in this mixed convection space, there is no piece of work that fill this gap completely in the sense that the solution space for mixed convection is enveloped by the four well-established cornerstones. This work tries to fill this gap completely by introducing a unified formulation of the two-phase boundary layer to study condensation in the free, mixed, or forced regimes in the absence or presence of noncondensables and to obtain the solution space enveloped by the known results of Koh et al. [2], Koh [3], Sparrow and Lin [4], and Sparrow et al. [5].

When vapor, which may contain a noncondensable gas and whose bulk velocity is not necessarily restricted to zero, is condensed along a cooled vertical plate (Fig. 1), a two-phase laminar boundary layer may exist with the inner boundary consisting of the liquid phase and the outer boundary consisting of the gas phase. In the liquid phase, the condensate film is driven by the gravity force and the interfacial shear force. The interfacial shear force is due to the relative motion of vapor with regard to liquid. If the vapor bulk velocity is zero, the motion of vapor is induced by the motion of liquid for pure vapor condensation in the free convection regime [2] or by natural convection caused by temperature and concentration differences in the gas boundary layer for condensation with noncondensables in the free convection regime [4]. On the other hand, if the vapor bulk velocity is not restricted to zero, the interfacial shear force is also due to the forced convection bulk flow [3,5].

The mass, momentum, energy, and species conservation principles for steady laminar flow of the liquid and gas phases can be written in the Fig. 1 coordinate system as follows, respectively [2,4]:

$$\frac{\partial u_L}{\partial x} + \frac{\partial v_L}{\partial y} = 0$$

$$u_L \frac{\partial u_L}{\partial x} + v_L \frac{\partial u_L}{\partial y} = g + \nu_L \frac{\partial^2 u_L}{\partial y^2}$$

$$u_L \frac{\partial T_L}{\partial x} + v_L \frac{\partial T_L}{\partial y} = \alpha_L \frac{\partial^2 T_L}{\partial y^2} \tag{1}$$

$$\frac{\partial u_G}{\partial x} + \frac{\partial v_G}{\partial y} = 0$$

$$u_G \frac{\partial u_G}{\partial x} + v_G \frac{\partial u_G}{\partial y} = \beta(W - W_\infty)g + \nu_G \frac{\partial^2 u_G}{\partial y^2}$$

$$u_G \frac{\partial W}{\partial x} + v_G \frac{\partial W}{\partial y} = D \frac{\partial^2 W}{\partial y^2} \tag{2}$$

It is assumed that the liquid phase density is much larger than the gas phase density. For the gas phase, the energy equation is neglected because sensible heat transfer is considered to be relatively small compared to condensation heat transfer; the first term on the right hand side of the momentum equation is due to buoyancy force resulting from concentration difference [4].

Contributed by the Heat Transfer Division of ASME for publication in the JOURNAL OF HEAT TRANSFER. Manuscript received December 8, 2009; final manuscript received May 5, 2010; published online July 27, 2010. Assoc. Editor: Patrick H. Oosthuizen.

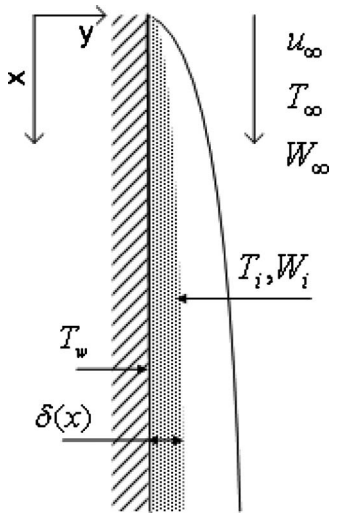

Fig. 1 Schematic of the physical and coordinate system

2 Mathematical Formulation for Mixed Convection Condensation

A mixed convection number is introduced herein to indicate the relative importance of forced convection (u_∞^2) over free convection (gx):

$$\xi = \frac{1}{1+[u_\infty^2/(gx)]^{1/4}} \tag{3}$$

When the vapor-gas flow with a finite bulk velocity is condensed along a vertical flat plate, its motion can be characterized by the relative importance of forced convection (u_∞^2) over free convection (gx). At the leading edge of the plate, forced convection dominates over free convection $u_\infty^2 \gg gx$; therefore, $\xi \to 0$. At the far field of the plate, free convection dominates over forced convection $gx \gg u_\infty^2$; therefore, $\xi \to 1$. In between is the mixed convection regime: $0 < \xi < 1$.

2.1 Transformation of Conservation Equations. Upon introducing the pseudosimilarity variables, $\eta_L = c_L y/(x^{1/4}\xi)$ and $\eta_G = c_G[y-\delta(x)]/(x^{1/4}\xi)$, for the liquid and gas phases, respectively, and the stream functions, $\psi_L = 4\nu_L c_L x^{3/4} F(\eta_L, \xi)/\xi$ and $\psi_G = 4\nu_G c_G x^{3/4} f(\eta_G, \xi)/\xi$, for the liquid and gas phases, respectively, the velocity components in the (x,y) coordinate system are transformed herein into the (ξ, η) coordinate system using the chain rule for derivatives for the liquid and gas phases, respectively as

$$u_L = \frac{\partial \psi_L}{\partial y} = 4\nu_L c_L^2 x^{1/2} F'/\xi^2$$

$$v_L = -\frac{\partial \psi_L}{\partial x} = -\frac{4\nu_L c_L}{x^{1/4}\xi}\left[\frac{2+\xi}{4}F + xF'\frac{\partial \eta_L}{\partial x} + x\frac{d\xi}{dx}\frac{\partial F}{\partial \xi}\right]$$

$$\frac{\partial u_L}{\partial y} = 4\nu_L c_L^3 x^{1/4} F''/\xi^3 \tag{4}$$

$$u_G = \frac{\partial \psi_G}{\partial y} = 4\nu_G c_G^2 x^{1/2} f'/\xi^2$$

$$v_G = -\frac{\partial \psi_G}{\partial x} = -\frac{4\nu_G c_G}{x^{1/4}\xi}\left[\frac{2+\xi}{4}f + xf'\frac{\partial \eta_G}{\partial x} + x\frac{d\xi}{dx}\frac{\partial f}{\partial \xi}\right]$$

$$\frac{\partial u_G}{\partial y} = 4\nu_G c_G^3 x^{1/4} f''/\xi^3 \tag{5}$$

where the primes denote differentiation with respect to the pseudosimilarity variables, η_L and η_G.

Upon introducing a dimensionless temperature, $\theta = (T_L - T_i)/(T_w - T_i)$, the liquid phase momentum and energy conservation equations are derived herein in the (ξ, η_L) coordinate system using the transformed velocity components as

$$F''' + (2+\xi)FF'' - 2\xi(F')^2 + \xi^4 = \xi(1-\xi)\left(F'\frac{\partial F'}{\partial \xi} - F''\frac{\partial F}{\partial \xi}\right) \tag{6}$$

$$\theta'' + (2+\xi)\mathrm{Pr}_L F\theta' = \mathrm{Pr}_L \xi(1-\xi)\left(F'\frac{\partial \theta}{\partial \xi} - \theta'\frac{\partial F}{\partial \xi}\right) \tag{7}$$

Upon introducing a transformed variable for the gas mass fraction, $\varphi = W - W_\infty$, the gas phase momentum and species conservation equations are derived herein in the (ξ, η_G) coordinate system using the transformed velocity components as

$$f''' + (2+\xi)ff'' - 2\xi(f')^2 + \xi^4\varphi = \xi(1-\xi)\left(f'\frac{\partial f'}{\partial \xi} - f''\frac{\partial f}{\partial \xi}\right) \tag{8}$$

$$\varphi'' + (2+\xi)\mathrm{Sc} f\varphi' = \mathrm{Sc}\xi(1-\xi)\left(f'\frac{\partial \varphi}{\partial \xi} - \varphi'\frac{\partial f}{\partial \xi}\right) \tag{9}$$

2.2 Transformation of Interfacial Closure Equations. The transformed velocity components in Eq. (4) for the liquid phase and in Eq. (5) for the gas phase are evaluated at the interface $y = \delta(x)$ to derive herein the closure equations for balance of mass, continuity of velocity, balance of tangential shear, balance of energy, and interface impermeable to noncondensables.

Continuity of velocity. The longitudinal gas and liquid velocities at the interface must equal for the nonslip condition: $(u)_{G,i} = (u)_{L,i}$. Using the transformed velocity components, it is immediately recognized that

$$f_i' = (\beta)^{-1/2} F_i' \tag{10}$$

Balance of mass. The vapor transferred to the interface must be equal to the liquid transferred from the interface to the condensate film: $[\rho(v - ud\delta/dx)]_{G,i} = [\rho(v - ud\delta/dx)]_{L,i}$. Using $\delta = \eta_{L,i} x^{1/4}\xi/c_L$ and the transformed velocity components, mass balance written in the new coordinate system is derived herein as

$$(2+\xi)f_i + \xi(1-\xi)\left(\frac{\partial f}{\partial \xi}\right)_i = \left(\frac{\rho_L \mu_L}{\rho_G \mu_G}\right)^{1/2}(\beta)^{-1/4}\left[(2+\xi)F_i + \xi(1-\xi) \times \left(\frac{\partial F}{\partial \xi}\right)_i\right] \tag{11}$$

Balance of tangential shear. The balance of tangential shear can be written as $(\mu \partial u/\partial y)_{G,i} = (\mu \partial u/\partial y)_{L,i}$. Upon substituting the transformed velocity components, it is obtained herein that

$$f_i'' = \left(\frac{\rho_L \mu_L}{\rho_G \mu_G}\right)^{1/2}(\beta)^{-3/4} F_i'' \tag{12}$$

Balance of energy. When the gas sensible heat transfer can be neglected, the latent heat of condensation is balanced by the overall heat transfer from the interface to the condensate film: $[\rho(v - ud\delta/dx)]_{L,i} h_{fg} = k_L(\partial T/\partial y)_{L,i}$, which in the new coordinate system is derived herein as

$$\frac{c_{pL}(T_i - T_w)}{\mathrm{Pr}_L h_{fg}} = -\frac{(2+\xi)F_i + \xi(1-\xi)\left(\frac{\partial F}{\partial \xi}\right)_i}{\theta_i'} \tag{13}$$

Interface impermeable to noncondensables. At the interface, the

convective mass flow must be balanced by the diffusive mass flow for the noncondensable gas: $[\rho_g(v_G - u_G d\delta/dx)]_i = (\rho_G D \partial W/\partial y)_i$, or in terms of the transformed variables it is derived herein that

$$\varphi_i' = -(\varphi_i + W_\infty)\mathrm{Sc}\left[(2+\xi)f_i + \xi(1-\xi)\left(\frac{\partial f}{\partial \xi}\right)_i\right] \tag{14}$$

2.3 Transformation of Boundary Closure Equations. The liquid longitudinal and transverse velocities are zero at the wall: $u_{L,w} = v_{L,w} = 0$, and the liquid temperature is the given wall temperature: $T_{L,w} = T_w$. In terms of the transformed variables, the boundary conditions at the wall ($\eta_L = 0$) are expressed herein by

$$F'_{\eta_L=0} = 0 \tag{15}$$

$$F_{\eta_L=0} = -\xi(1-\xi)\left(\frac{\partial F}{\partial \xi}\right)_{\eta_L=0}/(2+\xi) \tag{16}$$

$$\theta_{\eta_L=0} = 1 \tag{17}$$

By the definition of the transformed variable, $\theta = (T_L - T_i)/(T_w - T_i)$, the liquid temperature at the two-phase interface ($\eta_L = \eta_{L,i}$) in terms of the transformed variable is simply

$$\theta_{\eta_L=\eta_{L,i}} = 0 \tag{18}$$

Upon substituting the given gas bulk velocity $u_G = u_\infty$ into the transformed velocity and the given noncondensable gas mass fraction $W = W_\infty$ into the definition of the transformed mass fraction $\varphi = W - W_\infty$, it is obtained herein that

$$f'_{\eta_G=\infty} = (\beta)^{-1/2}(1-\xi)^2/2 \tag{19}$$

$$\varphi_{\eta_G=\infty} = 0 \tag{20}$$

3 Solution for Condensation in the Free, Forced, Mixed Convection Regimes With or Without Noncondensables

Condensation with or without noncondensables can be studied by varying the mixed convection number ξ continuously from 0 to 1 and by varying the condensable gas mass fraction W_∞ continuously from 0 to 1 to completely explore the space of mixed convection. The two limiting cases for condensation without noncondensables ($W_\infty = 0$) in the free convection regime ($\xi = 1$) and the forced convection regime ($\xi = 0$) were solved by Koh et al. [2] and Koh [3]. The other two limiting cases for condensation with noncondensables ($W_\infty \neq 0$) in the free convection regime ($\xi = 1$) and the forced convection regime ($\xi = 0$) were solved by Sparrow and Lin [4] and Sparrow et al. [5]. This section first discusses the solutions for these four limiting cases using the current formulation in light of the known solutions in the pioneering work and then presents the solution for the gap in between.

3.1 Limiting Case for Condensation Without Noncondensables in Free Convection Regime. This limiting case corresponds to $W_\infty = 0$ and $\xi = 1$ solved by Koh et al. [2]. As $W_\infty = 0$, the gas phase species conservation equation (Eq. (9)) need not be considered. As $\xi = 1$, the right hand sides of the transformed equations (Eqs. (6)–(8)) reduce to zero, and it is immediately recognized that the current reduced transformed equations are identical to their counterparts in the work of Koh et al. (Eqs. 14, 15, and 19 in Ref. [2]). Keeping in mind that this is a factor of $\beta^{1/4}$ difference in the definition of c_G between the present work and that of Koh et al. [2], it is not difficult to confirm that the nine closure equations (Eqs. (10)–(13) and Eqs. (15)–(19)) are also identical to their counterparts in the work of Koh et al.: Eqs. (21), (23), (25), and (26), 29, 30, 28, and 32 in Ref. [2], respectively, when $\xi \to 1$ and $\rho_v \ll \rho_L$. Therefore, the current boundary layer formulation is demonstrated to have the limit solution for free convection without noncondensables identical to that in the work of Koh et al. [2].

3.2 Limiting Case for Condensation Without Noncondensables in Forced Convection Regime. This limiting case corresponds to $W_\infty = 0$ and $\xi = 0$ solved by Koh [3]. As $\xi = 0$, the liquid momentum equation (Eq. (6)) reduces to

$$F''' + 2FF'' = 0 \tag{21}$$

At first glance, Eq. (21) looks different from its counterpart in Koh's work (Eq. 1 of Ref. [3]). Actually, they are equivalent if the difference in the respective scaling factors for the similarity variable (η_L) and the dimensionless stream function (F) used in carrying out the transformation of the conservation equation is carefully taken into account. The assumption $\rho_v \ll \rho_L$ is used in the following proof.

From the definition of ξ, it follows that $\xi = (gx/u_\infty^2)^{1/4}(1-\xi)$, which is substituted into the definition of η_L to obtain $\eta_L = c_L y/[x^{1/4}(gx/u_\infty^2)^{1/4}(1-\xi)]$, or $\eta_L = (y/x)\sqrt{u_\infty x/\nu_L}/[\sqrt{2}(1-\xi)]$. From the definition of the similarity variable used by Koh, when $\xi \to 0$ it is obtained that

$$\eta_L = \eta_{L,\mathrm{Koh}}/\sqrt{2} \tag{22}$$

where $\eta_{L,\mathrm{Koh}}$ denotes the similarity variable used by Koh [3].

Upon substituting $\xi = (gx/u_\infty^2)^{1/4}(1-\xi)$ into the definition of ψ_L, the liquid phase stream function is expressed as $\psi_L = 2\sqrt{2}\sqrt{\nu_L u_\infty x}F/(1-\xi)$. From the definition of the stream function used by Koh and equating the stream functions $\psi_L = \psi_{L,\mathrm{Koh}}$, it follows that when $\xi \to 0$,

$$F = F_{\mathrm{Koh}}/(2\sqrt{2}) \tag{23}$$

where $\psi_{L,\mathrm{Koh}}$ and F_{Koh} denote, respectively, the stream function and the dimensionless stream function used by Koh [3].

Substituting η_L in Eq. (22) and F in Eq. (23) into $F' = dF/d\eta_L$, it leads to $F' = (dF_{\mathrm{Koh}}/d\eta_{L,\mathrm{Koh}})/2 = F'_{\mathrm{Koh}}/2$. Similarly, it can be shown that $F'' = F''_{\mathrm{Koh}}/\sqrt{2}$ and $F''' = F'''_{\mathrm{Koh}}$. Upon substituting F, F'', F''' into the transformed liquid momentum equation (Eq. (21)), it follows that $F'''_{\mathrm{Koh}} + F_{\mathrm{Koh}}F''_{\mathrm{Koh}}/2 = 0$, which is exactly the formulation used in Koh's work for forced convection (Eq. 1 of Ref. [3]). In a similar way, it can also be shown that the other transformed conservation equations are equivalent to their counterparts in Koh's work [3]. Therefore, the current boundary layer formulation is shown to have the limit solution for forced convection identical to that in Koh's work [3].

3.3 Limiting Case for Condensation With Noncondensables in Free Convection Regime. This limiting case corresponds to $W_\infty \neq 0$ and $\xi = 1$ solved by Sparrow and Lin [4]. Herein, it is proved that as $\xi \to 1$, if the current formulation neglects inertia force and energy convection in the liquid conservation equations, the current formulation coincides with the work of Sparrow and Lin [4] on condensation with noncondensables in the free convection regime. It is worth pointing out that although Sparrow and Lin [4] did not consider these terms, the present work will take them into account in the numerical solution presented later.

First, regarding the transformed gas phase equations (Eqs. (8) and (9)), it is immediately recognized that when $\xi \to 1$, they are identical to their counterparts in the work of Sparrow and Lin (Eqs. 13 and 14 of Ref. [4]). Next, the transformed liquid phase equations (Eqs. (6) and (7)) can reduce to $F''' + 1 = 0$, $\theta' = 0$ if $\xi \to 1$, and the inertia force term $(2+\xi)FF'' - 2\xi(F')^2$ is omitted for the momentum equation and the energy convection term $(2+\xi)\mathrm{Pr}_L F\theta'$ is omitted for the energy equation. The reduced liquid conservation equations are equivalent to those treated by Nusselt, whose solutions were used in the work of Sparrow and Lin (Eqs. 2–5 of Ref. [4]). It is rather lengthy but not difficult to show that when $\xi \to 1$ the closure equations for solving the transformed equations in the current work are also identical to their counter-

parts in the work of Sparrow and Lin [4]. Therefore, it has been proved that the current boundary layer formulation has the limit solution for free convection identical to the work of Sparrow and Lin [4], which will also be confirmed later by presenting the comparison of numerical results.

3.4 Limiting Case for Condensation With Noncondensables in Forced Convection Regime. This limiting case corresponds to $W_\infty \neq 0$ and $\xi = 0$ solved by Sparrow et al. [5]. Herein, it is proved that as $\xi \to 0$, if the current formulation neglects inertia force and energy convection in the liquid conservation equations, the current formulation coincides with the work of Sparrow et al. [5] on condensation with noncondensables in the forced convection regime. It is worth pointing out that although Sparrow et al. [5] did not consider these terms, the current work will take them into account in the numerical solution presented later.

As $\xi \to 0$, the transformed gas phase momentum equation (Eq. (8)) is simplified to

$$f''' + 2ff'' = 0 \tag{24}$$

At first glance, the current transformed equations look different from their counterparts in the work of Sparrow et al. (Eq. 14 of Ref. [5]). Actually, they are equivalent if the difference in the respective scaling factors for the similarity variable (η_G) and the dimensionless stream function (f) used in carrying out the respective transformation of the conservation equations is carefully taken into account.

From the definition of ξ, it follows that $\xi = (gx/u_\infty^2)^{1/4}(1-\xi)$, which is substituted into the definition of η_G to get $\eta_G = c_G[y - \delta(x)]/[x^{1/4}(gx/u_\infty^2)^{1/4}(1-\xi)]$ or $\eta_G = \beta^{1/4}[y-\delta(x)]\sqrt{u_\infty/(\nu_G x)}/[\sqrt{2}(1-\xi)]$. From the definition of the similarity variable used by Sparrow et al. [5], it follows that when $\xi \to 0$, $\eta_G = [\beta^{1/4}/\sqrt{2}]\eta_{G,\mathrm{Sp}}$, where $\eta_{G,\mathrm{Sp}}$ denotes the similarity variable used by Sparrow. Upon substituting $\xi = (gx/u_\infty^2)^{1/4}(1-\xi)$ into the definition of ψ_G, it follows that $\psi_G = 2\sqrt{2}\beta^{1/4}\sqrt{u_\infty \nu_G x} f/(1-\xi)$. From the definition of the stream function used by Sparrow, it follows that when $\xi \to 0$, $\psi_G = \psi_{G,\mathrm{Sp}} \to f = f_{\mathrm{Sp}}/(2\sqrt{2}\beta^{1/4})$, where $\psi_{G,\mathrm{Sp}}$ and f_{Sp} denote, respectively, the stream function and the dimensionless stream function used by Sparrow et al. [5]. Since $f' = df/d\eta_G$, it leads to $f' = (df_{\mathrm{Sp}}/d\eta_{G,\mathrm{Sp}})/(2\beta^{1/2}) = f'_{\mathrm{Sp}}/(2\beta^{1/2})$. Similarly, it can be shown that $f'' = f''_{\mathrm{Sp}}/(\sqrt{2}\beta^{3/4})$ and $f''' = f'''_{\mathrm{Sp}}/\beta$. Upon substituting f, f'', f''' into the transformed momentum equation (Eq. (24)), it follows that $(f'''_{\mathrm{Sp}} + f_{\mathrm{Sp}} f''_{\mathrm{Sp}}/2)/\beta = 0$ or $f'''_{\mathrm{Sp}} + f_{\mathrm{Sp}} f''_{\mathrm{Sp}}/2 = 0$, which is exactly the one used in Sparrow's work for forced convection (Eq. 14 of Ref. [5]). In a similar way, it can also be shown that the transformed species conservation equation (Eq. (9)) is equivalent to its counterpart in the work of Sparrow et al. (Eq. 29 of Ref. [5]).

Next, regarding the transformed liquid conservation equations, it should be recalled that in the work of Sparrow et al. [5] the inertia force term $(2+\xi)FF'' - 2\xi(F')^2$ was omitted for the momentum equation and the energy convection term $(2+\xi)\mathrm{Pr}_L F\theta'$ was omitted for the energy equation. When these terms are neglected and keeping in mind that $\xi \to 0$, the current transformed liquid conservation equations (Eqs. (6) and (7)) reduce to $F''' = 0$, $\theta'' = 0$, which are equivalent to those used in the work of Sparrow et al. (Eq. 2 of Ref. [5]). It can be shown without difficulty that the current closure equations for $\xi \to 0$ are equivalent to their counterparts in the work of Sparrow et al. [5], but the lengthy demonstration is omitted herein for brevity. Therefore, it has been proved that the current boundary layer formulation also has the limit solution for forced convection identical to that in the work of Sparrow et al. [5], which will also be confirmed later by presenting the comparison of numerical results.

3.5 Solution for the Entire Mixed Convection Regime. When $\xi \to 0$ or $\xi \to 1$, the right hand sides of the current transformed equations (Eqs. (6)–(9)) reduce to 0, which are equivalent to a system of ten first order ordinary differential equations (ODE) involving ten unknown variables (which include three for the third order ODE about F, two for the second order ODE about θ, three for the third order ODE about f, and two for the second order ODE about φ). In addition to these ten unknown variables, there is one unknown variable, $\eta_{L,i}$, in the closure equations. On the other hand, there are altogether 11 closure equations: Eqs. (10)–(20). Therefore, the system prescribed by Eqs. (6)–(9) is definite.

When $0 < \xi < 1$, the solution of the current transformed equations becomes more complicated due to additional unknown variables emerging from the right hand sides of Eqs. (6)–(9) about the first order differentiation with respect to ξ: $\partial F/\partial\xi, \partial\theta/\partial\xi, \partial f/\partial\xi, \partial\varphi/\partial\xi$. But they can be solved using the local nonsimilarity method [7]. The main idea of the local nonsimilarity method is to reduce a set of partial differential equations to a set of ODEs that is easier to solve. When introducing new variables ($R = \partial F/\partial\xi$, $S = \partial\theta/\partial\xi$, $r = \partial f/\partial\xi$, and $s = \partial\varphi/\partial\xi$) and differentiating both sides of Eqs. (6)–(9) with respect to the mixed convection number ξ, the resulting equations become ordinary differential equations if the truncation errors due to the terms involving differentiation with respect to ξ with orders equal and greater than 2 are neglected (the second level approximation). Higher level of accuracy can be achieved by continuing this process to retain the terms involving the second order differentiation with respect to ξ while truncating the terms with differentiation orders equal and greater than 3 (the third level approximation).

When carrying out the local nonsimilarity method in this way for the second level approximation, the ordinary differential equations about R, S are derived herein from differentiating both sides of Eqs. (6) and (7) with respect to ξ and truncated the terms involving differentiation with respect to ξ with orders equal and greater than 2 to obtain

$$R''' + (2+\xi)FR'' + \xi(1-\xi)RR'' - (1+2\xi)F'R' - \xi(1-\xi)(R')^2 + (3-\xi)F''R + FF'' - 2(F')^2 + 4\xi^3 = 0$$

$$S''/\mathrm{Pr}_L + (2+\xi)FS' + \xi(1-\xi)RS' - (1-2\xi)F'S - \xi(1-\xi)R'S + (3-\xi)\theta'R + F\theta' = 0 \tag{25}$$

The ordinary differential equations about r, s are derived herein from Eqs. (8) and (9) in a similar way as

$$r''' + (2+\xi)fr'' + \xi(1-\xi)rr'' - (1+2\xi)f'r' - \xi(1-\xi)(r')^2 + (3-\xi)f''r + ff'' - 2(f')^2 + 4\xi^3\varphi + \xi^4 s = 0$$

$$s''/\mathrm{Sc} + (2+\xi)fs' + \xi(1-\xi)rs' - (1-2\xi)f's - \xi(1-\xi)r's + (3-\xi)\varphi'r + f\varphi' = 0 \tag{26}$$

When $W_\infty, T_\infty, u_\infty, T_w$ are prescribed for the condensation process along the vertical plate, the heat transfer characteristics and the thermal-dynamic as well as transport properties should be determined. The current formulation assumed constant property, but the variable property effect can be captured satisfactorily using the reference temperature and mass fraction to evaluate the fluid properties [8]. With the reference property method, the constant property boundary layer formulation was shown to be able to predict results virtually identical to those predicted by the variable property boundary layer formulation [8]. Therefore, the current solution employs the reference property method to account for the variable property effect.

Now, the iterative steps for solving the basic equations (Eqs. (6)–(9)) and the auxiliary equations (Eqs. (25) and (26)) with the aim to determine the noncondensable gas mass fraction at the interface are presented herein for the given mixed convection number ξ.

(i) Assume a guess value each for $\eta_{L,i}$ and F''_i, which will be iteratively updated.

(ii) With the assumed F_i'', only two additional closure equations are needed to solve the liquid phase momentum equation (Eq. (6))—these are Eqs. (15) and (16); two closure equations are needed to solve the liquid phase energy equation (Eq. (7))—these are Eqs. (17) and (18); three closure equations are needed to solve the gas phase momentum equation (Eq. (8))—these are Eqs. (11), (12), and (19); two closure equations are needed to solve the gas phase species equation (Eq. (9))—these are Eqs. (14) and (20); the closure equations for the auxiliary equations (Eqs. (25) and (26)) can be derived from differentiating both sides of the closure equations for the basic equations with respect to the mixed convection number ξ; a routine ODE solver is applied to all these ordinary differential equations.

(iii) Once the equations are solved, the respective temporary value is known for f_i' and F_i', which can be used by one remaining closure equation (Eq. (10)) to update F_i''.

(iv) In a similar way, another remaining closure equation (Eq. (13)) is used to update $\eta_{L,i}$ by making use of the respective temporary value for the involved variables.

(v) Repeat the above steps until both $\eta_{L,i}$ and F_i'' converge.

(vi) As the iterative algorithm converges, the transformed variables (F, θ, f, φ) have been solved. The noncondensable gas mass fraction at the interface W_i is obtained from the converged solution of $\varphi_i = W_i - W_\infty$. The liquid temperature gradient at the wall θ_w' among others is also a result of the solution.

4 Results

When the noncondensable gas mass fraction at the interface W_i has been solved, the interface temperature T_i can also be resolved using the vapor saturation temperature corresponding to the vapor partial pressure. The heat transfer rate at the wall can therefore be calculated with T_i:

$$q = k_L \left(\frac{\partial T}{dy} \right)_w = k_L (T_i - T_w) \theta_w' \frac{c_L}{x^{1/4} \xi} \tag{27}$$

Letting subscript 0 denote the condensation of pure vapor, the heat transfer degradation effect of the noncondensable gas can therefore be expressed with

$$\frac{q}{q_0} = \frac{k_L}{k_{L,0}} \frac{T_i - T_w}{T_\infty - T_w} \frac{\theta_w'}{\theta_{w,0}'} \sqrt{\frac{\nu_{L,0}}{\nu_L}} \tag{28}$$

where q_0 is calculated by letting $W_\infty \to 0$. Figure 2 shows the current solution for the heat transfer degradation effect (q/q_0) of air as a noncondensable gas on steam condensation in the full spectrum of the mixed convection regime $(0 \le \xi \le 1)$. The analytical results in Fig. 2 are for the steam bulk temperature $T_\infty = 100\,^\circ\mathrm{C}$, with $T_\infty - T_w$ varying from $5\,^\circ\mathrm{C}$ to $20\,^\circ\mathrm{C}$ and the air bulk mass fraction W_∞ varying from 0.005 to 0.1. In Fig. 2, the two limiting cases of mixed convection are compared with the known solutions reported by Sparrow et al. [5] for free convection $(\xi \to 1)$ or forced convection $(\xi \to 0)$. Without surprise, the current solutions for the two limiting cases of mixed convection coincide with results in the pioneering work because it has been proved that the current generic boundary layer formulation is reduced to two specific formulations in the pioneering work for the two limiting cases. There is some minor difference in the comparison though, which may result from several terms (inertia force and energy convection) neglected by the pioneering work but accounted for by the current work, as discussed in Sec. 3.

Next, attention is shifted to the results for the mixed convection regime $(0 < \xi < 1)$ in Fig. 2. The full spectrum of the mixed convection regime can be investigated by starting from observation of a stagnant bulk flow $u_\infty = 0$ $(\xi \to 1)$. As the bulk velocity increases (ξ becomes progressingly away from 1), the bulk flow blows away more noncondensable gases accumulating near the interface, resulting in an elevated condensation driving force. Therefore, the noncondensable gas heat transfer degradation effect becomes less prominent when the mixed convection flow behaves more closely to the forced convection flow (ξ becomes progressingly close to 0).

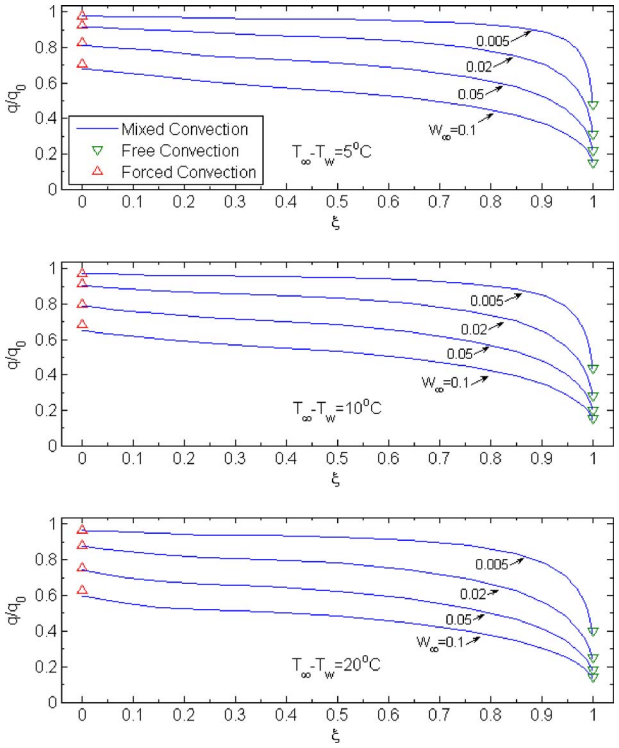

Fig. 2 Noncondensable gas effect in the entire mixed convection regime

Although a slight vapor flow imposed on free convection condensation in the absence of noncondensable gases has little effect because the imposed vapor flow is coupled to the liquid flow by interfacial shear, which is insignificant for a slowly moving vapor flow, it is found that a slight gas flow imposed on free convection condensation in the presence of noncondensable gases can drastically affect the mass transfer boundary. The reason may be that the coupling between hydrodynamics and convective mass diffusion in the gas mass transfer boundary depends strongly on the motion of the gas flow. Therefore, while the effect of a slowly moving bulk flow may be neglected on pure vapor condensation, its effect on condensation with noncondensable gases must be accounted for since the imposed flow can drastically decrease the accumulation of gas at the two-phase interface.

5 Conclusions

The laminar film condensation boundary layer theory was revisited and extended to the entire mixed convection regime for condensation with or without noncondensables. The two-phase boundary layer equations were reformulated so that the solution space for mixed convection enveloped by the known results in the pioneering work can be explored completely using a mixed convection number and the noncondensable gas mass fraction, and the known solutions in the pioneering work were shown to be merely four specific cases of the current formulation. In this sense, this work solves an essential problem in laminar film condensation.

Nomenclature

c_G = $[g\beta/(4\nu_G^2)]^{1/4}$, constant, $m^{-3/4}$
c_L = $[g/(4\nu_L^2)]^{1/4}$, constant $m^{-3/4}$
c_{pL} = liquid specific heat, J kg^{-1} K^{-1}
D = gas mass diffusivity, m^2 s^{-1}
f = gas dimensionless stream function
F = liquid dimensionless stream function
g = gravity constant, m s^{-2}
h_{fg} = latent heat, J kg^{-1}
k_L = liquid thermal conductivity, W m^{-1} K^{-1}
M = molecular weight, kg mol^{-1}
Pr_L = liquid Prandtl number
q = heat transfer rate, W m^{-2}
Sc = gas Schmidt number
T = temperature, K
u = longitudinal velocity, m s^{-1}
v = transverse velocity, m s^{-1}
x = longitudinal coordinate, m
y = transverse coordinate, m
W = gas mass fraction

Greek Symbols

α_L = liquid thermal diffusivity, m^2 s^{-1}
β = $(M_g-M_v)/[M_g-(M_g-M_v)W_\infty]$, volumetric expansion coefficient
δ = liquid film thickness, m
φ = $W-W_\infty$
η = pseudosimilarity variable
μ = absolute viscosity, kg s^{-1} m^{-1}
ν = kinematic viscosity, m^2 s^{-1}
θ = $(T_L-T_i)/(T_w-T_i)$
ξ = mixed convection number
ρ = density, kg m^{-3}
ψ = stream function

Subscripts

0 = pure vapor
g = noncondensable gas
G = gas phase
i = two-phase interface
L = liquid phase
v = vapor
w = wall
∞ = gas bulk

References

[1] Sparrow, E. M., and Gregg, J. L., 1956, "A Boundary-Layer Treatment of Laminar-Film Condensation," ASME J. Heat Transfer, **81**, pp. 13–18.
[2] Koh, J. C. Y., Sparrow, E. M., and Hartnett, J. P., 1961, "The Two Phase Boundary Layer in Laminar Film Condensation," Int. J. Heat Mass Transfer, **2**, pp. 69–82.
[3] Koh, J. C. Y., 1962, "Film Condensation in a Forced-Convection Boundary-Layer Flow," Int. J. Heat Mass Transfer, **5**, pp. 941–954.
[4] Sparrow, E. M., and Lin, S. H., 1964, "Condensation Heat Transfer in the Presence of Noncondensable Gas," ASME J. Heat Transfer, **86**, pp. 430–436.
[5] Sparrow, E. M., Minkowycz, W. J., and Saddy, M., 1967, "Forced Convection Condensation in the Presence of Noncondensables and Interfacial Resistance," Int. J. Heat Mass Transfer, **10**, pp. 1829–1845.
[6] Tamm, G., Boettner, D. D., Van Poppel, B. P., and Benson, M. J., 2009, "On the Similarity Solution for Condensation Heat Transfer," ASME J. Heat Transfer, **131**, p. 111501.
[7] Sparrow, E. M., and Yu, H. S., 1971, "Local Nonsimilarity Thermal Boundary Layer Solutions," ASME J. Heat Transfer, **93**, pp. 328–334.
[8] Liao, Y., and Vierow, K., 2009, "Variable Property Effects on Vapor Condensation With a Noncondensable Gas," Nucl. Technol., **167**, pp. 13–19.

Forced Flow of Vapor Condensing Over a Horizontal Plate (Problem of Cess and Koh): Steady and Unsteady Solutions of the Full 2D Problem

S. Kulkarni

A. Narain
e-mail: narain@mtu.edu

S. Mitra

Department of Mechanical Engineering-Engineering Mechanics,
Michigan Technological University,
Houghton, MI 49931

Accurate steady and unsteady numerical solutions of the full 2D governing equations—which model the forced film condensation flow of saturated vapor over a semi-infinite horizontal plate (the problem of Cess and Koh)—are obtained over a range of flow parameters. The results presented here are used to better understand the limitations of the well-known similarity solutions given by Koh. It is found that steady/quasisteady filmwise solution exists only if the inlet speed is above a certain threshold value. Above this threshold speed, steady/quasisteady film condensation solutions exist and their film thickness variations are approximately the same as the similarity solution given by Koh. However, these steady solutions differ from the Koh solution regarding pressure variations and associated effects in the leading part of the plate. Besides results based on the solutions of the full steady governing equations, this paper also presents unsteady solutions that characterize the steady solutions' attainability, stability (response to initial disturbances), and their response to ever-present minuscule noise on the condensing-surface. For this shear-driven flow, the paper finds that if the uniform vapor speed is above a threshold value, an unsteady solution that begins with any reasonable initial-guess is attracted in time to a steady solution. This long time limiting solution is the same—within computational errors—as the solution of the steady problem. The reported unsteady solutions that yield the steady solution in the long time limit also yield "attraction rates" for nonlinear stability analysis of the steady solutions. The attraction rates are found to diminish gradually with increasing distance from the leading edge and with decreasing inlet vapor speed. These steady solutions are generally found to be stable to initial disturbances on the interface as well as in any flow variable in the interior of the flow domain. The results for low vapor speeds below the threshold value indicate that the unsteady solutions exhibit nonexistence of any steady limit of filmwise flow in the aft portion of the solution. Even when a steady solution exists, the flow attainability is also shown to be difficult (because of waviness and other sensitivities) at large downstream distances. [DOI: 10.1115/1.4001636]

Keywords: film condensation, phase-change heat transfer, two-phase flows, stability, instability, interfacial waves

1 Introduction

1.1 The Cess and Koh Problem and Related Similarity Solutions. The problem studied by Cess [1] and Koh [2] deals with forced flow of saturated vapor (with a uniform upstream speed U_∞) that approaches a semi-infinite horizontal plate and starts experiencing filmwise condensation over the plate (see Fig. 1). The central interest of this paper is to solve the steady and unsteady governing equations for the full two dimensional version of this problem, compare the steady solutions with the relevant classical similarity solutions offered by Cess [1] and Koh [2], and to improve our understanding of the feasibility of the filmwise condensation assumption underlying the Cess [1] and Koh [2] solutions. The results of Koh [2] have been pivotal to the studies that rely on (e.g., Ref. [3]) or use (e.g., Ref. [4]) this solution to predict or estimate the features of shear-driven external condensing flows. The ordinary differential equations associated with the solution of Koh [2], which are numerically solved, result from a boundary layer and constant pressure approximation of an assumed filmwise condensation behavior and a "similarity" solution formulation of the resulting model equations. This solution's approach is very similar to other similarity solutions [5,6] for gravity-driven condensing flows that are well-cited in literature. One reason why this similarity solution for the shear-driven condensate case [2] has not been experimentally verified is, perhaps, significant differences exist between shear-driven and gravity-driven flows with regard to ease of attainment of filmwise or annular condensation and another reason is the difficulty in implementing a suitable experiment that meets the requirements of the theory [1,2]. This is in contrast with the similarity solutions [5,6] for filmwise condensation over a plate under conditions of gravity-driven condensate motion. The gravity-driven cases' similarity solutions are in good agreement with the Nusselt solution [7] and, also, known to be experimentally feasible and in reasonable agreement with related experiments [8]. With regard to ease of achieving filmwise or annular condensation, similar differences are known to exist between gravity-driven and shear-driven inter-

Contributed by the Heat Transfer Division of ASME for publication in the JOURNAL OF HEAT TRANSFER. Manuscript received December 10, 2009; final manuscript received March 13, 2010; published online July 29, 2010. Editor: Yogesh Jaluria.

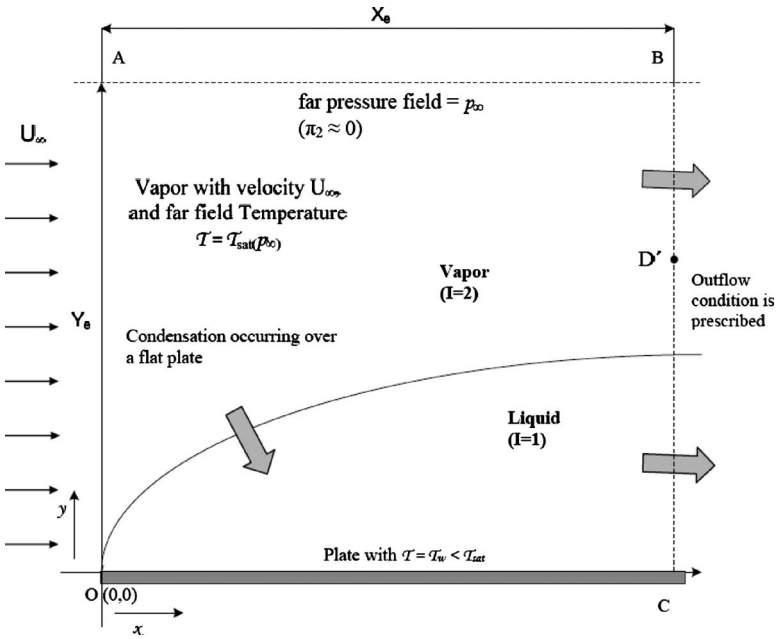

Fig. 1 The figure shows a schematic for a typical finite computational domain for a film condensation flow over a horizontal plate due to a forced uniform vapor flow at the left inlet

nal condensing flows. The experiments involving gravity-driven internal condensing flows inside a vertical tube (see Refs. [9,10], etc.) or large hydraulic diameter slightly inclined (downward) channels demonstrate easy attainment of a rather robust quasi-steady wavy annular (or film condensation) flows but annular or filmwise shear-driven internal condensing flows in millimeter- to micron-scale horizontal tubes and channels are more difficult to achieve and show [11–14] more complex vapor-liquid morphologies (such as steady or intermittent injection annular, mist, slug/plug, bubbly, etc.).

1.2 Steady and Unsteady Results Presented in This Paper. The computationally obtained steady solutions of the problem studied by Cess [1] and Koh [2] and their comparison with the well-known analytical results of Koh [2] have been discussed in this paper. It is shown here that, for a certain range of vapor speeds and vapor-to-wall temperature differences, Koh's analytical solution [2] of this external condensing flow problem agrees well with the reported computational solution's steady film thickness predictions. However, the reported simulations differ from the Koh solution [2] in pressure and associated variables' variation near the leading edge of the plate. While the analytical solution of Koh [2] assumes that the pressure stays constant even in the interior of the flow, the steady solutions presented in this paper show that there are significant pressure variations near the leading edge part of the plate and though the resulting pressure differences are miniscule in value relative to the far-field pressure p_∞, they are very important for determining the dynamics of the flow and in determining the feasibility of maintaining filmwise condensation at low vapor speeds. It is found that the leading edge pressure gradients become large as the vapor speed U_∞ becomes sufficiently small.

The unsteady solutions reported in this paper help assess attainability of the steady solutions. This is done here by looking at limiting solutions (as $t \to \infty$) of the unsteady problem obtained for different initial-guesses. Additionally, important assessments of stability through unsteady response (to initial disturbances as well as to ever-present bottom wall noises) of these flows are obtained and discussed. The effort to obtain and analyze unsteady solutions results in introduction and quantification of the following features of the steady solutions: (i) "attraction rate" values that measure the attainability of the steady solutions from different initial-guesses, (ii) response of the steady solutions to initial disturbances, and (iii) noise-sensitivity of the steady solutions to ever-present minuscule noise and, as a result, expected waviness levels on the steady solutions.

For the range of vapor speeds (0.2–20 m/s) considered for investigation of filmwise condensation of typical nonmetallic vapors (R113, FC-72, etc.), when an arbitrary initial-guess (at $t=0$) is used to obtain an unsteady solution in the idealized case of no condensing-surface vibrations (no matter how minuscule), it is shown that the unsteady solutions tend to a smooth wave free long-term steady solution. The limiting steady solution, when obtained this way as opposed to obtaining it as a steady solution of the steady governing equations, is termed a steady "attractor." This unsteady attraction process is studied and attraction rates to the limiting steady solution are defined. Though the reported attraction rates associated with attainability of a steady solution may appear to be a new idea, it is related to the well-known idea of "decay rates" in linearized stability analyses that assume exponential time evolution of initial disturbances. Thus increased monotonic (i.e., nonoscillatory) attraction rates reported here correlate with the idea of stronger decay rates (i.e., larger, real, and negative coefficients multiplying time in the exponential decay assumption in linear stability analyses). That is, large attraction rates mean both attainability and stronger stability of the steady solution. The attraction rates are used here because, in the present nonlinear context, they are both more general and computationally easier to obtain than decay rates in the linear context. It is found that this attraction rate when plotted as a function of time for any given point on the steady solution (which is close to Koh solution [2]—at least as far as steady film thickness values are concerned) may, in general, depend on the steady solution of the system (that is, the underlying partial differential equations under no-noise conditions) as well as the starting initial conditions. However, we show here that a proper segment of the time-history associated with the rate of change in film thickness yields a definition of attraction rate, which is more or less independent of the choice of initial-guess. This properly chosen measure of attraction rate is

shown to diminish with increasing distance from the leading edge and also with decreasing speed U_∞. As a result, it is found that the assumed filmwise steady condensation is difficult to achieve at very low freestream speeds and, for freestream speeds that are sufficiently large, attainment difficulty is predicted for large downstream distances.

For example, unsteady results find that at low vapor speeds ($U_\infty < U_\infty^* \approx 0.2$ m/s for the case discussed here), a long-term steady limit is not reached and hence a filmwise steady solution or a steady attractor does not exist. This result is further supported by the fact that the steady attractor (for $U_\infty > 0.2$ m/s in the example considered here) exhibits an approach to near zero mechanical energy availability for viscous dissipation in the interior of any chosen control volume.

For sufficiently fast vapor speeds, since the attraction rate diminishes with downstream distance, one expects sensitivity to the effects of transverse gravity (see Ref. [9] for similar effects for condensation inside a horizontal channel), to unintended variations in the far-field uniform pressure p_∞, and to ever-present minuscule noise on the condensing-surface. Considering limitations imposed by our computational approach and the scope of the paper, this paper limits itself to demonstrating increasing downstream waviness associated with persistent but minuscule condensing-surface noise. It is shown that when an arbitrary initial-guess (at $t=0$) is used to obtain an unsteady solution (for $t>0$) in the presence of minuscule noise on the condensing-surface (defined later in the paper through a representative Fourier component), the underlying long-term solution's diminishing attraction rates with distance cause the noise-induced interfacial waves to grow with the distance from the leading edge. A measure of spatial growth, as well as its growth rate with distance, is reported in this paper.

1.3 Trustworthiness of the Employed Computational Tool. The computational tool employed to solve the Koh problem [2] in this paper has been successfully used to solve internal as well as external condensing flow problems reported in Refs. [15–20]. The steady and unsteady simulation results and stability results for the classical Nusselt problem [7,21] by the tools employed in this paper have been already reported elsewhere in Ref. [16]. The agreement of steady computational results in Ref. [16] with the Nusselt solution [7], as well as successful comparison of computational results in Refs. [15–20] for internal condensing flows with relevant semi-analytical [9,15] and experimental results [9,15], further strengthen the confidence in the results reported here.

2 Governing Equations and Formulation for the Computational Problem

The liquid and vapor phases in the flow (e.g., see Fig. 1) are denoted by a subscript I: $I=1$ for liquid and $I=2$ for vapor. As shown in Fig. 1, the far upstream speed of the forced vapor flow is a uniform U_∞. The fluid properties (density ρ, viscosity μ, specific heat C_p, and thermal conductivity k) with subscript I are assumed to take their representative constant values for each phase ($I=1$ or 2). Let $\mathcal{T}_I$ be the temperature field (K), p_I be the pressure field (N/m^2), $\mathcal{T}_s(p)$ be the saturation temperature of the vapor (K) as a function of local pressure p, Δ be the film thickness (m), $\dot{m}$ be the local interfacial mass-flux ($kg/(s\,m^2)$), $\mathcal{T}_w(x)$ be a *known* temperature variation (here, often, $\mathcal{T}_w(x)=\text{const}=\mathcal{T}_w(0)<\mathcal{T}_s(p)$) of the cooled bottom plate (K), and $\mathbf{v}_I=u_I\hat{\mathbf{e}}_x+v_I\hat{\mathbf{e}}_y$ be the velocity field (m/s). It is assumed here that $\Delta\mathcal{T}\equiv\mathcal{T}_s(p_\infty)-\mathcal{T}_w(0)$ is always sufficiently large to allow film condensation at all x, including the $x\sim 0$ zone. For common metallic condensing-surfaces and nonmetallic (refrigerant) vapors, if $\Delta\mathcal{T}$ is larger than $1-2\,^\circ$C and other surface-energy conditions are supportive, annular/stratified or film condensation can be assumed/realized and conditions for its attainment can be theoretically/experimentally assessed.

As shown in Fig. 1, instead of the original infinite domain ($x\geq 0$ and $y\geq 0$), solutions for this problem are to be computationally obtained over a finite domain ($0\leq x\leq X_e$ and $0\leq y\leq Y_e$). For convenience, the characteristic length for this problem is chosen to be Y_e, where Y_e can be chosen to be a known numerical multiple of the well-known physical value of steady film thickness for an altogether different problem—the one associated with a vertical inclination of the plate (gravity-driven condensate) and for $U_\infty=0$—viz., the Nusselt problem (see Refs. [7,16]). That is, $Y_e \equiv c_1\cdot\Delta_N(X_e)$, where $c_1=47$ for most of the cases considered here and $\Delta_N(X_e)$ is the Nusselt film thickness at $x=X_e$. An equivalent alternative is $Y_e\equiv(c_2\cdot\mu_1)/(\rho_1\cdot h_{fg})^{0.5}$, where $c_2=1.133\times 10^5$ for most of the cases considered here. These choices make Y_e an a priori known number that is sufficiently large to capture all the relevant vapor flow domains of interest here. Though other choices of intrinsic characteristic length Y_e are also possible (e.g., $Y_e=\mu_1/(\rho_1\cdot U_\infty)$ or $Y_e=\mu_1^{3/4}k_1^{1/4}\Delta\mathcal{T}^{-1/2}C_{p1}^{-3/4}\rho_1^{-1}$), the earlier two choices suffice here. Furthermore, as discussed in Sec. 5, either of the two choices of Y_e is a posteriori verified to be effective by showing that the numerically obtained values of the flows' physical variables are independent of different choices of the number for Y_e. The above choices of Y_e for characteristic length and U_∞ for characteristic speed are used for defining the nondimensional variables whose computationally obtained values are reported in this paper. As needed, these values can easily be related to the results obtained from other commonly used choices of characteristic length and speed. Let g_y be gravitational acceleration acting along the y axis (gravity along the x direction is zero for this horizontal flow), p_∞ be the pressure of the far-field vapor at $y\geq Y_e$, $\Delta\mathcal{T}\equiv\mathcal{T}_s(p_\infty)-\mathcal{T}_w(0)$ be the representative controlling temperature difference between the vapor and the bottom plate, and h_{fg} be the heat of vaporization at saturation temperature $\mathcal{T}_s(p)$. With ℓ representing the physical time, a new list of fundamental nondimensional variables is introduced through the following definitions:

$$\{x,y,\delta,u_I,\dot{m}\}\equiv\left\{\frac{x}{Y_e},\frac{y}{Y_e},\frac{\Delta}{Y_e},\frac{u_I}{U_\infty},\frac{\dot{m}}{\rho_1 U_\infty}\right\}$$
$$\{v_I,\theta_I,\pi_I,t\}\equiv\left\{\frac{v_I}{U_\infty},\frac{\mathcal{T}_I}{\Delta\mathcal{T}},\frac{p_I-p_\infty}{\rho_I U_\infty^{\,2}},\frac{\ell}{(Y_e/U_\infty)}\right\} \quad (1)$$

In what follows, all governing equations are presented in their more general unsteady forms.

2.1 Interior Equations. The nondimensional differential forms of mass, momentum (x- and y-components), and energy equations for flow in the interior of either of the phases are well-known and are given in Eqs. (A1)–(A4) of the Appendix. The simplified forms that are used in obtaining the Koh formulation [2] and its solution are given by Eqs. (A1) and (A6) of the Appendix.

2.2 Interface Conditions. The nearly exact *physical variable forms* of general interface conditions [22] for condensing flows, with some approximations, are used here and, in the form used here, they are given in Eqs. (A1)–(A9) of Ref. [18]. Utilizing a superscript, i for values of the flow variables at the interface given by $\mathcal{H}\equiv y-\Delta(x,\ell)=0$, the *nondimensional* forms of the interface conditions are given in Eqs. (2)–(8). The Koh formulation [2] uses simplified versions of Eqs. (2)–(7) given below and they are, respectively, given as Eqs. (A7)–(A11) of the Appendix.

- The nondimensional form of the requirement of continuity of tangential component of velocities (Eq. (A2) of Ref. [18]) becomes

$$u_2^i = u_1^i - \delta_x(v_2^i - v_1^i) \quad (2)$$

where $\delta_x\equiv\partial\delta/\partial x$.

- The nondimensional form of the normal component of momentum balance at the interface (Eq. (A3) of Ref. [18]) becomes

$$\pi_1^i = \frac{\rho_2}{\rho_1}\pi_2^i - \frac{1}{We}\left(\frac{\delta_{xx}}{[1+\delta_x^2]^{3/2}}\right) + \dot{m}^2\left(\frac{\rho_1}{\rho_2} - 1\right) \tag{3}$$

where $We^{-1} \equiv \sigma/\rho_1 U_\infty{}^2 Y_e$ and σ is the surface tension with $\sigma = \sigma(\mathcal{T})$ being a function of interfacial temperature $\mathcal{T}$. Though surface tension term is included here, over the range of computational investigations reported here, the presence or absence of the second and third terms on the right side of Eq. (3) was found to have none to negligible impact on simulation results reported here. Because of near constancy of interfacial saturation temperature (as interfacial pressure variations are not strong enough to change it), and resulting absence of Marangoni effects (see Eq. (4)), the surface tension variation effect also shows no qualitative impact on the unsteady solutions reported here.
- The tangential component of momentum balance at the interface (Eq. (A4) of Ref. [18]) becomes

$$\left.\frac{\partial u_1}{\partial y}\right|^i = \frac{\mu_2}{\mu_1}\left.\frac{\partial u_2}{\partial y}\right|^i + [t] \tag{4}$$

The resulting term $[t]$ used here is defined by Eq. (A5) of the Appendix.
- The nondimensional forms $\dot{m}_{LK}$ and $\dot{m}_{VK}$ of the nonzero physical values of interfacial mass-fluxes $\dot{m}_{\mathcal{LK}}$ and $\dot{m}_{\mathcal{VK}}$ (defined in Eq. (A5) of Ref. [18]) impose kinematic constraints on the interfacial values of the liquid and vapor velocity fields and are given by

$$\dot{m}_{LK} \equiv [u_1^i(\partial\delta/\partial x) - (v_1^i - \partial\delta/\partial t)]/\sqrt{1+(\partial\delta/\partial x)^2} \text{ and}$$
$$\dot{m}_{VK} \equiv (\rho_2/\rho_1)[u_2^i(\partial\delta/\partial x) - (v_2^i - \partial\delta/\partial t)]/\sqrt{1+(\partial\delta/\partial x)^2} \tag{5}$$

- The nondimensional form $\dot{m}_{\text{energy}}$ of the nonzero physical values of interfacial mass-flux $\dot{m}_{\text{energy}}$ (as given by Eq. (A6) of Ref. [18]) represents the constraint imposed on mass-flux by the balance equation for the net energy transfer across the interface, and is given by

$$\dot{m}_{\text{energy}} \equiv \text{Ja}/(\text{Re}_1\ \text{Pr}_1)\{\partial\theta_1/\partial n|^i - (k_2/k_1)\,\partial\theta_2/\partial n|^i\} \tag{6}$$

where $\text{Ja} \equiv C_{p1}\Delta\mathcal{T}/h^0{}_{fg}$ and $h^0{}_{fg} \equiv h_{fg}(\mathcal{T}_s(p_\infty)) \cong h_{fg}(\mathcal{T}_s(p_2^i))$.
- The interfacial mass balance requires that the net mass-flux (in $kg/m^2/s$) at a point on the interface, as given by Eq. (A7) of Ref. [18], be single-valued regardless of which physical process is used to obtain it. The nondimensional form of this requirement becomes

$$\dot{m}_{LK} = \dot{m}_{VK} = \dot{m}_{\text{energy}} \equiv \dot{m} \tag{7}$$

It should be noted that negligible interfacial thermal resistance and equilibrium thermodynamics on either side of the interface are assumed to hold at all values of x downstream of the origin (i.e., second or third computational cell onwards). Hence, as in Koh solution [2] and as per discussions in the Appendix of Ref. [18] (see Eq. (A8) of Ref. [18]), no nonequilibrium thermodynamic model for the interfacial mass-flux $\dot{m}$ is needed to obtain a solution.
- The nondimensional thermodynamic restriction on interfacial temperatures (as given by Eq. (A8) in Ref. [18]) becomes

$$\theta_1^i \cong \theta_2^i = \mathcal{T}_s(p_2^i)/\Delta\mathcal{T} \equiv \theta_s(\pi_2^i) \tag{8}$$

Within the vapor domain, for any of the typical refrigerants (such as R113 considered here), typical changes in absolute pressure relative to the inlet pressure are small but sufficient to affect vapor motion, though, at the same time, they are too small to affect saturation temperature values even for the largest adverse pressure gradient zone in the leading edge. This allows the approximation $\theta_s(\pi_2^i) \cong \theta_s(0)$ to be a valid one.

2.3 Boundary-Conditions. Since the vapor flow is nearly uniform at locations at large y, appropriate boundary-conditions are prescribed along lines OA ($x=0$), AB ($\mathscr{y}=Y_e$ or $y=1$), and BC ($\mathscr{x}=X_e$ or $x=x_e=X_e/Y_e$) in Fig. 1. Assuming onset of condensation at $x=0$ (i.e., $\Delta(0,\mathscr{t})=0$), the boundary-conditions are as follows.

Inlet. At the inlet $x=0$, we have

$$\mathscr{u}_2(0,\mathscr{y},\mathscr{t}) = U_\infty, \quad \partial v_2/\partial x|_{x=0} = 0 \text{ on } OA \text{ in Fig. 1} \tag{9}$$

Pressure is not prescribed across the inlet boundary but is prescribed to be the far-field pressure p_∞ at the top corner reference location (point A with $\mathscr{x}=0$ and $\mathscr{y}=OA$ in Fig. 1) on the inlet boundary. Pressures within the entire domain, including the inlet values $p_2(0,\mathscr{y},\mathscr{t})$, are calculated as part of the solution of the problem being considered. However, outside and above the control volume, one expects the far-field pressures to be $p_2 - p_\infty \equiv (\rho_2 \cdot U_\infty{}^2)\cdot\pi_2(0,\mathscr{y},t) = 0$ for $y \geq OA$ (see Fig. 1) or $y \geq 1$. For temperature, one also iteratively imposes the condition $\mathcal{T}_2(0,\mathscr{y},\mathscr{t}) = \mathcal{T}_{\text{sat}}(p_2(0,\mathscr{y},\mathscr{t}))$—which is, in principle, a nonconstant prescription of vapor temperature at the inlet.

It should be noted that prescription of pressure at reference location (point A in Fig. 1) does not make inlet boundary-condition one of the pressure-inlet. It remains a boundary where the x-component of vapor velocity u_2 is uniform but the y-component of vapor velocity v_2 is given the requisite freedom through the condition $\partial v_2/\partial x|_{x=0} = 0$.

Top. On the top boundary, where $\mathscr{y}=OA$ (see Fig. 1) or $y=1$, the pressure is p_∞ and shear stress is nearly zero. This leads to standard far-field boundary modeling condition

$$\pi_2(x,1,t) = 0 \quad \text{and} \quad \partial u_2/\partial y|_{(x,1,t)} = 0 \text{ on } AB \text{ in Fig. 1} \tag{10}$$

The temperature at the top boundary is also considered to be one of saturated vapor, i.e., $\mathcal{T}_2(\mathscr{x},Y_e,\mathscr{t}) = \mathcal{T}_{\text{sat}}(p_\infty)$. Therefore, according to Eq. (1), $\theta_2(x,1,t) = \mathcal{T}_{\text{sat}}(p_\infty)/\Delta\mathcal{T}$. If the temperature at the top boundary is allowed some superheat (5–10°C), a nonzero thickness for the temperature boundary layer develops near the interface. For *saturated* vapor flow conditions considered here, this thermal boundary-layer thickness is not present. Even if the boundary layer has nonzero thickness because of the presence of vapor superheat, a nonzero superheat has no impact on the reported results for most vapors (we have computationally verified this and the physical reasons are discussed later).

Exit. As far as exit condition is concerned, none is needed for temperature. For the Koh problem [2], and the steady solution, the exit pressure remains externally unspecified and, as a result, it remains close to the far-field pressure p_∞ if the exit is sufficiently far from the inlet. This is not only the original assumption of Koh formulation [2] but is also the assumption for most parabolic external flow problems (such as single phase flow over a flat plate, etc.). For this modeling, either of the two formulations (A) or (B) below is used.

(A) The pressure is prescribed to be the uniform steady pressure p_∞ (i.e., nondimensional pressure π_2 of zero) along some of the vapor phase at the exit section (along BD' in Fig. 1) that is close to the top boundary. Thus the best way to faithfully reproduce the above assumption for pressure at the exit is

$$\pi_2(x_e,y,t) \approx 0 \quad \text{and} \quad \left.\frac{\partial v_2}{\partial x}\right|_{(x_e,y,t)} \cong 0 \tag{11}$$

whenever X_e and $\mathscr{y}$ are sufficiently large (i.e., $\mathscr{y}$ is on $D'B$ in Fig. 1). For smaller $\mathscr{y}$ values (i.e., $\mathscr{y}$ on CD' in Fig. 1 where the point D' at $\mathscr{x}=X_e$ can be taken to be any point

that is sufficiently close to the interface), no boundary-condition is prescribed except for the "outflow" boundary-condition. The outflow condition is simply that the mass flow across CD'—which specifically includes the liquid portion $0 \le \mathscr{y} \le \Delta(X_e, \mathscr{t})$—is such that it satisfies the overall mass balance for a control volume formed by the bounding surfaces $\mathscr{x}=0$, $\mathscr{x}=X_e$, $\mathscr{y}=0$, and $\mathscr{y}=Y_e$.

(B) The pressure is left unspecified along the entire (or most) vapor phase at the exit section (along *BC* in Fig. 1). Because uniform pressure p_∞ is already prescribed along the top (*AB* in Fig. 1), only an outflow condition at the exit section is enforced to preserve an overall mass balance for the entire control volume (see *OABC* in Fig. 1). This formulation is adequate as the resulting computational solution obtained under this formulation also satisfies the requisite $\pi_2(x_e, y, t) \approx 0$ condition. This steady or unsteady solution obtained under (B) is found to be nearly identical (within computational convergence bounds) to the solution under (A) above. So, from here and henceforth, unless otherwise stated, this exit formulation (B) is used to closely follow the original intent of the Koh formulation [2]—that is to assume that the uniform far-field pressure ($=p_\infty$) condition holds for the exit section if it is sufficiently far from the inlet and, as a result, at these locations no significant adjustments in cross-sectional kinetic energy takes place.

Condensing-surface. At the condensing-surface ($y=0$), we have

$$u_1(x,0,t) = v_1(x,0,t) = 0 \quad \text{and} \quad \theta_1(x,0,t) = \theta_w \equiv \mathcal{T}_w/\Delta\mathcal{T} \tag{12}$$

Preliminary remarks about the steady formulation and solution. For the steady problem, all variables are considered time independent and all time derivatives are dropped. The temperature variations in the vapor field were computed but the variations were found to be, as is well-known, quite insignificant for zero (or small) superheat. Therefore, for all practical purposes, vapor can be assumed to be at uniform saturation temperature—i.e., $\theta_2(x,y,t) \cong \theta_s(0)$ at all locations in the vapor domain. This is reasonable because the effects of superheat $\Delta\mathcal{T}_{\text{sup}}$ (in the typical 5–10°C range) are verifiably negligible because of the typically small values of vapor Jakob number ($\text{Ja}_2 \equiv C_{p2} \cdot \Delta\mathcal{T}_{\text{sup}}/h_{fg}$) and thermal conductivity ratio k_2/k_1 (see Eq. (6)) that are encountered for most nonmetallic vapor flow conditions of interest here.

Preliminary remarks about the unsteady formulation. The governing equations and the interface conditions given above are valid under the *continuum* assumption and, therefore, they cannot model and incorporate various intermolecular forces that are important in determining the time evolution of very thin (10–100 nm) condensate film thickness $\delta(x,t)$. As a result, for solving unsteady problems, $t=0$ cannot be chosen to be the time when saturated vapor first comes in contact with and condenses on the dry subcooled ($\mathcal{T}_w(x) < \mathcal{T}_s(p_\infty)$) horizontal condensing-surface. With the above modeling limitations, the strategy for obtaining unsteady solutions is to start at a time ($t=0$) for which one either has a sufficiently thick *steady* solution of the continuum equations (where all the governing equations clearly apply) or one has *any* reasonable, but sufficiently thick, initial-guess. Then, from there, one can obtain the unique large time ($t \to \infty$) smooth or wavy (steady/quasisteady) condensate flow solution/behavior—if one exists—with the help of the unsteady continuum equations. The reported computational results verify the fact that the large times (or long-term) unsteady solutions are independent of the choice of initial condition and thus represent (also see Ref. [9]) steady or unsteady features of the limiting steady solution for this flow.

Initial conditions for the unsteady formulation. In the context of the above discussion, if $\phi(x,y,t)$ is any variable (such as u_I, v_I, π_I, θ_I, etc.), the initial values of ϕ and film thickness $\delta(x,t)$ are given as

$$\phi(x,y,0) = \phi_{\text{steady}}(x,y) \quad \text{or} \quad \phi_{\text{initial-guess}}(x,y) \quad \text{and}$$
$$\delta(x,0) = \delta_{\text{steady}}(x) \quad \text{or} \quad \delta_{\text{initial-guess}}(x) \tag{13}$$

where $\phi_{\text{initial-guess}}$ and/or $\delta_{\text{initial-guess}}$ are reasonable initial-guesses and ϕ_{steady} and/or δ_{steady} are the solutions of the governing equations obtained by dropping all time dependencies in Eqs. (2)–(12).

An inspection of all the nondimensional governing equations, interface conditions, and boundary-conditions reveals the fact that the computational solutions given here are affected by the following set of seven independent nondimensional parameters:

$$\left\{ \text{Re}_1, \text{Ja}, \text{Fr}_y^{-1}, \frac{\rho_2}{\rho_1}, \frac{\mu_2}{\mu_1}, \text{Pr}_1, \text{We} \right\} \tag{14}$$

where $\text{Fr}_y^{-1} = {U_\infty}^2/g_y Y_e$ and $\text{Re}_1 \equiv \rho_1 U_\infty Y_e/\mu_1$. As we see later, for the downstream distances considered in this paper, the role of Fr_y^{-1} is insignificant. The role of surface tension, through We, is also found to be insignificant for the cases considered here.

3 Koh's Formulation for a Similarity Solution of the Steady Problem

The formulation for this problem (see Ref. [1] or Ref. [2]) is posed by governing Eqs. (A1) and (A6) of the Appendix along with the interface and boundary-conditions given in Eqs. (A7)–(A12) of the Appendix. The similarity formulation is sought after rewriting Eqs. (A1) and (A6) following an introduction of certain assumed forms of velocity and temperature functions in terms of two new similarity variables (η for the liquid phase and ξ for the vapor phase) that replace $\mathscr{x}$ and $\mathscr{y}$. These "new" similarity variables are defined as

$$\eta(\mathscr{x},\mathscr{y}) \equiv \mathscr{y}\sqrt{\frac{U_\infty}{\nu_1 \mathscr{x}}}, \quad \xi(\mathscr{x},\mathscr{y}) \equiv (\mathscr{y} - \Delta(\mathscr{x}))\sqrt{\frac{U_\infty}{\nu_2 \mathscr{x}}} \tag{15}$$

The physical variables of velocity and temperature are sought as functions (viz., f_1, f_2, g_1, and g_2) of the variables introduced above. The defining relations for these physical variables (see Ref. [2]) are

$$p_I(\mathscr{x},\mathscr{y}) = p_\infty = \text{const} \quad (I = 1 \text{ or } 2), \tag{16}$$

$$\Delta(\mathscr{x}) \equiv \Delta_{\text{Koh}}(\mathscr{x}) \equiv \eta_\delta \sqrt{\frac{\nu_1 \mathscr{x}}{U_\infty}}, \quad \mathscr{u}_1(\mathscr{x},\mathscr{y}) \equiv U_\infty f_1'(\eta)$$

$$\mathscr{u}_2(\mathscr{x},\mathscr{y}) \equiv U_\infty f_2'(\xi), \quad \mathcal{T}_1(\mathscr{x},\mathscr{y}) - \mathcal{T}_w \equiv \Delta\mathcal{T} \cdot g_1(\eta),$$
$$\mathcal{T}_2(\mathscr{x},\mathscr{y}) - \mathcal{T}_w \equiv \Delta\mathcal{T} \cdot g_2(\xi) \tag{17}$$

Equations (15)–(17) transform governing equations (A1) and (A6), and interface/boundary-conditions (A7)–(A12) given in the Appendix for the Koh formulation [2] to (also see Ref. [2]) a set of ordinary differential equations (ODEs) over the liquid ($0 \le \eta \le \eta_\delta$) and vapor ($0 \le \xi < \infty$) domains with proper boundary-conditions at $\eta=0$, $\eta=\eta_\delta$, $\xi=0$, and $\xi \to \infty$. This ODE formulation—unlike the formulation in Sec. 2—is *always* such that a unique steady solution exists and can be numerically obtained by a suitable method (e.g., fourth order Runge–Kutta method combined with a shooting technique that can satisfy all the boundary-conditions). Thus, the steady Koh formulation (which is always well-posed and solvable for plates of large finite length) cannot, by itself, assess attainability issues for these solutions. The solution obtained by Koh's method, based on the results presented here, are found to represent a meaningful approximate solution, when a solution exists, either as a *steady* solution of the steady version of the formulation in Sec. 2 or as the long-term steady limit of the *unsteady* formulation in Sec. 2.

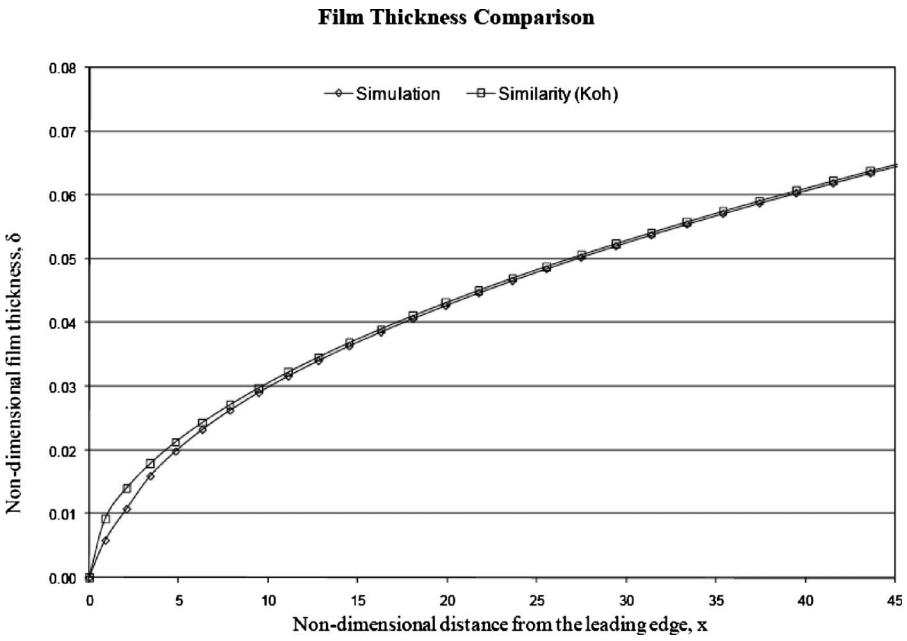

Fig. 2 For flow of R113 vapor with $U_\infty=2$ m/s, $\Delta T=5°C$, $p_\infty=1$ atm, $x_e=45$, $g_y=0$, and $Y_e=0.004$ m, this figure compares nondimensional film thickness (δ) values for the steady solution (obtained from solving the steady governing equations) with those obtained from Koh's similarity solution [2]

4 Computational Approach

A detailed description of the 2D steady/unsteady computational approach utilized in this paper is given in Sec. 3 of Ref. [18]. A brief description of all essential features of computational approach is also available in Sec. 3 of Ref. [19]. Since this paper investigates an external flow problem, unlike the internal flows discussed in Refs. 18 and 19, the imposition of the top and exit boundaries for this external flow is different from the internal flow situations but is the same as the one given by us in Ref. [16] for the external flow Nusselt problem [7]. The difference is primarily another use of the earlier established [14] τ-p method toward prescribing stress boundary-conditions—i.e., pressure (with τ =normal derivative of the tangential velocity component=0) on the top (AB in Fig. 1) and side (BD' in Fig. 1) boundaries. The τ-p method was originally developed (see Ref. [18]) for prescribing τ (tangential velocity gradient in the normal direction) and p (pressure) at the interface.

5 Computational Results Obtained for Steady Solutions

5.1 Results Obtained for the Full Steady Problem and Comparison With Koh Solution. Even though refrigerant R113's properties were used to run most of the computational simulations presented in this paper, similar results are expected, in principle, for any nonmetallic pure vapor flowing over a flat plate.

The Koh formulation [2] discussed in Sec. 3 is best represented by solution of the steady problem under unspecified exit conditions (see Eq. (11)) as described in Sec. 2. After establishing near equivalence of solutions obtained by imposing exit conditions under formulations (A) and (B) of Sec. 2, formulation (B) is used here to obtain the computational solutions of the steady problem and to discuss their comparisons with the corresponding Koh solutions [2]. For a representative R113 flow case, specified by sufficiently fast $U_\infty=2$ m/s, $x_e=45$, $\Delta T=5°C$, and $g_y=0$, the results obtained from steady solution are shown in Figs. 2–6. Figure 2 compares, for a representative case, nondimensional film thickness values predicted by computational solution of the complete steady version of the formulation described in Sec. 2 with the numerical solution of the Koh formulation [2] described in Sec. 3.

It is seen that the computationally obtained values of film thickness are in good agreement with the classical similarity solution as the underlying boundary-layer approximations for the Koh formulation [2] are approximately valid. For the case in Fig. 2, comparisons of vapor and liquid u-velocity profiles and liquid and vapor temperature profiles as obtained from the two different solution approaches were found to agree with each other (not shown here for brevity).

Thus film thickness, velocity profiles, and the temperature profiles from our simulations are in good agreement with Koh's approximate solution. This establishes that, for the ranges of vapor speeds investigated here, the solution obtained from Koh's similarity formulation (see summary in Sec. 3) yields film thickness, velocity, and temperature profiles with reasonable accuracy (e.g., both the formulations yield, as expected, linear velocity and temperature profiles in the liquid domain for the laminar condensate flow).

For the case in Fig. 2, Fig. 3 shows the nondimensional pressure variation $\pi_2(x,y)$ for $0\le x\le 45$ in the vapor domain along the x direction at $y=0.8$ (note that, for the corresponding case in Fig. 2, $\delta(x_e)<0.8$ and, therefore, $y=0.8$ is entirely in the vapor). The Koh formulation [2] in Sec. 3 neglects the pressure gradient terms in the governing momentum equations but, as seen from Fig. 3, there is a zone $0<x\le x^*$ near the leading edge, up to which there exists a significant adverse pressure gradient that is needed to slow the vapor down by the amount that is consistent with the slow motion of the adjacent condensate and mass transfer across its interface. After this length x^* (= x^*/Y_e), pressure gradient $d\pi_2/dx$ reduces nearly to zero value and Koh's [2] assumption of uniform pressure is valid. The pressure gradient in this frontal zone ($0<x\le x^*$) is very significant in determining the vapor and condensate dynamics for this horizontal condensing flow problem. As the vapor speed reduces, this pressure gradient is found to increase. For the same case, the nondimensional pressure profiles (values of $\pi_2(y)$ for $y\ge\delta(x)$ and values of $\rho_1\pi_1(y)/\rho_2$ for $0\le y\le\delta(x)$) across the plate at different cross sections are shown in Fig. 4. The pressure discontinuities across the interface in Fig.

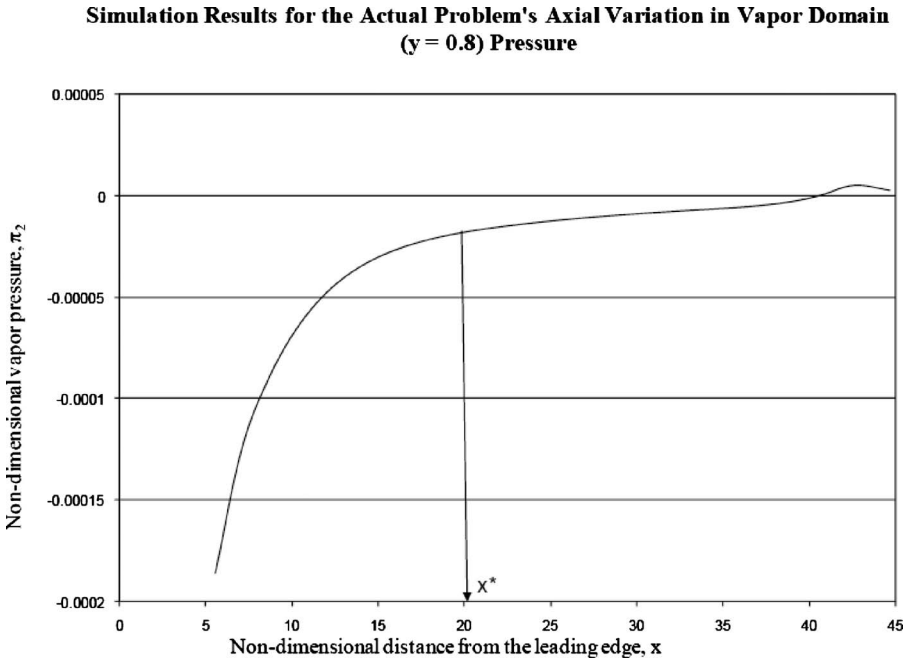

Fig. 3 For the steady solution of Fig. 2, this figure shows, at a fixed $y=0.8$ location, computationally obtained variation of nondimensional pressure π_2 with nondimensional distance x

4 arise from the last two terms on the right side of Eq. (3) and are found to be inconsequential because of their smallness. The cross-sectional pressure rise seen in Fig. 4 over the same frontal part is needed to provide the necessary centripetal acceleration for bending some of the streamlines (see Fig. 5) toward the condensate. As seen from Fig. 3, the pressure variations over the locations $x \geq x^*$ are insignificant as $\pi_2\ (x, y=0.8) \approx 0$. In the computational results obtained from the formulation described in Sec. 2, this bending of streamlines is assisted by pressure variations along and across the vapor domain as well as the variations in interfacial velocities (see, e.g., $u_1^{\,i}$ variations in Fig. 6). Unlike this solution of the full formulation, in the similarity solution obtained from the formulation summarized in Sec. 3, the pressure and interfacial velocity variations are not present and the bending of the streamline is kinematically enforced by an assumed constant value of pressure, constant value of interfacial velocity ($u_1^{\,i} \approx u_2^{\,i}$) independent of x, and condensate thickness values constrained by Eq. (16). Though, in the frontal portion of the plate, the computational

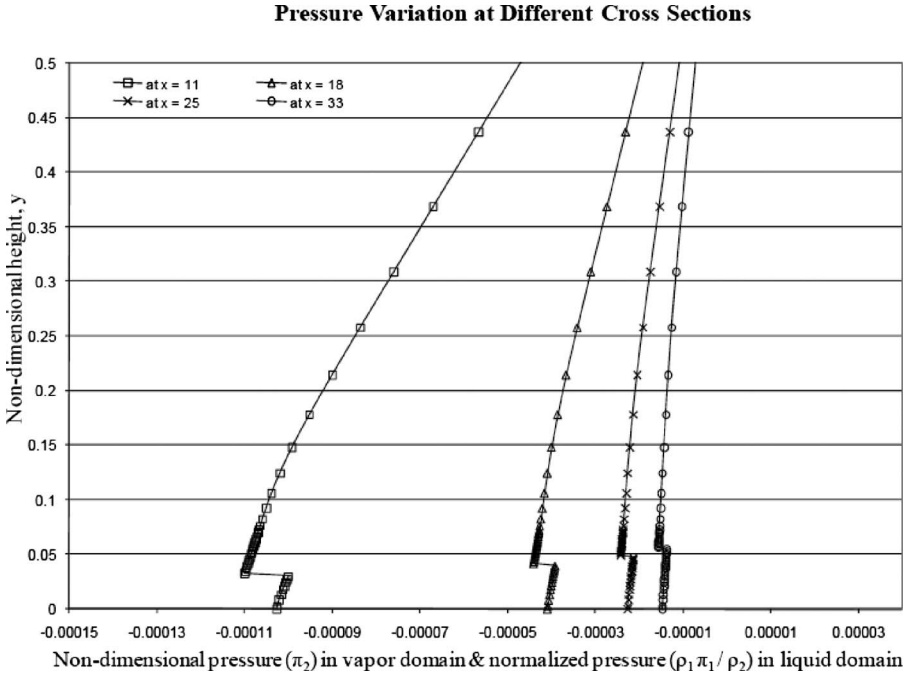

Fig. 4 For the steady solution of Fig. 2, Fig. 4 shows computationally obtained y-directional variation of nondimensional pressure π across different cross sections along the domain. The pressure in vapor domain above condensate film is represented by π_2 and pressure in liquid domain below the interface is represented by $(\rho_1/\rho_2)\pi_1$.

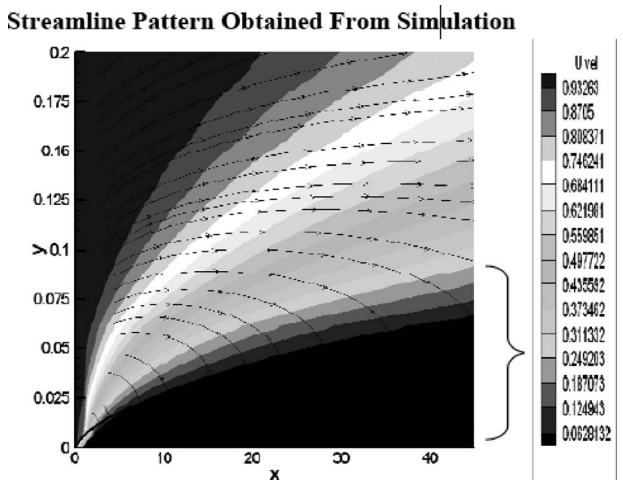

Fig. 5 The figure shows the streamline pattern for the case in Fig. 2. The pattern is obtained from the reported simulation technique. The contour on the background represents the magnitude of u_l velocities.

solution of the full problem significantly differs in its pressure predictions from the Koh solution [2] obtained under the assumption of constant pressure, the two solutions differ by less than 1% in the important heat transfer rate controlling values of film thickness variation. This agreement (within 1–2%) for film thickness variations was found to be valid over a range of flow parameters ($2\times10^5\leq \mathrm{Re}_x\leq 6\times10^7$, $0.02\leq \mathrm{Ja}\leq 0.12$, $0.0052\leq(\rho_2/\rho_1)\leq 0.00526$, $0.020\leq(\mu_2/\mu_1)\leq 0.0212$, and $7\leq \mathrm{Pr}_1\leq 7.5$) investigated by us.

The differences in the pressure fields cause the differences between the simulation and the Koh solution in the converged values of the vertical and horizontal components of condensate velocities at the interface, viz., $v_1{}^i=v_1(x,\delta(x))$ (not shown) and in $u_1{}^i=u_1(x,\delta(x))$ shown in Fig. 6. Figure 6 shows a mismatch between the horizontal components of interfacial velocities as obtained by computational solution of the full steady problem and those obtained by the Koh similarity solution [2]. This mismatch occurs over a leading edge zone ($0\leq x\leq x^*$) that is the same for which there is significant variation in vapor pressure field (see Fig. 3).

The streamline pattern (Fig. 5) obtained from computations has been compared with the streamline pattern (not shown) obtained from the Koh solution [2] for the same case. Both of the patterns were found to be very similar to each other. It is seen that the streamlines bend at the interface and that this bending reduces at the interface as one moves further downstream in the x direction.

It is also found that, over the relatively short distances and vapor speeds considered in this paper, the transverse component of gravity insignificantly affects the film thickness values and velocity profiles of the steady solution. The transverse component of gravity does, however, affect the condensate pressure profiles in the y direction and we also know—from the results given [9] for internal condensing flows in horizontal channels—that the transverse component of gravity does affect the flow at sufficiently long downstream distances once condensate thickness is "sufficiently" large. This version of our simulation tool for this external flow problem is not able to go far enough downstream to detect the phenomena we have observed, in Ref. [9], for internal flows in horizontal channels.

The above discussions for $U_\infty=2$ m/s describe a region $0\leq x\leq x^*(\approx 20)$ for which the pressure variations in the vapor phase (Figs. 3 and 4) and interfacial speed $u_1{}^i$ (Fig. 6) differ from the Koh solution [2] and yet the film thickness variations in Fig. 2 are close to the Koh solution [2] for all $x>2$ and not just $x>20$. If U_∞ is reduced, it is found that the value of x^* decreases, film thickness values increase, and the physical values of interfacial shear $S^i\approx\mu_1(\partial u_1/\partial y)|^i$ also decrease as per Koh [2] predictions.

5.2 Numerical Accuracy and Regularities of the Computationally Obtained Solutions. The computational procedure for obtaining steady and unsteady solutions as described above was verified for accuracy and consistency with regard to different choices of the number of grid points as well as different choices of the characteristic length Y_e appearing in Fig. 1 and in the definition of nondimensional parameters listed in Eq. (14).

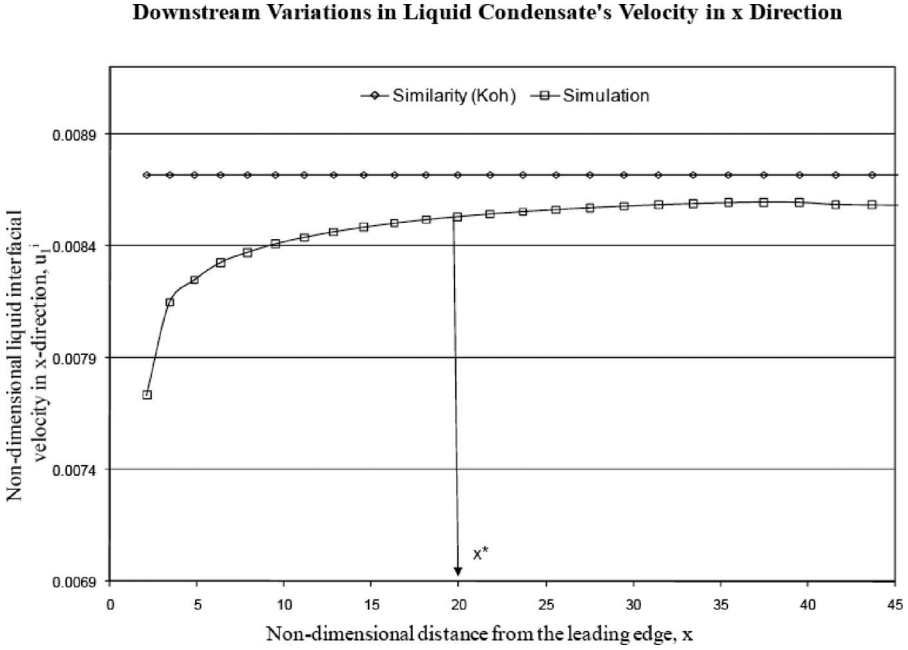

Fig. 6 For the steady solution of Fig. 2, this figure compares nondimensional values of x-directional liquid velocities at the interface ($u_1{}^i$) as obtained from the similarity solution [2] with those obtained from the computational solution

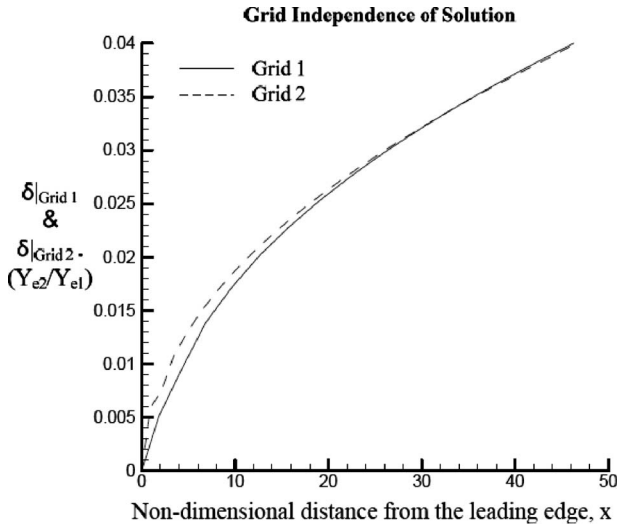

Fig. 7 For flow of R113 vapor with $U_\infty=2$ m/s, $\Delta\mathcal{T}=5°C$, $p_\infty=1$ atm, $x_e=50$, and $g_y=0$, this figure compares nondimensional values of film thickness δ obtained from simulations for the same steady conditions under two different choices of grids ($ni\times nj$) and domain heights Y_e. Grid 1 corresponds to the grid size of 30×50 with $Y_{e1}=0.004$ m and Grid 2 corresponds to the grid size of 35×70 with $Y_{e2}=0.008$ m. Nondimensional values of δ and x for Grid 2 are converted and compared in terms of Grid 1 (by multiplying them by Y_{e2}/Y_{e1}).

We only show here the grid independence for the steady solution scheme employed here though similar grid independence has also been established for the reported unsteady solution scheme. In Fig. 7, film thickness variations for the same flow situation are computationally obtained for two different grids and two different choices of Y_e values. In Fig. 7, $Y_e=0.004$ m is used for "Grid 1" and $Y_e=0.008$ m is used for "Grid 2." Furthermore, for Grid 1 and Grid 2, the numbers of grid points represented by $ni\times nj$ values (see Ref. [18]) are, respectively, given as 30×50 and 35×70. Although Fig. 7 only shows the nearly equal values of the two equivalent nondimensional film thickness values, similar proximity of the two solutions was confirmed for velocity, temperature, and relative pressure profiles as well. From computational point of view, it should be observed that shear-driven horizontal condensing flows, as opposed to gravity-driven flows [15–20], require more iterations to converge.

5.3 Other Comments/Results. Since the computational cases deal with high vapor velocities ($U_\infty=0.2-20$ m/s), it is natural to ask whether the Koh [2] assumption of *laminar* nature of the vapor flow holds for the near interface region. Since the near interface vapor flow is qualitatively similar to a boundary-layer flow with suction, it can be assumed that the transition to turbulence criteria for such boundary-layer flows—as given by Eq. (17.10) of Ref. [23]—will yield reasonable estimates for determining whether or not the vapor boundary-layer flow in the Koh problem [2] is laminar or turbulent. The computationally obtained vapor boundary-layer (momentum) thickness Δ_v values in the Koh solution, as well as the values obtained from the computational solution, were used to verify that Eq. (17.10) of Ref. [23], viz., $\rho_2 U_\infty \Delta_v(x)/\mu_2 \ll 70{,}000$, holds for all cases considered here. That is, these vapor flows, because of the suction effects, appear to be strongly laminar at all x locations considered here. However, such vapor-phase boundary-layer stability arguments based on vapor suction rates, may miss "stability" or "noise-sensitivity" of the associated condensate motion and this must be separately assessed in determining attainability and waviness of these flows.

6 Computational Results Obtained From Unsteady Solutions

6.1 Unsteady Simulation Results That Indicate the Domain and Attraction Rates of the Steady Solution. The unsteady computational solution based investigations cover speeds U_∞ in a range of $0.2\ \text{m/s}<U_\infty<20$ m/s (for the reported R113 and similar vapors) and, for temperature difference $\Delta\mathcal{T}$, a range of $3-15°C$ is covered. For this range, it is found that, if the unsteady solution was started at $t=0$ from a reasonable initial-guess for $\delta(x,0)$, it would always seek a long-term time independent steady solution. The long-term ($t\to\infty$) steady solution of the unsteady governing equations is found to be computationally equal (within 3–5% of computational error) to the steady solution obtained by solving the steady governing equations. This long-term ($t\to\infty$) steady solution obtained this way is termed an attractor because unsteady solutions starting at different initial-guesses are attracted to it.

Though these solutions in Fig. 8 show the existence of a steady attractor, we observe that the phenomenon of attraction in Fig. 8 shows a different attraction rate to the steady solution at different downstream locations. The example shown in Fig. 8 is for R113 vapor at $U_\infty=1.7$ m/s and $\Delta\mathcal{T}=5°C$. In Fig. 8, the unsteady solution is started at $t=0$ with an initial-guess of $\delta(x,0)$ that is about 16% below the final attracting steady solution. A similar attracting behavior, though not shown here, exists if the initial-guess was somewhat above the long-term steady solution. It is seen from Fig. 8 that the attraction to the steady solution takes progressively longer times for locations that are farther and farther downstream of the inlet. The steady solution attractor in Fig. 8 is said to have a "strength," which diminishes with x. Here, by strength, one means the rate of steadily falling values of $\partial\Delta/\partial t$ as indicated by representative slopes of "$\partial\Delta/\partial t$ versus t" curves for different values of x (these slopes are indicated by representative line segments AB, $A'B'$, etc., in Fig. 9). As shown in Fig. 9, for the no-noise unsteady simulation results at $x=0.12$ m, initial-guess at any x has a delay time τ_{D1} over which the attraction speed $\partial\Delta/\partial t|_{\text{init}}$ does not change much. Following this, over time duration τ_{eff}, there is a nearly constant representative deceleration rate $|\partial^2\Delta/\partial t^2|_{\text{rep|(no-noise)}}$ (termed attraction rates and measured by the slopes of lines AB, $A'B'$, etc.). This deceleration rate is needed to impede the attracting solution so it can reach a nearly steady ($\partial\Delta/\partial t\approx0$) behavior over a subsequent time duration τ_{D2}.

Figure 10 shows $\partial\Delta/\partial t$ versus t curves at $x=30$ for three different vapor speeds. For all the speeds compared in Fig. 10, initially guessed $\delta(x,0)$ values were approximately 16% below their corresponding long-term steady solutions. In Fig. 10, it can be seen that the attraction rate $|\partial^2\Delta/\partial t^2|_{\text{rep|(no-noise)}}$ increases with increasing speed U_∞ and, through Fig. 9, it can be seen that the attraction rate decreases with downstream distance.

Figure 11 shows, at $x=23$ and $U_\infty=2$ m/s, $\partial\Delta/\partial t$ versus t curves for different initial-guesses. It is shown in this figure that the attraction rates obtained over the time segment τ_{Rep} are, indeed, more or less independent of initial conditions and thus represent the inherent character of the attracting steady solution. This justifies the use of the magnitude of deceleration rates—given by the approximate slopes of the line segments AB, $A'B'$, etc.—as attraction rates.

The above described trends were established for R113 flows for a range of vapor speeds $0.2\ \text{m/s}\le U_\infty\le20$ m/s, a range of temperature differences $3°C\le\Delta\mathcal{T}\le15°C$, and a range of domain lengths $0\le X_e\le0.4$ m.

6.2 Stability of the "Steady Attractors"/Steady Solutions to Initial Interfacial Disturbances. The long-term steady limit of the unsteady solution was found to exist (and be the same as the steady solution of the steady problem) for this horizontal external flow problem if the inlet speed U_∞ was above a certain threshold

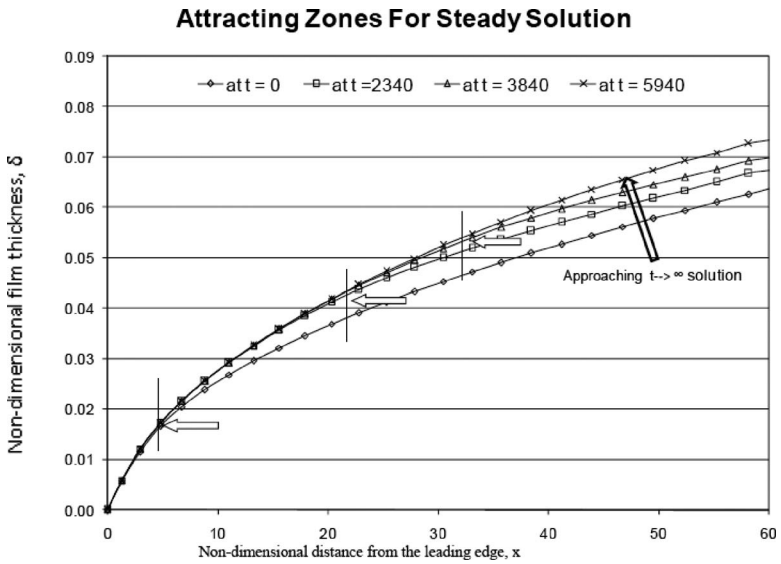

Fig. 8 For flow of R113 vapor with U_∞=1.7 m/s, $\Delta\mathcal{T}$=5°C, and g_y=0, this figure shows nondimensional film thickness values at different nondimensional times given by the unsteady solution of the problem. An initial-guess given at time t=0 (about 16% below the final long-term solution) is seen to get attracted to the long-term steady solution at different rates. The markings, at different times, demarcate the zones that have "nearly" converged to the steady solution from the zones that have not.

value (about 0.2 m/s for the example case discussed here). These solutions were tested for their response to the initial disturbances on the interface. Different vapor speeds ranging from 0.2 m/s to 25 m/s were tested for interfacial disturbances of different nondimensional wavelengths ranging from 5 to 30. Over the downstream distances investigated here, these external flows of vapor were found to be quite stable to the forward moving disturbances on the interface—whether or not transverse gravitational field was present. A representative example of this stable response to interfacial disturbances is shown in Fig. 12 where—even in the absence of the transverse component of gravity—the large initial disturbances die out for the inlet vapor speed of U_∞=3 m/s and $\Delta\mathcal{T}$=5°C. Computations show very stable response to these disturbances and all of these disturbances die out as the waves move downstream. The response to imposed disturbances in the initial (t=0) values of velocities (not shown here) was found to be similar to the ones in Fig. 12. However, the unsteady solutions, as expected, showed longer persistence (i.e., smaller decay rates) in the weakly attracting (i.e., smaller attraction rates) downstream portions of the flow. Recall that this paper has chosen the measure of attraction rates over decay rates because (a) they are computationally easier to obtain, (b) they are physically meaningful even in the nonlinear context (i.e., without the requirement of modeling time behavior by an exponential function of time), and (c) they also relate to physical attainability of steady flows. The response of the solution to disturbances when transverse downward component of gravity is present was also found to be equally stable because of the thinness of the film over the distances our computations could be implemented.

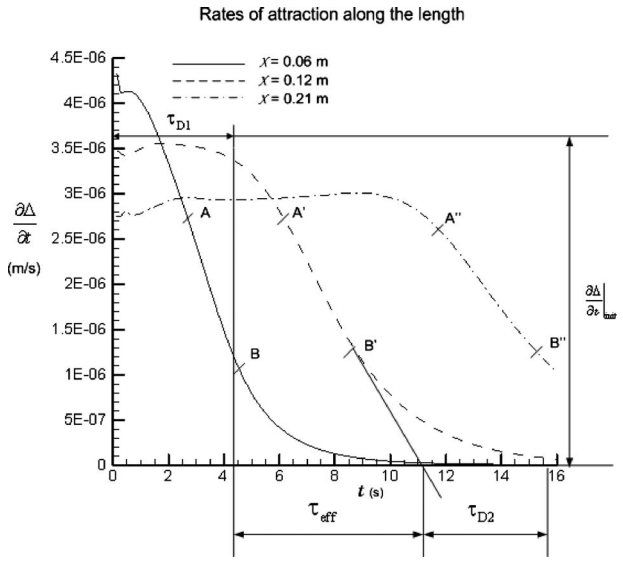

Fig. 9 For flow of R113 with U_∞=1.7 m/s, $\Delta\mathcal{T}$=5°C, and g_y=0, this figure shows different rates of attraction versus time—as indicated by different representative deceleration rates—for different x values along the length of the plate. The value of the initial attraction rate $\partial\Delta/\partial t\,(x,0)\equiv\partial\Delta/\partial t|_{\text{init}}$, as well as the strength of the attractors (as marked by the representative magnitude of deceleration rates associated with the slopes of the lines AB, $A'B'$, etc.), decreases with increasing x. The initial-guess of $\delta(x,0)$ for the unsteady solution was 16% below the long-term steady solution.

The above described response is different from the response [16] for the gravity-driven external flow problem of Nusselt [7], where the gradually speeding condensate allows disturbances on the interface to grow only after a certain critical distance x and only for wavelengths $\lambda \geq \lambda_{cr}$, where λ_{cr} is a certain critical wavelength. For gravity-driven flows, it was this inertial instability associated with speeding condensate that marked the transition from smooth laminar to wavy laminar flows. This typically happened when the condensate Reynolds number Re_δ ($\equiv 4\int_0^\Delta \rho_1 u_1(x,y)\cdot dy/\mu_1$)—which represents the size of inertia to viscous forces associated with fluctuations (a quantity which increases with x)—was computationally found to be higher than some critical value in the range of $20 \leq \mathrm{Re}_\delta \leq 40$. In contrast, the above described stable response for the Koh problem involved a much more weakly increasing Re_δ values with $\mathrm{Re}_\delta \leq 10$.

Therefore the reasons for this external flow showing very strong and stable response to initial disturbances are as follows.

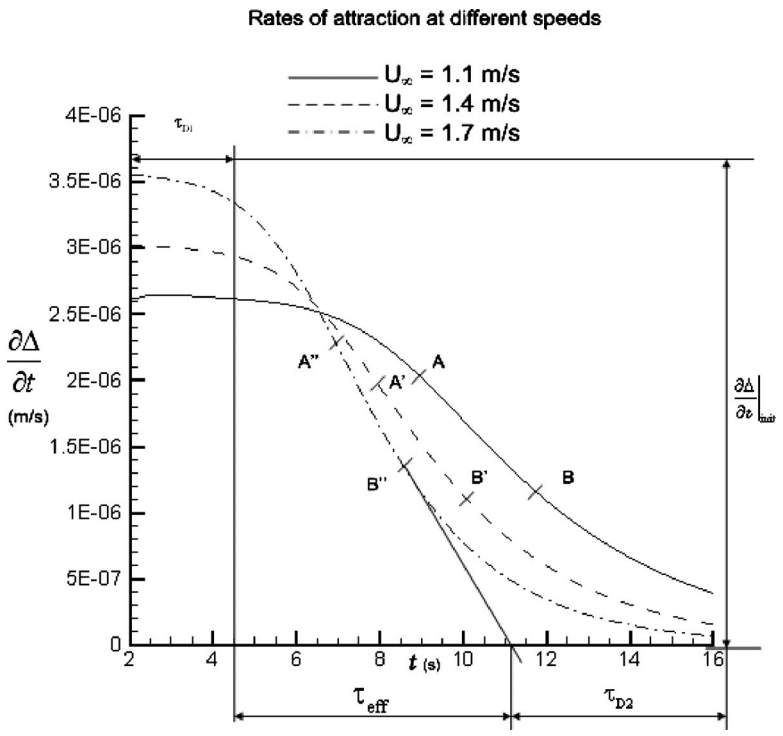

Fig. 10 For flow of R113 with $\Delta\mathcal{T}=5°C$, $g_y=0$, and $x=30$, the figure shows different rates of attraction versus time—as indicated by different representative magnitudes of deceleration rates associated with the slopes of the lines *AB*, *A′B′*, etc.—at different vapor speeds. The initial-guess of $\delta(x,0)$ for the unsteady solution was 16% below the long-term steady solution. The figure demonstrates higher rates of attraction for higher speeds.

- The condensate flow is slow because it is not driven by gravity, and hence, the mechanism for the wave evolution on the interface is very different as compared with the gravity-driven flows in which the liquid condensate accelerates.
- The well defined far-field pressure prescription of p_∞ (along *AB* and *BD′* in Fig. 1) and the process of condensation (mass transfer at the interface) make the flow more stable as compared with the known Kelvin–Helmholtz instability (see Refs. [24,25]) for adiabatic (air water type) flows, which do not involve gas-phase suction or mass transfer into the liquid phase. As shown in Fig. 12, this well-known dynamic instability for adiabatic flows is truly suppressed. This suppression of Kelvin–Helmholtz instability for the interface is over and above the earlier described issue of delayed transition to turbulence in the vapor boundary layer due to vapor suction effects.

Despite the fact that, in the presence of nonzero interfacial mass-flux, these flows show no instabilities over the distances considered, one still expects that at larger downstream distances, the flow will undergo transition to waviness whether or not transverse gravity is present.

6.3 Sensitivity of "Attractors"/Steady Solutions to Persistent Condensing-Surface Noise. Irrespective of their stability to initial disturbances superposed on the interface, the stable solutions obtained for this external condensing flow over a horizontal plate are found to be sensitive to small and persistent condensing-surface noise of standing wave types—whose single representative Fourier component is modeled, as shown in Fig. 13. While response of condensing flows to these types of noise has been considered for internal condensing flows in Refs. [18,19] and also for an external condensing flow [16], this paper reports, for the first time, a quantitative analysis of the resulting wave forms along with a quantitative measurement of the resulting noise-sensitivity. The ever-present miniscule condensing-surface noise is assumed to have a standing wave pattern in transverse displacement of the plate (of the type indicated in Fig. 13) with a representative Fourier component of the form

$$\mathcal{D}_w(x,t) = \mathcal{D}_{\max} \sin\frac{2\pi x}{\lambda_p} \cdot \cos 2\pi f_p t \tag{18}$$

where $\lambda_p(\equiv \lambda \cdot Y_e)$ is a physical wavelength ($\geq$ 0.02 m), f_p ($\equiv f \cdot U_\infty / Y_e$) is a physical frequency (0–15 Hz), and $\mathcal{D}_{\max}$ is a physical amplitude ($0-5$ μm) with which the condensing-surface is likely to vibrate under typical ever-present noise conditions that are neither seen nor heard. The flow sees this noise through the following boundary-condition for the vertical component of liquid velocity at the bottom wall location ($y=0$):

$$v_1(x,0,t) = v_{\max} \sin(2\pi x/\lambda_p) \cdot \sin(2\pi f_p t) \tag{19}$$

Since, $v_1(x,0,t) = \partial \mathcal{D}_w(x,t)/\partial t$, it follows that the amplitude $v_{\max}(\equiv \varepsilon_w \cdot U_\infty)$ in Eq. (19) above is related to $\mathcal{D}_{\max}$ in Eq. (18) by

$$v_{\max} = -2\pi \mathcal{D}_{\max} f_p \tag{20}$$

It has been established—by postprocessing the details of the resulting wave forms—that the response of the interface is of the form

$$\Delta(x,t) - \Delta(x)_{\text{steady}} = \{a(x)\sin[(2\pi x/\lambda_p) + \gamma_0(t)] \cdot \cos[(2\pi f_p t) + \psi_0(x)]\} \tag{21}$$

where $a(x)$ is the x-dependent amplitude of the resulting standing wave pattern on the interface. Thus, waves on the interface, in response to the bottom wall noise, do have the same spatial wavelength λ_p and temporal frequency f_p as that of the displacement

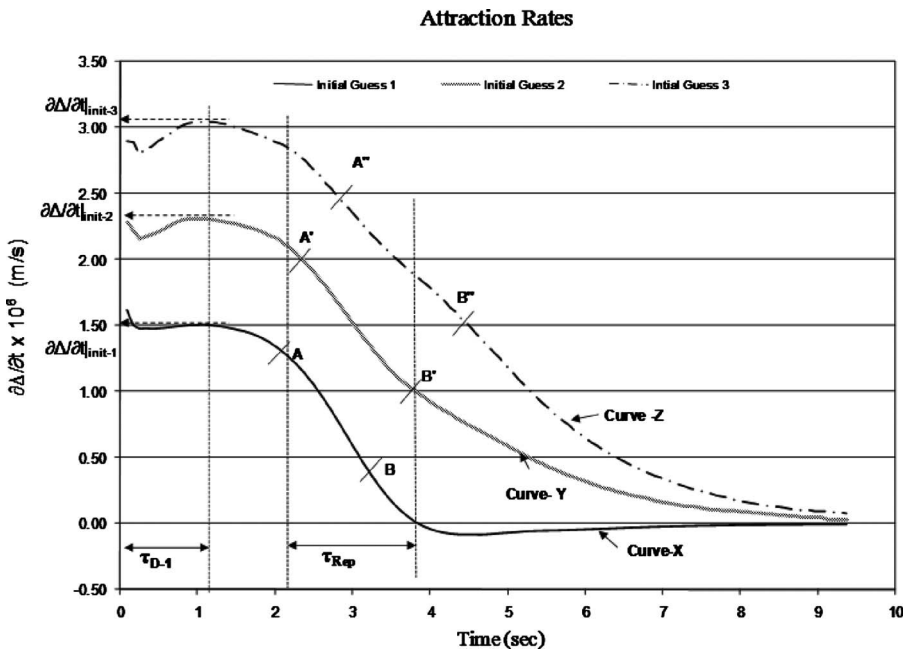

Fig. 11 This figure shows computationally obtained curves depicting the rate of change in film thickness at $x=23$ when the unsteady solutions approach the same long-term steady attractor from three different initial-guesses for flow of R113 vapor at $U_\infty=2$ m/s, $g_y=0$, and $\Delta\mathcal{T}=5°C$. The three initial-guesses 1, 2, and 3 are, respectively, 2%, 5%, and 7% away from the unique long-term steady attractor. The subsequent time duration (marked τ_{Rep}) over which a nearly constant deceleration rate ($\partial^2\Delta/\partial t^2$) exists is marked by nearly equal constant decelerating slopes of lines AB, $A'B'$, and $A''B''$ on curves X, Y, and Z. This shows that for a given vapor speed, the above characterized attraction rates over τ_{Rep} are associated with the long-term steady solutions rather than the values of the initial-guesses.

noise component $\mathcal{D}_w(x,t)$ experienced by the condensing-surface. However, the phases of the interfacial waves slightly differ from that of the condensing-surface's transverse displacement wave. The spatial phase difference is time dependent and is denoted by $\gamma_0(t)$ and the temporal phase difference is location dependent and is denoted by $\psi_0(x)$. Figure 14 shows the unsteady interface at

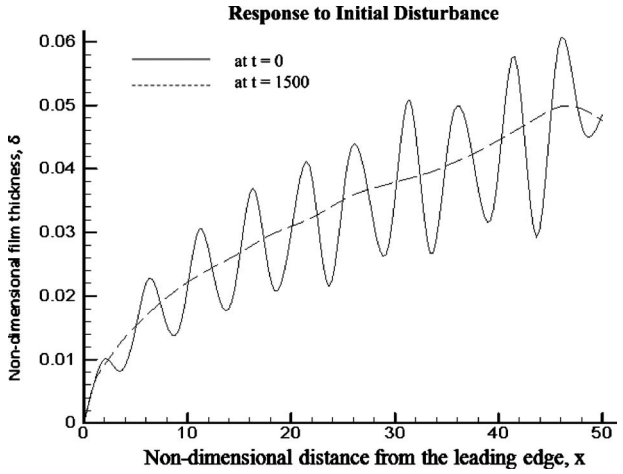

Fig. 12 For flow of R113 vapor with $U_\infty=3$ m/s, $x_e=50$, $\Delta\mathcal{T}=5°C$, and $g_y=0$, this figure shows the stable response of the long-term steady solution to the rather large initial disturbance given at time $t=0$. The nondimensional disturbance is given as $\delta(x,0)=\delta_{steady}(x)\ [1+\varepsilon_o\delta'(x,0)]$, where $\delta'(x,0)\equiv\sin(2\pi x/\lambda_o)$, $\varepsilon_o=0.35$, and $\lambda_o=5$. The disturbance dies out, almost completely, by the time $t=1500$.

different times in response to the representative condensing-surface noise. For the cases considered in this paper, over a wide range of different affecting parameters, it is found that the amplitude $a(x)$ of these interfacial waves increases with x and can be determined. However, spatial phase difference function $\gamma_0(t)$ is a sufficiently weak function of time and the temporal phase difference $\psi_0(x)$ is a sufficiently weak function of space that they cannot be determined, with sufficient precision, with the help of the simulation tool employed here. The spatially growing noise-induced waves are expected to be related to Re_δ values—which represent both the cross-sectional liquid mass-flux and the effects of local interfacial mass-flux $\dot{m}$. The noise-sensitive values of the amplitudes $a(x)(\equiv a(x)/Y_e)$ of these interfacial waves were computationally obtained for different flow cases for a range of different nondimensional parameters, viz., wavelength $\lambda(\equiv\lambda_p/Y_e)$, bottom wall velocity amplitude $\varepsilon_w(\equiv v_{w\max}/U_\infty)$, and frequency $f(f\equiv 1/T_w\equiv f_p\cdot Y_e/U_\infty)$. The amplitude $a(x)$ values were measured by looking at several peak values of computationally obtained $\delta(x,t)-\delta(x)_{steady}$ signals in the space-time domain. After obtaining the values of $a(x)$ at different x locations, for different flow cases involving different $\mathcal{D}_{max}$ values, linear curves—as in Fig. 15—were found to be adequate fits to the data of $a(x)$ over the range of distances considered. This linear relation can be expressed as

$$a(x)/\mathcal{D}_{max}=\overline{c_1}x+c_2 \tag{22}$$

where $\overline{c_1}$ and c_2 are, respectively, found to be 120.9 (m^{-1}) and 3.00 for R113 flow parameters indicated in the inset of Fig. 15.

6.4 Nonattainability of Steady Film Flows at Lower Vapor Speeds. The computational results presented earlier in this paper were mainly for R113 vapor flows at speeds 10 m/s $> U_\infty$

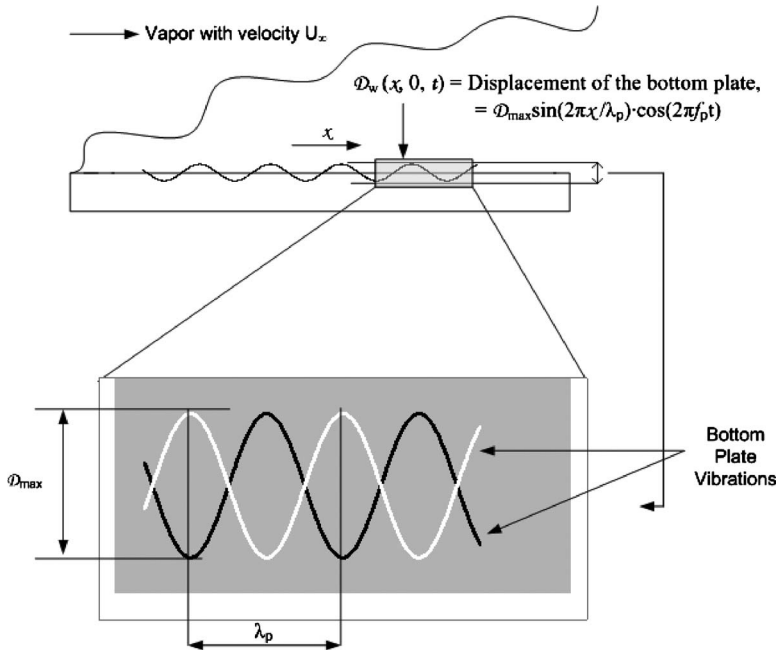

Fig. 13 This figure depicts the definition of the type of miniscule ever-present noise given to the condensing-surface to investigate the sensitivity of condensing flows to persistent disturbances. The inset shows the displacement profile of the condensing-surface at two out-of-phase instants associated with a mode of the standing wave.

>0.2 m/s. As one approaches the lower vapor speeds ($U_\infty \leq 0.2$ m/s) in Fig. 16, unsteady solutions show nonexistence of a steady long-term ($t\to\infty$) limit that exists for $U_\infty > 0.2$ m/s. One is tempted to say that the steady solution for $U_\infty > 0.2$ m/s loses stability as speed U_∞ is lowered further but the situation is different because one does not find, at least computationally, a steady solution for $U_\infty < 0.2$ m/s. Since one does not have a steady solution in this range, one cannot say that the steady solution for $U_\infty < 0.2$ m/s has lost its stability. This nonexistence of a steady limit is a gradual phenomenon, which is depicted in Fig. 16. The

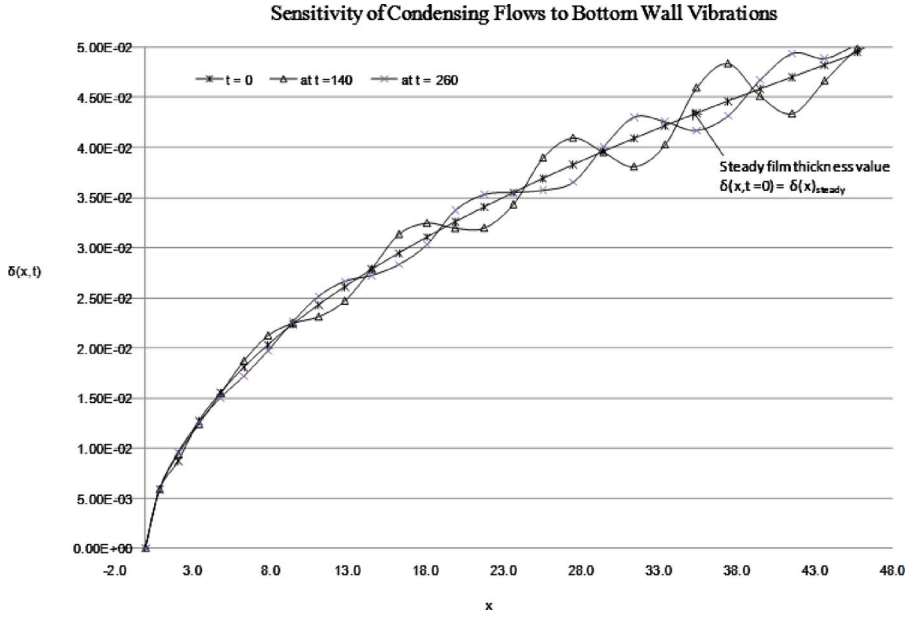

Fig. 14 For R113 vapor with $U_\infty = 3$ m/s, $x_e = 48$, $\Delta\mathcal{T} = 5°C$, and $g_y = 0$, this figure shows unsteady response of the flow to the typical condensing-surface noise with $\lambda(\equiv\lambda_p/Y_e) = 10$, $T_w(\equiv U_\infty/(f_p\cdot Y_e)) = 240$, and $\varepsilon_w(\equiv v_{max}/U_\infty) = 3\times10^{-6}$. The noise given to the condensing-surface is represented as $v_1(x,0,t) = v_{max}\sin(2\pi x/\lambda_p)\cdot\sin(2\pi f_p t)$, where $v_1(x,0,t)$ is condensing-surface velocity. The figure shows nondimensional film thickness $\delta(x,t)$ plotted versus x at two different nondimensional times $t = 140$ and $t = 260$. The steady film thickness values $\delta(x)_{steady}$ are shown as an initial solution at time $t = 0$.

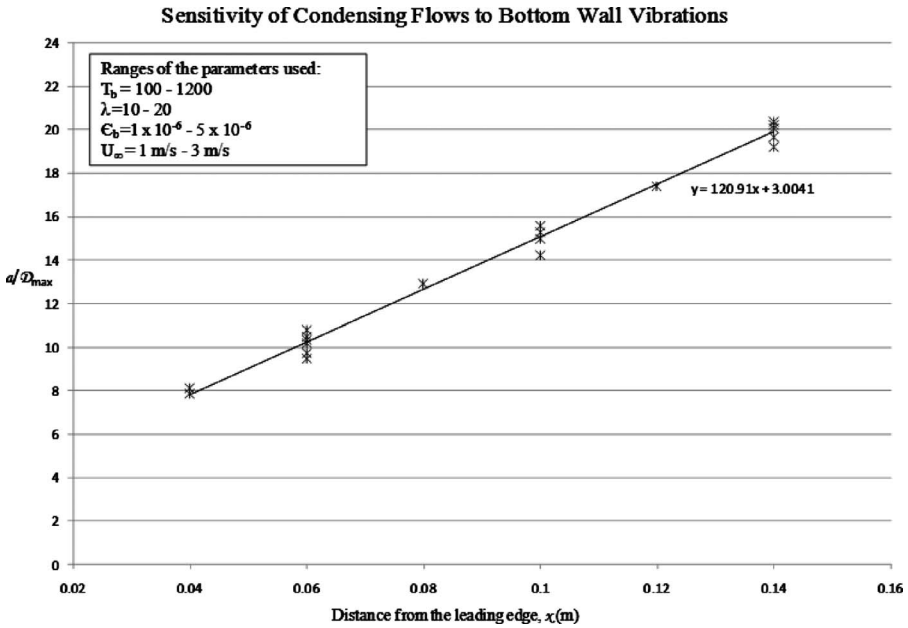

Fig. 15 For different ranges of non-dimensional condensing-surface noise parameters, namely: time period $T_w=T_b$, wavelength λ, and condensing-surface velocity vibration amplitude $\varepsilon_b=\varepsilon_w$, and different vapor speeds U_∞; this figure plots computationally obtained nondimensional $a/\mathcal{D}_{max}$ values (amplitude of interfacial waves divided by amplitude of bottom wall displacement waves) against dimensional values of $x(=x\cdot Y_e)$. The range of R113 vapor (with $g_y=0$) flows considered here is described in the inset.

signs of nonexistence of a steady limit is especially apparent in the aft portion of the flow for vapor speed $U_\infty=0.08$ m/s. This is different than noise-sensitive steady limits discussed earlier for higher speeds (also see $U_\infty=0.2$ m/s in Fig. 16, which exhibits existence of a steady limit). This fact is more apparent through Fig. 17, which plots long-term physical values of rate of change in film thickness ($\partial\Delta/\partial t$) at a fixed x location ($x=30$). It can be seen that as vapor speed reduces below some critical value (below 0.2 m/s), the rate of change in film thickness starts increasing indicating above its effectively zero value (which is defined in Fig. 17,

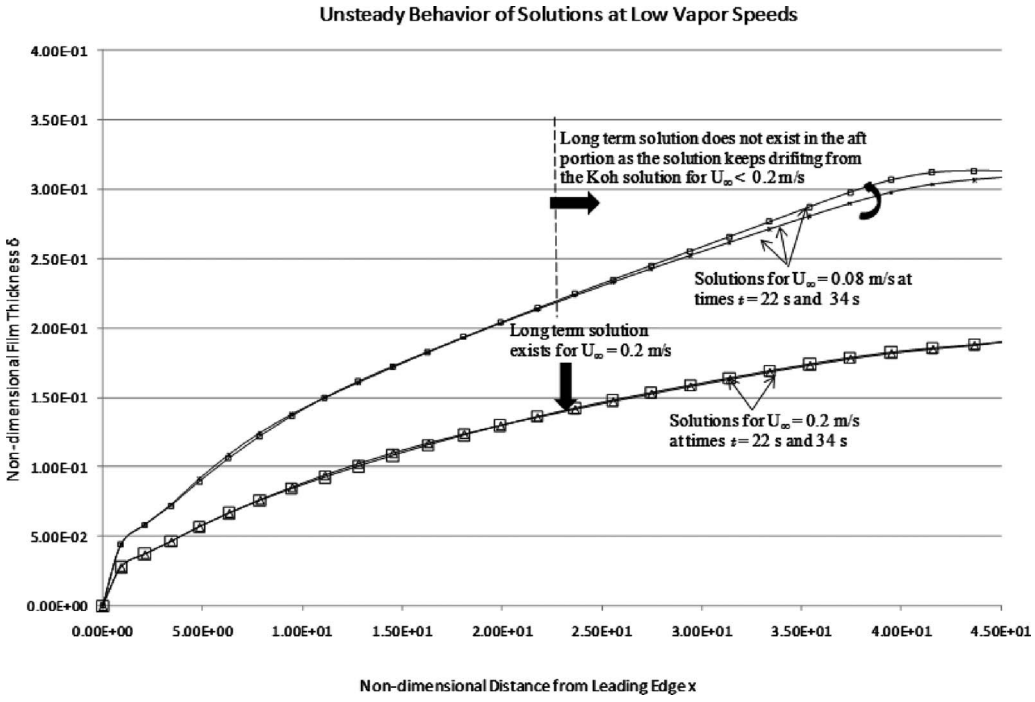

Fig. 16 The figure plots two different sets (for $U_\infty=0.2$ m/s and $U_\infty=0.08$ m/s) of long-term film thickness values $\delta(x,t)$ with x at large nondimensional times $t=22$ s and 34 s. The flows are of R113 vapor at $\Delta\mathcal{T}=5$°C and initial conditions (not shown) for each of these cases were the Koh similarity solution [2]. For $U_\infty<0.2$ m/s, the aft portions of these curves suggest nonexistence of $\lim_{t\to\infty}\delta(x,t)$.

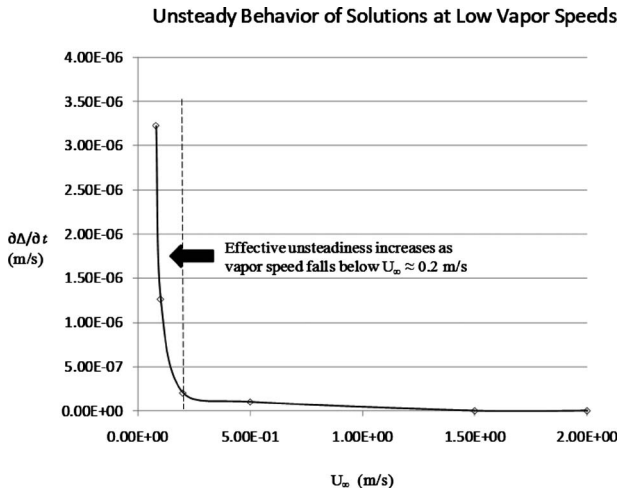

Fig. 17 The figure plots long-term steadiness measure $|\partial\Delta/\partial\mathcal{T}|$ (estimated at $x=40$) with freestream speed U_∞. The flows are of R113 vapor at $\Delta\mathcal{T}=5°C$. The values of $|\partial\Delta/\partial\mathcal{T}|$ for $U_\infty > 0.2$ m/s is considered effectively zero within computational error. This suggests existence of a long time steady solution. However, the rising positive values of $|\partial\Delta/\partial\mathcal{T}|$ for $U_\infty < 0.2$ m/s suggest nonexistence of a long time steady solution.

within computational errors, to be 1.5×10^{-7}). This sustained unsteadiness at such low vapor speeds implies nonattainment of any limiting steady solution of the film condensation type, and one expects an eventual long time behavior that involves a more complex liquid-vapor morphology.

It is known that, as vapor speed reduces, the available shear stress for driving the thin liquid film reduces and, also, more kinetic energy of the vapor is deflected away from the condensate (the upward bending streamlines in Fig. 5 cover more of the leading edge and pressure gradients near the leading edge—as shown in Figs. 3 and 4—become sharper). The gradualness of the loss of the above described steady limit (i.e., existence of steady filmwise solution) is further demonstrated by insufficient availability of mechanical energy (i.e., near zero values of viscous dissipation rates in Fig. 18).

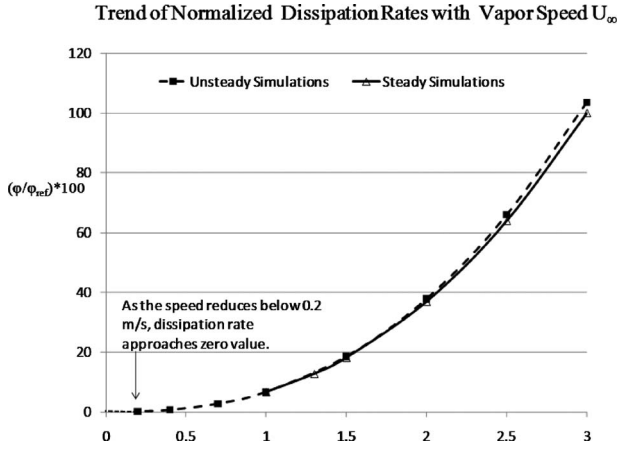

Fig. 18 For flow of R113 vapor with $\Delta\mathcal{T}=5°C$, $X_e=0.2$ m, and $g_y=0$, this figure plots normalized viscous dissipation rates φ/φ_{ref} (see Eq. (A13) in the Appendix for the definition of φ) obtained from steady and unsteady (long-term) steady solutions in a representative control volume given by $0<x<40$ and $0<y<0.5$. As the vapor speed U_∞ reduces below 0.2 m/s, dissipation rates can be seen becoming effectively equal to the zero value associated with $U_\infty=0$.

When we plot, in Fig. 18, the viscous dissipation rate φ (see Eq. (A13) in the Appendix) at which energy is dissipated in the interior of the vapor and the liquid phases inside any representative control volume for which long-term steady solutions exist, it is observed that, as vapor speed decreases (and approaches values below $U_\infty=0.2-0.3$ m/s), the dissipative energy *asymptotically* approaches negligible or near zero values. Figure 18 shows normalized dissipative energies (φ/φ_{ref}) as obtained by steady as well as long-term steady solutions of this problem in a representative control volume defined by $0<x<40$ and $0<y<0.5$. Even though the energy dissipated in any control volume depends on its size, it was observed that the normalized values follow exactly the same trend irrespective of the size of the control volume. Here the normalizing dissipation rate φ_{ref} is the value of φ for the chosen control volume at speed $U_\infty=3$ m/s. In Fig. 18, the value of $\varphi_{ref}=3.48\times10^{-2}$ W for $U_\infty=3$ m/s and a control volume defined by $0<x<40$ and $0<y<0.5$. For vapor speeds between 1 m/s $<U_\infty<3$ m/s, the thick line in Fig. 18 shows φ/φ_{ref} values as obtained from the steady solutions while the dotted line in Fig. 18 shows φ/φ_{ref} values obtained from long-term steady limits of unsteady solutions for 0.2 m/s $<U_\infty<3$ m/s. There were some algorithmic issues in the steady solver for 0.2 m/s $<U_\infty<1$ m/s whose improvements were not considered necessary and therefore were not included for results in Fig. 18. It should be noted that the integral *theorem on expended mechanical power* (see Chap. 15, Ref. [26]) or the integral form of *mechanical energy equation* (see Eq. (5.4.13) of Ref. [27]) says that a steady solution exists if and only if $\varphi/\varphi_{ref}>0$, and this condition is hard to satisfy in Fig. 18 for 0 m/s $<U_\infty<0.2$ m/s because the energy for $U_\infty=0$, where the theorem is violated, is effectively equivalent to the energy at $U_\infty=0.2$ m/s. This fact that energy available to dissipate at $U_\infty<0.2$ m/s (say, $U_\infty=0.08$ m/s) is effectively the zero value associated with $U_\infty=0$ should lead to a response that is also somewhat similar to what is expected at $U_\infty=0$ and fixed $\Delta\mathcal{T}$. Clearly, for $U_\infty=0$ and fixed $\Delta\mathcal{T}$, one expects a rising unsteady film type solution, which is similar to what is being found in Fig. 17. However, the flow for $0<U_\infty<0.2$ m/s also has an option to come to a new quasisteady flow under a more complex liquid/vapor morphology.

Because of the mutually supportive nature of the above described independent facts, one can reliably state that filmwise steady condensation solution for this problem is not possible for effectively zero inlet speeds that correspond to a certain finite range of values of the type $0<U_\infty<U_\infty^*$. This result states that Koh solution [2] for $0<U_\infty<U_\infty^*$ is not valid.

6.5 Additional Sensitivity of These Shear-Driven Flows. The above described steady solution, under uniform far-field pressure ($p=p_\infty$) assumption, shows stability for $U_\infty>U_\infty^*$ with possible attainability issues (for nonzero transverse gravity) and increasing waviness issues only after a sufficiently large downstream distance x. Note that shear-driven film condensation flows are extremely sensitive because, unlike gravity-driven flows, the liquid condensate motion is driven by vapor motion and it takes minuscule pressure differences to change vapor motion. Therefore any difficulty in experimentally achieving far-field uniform pressure ($p=p_\infty$) condition—particularly near the downstream zones of far-field locations—will additionally limit the attainability of steady filmwise condensation for this problem. Furthermore, besides the fact that similar sensitivity is found for shear-driven internal condensing flows (as described in the Introduction), the role of various boundary-conditions was also discussed, for finite horizontal plates, by Prasad and Jaluria [28]. It should be further noted that these "structural" sensitivities and instabilities associated with shear-driven annular or film condensation flows are not present for the gravity-driven condensing flows [7,16].

7 Conclusions

For the ranges of the flow parameters investigated, the Koh solution [2] for film thickness is found to be reasonably accurate for horizontal condensing flows over a flat plate under conditions of sufficiently fast vapor speeds and nearly uniform far-field pressure p_∞. Over this range, it is found that there is some departure from the Koh solution [2] in the frontal portion of the plate with regard to the values of interfacial velocities and pressure variations in the liquid and vapor domains. The gradients in pressure become sharper as vapor speed reduces and such dynamics cannot be captured using the analytical solution of Koh [2].

The results show that the presence or absence of transverse component of gravity does not change the steady solution by much if only a certain length from the leading edge (lengths investigated here) is considered. Over this length only changes in the hydrostatic pressure variations, resulting from presence or absence of gravitational component of pressure, are observed in the liquid film.

For the ranges of the flow parameters investigated here for R113, unsteady solutions predicted that there exists a long-term ($t \to \infty$) steady solution (*attractor*) for this external condensing flow problem. A measure termed attraction rate is introduced for the reported "nonlinear" stability analysis. This value decreases with increasing distance and increases with increasing vapor speeds. The qualitative and quantitative variations in the strength of the attractor are presented for the cases of $U_\infty > 0.2$ m/s. Unsteady results, along with several supporting results, find that at low vapor speeds ($0 < U_\infty < U_\infty^* \approx 0.2$ m/s) a filmwise steady solution does not exist.

It is established here that the steady solutions for sufficiently fast external flows and up to certain downstream distances are sensitive to persistent noise leading to increasing wave amplitudes with distance. However, the smooth underlying steady solutions for these cases are stable to the momentary initial disturbances (of various wavelengths and amplitudes) on the interface.

The computational results and physics indicate that the stable attracting solutions for this condensing flow over a horizontal plate are not only expected to become very sensitive, at large downstream distances, to persistent but minuscule condensing-surface noise but, also, perhaps to presence of transverse gravity and any experimental difficulties in maintaining uniform pressure conditions in the far-field downstream regions.

Acknowledgment

This work was supported by NASA Grant No. NNC04GB52G.

Nomenclature

C_p = specific heat, J/(kg K)
$\mathcal{D}_{\max}$ = displacement amplitude of waves on the condensing-surface, m
f = nondimensional frequency f_p of bottom wall vibrations given by $1/T_b \equiv f_p \cdot Y_e/U_\infty$
f_p = physical value of frequency of bottom wall vibrations, Hz
Fr = Froude number U_∞^2/gY_e
Ja = Jakob number given by $C_{p1}\Delta\mathcal{T}/h_{fg}$
h_{fg} = latent heat, J/kg
k = thermal conductivity, W/(m K)
$\dot{m}$ = nondimensional value of interfacial mass-flux, $\dot{m} \equiv \dot{m}/(\rho_1 \cdot U_\infty)$
$\dot{m}$ = physical value of interfacial mass-flux, kg/(m^2 s)
ni = representative number of grid points in the x direction for simulations
nj = representative number of grid points in the y direction for simulations
p = pressure, N/m^2
p_∞ = pressure far field, N/m^2
Pr_I = Prandtl number $\mu_I C_{pI}/k_I$
Re_δ = film Reynolds number, $4\rho_1 u_{1\mathrm{avg}}(x)\Delta(x)/\mu_1$
T_w = nondimensional time period of condensing-surface vibrations
$\mathcal{T}$ = temperature, K
t = physical value of time, s
U_∞^* = lower threshold of vapor speed U_∞ given by simulations for filmwise condensation, m/s
U_∞ = far upstream vapor speed, m/s
(u,v) = values of x- and y-components of velocity, m/s
(u,v) = nondimensional values of u and v, $(u,v) \equiv (u/U_\infty, v/U_\infty)$
$v_{\max}$ = physical value of the amplitude of a standing velocity wave associated with condensing-surface noise, m/s
We = Weber number, $\rho_1 U_\infty^2 Y_e/\sigma$
x_e = nondimensional value of domain length, X_e/Y_e
x^* = distance from the leading edge beyond which pressure gradient in liquid or vapor domain is nearly equal to zero, m
x^* = nondimensional value of $x^*, x^*/Y_e$
X_e = physical value of domain length (distance from leading edge *BC* in Fig. 1), m
x_e = nondimensional value of domain length, X_e/Y_e
x = physical value of distance along x direction, m
(x,y,t) = nondimensional values of $(x,y,t) \equiv (x/Y_e, y/Y_e, (t \cdot U_\infty/Y_e))$ in the computational and problem formulation context
Y_e = characteristics length (*OA* in Fig. 1), m
y = physical value of distance along y direction, m
$\Delta\mathcal{T}$ = temperature difference between the vapor and the condensing-surface, °C
φ = rate of energy dissipation inside a flow domain, W

Greek Symbols

π_I = nondimensional pressure, $p_I/(\rho_I \cdot U_\infty^2)$
θ = nondimensional temperature, $\mathcal{T}/\Delta\mathcal{T}$
ρ = density, kg/m^3
μ = viscosity, Pa s
Δ = physical value of condensate film thickness, m
δ = nondimensional value of condensate thickness, Δ/Y_e
ν = kinematic viscosity μ/ρ, m^2/s
σ = surface tension, N/m
λ = nondimensional wavelength for the bottom wall vibrations ($\lambda = \lambda_p/Y_e$)
λ_p = physical/dimensional value of wavelength for the bottom wall vibrations, m
λ_o = nondimensional wavelength for the initial disturbance $\delta'(x,0)$ on the interface
δ' = nondimensional value of disturbance on the interface

Subscripts

I = it takes a value of 1 for liquid phase and 2 for vapor phase
s = saturation condition
w = condensing-surface

Superscripts

i = value of a variable at an interface location

Appendix

The differential forms of mass, momentum (x- and y-components), and energy equations in terms of nondimensional

variables for flows in the interior of either of the phases ($I=1$ or 2) for this external flow are given as

$$\frac{\partial u_I}{\partial x} + \frac{\partial v_I}{\partial y} = 0 \tag{A1}$$

$$\frac{\partial u_I}{\partial t} + u_I\frac{\partial u_I}{\partial x} + v_I\frac{\partial u_I}{\partial y} = -\left(\frac{\partial \pi_I}{\partial x}\right) + \frac{1}{\mathrm{Re}_I}\left(\frac{\partial^2 u_I}{\partial x^2} + \frac{\partial^2 u_I}{\partial y^2}\right) \tag{A2}$$

$$\frac{\partial v_I}{\partial t} + u_I\frac{\partial v_I}{\partial x} + v_I\frac{\partial v_I}{\partial y} = -\left(\frac{\partial \pi_I}{\partial y}\right) + \mathrm{Fr}_y^{-1} + \frac{1}{\mathrm{Re}_I}\left(\frac{\partial^2 v_I}{\partial x^2} + \frac{\partial^2 v_I}{\partial y^2}\right) \tag{A3}$$

$$\frac{\partial \theta_I}{\partial t} + u_I\frac{\partial \theta_I}{\partial x} + v_I\frac{\partial \theta_I}{\partial y} \approx \frac{1}{\mathrm{Re}_I\ \mathrm{Pr}_I}\left(\frac{\partial^2 \theta_I}{\partial x^2} + \frac{\partial^2 \theta_I}{\partial y^2}\right) \tag{A4}$$

where $\mathrm{Re}_1 \equiv \rho_1 U_\infty Y_e/\mu_1$, $\mathrm{Pr}_1 \equiv \mu_1 C p_1/k_1$, and $\mathrm{Fr}_y^{-1} \equiv g_y Y_e/U_\infty{}^2$.

The term $[t]$ on the right side of Eq. (4) is given by

$$[t] = \left\{ \frac{\mu_2}{\mu_1}\frac{\partial v_2}{\partial x}\bigg|^i - \frac{\partial v_1}{\partial x}\bigg|^i \right\} + \frac{2\delta_x}{[1-\delta_x^2]}\left\{ \frac{\partial u_1}{\partial x}\bigg|^i - \frac{\partial v_1}{\partial y}\bigg|^i \right\} - \frac{2\delta_x}{[1-\delta_x^2]}\frac{\mu_2}{\mu_1}\left\{ \frac{\partial \mu_2}{\partial x}\bigg|^i - \frac{\partial v_2}{\partial y}\bigg|^i \right\} + \frac{\mathrm{Ma}(\partial \pi_2/\partial x|^i)}{\sqrt{1+\delta_x^2}} \tag{A5}$$

where $\mathrm{Ma} \equiv \rho_2 U_\infty c_1 d_1/\mu_1$ is a Marangoni number, $c_1 \equiv d\mathcal{T}_s/dp$, and $d_1 \equiv -d\sigma/d\mathcal{T}$.

Under the assumptions of uniform pressure throughout the flow, steadiness ($\partial/\partial t = 0$), horizontalness ($g_x = 0$), and boundary-layer approximations ($\partial/\partial x \ll \partial/\partial y$ and $v_I \ll u_I$) associated with thin condensate flow; the Koh formulation [2] effectively replaces Eqs. (A2)–(A4) with

$$u_I\frac{\partial u_I}{\partial x} + v_I\frac{\partial u_I}{\partial y} \cong \frac{1}{\mathrm{Re}_I}\frac{\partial^2 u_I}{\partial y^2}$$

$$-\frac{\partial \pi_1}{\partial y} + \mathrm{Fr}_y^{-1} \cong 0 \tag{A6}$$

$$u_I\frac{\partial \theta_I}{\partial x} + v_I\frac{\partial \theta_I}{\partial y} \approx \frac{1}{\mathrm{Re}_I\ \mathrm{Pr}_I}\left(\frac{\partial^2 \theta_I}{\partial y^2}\right)$$

In addition to the above, the Koh formulation [2] also assumes negligible interfacial slope approximation ($\delta'(x)^2 \ll 1$) and, as a result, interface conditions given by Eqs. (2)–(6) in Sec. 2 are simplified and, respectively, replaced with

$$u_2^i = u_1^i \tag{A7}$$

$$\pi_1^i = \frac{\rho_2}{\rho_1}\pi_2^i \tag{A8}$$

$$\frac{\partial u_1}{\partial y}\bigg|^i = \frac{\mu_2}{\mu_1}\frac{\partial u_2}{\partial y}\bigg|^i \tag{A9}$$

$$\dot{m}_{LK} \equiv [u_1^i(d\delta/dx) - v_1^i]$$
$$\dot{m}_{VK} \equiv (\rho_2/\rho_1)[u_2^i(d\delta/dx) - v_2^i] \tag{A10}$$

$$\dot{m}_{\mathrm{energy}} \equiv \mathrm{Ja}/(\mathrm{Re}_1\ \mathrm{Pr}_1)\{\partial\theta_1/\partial y|^i - (k_2/k_1)\,\partial\,\theta_2/\partial y|^i\} \tag{A11}$$

The remaining interface conditions given by Eqs. (7) and (8) in Sec. 2 continue to hold as they need no further approximations. Furthermore, for the Koh formulation [2], no top or exit condition regarding pressure is necessary. Instead, the inlet and the far-field conditions, respectively, become

$$u_2(0,y) = U_\infty \quad \text{and} \quad \lim_{y\to\infty} u_2(x,y) = U_\infty \tag{A12}$$

Total *integral* viscous dissipation rate $\varphi(=\varphi_1+\varphi_2)$ inside any control volume is obtained from *power law theorem* [26] or the integral form of *mechanical energy equation* (see Ref. [27]) for individual liquid and vapor domains and then adding them together. For any control-volume "CVf-total" of the type *OABD* in Fig. 1, if one denotes the liquid-vapor interface by Σ, the bounding surface by "CSf-total," unit normal on the bounding surface by **n**, it results in the following expression:

$$\varphi = \int_{\text{Csf-total}} -p_{\mathrm{rel}}(\mathbf{n}\cdot\mathbf{V})da + \int_\Sigma \left[\frac{\dot{m}}{\rho_1} - \frac{\dot{m}}{\rho_2}\right]p_{\mathrm{rel}}da - 0.5\int_{\text{Csf-total}} \rho|\mathbf{V}|^2(\mathbf{n}\cdot\mathbf{V})da - 0.5\int_\Sigma \dot{m}[|\mathbf{V}_2^i|^2 - |\mathbf{V}_1^i|^2]da \tag{A13}$$

where $p_{\mathrm{rel}} \equiv p - p_\infty$ is the relative value of absolute pressure $p = p_I$ ($I=1$ or 2) with respect to the far-field pressure p_∞.

References

[1] Cess, R. D., 1960, "Laminar Film Condensation on a Flat Plate in the Absence of a Body Force," Z. Angew. Math. Phys., **11**, pp. 426–433.

[2] Koh, J. C. Y., 1962, "Film Condensation in a Forced-Convection Boundary-Layer Flow," Int. J. Heat Mass Transfer, **5**, pp. 941–954.

[3] Rose, J. W., 1998, "Condensation Heat Transfer Fundamentals," Trans. Inst. Chem. Eng., Part A, **76**, pp. 143–152.

[4] Balasubramaniam, R., Nayagam, V., Hasan, M. M., and Khan, L., 2006, "Analysis of Heat and Mass Transfer During Condensation Over a Porous Substrate," Ann. N.Y. Acad. Sci., **1077**, pp. 459–470.

[5] Sparrow, E. M., and Gregg, G. L., 1959, "A Boundary Layer Treatment of Laminar Film Condensation," ASME J. Heat Transfer, **81**, pp. 13–18.

[6] Koh, J. C. Y., Sparrow, E. M., and Hartnett, J. P., 1961, "The Two-Phase Boundary Layer in Laminar Film Condensation," Int. J. Heat Mass Transfer, **2**, pp. 69–82.

[7] Nusselt, W., 1916, "Die Oberflächenkondesation des Wasserdampfes," Z. Ver. Dtsch. Ing., **60**(27), pp. 541–546.

[8] Incropera, F. P., and DeWitt, D. P., 1996, *Fundamentals of Heat and Mass Transfer*, 4th ed., Wiley, New York.

[9] Mitra, S., Narain, A., Kulkarni, S., Naik, R., and Kurita, J. H., 2009, "Annular/Stratified Internal Condensing Flows in Millimeter to Micrometer Scale Ducts," *Proceedings of the ASME Second Micro/Nanoscale Heat and Mass Transfer International Conference*, Shanghai, China, Dec. 18–22, Paper No. MNHMT 2009-18507.

[10] Rabas, T. J., and Arman, B., 2000, "Effects of the Exit Condition on the Performance of In-Tube Condensers," Heat Transfer Eng., **21**(1), pp. 4–14.

[11] Chen, Y. P., and Cheng, P., 2005, "Condensation of Steam in Silicon Microchannels," Int. Commun. Heat Mass Transfer, **32**, pp. 175–183.

[12] Wu, H. Y., and Cheng, P., 2005, "Condensation Flow Patterns in Microchannels," Int. J. Heat Mass Transfer, **48**, pp. 2186–2197.

[13] Coleman, J. W., and Garimella, S., 2003, "Two-Phase Flow Regimes in Round, Square, and Rectangular Tubes During Condensation of Refrigerant R134a," Int. J. Refrig., **26**, pp. 117–128.

[14] Garimella, S., 2004, "Condensation Flow Mechanisms in Microchannels: Basis for Pressure Drop and Heat Transfer Models," Heat Transfer Eng., **25**, pp. 104–116.

[15] Mitra, S. A., Narain, R., and Kulkarni, S. D., 2010, "A Quasi One Dimensional Method and Results for Steady Annular/Stratified Shear and Gravity Driven Condensing Flows," Int. J. Heat Mass Transfer, submitted.

[16] Phan, L., and Narain, A., 2007, "Nonlinear Stability of the Classical Nusselt Problem of Film Condensation and Wave Effects," ASME J. Appl. Mech., **74**(2), pp. 279–290.

[17] Narain, A., Kurita, J. H., Kivisalu, M., Siemionko, A., Kulkarni, S., Ng, T., Kim, N., and Phan, L., 2007, "Internal Condensing Flows Inside a Vertical Pipe—Experimental/Computational Investigations of the Effects of Specified and Unspecified (Free) Exit Conditions at Exit," ASME J. Heat Transfer, **129**, pp. 1352–1372.

[18] Narain, A., Liang, Q., Yu, G., and Wang, X., 2004, "Direct Computational Simulations for Internal Condensing Flows and Results on Attainability/Stability of Steady Solutions, Their Intrinsic Waviness and Their Noise-Sensitivity," ASME J. Appl. Mech., **71**, pp. 69–88.

[19] Liang, Q., Wang, X., and Narain, A., 2004, "Effect of Gravity, Shear and Surface Tension in Internal Condensing Flows—Results From Direct Computational Simulations," ASME J. Heat Transfer, **126**(5), pp. 676–686.

[20] Phan, L., Wang, X., and Narain, A., 2006, "Exit Condition, Gravity and Surface-Tension Effects on Stability and Noise Sensitivity Issues for Steady Condensing Flows Inside Tubes and Channels," Int. J. Heat Mass Transfer, **49**(13–14), pp. 2058–2076.

[21] Carey, V. P., 1992, *Liquid-Vapor Phase-Change Phenomena* (Series in Chemical and Mechanical Engineering), Hemisphere Publication Corporation, New York.
[22] Delhaye, J. M., 1974, "Jump Conditions and Entropy Sources in Two-Phase Systems; Local Instant Formulation," Int. J. Multiphase Flow, **1**, pp. 395–409.
[23] Schlichting, H., 1968, *Boundary Layer Theory*, 6th ed., McGraw-Hill, New York.
[24] Turner, J. S., 1973, *Buoyancy Effects in Fluids*, Cambridge University Press, London.
[25] Kundu, P. K., 1990, *Fluid Mechanics*, Academic, San Diego, CA.
[26] Gurtin, M. E., 1981, *An Introduction to Continuum Mechanics*, Academic, New York.
[27] Whitaker, S., 1977, *Fundamental Principles of Heat Transfer*, Pergamon, New York.
[28] Prasad, V., and Jaluria, Y., 1982, "Transient Film Condensation on Finite Horizontal Plate," Chem. Eng. Commun., **13**, pp. 327–342.

Effect of Upstream Shear on Flow and Heat (Mass) Transfer Over a Flat Plate—Part I: Velocity Measurements

K. Ghosh
Postdoctoral Associate
e-mail: kalmech@me.umn.edu

R. J. Goldstein[1]
Regents' Professor
Mem. ASME
e-mail: rjg@me.umn.edu

Department of Mechanical Engineering,
Heat Transfer Laboratory,
University of Minnesota,
Minneapolis, MN 55455

A parametric study investigates the effects of wall shear on a two-dimensional turbulent boundary layer. A belt translating along the direction of the flow imparts the shear. Velocity measurements are performed at 12 streamwise locations with four surface-to-freestream velocity ratios (0, 0.38, 0.52, and 0.65) and a momentum-based Reynolds number between 770 and 1776. The velocity data indicate that the location of the "virtual origin" of the turbulent boundary layer "moves" downstream toward the trailing edge of the belt with increasing surface velocity. The highest belt velocity ratio (0.65) results in the removal of the "inner" region of the boundary layer. Measurements of the streamwise turbulent kinetic energy show an inner scaling at locations upstream and downstream of the belt, and the formation of a new self-similar structure on the moving surface itself. Good agreement is observed for the variation in the shape factor (H) and the skin friction coefficient (c_f) with the previous studies. The distribution of the energy spectrum downstream of the belt indicates peak values concentrated around 1 kHz for the stationary belt case in the near wall region ($30<y^+<50$). However, with increasing belt velocity, this central peak plateaus over a wide frequency range (0.9–4 kHz).
[DOI: 10.1115/1.4001608]

Keywords: turbulent flow, wall shear, Clauser technique, boundary layer, scaling laws

1 Introduction

The two-dimensional turbulent boundary layer (2DTBL) on a stationary flat surface can be divided into an "inner" and an "outer" region. The outer edge of the "inner-outer" overlap region corresponds approximately to $y/\delta_{99}\sim 0.2$ [1]. The production of the Reynolds stresses and turbulent kinetic energy is limited to the inner region. Hence, the study and control of this region is pertinent to reducing separation and drag on aerodynamic structures.

Favre [2] demonstrated delayed separation on an airfoil blade running an endless belt on its upper surface. However, no boundary layer measurements were reported. Sakiadis [3] studied the boundary layer on a continuous moving surface using a one-seventh power law for the velocity profile. The experimental and analytical studies of Tsou et al. [4] compared the velocity and thermal boundary layer profiles over a rotating cylinder for laminar and turbulent flows. Similar velocity measurements using a hotwire with a rotating cylinder [5] showed that the outer region of the boundary layer was unaffected by the wall shear. Delayed separation and drag reduction were reported in a number of studies involving rotating cylinders at the leading edges of bluff bodies and aerofoils [6–8].

In a study closely related to the present work, Hamelin and Alving [1] were the first to explore the effects of an outer only region of the boundary layer on the turbulence characteristics. Hotwire measurements using boundary layer and cross-wire probes were conducted for a fixed belt-freestream ratio of $u_w/u_\infty = 0.61$, at which the inner region was completely removed. Only a few locations downstream of the belt were probed. These experimental results were later used to verify a number of turbulence models [9], which includes the algebraic, one-equation eddy viscosity transport, $k-\varepsilon$, and $k-\omega$ SST models. The mean flow characteristics were well predicted using these models, and it was inferred that the turbulent outer layer on the moving belt could be considered fully developed at a distance of $100\delta_o$ downstream from the leading edge, where δ_o is the boundary layer thickness at the start of the perturbation (belt). Brungart et al. [10] conducted similar experiments with $u_w=u_\infty$ and observed that the velocity defect in the boundary layer decreased with downstream position (over the belt) and appeared to asymptotically approach a shear-free turbulent layer profile.

In most previous studies, velocity measurements have been concentrated at locations upstream and on the moving surface itself, and not on the downstream stationary region. This paper presents a comprehensive investigation on the aerodynamic effects of a belt moving in the direction of the flow for four surface-to-freestream velocity ratios. This article is primarily a fundamental study. However, the transition from a moving to a fixed surface can be thought of as a suddenly stopped continuous moving surface, which finds many applications in the processing industry. In addition, it depicts the use of a moving wall as an active boundary layer control mechanism. The companion paper (Part II) studies the heat (mass) transfer downstream of the moving surface using the heat/mass transfer analogy.

2 Experimental Apparatus and Measurement Technique

The moving wall apparatus (Fig. 1(*a*)), previously used by Srinivasan and Goldstein [11], is placed in a suction type wind tunnel, as shown in Fig. 1(*b*). It consists of a rubber belt, translating over three cylindrical rollers. Barely any vibration was noticed using a high-speed camera for the range of the belt velocities concerned (0–10 m/s). The motor speed is controlled by an Altivar, Palatine, IL, ATV drive controller, and the belt speed is mea-

[1]Corresponding author.

Contributed by the Heat Transfer Division of ASME for publication in the JOURNAL OF HEAT TRANSFER. Manuscript received April 10, 2009; final manuscript received April 1, 2010; published online August 3, 2010. Assoc. Editor: Cholik Chan.

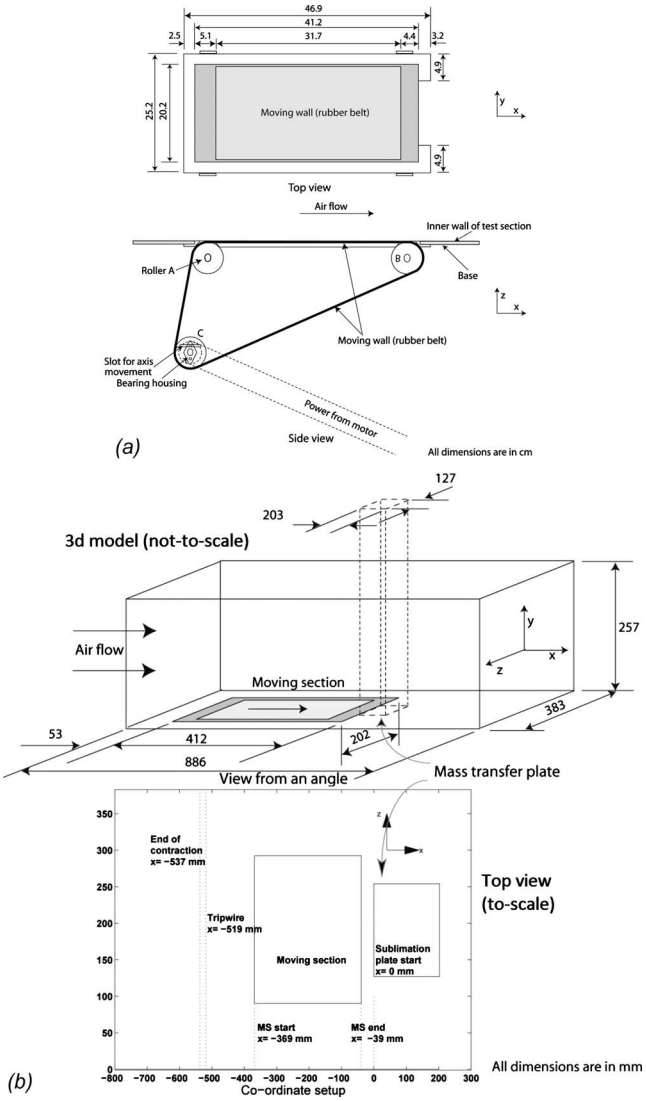

Fig. 1 Schematic of the experimental apparatus

sured using a handheld digital tachometer (Electromatic Equipment, Cedarhurst, NY, DT-105A). As shown in Fig. 1(*b*), a 1.4 mm diameter trip wire initiates the turbulent boundary layer.

The boundary layer hot-wire probe (TSI 1218-T1.5) was used to measure the mean and fluctuating components of the streamwise velocity (u). The sensing portion of this probe consists of a platinum coated tungsten wire of diameter 3.8 μm with an active sensing length of 1.27 mm ($l/d=333$). It was run in a constant temperature (CTA) mode with the operating temperature fixed at 250°C and the reference temperature set at 25°C. Signal from the hot wire was transmitted by a RG58A/U cable to a two-channel IFA-100 (intelligent flow analyzer) anemometer (from TSI, Shoreview, MN). Each channel of the anemometer is equipped with a signal conditioner (TSI 157) for amplifying and filtering the raw signal. The amplified output was read into a high-speed dual-channel Keithley-194 voltage meter, which routed it to a Linux workstation through a general purpose interface bus (GPIB). An oscilloscope (BK precision model 477) was used to monitor the output signal from the anemometer. The hot-wire probe is previously calibrated against a pitot probe by varying the freestream velocity in the wind tunnel in the range 3–20 m/s. The calibration is dependent on the flow temperature, and the anemometer output voltage was normalized to 25°C, by multiplying it with the correction factor $(250-25)/(250-T_\infty)$. The hot-wire probe is attached to a five-axis moving mechanism [12] and is traversed across the boundary layer to obtain the velocity profile. The uncertainty in the velocity measurements is primarily dependent on the location of the probe (an uncertainty of 0.1 mm in locating the wall).

3 Results and Discussion

Velocity measurements were carried out using the boundary layer probe at 12 streamwise locations, distributed upstream, on, and downstream of the moving belt (Table 1). Here, the streamwise distances are measured with respect to the location of the leading edge of the sublimation plate ($x=0$) used for the mass transfer measurements. US denotes upstream, B denotes on, and DS denotes a location downstream of the belt. With a constant freestream velocity $u_\infty=15.4$ m/s measured at position 7, the belt was run at $u_w=0$ m/s, 6, 8 m/s, and 10 m/s, leading to the velocity ratios $r(u_w/u_\infty)=0$, 0.38, 0.52 and 0.65, respectively. Based on the review by Fernholz and Finley [13], a lower limit of Re_{δ_2} for having a logarithmic profile in the turbulent boundary layer is of the order of 350. In the current study, the value of Re_{δ_2} at location 1 (US) is 770 for $r=0$. Freestream turbulence levels are in the range 0.3–0.4%. Multiple runs are conducted to verify the repeatability of the results.

4 Velocity Profiles

4.1 Case 1—Stationary Belt. For the stationary belt, the variation in u_∞ with x and the velocity profiles at locations 1–12 are shown in Fig. 2(*a*). The freestream velocity increases from 14.65 m/s (position 1) to 15.6 m/s (position 12) over a streamwise distance of 558 mm, and Re_{δ_2} changes from 770 to 1776. The boundary layer thickness (δ_o) at position 1 is 8.2 mm. The Clauser technique was used to fit the data to the law of the wall as formulated by Gersten and Herwig [14] (Eq. (1)) in the range of $5<y^+<200$.

$$u^+=\frac{1}{\Lambda}\left[\frac{1}{3}\ln\frac{\Lambda y^+ +1}{\sqrt{(\Lambda y^+)^2-\Lambda y^+ +1}}+\frac{1}{\sqrt{3}}\left(\arctan\frac{2\Lambda y^+ -1}{\sqrt{3}}+\frac{\pi}{6}\right)\right]+\frac{1}{4\kappa}\ln(1+\kappa B_1 y^{+4}) \quad (1)$$

with $\kappa=0.41$, $A=6.1\times10^{-4}$, $B_1=1.43\times10^{-3}$, and $\Lambda=(A+B_1)^{1/3}=0.127$. It should be noted that Eq. (1) reduces to the more familiar logarithmic law of the wall

$$u^+=\frac{1}{\kappa}\ln y^+ + B_2 \quad (2)$$

with $\kappa=0.41$ and $B_2=5.0$, for $y^+\to\infty$. Figure 2(*b*) shows the data fit along with the Van Driest formulation of the buffer region for

Table 1 Streamwise locations for velocity measurements

	1	2	3	4	5	6	7	8	9	10	11	12
x (mm)	−376.7	−351.3	−275.1	−198.9	−46.5	−33.8	−8.4	93.2	144.0	156.7	169.4	182.1
Position	US	B	B	B	B	DS	DS	DS	DS	DS	DS	DS
Symbol	△		○	×		□		◁		▷		◇

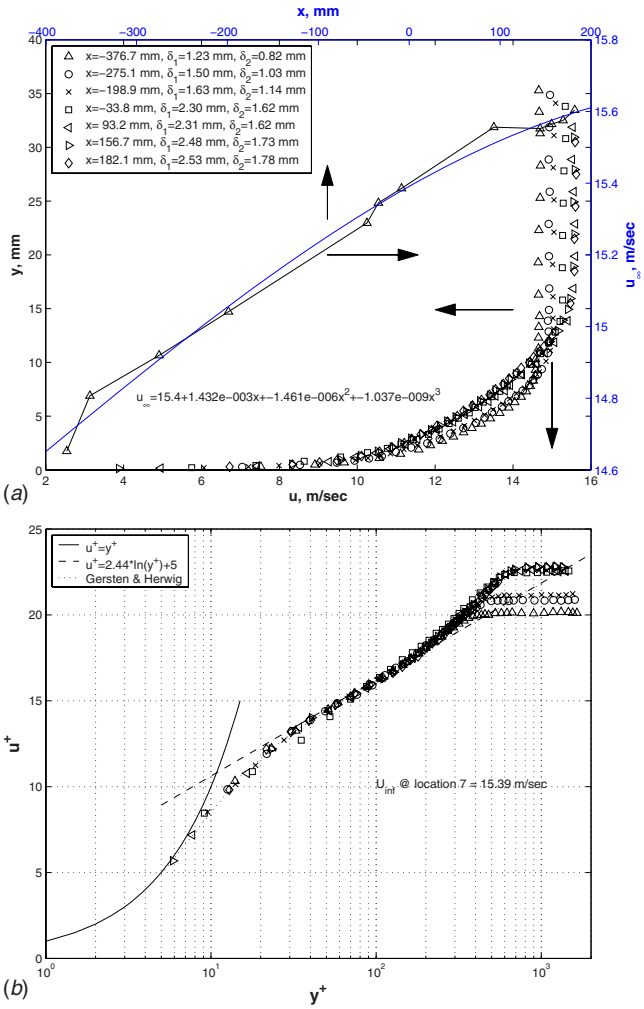

Fig. 2 Velocity profiles, case 1 (stationary belt)

the stationary belt. For much of the boundary layer, a $1/n$ power law profile could be assumed, which gives

$$\frac{u}{u_\infty} = \left(\frac{y}{\delta}\right)^{(1/n)} \tag{3}$$

Subsequently, the displacements and momentum thicknesses are $\delta_1/\delta = 1/(n+1)$ and $\delta_2/\delta = n/[(n+1)(n+2)]$, and

$$u/u_\infty \propto (y/\delta_1)^{(1/n)} \tag{4a}$$

$$\propto (y/\delta_2)^{(1/n)} \tag{4b}$$

The value of "n" is determined from the slope of the linear portion of the variation in the nondimensional velocity (u/u_∞) versus the nondimensional distance from the wall $(y/\delta_1$ or $y/\delta_2)$ in a log-log scale, as shown in Fig. 3(a).

In this study, the same methodology as applied by Hamelin and Alving [1] is used to determine the wall velocity, which would completely remove the inner turbulence-producing region of the boundary layer. At location 1 ($x=-376.7$ mm, Fig. 2(b)), the slope of the velocity profile at $y/\delta_{99}=0.2$ is determined from the power law profile ($n=5.5$). Its projection on the x-axis gives a wall velocity of $u_{w,c}=8.85$ m/s as this "limiting" velocity to remove the inner region.

4.2 Cases 2, 3, and 4—Belt Velocity (u_w=6 m/s, 8 m/s, and 10 m/s). A parametric study was conducted for three belt velocities, with two lower and one higher than $u_{w,c}$ to study the

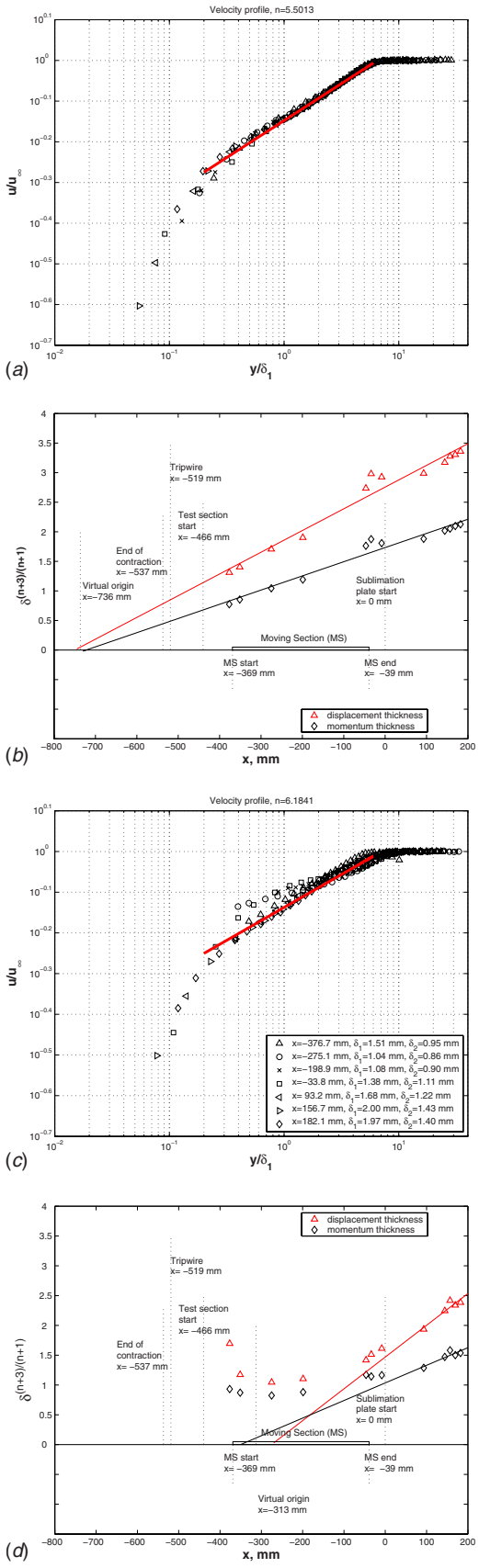

Fig. 3 Determination of the virtual origin

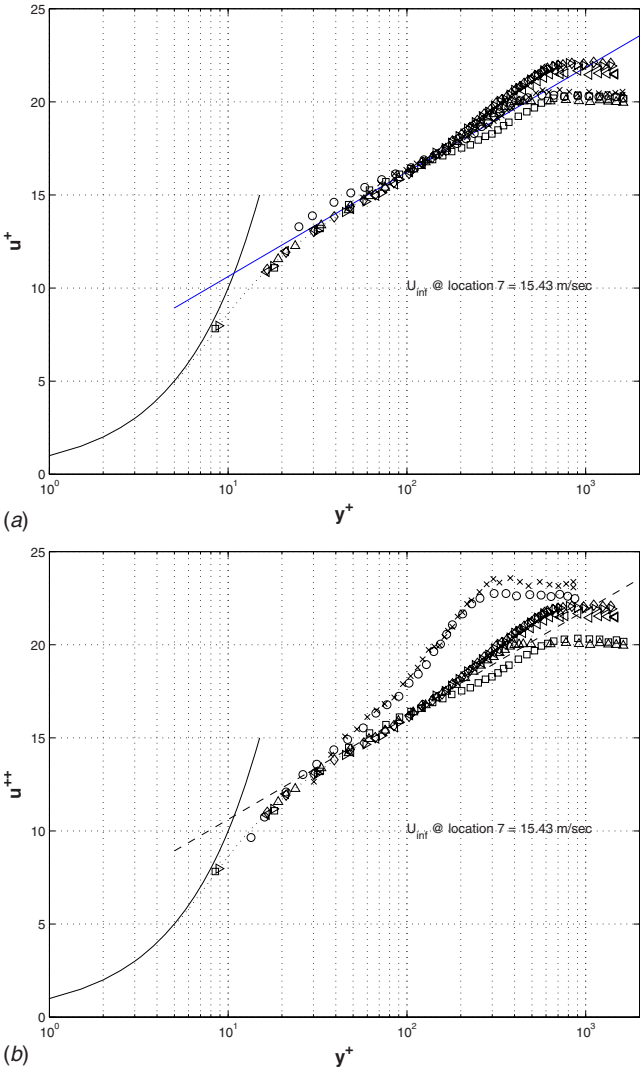

Fig. 4 Universal velocity profiles based on pseudo and true scalings (u_w=6 m/s)

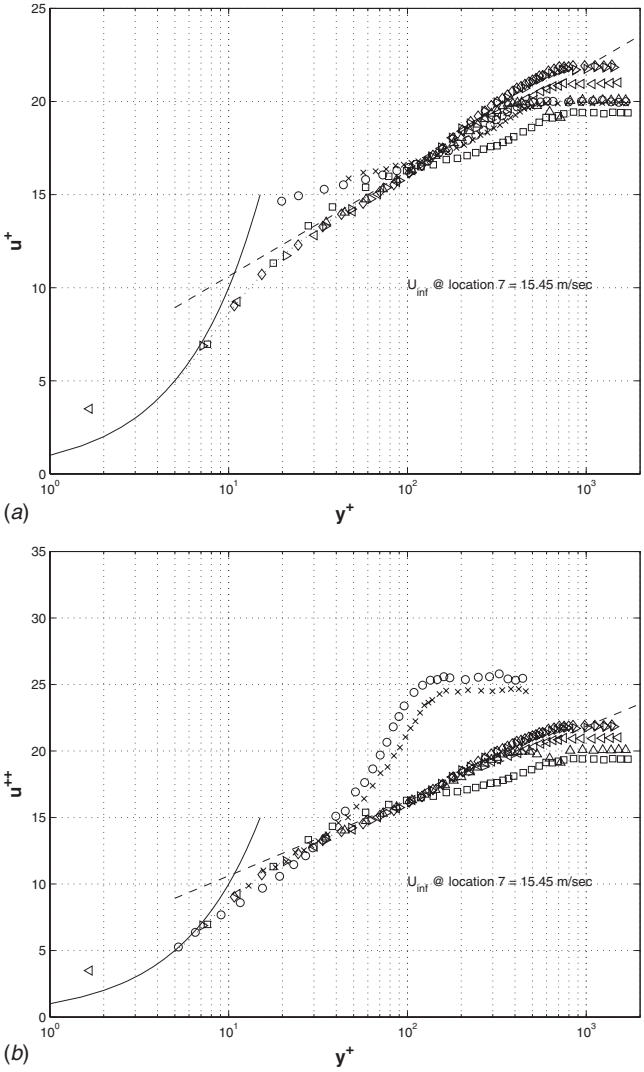

Fig. 5 Universal velocity profiles based on pseudo and true scalings (u_w=10 m/s)

transition of the velocity boundary layer, on, and more importantly, downstream of the moving belt to confirm that self-similarity had been restored.

With an increase in the belt speed, the velocity difference ($u - u_w$) in the boundary layer is reduced. Velocity profiles for $u_w = 6$ m/s are shown in Figs. 4(*a*) and 4(*b*). In Fig. 4(*a*), the value of the friction velocity on the belt is determined as if a stationary boundary is present ($u^+ = (u/u_{\tau,p})$). A least-square fit of the data with Eq. (1) in the logarithmic region $100 < y^+ < 200$ ($y^+ = (yu_{\tau,p}/\nu)$), gives the "pseudo inner-scaled" friction velocity ($u_{\tau,p}$). However, the true scaling of the inner region should be in the reference frame of the moving surface. This is shown in Fig. 4(*b*). Here, for velocity measurements on the moving wall (symbols—○ and ×, Table 1), the least-square technique is used to obtain the "true inner-scaled" friction velocity ($u_{\tau,t}$) by fitting the nondimensional velocity $u^{++} = (u - u_w/u_{\tau,t})$ in the buffer region ($5 < y^+ < 20$, $y^+ = yu_{\tau,t}/\nu$, Eq. (1)). It should be noted that the velocity profiles upstream (position 1) and downstream of the belt (positions 6–12) are the same in Figs. 4(*a*) and 4(*b*). The corresponding velocity plots for the highest belt-freestream ratio (Figs. 5(*a*) and 5(*b*)) show increased velocity defect compared with the 6 m/s case.

The flow downstream of the belt is strongly affected by the moving belt. Velocity profiles until position 7, 30.3 mm downstream of the belt, carry the signature of the upstream wall shear. The velocity profile is restored to the logarithmic law of the wall only to $y^+ \sim 100$ (y^+ based on $u_{\tau,t}$) at this streamwise location. The deviation of the velocity profile from the logarithmic law beyond $y^+ \sim 100$ is most pronounced at the highest belt velocity, as evident in Fig. 5(*b*) (symbols—○ and ×). The law of the wall is eventually restored at the streamwise location $x = 93.2$ mm (position 8).

Based on these measurements, the value of the exponent n for the new power law profile of the relaxed two-dimensional turbulent boundary layer is determined as the mean slope of the linear portion of the $\log(u/u_\infty)$ versus $\log(y/\delta_1)$ plot (Fig. 3(*a*)) at positions 8–12 (Table 1). The importance of selecting these five locations for characterizing the relaxed flow is later verified from the turbulence kinetic energy measurements. With an increase in the belt speed, an increase in the value of n is observed, which is a direct consequence of a reduction in the boundary layer thickness ($n = 5.5$ for $r = 0$ and $n = 6.2$ for $r = 0.65$).

5 Determining Virtual Origin

5.1 Case 1—Stationary Belt. The virtual origin of the boundary layer is defined as the location where the turbulent boundary layer would have started in the absence of preceding laminar and transition regions. The analytical integration of the

Table 2 Movement of the virtual origin

Ratio (u_w/u_∞)	x_o (mm)
0	−736
0.38	−458
0.52	−448
0.65	−313

boundary layer momentum equation using a power law velocity profile shows that the displacement (δ_1) and momentum thicknesses (δ_2) increase along the streamwise direction proportional to $X^{(n+1)/(n+3)}$. Here, X is the streamwise distance measured from the start of the boundary layer. Therefore, $X=x-x_o$, where x_o is the distance of the virtual origin from $x=0$. Therefore, a plot of $\delta_i^{(n+3)/(n+1)}$ versus X demonstrates a linear variation, which can be extrapolated to obtain the location of the virtual origin $(X=0)$. As shown in Fig. 3(*b*), the virtual origin for the stationary belt is located at a distance 736 mm upstream of the naphthalene plate.

5.2 Cases 2, 3, and 4 (u_w=6 m/s, 8 m/s, and 10 m/s). With an increase in the belt velocity, the virtual origin would be expected to "move" toward the trailing edge of the belt. For the special case, when the wall velocity is equal to the freestream $(u_{\text{wall}}=u_\infty)$, a uniform velocity profile is expected far downstream on the moving belt. As shown in Fig. 3(*d*), for $u_w=10$ m/s, the virtual origin has moved considerably downstream. It should be noted that in this case, the virtual origin is determined by extrapolating $\delta_i^{(n+3)/(n+1)}$ at positions 8–12 (from the analysis in Sec. 5.1). The 'movement' of the virtual origin downstream toward the trailing edge of the belt with increasing belt velocity is tabulated in Table 2.

6 Shape Factor and Skin Friction Coefficient

The variation in the shape factor $H=\delta_1/\delta_2$ and the skin friction coefficient c_f $(=u_\tau^2/(2u_\infty^2))$ are shown in Figs. 6 and 7 along with a comparison with the previous data from the review paper of Fernholz and Finley [13]. It should be noted that data from this paper are for a zero pressure gradient boundary layer. On the moving belt, considerably reduced values of H are observed due to the reduction in δ_1 on the belt itself. For $u_w=u_\infty$, the shape factor far downstream on the moving belt would be approximately zero. The skin friction coefficient (c_f) on the moving belt is reduced by as much as 88% for the highest velocity ratio $(r=0.65)$.

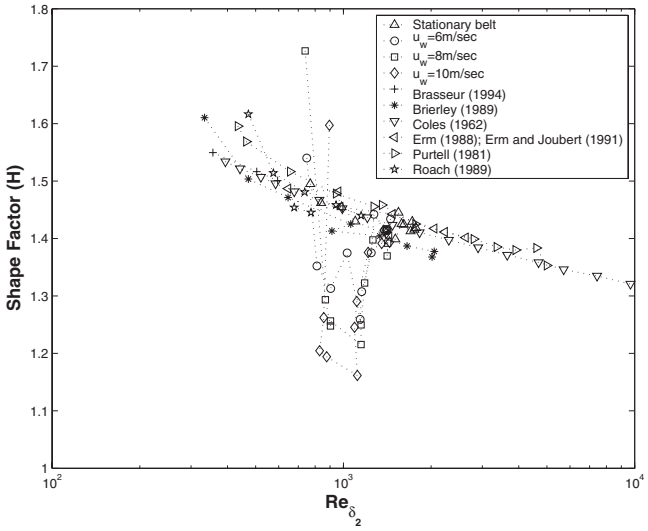

Fig. 6 Variation in the shape factor

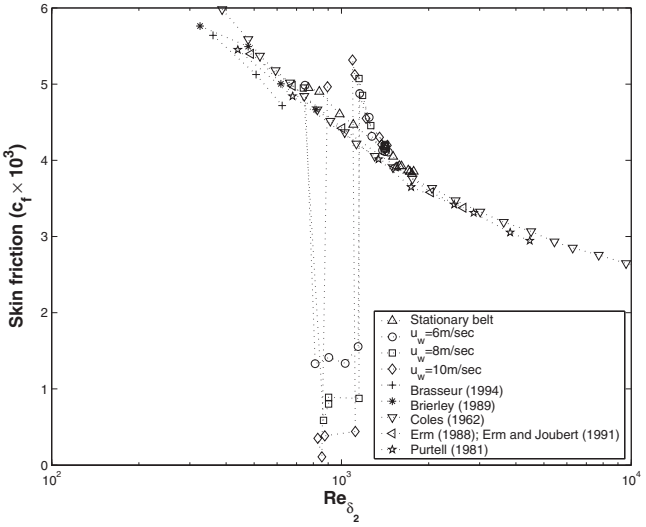

Fig. 7 Variation in the skin friction coefficient

7 Scaling Parameters

7.1 Case 1—Stationary Belt. As has been noted in many studies, the easiest turbulent parameter that can be measured in two-dimensional turbulent flows is the streamwise turbulent intensity $(\sqrt{\overline{u'^2}}/u_\infty)$, the square of which is the nondimensional streamwise turbulent kinetic energy (STKE). For the stationary belt, the variation in this parameter across the boundary layer is shown in Fig. 8(*a*). Except for the variation in the STKE near the leading and trailing edges of the belt, an inner scaling is observed for the entire range of the Reynolds number (Re_{δ_2}). Here, the main idea of the scaling technique is that a similarity formulation can be obtained for the variation in the STKE versus y^+ for all Re_{δ_2} [15,16]. The similarity formulation describes Reynolds number effects on the variation in the STKE. This scaling has been shown to depend on the parameter Re_τ $(\text{Re}_\tau=\delta u_\tau/\nu)$, which is the Karman number (Eq. 2 in Ref. [15]). Therefore, the similarity formulation is in a way dependent on u_w.

Peak values of the STKE, which is a qualitative measure of the largest eddies in the boundary layer, are observed near $y^+=15$. The fact that the peak remains unchanged for all Re_{δ_2} suggests that the scale of the largest eddies is independent of Re_{δ_2}. In the current study, a similarity in the wall units is observed until $y^+\approx 80$. This is much lower in comparison with a value of $y^+\approx 200$, until which a similarity is observed in case of the mean velocity profiles (Fig. 2(*b*)). It has previously been suggested that this higher decrease in the STKE is a result of the suppression of all but the largest scales in the turbulent boundary layer with decreasing Reynolds number [17].

7.2 Case 2 (u_w=6 m/s). Figure 8(*b*) shows the variation in the STKE for $u_w=6$ m/s. It should be noted that the true value of the friction velocity (from $u^{++}=(u-u_w/u_{\tau,t})$) is used to define the wall units $(y^+=(yu_{\tau,t}/\nu))$. Except for positions 2–7 (Table 1), an inner scaling and associated peaks (near $y^+=15$) is observed in the variation in the STKE, similar to the stationary belt case. On the moving belt (positions 2–5), reduced values of the energy levels are observed. This suggests smaller scales of the corresponding eddies. It is also evident that as the turbulent boundary layer develops on the moving surface, a "newer" scaling in the inner region gradually begins to develop (positions 3–5). Immediately downstream of the moving belt (position 6, "□," the STKE profile falls in between the profiles on the moving belt and those far downstream. The energy levels in the "buffer" $(y^+<50)$ and "wake" $(y^+>400)$ regions are restored immediately. However, in the region $60<y^+<300$, which is essentially the logarithmic por-

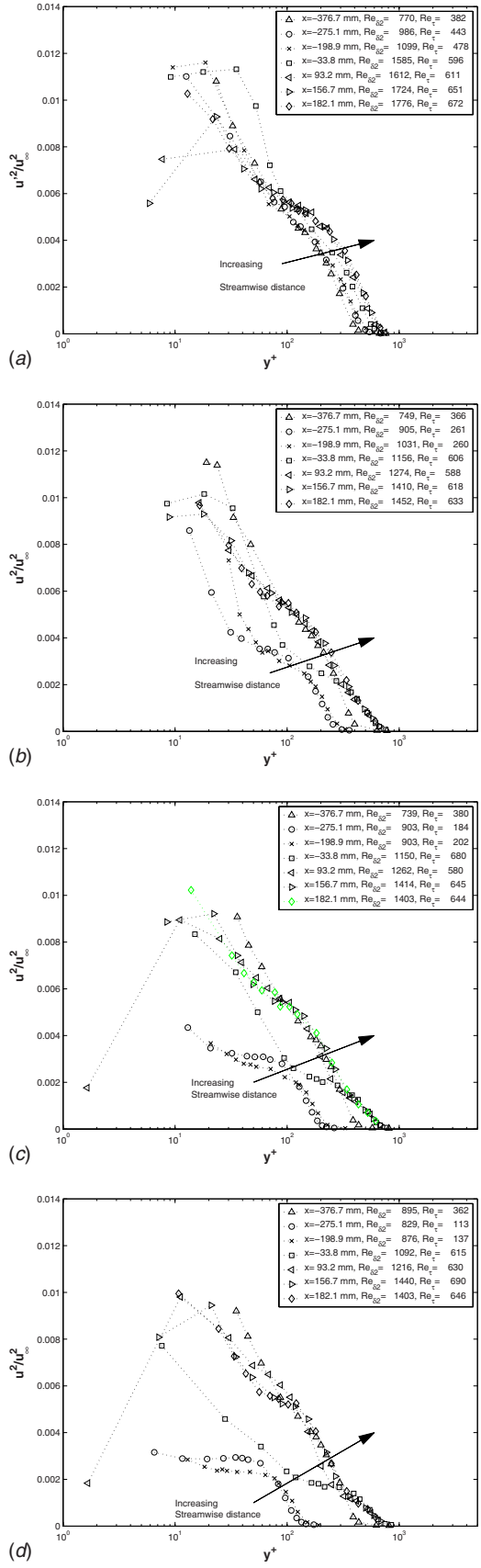

Fig. 8 Nondimensionalized streamwise TKE

tion of the turbulent boundary layer, greatly reduced values of the STKE are observed for some distance downstream of the belt. This signifies smaller scales associated with the logarithmic region, even as the stationary wall and the freestream boundary conditions restore the turbulent characteristics of the flow almost immediately.

As the flow relaxes downstream, this energy defect is reduced, and the kinetic energy profile approaches that of an undisturbed boundary layer. It is evident that the profile similarity is observed for positions 8–12. This verifies the usage of the velocity profiles at these streamwise positions to determine the value of n to get the effective origin of the turbulent boundary layer with the moving belt.

7.3 Case 3 (u_w=8 m/s). At a higher belt velocity, the turbulence levels on the belt are even further reduced as compared with the 6 m/s case. As shown in Fig. 8(c), the formation of the newer inner scaling for the boundary layer on the moving surface is more pronounced. As before, at the location immediately downstream of the trailing edge (position 6, □), the TKE levels in the buffer and wake regions are restored. However, the energy deficit is spread over a much wider part of the logarithmic region in this case ($40<y^+<300$) compared with u_w=6 m/s.

7.4 Case 4 (u_w=10 m/s). At u_w=10 m/s, the belt motion eventually "removes" the inner (turbulence-producing) region of the boundary layer. Figure 8(d) indicates that the energy levels above the moving surface are substantially lower than all the previous cases. The profiles of the kinetic energy on the moving surface itself (positions 3–5) appear as scaled-down prototypes of the profiles for an unperturbed boundary layer. The peaks disappear, as found earlier by Hamelin and Alving [1]. At position 6, only the wake region of the boundary layer STKE levels are restored. The energy defect in this case does not remain limited to the logarithmic region, but penetrates well into the buffer region. The gradual restoration of the STKE further downstream location (position 7) is observed. As before, the profile similarity is restored only at positions 8–12.

8 Spectral Measurements

The variation in the energy spectrum in the boundary layer for the stationary belt is shown in Fig. 9(a). The streamwise positions for these variations are tabulated in Table 3. The four locations within the boundary layer at each streamwise position are selectively chosen to lie in each of the following ranges of y^+: [0,100], [100,200], [200,300], and [300,400]. In these plots, the u'^2 power spectral density (PSD) (m^2/s) is premultiplied with the frequency (Hz). Therefore, the area within a section of the spectrum gives the energy content within that range of frequencies. The energy spectra are distributed around 1 kHz for the stationary belt test. Figures 9(b)–9(d) show the distribution of the energy spectra for u_w=6 m/s, 8 m/s, and 10 m/s, respectively. With increasing belt velocity, this central peak plateaus over a wider frequency range (0.9–4 kHz), and a local minimum in the energy level seems to be more prominent (Fig. 9(d)). This is more conspicuous in the distribution at y^+=118 (lying in the logarithmic region) for the 10 m/s belt speed. This corroborates the findings related to the relaxation of the STKE from the moving to the stationary boundary (Fig. 8(d)), where the logarithmic region responds the slowest as the flow transitions over the stationary surface.

9 Conclusions

A series of velocity measurements have been conducted to better understand the relaxation of a turbulent boundary layer downstream of a moving belt. The key features are as follows:

1. A reduction in the peak values of the TKE on the moving belt, which is more pronounced with increasing belt

Table 3 Location of the spectral data

x (mm)	y^+ range, case 1				y^+ range, case 2			
	[0,100]	[100,200]	[200,300]	[300,400]	[0,100]	[100,200]	[200,300]	[300,400]
−376.7	23	126	224	293	33	127	212	352
−198.9	19	123	255	300	71	127	198	339
−46.5	28	138	204	314	44	144	215	340
144.0	22	135	223	310	47	110	223	314
	y^+ range, case 3				y^+ range, case 4			
−376.7	36	125	223	387	35	125	224	389
−198.9	49	126	226	350	47	130	232	353
−46.5	44	140	217	342	41	131	221	345
144.0	34	116	231	322	39	118	234	327

velocity. Development of a new inner scaling on the moving surface is evident.

2. The almost immediate restoration of the wake region of the boundary layer on the stationary surface. This is followed by a restoration of the "viscous sublayer" region to its undisturbed values. Velocity and TKE profiles in the logarithmic region ($100<y^+<500$) relaxes back to the undisturbed turbulent layer values last.
3. The "movement" of the "virtual origin" of the boundary layer downstream is important while comparing results from the mass transfer measurements studies, which are described in the companion paper.

Nomenclature

c_f = skin friction coefficient
H = shape factor, δ_1/δ_2
n = power law exponent
r = velocity ratio, u_w/u_∞
Re_x = distance-based Reynolds number, $\mathrm{Re}_x=(u_{\mathrm{in}}|x-x_o|/\nu)$
Re_{δ_2} = momentum-based Reynolds number, $\mathrm{Re}_{\delta_2}=(u_{\mathrm{in}}\delta_2/\nu)$
Re_τ = Karman number, $\mathrm{Re}_\tau=(\delta u_\tau/\nu)$
T_∞ = freestream temperature
u = velocity along the x-direction
u' = fluctuating x-velocity component
u^+ = nondimensional velocity, u/u_τ
u^{++} = nondimensional velocity, $(u-u_w)/u_{\tau,t}$
u_{in} = freestream velocity at position 7
u_w = belt velocity
$u_{w,c}$ = limiting belt velocity
u_τ = friction velocity, $u_\tau=\sqrt{\tau_w/\rho}$
$u_{\tau,p}$ = pseudo friction velocity on the moving belt, $u_{\tau,p}=\sqrt{\tau_{w,p}/\rho}$
$u_{\tau,t}$ = true friction velocity on moving belt, $u_{\tau,t}=\sqrt{\tau_{w,t}/\rho}$
$\overline{u'^2}$ = streamwise kinetic energy
u_∞ = freestream velocity
x = distance measured from the leading edge of the mass transfer plate
x_o = distance of the virtual origin from the leading edge of the mass transfer plate
y^+ = wall coordinates, $y^+=yu_\tau/\nu$
y = direction normal to the belt
z = spanwise direction

Greek Symbols

δ_o = boundary layer thickness at the start of perturbation
δ = boundary layer thickness at $u=u_\infty$
δ_{99} = boundary layer thickness at $u=0.99u_\infty$
δ_1 = displacement thickness
δ_2 = momentum thickness
ν = kinematic viscosity
ρ = density of air
τ_w = wall shear stress without belt motion
$\tau_{w,p}$ = pseudo shear stress on the moving belt
$\tau_{w,t}$ = true shear stress on the moving belt
ν = kinematic viscosity

Constants

$A, B_1, B_2, \Lambda, \kappa$

References

[1] Hamelin, J., and Alving, A., 1996, "A Low-Shear Turbulent Boundary Layer," Phys. Fluids, **8**(3), pp. 789–804.
[2] Favre, A., 1938, "Contribution a l'etude experimentale des mouvements hydrodynamques a deux dimensions," These Universite de Paris thesis, University of Paris, France.
[3] Sakiadis, B., 1961, "Boundary Layer on Continuous Solid Surface. III The Boundary Layer on a Continuous Cylindrical Surface," AIChE J., **7**, pp. 467–472.
[4] Tsou, F., Sparrow, E., and Goldstein, R., 1967, "Flow and Heat Transfer in the Boundary Layer on a Continuous Moving Surface," Int. J. Heat Mass Transfer, **10**, pp. 219–235.
[5] Tennant, J., and Yang, T., 1973, "Turbulent Boundary-Layer Flow From Stationary to Moving Surfaces," AIAA J., **11**, pp. 1156–1160.
[6] Chew, Y., Pan, L., and Lee, T., 1998, "Numerical Simulation of the Effect of a Moving Wall on Separation of Flow Past a Symmetrical Aerofoil," Proc. Inst. Mech. Eng., Part A, **212**, pp. 69–77.
[7] Munshi, S., Modi, V., and Yokomizo, T., 1999, "Fluid Dynamics of Flat Plates and Rectangular Prisms in the Presence of Moving Surface Boundary-Layer Control," J. Wind Eng. Ind. Aerodyn., **79**, pp. 37–60.
[8] Singh, S., Rai, L., Puri, P., and Bhatnagar, A., 2005, "Effect of Moving Surface on the Aerodynamic Drag of Road Vehicles," Proc. Inst. Mech. Eng., Part D (J. Automob. Eng.), **219**, pp. 127–134.
[9] Bassina, I., Strelets, M., and Spalart, P. R., 2001, "Response of Simple Turbulence Models to Step Changes of Slip Velocity," AIAA J., **39**(2), pp. 201–210.
[10] Brungart, T., Lauchle, G., Deutsch, D., and Riggs, E., 2001, "Effect of a Moving Wall on a Fully Developed, Equilibrium Turbulent Boundary Layer," Exp. Fluids, **30**, pp. 418–425.
[11] Srinivasan, V., and Goldstein, R., 2003, "Effect of Endwall Motion on Blade Tip Heat Transfer," ASME J. Turbomach., **125**, pp. 267–273.
[12] Han, S., and Goldstein, R., 2007, "Heat Transfer Study in a Linear Turbine Cascade Using a Thermal Boundary Layer Measurement Technique," ASME J. Heat Transfer, **129**, p. 1384.
[13] Fernholz, H., and Finley, P., 1996, "The Incompressible Zero-Pressure-Gradient Turbulent Boundary Layer: An Assessment of the Data," Prog. Aerosp. Sci., **32**, pp. 245–311.
[14] Gersten, K., and Herwig, H., 1992. "Grundlagen der impuls," *Waerme-Stoffeubertrag.* (from *Boundary Layer Theory*, by H. Schlichting and K. Gersten, 2000, 8th ed.).
[15] Marusic, I., and Kunkel, G., 2003, "Streamwise Turbulence Intensity Formulation for Flat-Plate Boundary Layers," Phys. Fluids, **15**(8), pp. 2461–2464.
[16] Marusic, I., Uddin, A., and Perry, A., 1997, "Similarity Law for the Streamwise Turbulence Intensity in Zero-Pressure-Gradient Turbulent Boundary Layers," Phys. Fluids, **9**(12), pp. 3718–3726.
[17] Purtell, L., Klebanoff, P., and Buckley, F., 1981, "Turbulent Boundary Layer at Low Reynolds Number," Phys. Fluids, **24**, p. 802.

Effect of Upstream Shear on Flow and Heat (Mass) Transfer Over a Flat Plate—Part II: Mass Transfer Measurements

K. Ghosh
Postdoctoral Associate
e-mail: kalmech@me.umn.edu

R. J. Goldstein[1]
Regents' Professor
Mem. ASME
e-mail: rjg@me.umn.edu

Department of Mechanical Engineering,
Heat Transfer Laboratory,
University of Minnesota,
Minneapolis, MN 55455

Mass transfer measurements on a flat plate downstream of a belt moving in the same direction of the freestream study the effect of the upstream shear on the heat (mass) transfer for four belt-freestream velocity ratios. With an increase in this ratio, the "virtual origin" of the turbulent boundary layer "moves" downstream toward the trailing edge of the belt. This is verified from the variation of the Stanton number versus the Reynolds number plots. As the "inner" region of the boundary layer is removed for a belt speed of $u_w = 10$ m/s (freestream velocity $u_{in} \approx 15.4$ m/s), a corresponding local minimum in the variation of the Stanton number is observed. Downstream of this minimum, the characteristics of the turbulent boundary layer are restored and the data fall back on the empirical variation of Stanton with Reynolds number. [DOI: 10.1115/1.4001609]

Keywords: heat/mass transfer analogy, naphthalene sublimation, turbulent flow, wall motion, boundary layer, constant temperature, constant concentration

1 Introduction

The heat transfer characteristics of a translating heated surface in quiescent conditions have been studied over the years. These studies have generally been limited to experimental or analytical studies on the surface itself and not downstream of it. Most of these studies are associated with manufacturing processes such as stretching, rolling, and extrusion.

Erickson et al. [1] presented analytical solutions for the thermal boundary layer on a moving continuous sheet using the Karman–Pohlhausen integral method. One of the earliest measurements of the heat transfer associated with a moving surface in turbulent flow conditions was by Tsou et al. [2]. In this study, the experimental conditions closely approximated a uniform surface temperature condition. The authors noted that the analytically derived temperature profiles, which were for a uniform heat flux condition, were very close to the measured profiles. They concluded that in turbulent flow conditions, the temperature profiles were relatively insensitive to the thermal boundary condition. Local skin friction coefficient and Nusselt number were independently obtained by Abdelhafez [3] and Chappidi and Gunnerson [4] using similarity and integral methods, and good agreement between these solutions were reported. Sparrow and Abraham [5] studied the streamwise variation of temperature on a moving sheet in the presence of a coflowing fluid. They reported a number of universal solutions for laminar flow conditions. Cortell [6] carried out a numerical solution for the momentum and heat transfer on a moving sheet for both constant and power-law surface temperature.

Recently, simulations involving rotating cylinders placed on a bluff body have shown promise in controlling drag forces as related to moving vehicles [7]. Part I of this paper [8] investigates the aerodynamic effects of a belt translating "along" the freestream flow. The belt can remove the "inner" region of the boundary layer, when translating at a high velocity thereby reducing turbulence production. The study of the heat transfer downstream of a belt represents a fundamental problem. It demonstrates the effects of the addition of momentum at the wall boundary. The objective of the present study is to investigate the variation of the Sherwood number on a flat plate placed downstream of a surface moving in the direction of the flow. Mass transfer experiments using the naphthalene sublimation technique have been conducted. The heat transfer variation is subsequently obtained using the heat/mass transfer analogy.

2 Heat/Mass Transfer Analogy

The heat/mass transfer analogy is applicable in incompressible constant property flows, where temperature and concentration (nonreacting species) are passive scalars and have no bearing on the fluid dynamics [9,10]. The transport equations for the nondimensional thermal and mass concentration in a turbulent boundary layer are given by [11]

$$\frac{D\theta}{D\tau} = \frac{1}{\mathrm{Re}_x\ \mathrm{Pr}} \frac{\partial}{\partial \hat{x}_i}\left(\left(1 + \frac{\varepsilon}{\nu}\frac{\mathrm{Pr}}{\mathrm{Pr}_t}\right)\frac{\partial \theta}{\partial \hat{x}_i}\right) \quad \text{heat transfer} \qquad (1a)$$

$$\frac{D\Phi}{D\tau} = \frac{1}{\mathrm{Re}_x\ \mathrm{Sc}} \frac{\partial}{\partial \hat{x}_i}\left(\left(1 + \frac{\varepsilon}{\nu}\frac{\mathrm{Sc}}{\mathrm{Sc}_t}\right)\frac{\partial \Phi}{\partial \hat{x}_i}\right) \quad \text{mass transfer} \qquad (1b)$$

A review of the mass transfer analogy and the experimental technique is given in Goldstein and Cho [11]. A mass transfer study is often more convenient as compared with a heat transfer experiment, as errors associated with wall conduction and radiation are not present with mass transfer. However, as pointed out by Eckert et al. [12], the boundary conditions should be equivalent for the analogy to be valid. For the heat/mass transfer analogy considered in this study, the similarity variables are as follows: heat transfer: $\mathrm{Re}_x, \mathrm{Pr}, T_w = \text{const}$, model shape and mass transfer: $\mathrm{Re}_x, \mathrm{Sc}, c_w = \text{const}$, model shape.

3 Naphthalene Sublimation Technique

The naphthalene sublimation procedure has been extensively used in the Heat Transfer Laboratory at the University of Minnesota to measure local mass transfer coefficients on various surface geometries, including circular cylinders in crossflow and in turbine cascade passages. The procedure has five steps: (1) The test surface is cast with naphthalene; (2) the surface profile is mea-

[1]Corresponding author.

Contributed by the Heat Transfer Division of ASME for publication in the JOURNAL OF HEAT TRANSFER. Manuscript received April 16, 2009; final manuscript received April 1, 2010; published online August 3, 2010. Assoc. Editor: Cholik Chan.

Table 1 Measurement conditions for mass transfer experiments

Run	u_w (m/s)	u_{in} (m/s)	x_o (mm)
1	0	15.7	−736
2, 3	6	15.4	−458
4, 5, 6	8	15.8	−448
7, 8, 9	10	15.8	−313

sured using a linear variable differential transformer (LVDT) probe; 3) the mold is placed in the wind tunnel under desired flow conditions for approximately 40 min. The average sublimation depth during this period (≈ 40 μm) is of a much larger value than the natural convection (≈ 1.5 μm); (4) the surface profile of the mass transfer plate is measured again using the LVDT probe. The sublimation depth of naphthalene during the experiment is obtained from the difference in LVDT measurements before and after the run; (5) finally, the local mass transfer coefficients on the surface of the plate are determined from

$$h_m = \frac{\dot{m}}{\rho_{v,w} - \rho_{v,\infty}} = \frac{\rho_s \delta y / \delta \tau}{\rho_{v,w}} \tag{2}$$

Subsequently, the mass transfer Stanton number (St_m) at each x location is obtained from

$$St_m = \frac{h_m}{u_{in}} \tag{3}$$

where u_{in} is the freestream velocity near the leading edge of the mass transfer plate (position 7 in Table 1, Part I). The uncertainty in the value of St_m is calculated using the method outlined by Kline and McClintock [13] for single sample experiments. The result is expressed as

$$\frac{\Delta St}{St} = \left[\left(\frac{\Delta \rho_s}{\rho_s} \right)^2 + \left(\frac{\Delta \rho_{v,w}}{\rho_{v,w}} \right)^2 + \left(\frac{\Delta \delta y}{\delta y} \right)^2 + \left(\frac{\Delta \delta \tau}{\delta \tau} \right)^2 \right]^{1/2} \tag{4}$$

and is approximately 5%. Note that much of this is the bias error due to uncertainty in the properties of naphthalene (3.8% uncertainty in the vapor density of naphthalene).

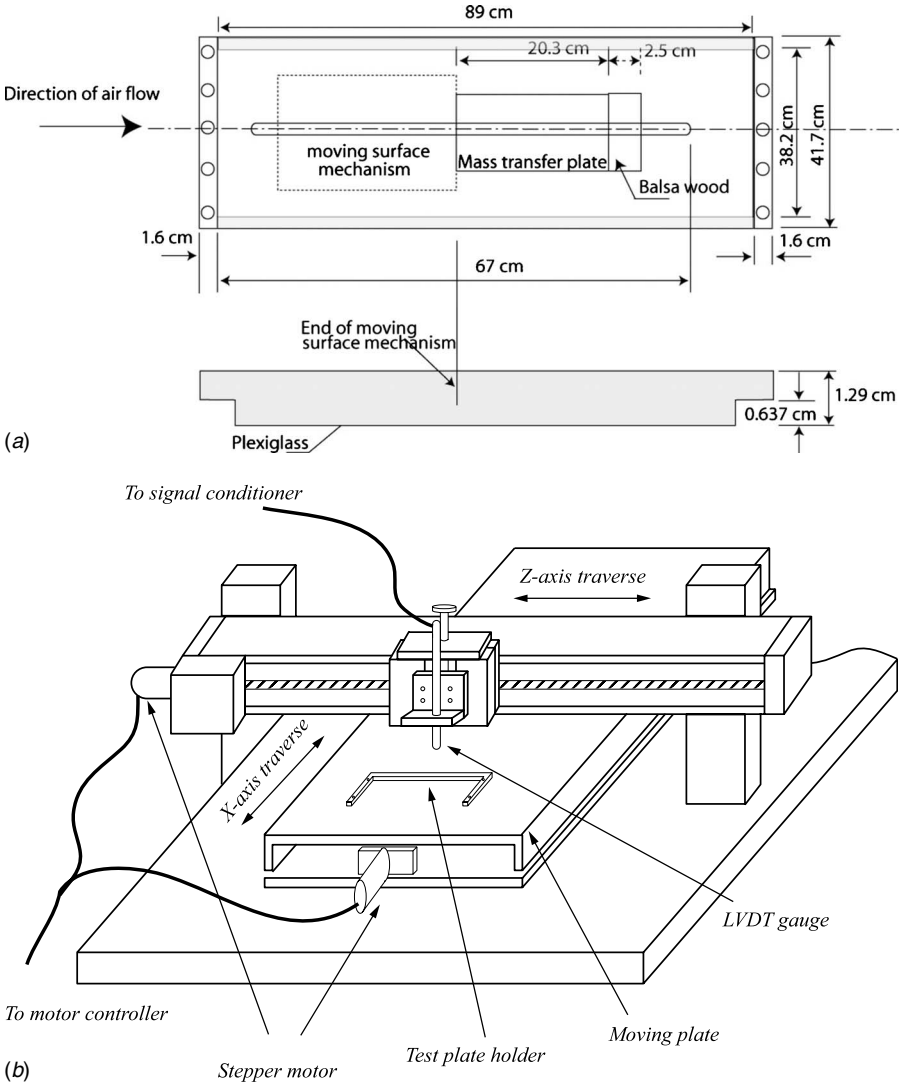

Fig. 1 Mass transfer experimental setup

4 Experimental Setup

The mass transfer experiments are conducted in a suction wind tunnel as described in Part I. The position of the mass transfer plate is shown in Fig. 1(*a*).

5 *XYZ* Table for Surface Profile Measurement

The two-axis sublimation surface profile measurement system [14] consists of a motor controller (NF-90), a linear signal conditioner (Schaevitz/Measurement Specialties, Hampton, VA, CAS-025), a linear variable differential transformer depth gauge (Schaevitz/Measurement Specialties, Hampton, VA, PCA-220-010 LVDT), two stepper motors (Superior Electric Co., Farmington, CT, SLO-SYN MN-63), two single axis unislides (Velmex Inc., Bloomfield, NY, and Design Components Inc., Palatine, IL), and a Keithley 2000 multimeter. The entire system is controlled by an IBM Linux computer. The working principle behind the profile measurement is that the voltage response from the LVDT gauge is directly proportional to its displacement. A schematic of the measurement table is shown in Fig. 1(*b*).

The LVDT is mounted on a single axis unislide that moves it in the *x*-direction and the other unislide moves the table in the *z*-direction. The two unislides are individually driven by the two synchronous stepper motors, which are controlled by the motor controller through the Linux terminal. The signal conditioner is used to convert the ac voltage output from the LVDT to dc voltage as well as amplify the signal. The LVDT depth gauge has a resolution of 25.4 nm with a linear range of 0.5 mm. With the average sublimation depth being approximately 60 μm during an experiment, the system has adequate resolution to measure the profile very precisely.

6 LVDT Calibration

The LVDT probe is calibrated against a set of precision gage blocks. The variation of the voltage with displacement is shown in Fig. 2(*a*). For this probe, a voltage reading of 1 V corresponds to a displacement of 18.968 μm. The total error consists of the summation of the random error (scatter) and the deviation of the data from the linear fit. The standard deviation of the data from the linear fit is ± 0.1 μm. This is also equal to the total error for this calibration set as the scatter in the data is less by an order of 2.

7 Mock Sublimation Test

Figure 2(*b*) shows the results from a mock sublimation test. In this test, a square aluminum plate is scanned by the LVDT probe, removed from the *XYZ*-table, then returned to the *XYZ*-table and scanned a second time. The active naphthalene surface is replaced by a passive surface in this case. Ideal results from this mock test would be identically zero difference. However, the scatter in the LVDT voltage gives a mean displacement of 65 nm having a standard deviation of 114 nm. The results from the LVDT calibration and the mock sublimation test verify the accuracy of the measurement probe. The total errors are two orders of magnitudes less the displacements in an experimental run.

7.1 Natural Convection Correction. In addition to the sublimation during exposure in the wind tunnel, sublimation occurs due to natural convection in between and during the *XYZ*-table measurements. The rate of natural convection loss is estimated by measuring the depth change over 6 h at intervals of 2 h. Subsequently, the depth change in an experimental run is corrected for the time the naphthalene surface is exposed to ambient conditions.

8 Results and Discussion

The mass transfer experiments are performed in conjunction with the velocity measurements presented in Part I. The measurement conditions for the parallel motion of the rubber belt are tabulated in Table 1.

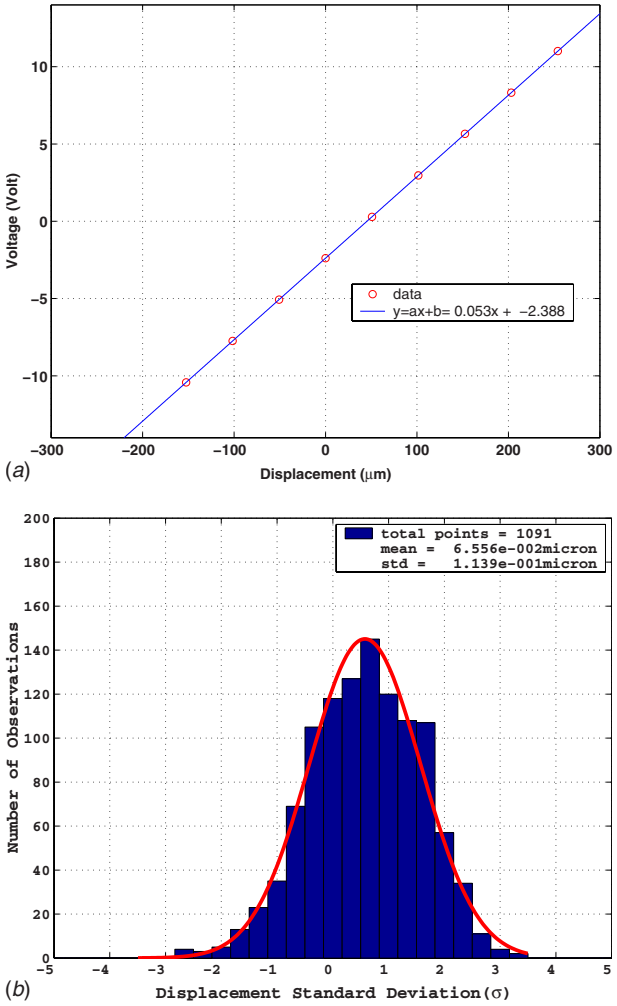

Fig. 2 LVDT calibration and mock test

8.1 Run 1: Stationary Belt. The distribution of the mass transfer Stanton number on the flat plate for the stationary belt is shown in Fig. 3(*a*). Here, Re_x is defined as $\mathrm{Re}_x = (u_{\mathrm{in}}|x - x_o|)/\nu$, where x_o is the location of the "virtual origin" of the turbulent boundary layer from the leading edge of the mass transfer plate ($x=0$) and u_{in} is the freestream velocity at position 7. The experimental results are compared with the empirical relations from Kays and Crawford [15] (Eq. (5*a*)) and Eckert and Drake [16] (Eq. (5*b*)), by replacing the Prandtl with the Schmidt number. However, it should be kept in mind that these relations are for a $1/n = 1/7$ power-law velocity profile, whereas in the current study n varies between 5.4–5.6 for the stationary belt case. As a comparison, the analytical solution for the variation of the St_m with Re_x is determined for $n=5.6$ (Eq. (5*c*)) and is plotted against the other values.

$$\mathrm{St}_m = 0.0287\ \mathrm{Re}_x^{-0.2}\ \mathrm{Pr}^{-0.4}(1 - (x_o/x)^{9/10})^{-1/9} \tag{5a}$$

$$\mathrm{St}_m = 0.0297 \frac{\mathrm{Re}_x^{-0.2}}{1 + 1.48\ \mathrm{Re}^{-0.1}\ \mathrm{Pr}^{-1/6}(\mathrm{Pr} - 1)}(1 - (x_o/x)^{9/10})^{-1/9} \tag{5b}$$

$$\mathrm{St}_m = 0.041\ \mathrm{Re}_x^{-0.22}\ \mathrm{Pr}^{-0.4}(1 - (x_o/x)^{0.866})^{-1/7.7} \tag{5c}$$

Except near the leading and trailing edges of the mass transfer plate, the measured values of St_m show good agreement with the empirical solutions as well as for $n=5.6$.

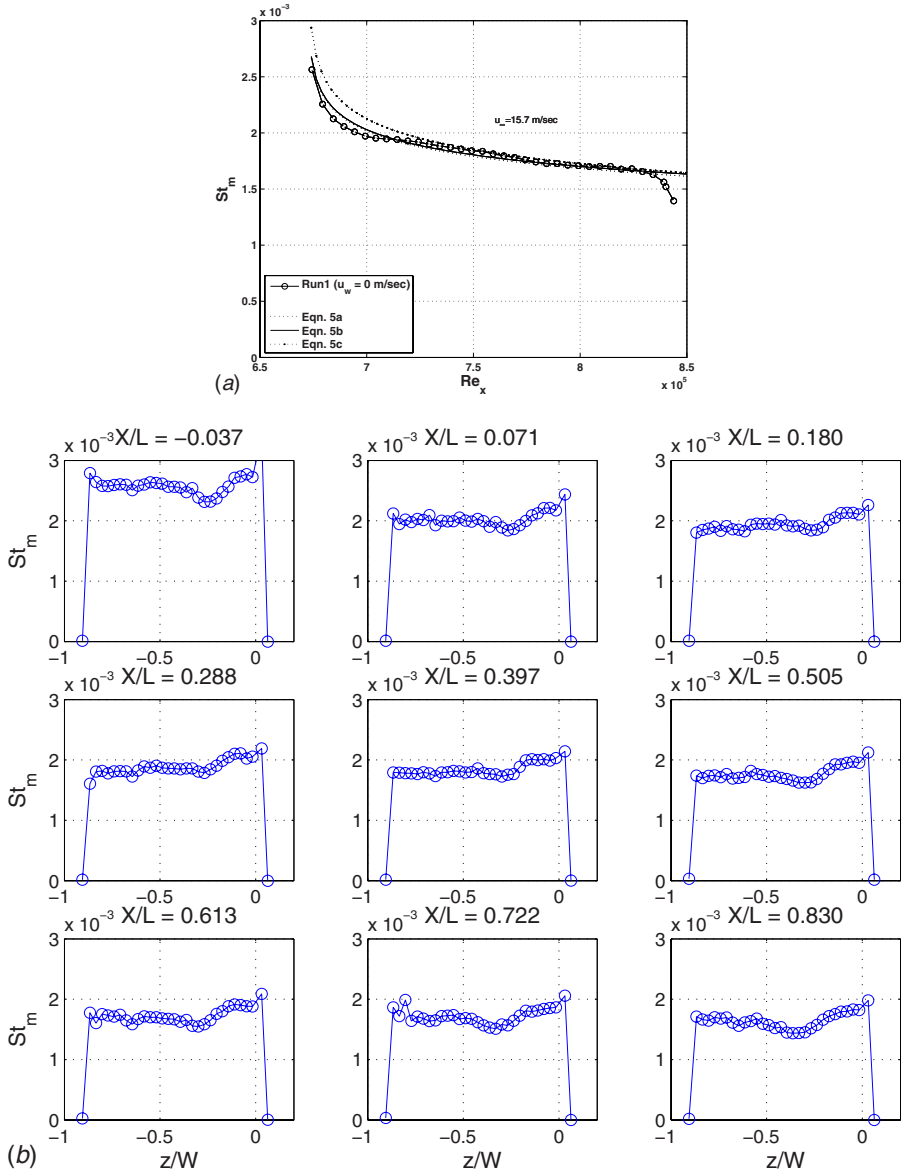

Fig. 3 Distribution of Stanton number (run 1)

The spanwise variation of St_m over the surface plate is shown in Fig. 3(*b*). Here L and W are the measures of the length and width of the mass transfer plate (Fig. 1(*a*)). Note that $x/L=0$ represents a transverse plane at the leading edge of the plate and $x/L=1$ represents the trailing edge of the plate. Similarly, the nondimensional transverse location varies from $z/W=0$ to -1. These plots give an estimate of the uniformity of the mass transfer distribution on the surface of the plate during the experimental conditions.

8.2 Runs 2 and 3 ($u_w=6$ m/s). With the belt moving in the direction of the freestream, the displacement and momentum thicknesses on and downstream of the belt are reduced. Table 1 lists the measurement conditions for this case. Figure 4(*a*) shows the variation of the St_m with Re_x. The total distance from the virtual origin ($x_o=-458$ mm, see Table 1) is used to calculate the Reynolds number. The results are in good agreement with previous correlations. Subsequently, the experimental data are compared with the same relations using the virtual origin for the stationary case ($x_o=-736$ mm). As observed in Fig. 4(*b*), the values of St_m in the latter case are overpredicted by approximately 6%.

8.3 Runs 7–9 ($u_w=10$ m/s). At the highest belt-freestream velocity ratio used (resulting in the removal of the inner region of the turbulent boundary layer), the virtual origin ($x_o=-313$ mm) moves even closer to the trailing edge of the moving surface. The variation of St_m with Re_x (Runs 7–9) are shown in Fig. 5(*a*). Figure 5(*b*) shows the same data using the virtual origin for the stationary belt ($x_o=-736$ mm). In this case, the overprediction is as much as 12%. Note the local minimum in the variation of St_m with Re_x. This is probably due to lower turbulence production in the boundary layer associated with the removal of the "inner region." This local minimum is not observed for the other velocity ratios. This result tends to confirm the methodology for determining the "limiting" velocity ($u_{w,c}$) of the belt as described in Part I. With the freestream velocity at 15.7 m/s the value of $u_{w,c}$ was obtained to be 8.85 m/s. Further downstream, the variation of St_m readjusts with the flow. Figure 6 shows the spanwise variation of St_m at various downsream positions on the mass transfer plate. There is a clear nonuniformity near the leading edge of the naph-

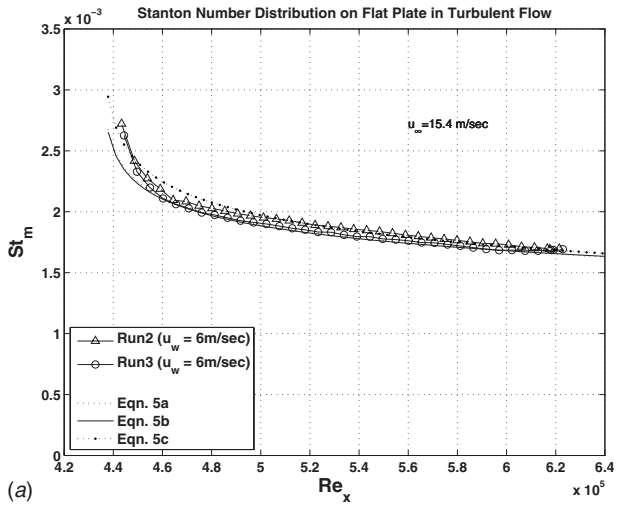

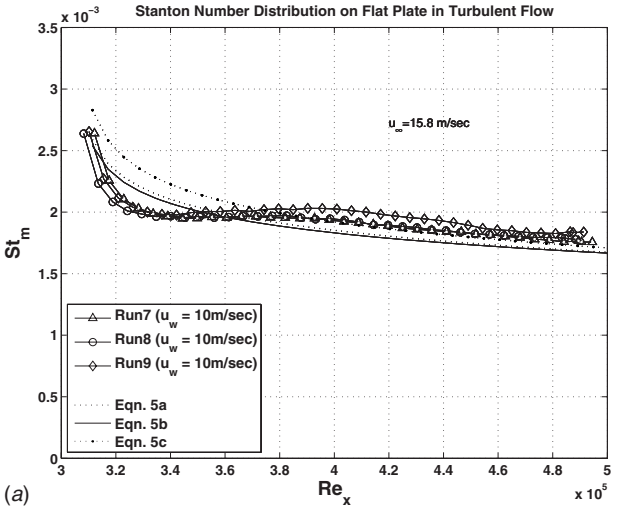

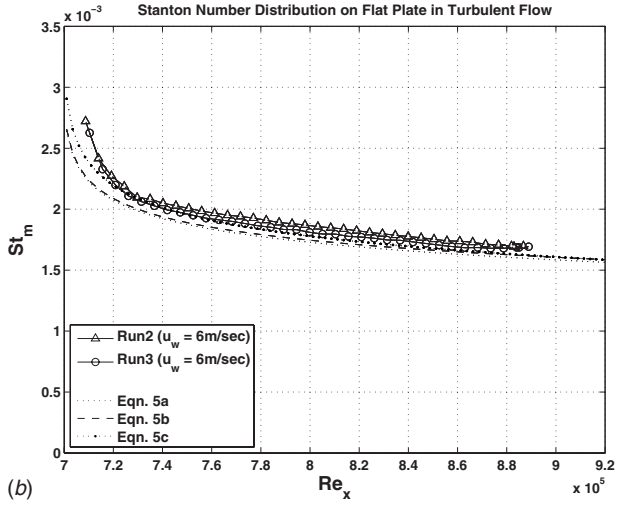

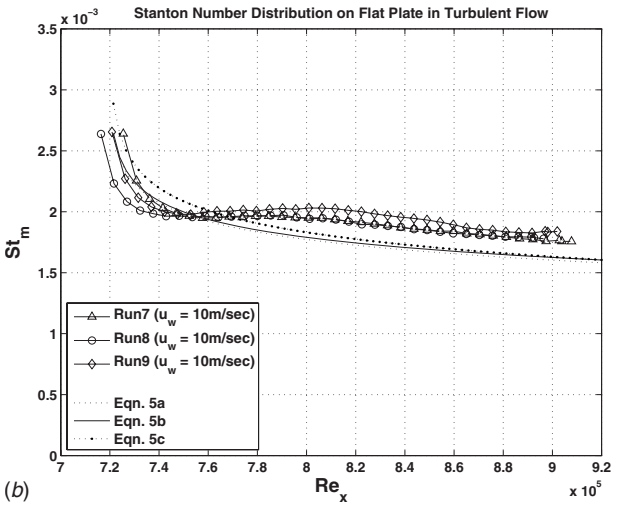

Fig. 4 Effect of modified virtual origin on the variation of Stanton number (runs 4–6)

Fig. 5 Effect of modified virtual origin on the variation of Stanton number (runs 7–9)

thalene plate, which may be due to slight irregularities in the moving belt surface, and diminishes further downstream.

9 Conclusions

Mass transfer experiments have been conducted to study the heat (mass) transfer variation, downstream of a moving belt using the heat/mass transfer analogy for four belt-freestream velocity ratios. With an increase in the surface velocity, the virtual origin of the turbulent boundary layer "moves" toward the trailing edge of the belt. This requires using a modified virtual origin for the boundary layer (a function of the velocity ratio, r) to compare well with mass transfer predictions. A high belt speed (u_w=10 m/s) removes the inner region of the turbulent layer as reported in Part I. It results in the reduction in the turbulence production over the belt itself and also at streamwise locations immediately downstream. This manifests itself as a local minimum in the streamwise distribution of St_m.

Nomenclature

$\hat{x}_i (i=1,2,3)$ = dimensionless spatial coordinates
c_w = local wall concentration
D_{naph} = mass diffusion coefficient, m^2/s
h_m = convective mass transfer coefficient, m/s
$\dot{m}$ = mass transfer rate during experiment, $\mathrm{kg}/\mathrm{m}^2\,\mathrm{s}$
Pr = Prandtl number, $\mathrm{Pr}=\nu/\alpha$
Pr_t = turbulent Prandtl number, $\mathrm{Pr}_t=\varepsilon/\varepsilon_H$
Re_x = distance-based Reynolds number, $\mathrm{Re}_x=(u_{\mathrm{in}}|x-x_o|)/\nu$
Sc = Schmidt number, $\mathrm{Sc}=\nu/D_{\mathrm{naph}}$
Sc_t = turbulent Schmidt number, $\mathrm{Sc}_t=\varepsilon/\varepsilon_M$
St = Stanton number, $\mathrm{St}=\mathrm{Nu}/\mathrm{Re}_x$ $\mathrm{Pr}=h/\rho c_p u_{\mathrm{in}}$
St_m = mass transfer Stanton number, $\mathrm{St}_m=\mathrm{Sh}/\mathrm{Re}_x$ Sc $=h_m/u_{\mathrm{in}}$
T_w = local wall temperature, °C
T_∞ = freestream temperature, °C
u_w = belt velocity, m/s
u_{in} = freestream velocity at position 7, Part I, m/s
x = streamwise direction, m
x_o = distance of virtual origin from leading edge of mass transfer plate, m
y = direction away from wall
z = spanwise direction

Greek Symbols

$\delta\tau$ = time duration of data run
δy = local sublimation depth
ε = turbulent momentum diffusivity
ε_H = turbulent thermal diffusivity
ε_M = turbulent mass diffusivity
ν = kinematic viscosity

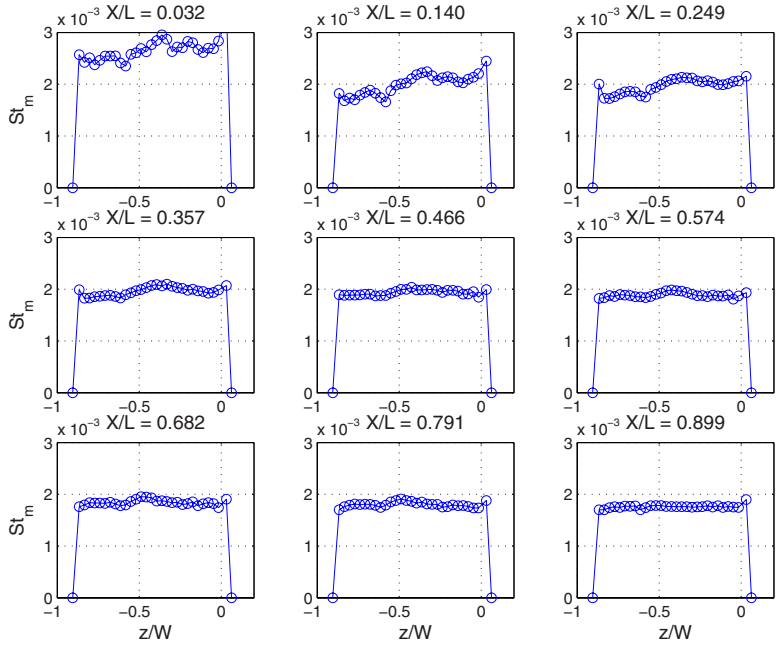

Fig. 6 Variation of Stanton number (run 7)

Φ = dimensionless mass fraction $((\omega-\omega_\infty)/(\omega_w-\omega_\infty))$
$\rho_{v,w}$ = naphthalene vapor density on the surface
ρ_s = density of solid naphthalene
$\rho_{v,\infty}$ = naphthalene vapor density at freestream
θ = dimensionless temperature difference $((T-T_\infty)/(T_w-T_\infty))$
τ = time

References

[1] Erickson, L., Cha, L., and Fan, L., 1966, "The Cooling of a Moving Continuous Flat Sheet," (AIChE Chemical Engineering Progress Symposium Series).
[2] Tsou, F., Sparrow, E., and Goldstein, R., 1967, "Flow and Heat Transfer in the Boundary Layer on a Continuous Moving Surface," Int. J. Heat Mass Transfer, **10**, pp. 219–235.
[3] Abdelhafez, T., 1985, "Skin Friction and Heat Transfer on a Continuous Flat Surface Moving in a Parallel Free Stream," Int. J. Heat Mass Transfer, **28**(6), pp. 1234–1237.
[4] Chappidi, P., and Gunnerson, F., 1989, "Analysis of Heat and Momentum Transport Along a Moving Surface," Int. J. Heat Mass Transfer, **32**(7), pp. 1383–1386.
[5] Sparrow, E., and Abraham, J., 2005, "Universal Solutions for the Streamwise Variation of the Temperature of a Moving Sheet in the Presence of a Moving Fluid," Int. J. Heat Mass Transfer, **48**, pp. 3047–3056.
[6] Cortell, R., 2007, "Flow and Heat Transfer in a Moving Fluid Over a Moving Flat Surface," Theor. Comput. Fluid Dyn., **21**(6), pp. 435–446.
[7] Singh, S., Rai, L., Puri, P., and Bhatnagar, A., 2005, "Effect of Moving Surface on the Aerodynamic Drag of Road Vehicles," Proc. Inst. Mech. Eng., Part D (J. Automob. Eng.), **219**, pp. 127–134.
[8] Ghosh, K., and Goldstein, R., 2010, "Effect of Upstream Shear on Flow and Heat (Mass) Transfer Over a Flat Plate Part I: Velocity Measurements," ASME J. Heat Transfer, **132**, p. 101701.
[9] Schmidt, E., 1929, "Verdunstung und warmeugergang," Gesund.-Ing., **29**, pp. 525–529.
[10] Nusselt, W., 1930, "Wärmeübergang, Diffusion und Verdunstung," ZAMM, **10**(2), pp. 105–121.
[11] Goldstein, R., and Cho, H., 1995, "Review of Mass Transfer Measurements Using Naphthalene Sublimation," Exp. Therm. Fluid Sci., **10**(4), pp. 416–434.
[12] Eckert, E., Sakamoto, H., and Simon, T., 2001, "The Heat/Mass Transfer Analogy Factor, Nu/Sh, for Boundary Layers on Turbine Blade Profiles," Int. J. Heat Mass Transfer, **44**, pp. 1223–1233.
[13] Kline, S., and McClintock, F., 1953, "Describing Uncertainty in Single-Sample Experiments," Mech. Eng. (Am. Soc. Mech. Eng.), **75**, pp. 3–8.
[14] Han, S., 2004. "The Heat and Mass Transfer Analogy Factor, Nu/Sh for 2-d and 3-d Boundary Layers," Ph.D. thesis, University of Minnesota, Minneapolis, MN.
[15] Kays, W., and Crawford, M., 1993, *Convective Heat and Mass Transfer*, McGraw-Hill, New York.
[16] Eckert, E., and Drake, R., 1972, *Analysis of Heat and Mass Transfer*, McGraw-Hill, New York.

Second-Law Thermodynamic Comparison and Maximal Velocity Ratio Design of Shell-and-Tube Heat Exchangers With Continuous Helical Baffles

Qiu-Wang Wang[1]
e-mail: wangqw@mail.xjtu.edu.cn

Gui-Dong Chen
e-mail: chengd514@163.com

Jing Xu
e-mail: xujing_nanjing@163.com

Yan-Peng Ji
e-mail: jyp.2008@stu.xjtu.edu.cn

State Key Laboratory of Multiphase Flow in Power Engineering,
School of Energy and Power Engineering,
Xi'an Jiaotong University,
Xi'an 710049, China

Shell-and-tube heat exchangers (STHXs) have been widely used in many industrial processes. In the present paper, flow and heat transfer characteristics of the shell-and-tube heat exchanger with continuous helical baffles (CH-STHX) and segmental baffles (SG-STHX) were experimentally studied. In the experiments, these STHXs shared the same tube bundle, shell geometrical structures, different baffle arrangement, and number of heat exchange tubes. Experimental results suggested that the CH-STHX can increase the heat transfer rate by 7–12% than the SG-STHX for the same mass flow rate although its effective heat transfer area had 4% decrease. The heat transfer coefficient and pressure drop of the CH-STHX also had 43–53% and 64–72% increase than those of the SG-STHX, respectively. Based on second-law thermodynamic comparisons in which the quality of energy are evaluated by the entropy generation number and exergy losses, the CH-STHX decreased the entropy generation number and exergy losses by 30% and 68% on average than the SG-STHX for the same Reynolds number. The analysis from nondimensional correlations for Nusselt number and friction factor also revealed that if the maximal velocity ratio $R > 2.4$, the heat transfer coefficient of CH-STHX was higher than that of SG-STHX, and the corresponding friction factor ratio kept at constant $f_{o,CH}/f_{o,SG} = 0.28$. [DOI: 10.1115/1.4001755]

Keywords: continuous helical baffles, segmental baffles, entropy generation number, exergy losses, second-law thermodynamic analysis, shell-and-tube heat exchangers

1 Introduction

Heat exchangers are widely used in chemical engineering processes, power plants, environmental protection, oil refining engineering, etc. Among different types of heat exchangers, shell-and-tube heat exchangers (STHXs) are still commonly used due to their simple manufacturing and adaptability operation conditions [1,2]. In order to enhance heat transfer performance and compactness of the STHXs, baffles have been used in the shell side to increase fluid flow velocity, mixing, and turbulence [3]. In addition, baffles can provide supports for the tube bundles. Many different types of baffles have been invented with the development of STHXs such as segmental baffles, deflecting baffles, disk-and-doughnut baffles, overlapped helical baffles, rod baffles, etc. [4–7]. The traditional segmental baffles have many problems, which were described in Refs. [8,9]. On the other hand, helical baffles [10] offer a possible alternative to the segmental baffles by circumventing some problems of conventional segmental baffles. Most of the early helical baffles are formed by overlapped fans, or oval shaped plates, and named as discontinuous helical baffles. These discontinuous helical baffles are normally arranged by a central pole and the volume of the central pole is relatively small. Fluid flows in the shell pass and rushes across the tube bundle in a close helix manner. However, serious leakage are induced by the triangle zones and they reduce the heat transfer coefficient of the STHX greatly. Many studies (Nemcansky and co-workers [11,12], Kral et al. [13], Wang et al. [14], Zhang et al. [15], and Zhang and Wang [16]) have confirmed that STHXs with discontinuous helical baffles (DCH-STHXs) often have higher heat transfer coefficient per pressure drop than conventional STHXs with segmental baffles. As a great improvement of discontinuous helical baffles, Wang and co-workers [17–19] introduced a manufacturing technique for continuous helical baffles and found that the STHXs with continuous helical baffles have better heat transfer performance than the STHXs with segmental baffles and discontinuous helical baffles. In our previous works, Peng et al. [20] carried out an experimental investigation on heat exchanger with continuous helical baffles. The results indicated that heat transfer coefficient of the STHX with continuous helical baffles was nearly 10% higher than that of the STHX with segmental baffles for the same shell-side mass flow rate. Wang et al. [21] applied the genetic algorithm to optimize correlations for STHXs with helical baffles and segmental baffles. The whole heat exchanger models and periodic models were also used in numerical simulations to study the flow and heat transfer performance of STHXs with continuous helical baffles (Wang and co-workers [22–26]).

However, almost all the experimental and numerical studies on continuous helical baffles mentioned above mainly focus on pressure drop and heat transfer rate or heat transfer coefficient, which are based on first-law thermodynamic analysis comparisons. Compared with the first-law thermodynamic analysis comparisons, the second-law thermodynamic analysis comparison, which are mostly evaluated by the entropy generation and exergy losses, concern the quality of energy. Many studies have been performed on the second-law thermodynamic analysis of heat exchangers [27–30]. Entropy generation in a counterflow heat exchanger has

[1]Corresponding author.

Contributed by the Heat Transfer Division of ASME for publication in the JOURNAL OF HEAT TRANSFER. Manuscript received December 10, 2009; final manuscript received March 24, 2010; published online July 27, 2010. Assoc. Editor: Giulio Lorenzini.

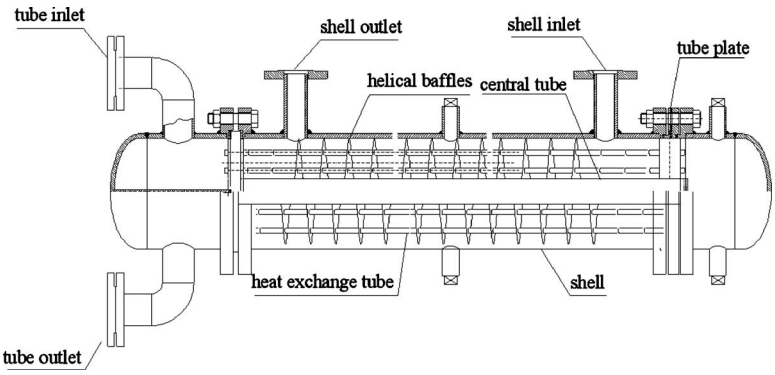

Fig. 1 Schematic of continuous helical baffled STHX (CH-STHX)

been analyzed in detail and expressions were derived in terms of relevant nondimensional parameters by Sarangi and Chowdhury [31]. Hesselgreaves [32] had a review of the various approaches to second-law thermodynamic analysis. Yilmaz et al. [33] presented second-law based performance evaluation criterion to evaluate performance of heat exchangers. Theoretical and experimental results of the second-law thermodynamic analysis on the heat transfer and flow of horizontal concentric tube heat exchanger were carried out by Naphon [34]. Recently, He et al. [35] carried out experimental and second-law based thermodynamic analysis on shell-and-tube heat exchangers with discontinuous helical baffles. However, there is few literature available for designing shell-and-tube heat exchangers with continuous helical baffles.

In the present paper, first, two different shell-and-tube heat exchangers with different baffles are designed and tested, second, heat transfer rate, heat transfer coefficient, and pressure drop of the STHXs based on first-law thermodynamic analysis are compared with each other, third, entropy generation number and exergy losses comparisons of the two STHXs are presented, then fourth, correlations of Nusselt number and friction factor versus Reynolds number are established and compared with previous studies, and, finally, maximal velocity ratio design method is proposed for designing CH-STHX.

2 Configurations of Heat Exchangers

Figure 1 shows the schematic of the shell-and-tube heat exchangers with continuous helical baffles (CH-STHX). In the shell side of the CH-STHX, the center tube, the continuous helical baffles, and the shell work together to form a continuous helix flow channel. The continuous helical baffle circles are linking end to end along the axial direction. In the tube side, the working fluid has a two-passage-layout arrangement and the tube inlet and tube outlet are designed on the same side of the shell. In the shell-and-tube heat exchangers with segmental baffles (SG-STHX), the continuous helical baffles are replaced by segmental baffles and there is no central tube. Because no heat exchange tubes can be set in the central tube, there are more heat exchange tubes in the SG-STHX than those in the CH-STHX.

Figures 2 and 3 show the baffle layout and tube bundle of the CH-STHX and SG-STHX, respectively. Detailed geometrical parameters of the present STHXs in the experiments are listed in Table 1.

3 Experiment Setup and Data Reduction

3.1 Experimental Setup. The experiments are carried out on an oil/water-water/water test stand. The experimental system consists of two loops: the hot oil loop and the cooling water loop, as shown in Fig. 4. The detailed descriptions of the two loops are given as follows.

Hot oil loop: There is a filter loop existing in the hot oil loop (it is not shown in Fig. 4) to clean the oil at the test-preparing stage for preventing blockage of measure equipments. In the oil loop, the oil is filled into the eclectic oil heater from the oil tank. Heated oil is elicited by the oil pump, first, flows through the turbine flow meter, then flows downstream through the shell side of the test heat exchanger, and finally goes back into the oil heater.

Cooling water loop: Cold water in the water tank is elicited by the water pump, water from the water pump partially turns back into the water tank through the bypass channel and the others flow through the turbine flow meter, flows into the tube side of test heat exchanger, then flows into cooling tower, and finally goes back into the water tank.

As shown in Fig. 4, ten parameters should be measured during the experimental process: inlet and outlet temperatures of the hot oil (shell side) $t_{o,in}$ and $t_{o,out}$, inlet and outlet temperatures of the cold water (tube-side) $t_{w,in}$ and $t_{w,out}$, volumetric flow rates of both sides V_o and V_w, pressure drops in the both sides Δp_o and Δp_w, and static pressure on the outlet of both sides $p_{o,out}$ and $p_{w,out}$. All digital data obtained for the above parameters are collected by a data acquisition system.

During the experiments, the water flow rate is set at a certain value first through which the tube-side Reynolds number is higher than 3000($>$2300) and then the Gnielinski's correlations can be effectively used to calculate the tube-side heat transfer coefficient.

(a) CH-STHX

(b) SG-STHX

Fig. 2 Baffle layout of heat exchangers

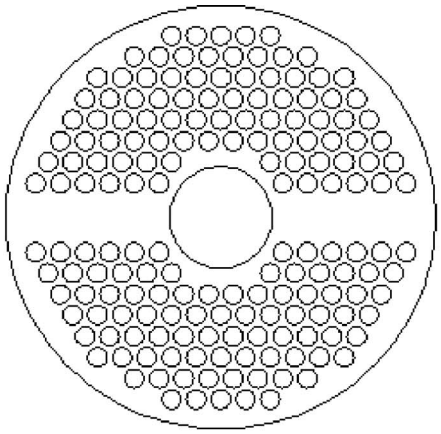

(a) CH-STHX

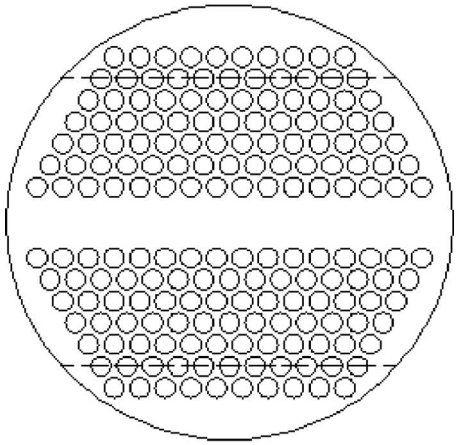

(b) SG-STHX

Fig. 3 Heat exchanger tube arrangement

The shell-side flow rates of the hot oil are adjusted by a valve from 0.8 kg/s to 2.0 kg/s. For each case, the deviation of heat transfer rate between the tube side and the shell side is controlled less than 5%.

3.2 Data Reduction. The shell-side, tube-side, and total heat transfer rates are defined by Eqs. (1)–(3).

$$Q_o = \frac{V_o \rho_o}{3600} c_{p,o}(t_{o,in} - t_{o,out}) \tag{1}$$

$$Q_w = \frac{V_w \rho_w}{3600} c_{p,w}(t_{w,out} - t_{w,in}) \tag{2}$$

$$Q_{ave} = \frac{Q_o + Q_w}{2} \tag{3}$$

The relative deviation of heat transfer rate between the shell side and tube side is controlled by

$$\varepsilon = \frac{|Q_o - Q_w|}{Q_{ave}} \times 100\% \leq 5\% \tag{4}$$

where V_o and V_w are the volumetric flow rates of oil and water and $c_{p,o}$ and $c_{p,w}$ are the specific heats of oil and water. All the thermodynamic and transport properties of oil and water are list in Table 2, where $t_{f,o}$ and $t_{f,w}$ are the average temperatures of the inlet and outlet in the shell side and the tube side.

Table 1 Geometric parameters of CH-STHX and SG-STHX

Item	Unit	Dimensions and description	
		SG-STHX	CH-STHX
Shell parameters			
D_o/D_i	mm	219/210	219/210
Material	-	Carbon steel	Carbon steel
Length of the shell (L)	mm	2016	2016
Tube parameters			
d_o/d_i	mm	9.8/9.2	9.8/9.2
Material	-	Cu	Cu
Effective length (L_t)	mm	1598	1598
Number (N_t)	-	182	174
Layout pattern	deg	30	30
Tube pitch (P_t)	mm	11.5	11.5
Baffle parameters			
Cut ratio	%	17	-
Helical angle (β)	deg	-	8.5
Thickness	mm	2	2
Number (N_b)	-	27	28
Baffles pitch (P_b)	mm	50	48
Central tube			
D_c	mm	-	45
Material	-	-	Carbon steel

The overall heat transfer coefficient U can be determined by

$$U = \frac{Q_{ave}}{A \Delta t_m} \tag{5}$$

where the heat transfer area A is the total effective outside tube area and Δt_m is the logarithmic-mean temperature difference, which can be determined by

$$A = N_t \pi d_o L_t \tag{6}$$

$$\Delta t_m = F \Delta t_c \tag{7}$$

where F is the correction factor and Δt_c is the counterflow log mean temperature difference [36].

$$\Delta t_c = \frac{(t_{o,in} - t_{w,out}) - (t_{o,out} - t_{w,in})}{\ln\left(\frac{t_{o,in} - t_{w,out}}{t_{o,out} - t_{w,in}}\right)} \tag{8}$$

$$F = \frac{\sqrt{R'^2 + 1}}{R' - 1} \frac{\ln\left(\frac{1 - P'}{1 - P'R'}\right)}{\ln\left(\frac{2 - P'(1 + R' - \sqrt{R'^2 + 1})}{2 - P'(1 + R' + \sqrt{R'^2 + 1}}\right)} \tag{9}$$

$$P' = \frac{t_{w,out} - t_{w,in}}{t_{o,in} - t_{w,in}} R' = \frac{t_{o,in} - t_{o,out}}{t_{w,out} - t_{w,in}} \tag{10}$$

The shell-side heat transfer coefficient h_o is determined from the overall heat transfer resistance relationship

$$\frac{1}{h_o} = \frac{1}{U} - R_o - \frac{d_o}{2\lambda_t} \ln\left(\frac{d_o}{d_i}\right) - \frac{d_o}{d_i} \frac{1}{h_w} - \frac{d_o}{d_i} R_w \tag{11}$$

where d_o and d_i are the outside and inside diameters of the heat exchange tubes, respectively, R_o and R_w are the fouling resistances in the shell side and tube side, both of them are neglected in the experiment because the test heat exchangers are new, λ_t is the thermal conductivity of the tube material, and h_w is the tube-side heat transfer coefficient, which is calculated by the semi-empirical correlation of Gnielinski [37].

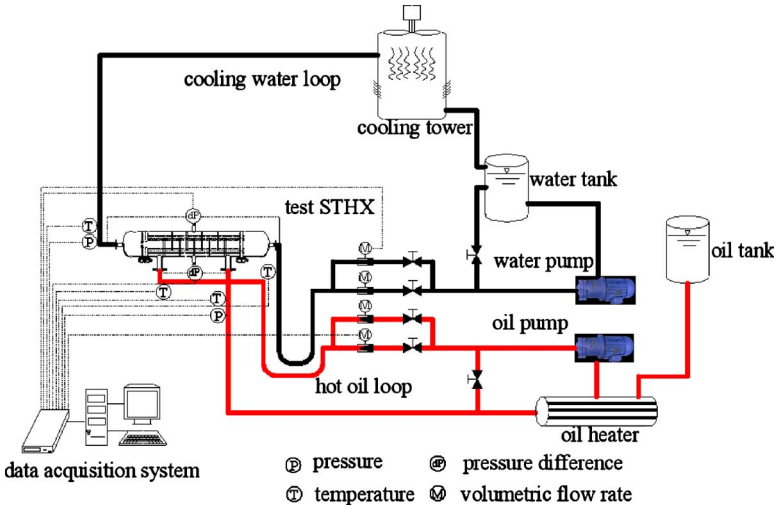

Fig. 4 Experimental loops

$$h_w = \left(\frac{\lambda_w}{d_i}\right)\frac{(f_w/8)(\mathrm{Re_t}-1000)\mathrm{Pr_t}}{1+12.7\sqrt{f_w/8}(\mathrm{Pr_t}^{2/3}-1)}\left[1+\left(\frac{d_i}{L_t}\right)^{2/3}\right] \quad (12)$$

$$f_w = (1.82\log_{10}\mathrm{Re_w}-1.64)^{-2} \quad (13)$$

$$\mathrm{Re_w} = u_{w,\max}d_i/\upsilon_w \quad (14)$$

After calculating the shell-side heat transfer coefficient h_o, the shell-side Nusselt number is computed by

$$\mathrm{Nu_o} = h_o\frac{d_o}{\lambda_o} \quad (15)$$

On the other hand, the flow friction characteristics can be presented by the friction factor f_o, which is defined as

$$f_o = \frac{2\Delta p_o}{\rho_o u_{o,\max}^2}\frac{d_o}{L_t} \quad (16)$$

where $u_{o,\max}$ is the velocity at the minimum free flow area $A_{o,\min}$.

For the CH-STHX

$$A_{o,\min} = 0.5P_hD_i\left(1-\frac{d_o}{P_t}\right)\left(1-\frac{D_c}{D_i}\right) \quad (17)$$

For the SG-STHX

$$A_{o,\min} = P_hD_i\left(1-\frac{d_o}{P_t}\right) \quad (18)$$

$$u_{o,\max} = \frac{V_o}{3600A_{o,\min}} \quad (19)$$

In addition, the Reynolds numbers in the shell side is defined as

$$\mathrm{Re_o} = \frac{u_{o,\max}d_o}{\upsilon_o} \quad (20)$$

3.3 Experimental Uncertainty. The method presented by Kline and McClintock [38] was used to calculate the experimental uncertainty and this method was described in detail by Peng et al. [20]. In the experiments, the relative uncertainties of temperature, flow rate, heat transfer rate, and heat transfer coefficient calculated by the method mentioned above are less than 1.8%, 0.14%, 2.5%, and 3.7%, respectively.

4 Results and Discussion

In the experiments, the hot oil flows in the shell side and cold water flows in the tube side. In order to have a comparison between the SG-STHX and CH-STHX under the same working conditions, the hot oil inlet temperature is set at $45\pm0.5°C$, the cold water inlet temperature is set at $22\pm0.5°C$, and the cold water flow rate is set at 1.38 kg/s.

4.1 Data Validation. Because there is no experimental data and experimental correlations for the heat transfer and pressure drop on the CH-STHX, which has the same helical angle with the test CH-STHX in the experiment, the verification of the measuring system is conducted on the SG-STHX. The heat transfer coefficient and pressure drop obtained from the experiments are compared with the data from the Bell–Delaware design method (Bell [39–41]). From Fig. 5, it is found that the average deviations in the heat transfer coefficients and pressure drops are 9.4% and 12.6%, respectively. These results demonstrate that the measuring system in the present experimental study is reliable.

4.2 Heat Transfer and Pressure Drop. The variation in the heat transfer rate Q versus the shell-side mass flow rate m_o is shown in Fig. 6 for the test CH-STHX and SG-STHX. It is suggested that the heat transfer rate increases with the increase in mass flow rate in both the CH-STHX and SG-STHX. The continuous helical baffles enhance the transfer rates by 7–12% than

Table 2 Thermophysical properties of oil and water

Item	Unit	Parameter value	
		Oil (320#)	Water
c_p	J/(kg K)	$853.436-0.631t_{f,o}$	$1000.44-0.141t_{f,w}$
υ	$m^2/s(\times10^{-6})$	$26.05-0.445t_{f,o}+0.00277{t_{f,o}}^2-5.893\times10^{-6}{t_{f,o}}^3$	$1.789-0.060t_{f,w}+0.00134{t_{f,w}}^2-1.4\times10^{-5}{t_{f,w}}^3$
ρ	kg/m^3	$2.159+2.677\times10^{-3}t_{f,o}-2.304\times10^{-6}{t_{f,o}}^2$	$4.211-2.12\times10^{-3}t_{f,w}-3.0\times10^{-6}{t_{f,w}}^2$
λ	W/(m K)	$0.137-1.040\times10^{-4}t_{f,o}-8.899\times10^{-8}{t_{f,o}}^2$	$0.551+2.56\times10^{-3}t_{f,w}-1.0\times10^{-5}{t_{f,w}}^2$

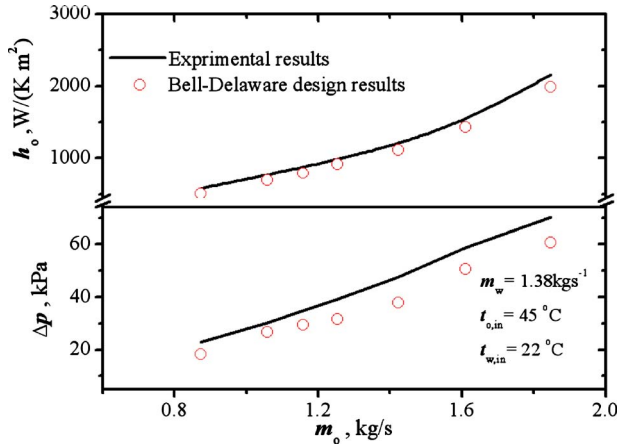

Fig. 5 Comparison of experimental data with results from Bell–Delaware design method

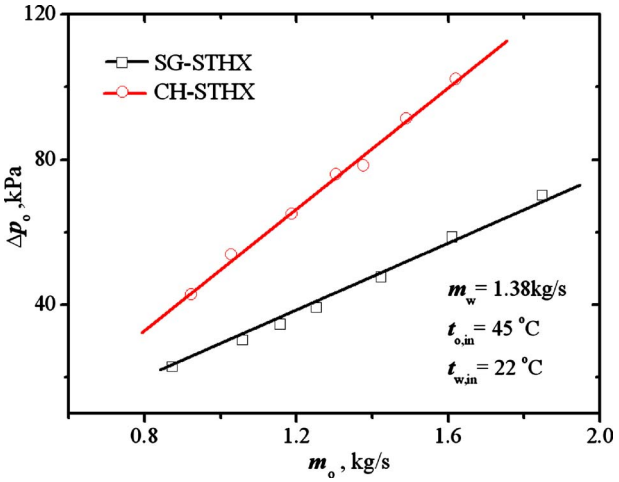

Fig. 7 Pressure drop versus mass flow rate

the segmental baffles for the same mass flow rate. It can be noticed from the geometrical parameters listed in Table 1 that the CH-STHX has less heat exchange tubes, in other words, the CH-STHX (with 174 tubes) has less effective heat transfer area than the SG-STHX (with 182 tubes). Therefore, as to the heat transfer coefficient of the two STHXs, the CH-STHX increases it by 43–53% in the test mass flow rate range. It confirms that the test CH-STHX has better heat transfer performance than the SG-STHX. The reasons for better heat transfer performance can be explained as follows. First, the completely helical flow manner is closer to "plug flow" and it can increase the temperature difference to drive heat transfer process. Second, the helical flow manner avoids local "dead zones" and can make the heat transfer process more evenly and in higher efficiency, in particular, the baffle pitch of the continuous helical baffles is much smaller than the segmental baffles. Finally, the minimal flow area of the CH-STHX has been greatly decreased and the velocity, turbulence, and mixing have been greatly increased.

The variation in the pressure drop Δp_o versus shell-side mass flow rate m_o is shown in Fig. 7. It can be seen that the pressure drop increases with the increase in the mass flow rate in the shell side in both the CH-STHX and SG-STHX. The pressure drops of the two STHXs have linear relationships with the mass flow rates and the CH-STHX has faster increase than the SG-STHX. The CH-STHX increases the pressure drop by 64–72% in the test mass flow rate range. It indicates that the test CH-STHX has worse pressure drop performance than the SG-STHX. The possible reason resulted in the worse pressure drop performance of CH-STHX is that the baffle pitch of the continuous helical baffles is much smaller than that of the segmental baffles.

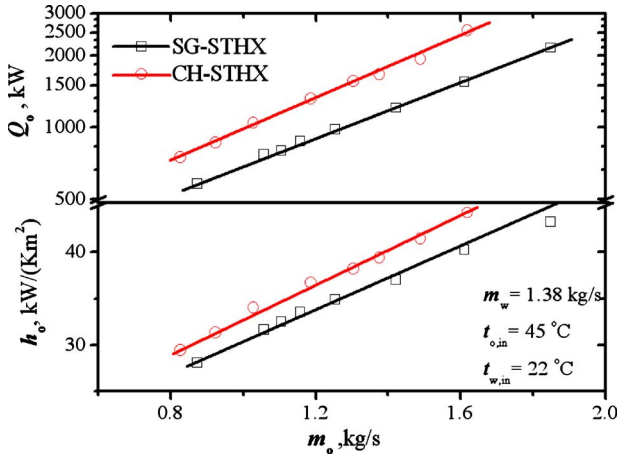

Fig. 6 Heat transfer rate and heat transfer coefficient versus mass flow rate

4.3 Entropy Generation Number and Exergy Losses. In order to evaluate the comprehensive performance of the two STHXs, entropy generation number and exergy losses, which are based on second-law thermodynamic analysis, are introduced. The entropy generation rate for a heat exchanger is defined as [32–34]

$$S'_{\text{seg}} = (m_o c_{p,o})_s \ln\left(\frac{T_{o,\text{out}}}{T_{o,\text{in}}}\right) + (m_w c_{p,w})_t \ln\left(\frac{T_{w,\text{out}}}{T_{w,\text{in}}}\right) - (m_o R)_s \ln\left(\frac{p_{o,\text{out}}}{p_{o,\text{in}}}\right) - (m_w R)_t \ln\left(\frac{p_{w,\text{out}}}{p_{w,\text{in}}}\right) \quad (21)$$

where the first two terms on the right side represent the shell-side and tube-side heat transfer irreversibility and the last two terms represent the shell-side and tube-side pressure drop irreversibility. What should be emphasized is that the pressure drops at the inlet and outlet in both sides used here are the total pressure drops initially, however, it is difficult to measure them and, therefore, the static pressure drops at the inlet and outlet in both sides are used instead in Eq. (21).

The entropy generation number is defined as [32–34]

$$N_s = \frac{S'_{\text{seg}}}{(mc_p)_{\min}} (mc_p)_{\min} = \min[m_w c_{p,w}, m_o c_{p,o}] \quad (22)$$

Exergy losses are the amount of work obtained at the end of the reversible process. The relationship between the irreversible production (exergy loss) and entropy generation can be expressed as

$$I' = T_e S'_{\text{seg}} \quad (23)$$

The variation in the entropy generation number N_s and exergy loss (I') with the shell-side Reynolds number Re_o is shown in Fig. 8. It can be seen that the entropy generation number of the SG-STHX is obviously higher than that of the CH-STHX for the same Reynolds number, which indicates that the SG-STHX has higher irreversibility losses of the heat transfer and pressure drop. In comparison, the CH-STHX decreases the entropy generation number by 30% on average than the SG-STHX. The total exergy losses, including the temperature difference and pressure drop in both sides, have similar trend as N_s with the Reynolds number and the CH-STHX decreases the exergy losses by 68% on average. From the results mentioned above, it can be concluded that the test CH-STHX has better heat transfer quality than the SG-STHX.

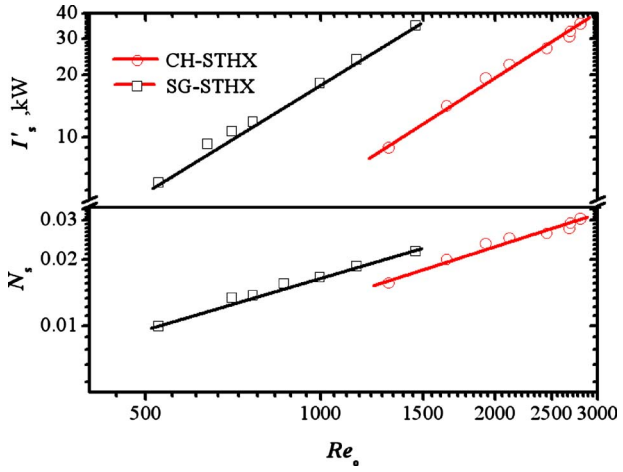

Fig. 8 Entropy generation number and exergy loss versus Reynolds number

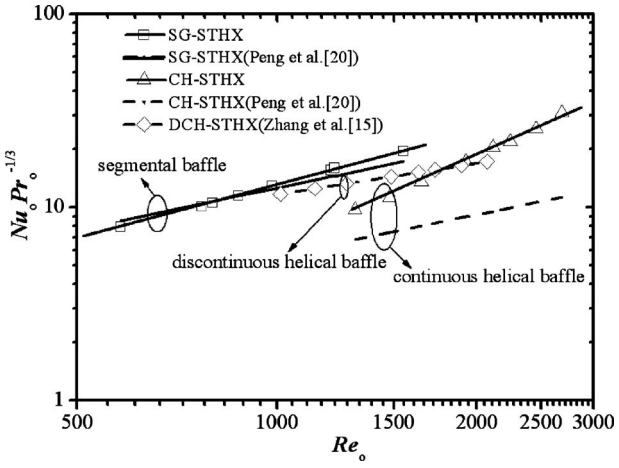

Fig. 9 Nusselt number versus Reynolds number

4.4 Correlations for Friction Factor and Nusselt Number. The data on heat transfer coefficients and pressure drops for different mass flow rates obtained from the experiments are used to fit correlations between the Nusselt numbers Nu_o, friction factors f_o and Reynolds numbers Re_o. The reduction results are fitted into the following correlations:

$$Nu_o\, Pr_o^{-1/3} = c_1\, Re_o^{m_1} \tag{24}$$

$$f_o = c_2\, Re_o^{m_2} \tag{25}$$

In order to have a comparison, the forms of the correlations are the same with previous studies [20,21] and the exponent in the fluid Prandtl number is fixed at $-1/3$, which was cited from Refs. [42,43]. The constants c_1, c_2, m_1, and m_2 for the test CH-STHX and SG-STHX are listed in Table 3.

Comparing with the experimental results and results from previous correlations fitted by Peng et al. [20] on SG-STHX, good agreement can be obtained. As shown in Fig. 9, the biggest difference is less than 12%. On the other hand, the present experimental results for CH-STHX are much higher than those in the previous work [20]. What should be emphasized here is that the helical angle in Peng et al. [20] is β=9.5 deg while that in the present work is β=8.5 deg. Smaller helix angle means smaller flow area, which can result in higher velocities, turbulence, and better heat transfer performance. The experimental results also indicate that the SG-STHX has better heat transfer performance than the CH-STHX for the same Reynolds number. When comparing with the results for DCH-STHX by Zhang et al. [15], the results also indicated that the CH-STHX has higher Nusselt number than the DCH-STHX in the higher Reynolds number region.

As shown in Fig. 10, the friction factors obtained by previous correlations [20] and the experimental results on both SG-STHX and CH-STHX have similar changes with the increase in Reynolds number and the experimental results are much higher than the results from previous correlations [20]. The experimental results indicate that the SG-STHX has higher friction factors than the CH-STHX and DCH-STHX for the same Reynolds number. The higher friction factors of the SG-STHX results from sudden contraction and expansion of the flow in the shell side and the fluid impinging on the shell walls caused by segmental baffles. It is also suggested that both the SG-STHX and CH-STHX have higher friction factors than the previous correlations [20]. This is perhaps because the effects of inlet and outlet sections are included in the present study while those in Ref. [20] are excluded.

4.5 Maximal Velocity Ratio Design Method. In practical industries, the tube bundle of shell-and-tube heat exchangers sometimes need to be redesigned or replaced because of failure or improvement in their heat transfer efficiency. How to design new tube bundle and baffle arrangements to make the CH-STHX has better performance than the original SG-STHX in the same shell structure is very important for designers. From the correlations mentioned above, it can be concluded that the maximal velocity in the minimum flow area, which determines the Reynolds number, can affect the heat transfer performance greatly. In order to enhance heat transfer performance of the CH-STHX, one effective method is to increase the maximal velocity in the shell side for the

Table 3 Constants in Nusselt number and friction factor correlations

STHX	c_1	m_1	RMSD (%)	Reynolds number	Reference
SG	0.0124	1.009	0.23	$580 < Re_o < 1560$	Present experiment
	0.7170	0.0889	0.14	$300 < Re_o < 2000$	Peng et al. [20]
CH	0.0001	1.602	0.42	$1300 < Re_o < 2690$	Present experiment
	0.6690	0.0450	0.18	$1100 < Re_o < 9000$	Peng et al. [20]
	c_2	m_2	RMSD (%)	Reynolds number	
SG	5.982	−0.303	0.27	$580 < Re_o < 1560$	Present experiment
	1.440	−1.670	0.10	$752 < Re_o < 2000$	Peng et al. [20]
CH	10.554	−0.534	0.28	$1300 < Re_o < 2690$	Present experiment
	0.226	−0.206	0.35	$2757 < Re_o < 9000$	Peng et al. [20][a]

[a]RMSD is the root mean square deviation.

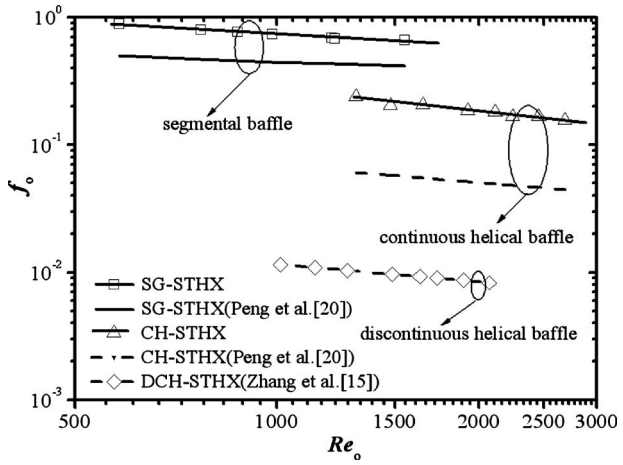

Fig. 10 Friction factor versus Reynolds number

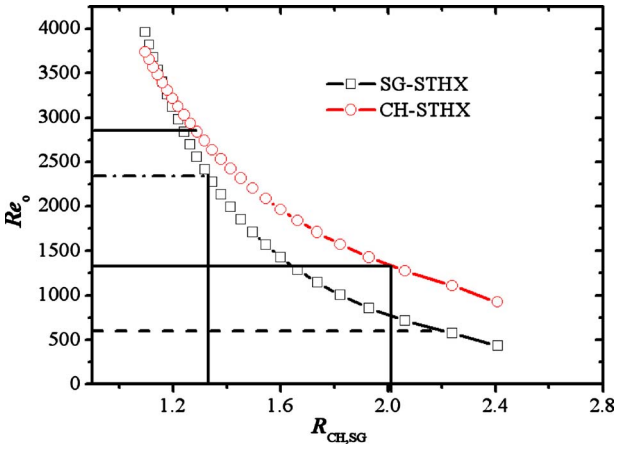

Fig. 12 Reynolds number versus maximal velocity ratio

same mass flow rate. The maximal velocity ratio R is defined as follows when the CH-STHX and the SG-STHX have the same heat transfer coefficient in the shell side:

$$R = \frac{u_{\mathrm{CH,max}}}{u_{\mathrm{SG,max}}} \tag{26}$$

where $u_{\mathrm{CH,max}}$ and $u_{\mathrm{SG,max}}$ are the maximal velocities in the minimum flow area for helical baffled heat exchangers and segmental baffled heat exchangers, respectively.

As shown in Fig. 11, the maximal velocity ratios decrease with an increase in the heat transfer coefficient in the shell side. When the maximal velocity ratios are above the line with circle points ($R>2.4$), the heat transfer coefficient of CH-STHX will be higher than that of SG-STHX. On the other hand, the corresponding friction factor ratios between the CH-STHX and the SG-STHX keep almost constant $f_{o,CH}/f_{o,SG}=0.28$ with the increase in heat transfer coefficient in the shell side. Figure 12 shows the maximal velocity ratio range obtained by the experimental data and the extrapolated maximal velocity ratio range obtained by correlations.

In order to validate the maximal velocity ratio design method, two other shell-and-tube heat exchangers with continuous helical baffles and segmental baffles in smaller scale are designed and tested. The geometrical parameters in detail are listed in Table 4. As shown in Table 4, when the maximal velocity ratio is set at 2.6, which is higher than 2.4, the shell-side heat transfer coefficient of the test CH-STHX is 18% higher than that of the test SG-STHX. In the meantime, the pressure drop cost of the CH-STHX has 20% increases than that of the SG-STHX.

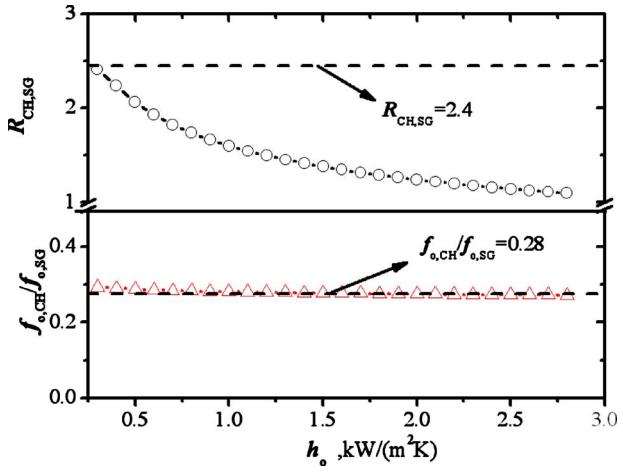

Fig. 11 Maximal velocity ratio versus heat transfer coefficient

5 Conclusions

The performances of the STHXs with continuous helical baffles and segmental baffles have been experimentally studied based on second-law thermodynamic comparisons and the maximal velocity ratio design method is proposed for designing the continuous helical baffled heat exchangers. The main conclusions can be summarized as follows.

(1) For the same mass flow rate, the shell-side heat transfer rate, heat transfer coefficient, and pressure drop of the CH-STHX are higher than those of the SG-STHX by 7–12%, 43–53%, and 64–72%, respectively. The test CH-STHX has better heat transfer performance.
(2) For the same Reynolds number, the entropy generation number, and exergy losses of the CH-STHX decrease by 30% and 68% on average than the SG-STHX. The test CH-STHX has better performance in reducing entropy generation and exergy losses.
(3) Correlations in the form of $\mathrm{Nu_o\,Pr_o^{-1/3}}=c_1\,\mathrm{Re_o}^{m_1}$ and $f_o=c_2\,\mathrm{Re_o}^{m_2}$ are developed for thermal design of similar shell-and-tube heat exchangers with continuous helical baffles and segmental baffles.
(4) If the maximal velocity ratio $R>2.4$, the heat transfer coefficient of CH-STHX is higher than that of the SG-STHX and the corresponding friction factor ratio keeps at constant $f_{o,CH}/f_{o,SG}=0.28$.

Acknowledgment

This work is supported by National Nature Science Foundation of China (Grant No. 50776068).

Nomenclature

A = heat transfer area, m^2
A_{mim} = minimum transverse area, m^2
c_1, c_2 = constants
c_p = specific heat, J/(kg K)
D, D_c = diameter of shell and central tube, mm
D_i = inner diameter of shell, mm
d_i = inner diameter heat exchange tube, mm
d_o = outer diameter heat exchange tube, mm
F = correction factor
f = friction factor
h = heat transfer coefficient, W/(m^2 K)
I' = exergy loss, kW

Table 4 Test results of shell-and-tube heat exchangers

Items	Variable	Unit	Value	
Heat exchangers			SG-STHX	CH-STHX
Inner diameter of shell	D_i	mm	207	207
Center tube diameter	D_c	mm	-	48
Diameter of tube	d_t	mm	10	10
Distance between tubes	P_t	mm	12.5	12.5
Distance between baffles	P_h	mm	70	48
Number of baffles	N_b		7	9
Maximal velocity ratio	R		1	2.6
Number of tubes	N_t		176	158
Layout of tubes		deg	30	30
Length of tubes	L	mm	620	620
Mass flow rate (oil)	m_o	kg/s	2.62	2.62
Mass flow rate (water)	m_w	kg/s	1.32	1.32
Inlet temperature (oil)	$t_{o,in}$	°C	60	60
Outlet temperature (oil)	$t_{o,out}$	°C	53.4	52.9
Inlet temperature (water)	$t_{w,in}$	°C	31.0	31.0
Outlet temperature (water)	$t_{w,out}$	°C	37.8	38.2
Pressure drop	Δp	kPa	10.1	12.7
Shell-side heat transfer Coefficient	h	W/(m K)	803	927

L = shell length, mm
L_t = effective length of tubes, mm
m = mass flow rate, kg/s
m_1, m_2 = constants
Nu = Nusselt number
N_t = number of heat exchange tubes
N_b = number of baffles
N_s = entropy generation number
p = static pressure drop, kPa
P' = correction factor
P_b = distance between baffles, mm
Pr = Prandtl number
P_t = distance between tube, mm
Δp = pressure drop, kPa
Q = heat transfer rate, W
Re = Reynolds number
R_o, R_w = fouling resistance, m^2 K/W
R = ideal gas constant, J/(kg K); maximal velocity ratio
R' = correction factor
S'_{seg} = entropy generation, kW/K
t = temperature, °C
t_f = average fluid temperature, °C
T = temperature, K
Δt_m = log mean temperature difference, °C
Δt_c = log mean temperature difference for counterflow, °C
U = overall heat transfer coefficient, W/(m^2 K)
u = velocity, m/s
V = volumetric flow rate, m^3/h

Greek Symbols

β = helix angle, deg
ε = heat balance deviation
ρ = density, kg/m^3
λ = thermal conductivity, W/(m K)
λ_t = thermal conductivity for tube material, W/(m K)
υ = kinematic viscosity, m^2/s

Subscripts

ave = average
b = baffle
CH = continuous helical baffles
e = environment
in = inlet
max = maximal
min = minimal
o = oil
out = outlet
SG = segmental baffles
w = water

References

[1] Gulyani, B. B., 2000, "Estimating Number of Shells in Shell and Tube Heat Exchangers: A New Approach Based on Temperature Cross," ASME J. Heat Transfer, **122**, pp. 566–571.
[2] Master, B. I., Chunangad, K. S., Boxma, A. J., Kral, D., and Stehlik, P., 2006, "Most Frequently Used Heat Exchangers From Pioneering Research to Worldwide Applications," Heat Transfer Eng., **27**(6), pp. 4–11.
[3] Nasiruddin, K., and Siddiqui, M. H., 2007, "Heat Transfer Augmentation in a Heat Exchanger Using a Baffle," Int. J. Heat Fluid Flow, **28**, pp. 318–328.
[4] Stehlík, P., and Wadekar, V. V., 2002, "Different Strategies to Improve Industrial Heat Exchanger," Heat Transfer Eng., **23**(6), pp. 36–48.
[5] Reppich, R. M., and Zagermann, S., 1995, "A New Design Method for Segmentally Baffled Heat Exchangers," Comput. Chem. Eng., **19**, pp. 137–142.
[6] Anthony, J., 1998, "Tube and Shell Heat Exchanger With Baffle," U.S. Patent No. US5,832,991.
[7] Gentry, C. C., 1998, "Rod Baffle Heat Exchanger," Appl. Therm. Eng., **18**(6), pp. VII–VIII.
[8] Li, H. D., and Kottke, V., 1998, "Effect of Leakage on Pressure Drop and Local Heat Transfer in Shell-and-Tube Heat Exchangers for Staggered Tube Arrangement," Int. J. Heat Mass Transfer, **41**(2), pp. 425–433.
[9] Gaddis, E. S., and Gnielinski, V., 1997, "Pressure Drop on the Shell Side of Shell-and-Tube Heat Exchangers With Segmental Baffles," Chem. Eng. Prog., **36**, pp. 149–159.
[10] ABB Lummus Global, Inc., 2004, "Heat Exchanger," U.S. Patent No. US 6,827,138 Bl.
[11] Lutcha, J., and Nemcansky, J., 1990, "Performance Improvement of Tubular Heat Exchangers by Helical Baffles," Chem. Eng. Res. Des., **68**, pp. 263–270.
[12] Stehlík, P., Nemcansky, J., Kral, D., and Swanson, L. W., 1994, "Comparison of Correction Factors for Shell-and-Tube Heat Exchangers With Segmental or Helical Baffles," Heat Transfer Eng., **15**(1), pp. 55–65.
[13] Kral, D., Stehlik, P., Van Der Ploeg, H. J., and Master, B. I., 1996, "Helical Baffles Shell-and-Tube Heat Exchangers, Part 1: Experimental Verification," Heat Transfer Eng., **17**(1), pp. 93–101.
[14] Wang, Q. W., Luo, L. Q., Zeng, M., Wang, L., Tao, W. Q., and Huang, Y. P., 2005, "Shell-side Heat Transfer and Pressure Drop of Shell-and-Tube Heat Exchangers With Overlap Helical Baffles," J. Chem. Ind. Eng., **56**(4), pp. 598–601.
[15] Zhang, J. F., Li, B., Huang, W. J., Lei, Y. G., He, Y. L., and Tao, W. Q., 2009, "Experimental Performance Comparison of Sell-Side Heat Transfer for Shell-and-Tube Heat Exchangers With Middle-Overlapped Helical Baffles and Segmental Baffles," Chem. Eng. Sci., **64**(8), pp. 1643–1653.
[16] Zhang, D. J., and Wang, Q. W., 2005, "Numerical Simulation of Flow Performance in Shell Side of Shell-and-Tube Heat Exchanger With Discontinuous

Helical Baffles," Proceedings of the Second International Symposium on Thermal Science and Technology, Beijing, pp. 181–185.
[17] Wang, Q. W., Chen, Q. Y., Peng, B. T., and Zeng, M., Luo, L. Q., and Wu, Y. N., 2005, "Continuous Helical Baffled Shell-and-Tube Heat Exchanger," China Patent No. CN: ZL200510043033.5.
[18] Wang, Q. W., Chen, G. D., Chen, Q. Y., and Zeng, M., 2008, "Recent Patents in Shell-and-Tube Heat Exchangers With Helical Baffles," Recent Patents on Mechanical Engineering, **1**, pp. 88–95.
[19] Wang, Q. W., Chen, G. D., Chen, Q. Y., and Zeng, M., 2010, "Review of Improvements on Shell-and-Tube Heat Exchangers With Helical Baffles," Heat Transfer Eng., **31**(10), pp. 836–853.
[20] Peng, B. T., Wang, Q. W., Zhang, C., Xie, G. N., Luo, L. Q., Chen, Q. Y., and Zeng, M., 2007, "An Experimental Study of Shell-and-Tube Heat Exchangers With Continuous Helical Baffles," ASME J. Heat Transfer, **129**(10), pp. 1425–1431.
[21] Wang, Q. W., Xie, G. N., Peng, B. T., and Zeng, M., 2007, "Experimental Study and Genetic-Algorithm-Based Correlation on Shell-Side Heat Transfer and Flow Performance of Three Different Types of Shell-and-Tube Heat Exchangers," ASME J. Heat Transfer, **129**(9), pp. 1277–11285.
[22] Wang, Q. W., Chen, Q. Y., and Chen, G. D., 2009, "Numerical Investigation on Combined Multiple Shell-Pass Shell-and-Tube Heat Exchangers With Continuous Helical Baffles," Int. J. Heat Mass Transfer, **52**(5–6), pp. 1214–1222.
[23] Wang, Q. W., Chen, G. D., Chen, Q. Y., Zhang, D. H., and Zeng, M., 2008, "Numerical Studies of a Novel Combined Multiple Shell-Pass Shell-and-Tube Heat Exchangers With Helical Baffles," ASME Paper No. HT2008-56217.
[24] Chen, G. D., Zeng, M., and Wang, Q. W., 2008, "Numerical Studies of Combined Multiple Shell-Pass Shell-and-Tube Heat Exchangers With Helical Baffles," Seventh International Symposium on Heat Transfer, Beijing, China.
[25] Chen, G. D., Wang, Q. W., and Zeng, M., 2009, "Numerical Studies on a Novel Shell-and-Tube Heat Exchanger With Combined Helical Baffles," Seventh International Conference on Enhanced, Compact and Ultra-Compact Heat Exchangers: From Microscale Phenomena to Industrial Applications, Heredia, Costa Rica, Paper No. CHE 2009-17.
[26] Chen, G. D., Wang, Q. W., and Peng, B. T., 2009, "Experimental and Numerical Studies of Shell-and-Tube Heat Exchangers With Helical Baffles," ASME Paper No. HT2009-88174.
[27] Bejan, A., 1977, "The Concept of Irreversibility in Heat Exchanger Design: Counterflow Heat Exchanger for Gas-Gas Application," ASME J. Heat Transfer, **99**, pp. 374–380.
[28] Bejan, A., 1979, "A Study of Entropy Generation in Fundamental Convective Heat Transfer," ASME J. Heat Transfer, **101**, pp. 374–380.
[29] Prasad, R. C., and Shen, J., 1993, "Performance Evaluation of Convective Heat Transfer Enhancement Devices Using Exergy Analysis," Int. J. Heat Mass Transfer, **36**, pp. 4193–4197.
[30] Sahin, A., 2000, "Entropy Generation in Turbulent Liquid Flow Through a Smooth Duct With Constant Wall Temperature," Int. J. Heat Mass Transfer, **43**, pp. 1469–1478.
[31] Sarangi, S. K., and Chowdhury, K., 1982, "On the Generation of Entropy in a Counterflow Heat Exchanger," Cryogenics, **22**(2), pp. 63–65.
[32] Hesselgreaves, J. E., 2000, "Rationalisation of Second Law Analysis of Heat Exchangers," Int. J. Heat Mass Transfer, **43**(22), pp. 4189–4204.
[33] Yilmaz, M., Sara, O. N., and Karsli, S., 2001, "Performance Evaluation Criteria for Heat Exchangers Based on Second Law Analysis," Int. J. Heat Mass Transfer, **1**(4), pp. 278–294.
[34] Naphon, P., 2006, "Second Law Analysis on the Heat Transfer of the Horizontal Concentric Tube Heat Exchanger," Int. Commun. Heat Mass Transfer, **33**(8), pp. 1029–1041.
[35] He, Y. L., Lei, Y. G., Zhang, J. F., Chu, P., and Li, R., 2009, "Second-Law Based Thermodynamic Analysis of a Novel Heat Exchanger," Chem. Eng. Technol., **32**(1), pp. 86–92.
[36] Bowman, R. A., Mueller, A. C., and Nagle, W. M., 1940, "Mean Temperature Difference in Design," Trans. ASME, **26**, pp. 283–294.
[37] Gnielinski, V., 1976, "New Equations for Heat and Mass Transfer in Turbulent Pipe and Channel Flows," Int. Chem. Eng., **16**, pp. 359–368.
[38] Kline, S. J., and McClintock, F. A., 1953, "Describing Uncertainties in Single-Sample Experiments," Mech. Eng. (Am. Soc. Mech. Eng.), **75**(1), pp. 3–8.
[39] Bell, K. J., 1981, "Delaware Method for Shell Side Design," *Heat Exchangers-Thermal-Hydraulic Fundamentals and Design*, S. Kakac, A. E. Bergles, and E. Mayinger, eds., Taylor & Francis, Washington, DC.
[40] Bell, K. J., 1986, "Delaware Method for Shell Side Design," *Heat Exchanger Sourcebook*, G. W. Pallen, ed., Hemisphere, New York.
[41] Bell, K. J., 1988, "Delaware Method for Shell-Side Design," *Heat Transfer Equipment Design*, R. K. Shah, E. C. Sunarao, and R. A. Mashelkar, eds., Taylor & Francis, New York.
[42] Cengel, Y. A., 1998, *Heat Transfer, A Practical Approach*, WCB McGraw-Hill, Boston.
[43] Churchill, S. W., and Bernstein, M., 1977, "A Correlating Equation for Forced Convection From Gases and Liquids to a Circular Cylinder in Cross Flow," ASME J. Heat Transfer, **99**(1), pp. 300–306.

Exergy Analysis of Coil-Spring Turbulators Inserted in the Horizontal Concentric Tubes

Haydar Eren
Department of Mechanical Engineering,
University of Firat,
23119 Elazig, Turkey

Nevin Celik[1]
Department of Mechatronic Engineering,
University of Firat,
23119 Elazig, Turkey
e-mail: nevincelik23@gmail.com

Irfan Kurtbas
Department of Mechanical Engineering,
University of Hitit,
19030 Corum, Turkey

Seyba Yildiz
Department of Mechanical Engineering,
University of Firat,
23119 Elazig, Turkey

In this study, to obtain definitive information about the effects of spring-type turbulators located in the inner pipe of a concentric heat exchanger, the rates of exergy transfer Nusselt number (Nu_e) and exergy loss (E^*) were obtained. The results were parametrized by the Reynolds number ($2500 < Re < 12{,}000$), the outer diameter of the spring ($D_s = 7.2$ mm, 9.5 mm, 12 mm, and 13 mm), the number of the springs ($n = 4$, 5, and 6), and the incline angle of the spring ($\theta = 0$ deg, 7 deg, and 10 deg). It is found that increasing those parameters results in a significant augmentation on exergy transfer comparative to the results of a smooth empty tube. A new term, exergy transfer Nusselt number, is derived in this paper. This term includes both irreversibility due to temperature gradient on the heat transfer surface and irreversibility due to pressure loss of the system. Hence, it is observed that optimum values of independent parameters for a constant surface temperature tube can be determined by this value. With regard to the maintained data, the irreversibility of heat transfer and pressure loss increases with increasing Re. However, at a certain value of Re, the increment rate of the irreversibility of heat transfer decreases, while the increment rate of the irreversibility of pressure loss increases. These results will contribute to adjust the system parameters such as the pump power and other independent parameters more easily. [DOI: 10.1115/1.4001926]

Keywords: heat transfer enhancement, heat exchangers, spring turbulator, exergy transfer

1 Introduction

The first law of thermodynamics deals with the quantity of energy and asserts that energy cannot be created and destroyed. The second law, however, deals with the quality of energy. More specifically, it is concerned with the degradation of energy during a process, entropy generation, and the lost opportunities to do work [1]. Since the second law analysis of the heat exchangers provides data for the users about the quality of energy, many researchers investigate the exergy and entropy analysis of the heat exchangers. The analysis is mostly done for turbulated heat exchangers [2–5].

In order to augment heat transfer and increase the system efficiency, turbulators with different geometries have been developed and many experimental investigations have been conducted to determine their thermodynamic characteristics. The coiled wire is one of the common heat transfer enhancement devices.

The thermal performance of a coiled wire inserted in heat exchangers is previously investigated by some researchers based on the first law of thermodynamics [6–11], especially the variations in Nusselt number and friction factor with regard to the parametric values of the coiled wire; such as the pitch [6–9] and diameter of the wire [7,9] and the length and segmentation of the coiled spring [11]. The effects of the orientation angle, number, and diameter of the coil springs inserted in a heat exchanger were also analyzed experimentally in detail by Eren et al. [12].

To the best of the authors' knowledge, despite the great number of papers in literature, there is not much work that provides detailed information on the second law analysis of coil-spring turbulators. Prasad and Shen [13] studied the performance evaluation of several wire-coil inserts using the exergy analysis method. It was seen that the minimum exergy destruction criterion results in a thermodynamically optimum choice. However, the heat transfer improvement number and the exergy destruction number provide realistic criteria for comparing the performance of augmentation devices.

The properties of vortex flow (vortex)–acoustic coupling and the relation between entropy generation and vortex characteristics in a coiled wire inserted tube were investigated experimentally by Yakut and Sahin [14]. It was observed that coiled wires were thermodynamically advantageous ($Ns < 1$) up to 13,000 Reynolds number.

In present study, the exergy analysis of long coil springs inserted through a horizontal heat exchanger was performed in terms of mean exergy transfer Nusselt number Nu_e, exergy transfer Nusselt number due to pressure loss Nu_P, exergy transfer Nusselt number due to temperature differences Nu_T, and nondimensional exergy transfer rate E^*. The investigation includes the effects of the numbers ($n = 4$, 5, and 6), the incline angles ($\theta = 0$ deg, 7 deg, and 10 deg), and the outer diameters of the coil springs ($D_s = 7.2$ mm, 9.5 mm, 12 mm, and 13 mm) on the mentioned terms. Coils were used as turbulators in a heat exchanger whose inner tube is heated by constant temperature water vapor on all surfaces. The Reynolds number varied from 2500 to 12,000, which means that turbulent flow is considered as the flow region. The results obtained from the tube with a coil-spring insert are compared with those without a coil-spring insert.

2 Experimental Setup

The experimental setups used in the heat transfer and pressure loss experiments were explained in another study of the authors of this paper [12]. A schematic view of the setup is presented in Fig. 1.

The heat exchanger is a classical-type concentric tube; the outer surface of the inner tube is heated by the condensation of a stream

[1]Corresponding author.

Contributed by the Heat Transfer Division of ASME for publication in the JOURNAL OF HEAT TRANSFER. Manuscript received October 27, 2009; final manuscript received April 19, 2010; published online July 29, 2010. Assoc. Editor: Giulio Lorenzini.

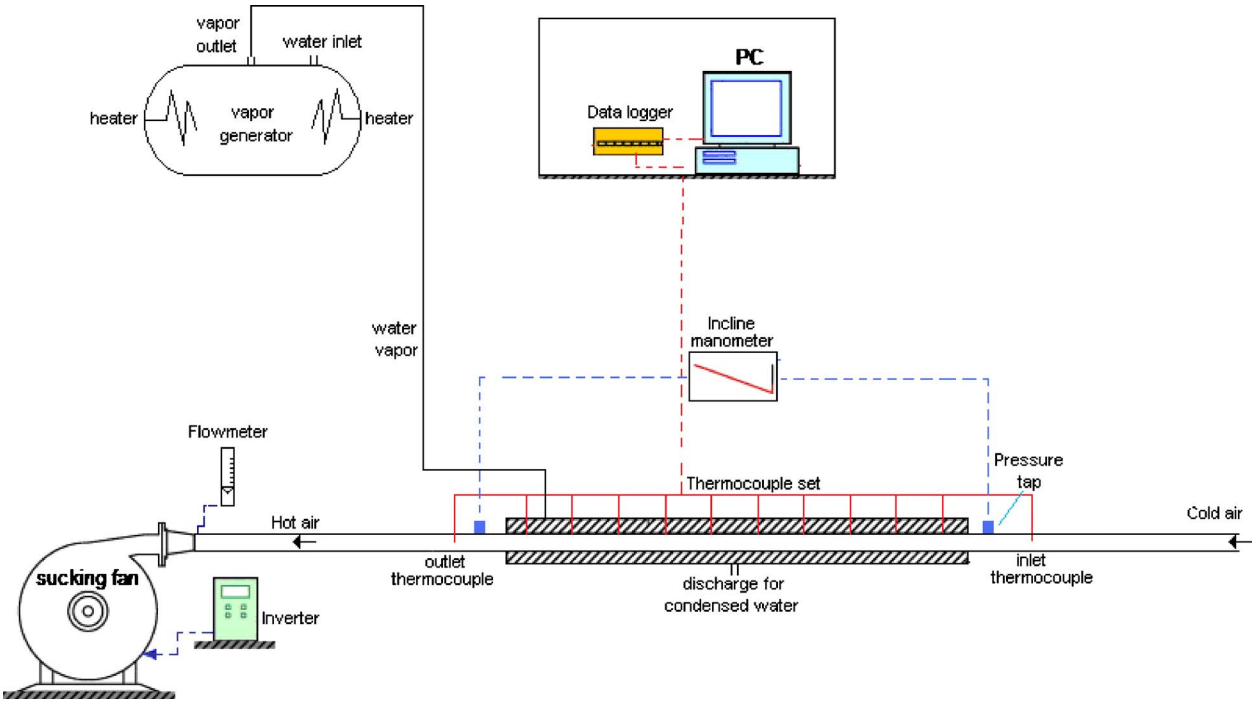

Fig. 1 Schematic view of whole setup

of flowing water vapor. The inner and outer diameters of the inner tube are, respectively, 60 mm and 62 mm, and the length of the tube is 900 mm. As an outer tube, a 1 mm thick flat plate with dimensions of 700×1200 mm^2 is rolled to obtain a circular tube with a diameter of 210 mm.

The outer surface of the inner tube was kept at a constant temperature (100°C) by continuous contact with saturated water vapor introduced and filled into the annular space between the inner and outer tubes and discharged by a channel. The surface temperatures were measured by T-type thermocouples located every 50 mm distance along the tube length. The mean local wall temperature was determined by means of calculations based on the readings of the thermocouples. The inner and outer temperatures of air were also measured at certain points inside the tube. The pressure loss was maintained by an inclined manometer [12].

Turbulators inserted in the horizontal concentric tube are coil springs. Figure 2 shows detailed instructions about the coil springs. In literature, *coil diameter* or *wire diameter* terms [6–11,13,14] are generally used to define the diameter of the coil wire, whereas in the present paper the *diameter of the spring* term (D_s) defines the outer diameter of a spring pretending to be a rod, as seen in Fig. 2(*a*). Cross sections of the spring are presented both from the front-side view and the left-side view in the figure. In Fig. 2(*b*), the incline angles of the springs are shown schematically [12].

3 Formulation of Exergy Analysis

In a thermodynamic process, the loss of exergy is primarily due to the associated irreversibility, which generates entropy. Most convective heat transfer processes are characterized by two types of exergy loss, i.e., loss due to fluid friction and loss due to heat transfer across a finite temperature difference. The above two inter-related phenomena are manifestations of thermodynamic irreversibility, and the investigation of a process from this standpoint is known as the second law analysis. However, there exists a direct proportionality between the wasted power (the rate of available work lost) and the entropy generation rate. If engineering systems and their components are to operate such that their lost work is minimized, then the conceptual design of such systems and components must comply with the minimization of entropy generation [15–18].

Fluid flow and heat transfer inside a circular duct for different boundary conditions are fundamental areas of research in engineering. Circular ducts appear in many engineering applications as a single unit or in combination, such as in heat exchangers used in power and process industries to transfer heat from one fluid stream to another. Efficient utilization of energy is the primary objective in the design of fluid flow and heat transfer processes. The second law analysis is the gateway for optimization in thermal equipments and systems, which makes good engineering sense to focus on the irreversibility of fluid flow and heat transfer processes.

Entropy generation or exergy destruction due to heat transfer and fluid flow through a duct has been investigated by many researchers, and nondimensional entropy generation number is always employed in the irreversibility examination of convective heat transfer [19]. Consider a constant cross-sectional area circular duct of inner diameter D_i and length L, as shown schematically in Fig. 3. The wall temperature T_w remains constant. An incompressible viscous fluid with mass flow rate G and inlet temperature T_{fi} enters the duct, and the exit temperature is T_{fo}. The convective heat transfer occurred under steady state condition and the fluid was thermally and hydrodynamically fully developed. The average convective heat transfer coefficient h is constant. In addition, the physical properties of the fluid are assumed to be constant within the range of temperatures considered in this study; the axial heat conduction, viscous dissipation, and heat losses of the duct are neglected.

Even though exergy is not conserved because of irreversibility caused by temperature difference heat transfer and viscous flow pressure drop, the aim of exergy change of working fluids is consistent with that of exergy transfer. So, the assumption that the exergy change rate of working fluids is equal to the exergy transfer rate of the convective heat transfer process is accepted (see Refs. [19,20] for more complete and detailed discussion). In this case, we can find the local exergy transfer coefficient and Nusselt number as follows:

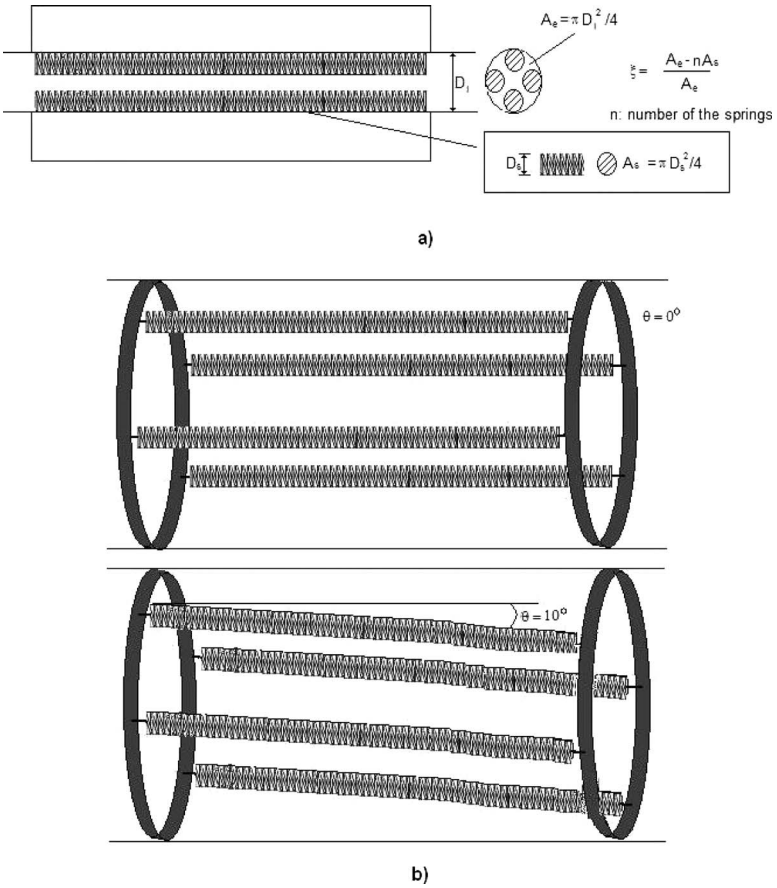

Fig. 2 Specifications of the springs: (*a*) dimensions of the springs and (*b*) incline angle of the springs

$$h_{ex} = h\left(1 - \frac{1}{N_{Tw1} - N_{Ti}e^{-4StX}}\right) - f\mathrm{Re}^3\frac{\eta C_p}{8N_{Ti}N_{Tw2}D_i}\frac{1}{e^{-4StX}(1-\tau e^{-4StX})} \quad (1)$$

$$\mathrm{Nu}_{ex} = \frac{h_{ex}D_i}{\lambda} = \mathrm{Nu}\left(1 - \frac{1}{N_{Tw1} - N_{Ti}e^{-4StX}}\right) - f\mathrm{Re}^3\mathrm{Pr}\frac{1}{8N_{Ti}N_{Tw2}}\frac{1}{e^{-4StX}(1-\tau e^{-4StX})} \quad (2)$$

The nondimensional groups appear in Eqs. (1) and (2) and are defined as follows:

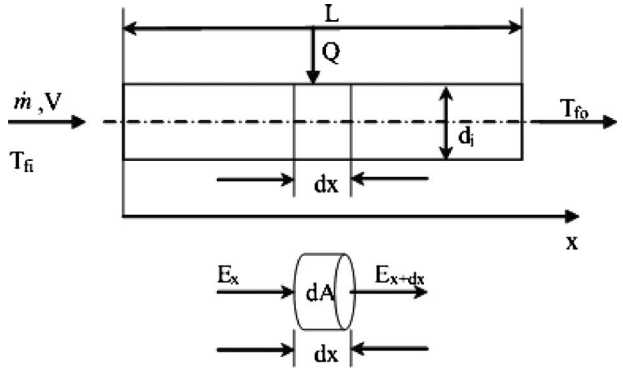

Fig. 3 Description of exergy analysis method

$$N_{Ti} = \frac{\Delta T_i}{T_o} \quad (3a)$$

$$N_{Tw1} = \frac{T_w}{T_o} \quad (3b)$$

$$N_{Tw2} = \frac{T_w}{\eta^2/\rho^2 C_p D_i^2} \quad (3c)$$

$$\tau = \frac{\Delta T_i}{T_w} = \frac{N_{Ti}}{N_{Tw1}} \quad (3d)$$

$$X = \frac{x}{D_i} \quad (3e)$$

The mean exergy transfer coefficient is defined as

$$h_e A \Delta T = \int_0^L h_{ex}\pi D_i(T_w - T_f)dx \quad (4)$$

As known, exergy is called the amount of maximum work obtained theoretically at the end of a reversible process in which equilibrium with environment should be obtained. As for the exergy destroyed, it is related directly to the irreversible production of entropy in a heat exchanger. By this definition, in order to calculate exergy, the environmental conditions should be known [18]. From Eqs. (1) and (4), the convective exergy transfer coefficient is related to the heat transfer across a finite temperature difference and viscous flow of fluid, which is different from the convective heat transfer coefficient. In other words, the convective

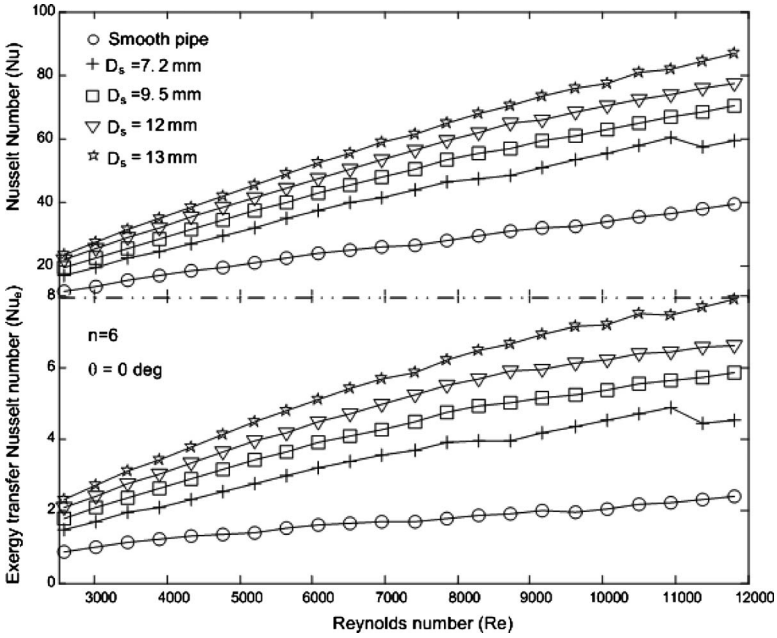

Fig. 4 Variations in Nu and Nu_e versus Re, with respect to coil diameters, for $n=6$ and $\theta=0$ deg

heat transfer coefficient is a function of both fluid's thermophysical properties and temperature difference. On the other hand, the convective exergy transfer coefficient is related not only to the two mentioned functions, but also to the friction of the fluid. The mean exergy transfer Nusselt number is

$$\mathrm{Nu}_e = \frac{h_e D_i}{\lambda} = \mathrm{Nu} + \frac{\mathrm{Nu}}{N_{Ti}(e^{-4\mathrm{St}N_L}-1)}\ln\frac{1-\tau e^{-4\mathrm{St}N_L}}{1-\tau} - \frac{f\mathrm{Re}^3\mathrm{Pr}}{8N_{Ti}N_{Tw2}e^{-4\mathrm{St}N_L}-1}\left(-4\mathrm{St}N_L + \ln\frac{1-\tau}{1-\tau e^{-4\mathrm{St}N_L}}\right) \quad (5)$$

where

$$\mathrm{St} = h/\rho V C_p \quad \text{and} \quad N_L = L/D_i$$

Equation (5) can be rewritten and the exergy transfer Nusselt number due to fluid friction Nu_P and those due to heat transfer across a finite temperature difference Nu_T can be found:

$$\mathrm{Nu}_e = \mathrm{Nu}_{eT} - \mathrm{Nu}_{eP} \quad (6)$$

$$\mathrm{Nu}_{eT} = \mathrm{Nu} + \left[1 + \frac{1}{N_{Ti}(e^{-4\mathrm{St}N_L}-1)}\ln\frac{1-\tau e^{-4\mathrm{St}N_L}}{1-\tau}\right] \quad (7)$$

$$\mathrm{Nu}_{eP} = \frac{f\,\mathrm{Re}^3\mathrm{Pr}}{8N_{Ti}N_{Tw2}e^{-4\mathrm{St}N_L}-1}\left(-4\mathrm{St}N_L + \ln\frac{1-\tau}{1-\tau e^{-4\mathrm{St}N_L}}\right) \quad (8)$$

4 Results and Discussion

In this section, the results of analysis will be presented by emphasizing the effects of design parametric values (diameter D_s, number n, and incline angle θ of the coil springs) on the exergy transfer Nusselt number. The presentation begins with two separate curve sets that are plotted to show the effects of the spring diameter D_s on Nu and Nu_e in Fig. 4. The incline angle and the number of the coil springs are constant at $\theta=0$ deg and $n=6$ in this figure. Also, the results of the smooth empty tube are added in the figures.

Four major results are apparently seen from the lines regarding $D_s=7.2$ mm, 9.5 mm, 12 mm, and 13 mm.

(i) Increasing the diameter causes significant increases in both Nusselt number Nu and exergy transfer Nusselt number Nu_e, If the attention is turned to Eq. (5), it will be seen that exergy transfer increases with increasing heat transfer (Nu) but decreases with increasing friction factor (f). According to the experimental data, increasing the spring diameter (D_s) results in the enhancement of heat transfer. It should be noticed that the pressure loss increases meanwhile. If Fig. 4 and Eq. (5) are hold under a microscope at the same time, the effect of the increment level of heat transfer is much more dominant than the effect of the increment of friction loss on the exergy transfer. It is also evident from Fig. 5 that Nu_T affects the exergy transfer Nusselt number much more dominantly than Nu_P does.

(ii) Nu and Nu_e values for the turbulated tube are much higher than the values for the smooth tube.

(iii) Nu and Nu_e monotonically increase with the increase in Re.

(iv) There is no optimal Re to make Nu_e maximal.

It is now appropriate to compare the results of the Nu_T and Nu_P. Both values increase with the increase in Re. For the case when Re is higher than a certain value (up to ~8000), the available energy loss caused by the viscous friction increases quickly. However, considering the curves of Nu_{eP} and Nu_{eT} will show that an increase in Nu_{eP} is quite higher than an increase in Nu_{eT} based on Re. In this case, when Re is larger than a certain value, Nu_{eP} can become higher than Nu_{eT}, and then Nu_e can be less than zero, which has no significance in engineering.

Figure 6 demonstrates the effect of the number of the coil springs (n) on Nu_e, Nu_T, and Nu_P for a fixed diameter and incline angle ($D_s=13$ mm and $\theta=0$ deg). As seen in the figure, Nu_e and Nu_T have higher increments than those of the smooth pipe. Nu_e, Nu_T, and Nu_P increase with increasing spring numbers n. The effect of Re on Nu_e and Nu_T has a decreasing curve, while it has an increasing trend for Nu_P. It is apparent that these trends are similar for the incline angle of the springs θ (Fig. 7). Although Nu_e is proportional to θ and D_s, the quantities are different from each other. The effect of both D_s and θ on Nu_e becomes higher at high Re values. Also, the effect of θ on Nu_e is less than that of D_s.

In Fig. 7, it is seen that for $D_s=13$ mm, the exergy transfer

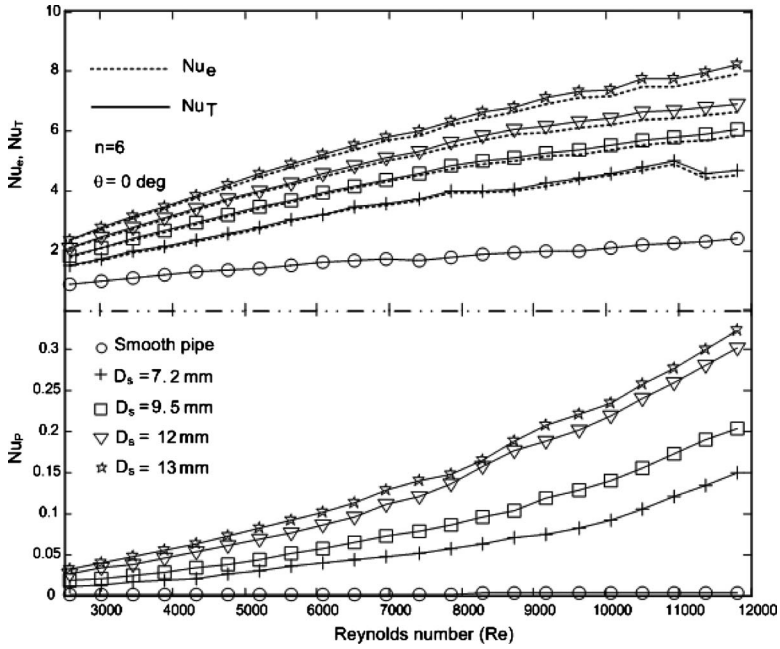

Fig. 5 Variations in Nu_e, Nu_P, and Nu_T versus Re, with respect to coil diameters, for $n=6$ and $\theta=0$ deg

Nusselt numbers with $\theta=0$ deg are higher than those with $\theta=10$ deg at low Reynolds numbers; however, the opposite trend is found at high Reynolds numbers. For $D_s=13$ mm, the pressure loss at $\theta=0$ deg is measured to be the lowest; hence, the exergy transfer Nusselt number is high. Meanwhile, for the angle $\theta=10$ deg, the pressure loss is measured to be the highest for all tested ranges of Re. However, the temperature differences apparently increase above a certain value of Re number ($Re>7000$), and the effects of temperature differences become stronger than the effects of pressure loss at that range. It should be briefly noted that the magnitudes of both Reynolds number and pressure loss shape the destiny of the trend of the exergy transfer. Also, it is evident that this kind of trend is not observed at the tests with lower spring diameters.

Furthermore, it is clear in Figs. 7 and 8 that the curves have similar changing trends, but the rate of change is not the same. For instance, with the increase in Re from 2800 to 12,000, while Nu_e increases up to approximately 3.7 times, Nu_P increases up to approximately 11 times. Besides, the higher Re is, the more obvious the trend is.

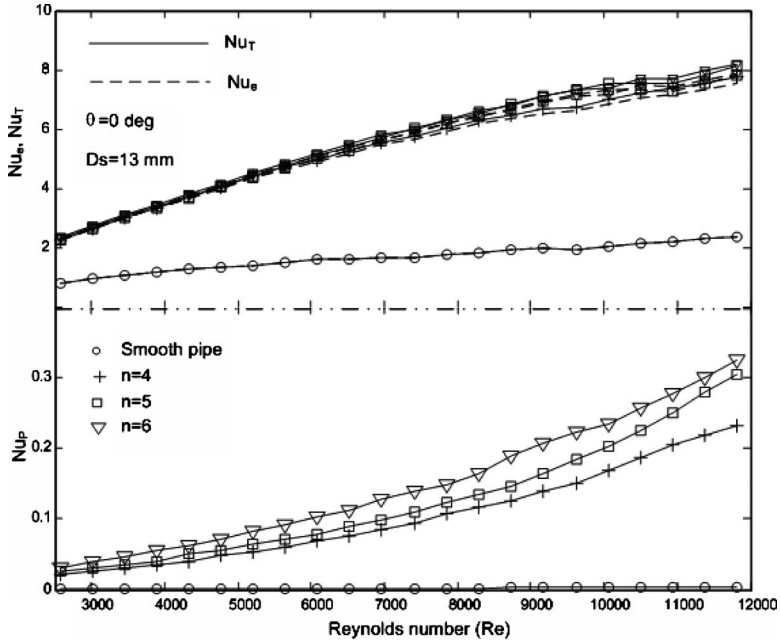

Fig. 6 Variations in Nu_e, Nu_P, and Nu_T versus Re, with respect to coil numbers, for $D_s=13$ mm and $\theta=0$ deg

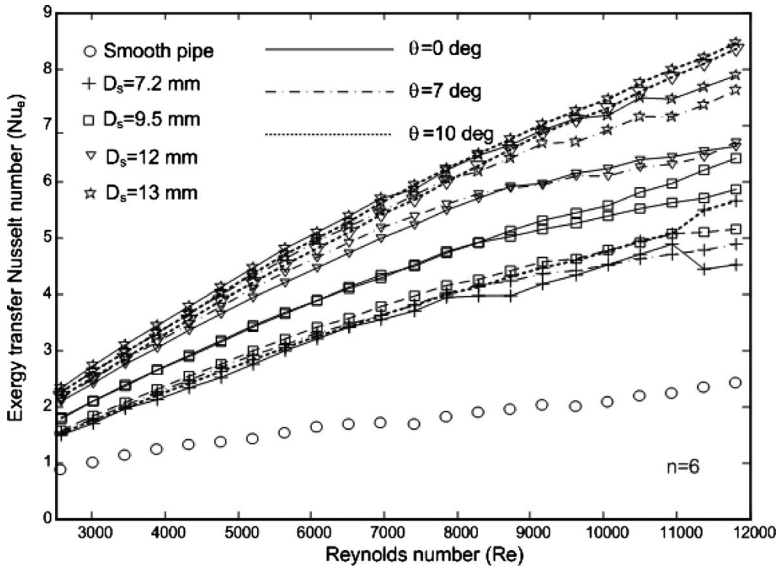

Fig. 7 Variation in Nu_e versus Re, with respect to coil diameters and incline angles, for $n=6$

Attention now will be turned to the nondimensional exergy transfer rate E^*. This term can be useful for the extensive knowledge of the system. It is defined as

$$E^* = E_T - E_P \tag{9}$$

$$E^* = \frac{E}{\dot{m}C_pT_0} = N_{Ti}(1-e^{-4\mathrm{St}N_L}) - \ln\frac{1-\tau e^{-4\mathrm{St}N_L}}{1-\tau} + \frac{f\,\mathrm{Re}^3\mathrm{Pr}}{8N_{Ti}N_{Tw2}}\left(-4\mathrm{St}N_L + \ln\frac{1-\tau}{1-\tau e^{-4\mathrm{St}N_L}}\right) \tag{10}$$

E_T^* is the derived exergy transfer rate owing to temperature difference heat transfer and is equal to [19]

$$E_T^* = N_{Ti}(1-e^{-4\mathrm{St}N_L}) - \ln\frac{1-\tau e^{-4\mathrm{St}N_L}}{1-\tau} \tag{11}$$

E_P^* is the lost exergy transfer rate owing to flow friction and is defined as follows:

$$E_P^* = -\frac{f\,\mathrm{Re}^3\mathrm{Pr}}{8N_{Ti}N_{Tw2}}\left(-4\mathrm{St}N_L + \ln\frac{1-\tau}{1-\tau e^{-4\mathrm{St}N_L}}\right) \tag{12}$$

In light of the above equations, he_x, he, Nu_e, E^*, etc., may be less than zero when the nondimensional parameters Re, Pr, N_{w1}, N_{w2}, N_L, etc., are beyond the change range, which has no significance in engineering and gives rise to our attention to the fact that the noteworthy parameters such as the process parameters and con-

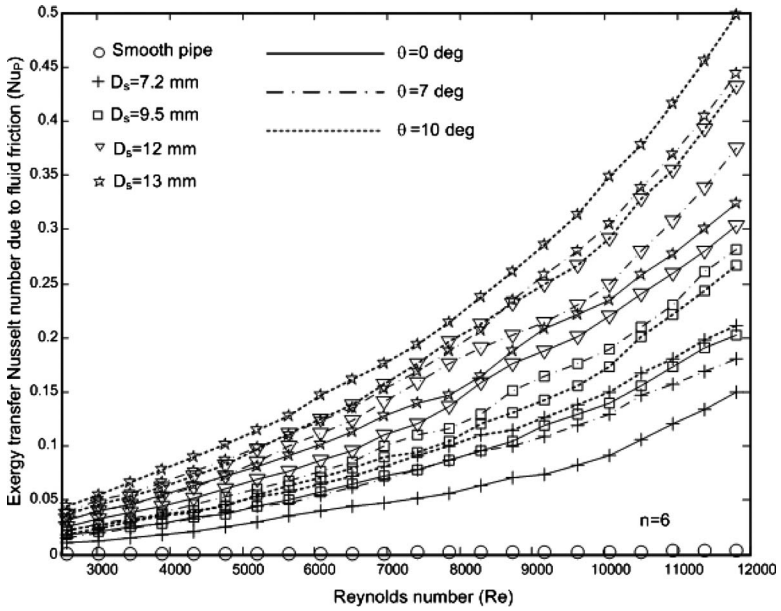

Fig. 8 Variation in Nu_P versus Re, with respect to coil diameters and incline angles, for $n=6$

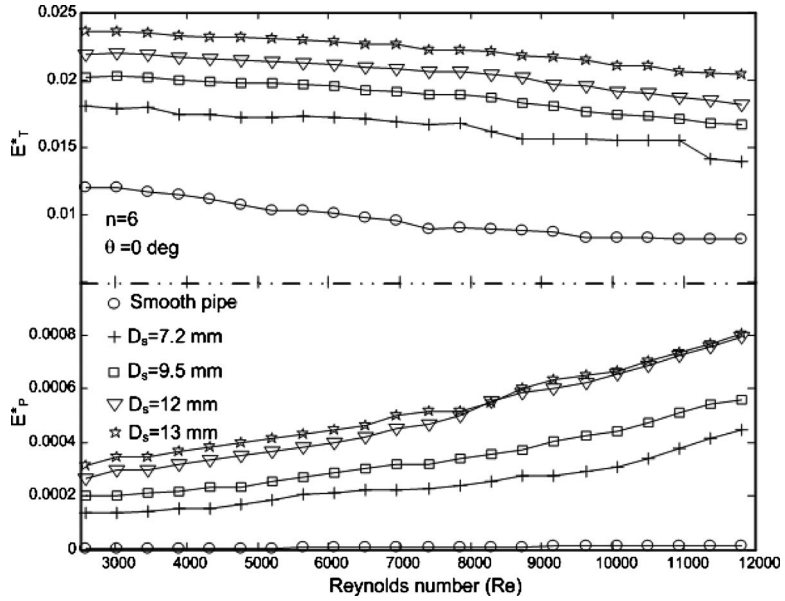

Fig. 9 Variations in E_P^* and E_T^* versus Re, with respect to coil diameters, for $n=6$ and $\theta=0$ deg

figuration must be within the limits permitted by exergy transfer [19].

Figure 9 reveals that the exergy transfer rate owing to temperature difference heat transfer (E_T^*) decreases with the increase in Re. This case can be explained by the fact that exergy transfer increase is less than the increase in fluid's thermal capacity. Namely, when Re increases, E_T^* decreases, but E_P^* increases quickly. In addition, when Re increases, the increasing trend of E_P^* and the effect of D_s on E_P^* become apparent.

Figure 10 demonstrates the effect of the number of the springs (n) on E_T^* and E_P^*. The lost exergy transfer rate owing to flow friction (E_P^*) is far smaller than the exergy transfer rate owing to temperature difference heat transfer (E_T^*). Although the E_P^* is proportional to Re, the E_T^* is reversely proportional to Re. This situation is similar to the exergy transfer Nusselt number. As a result, E^* decreases with the increase in Re. If the D_s and θ increase, the E^* will increase too, as seen in Fig. 11.

The effects of fluid flow (Reynolds number) and design parameters (spring number, diameter, and positioning) on heat transfer are found based on the obtained data; i.e., Reynolds number (Re), 48%; spring diameter (D_s), 36%; spring number (n), 12%; and spring angle (θ), 4%. The effects of all mentioned parameters on the exergy transfer Nusselt number are quite different. The effects of Reynolds number, spring diameter, spring number, and positioning angle are, respectively, 38%, 42%, 16%, and 8%. Two conclusions can be claimed evidently from the percentages: (i) the

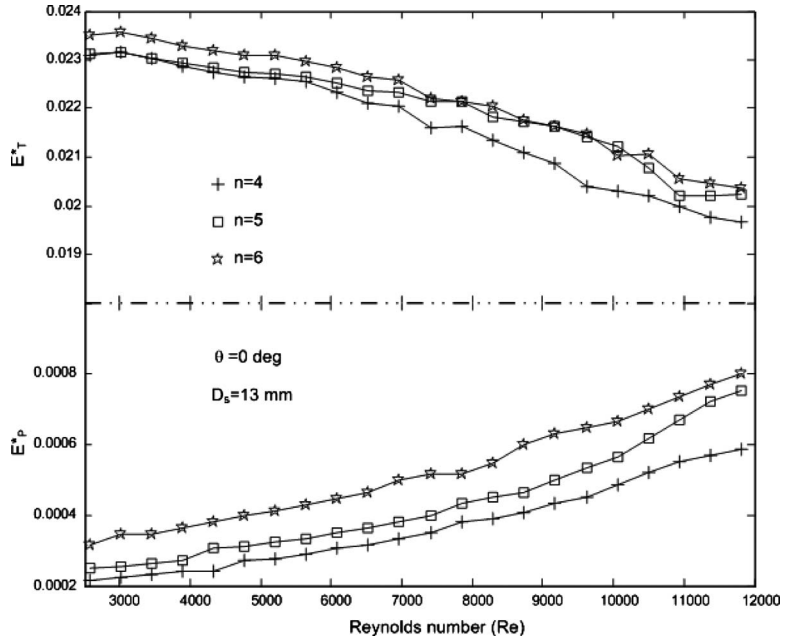

Fig. 10 Variations in E_P^* and E_T^* versus Re, with respect to coil numbers, for $D_s=13$ mm and $\theta=0$ deg

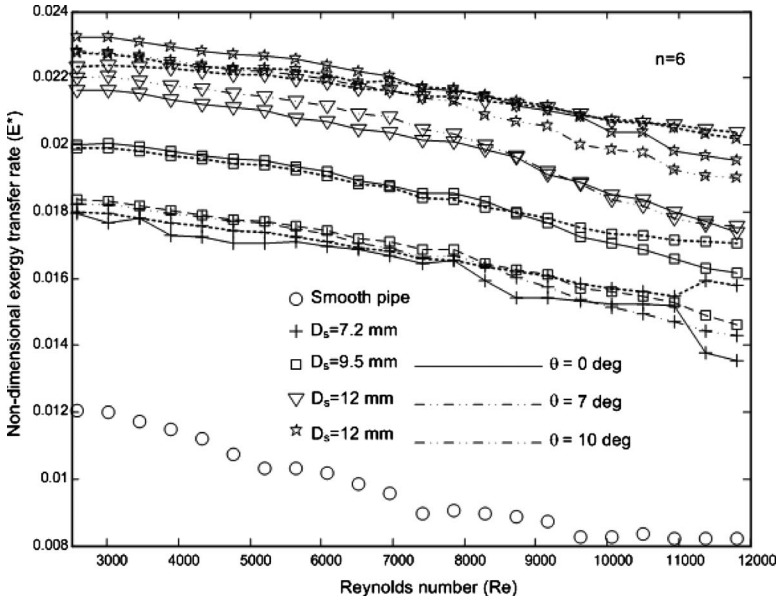

Fig. 11 Variation in E^* versus Re, with respect to coil diameters and incline angles, for $n=6$

most dominant parameter on heat transfer is Re, and (ii) the most dominant parameter on exergy transfer Nusselt number is spring diameter.

As mentioned before, exergy transfer consists of the irreversibility of the system. These irreversibilities are a kind of measurement of heat transfer and pressure loss. According to the exergy analysis of the present work, based on the spring diameter, maximum heat transfer occurs with the minimum pressure loss. In other words, a coil-spring turbulated system should be designed with first taking the Reynolds number and spring diameter into account. Therefore, the relationship between the irreversibility and the exergy transfer should be determined. Information is conveyed in Fig. 12. The variation in exergy transfer Nusselt number Nu_e with the entropy generation rate $\dot{S}_{\mathrm{gen}}$ is presented in the figure. Nu_e and $\dot{S}_{\mathrm{gen}}$ include irreversibility both from pressure loss and temperature differences. Entropy generation rate $\dot{S}_{\mathrm{gen}}$ can be defined as follows [18,21]:

$$\dot{S}_{\mathrm{gen}} = Q\frac{\phi_o}{T_i T_o} + \frac{32\dot{m}f}{\rho^2\pi^2 D_i^5}\frac{L}{T_w} \tag{13}$$

where ϕ_o is the temperature difference. It is evident that the trends of Nu_e and $\dot{S}_{\mathrm{gen}}$ are different from each other. For instance, Nu_e accelerates up to a critical value of $\dot{S}_{\mathrm{gen}}$ for the coil springs D_s = 12 and 13 mm. This critical value is 0.34 W/K for D_s = 12 mm

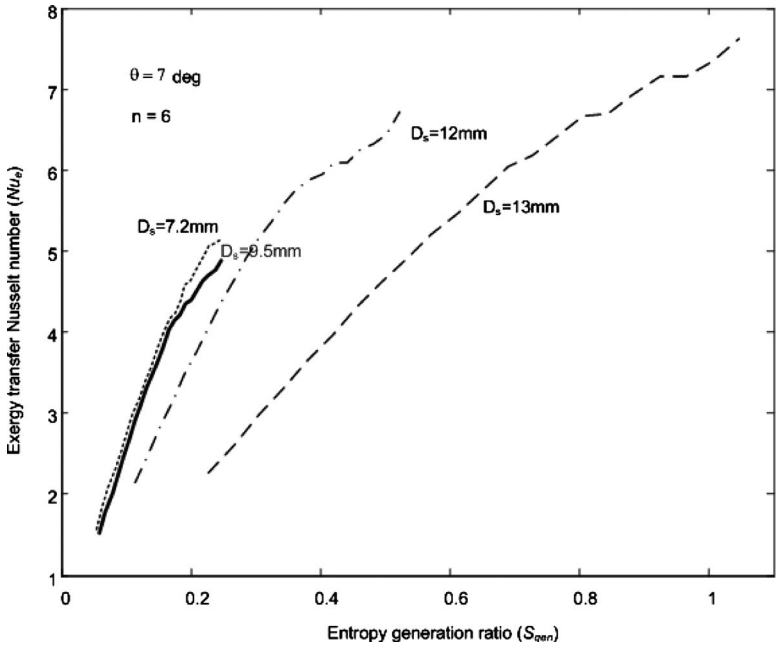

Fig. 12 Variation in Nu_e versus $\dot{S}_{\mathrm{gen}}$, with respect to coil diameters, for $n=6$ and $\theta=7$ deg

and 0.69 W/K for $D_s=13$ mm. The speed of increment of Nu_e becomes slower and more discontinuous above this value.

5 Conclusions

The major difference between the concepts of energy and exergy is in the value of the utilization of a particular energy potential with respect to a selected reference level. The present method thus permits an examination of exergy transfer characteristics in a convective heat transfer process.

In the present work, the second law analysis of a turbulated heat exchanger was performed. The results were presented with the following terms: exergy transfer Nusselt number Nu_e, exergy transfer Nusselt number due to pressure loss Nu_P, and exergy transfer Nusselt number due to heat transfer caused by temperature difference Nu_T. The nondimensional exergy rate also presented both in terms of pressure loss and heat transfer. Major results of the exergy analysis based on experimental data are as follows:

- The diameter of the springs has a great effect on exergy transfer Nusselt number. Increasing the diameter causes significant increases in Nu_e, Nu_T, and Nu_P.
- For the smallest incline angle of the springs, $\theta=0$ deg, Nu_e, Nu_T, and Nu_P have their lowest values, while for the largest angle, $\theta=10$ deg, they have their highest values.
- Nu_e, Nu_T, and Nu_P increase with increasing spring numbers, n, but the strength of the effect of n is not the same for each of them.
- Nu_e increases with increasing Re.
- Increasing Re results in decreases in Nu_T but increases in Nu_P. By the way, the total nondimensional exergy rate decreases with increasing Re.
- It appears that different pump powers will be needed for an optimum value of design parameters D_s, n, and θ.
- The analyses of first and second laws of thermodynamics applied to the present problem are necessarily limited with a constant surface temperature and a small range of Re ($2500<\mathrm{Re}<12{,}000$), which reflects the absence of a wide range of Re and different surface temperatures. The authors would like to suggest it to be done.

Nomenclature

A = area (m^2)
C_p = specific heat capacity at constant pressure (J/kg K)
D_i = inner diameter of the inner tube (mm)
D_s = outer diameter of the spring (m)
E = exergy transfer rate (W)
E^* = nondimensional exergy transfer rate
f = friction factor
h = convective heat transfer coefficient (W/m K)
h_e = mean convective exergy transfer coefficient (W/m^2 K)
h_{ex} = local convective exergy transfer coefficient (W/m^2 K)
L = length of tube (m)
$\dot{m}$ = mass flow rate (kg/s)
n = number of the springs
N_l = nondimensional tube length
$N_{Ti}N_{Tw1},N_{Tw2}$ = nondimensional temperatures
Nu = Nusselt number
Nu_e = mean exergy transfer Nusselt number
Nu_{ex} = local exergy transfer Nusselt number
Nu_P = exergy transfer Nusselt number due to fluid friction
Nu_T = exergy transfer Nusselt number due to heat transfer across a finite temperature difference
Pr = Prandtl number
Q = heat transfer rate (W)
Re = Reynolds number
St = Stanton number
$\dot{S}_{gen}$ = entropy generation rate (W/K)
T = temperature (K)
X = nondimensional cross-section position, $X=x/D_i$

Greek Symbols

ρ = density of fluid (kg/m^3)
τ = nondimensional temperature notation
λ = thermal conductivity (W/m K)
μ = dynamic viscosity (kg/m s)
ϕ_o = temperature difference between wall and fluid at $x=L$ (K)
θ = incline angle of the spring (deg)

Subscripts

e = exergy
f = fluid
gen = generated
i = inlet
o = outlet
P = pressure
T = temperature
w = wall
0 = environment

References

[1] Naphon, P., 2006, "Second Law Analysis on the Heat Transfer of the Horizontal Concentric Tube Heat Exchanger," Int. Commun. Heat Mass Transfer, **33**, pp. 1029–1041.
[2] Durmus, A., 2002, "Heat Transfer and Exergy Loss in a Concentric Heat Exchanger With Snail Entrance," Int. Commun. Heat Mass Transfer, **29**(3), pp. 303–312.
[3] Durmus, A., 2004, "Heat Transfer and Exergy Loss in Cut-Out Conical Turbulators," Energy Convers. Manage., **45**, pp. 785–796.
[4] Durmus, A., Kurtbas, I., Gulcimen, F., and Turgut, E., 2004, "Investigation of the Effect of Co-Axis Free Rotating Propeller-Type Turbulators on the Performance of Heat Exchanger," Int. Commun. Heat Mass Transfer, **31**(1), pp. 133–142.
[5] Akpinar, K. E., 2006, "Evaluation of Heat Transfer and Exergy Loss in a Concentric Double Tube Exchanger Equipped With Helical Wires," Energy Convers. Manage., **47**, pp. 3473–3486.
[6] Naphon, P., 2006, "Effect of Coil-Wire Insert on Heat Transfer Enhancement and Pressure Drop of the Horizontal Concentric Tubes," Int. Commun. Heat Mass Transfer, **33**, pp. 753–763.
[7] Promvonge, P., 2008, "Thermal Performance in Circular Tube Fitted With Coiled Square Wires," Energy Convers. Manage., **49**(5), pp. 980–987.
[8] Promvonge, P., 2008, "Thermal Augmentation in Circular Tube With Twisted Tape and Wire Coil Turbulators," Energy Convers. Manage., **49**, pp. 2949–2955.
[9] Garcia, A., Vicente, P. G., and Viedma, A., 2005, "Experimental Study of Heat Transfer Enhancement With Wire Coil Inserts in Laminar-Transition-Turbulent Regimes at Different Prandtl Numbers," Int. J. Heat Mass Transfer, **48**, pp. 4640–4651.
[10] Uttawara, S. B., and Raja Rao, M., 1985, "Augmentation of Laminar Flow Heat Transfer in Tubes by Means of Wire Coil Inserts," ASME J. Heat Transfer, **5**, pp. 930–935.
[11] Shoji, Y., Sato, K., and Oliver, D. R., 2003, "Heat Transfer Enhancement in Round Tube Using Coiled Wire: Influence of Length and Segmentation," Heat Transfer Asian Res., **32**(2), pp. 99–107.
[12] Eren, H., Celik, N., Yildiz, S., and Durmus, A., 2010, "Heat Transfer and Friction Factor of Coil Springs Inserted in the Horizontal Concentric Tubes," ASME Trans. J. Heat Transfer, **132**(1), p. 011801.
[13] Prasad, R. C., and Shen, J., 1994, "Performance Evaluation Using Exergy Analysis—Application to Wire-Coil Inserts in Forced Convection Heat Transfer," Int. J. Heat Mass Transfer, **37**(15), pp. 2297–2303.
[14] Yakut, K., and Sahin, B., 2004, "The Effects of Vortex Characteristics on Performance of Coiled Wire Turbulators Used for Heat Transfer Augmentation," Appl. Therm. Eng., **24**, pp. 2427–2438.
[15] Bejan, A., 1994, *Entropy Generation Through Heat and Fluid Flow*, Wiley, New York, pp. 105–109.
[16] Bejan, A., 1996, "Entropy Generation Minimization: The New Thermodynamics of Finite Size Devices and Finite-Time Processes," J. Appl. Phys., **79**, pp. 1191–1218.
[17] Satapathy, A. K., 2009, "Thermodynamic Optimization of a Coiled Tube Heat Exchanger Under Constant Wall Heat Flux Condition," Energy, **34**, pp. 1122–1126.
[18] Kurtbas, I., Durmus, A., Eren, H., and Turgut, E., 2007, "Effect of Propeller

Type Swirl Generators on the Entropy Generation and Efficiency of Heat Exchangers," Int. J. Therm. Sci., **46**, pp. 300–307.
[19] Wu, S. Y., Li, Y. R., Chen, Y., and Xiao, L., 2007, "Exergy Transfer Characteristics of Forced Convective Heat Transfer Through a Duct With Constant Wall Temperature," Energy, **32**, pp. 2385–2395.
[20] Demirel, Y., and Sandler, S. I., 2001, "Linear Non-Equilibrium Thermodynamics Theory for Coupled Heat and Mass Transport," Int. J. Heat Mass Transfer, **44**, pp. 2439–2451.
[21] Zimparov, V., 2000, "Extended Performance Evaluation Criteria for Enhanced Heat Transfer Surface: Heat Transfer Through Ducts With Constant Wall Temperature," Int. J. Heat Mass Transfer, **43**, pp. 3137–3155.

Front Tracking Based Macroscopic Calculations of Columnar and Equiaxed Solidification of a Binary Alloy

M. Seredyński
e-mail: msered@itc.pw.edu.pl

J. Banaszek
e-mail: banaszek@itc.pw.edu.pl

Warsaw University of Technology,
Warsaw 00-665, Poland

The paper explores the potential of a recently developed special front tracking method in the identification of the interface between columnar and equiaxed structures formed during a binary alloy solidification, driven by thermosolutal convection. The method, based on theoretical and experimental dendrite tip kinetics, is capable of directly distinguishing between the columnar mush and the undercooled liquid/equiaxed region developing ahead of the dendrite tip curve. A new numerical model and its computational algorithm are proposed, where the classical Eulerian volume averaged description of the transport processes is coupled with the Lagrangian front tracking method on a fixed control-volume grid. Having thus distinguished zones of different dendrite structures, distinct simulation models are used within each of the zones, e.g., the Darcy's porous medium model in the stationary dendrite region, and a model of slurry with floating dendrites in the equiaxed part of the mush. The calculated temperature and solute concentration fields are compared with the relevant results of the classical enthalpy-porosity model, for an example problem of Pb-48 wt % Sn alloy solidification driven by diffusion and thermosolutal convection. And a good match with both solutions is exhibited. A preliminary validation study is also presented by comparing the available experimental data with the model predictions. Possible reasons for some observed discrepancies between the calculations and the experimental findings are discussed. Finally, the proposed front tracking approach is used to address the question of the impact of dendrites floating in the liquid on the flow pattern and macrosegregation in the solidifying alloy.
[DOI: 10.1115/1.4001362]

Keywords: solidification, front tracking, binary alloy

1 Introduction

Solidification of a binary alloy is a very complex multiscale phenomenon where a two-phase solid-liquid region, referred to as a *mushy zone*, develops. It consists of two different grain structures, i.e., columnar and equiaxed. Motionless columnar dendrites, immersed in an interdendritic liquid, grow from cooled walls into the melt in the direction opposite to the heat flow. This two-phase mixture, which resembles a dynamically changing porous medium, has strongly directional structure and anisotropic properties. In front of columnar dendrite tips, in the undercooled liquid, equiaxed grains can grow freely, forming a zone of crystals, which can float in the liquid, impinge or drop down due to both density differences of the solid and the liquid phases and thermosolutal buoyancy forces. Equiaxed crystals forming in the undercooled melt can block the advance of the columnar front—the phenomenon known as the columnar-to-equiaxed transition (CET). Macroscopic thermal and solutal convection in the liquid metal causes a macrosegregation, which manifests itself by a nonhomogeneous solute distribution of the solute in a mold.

Since all the multiscale phenomena accompanying binary alloy solidification determine on a final casting product quality, numerical modeling of micro- and macroscopic structures, developing during binary alloy solidification, has attracted researchers over the last 3 decades. Their efforts have led to the development of sophisticated computer simulation models of transport phenomena accompanying the liquid-solid phase transition across the whole spectrum of length scales. At the microscale, simulation of growth of individual grains and of developing dendrite structures requires precise modeling of a very complex local shape of the solid-liquid interface. Two different categories of methods have been developed for this purpose, i.e., the ones, which track a sharp interface between the liquid and solid phases on a microscopic discretization grid [1] and the nontracking front methods, which assume a diffusive nature of this boundary. Among the latter techniques, the phase field method [2] is the most promising technique used for numerical simulation of the growth of a single crystal or a small group of crystals. For example, Badillo and Beckermann [3] used the method for 2D simulation of the developing columnar and equiaxed microstructure during the directional solidification of Al−3 wt %Cu driven by solute diffusion. They analyzed the effects of the applied temperature gradient, pulling speed, nucleation undercooling, and crystalline anisotropy strength on the CET. A micromacroscopic approach to modeling different dendritic structures in the mush was presented by Gandin et al. [4] and Dong and Lee [5]. They applied the cellular automaton (CA) method for simulation of nucleation and growth of individual crystals and the formation of grain microstructures. The CA method is characterized by a set of algebraic and logical rules for determining a future state of each microscopic cell, determined from the previous state of these cells and their neighboring cells. The KGT model of dendrite tip kinetics [6] was used in Ref. [4], whereas Dong and Lee [5] directly solved the solute conservation equation, accounting for the equilibrium conditions at the solid/liquid interface. The temperature field, needed in the nucleation and solid growth models, was obtained by solving the macro-

Contributed by the Heat Transfer Division of ASME for publication in the JOURNAL OF HEAT TRANSFER. Manuscript received March 27, 2009; final manuscript received February 22, 2010; published online July 23, 2010. Assoc. Editor: Cholik Chan.

scopic heat conduction equation on a finite element grid [4] or a finite difference grid [5]. The computational models based on the CA approach are capable for reproducing most of the underlying features of the developing microstructure, such as the growth of columnar and equiaxed grains and the CET.

However, all microscopic simulation models, which involve calculations on a very fine geometrical mesh, are computationally intensive and, because of yet restricted computer facilities, they are ineffective when applied to a whole casting domain, where a great number of interacting elements exist. Therefore, at present, pure microscopic simulations are far from industrial applications.

To resolve this problem, a macroscopic approach has been developed, where key calculations are performed on a macroscopic scale (i.e., scale of a mold) and special microsegregation and porous medium models are used to include information of the microscopic structure of the mushy zone in effective macroscopic properties. Macroscopic conservation equations of mass, species, momentum, and energy are obtained from the relevant microscopic equations through the process of averaging. Three different averaging techniques are commonly used here—i.e., a model based on the mixture theory [7,8], the volume averaging method [9,10], and the ensemble averaging method [11,12]. Two different approaches are possible in the development of these averaged models. In the first one, a two-phase (two-continuum) heterogeneous medium is replaced by two fictitious media (phases) with continuously varying phase effective properties (*a two-phase* or *two-continuum approach,* e.g., Ref. [10]).

In the second, a two-phase heterogeneous medium is substituted by a single fictitious counterpart with continuously varying effective properties (*a single-phase* or *single-continuum approach*) [7,8]. In the single-continuum approach, to which the further analysis is restricted, the latent heat effect is usually treated by the general enthalpy formulation [13,14], and Darcy's source term is added in the momentum equation to account for the resistance encountered by the interdendritic liquid during its flow in the mushy zone [7].

Distinct grain morphology developing within the two-phase region causes some problems in macroscopic single-continuum modeling of binary alloy solidification, since it requires both special techniques to distinguish the columnar and equiaxed zones, and the application of different simulation models in each of these regions. In the commonly used enthalpy-porosity model [7,13,14], the interface between the columnar dendrites region, growing from the cooled walls into the superheated melt and the equiaxed grain region, developing in the undercooled and solute reach liquid, is not directly tracked. These two different structures are distinguished by the inspection of the solid volume fraction—when it exceeds some previously specified characteristic value, called a *coherency point*, the region is treated as a stationary columnar mush, or otherwise as an equiaxed zone, where a model of slurry can be used. Some examples are given below.

Christenson et al. [15] developed a simplified model of the mushy zone, based on the theory of mixtures, where the entire two-phase region was treated as an isotropic porous medium—the stiff solid structure immersed in the liquid was assumed stationary regardless of local volume fraction values. The model was applied to calculate the solidification of an aqueous solution of ammonium chloride confined in a rectangular enclosure, and then the numerical predictions were compared with the experimental data reported by Christenson and Incropera [16]. The model satisfactorily simulates the basic transfer phenomena accompanying binary mixture solidification, but it underestimates both the solid phase extent and the mushy zone size.

Three different models of transfer processes in the mushy zone were analyzed by Voller et al. [13]. The first, called *the mushy fluid*, describes the situation where the solid phase is fully dispersed in the liquid and grains move with the liquid velocity. The *columnar dendritic with dispersed microstructure* model describes the case where the solid phase is stationary and the solute is ideally mixed in both phases, where the *lever rule* model of microdiffusion is valid. Finally, the model of *columnar dendritic with distinct microstructure* occurs when the solid phase is motionless and the solute microdiffusion is represented by the Scheil's function. The predicted macrosegregation patterns were compared for all these cases by solving the problem of the aqueous ammonium chloride solidification in a rectangular cavity with one side cooled and the others kept adiabatic. The latter two models provided comparable pictures of the solute distribution in the cavity, whereas the results of the mushy fluid model were completely different. This highlights the importance of a precise modeling of equiaxed grain behavior in the undercooled liquid.

Recently, Roux et al. [17] analyzed the simulation model, based on the volume averaging method for a stationary matrix of columnar dendrites, and compared the results obtained for three binary alloys with the experimental data available in the respective literature. An extensive analysis of the Darcy and Brinkman porosity models was carried out, but no slurry model was considered.

The simulation models, briefly discussed above, treat the solid phase as a stationary porous medium, in which the interdendritic fluid flow is modeled by Darcy's source terms included in the momentum equations. This approach is based on the assumption that the solid in the mushy zone consists of columnar dendrites or a solid skeleton formed immediately at the moment the solidification starts. Thus, these models do not account for the movement of equiaxed grains, which may have a substantial impact on: the extent of the undercooled zone, inhomogeneous properties of the solidified parts, and the actual structure of a casting.

Arnberg et al. [18] experimentally studied the effects of the grain impingement and the creation of a stiff solid skeleton in the slurry region of various metal alloys, and they determined the corresponding coherency points for various aluminum alloys for the solid volume fraction changing from 9% to 30%, depending on the alloy, cooling conditions, etc.

Based on these experimental findings, Vreeman and Incropera [19] developed a simple model of slurry, where the value of the solid volume fraction, which separated packed and floating dendrite zones, was estimated as 0.3 and it was assumed that the velocity of the solid phase was the same as that of the mixture. Specifying the characteristic dendrite diameter as 25 μm, the permeability of the packed bed of dendrites was estimated. However, the model was not validated.

Mat and Ilegbusi [20] elaborated a hybrid model, where the columnar mush was considered as an isotropic permeable matrix of stationary dendrites and the remaining part of the mushy zone was imitated by the slurry of floating equiaxed dendrites. Both regions were separated by the surface of constant solid volume fraction, where the coherency point was set at the upper limit of the data of Arnberg et al. [18], i.e., for the volume fraction equal to 0.3. Above the coherency point, the solid phase was stationary and Darcy's isotropic porous medium model was applied, whereas for the lower solid volume fraction, the melt was treated as a power-law fluid. The results obtained were compared with both the experimental data of Christenson and Incropera [16] and the numerical predictions of Christenson et al. [15] and good agreement was achieved.

All these models assume that when the solid volume fraction exceeds the *coherency point*, the dendrite structure is columnar-like, i.e., it is imitated by a porous medium model developed for the columnar mushy zone, regardless of the morphology differences occurring between a real stationary solid skeleton of columnar dendrites, growing from cooled walls into the melt, and the equiaxed grains rising freely in the undercooled liquid, impinging and mutually blocking their own movement.

To circumvent the problem, an actual position of the interface between the columnar mush and the region of equiaxed crystals needs to be known. Such information can be obtained by tracking the columnar zone boundary, on the assumption that this border can be represented by a curve or a surface drawn through the

columnar dendrite tips. For this purpose, the special front tracking method (FTM) on a fixed macroscopic control-volume grid was recently developed and combined with macroscopic calculations of mass, momentum, and energy transfer accompanying nonequilibrium binary alloy solidification in microgravity conditions [21], and in the presence of thermal buoyancy forces [22,23]. Based on the assumed dendrite tip kinetics, the advance, not of the strict solid-liquid interface, but an envelope of columnar dendritic structure, ahead of which everything is liquid and behind which a mushy zone exists, is modeled. Thus, the method allows a direct identification of different dendrite zones and uses distinct simulation models in each of these two different grain structures developing within the mush. The model was validated by comparison with thermocouple measurements from a carefully instrumented experiment of Al−7 wt %Si directional solidification, in which natural convection is limited by design [23]. Moreover, using the *equiaxed index* proposed by Browne [24], as a metric for relative tendency to form an undercooled-liquid/equiaxed zone (while actually modeling only columnar solidification), it was shown that in the case of thermal natural convection, the potential of forming equiaxed grains in copper alloys solidifying in a convectively cooled square cavity is roughly two times higher than that calculated for a pure conduction case [23].

However, all FTM models of a binary alloy solidification, presented so far (i.e., in Refs. [21–24]), do not include the effect of natural convection driven by solutal buoyancy forces—the phenomenon, which, along with thermal natural convection, induces a macroscopic compositional heterogeneity, known as macrosegregation. Moreover, in all, it was assumed that no equiaxed grains formed yet in the undercooled liquid region—the space just ahead of the columnar front was treated as completely liquid, although with temperatures lower than the equilibrium *liquidus* temperature.

Therefore, in this study, an account is given of the extension of the FTM as applied to modeling of binary alloy solidification controlled by both thermal and solutal buoyancy forces. The FTM simulation is then further developed by implementing different models of slurry to deal with the flow of the equiaxed mushy zone and by direct coupling of the two flow models—that in the fixed porous columnar solid with that in the particulate two-phase equiaxed mush. Provisionally, as in Refs. [22,23], the diffusion driven dendrite tip kinetics is applied for the columnar front advance to construct a surface separating the slurry and columnar dendrites regions. The proposed model is further compared with the classical enthalpy-porosity approach [25] by solving an example problem of Pb-48 wt % Sn alloy solidification driven by conduction and thermosolutal convection. A validation study of the front tracking model is also presented using the available experimental data [26], and possible reasons of some observed discrepancy between the calculations and the experimental findings are discussed. Eventually, the proposed front tracking approach is used to address the question of the impact of dendrites floating in the melt on the flow pattern and macrosegregation in the solidifying alloy.

2 Macroscopic Equations

Based on the volume averaging method Ni and Incropera [27] developed a comprehensive model of transfer processes, occurring in the part of the mushy zone where the solid phase is stationary. Its conservation equations for the liquid-solid mixture mass, its energy and species concentration are, respectively

$$\nabla \cdot (\rho V) = 0 \tag{1}$$

$$\frac{\partial}{\partial t}(\rho h) + \nabla \cdot (\rho V h) = \nabla \cdot \left(\frac{k}{c_S} \nabla h \right) + \nabla \cdot \left[\frac{k}{c_S} \nabla (h_S - h) \right] - \nabla \cdot [\rho (V - V_S)(h_L - h)] \tag{2}$$

$$\frac{\partial}{\partial t}(\rho C) + \nabla \cdot (\rho V C) = \nabla \cdot (\rho f_L D_L \nabla C) + \nabla \cdot (\rho f_L D_L \nabla (C_L - C)) - \nabla \cdot [\rho (V - V_S)(C_L - C)] \tag{3}$$

In the liquid and the slurry regions, the x-th and y-th momentum equations, respectively, take the form

$$\frac{\partial}{\partial t}(\rho u) + \nabla \cdot (\rho V u) = \nabla \cdot (\mu_L \nabla u) - \nabla \cdot (\mu_L f_S \nabla u_S) + \nabla \cdot (\mu_S g_S \nabla u_S) - \nabla \cdot \left[\left(\frac{\rho f_S}{f_L} \right) (V - V_S)(u - u_S) \right] - \frac{\partial p}{\partial x} \tag{4}$$

$$\begin{aligned} \frac{\partial}{\partial t}(\rho v) + \nabla \cdot (\rho V v) &= \nabla \cdot (\mu_L \nabla v) \\ &- \nabla \cdot (\mu_L f_S \nabla v_S) + \nabla \cdot (\mu_S g_S \nabla v_S) \\ &- \nabla \cdot \left[\left(\frac{\rho f_S}{f_L} \right) (V - V_S)(v - v_S) \right] \\ &- g_S \rho_S g [\beta_{T,S}(T - T_{\text{ref}}) + \beta_{C,S}(C_S - C_{\text{ref}})] \\ &- g_L \rho_L g [\beta_{T,L}(T - T_{\text{ref}}) + \beta_{C,L}(C_L - C_{\text{ref}})] - \frac{\partial p}{\partial y} \end{aligned} \tag{5}$$

Alternatively, the x-th and y-th momentum equations, which are valid in the rigid columnar mushy zone and in the completely solid phase, have the following forms, respectively

$$\frac{\partial}{\partial t}(\rho u) + \nabla \cdot (\rho V u) = \nabla \cdot (\mu_L \nabla u) - g_L \frac{\mu_L}{K} u - \nabla \cdot \left[\left(\frac{\rho f_S}{f_L} \right) V u \right] - g_L \frac{\partial p}{\partial x} \tag{6}$$

$$\frac{\partial}{\partial t}(\rho v) + \nabla \cdot (\rho V v) = \nabla \cdot (\mu_L \nabla v) - g_L \frac{\mu_L}{K} v - \nabla \cdot \left[\left(\frac{\rho f_S}{f_L} \right) V v \right] - g_L \rho_L g [\beta_{T,L}(T - T_{\text{ref}}) + \beta_{C,L}(C_L - C_{\text{ref}})] - g_L \frac{\partial p}{\partial y} \tag{7}$$

In previous applications of the FTM [21–23], a special form of the energy conservation equation in the mushy zone was developed on the basis of the known position of the tracked interface. Two different source terms have been carefully defined to account for both the advance of the solidification front and subsequent thickening of dendrites within the columnar part of the control volume [21,22]. Such modeling is, however, not applied in this study, where the classical enthalpy formulation of the energy conservation [7,13,14] is preferred and the tracing of the columnar front serves only to distinguish two different grain morphologies within the mushy zone control-volume. Hence, the mixture total specific enthalpy is defined by weighting the sum of the phase specific enthalpies, i.e., $h = f_S h_S + f_L h_L$, and upon the commonly used assumption of constant specific heats, the phase enthalpies are $h_S = c_S T$ and $h_L = c_L T + L$. Incorporating them into the energy equation (Eq. (2)) gives

$$\frac{\partial (\rho c_p T)}{\partial t} + \nabla \cdot (\rho c_p V T) = \nabla \cdot (k \nabla T) + \frac{\partial}{\partial t}(\rho f_s L) + \nabla \cdot (\rho V_s f_s L) \tag{8}$$

The above conservation equations must be supplemented with the following closure relationships.

1. The mutual linking between temperature and species concentration in the liquid is approximated by the assumption of the local thermodynamic equilibrium, and thus a *phase diagram* can be used to couple both these unknowns through

the *liquidus line*. Due to different solubility of the solute in the solid and liquid phases, discontinuity of the concentration appears at the phase interface. According to the thermodynamic equilibrium assumption, the phase concentrations at the interface are related by the phase partition coefficient [28,29]: $\kappa_p = C_S / C_L$.

2. Species concentration at the phase interface is different to the average value in a bulk phase; both are related through a model of microdiffusion. Two asymptotic cases are commonly used [29]. The first one is based on the *lever rule* when a full mixing (very rapid solute diffusion) in both phases is assumed. The second, known as Scheil's model, assumes ideal mixing in the liquid and no diffusion in the solid phase. More general formulae, which couples the solute concentrations in the liquid phase and in the mixture and assumes finite microdiffusion in the solid, may take the form Ref. [14]

$$C_L = \frac{C - C^0 + [1 - g_S^0 + \omega g_S^0 \kappa_p] C_L^0}{1 - g_S + \omega g_S \kappa_p + (1 - \omega)\kappa_p (g_S - g_S^0)} \tag{9}$$

Parameter ω depends on the intensity of microdiffusion in the solid (known as *back diffusion*). Its values lie between 0 and 1 that corresponds, respectively, to zero back diffusion (Scheil's assumption) and full diffusion (the lever rule). Coupling between solute concentration and temperature fields via the above described supplementary relations is based on the iterative algorithm proposed by Swaminathan and Voller [14].

3. In the momentum equations for the columnar mushy zone (Eqs. (6) and (7)), a simple model of an isotropic porous medium with the Darcy's damping source term is applied. But, bearing in mind the strong influence of the anisotropy of a growing porous structure on a final solutal segregation picture [30], the secondary dendrite arm spacing is taken as a characteristic dimension [25]. Then, the Darcy's term reads

$$K = \frac{\lambda_2^2 (1 - g_S)^3}{180 g_S^2}$$

4. Inside the undercooled liquid, solid grains can nucleate, grow, and can float by convection. Precise modeling of these multiscale phenomena is difficult. In the simplified model based on the solid-liquid mixture, an explicit relation between the phase velocities is required. Two cases are further studied. In the first one, the solid phase is stationary, so the phase velocities are given by $V_S = 0$ and $V_L = V / f_L$. In the second case, the mushy region is divided into two different regions by a curve joining the columnar dendrite tips. In front of this interface, a slurry zone develops, where equiaxed grains are freely floating. A simple relation between the phase velocities, developed by Ni and Incropera [31] is applied here, where, for the same phase densities, phase velocities are equal, $V_S = V_L = V$. Behind the dendrite tips curve, in the columnar zone, the solid phase is stationary; $V_S = 0$ and $V_L = V / f_L$. Switching between these two cases is based on the FTM identification of the temporal front position. Details of the algorithm are described in a subsequent chapter.

5. In the slurry zone, the solid grains interaction is modeled by increasing the dynamic viscosity. This property is no longer equal to the physical viscosity of a pure liquid μ_L, but is given by the expression derived from the rheological analysis [32,28]

$$\mu_m = \left(1 - \frac{g_S}{g_{Sp}}\right)^{-2.5 g_{Sp}} \mu_L$$

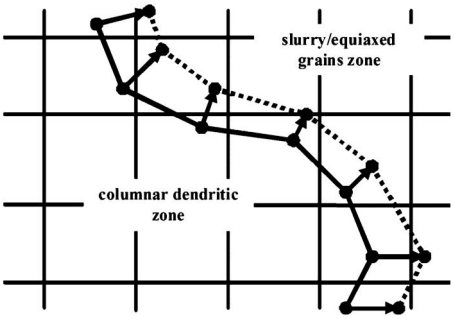

Fig. 1 Tracking an internal interface via markers on a fixed control-volume grid

6. Since the proposed FTM model predictions will be further verified by comparison with the solution of Ahmad et al. [25], the alloy properties, as well as boundary and initial conditions, are taken from their paper.

3 Computational Model

The above conservation equations have been discretized on a fixed control-volume grid. The developed computational procedure is based on the staggered grid approach to avoid checkerboard pressure modes and on the power-law *up-winding* to eliminate nonphysical spatial oscillations of the numerical solution [33]. To separately calculate pressure and velocity fields, the pressure correction method is used. Finally, the iterative segregated solution strategy is applied, which follows the SIMPLE algorithm [33], where linearized directional momentum and energy equations are solved consecutively. For the fully implicit time marching scheme used, the matching between temperature and concentration fields is reached in an additional inner iterative loop [14]. To account for different dendrite morphologies in the above described macroscopic modeling of the mushy zone (Eqs. (1)–(9)), the computational algorithm is further coupled with the front tracking technique on a fixed control-volume grid, where it is assumed that a local advance of the curve/surface embracing the columnar mush results from assumed dendrite tip kinetics [21]. In a consecutive iterative step, Eqs. (1), (4), (5), and (8) are solved within the distinguished columnar dendritic mush, whereas Eqs. (1)–(3) and (8) are used to calculate pressure, velocity, temperature, and concentration fields in the undercooled liquid/equiaxed region.

3.1 Front Tracking Technique on a Fixed Grid. The studied FTM employs a *Lagrangian* representation of a moving curve of columnar dendrite tips and *Eulerian* (fixed grid) calculations of mass, momentum energy, and species conservation equations [21–23]. To track the front between two different dendritic structures developing in the mushy zone, the idea originated by Shyy [34] was adopted, where a set of mass-less marker particles, connected by linear segments (Fig. 1), is used to represent this interface on a fixed control-volume grid. But unlike Ref. [34], the front tracking model is used here to treat the advance, not of the strict solid-liquid interface at the scale of an individual dendrite; but an envelope of dendritic structure ahead of which everything is undercooled liquid or slurry of the liquid and moving equiaxed grains. The columnar mushy zone exists behind this envelope. An initial position of a marker is assumed in accordance with both the initial state and thermal boundary conditions on the domain surfaces. At some time during solidification, the curve joining successive markers represents the current interface (a continuous line in Fig. 1). From this position, a marker advances in a direction perpendicular to the front, at the velocity specified by an assumed dendrite tip kinetics, which is a function of a local undercooling, determined from a current temperature field. New marker positions are calculated from the time interval Δt and local velocities

at the corresponding particle locations, and a new interface (dotted line in Fig. 1) is obtained by the linear interpolation between each pair of successive markers [34]. In the original work of Shyy [34], as well as in Refs. [21–23], thus obtained interface and is treated as a temporary one. In order to comply with the grid resolution, one more step is performed. The points at which this set of linear segments intersects the grid-lines become the new marker particles, and linear interpolation between these new markers positions (not shown in Fig. 1) creates a final representation of the interface after Δt. However, this geometrical dependence of the front interpolation on a control-volume grid makes the tracking algorithm complex and cumbersome for 3D extension. Therefore, the grid independent method of Glimm et al. [35] was adopted in this study, where the interface can also be represented by computational markers lying inside a control volume (Fig. 1), and special techniques are used to avoid marker particle rarefaction or accumulation [36].

Proper dendrite tip kinetics give rise to a fundamental issue in this special front tracking technique that can result from enhanced theoretical considerations (e.g., Refs. [37,6,38]) and/or from experiments. In the preliminary calculations presented in this study, it has been assumed that thermosolutal buoyancy forces have a negligible impact on the local growth of a columnar dendrite, and the commonly used KGT model [6] was applied. According to the KGT model, the columnar dendrite tip velocity w can be approximated in a polynomial form

$$w = 1.6891 \times 10^{-7}\Delta T^2 + 1.21745 \times 10^{-7}\Delta T^3$$

where the undercooling ΔT is computed as the difference between the liquidus temperature T_L for the nominal composition C_0 and the current temperature T.

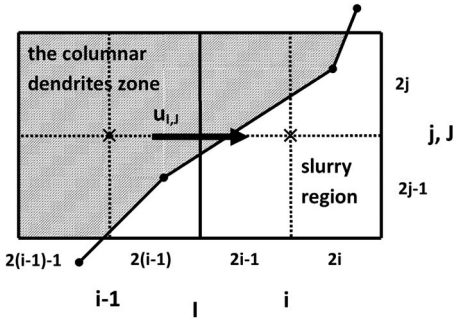

Fig. 2 A fragment of the front crossing a control-volume face

3.2 Interpolation of Phase Velocities. In a control volume, which encompasses the interface, two different zones coexist: the columnar dendrite region (a shaded area in Fig. 2), where the solid velocity is equal to zero and the slurry zone, where floating grains and the liquid move with the mixture velocity. The volume of the control-volume part occupied by the columnar dendrites is calculated on a grid of twice the density than that used in the discretization of the conservation equations. Both grids are shown in Fig. 2, along with the corresponding index notation. Thus, a dimensionless volume associated with the velocity $u_{I,J}$, at the node (I,J) located in the columnar mush (Fig. 2), is given by

$$\tilde{V} = \frac{\mathrm{Vol}(2(i-1),2j-1) + \mathrm{Vol}(2i-1,2j-1) + \mathrm{Vol}(2(i-1),2j) + \mathrm{Vol}(2i-1,2j)}{(\Delta x \Delta y)}$$

The solid and liquid phase velocities at this node read, respectively

$$V_S = (1-\tilde{V})V_L; \quad V_L = \frac{V}{f_L + (1-\tilde{V})(1-f_L)}$$

4 Results and Discussion

4.1 Model Verification and Validation. To verify the correctness and accuracy of the mathematical model and its computer simulation based on the FTM, the problem of Pb-48 wt % Sn solidification in a rectangular cavity was solved and the results obtained were compared with the numerical predictions of Ahmad et al. [25] and Roux et al. [17]. Ahmad et al. built their discrete model on the basis of the volume averaged mass, energy, and solute conservation in both phases, whereas the momentum conservation equation was volume averaged only over the liquid phase. The simple lever rule model of microsegregation (Eq. (9) with $\omega=1$) was used, along with the assumptions of equal phase densities and a stationary solid phase. Within these assumptions, the whole mushy zone was treated as the Carman–Kozeny porous medium. Roux et al. [17] also established their model of columnar solidification on volume averages of the local mass, energy, momentum, and solute concentration equations, supplemented by the enhanced closure models based on geometrical considerations of the columnar mush heterogeneity and on nonequilibrium chemical transfer at the solid-liquid interface [17].

In the carried out FTM calculations, the initial temperature was equal to the one arranged by Hebditch and Hunt [26] in their experiments, and data of the convective boundary condition on the left cooled wall were assumed in accordance with those estimated by Ahmad et al. [25], on the basis of the advance of solidification front reported by Hebditch and Hunt [26], i.e., a constant heat transfer coefficient was equal to 400 $\mathrm{W/(m^2\,K)}$ and an ambient temperature of 25°C. The alloy properties were taken from Ahmad et al. [25], and thermal and solutal expansions coefficients of the solid phase were estimated from the data given by Poirer [39]. All thermophysical data and parameters used in calculations are presented in Table 1.

Two different models of the mushy zone have been analyzed, i.e., the one with a stationary solid—further referred to as Case 1, and the second, where the effect of free floating dendrites in the slurry is accounted for—Case 2.

Streamlines (ψ) and the lines of constant solid volume fraction, obtained, for the model of a stationary solid (Case 1), on the grid of 60×60 control volumes and with the time increment changing from 0.01s to 0.05 s, are compared, respectively, in Figs. 3 and 4, with the corresponding reference solutions of Roux et al. [17] and Ahmad et al. [25]. A good agreement of the FTM results is only observed with those reported in Ref. [25]—the flow pattern (Figs. 3(b) and 3(c)) and the solid volume fraction distribution (Figs. 4(b) and 4(c)) predicted by both models are very similar.

Then, to address the question of how the proposed FTM model reflects the physics of a binary alloy solidification driven by thermosolutal buoyancy forces, a validation analysis was carried out.

Table 1 Thermophysical data of Pb-48 wt % Sn and parameters used in the calculation.

Initial mass fraction	wt % Sn	48.0
Melting temperature	°C	327.5
Eutectic temperature	°C	183.0
Liquidus slope	°C (wt %)$^{-1}$	−2.334
Partition coefficient	-	0.307
Eutectic mass fraction	wt %	61.9
Specific heat (liquid or solid)	J kg^{-1} K^{-1}	200.0
Thermal conductivity	W m^{-1} K^{-1}	50.0
Latent heat of fusion	J kg^{-1}	53,550.0
Reference density	kg m^{-3}	9000.0
Reference temperature	°C	232.0
Thermal expansion coefficient (liquid)	K^{-1}	1×10^{-4}
Solutal expansion coefficient (liquid)	(wt %)$^{-1}$	4.5×10^{-3}
Thermal expansion coefficient (solid)	K^{-1}	1.2×10^{-4}
Solutal expansion coefficient (solid)	(wt %)$^{-1}$	5.5×10^{-3}
Dynamic viscosity	kg m^{-1} s^{-1}	1×10^{-3}
Secondary dendrite arm spacing	μm	40.0
Molecular diffusion coefficient (liquid)	m^2 s^{-1}	1×10^{-9}
Molecular diffusion coefficient (solid)	m^2 s^{-1}	1×10^{-13}
Gibbs–Thomson coefficient	K m	1×10^{-7}

The calculated 2D macrosegregation pattern was compared with the experimental results obtained by Hebditch and Hunt [26]. In their experiments, Pb-48 wt % Sn alloy was solidified in the parallelepiped cavity of $6\times10\times1.3$ cm^3. The cavity was thermally insulated on all lateral surfaces, except the one through which the liquid alloy confined in the cavity was convectively cooled. Assuming that the fluid flow in the central cross section of the cavity (the one having an area of 0.1×0.06 m^2) is not influenced by the two parallel walls, the problem can be viewed as two-dimensional and the experimental data can be compared with the 2D calculations.

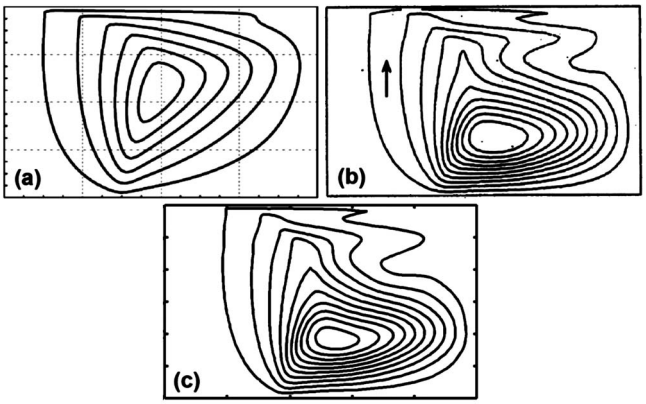

Fig. 3 Streamlines after 50 s of solidification, $\Delta\psi=3.67\times10^{-6}$: (*a*) model of Roux et al. [17], (*b*) model of Ahmad et al. [25], and (*c*) the proposed model—Case 1

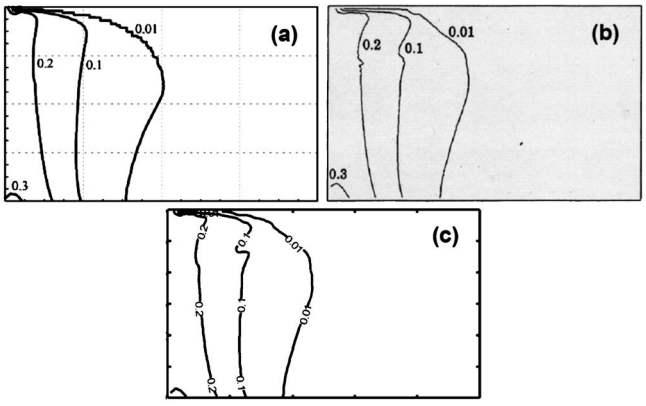

Fig. 4 Lines of constant solid fraction after 50 s of solidification: (*a*) model of Roux et al. [17], (*b*) model of Ahmad et al. [25], and (*c*) the proposed model—Case 1

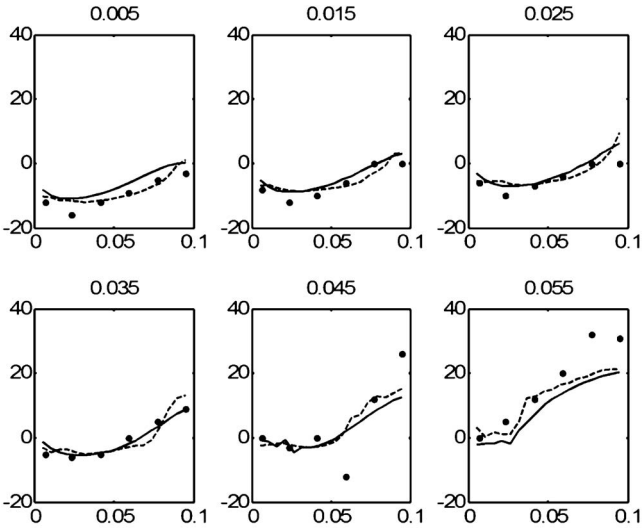

Fig. 5 Relative tin concentration in the completely solidified alloy along the selected horizontal lines of the cavity central cross section (measured in (m) from the left cooled wall): solid line—Case 1, dashed line—Case 2, and dots—experimental data by Hebditch and Hunt [26]

Such a comparison is shown in Fig. 5 in terms of tin concentration changes along the distance from the left cooling surface, at six selected height levels measured from the bottom of the cavity (shown in meters above the plots in Fig. 5). Two models of the two-phase region have been analyzed, i.e., Case 1, where the whole mushy zone is treated as a porous medium with a stationary solid, and Case 2, where the columnar dendrite front, traced by the FTM, separates the columnar mush and the undercooled liquid/equiaxed region and the effect of free floating dendrites in the slurry is accounted for. Thorough inspection of Fig. 5 shows that the latter model is a closer fit to the experimental findings of Hebditch and Hunt [26].

4.2 FTM Analysis of Macrosegregation. Thus, a verified and preliminary validated FTM model has been further used to address the issue of the impact of dendrites floating in the melt on the flow pattern and macrosegregation in the solidifying alloy. For this purpose, the problem of Pb-48 wt % Sn solidification in the rectangular cavity has been solved for the material data given in Table 1. Two models of the mushy zone have been analyzed, i.e., the first, where the whole mush is treated as a Darcy's porous medium with a stationary solid and where the front tracking method is not utilized—Case 1, and the second, where the columnar and equiaxed zones are identified by tracking the columnar front, Darcy's model is restricted to the columnar mush and the effect of free floating dendrites is accounted for in the undercooled/equiaxed zone—Case 2.

The fields of the relative mixture concentration, $(C-C_0)/C_0^*100\%$, velocity (in terms of streamlines) and the solid fraction, calculated for both these cases, are compared in Figs. 6–8, and in Figs. 9–11 at two different times of the solidification process, i.e., after 150 s and after 300 s, respectively.

Visible differences in the flow structure and the mixture concentration are caused by the different treatment of the solid phase in each of the two analyzed mushy zone models. When the entire

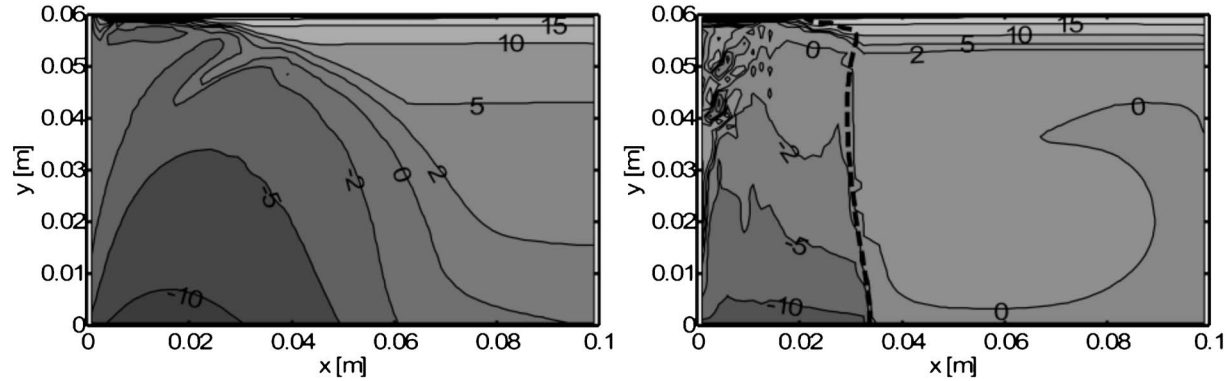

Fig. 6 Relative mixture concentration of Sn (in %) after 150 s of solidification: left—Case 1, right—Case 2; a dotted line—the columnar front position

solid confined in the two-phase region is assumed stationary (Case 1), the solutal buoyancy forces are dominant and the melt rich in solute is transported upwards (Fig. 7, left). On the bottom of the cavity, the mixture concentration is relatively small, making the liquidus temperature of the hypoeutectic alloy higher. The solidification takes place earlier in the other parts of the cavity. Conversely, a very high solute concentration in the upper narrow layer of the melt (Fig. 6, left) effectively prohibits the solidification (Fig. 8, left). On the contrary, when grains can freely move in the slurry, the liquid and equiaxed crystals are well mixed (Fig. 6, right). Moreover, the mixture concentration is virtually constant along the interface (Fig. 6, right) and the dynamics of dendrite growth is mainly related to the local temperature. Convective currents are much stronger in the model of floating dendrites (compare Fig. 7, left and Fig. 7, right). This is probably because of the assumption of stationary dendrites in the whole mushy zone (Case 1), implying the development of a large porous region, which weakens the strength of natural convection.

While solidification proceeds, the natural convection in Case 2 changes its orientation (compare Fig. 7, right, and Fig. 10, right) and becomes solutally driven, creating good solute mixing in the bottom-right corner. The stagnant region expands in the vertical direction, so the rich solute region, developing in an upper part of the cavity (Fig. 9), reduces the liquidus temperature and retards the columnar dendrites growth along the line of constant value of the solid fraction (value of about 0.001 in Fig. 11, right). The use of the slurry model in the undercooled region developing in front of the columnar dendrites, radically changes the character of the

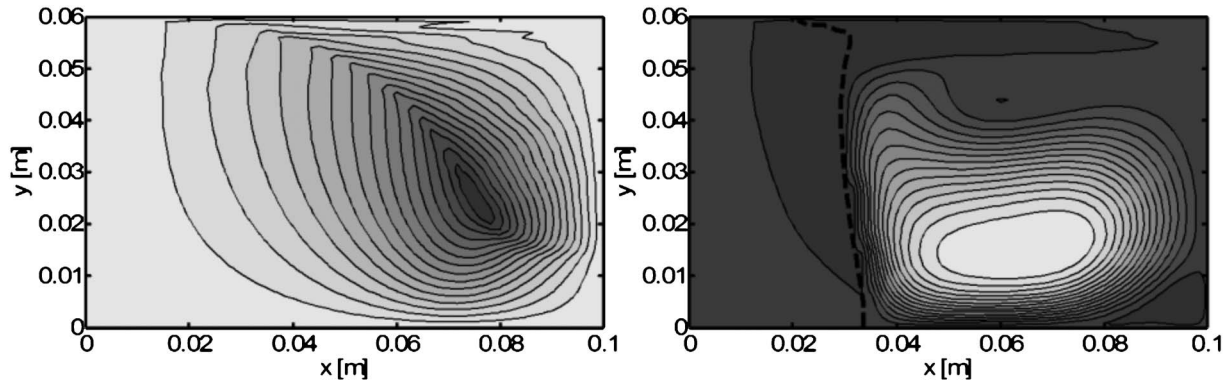

Fig. 7 Stream function after 150 s of solidification: left—Case 1, $\psi_{max}=8.8\times10^{-6}$, right—Case 2, $\psi_{max}=1.4\times10^{-4}$; a dotted line—the columnar front position

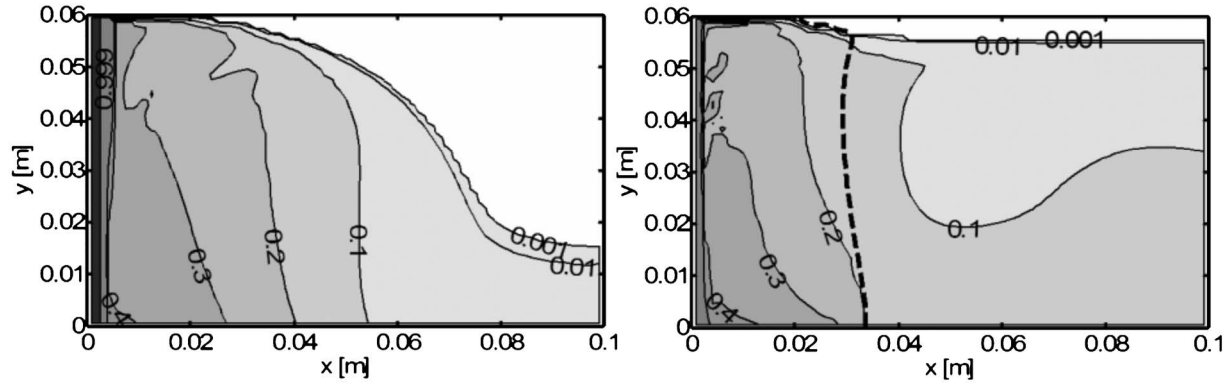

Fig. 8 Solid fraction after 150 s of solidification, left—Case 1, right—Case 2; a dotted line—the columnar front position

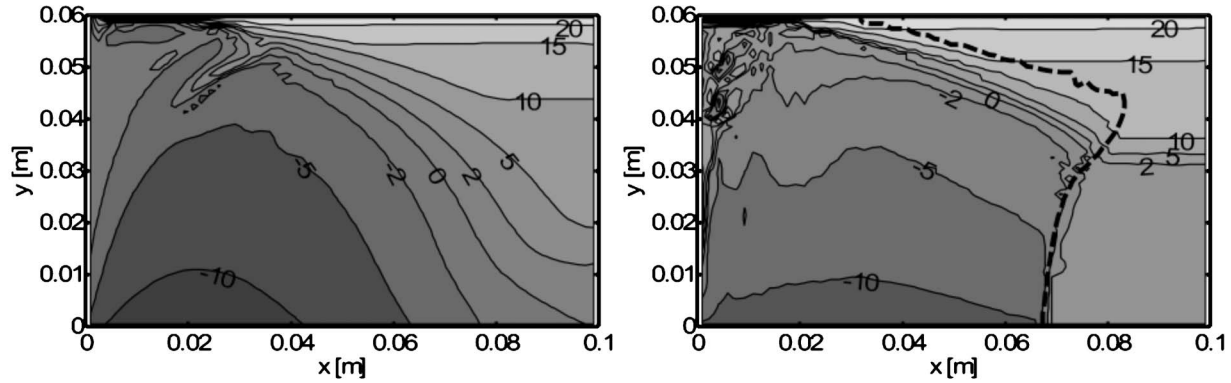

Fig. 9 Relative mixture concentration of Sn (in %) after 300 s of solidification: left—Case 1, right—Case 2; a dotted line—the columnar front position

flow field, what causes a visibly different pattern of macrosegregation. The good solute mixing observed, which promotes high values of the final solute fraction in an upper part of the cavity, gives results closer to the experimental data of Hebditch and Hunt [26] than those obtained in Case 1 (Fig. 5).

5 Concluding Remarks

The proposed FTM computer simulation model for macroscopic calculations of binary alloy solidification driven by diffusion and thermosolutal natural convection, differs from others available in the relevant literature by the coupling of the classical approach (based on the volume averaging) with a special Lagrangian technique of tracking the interface on a fixed control-volume grid. On the underlying assumption that local fragments of the columnar front advance into the undercooled liquid at a velocity resulting from the assumed dendrite tip kinetics, this combined Eulerian–Lagrangian approach is capable of distinguishing the interface between two different dendrite structures developing in the mushy zone, i.e., the columnar mush and the equiaxed grain region. Thus, the possibility is offered of using different computer simulation models in each of these two regions, thus, better reflecting the distinct physics of columnar and equiaxed dendrite solidification. Being evenly computationally efficient, the proposed FTM method appears to be an interesting alternative to the commonly used macroscopic enthalpy-porosity model, where zones of different grain structures are indirectly

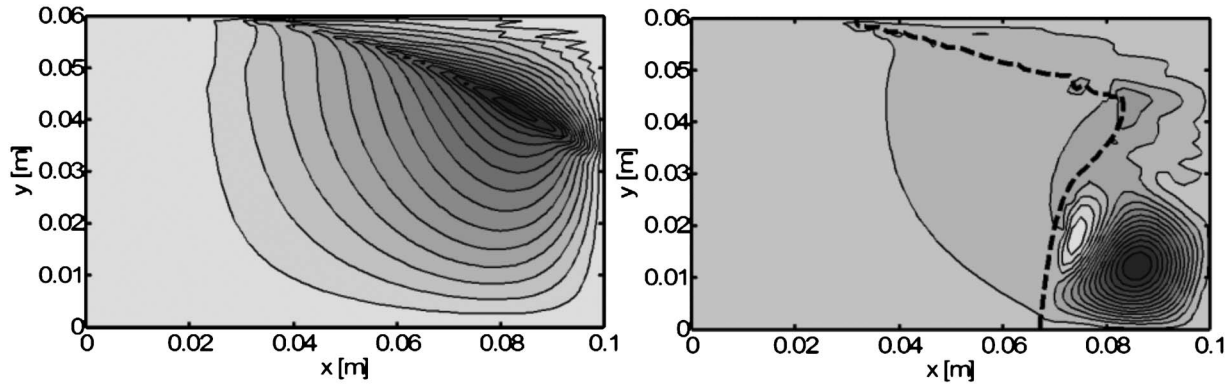

Fig. 10 Stream function after 300 s of solidification: left—Case 1, $\psi_{max}=2.8\times10^{-6}$, right—Case 2, $\psi_{max}=3.6\times10^{-5}$; a dotted line—the columnar front position

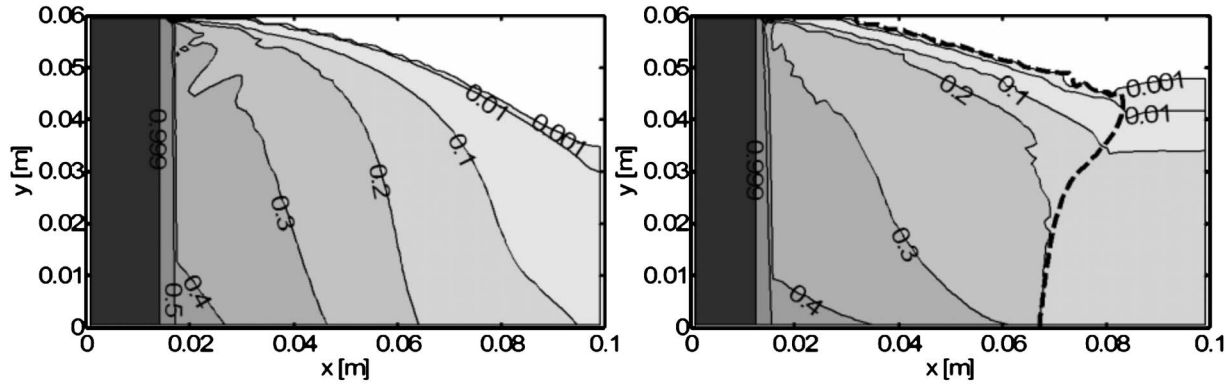

Fig. 11 Solid fraction after 300 s of solidification: left—Case 1, right—Case 2; a dotted line—the columnar front position

identified through *the coherency point*—a subjectively assumed value of the solid volume fraction.

Preliminary verification of the FTM calculations of Pb-48 wt % Sn solidification in a rectangular cavity demonstrates good fitting to the numerical results reported by Ahmad [25]. The subsequent validation, based on the comparisons between the numerical predictions and the experiment findings of Hebditch and Hunt [26], shows that the model, which distinguishes two different grain structures in the mushy zone and includes the specifics of the equiaxed region (through the model of slurry), gives a better match to the experimental data than the classical model with a stationary solid phase, especially in the upper and bottom parts of the cavity. Some remaining differences between FTM calculations and the experimental data can be caused by a simplified model of slurry, where grain sedimentation is not accounted for by the assumed isotropic porosity of the columnar mush and by the application of the simplified dendrite tip kinetics, where the role of thermosolutal convection is neglected. Alternatively, the lack of precise information on the boundary conditions occurring in the experiments [26] may also have contributed to these differences.

The main purposes of the study presented is the exploration of the potential of FTM in macroscopic modeling of the mushy zone in the presence of thermal and solutal buoyancy forces and preliminary verification and validation of the FTM numerical predictions, by their comparison with alternative calculations and experimental data. Therefore, rather simple models of the columnar mush permeability and the undercooled slurry zone of floating equiaxed crystals were adopted—those used in the reference solutions [17,25].

The authors are aware of the limitations and weaknesses of these models. Hence, the results of the current work, to be published elsewhere, have an entailed modification of the dendrite kinetics to account for the effect of thermosolutal buoyancy forces on grain growth (e.g., through combining the models developed in Refs. [39,40], refer to details given in Ref. [41]); implementing more enhanced model of slurry with sedimentation (e.g., by using data from Ref. [42]) and more realistic modeling of the columnar porous medium (e.g., from Ref. [43]).

Acknowledgment

The authors are grateful to the Polish Ministry of Science and Higher Education for funding from its Grant No. N N512 361634.

Nomenclature

C = concentration of solvent (wt %)
c_p = specific heat (J kg^{-1} K^{-1})
f = mass fraction
g = volumetric fraction
h = enthalpy (J)
k = thermal conductivity (W m^{-1} K^{-1})
K = permeability (m^2)
L = latent heat (J kg^{-1})
p = pressure (Pa)
t = time (s)
T = temperature (K)
u = velocity in the x-direction (m s^{-1})
v = velocity in the y-direction (m s^{-1})
V = velocity vector (m s^{-1})
Vol = volume of a control-volume part occupied by the columnar mush (m^3)
$\tilde{V}$ = dimensionless volume of a control-volume part occupied by the columnar mush
w = dendrite tip velocity (m s^{-1})
x,y = Cartesian coordinates (m)
β = expansion coefficient (K^{-1} or wt %)
κ_p = partition coefficient
λ_2 = secondary dendrite arm spacing (m)
μ = dynamic viscosity (kg m^{-1} s^{-1})
ρ = density (kg m^{-3})
ψ = stream function (m^2 s^{-1})
$\Delta x, \Delta y$ = grid increments in x and y directions, respectively (m)
Ω = supersaturation

Indices

0 = previous time step
C = solutal
E = eutectic
L = liquid
m = mushy zone
p = packing fraction
S = solid
T = thermal
$*$ = at the solid/liquid interface

References

[1] Juric, D., and Tryggvason, G., 1996, "A Front Tracking Method for Dendritic Solidification," J. Comput. Phys., **123**, pp. 127–148.
[2] Amberg, G., 2004, ""Solidification, Microstructure and Convection," Courses and Lectures—No. 449," *Phase Change With Convection: Modelling and Validation*, Springer-Verlag, Berlin, pp. 1–54.
[3] Badillo, A., and Beckermann, C., 2006, "Phase-Field Simulation of the Columnar-to-Equiaxed Transition in Alloy Solidification," Acta Mater., **54**, pp. 2015–2026.
[4] Gandin, Ch.-A., Desbiolles, J., Rappaz, M., and Thevoz, Ph., 1999, "A Three Dimensional Cellular Automaton Finite Element Model for the Prediction of Solidification Grain Structures," Metall. Mater. Trans. A, **30**, pp. 3153–3165.
[5] Dong, H. B., and Lee, P. D., 2005, "Simulation of the Columnar-to-Equiaxed Transition in Directionally Solidified Al–Cu Alloys," Acta Mater., **53**, pp. 659–668.
[6] Kurz, W., Giovanola, B., and Trivedi, R., 1986, "Theory of Micro-Structural Development During Rapid Solidification," Acta Metall., **34**, pp. 823–830.
[7] Bennon, W. D., and Incropera, F. P., 1987, "A Continuum Model for Momentum, Heat and Species Transport in Binary Solid-Liquid Phase Change Systems—I. Model Formulation," Int. J. Heat Mass Transfer, **30**, pp. 2161–2170.
[8] Prescott, P. J., Incropera, F. P., and Bennon, W. D., 1991, "Modelling of Dendritic Solidification Systems: Reassessment of the Continuum Momentum Equation," Int. J. Heat Mass Transfer, **34**, pp. 2351–2359.
[9] Beckermann, C., and Viskanta, R., 1993, "Mathematical Modelling of Transport Phenomena During Alloy Solidification," Appl. Mech. Rev., **46**, pp. 1–27.
[10] Wang, C. Y., and Beckermann, C., 1993, "A Multiphase Solute Diffusion Model for Dendritic Alloy Solidification," Metall. Trans. A, **24A**, pp. 2787–2802.
[11] Furmański, P., 2004, "Microscopic-Macroscopic Modelling of Transport Phenomena During Solidification in Hetero-Geneous Systems," *Courses and Lectures—No. 449 "Phase Change With Convection: Modelling and Validation"*, Springer-Verlag, Berlin, pp. 55–126.
[12] Ciobanas, A. I., and Fautrelle, Y., 2007, "Ensemble Averaged Multiphase Eulerian Model for Columnar/Equiaxed Solidification of Binary Alloy: I. The Mathematical Model," J. Phys. D, **40**, pp. 3733–3762.
[13] Voller, V. R., Brent, A. D., and Prakash, C., 1989, "The Modelling of Heat, Mass and Solute Transport in Solidification Systems," Int. J. Heat Mass Transfer, **32**, pp. 1719–1731.
[14] Swaminathan, C. R., and Voller, V. R., 1997, "Towards a General Numerical Scheme for Solidification Systems," Int. J. Heat Mass Transfer, **40**, pp. 2859–2868.
[15] Christenson, M. S., Bennon, W. D., and Incropera, F. P., 1989, "Solidification of an Aqueous Ammonium Chloride Solution in a Rectangular Cavity—II. Comparison of Predicted and Measured Results," Int. J. Heat Mass Transfer, **32**, pp. 69–79.
[16] Christenson, M. S., and Incropera, F. P., 1989, "Solidification of an Aqueous Ammonium Chloride Solution in a Rectangular Cavity—I. Experimental Study," Int. J. Heat Mass Transfer, **32**, pp. 47–68.
[17] Roux, P., Goyeau, B., Gobin, D., Fichot, F., and Quinard, M., 2006, "Chemical Non-Equilibrium Modelling of Columnar Solidification," Int. J. Heat Mass Transfer, **49**, pp. 4496–4510.
[18] Arnberg, L., Chai, G., and Backerund, L., 1993, "Determination of Dendritic Coherency in Solidifying Melts by Rheology Measurements," Mater. Sci. Eng., A, **173A**, pp. 101–103.
[19] Vreeman, C. J., and Incropera, F. P., 1999, "Numerical Discretization of Species Equation Source Terms in Binary Mixture Models of Solidification and Their Impact on Macro-Segregation in Semicontinuous Direct Chill Castings Systems," Numer. Heat Transfer, Part B, **36B**, pp. 1–14.
[20] Mat, M. D., and Ilegbusi, O. J., 2002, "Application of a Hybrid Model of Mushy Zone to Macro-Segregation in Alloy Solidification," Int. J. Heat Mass Transfer, **45**, pp. 279–289.

[21] Browne, D. J., and Hunt, J. D., 2004, "A Fixed Grid Front-Tracking Model of the Growth of a Columnar Front and an Equiaxed Grain During Solidification of an Alloy," Numer. Heat Transfer, Part B, **45**, pp. 395–419.
[22] Banaszek, J., and Browne, D. J., 2005, "Modelling Columnar Dendritic Growth Into an Under-Cooled Metallic Melt in the Presence of Convection," Mater. Trans., **46**, pp. 1378–1387.
[23] Banaszek, J., McFadden, S., Browne, D. J., Sturz, L., and Zimmermann, G., 2007, "Natural Convection and Columnar-to-Equiaxed Transition Prediction in a Front Tracking Model of Alloy Solidification," Metall. Mater. Trans. A, **38**, pp. 1476–1484.
[24] Browne, D. J., 2005, "A New Equiaxed Solidification Predictor From a Model of Columnar Growth," ISIJ Int., **45**(1), pp. 37–44.
[25] Ahmad, N., Combeau, H., Desbiolles, J.-L., Jalanti, T., Lesoult, G., Rappaz, J., Rappaz, M., and Stomp, C., 1998, "Numerical Simulation of Macro-Segregation: A Comparison Between Finite Volume Method and Finite Element Method Predictions and a Confrontation With Experiments," Metall. Mater. Trans. A, **29**, pp. 617–630.
[26] Hebditch, D. J., and Hunt, J. D., 1974, "Observations of Ingot Macro-Segregation on Model Systems," Metall. Trans., **5**, pp. 1557–1564.
[27] Ni, J., and Incropera, F. P., 1995, "Extension of the Continuum Model for Transport Phenomena Occurring During Metal Alloy Solidification—I. The Conservation Equations," Int. J. Heat Mass Transfer, **38**, pp. 1271–1284.
[28] Vreeman, C. J., Krane, M. J. M., and Incropera, F. P., 2000, "The Effect of Free-Floating Dendrites and Convection on Macro-Segregation in Direct Chill Cast Aluminum Alloys: Part I: Model Development," Int. J. Heat Mass Transfer, **43**, pp. 677–686.
[29] Kurz, W., and Fisher, D. J., 1998, *Fundamentals of Solidification*, 4th ed., Trans Tech Publication Ltd., Switzerland.
[30] Song, M., and Viskanta, R., 2001, "Lateral Freezing of an Anisotropic Porous Medium Saturated With an Aqueous Salt Solution," Int. J. Heat Mass Transfer, **44**, pp. 733–751.
[31] Ni, J., and Incropera, F. P., 1995, "Extension of the Continuum Model for Transport Phenomena Occurring During Metal Alloy Solidification—II. Microscopic Considerations," Int. J. Heat Mass Transfer, **38**, pp. 1285–1296.
[32] Ishii, M., and Zuber, N., 1979, "Drag Coefficient and Relative Velocity in Bubble, Droplet or Particulate Flows," AIChE J., **25**, pp. 843–855.
[33] Patankar, S. V., 1980, *Numerical Heat Transfer and Fluid Flow*, 1st ed., McGraw-Hill, New York.
[34] Shyy, W., 1994, *Computational Modelling for Fluid Flow and Interfacial Transport*, 1st ed., Elsevier, Amsterdam.
[35] Glimm, J., Li, X. L., and Liu, Y., 2003, "Conservative Front Tracking With Improved Accuracy," SIAM (Soc. Ind. Appl. Math.) J. Numer. Anal., **41**, pp. 1926–1947.
[36] Seredyński, M., and Banaszek, J., 2007, "Comparison of Two Front Tracking Techniques on a Fixed Grid in Modelling Binary Alloy Solidification," *Proceedings of the 13th Symposium on Heat and Mass Transfer*, Darlowko, Poland, pp. 933–940.
[37] Burden, M. H., and Hunt, J. D., 1974, "Cellular and Dendritic Growth I and II Part," J. Cryst. Growth, **22**, pp. 99–108.
[38] Gandin, Ch.-A., Guillemot, G., Appolaire, B., and Niane, N. T., 2003, "Boundary Layer Correlation for Dendrite Tip Growth With Fluid Flow," Mater. Sci. Eng., A, **342A**, pp. 44–50.
[39] Poirer, D. R., 1988, "Densities of Pb–Sn Alloys During Solidification," Metall. Trans. A, **19A**, pp. 2349–2354.
[40] Schrage, D. S., 1999, "A Simplified Model of Dendritic Growth in the Presence of Natural Convection," J. Cryst. Growth, **205**, pp. 410–426.
[41] Banaszek, J., and Furmanski, P., 2008, "Computer Simulation of Multi-Scale Transport Processes in Binary Mixture Solidification," *Proceedings of Fifth International Conference on Transport Phenomena in Multiphase Systems*, Bialystok, Poland, pp. 31–50.
[42] de Groh, H. C., III, Weidman, P. D., Zakhem, R., Ahuja, S., and Beckermann, C., 1993, "Calculation of Dendrite Settling Velocities Using a Porous Envelope," Metall. Trans. B, **24**, pp. 749–753.
[43] Furmanski, P., and Banaszek, J., 2006, "Modelling of the Mushy Zone Permeability for Solidification of Binary Alloys," Mater. Sci. Forum, **508**, pp. 411–418.

Hierarchical Modeling of Heat Transfer in Silicon-Based Electronic Devices

Javier V. Goicochea
Department of Mechanical Engineering,
Carnegie Mellon University,
Pittsburgh, PA 15213

Marcela Madrid
Pittsburgh Supercomputing Center,
Pittsburgh, PA 15213

Cristina Amon
Department of Mechanical and Industrial Engineering,
University of Toronto,
ON, M5S 1A4, Canada

A hierarchical model of heat transfer for the thermal analysis of electronic devices is presented. The integration of participating scales (from nanoscale to macroscales) is achieved by (i) estimating the input parameters and thermal properties to solve the Boltzmann transport equation (BTE) for phonons using molecular dynamics (MD), including phonon relaxation times, dispersion relations, group velocities, and specific heat, (ii) applying quantum corrections to the MD results to make them suitable for the solution of BTE, and (iii) numerically solving the BTE in space and time subject to different boundary and initial conditions. We apply our hierarchical model to estimate the silicon out-of-plane thermal conductivity and the thermal response of an silicon on insulator (SOI) device subject to Joule heating. We have found that relative phonon contribution to the overall conductivity changes as the dimension of the domain is reduced as a result of phonon confinement. The observed reduction in the thermal conductivity is produced by the progressive transition of modes in the diffusive regime (as in the bulk) to transitional and ballistic regimes as the film thickness is decreased. In addition, we have found that relaxation time expressions for optical phonons are important to describe the transient response of SOI devices and that the characteristic transport regimes, determined with Holland and Klemens phonon models, differ significantly. [DOI: 10.1115/1.4001644]

1 Introduction

The performance and reliability of modern electronic devices, such as microprocessors, is related to their ability to dissipate the heat generated from their operation. However, as their characteristic dimensions become comparable to or smaller than the mean free path or the relaxation time of the main energy carriers, the thermal conductivity of the constituent materials decreases from their bulk values. At subcontinuum scales, the interactions of the energy carriers become a fundamental part in the description of the heat transport. Lower values of thermal conductivity restrict heat dissipation and induce large thermal stresses and temperature changes. In semiconductor materials, these interactions are described in terms of quantized lattice vibrations or phonons [1]. Phonons are subject to complex collisions or scattering mechanisms (e.g., phonon-phonon, phonon-impurities, phonon-boundaries, and phonon-defects), which play a crucial role in describing how the heat is transported in the crystalline structure [2,3].

To model the thermal behavior of these devices, considering all scales involved, is a complex task. The complexity lies in the large variation in the participating spatial (from nanometers to centimeters) and temporal scales (from picoseconds to hours) in their intricate operation and in the physical behavior and nature of each scale. Even though the formulation of the thermal transport at the subcontinuum level has long been established [1–5], no mathematical method is able to fully resolve by itself the thermal response of electronic devices from nanoscale to macroscales. For instance, molecular dynamics (MD), which is a classical method, is essentially constrained to small (submicro) scales due to the expensive computations involved. The Boltzmann transport equation (BTE) on the other hand requires input parameters such as the relaxation time of phonons, which are difficult to estimate [6–10]. Likewise, the Fourier law, which is valid only at the macroscopic level, assumes instantaneous heat propagation and ignores interactions among phonons. From these methods, the solution of BTE under the single mode relaxation time (SMRT), approximation offers the possibility to model the heat transport from subcontinuum scales to continuum scales if the required phonons relaxation times are available.

There are several problems associated with the analytical estimation of the relaxation time of phonons. First, phenomenological models (derived from perturbation theory) are not reliable outside the range for which their parameters were fitted [11,12] and the effect of the approximations involved in their derivation (such as isotropic crystal, elastic continuum behavior, piecewise linear dispersion relations, third-order anharmonic expansions, etc.) are shadowed by the use of fitting parameters [13]. Second, since the relative contribution of the acoustic (A) and optical (O) and transverse (T) and longitudinal (L) phonons to the total thermal conductivity in semiconductors is still an open topic, these relaxation time models are not accurate. For instance, recent *ab initio* [14] and MD predictions obtained using the Stillinger–Weber (SW) potential for silicon [15] suggest that the contribution of acoustic modes is approximately 90–95% depending on the temperature of the system being the contribution of transverse acoustic (TA) about 30%. However, these results contrast with analytical estimations from Holland [4] and Hamilton and Parrott [16] who suggested that the TA modes were the dominant heat carriers at high temperatures. Sood and Roy [17] concluded that longitudinal acoustic (LA) phonons dominate heat transport in germanium at high temperatures being the contribution of the LA phonons more than 75% for $T > \theta_D$. Third, there is a lack of relaxation time expressions applicable to optical modes and frequently thermal estimations neglected their contribution. Different authors [7,18–20] have pointed out that optical phonons can have a significant effect on the creation of hotspots during transient Joule heating events due to the confinement of phonons, which can severely impact the operation temperature of silicon on insulator (SOI) devices. Notable are the works of Sinha et al. [18], Pop and co-workers [21,22], and, more recently, Rowlette and Goodson [6], who studied the scattering mechanisms of longitudinal optical (LO) phonons at hotspots and developed nonequilibrium electron and electron-phonon transport models, respectively, applicable to

Contributed by the Heat Transfer Division of ASME for publication in the JOURNAL OF HEAT TRANSFER. Manuscript received May 8, 2008; final manuscript received April 13, 2010; published online July 23, 2010. Assoc. Editor: Jayathi Murthy.

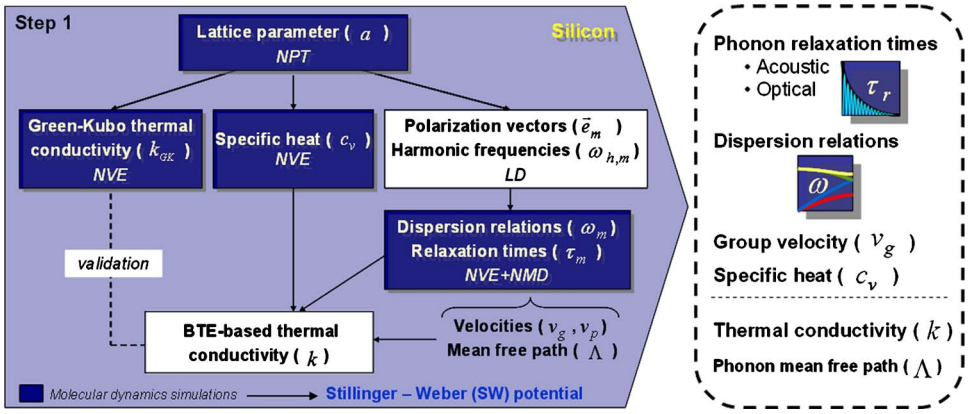

Fig. 1 Step 1: Estimation of different properties and relaxation times with MD

nanometer-scale field-effect transistors. Lastly, the accuracy of common relaxation time models in more complex semiconductors is unknown.

In this work, we present a hierarchical model of heat transfer for the thermal analysis of electronic devices. In the proposed methodology, the phonon relaxation times and the dispersion relations of silicon are estimated by means of MD simulations, removing in this way the need of fitting parameters. The methodology considers the effect of the anharmonicity of the potential energy function over the thermal expansion of the crystal and the change in the dispersion, which are particularly difficult to include in theoretical derivations [23] and might be important in systems, where the phonon vibration frequencies are expected to change significantly with temperature [24]. In addition, no explicit simplifications about the lattice structure or the contribution of anharmonic terms are required as it is commonly needed in theoretical derivations.

The integration of participating scales is achieved in three steps. First, we use MD simulations to estimate the properties required to solve the BTE for phonons. In the second step, we apply quantum corrections (QCs) to the MD results to make them suitable for BTE. This is required since MD and BTE interpret the physics of phonons differently. Lastly, we solve the BTE using these properties. Here, we use the SW potential to describe the interactions between silicon atoms and we solve the BTE using the lattice Boltzmann method (LBM) under the SMRT approximation. We apply our methodology to analyze the out-of-plane thermal conductivity and the thermal response of a SOI-like device subject to Joule heating.

2 Methodology

Our final goal is to numerically solve in space and time the BTE for phonons using the properties estimated from MD including phonon relaxation times ($\tau_{r,m}$), dispersion relations (ω_m), group velocity ($\boldsymbol{v}_{g,m}$), and specific heat (c_v). Under the SMRT approximation, the BTE can be written as follows:

$$\frac{\partial f_m}{\partial t} + \boldsymbol{v}_{g,m} \cdot \nabla f_m = -\frac{f_m - f_m^o}{\tau_{r,m}} \tag{1}$$

In the equation, f_m and f_m^o are the current and equilibrium distribution functions and t is the time. Phonons follow the equilibrium distribution function given by the Bose–Einstein distribution.

$$f_m^o = \left\{ \exp\left[\frac{\hbar \omega_m}{k_B T} \right] - 1 \right\}^{-1} \tag{2}$$

where $\hbar$ and k_B represent the Plank and Boltzmann constants and T is the equilibrium temperature.

We solve the BTE with the LBM using an isotropic and dispersive phonon formulation. The formulation includes acoustic and optical phonons (with longitudinal and transverse polarizations) whose properties depend on frequency. Details of the solution of the BTE using the LBM are presented in Appendix. In order to obtain the inputs needed to solve the BTE, first, we perform MD simulations using an NPT ensemble (constant number of atoms, pressure, and temperature) to determine the lattice parameter of silicon at 300 K and 1000 K. In this way, we consider the thermal expansion of the crystal. Then, as detailed below (see Fig. 1), we proceed to determine all other phonon properties using the lattice parameters obtained previously. For this, we perform additional MD simulations using an NVE ensemble (constant number of atoms, volume, and energy). For both ensembles, the instantaneous position and velocity of atoms are obtained by solving Newton's second law.

$$M \frac{d^2 \boldsymbol{r}}{dt^2} = \boldsymbol{F} \tag{3}$$

where M is the atom's mass, $\boldsymbol{r}$ is the position of the atom in the molecular domain, t represents the time, and $\boldsymbol{F}$ is the force.

The phonon relaxation times are computed from the energies obtained in the MD simulation using the normal mode decomposition method; specifically from the temporal decay of the autocorrelation function of the energy of each mode (m), where the energy of each mode is a function of the instantaneous position and velocity of each atom. This procedure was first proposed by Ladd et al. [25] and extended by McGaughey and Kaviany [24] for the determination of the phonon relaxation times and thermal conductivity of LJ argon under the isotropic approximation. Sun and Murthy [26], Henry and Chen [27], and, more recently, Goicochea et al. [15] used the environment-dependent interatomic potential (EDIP) and the SW potential to determine the relaxation times of silicon. Additionally, Turney et al. [28] presented four different methods for predicting phonon properties and thermal conductivity of argon based on lattice dynamics, on molecular dynamics, and on the solution Boltzmann transport equation. Their results indicate that the shape of the spectral thermal conductivity is closely related to the density of phonon states and that phonons with a frequency of half the maximum frequency are found to dominate thermal transport.

Under the harmonic approximation, the total energy of each mode can be written as [29]

$$E_{m,t} = \frac{\omega_{h,m}{}^2 Q_m^*(\boldsymbol{q},\lambda) Q_m(\boldsymbol{q},\lambda)}{2} + \frac{\dot{Q}_m^*(\boldsymbol{q},\lambda) \dot{Q}_m(\boldsymbol{q},\lambda)}{2} \tag{4}$$

where $\omega_{h,m}$ is the harmonic frequency and the first and second terms on the right hand side of the equation represent the potential energy and kinetic energy of the mode m, respectively. $Q_m(\boldsymbol{q},\lambda)$ is the normal mode of the system [29] given by

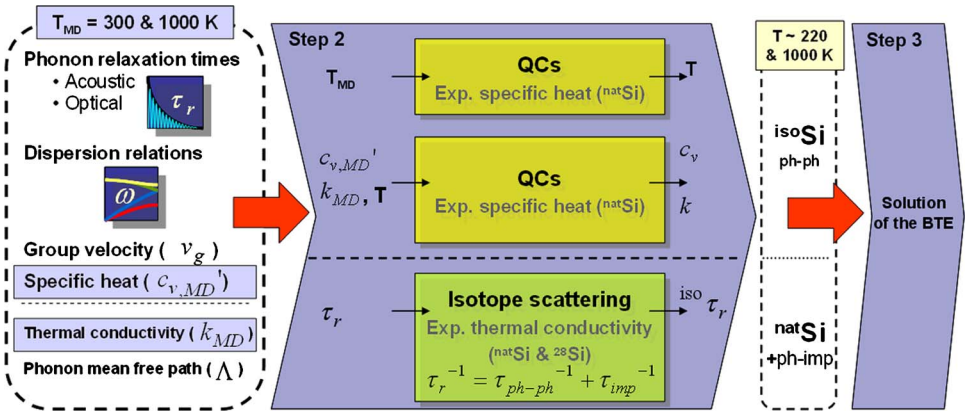

Fig. 2 Steps 2 and 3: Quantum correction of MD properties and solution of the BTE

$$Q_m(\boldsymbol{q},\lambda) = N^{-1/2}\sum_i M_i^{1/2}\exp(-\boldsymbol{q}\cdot\boldsymbol{r}_{i,0})\boldsymbol{e}_m^*(\boldsymbol{q},\lambda)\cdot\boldsymbol{u}_i(t) \quad (5)$$

where N is the number of atoms, M_i is the mass of atom i, and λ corresponds to the mode polarization (longitudinal or transverse) described by the polarization vector $\boldsymbol{e}_m^*(\boldsymbol{q},\lambda)$, i.e., its complex conjugate. $\boldsymbol{r}_{i,0}$ is the equilibrium position of atom i, and $\boldsymbol{u}_i(t)$ is the relative displacement of atom i at time t from its equilibrium position $(\boldsymbol{u}_i(t)=\boldsymbol{r}_i(t)-\boldsymbol{r}_{i,0})$.

Once the total energy $E_{m,t}$ of each mode is obtained for each time step in the MD simulation, the autocorrelation of the deviation of total energy from its mean value $(\delta E_{m,t}=E_{m,t}-\overline{E_m})$ is computed. The normalized autocorrelation produces a temporal decaying function that is fitted with an exponential function from which the relaxation time of mode m is extracted.

Likewise, the dispersion relations $\omega_m(\boldsymbol{q},\lambda)$ can be directly determined using the equipartition theorem between the kinetic and potential energy of each mode.

$$\omega_m(\boldsymbol{q},\lambda) = \sqrt{\frac{\langle \dot{Q}_m(\boldsymbol{q},\lambda)\dot{Q}_m(-\boldsymbol{q},\lambda)\rangle}{\langle Q_m(\boldsymbol{q},\lambda)Q_m(-\boldsymbol{q},\lambda)\rangle}} \quad (6)$$

Once the dispersion relations are obtained, the group and phase velocities are obtained as $v_g=\partial\omega/\partial q$ and $v_p=\omega/q$. The specific heat is computed using the procedures reported in Refs. [30,31]. We validate the MD obtained properties by comparing the silicon bulk thermal conductivity determined using the Green–Kubo method (k_{GK}) and that obtained from the steady state solution of the BTE (i.e., the thermal conductivity expression of Tiwari and Agrawal [32], which corresponds to the expression between curly brackets in Eq. (9)) at the studied temperatures.

Since MD is a classical method, before solving the BTE, the temperature, specific heat, and thermal conductivity have to be quantum corrected. This is particularly important at temperatures below the Debye temperature. (i.e., 645 K for Si [33]). Several strategies have been proposed to quantum correct the thermal conductivity and temperature [34–36]. We use the method proposed in Ref. [34], which includes the experimental specific heat to quantum correct both quantities. In addition, as explained below, we have extended this method to correct the thermal conductivity per phonon mode. In Ref. [34], the thermal conductivity is corrected as

$$k = \frac{dT_{\mathrm{MD}}}{dT}\{k_{\mathrm{MD}}\} \rightarrow k = \frac{c_{v,e}(T)}{3(N-1)k_B}\{k_{\mathrm{MD}}\} \quad (7)$$

where dT_{MD}/dT is defined as the ratio between the experimental $(c_{v,e})$ and the classical specific heat $(3(N-1)k_B)$. Likewise, the corrected temperature (T) is found integrating Eq. (7) as

$$T_{\mathrm{MD}}(T) = \frac{V}{3(N-1)k_B}\int_0^T c_{v,e}(T)dT + T^* \quad (8)$$

where T^* is the integration constant of the order of the Debye temperature [34].

To include the quantization of the energy of each mode at T and the change in the dispersion relations, we modify Eq. (7), considering that the corrected thermal conductivity is a function of the mode contribution to the specific heat $c_{v,a}(T,\omega)$, temperature, and of the ration between the total experimental and analytical specific heats $(c_{v,e}(T)/c_{v,a}(T))$

$$k = \frac{c_{v,e}(T)}{c_{v,a}(T)}\left\{\frac{4\pi}{3}\frac{1}{(2\pi)^3}\sum_{b,p}\left[\int_{\omega_{m,\min}}^{\omega_{m,\max}}\left(c_{v,a}(T,\omega)\frac{v_g}{v_p^2}\tau_r\right)\omega^2 d\omega\right]\right\} \quad (9)$$

For simplicity, the summation is performed in the [100] direction over all phonon branches and polarizations, where the relaxation times are determined. In Eq. (9), we assume that the crystal is isotropic, however, no changes are needed if an anisotropic model is considered. Lastly, the MD specific heat is corrected as $c_v(T,\omega)=c_{v,e}(T)c_{v,\mathrm{MD}}{}'(c_{v,a}(T,\omega)/c_{v,a}(T))$, where $c_{v,\mathrm{MD}}{}'$ is the MD specific heat per degree of freedom. $c_{v,\mathrm{MD}}{}'$ is 1.01 and 1.05 at 300 K and 1000 K, respectively.

To validate the second step of our methodology, we compare our estimated thermal conductivity with that obtained experimentally for natural Si ($^{\mathrm{nat}}$Si). For this, the isotope scattering is included in our phonon-phonon relaxation times $(\tau_{\mathrm{ph-ph}})$. In silicon, the isotope scattering is only important at temperatures approximately below 350 K [37]. $^{\mathrm{nat}}$Si has three stable isotopes (different forms of an element each having different atomic mass): ^{28}Si, ^{29}Si, and ^{30}Si in a proportion of 92.23%, 4.67%, and 3.1%, respectively. We include the phonon-isotope relaxation times (τ_{imp}) using an expression obtained from perturbation theory. The phonon-isotope relaxation times are included using Matthiessen's rule $(\tau_r^{-1}=\tau_{\mathrm{ph-ph}}^{-1}+\tau_{\mathrm{imp}}^{-1})$. Alternatively, the effect of isotope scattering can be modeled explicitly with MD using silicon atoms with different masses [38]. Klemens [2] and Carruthers [39] suggested two expressions for this type of scattering. Both of them are used to study the effect of isotope scattering.

$$\tau_{\mathrm{imp}}^{-1} = A\omega^4 \quad \text{and} \quad \tau_{\mathrm{imp}}^{-1} = Av_g^{-3}\omega^4 \quad (10)$$

where A is a fitted constant.

As shown in Fig. 2, the inclusion of the isotope scattering results in two sets of properties. One includes only phonon-phonon scattering ($^{\mathrm{iso}}$Si) and another includes the scattering with isotopes

Table 1 Relative contribution of each mode to the overall thermal conductivity at 300 K and 1000 K

From	T	$\frac{c_v}{k_B}$	k_{TA}	k_{LA}	k_{LO}	k_{TO}	k_{MD}	k_{GK}	A
MD	300	1.01	122.8 (33.87%)	202.590 (55.87%)	34.186 (9.43%)	2.953 (0.82%)	362.5	350.67	
+QC	220	See Sec. 2	119.656 (38.62%)	172.518 (55.67%)	16.530 (5.33%)	1.163 (0.38%)	309.9		
+ISO $A\omega^4$	220		116.186 (43.79%)	143.747 (53.83%)	6.004 (2.19%)	0.518 (0.19%)	265.3		1.57×10^{-45} (s^3/rad^4)
+ISO $\frac{A}{v_g^3}\omega^4$	220		107.750 (40.62%)	153.554 (57.88%)	3.973 (1.50%)	0.021 (0.01%)	265.3		2.47×10^{-34} (m^3/rad^4)
MD	1000	1.05	18.0 (29.99%)	35.385 (58.88%)	6.240 (10.38%)	0.438 (0.73%)	60.092		52.36

T is the temperature in (K), c_v/k_B is the nondimensional specific heat per unit of degree of freedom, k_{TA}, k_{LA} k_{LO} k_{TO} are the thermal conductivity contribution of the transverse and longitudinal acoustic and optical modes, respectively, k_{MD} is the BTE-based thermal conductivity obtained from MD results, and k_{GK} is the Green–Kubo thermal conductivity. MD, +QC, +ISO are the from molecular dynamics, after quantum corrections, and after isotope scattering, respectively. Thermal conductivity values in (W/m K).

(^{nat}Si). After these properties are quantum corrected, the BTE for phonons is solved and the methodology is applied to the study cases.

3 Results

In this section, results pertained to each of the steps of our hierarchical model are presented. Due to length considerations and since the first and second steps of the methodology have been presented individually [15,40,41], more emphasis is provided to the application of the methodology. For completeness, we also discuss the most important results found in the first two steps.

3.1 Step 1: Thermal Properties Estimation. We have found that the behavior of the phonon relaxation times for the different modes can be well-captured using power functions of the form: $1/\tau_r = a\omega^b$ [15]. At both temperatures the value of the exponents of the power functions for the acoustical modes (TA and LA) are approximately equal to 2 [15], which is in agreement with the theoretical predictions obtained from time-dependent perturbation theory for U-processes at high temperatures [3]. For optical modes, the value of the exponents is higher than 2, indicating that higher-order processes might be responsible for such behavior (as suggested in Ref. [15]).

It is observed that the anharmonic nature of the potential energy and the thermal expansion are responsible for the change in the dispersion relations with temperature. The change in the frequency of vibration is noticeable in the transverse modes, however, their change is relatively small compared with that obtained for argon [24] using the normal mode decomposition.

Table 1 shows the values obtained for specific heat and thermal conductivities of the TA, LA, LO, and transverse optical (TO) modes. As expected, the obtained specific heat is approximately k_BT. The small derivation from the classical specific heat at 1000 K is produced due to the anharmonic nature of the potential energy function. The relative contribution is obtained from the expression Tiwari and Agrawal considering that the specific heat is constant. At 300 K and 1000 K, we have found that the contribution of the TA and LA modes represents roughly 90% being about 30% from the TA mode and lower than 60% from the LA mode while the relative contribution of LO mode is 10%. The contribution from the TO mode for both temperatures is negligible (less 1%). In addition, both predictions match the overall thermal conductivity obtained with Green–Kubo. The difference between both thermal conductivities $(k-k_{GK})/k^*_{GK}100$ is 3.39% and 14.76% at 300 K and 1000 K, respectively. Both values fall within one standard deviation of the predicted values of the Green–Kubo method (i.e., 4.90% (17.38 W/m K) and 21.13% (11.16 W/m K) at 300 K and 1000 K, respectively). The agreement between these values validates the properties obtained with MD in this step. Furthermore, recent results for Ge [42] obtained using MD at high temperature agree very well with these predictions.

3.2 Step 2: Quantum Corrections and Isotope Scattering. Table 2 shows the QC temperatures calculated from Eq. (8) and using the experimental specific heat corresponds to that for natural silicon (^{nat}Si) [43]. In addition, due to the lack of experimental data for single Si isotopes and for comparison purposes, the temperature is also corrected replacing the experimental specific heat by the corresponding analytical expression (Eq. (11)).

$$c_{v,a}(T) = \sum_m \left\{ k_B(\hbar\omega_m/k_BT)^2 \frac{\exp(\hbar\omega_m/k_BT)}{[\exp(\hbar\omega_m/k_BT)-1]^2} \right\} \quad (11)$$

The frequency values used in Eq. (11) are those obtained from Eq. (6). Note that both estimations (experimental and analytical) provide similar results. At 300 K, the corrected temperature is roughly 220 K while at 1000 K, the correction is negligible (less than 1.2%). The analytical estimations are obtained for T^* = 790.94 K.

The QCs also affect the behavior of the specific heat with frequency. Figure 3 shows the mode specific heat as a function frequency at T_{MD} = 300 K. Before QCs, the specific heat is independent of the frequency of vibration of the modes, however, when the quantization of the energy is considered, the specific heat decreases as the frequency is increased. The quantum corrected specific heat starts at almost the same value of the corresponding for the classical anharmonic system, however, the difference becomes larger at higher frequencies. The small shift in the specific heat values observed at zero-frequency is produced due to the difference between the experimental and the analytic specific heats $(c_{v,e}(T)/c_{v,a}(T))$. The freezing of high-frequency modes translates in a reduction in their contribution to the overall thermal conductivity. As shown in Table 1, the relative contribution of the optical modes reduces from 10.25% before QCs to 5.70% after QCs while the one from acoustical modes increases from 89.75% to 94.30%.

To include the effect of isotope scattering, we find the value of A (in Eq. (10)) that produces the reduction in the experimental

Table 2 Quantum corrected temperatures

	T	
T_{MD}	Experimental	Analytical
300	218.5	220.6
1000	1011.3	1006.5

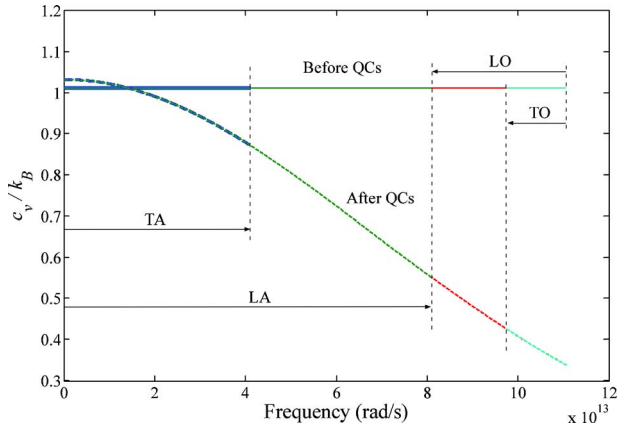

Fig. 3 Mode specific heat after quantum corrections. Arrows indicate the frequency range of each mode.

thermal conductivity due to isotope scattering. Based on experimental data reported by Kremer et al. [37] for ^{nat}Si and ^{28}Si (i.e., silicon enriched with isotope 28) at $T=220$ K, we estimate that such reduction (measured relatively to the ^{nat}Si thermal conductivity) is 16.80%.

As shown in Fig. 4, the inclusion of the isotope scattering term modifies the phonon relaxation times and all properties that depend on them (e.g., phonon mean free path, thermal conductivity, etc.). In particular, the phonon mean free path decreases as the frequency of each mode increases being the reduction more severe for high-frequency modes (i.e., LO and TO modes) and when the group velocity is considered in the phonon-impurity scattering term. Additionally, the relative contribution of high-frequency modes to the thermal conductivity is modified. As reported in Table 1, the contribution of optical modes reduces to less than 2.4% while the one from the acoustical modes increases to more than 97.6% when the first expression in Eq. (10) is used. Note that although both isotope scattering expressions yield to the same value of thermal conductivity, the reduction in the contribution of optical modes occurs regardless of the expression used for the phonon-isotope scattering. When the second expression of Eq. (10) is used, the contribution of TO modes becomes negligible.

3.2.1 Comparison With Experimental Data. Table 3 shows the comparison between the predicted thermal conductivity with that obtained experimentally for ^{nat}Si and ^{28}Si. The deviation of the predicted thermal conductivity before and after QCs are applied

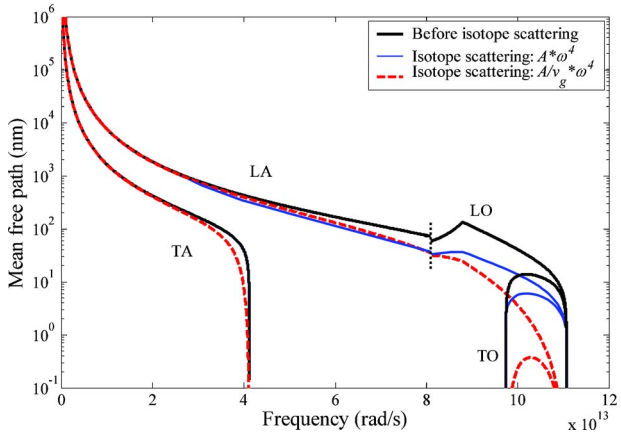

Fig. 4 Effect of the isotope scattering term in the phonon mean free path. The thin dotted line presents the edge of the BZ.

Table 3 Thermal conductivity comparison before and after isotope scattering with experimental data

From	k	$\left\lvert \frac{k}{k_e(^{28}\mathrm{Si})} - 1 \right\rvert$	$\left\lvert \frac{k}{k_e(^{nat}\mathrm{Si})} - 1 \right\rvert$
MD	362.5	44.48%	
+QC	309.9	23.48%	
+ISO	265.3		13.94%

$k_e(^{28}\mathrm{Si})=250.934$ W/m K [37], $k_e(^{nat}\mathrm{Si})=232.844$ W/m K [44], and k_e is the experimental thermal conductivity.

with respect to the experimental value is 44.48% and 23.48% for ^{28}Si. When the isotope scattering term is included, a deviation of 13.94% is found between our thermal conductivity predictions and the experimental value for ^{nat}Si. Hence, both the proposed quantum correction and the inclusion of the isotope scattering term improve the thermal conductivity predictions.

3.2.2 High Temperature Implications. At high temperatures, both the quantization of the energy and the presence of isotopes are expected to have a minor effect on the reduction in the thermal conductivity. Although there are no reported values of thermal conductivity for ^{28}Si at 1000 K, it is well known that at high temperatures phonon-phonon scattering is the main source of thermal resistance. It is interesting to note that the contribution to the thermal conductivity from the high-frequency modes would approach the ones estimated with MD (before QCs) as the temperature of the system is increased.

3.3 Step 3: Solution of the BTE and Study Cases. In this section, we discuss the results of the application of the methodology. Details of the solution of the BTE using the LBM are presented in Appendix. We apply the methodology to estimate the silicon out-of-plane thermal conductivity and the thermal response of an SOI device subject to Joule heating. The calculated phonon dispersion relations, specific heat, group velocity, and relaxation times are provided as input to solve the BTE.

3.3.1 Out-of-Plane Thermal Conductivity. The out-of-plane thermal conductivity is obtained for a thin film of thickness d. It is assumed that the length L of the film is several times larger than its thickness $L \gg d$. The film is modeled as a one-dimensional domain (see Fig. 5) with prescribed temperature at the top and bottom boundaries. All other boundaries are assumed to be adiabatic and no phonon-boundary scattering is possible with them. The procedure to determine the out-of-plane thermal conductivity is described in Ref. [45].

Figure 6 shows the out-of-plane thermal conductivity obtained with ^{nat}Si and ^{iso}Si at 220 K. For comparison, the out-of-plane conductivity obtained with relaxation times models of Escobar et al. [46] (i.e., gray formulation), Holland [4], and Han and Klemens [47]. In general, all conductivity curves have the same behavior; they approach their bulk values as the thickness increases. At 100 nm and 1000 nm, the difference between ^{nat}Si and ^{iso}Si is 15% and 23%, respectively. This is expected, since the bulk thermal conductivity of ^{iso}Si is higher than that for ^{nat}Si (see Table 3). Note that despite Holland [4] and Han and Klemens [47] models were designed to reproduce the bulk thermal conductivity of sili-

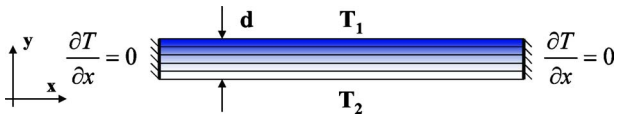

Fig. 5 One-dimensional domain used to estimate the out-of-plane thermal conductivity

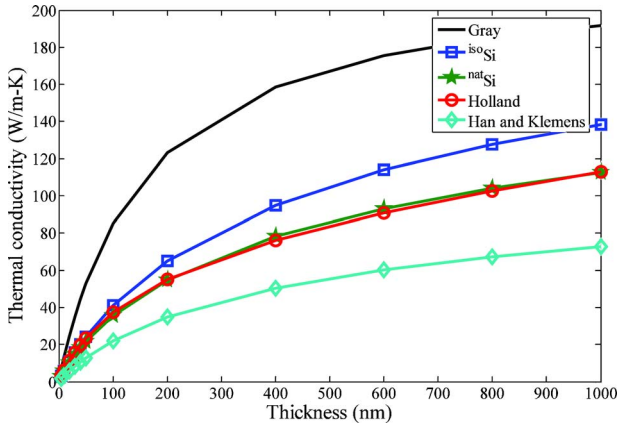

Fig. 6 Silicon thin film out-of-plane thermal conductivity as a function of film thickness at 220 K

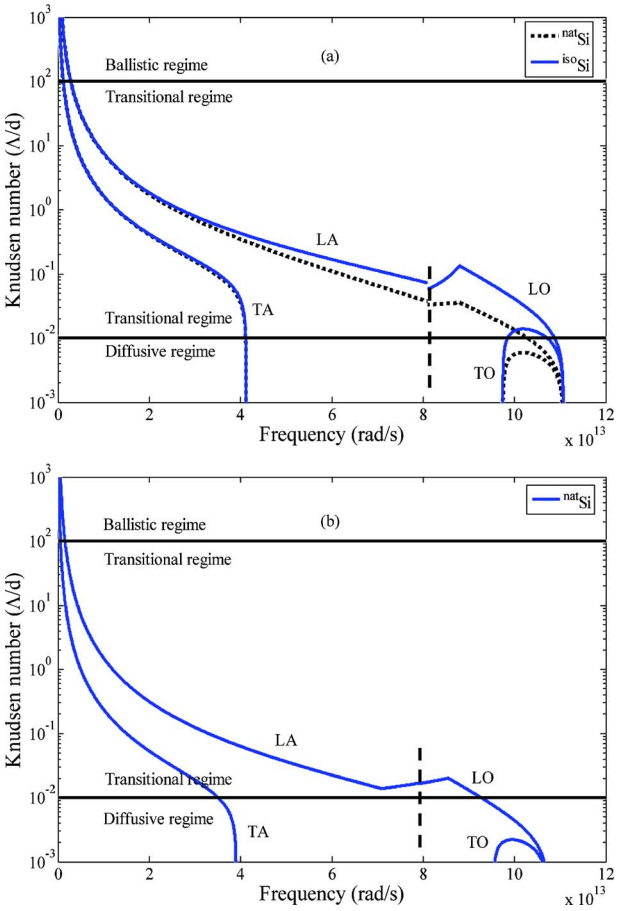

Fig. 7 Variation in Knudsen number with respect to frequency for a film thickness of 1000 nm at 220 K (*a*) and 1000 K (*b*). The dashed line represents the edge of the BZ.

con over a wide range of temperatures, their predictions obtained for the studied thicknesses differ significantly. Furthermore, despite 220 K the out-of-plane conductivity obtained with the Holland model is higher than that of the Han and Klemens model, the situation reverses at 1000 K for film thickness below 100 nm. Coincidentally, at 220 K Holland model predicts similar out-of-plane conductivities as those obtained with ^{nat}Si.

In Fig. 6, all phonon models have thermal conductivity values lower than that for the gray formulation. This is produced due to the transition of phonon modes from the diffusive transport regime to the ballistic regime as the thickness of the film reduces. This transition, observed in our LBM dispersive formulations, has been *qualitatively* explained due to the coexistence of different phonons [7]. Different transport regimes originate due to the existence of frequency-dependent phonons with different relaxation times, group velocities, and, hence, different mean free paths. For a given characteristic dimension of the film, this yield to phonons with different Knudsen number (Λ/d) coexisting in the same phonon system. A similar behavior has been previously observed in Ref. [7].

To elucidate this effect, Fig. 7 shows the frequency-dependent Knudsen number for a film of 1000 nm at 220 K and 1000 K. At both temperatures, only low-frequency TA and LA modes fall within the ballistic regime region at both temperatures. The rest of the LA modes are located in the transitional region. This is also the situation for the TA modes, except for those modes with higher frequency. At 1000 K most of the LO and TO modes are located in the diffusive region, however, at 220 K the low-frequency LO modes also fall within the transitional region. In general, the increase in temperature produces that more modes are locate within the transitional and diffusive regions, which corresponds to a decrease in the phonon mean free path for all modes and thermal conductivity. Contrarily, further reductions in the thickness will increase the number of modes falling within the ballistic and transitional regions, especially low-frequency modes. For phonons falling within the transitional and ballistic regimes, the phonon-boundary scattering becomes a major source of thermal resistance, reducing their contribution to the thermal conductivity.

The evidence of change in the contribution of the different modes to the thermal conductivity as a function of the thickness is shown in Fig. 8. In the figure, the variation in mode thermal conductivity of ^{iso}Si as a function of film thickness is shown. The mode thermal conductivity is determined for three different films of increasing thickness from 100 nm to 10000 nm and is calculated expressing Eq. (9) as

$$k = \sum_m \int_{\omega_{m,\min}}^{\omega_{m,\max}} k_m(\omega) d\omega \tag{12}$$

where the summation includes all branches and polarizations. Again an isotropic phonon space is assumed.

As shown in Fig. 8, the increase in the film thickness not only affects the mode contribution to the thermal conductivity (especially for those low-frequency modes) but the peaks for the TA

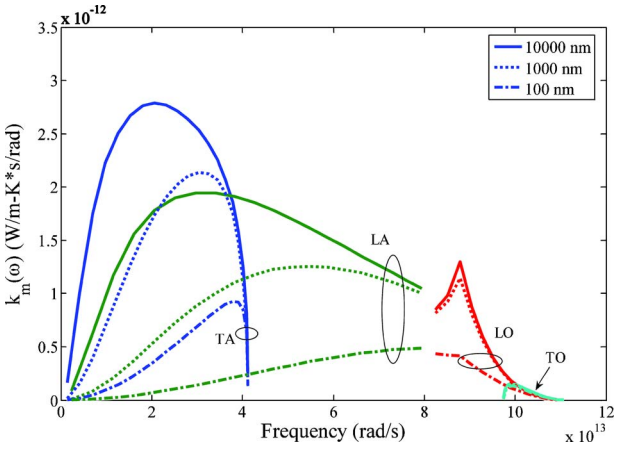

Fig. 8 Variation in mode thermal conductivity as a function of film thickness at 220 K

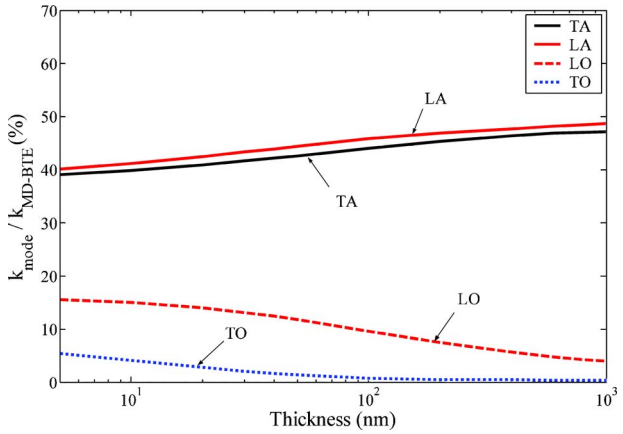

Fig. 9 Mode thermal conductivity contribution as a function of thickness

and LA modes are progressively displaced to the left. In the limit of a large film thickness (previously estimated to be of the order of millimeters [7,48]), the location of the peaks and the contribution of the low-frequency modes would correspond to that of the bulk case, as reported in Table 1. For small thicknesses the relative contribution of the modes to the overall thermal conductivity changes significantly due to phonon confinement.

Figure 9 shows how the contribution of the TA, LA, LO, and TO modes to the overall thermal conductivity changes as a function of film thickness for ^{nat}Si. For films of 10 nm, acoustical modes contribute about 80% while optical modes contribute 20%, being 15% and 5% the contribution of the LO and TO modes, respectively. This represents a substantial increase in the contribution of the optical modes from the bulk values (see Table 1). The behavior is also present in ^{iso}Si, where optical modes contribute about 22% for a 10 nm film and in the phonon relaxation time models of Holland and Han and Klemens (not shown). In Holland model, the contribution of the TA and LA modes decreases from 58.3% and 41.7% for bulk to 24.5% and 75.5% while in Han and Klemens model the contribution of the TA and LA modes changes from 33.0% and 67.0% for bulk to 24.4% and 75.6% at 10 nm and 220 K. To the best of our knowledge, this is the first time that this change in the thermal conductivity is quantitatively reported for Si.

3.3.2 Thermal Response of a SOI Device. The thermal response of a SOI device is modeled by considering a one-dimensional silicon layer of $L=100$ nm subject to self-heating. The heat generation occurs at the center of the domain in a region 1/10 smaller than the length of the silicon layer, as shown in Fig. 10. The top and bottom boundaries are considered adiabatic. Temperatures at the right and left boundaries are maintained at a constant value. The value of the phonon relaxation times depends on the initial temperature of the film. It is considered that the silicon layer is fabricated of ^{nat}Si and ^{iso}Si.

To study the thermal response of the SOI device, we analyze the transient behavior of temperature at the center of the hotspot. Pop et al. [21] determined phonon emission and energy dissipation rates, due to Joule heating, using a coupled electron-phonon

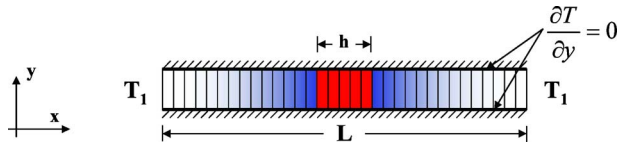

Fig. 10 One-dimensional domain used to model the silicon layer of a SOI transistor

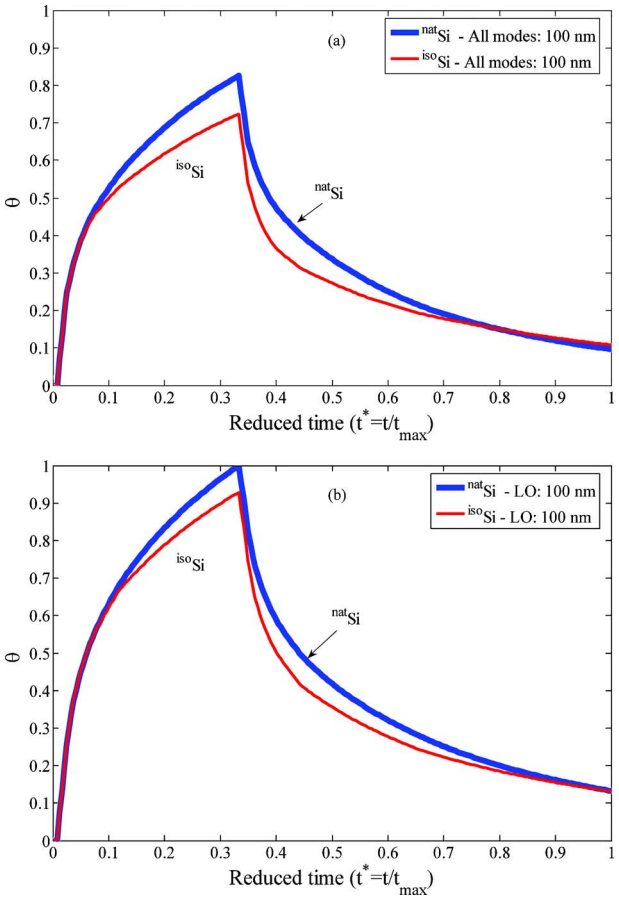

Fig. 11 Temperature evolution at the center of the hotspot for a film of 100 nm. (*a*) Heat generated is distributed over all phonon modes, (*b*) Heat generated is distributed only in LO mode.

model. Here, we use their results to model how the total heat generated due to the operation of the SOI device under low and high electric fields (5 kV/cm and 50 kV/cm) is distributed among the heat carriers. When a high electric field is applied, all heat generated is distributed in the LO, LA, and TO modes with a ratio about 1/2, 1/3, and 1/10, respectively. Conversely, for the low electric field case, all heat is distributed in the LO mode [21]. The same amount of heat is dissipated in both scenarios (i.e., 10×10^{12} W/cm^3). Figure 11 shows the nondimensionalized temperature as a function of time at the center of the hotspot subject to high and low electric fields. The temperature and thickness of the film have been nondimensionalized as $\theta=(T-T_{min})/(T_{max}-T_{min})$ and $\xi=x/d$, where T_{min} initial temperature inside of the layer and T_{max} is the maximum temperature found during all simulations. Likewise, the time scale is defined as $t^*=t/t_{max}$, where t and t_{max} are the actual and total simulation time, respectively. The total simulation time (t_{max}) is 60 ps and the heat pulse last 1/3 of the total time.

In the figure, an increase in the temperature during the first 20 ps is observed. The maximum peak temperature is found when the heat pulse is applied to ^{nat}Si and all the heat is distributed in the LO mode. This is produced due to the low thermal conductivity of the LO mode for which the isotope scattering further reduces the contribution of optical modes.

The temperature behavior of ^{iso}Si shows two characteristic effects of ballistic heat transport [7]. First, the slope of the temperature as a function of time during the application of the heat pulse is slower than for ^{nat}Si, especially for $t^*>0.1$. Second, despite the higher thermal conductivity of ^{iso}Si, its rate of cooling is lower

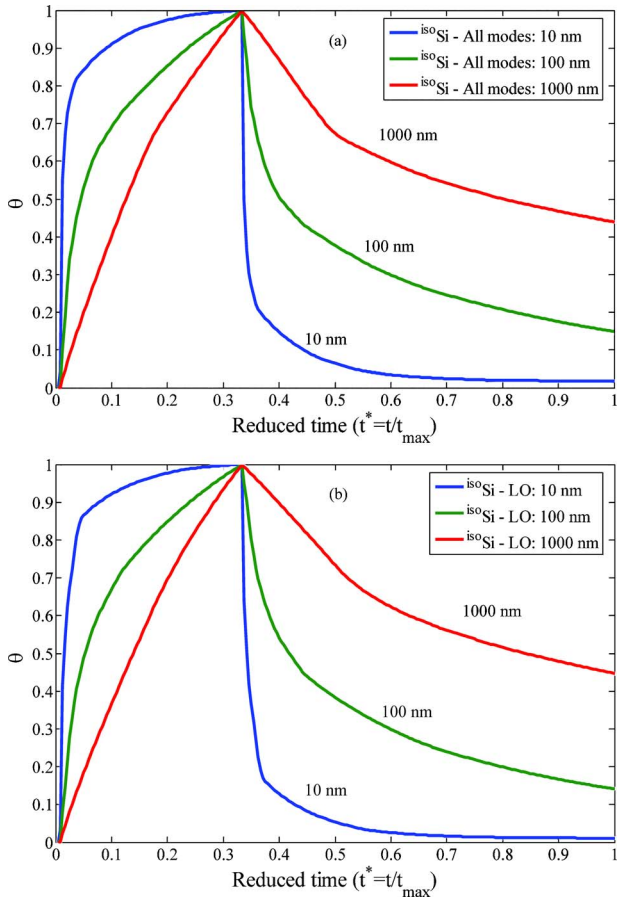

Fig. 12 Temperature evolution at the center of the hotspot for different film thicknesses. Hotspot size is 1/10 of the thickness of the film. Heat generated is distributed over all phonon modes (*a*) and through the LO mode (*b*).

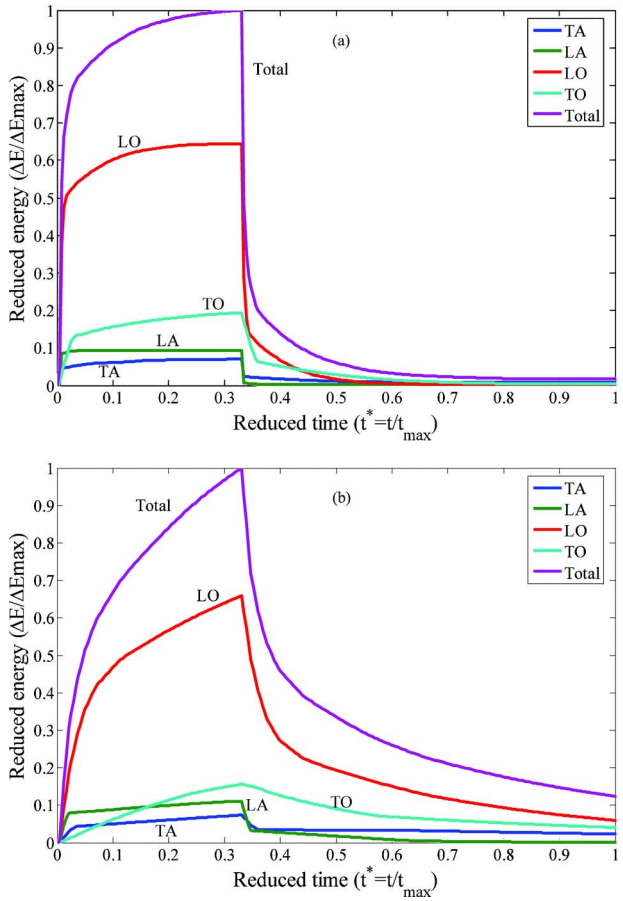

Fig. 13 Contribution of the TA, LA, LO, and TO modes to the reduced phonon total energy as a function of reduced time for films thicknesses of 10 nm (*a*) and 100 nm (*b*)

than that for ^{nat}Si. For ^{iso}Si, when the heat pulse is turned off, the temperature decreases rapidly followed by a slower rate of cooling. These effects are less noticeable in ^{nat}Si since more phonons fall within the transitional or diffusive regimes (Fig. 7(*a*)).

Figure 12 shows the temperature evolution at the center of the hotspot for film thicknesses of 10 nm, 100 nm, and 1000 nm and ^{iso}Si subject also the high and low electrical fields. For films of 1000 nm, the temperature increases roughly linear while the heat pulse is on, followed by a slow cooling rate. This behavior is characteristic of diffusive heat transport [7,48] and is essentially independent of how the generated heat is distributed among phonon modes. As the film thickness is reduced, the transient evolution of temperature changes. For 100 nm films, the hotspot increases more rapidly until $t^* < 0.1$ (approximately) followed by a reduction in the temperature slope. Then, when the heat pulse is turned off, the hotspot temperature reduces rapidly. Further reductions in the film thickness accentuate this behavior. For 10 nm films, the heating and cooling of the hotspot occurs abruptly. Initially, the increase in temperature is steep until it becomes almost flat, followed by quickly temperature drop produced after the heat pulse is turned off. A similar behavior in the hotspot temperature was observed by Escobar and Amon [7]. Similar temperature changes are also found for ^{nat}Si.

Figure 13 shows the change in the reduced energy (Eq. (13)) of each phonon branch and polarization as a function of the reduced time for films thicknesses of (a) 10 nm and (b) 100 nm. All generated heat is assumed distributed among all modes as described previously. The film is fabricated of ^{iso}Si. The reduced energy is defined as

$$\left(\frac{\Delta E}{\Delta E\ \max}\right)^t = \frac{E_p^t - E_p^{t=0}}{E_{\text{total}}^t - E_{\text{total}}^{t=0}} \tag{13}$$

where E_p^t is energy of each phonon branch and polarization (i.e., TA, LA, LO, and TO), E_{total}^t is the total energy of all phonons, and the superscript t represents the time.

The shape of the total energy curves follows the same behavior as the hotspot temperature (shown in Fig. 12(*a*)) for equivalent film thicknesses. Despite the heat generated is distributed among all modes, the contribution of each mode to the total energy varies significantly. Acoustic modes follow a similar trend to that observed in Fig. 12(*a*) for a film thickness of 10 nm (which is characteristic of ballistic transport [7]). These modes experience an abrupt change in their energy levels as the heat pulse is turned on or off since they fall in the ballistic and transitional regimes (see Fig. 7(*a*)). For both thicknesses, the LA mode is more excited than the TA mode. This is produced because 1/3 of the heat generated is transferred through the LA mode. On the other hand, the low thermal conductivity of optical modes produces a large increase in their energy levels, leading to phonon confinement. Phonon confinement is further promoted due to the distribution of 1/2 and 1/10 of the total heat generated into the LO and TO modes, respectively. For a film of 100 nm the energy of optical modes increases with a lower rate than for acoustic modes while the heat pulse is on, followed by a slower cooling rate. It can be verified that for a film of 100 nm, most optical phonons fall in the transitional and diffusive regimes. As the film thickness is reduced to 10 nm, most optical phonons fall in the transitional regime and the behavior approaches that of ballistic transport. Evidently, the behavior of the total phonon energy and temperature at the hotspot

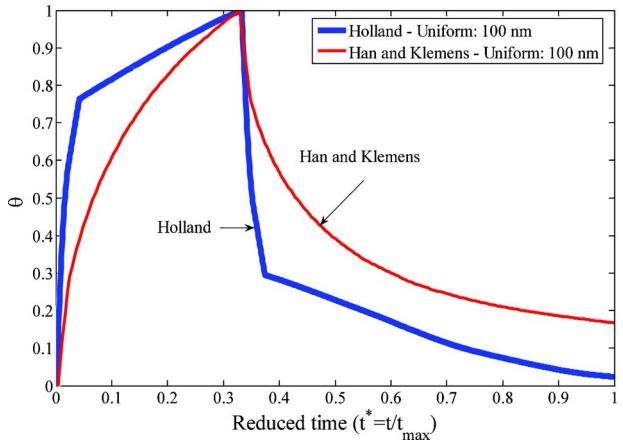

Fig. 14 Temperature at the center of the hotspot for a film of 100 nm as a function of time, obtained from Holland, and Han and Klemens phonon relaxation times models

are strongly affected by the confinement of optical modes.

Figure 14 compares the temperature at the center of the hotspot for a film of 100 nm obtained from Holland and Han and Klemens. In this case, all heat generated is distributed uniformly among the TA and LA modes. From the figure, the thermal predictions of both models differ drastically. Holland's model predict a behavior similar to that of ballistic transport while Han and Klemens' predict a hotspot temperature behavior similar to the transitional regime, resembling that obtained for ^{nat}Si for the same film thickness. As expected, the maximum temperature at the hotspot depends on the phonon model used. Holland's model predicts the lowest hotspot temperature, followed in increasing order by ^{iso}Si, ^{nat}Si, and Han and Klemens (which has the lowest thermal conductivity). The presence of optical modes in ^{iso}Si and ^{nat}Si increase their thermal resistance due to phonon confinement leading to higher temperatures at the hotspot.

4 Summary and Conclusions

A hierarchical modeling methodology for heat transfer of silicon-based electronic devices has been presented. The integration of participating scales has been achieved in three steps. These involve (i) the estimation of the thermal properties at different temperatures required to solve the BTE, including phonon relaxation times, dispersion relations, group velocity, and specific heat, (ii) their quantum correction to make them suitable for BTE, and (iii) the solution of this equation using an isotropic and dispersive lattice Boltzmann formulation for phonons. Nonlinear dispersion relations in the [100] direction for the acoustic and optical modes (longitudinal and transverse) were used to solve the BTE. The different steps of the methodology were validated using analytic or experimental data reported in literature.

It is found that the reduction in the out-of-plane conductivity is produced by a progressive transition of modes from diffusive regimes (as in the bulk case) to transitional or ballistic regime regions as the film thickness is reduced. This transition is characterized by a shift in the location of the mode thermal conductivity peaks for the acoustic modes as the film thickness is reduced, which at the same time modifies the relative contribution of all modes to the thermal conductivity. For ^{nat}Si and ^{iso}Si, the total contribution of the optical modes increases to 20% and 22% when the film thickness is reduced to 10 nm. At this thickness, the LO and TO modes contribute about 15% and 5% to the thermal conductivity, respectively. Similar changes are also found in the LA and TA modes for the models of Holland and Han and Klemens.

The thermal response of SOI-like transistors of decreasing size is characterized by temperature profiles that become progressively nonlinear. The transition to ballistic transport is observed as both the length and the hotspot size decreases. The hotspot temperature exhibits abrupt changes as the heat pulse is turned on or off, produced due to the sudden changes in the energy levels of each mode. It was found that acoustic modes dissipate the generated heat ballistically, whereas the behavior of optical modes is identified to be within the transitional and diffusive regimes. Under self-heating conditions, acoustic modes exhibit a saturation of their energy levels as the heat pulse is turned on while those of optical modes increase due to their lower thermal conductivity. The difference between transient behavior of temperature (in nondimensional units) obtained for ^{nat}Si and ^{iso}Si is not substantially different, however, notable differences are found using the models of Holland and Han and Klemens.

The value of hierarchical methodology stands out when the results obtained from different phonon relaxation time models are compared. Despite Holland and Han and Klemens, the models are able to reproduce the silicon bulk thermal conductivity, their predictions for out-of-plane thermal conductivity, and behavior of temperature at the hotspot differ drastically. The difference in the results obtained from Holland and Han and Klemens models reaffirms the importance of our proposed methodology, which can be extended to other semiconductor materials and to validate models for phonon relaxation times.

Acknowledgment

The authors gratefully acknowledge the funding of the National Science Foundation under Grant No. CTS-0103082 and the Pennsylvania Infrastructure Technology Alliance (PITA), a partnership of Carnegie Mellon, Lehigh University, and the Commonwealth of Pennsylvania's Department of Community and Economic Development (DCED). Most of the computations were performed on the National Science Foundation Terascale Computing System at the Pittsburgh Supercomputing Center under Grant No, CTS-070003P.

Nomenclature

A = fitted coefficient (s^3/rad^4 or m^3/rad^4)
c_v/k_B = nondimensional specific heat per degree of freedom
$c_{v,e}$ = experimental specific heat (kg/s^2 K)
$c_{v,a}$ = analytic specific heat (kg/s^2 K)
$c_{v,a}(T,\omega)$ = mode contribution to the specific heat as a function of temperature and frequency
d = silicon layer thickness (nm)
E_p^t = energy of each phonon branch and polarization (J)
E_{total}^t = total energy of all phonons (J)
f_m = phonon distribution function
$\hbar$ = Plank constant (J*s/rad)
k_e = experimental thermal conductivity (W/m K)
$k_e(^{28}\text{Si})$ = experimental thermal conductivity of enriched 28 silicon (W/m K)
$k_e(^{nat}\text{Si})$ = experimental thermal conductivity of natural silicon (W/m K)
k = quantum corrected thermal conductivity (W/m K)
k_B = Boltzmann constant (kg/s^2 K)
k_{GK} = Green–Kubo thermal conductivity (W/m K)
k_{MD} = BTE-based thermal conductivity (W/m K)
$k_m(\omega)$ = mode thermal conductivity as a function of frequency (W/m K*s/rad)
L = silicon layer length (nm)
N = number of atoms
q = wave vector (1/m)
Si = Silicon
t = time (s)

T = temperature (K)
T_{MD} = molecular temperature (K)
T^* = integration constant (K)
v_g, v_p = group and phase velocities (m/s)
w_m = LBM weighting factor

Greek Symbols

θ = nondimensional temperature
θ_D = Debye temperature (K)
Δx = lattice spacing
Δt = time step
Λ = mean free path (nm)
τ_m = relaxation time (s)
ω = frequency (rad/s)

Superscripts

O = equilibrium
* = nondimensional

Subscripts

m = phonon mode
max = maximum
min = minimum
TA, LA = transverse and longitudinal acoustics
TO, LO = transverse and longitudinal opticals

Appendix

LBM is a computational method originally developed for fluid simulation [49]. In this method, the spatial domain is discretized in lattices that only have a finite number of propagation directions. Since all our simulations are one-dimensional, we use the D1Q3 lattice [50], considering only two propagation directions (left and right). On each lattice, a discretized version of the BTE known as the lattice Boltzmann kinetic equation (LBKE) is solved. The latter was obtained after applying two different operators to the first and second terms on the right of Eq. (1): one forward in time (t) and one forward in time and space (x), respectively. One important characteristic of the LBM is that the lattice spacing and time are linked by the so-called light-cone rule [49] (i.e., $\Delta x = v^* \Delta t$). This results in Eq. (A1) (w_m is a weighting factor defined as $w_m = \Delta x / (|v_{g,m}| \tau_m) = \Delta t / \tau_m$).

$$f_{m,i}(x + dx, t + dt) = (1 - w_m) f_{m,i}(x,t) + w_m f^o_{m,i}(x,t) \qquad \text{(A1)}$$

In our dispersive LBM phonon formulation, multiple LBKEs are solved simultaneously in space and time. One equation per phonon is defined in the simulation domain [7]. Phonons are obtained from the discretization of the dispersion relations in bands of constant wave vector [7] or constant frequency [9]. This leads to phonon properties (e.g., group velocities) that depend on frequency. In our case, our dispersion relations obtained in the [100] direction are discretized using constant wave vector bands and all phonon properties are band-average with respect to frequency (i.e., $\overline{\alpha} = 1/\Delta\omega \int_{\Delta\omega} \alpha(\omega) d\omega$). Unlike a gray model [46], which include only a single phonon with one group velocity, in a dispersive formulation many phonons are defined.

The solution of each LBKE in space and time follows the next algorithm: (i) given a finite number of phonons defined in the simulation, the initial temperature of the system and its boundary conditions, we use Eq. (2) to obtain the initial phonon distribution functions in the domain. Since the temperature at the boundaries is typically prescribed, the equilibrium distribution at these locations for each phonon defined remains fixed during the entire simulation; (ii) multiple equations, such as Eq. (A1), are solved and (iii) at the end of each time step, the total phonon energy is computed on each lattice site and a new temperature distribution is obtained using Eq. (2). Steps ii and iii are repeated until the predefined simulation time is reached.

In the algorithm, it is implicitly assumed that the energy of the phonon system remains in quasi-equilibrium. Hence, the temperature of the system can be recovered from equilibrium distribution functions. In this way, all our results are strictly valid in the limit of low normal modes amplitudes. The impact of this approximation was discussed in Ref. [15]. Other nonequilibrium phonon formulation to solve BTE has been developed [6,10,21].

To maintain the accuracy at an acceptable level while keeping the computational effort at minimum, the sensitivity of the bulk thermal conductivity at 220 K to the number of bands (per branch) used to discretize the dispersion relations was evaluated. The sensitivity is defined as $[k(n_w) - k(n_w - 1)]/k(n_w)$, where k is the thermal conductivity and n_w is the number of bands per branch. For $n_w = 10$ or 40, the phonon defined (i.e., ten bands * four branches) the sensitivities of 3.7%, 5.2%, 0.03%, and 0.04% were found using the models of Holland, Han, and Klemens and for ^{nat}Si and ^{iso}Si, respectively. Additionally, since the LBM is a nonconservative method, the sensitivity with respect to the spatial discretization was also evaluated. All our results are independent of the number of cells used to discretize the domain. However, it is important to mention that the number of cells we use to discretize the domain varies with the domain size. The light-cone rule restriction is particularly severe in multiphonon systems, especially for phonons whose group velocity approach to zero (i.e., transverse modes near the BZ edge) and therefore the number of cell used is generally large enough for the results to be independent of spatial discretization [41]. Mesh independence was found with a minimum of 800 cells. For the film of 10,000 nm (see Fig. 8), approximately 30,000 cell were used.

References

[1] Peierls, R. E., 1955, *Quantum Theory of Solid*, Oxford University Press, London.
[2] Klemens, P. G., 1958, "Thermal Conductivity and Lattice Vibrational Modes," *Solid State Physics*, F. Seitz and D. Thurnbull, eds., Academic, New York, pp. 1–98.
[3] Klemens, P. G., 1969, "Theory of Thermal Conductivity of Solids," *Thermal Conductivity*, R. P. Tye, ed., Academic, London, pp. 1–68.
[4] Holland, M. G., 1963, "Analysis of Lattice Thermal Conductivity," Phys. Rev., **132**(6), pp. 2461–2471.
[5] Ziman, J., 1960, *Electrons and Phonons: The Theory of Transport Phenomena in Solids*, Oxford University Press, Oxford, UK.
[6] Rowlette, J., and Goodson, K., 2008, "Fully Coupled Nonequilibrium Electron–Phonon Transport in Nanometer-Scale Silicon FETs," IEEE Trans. Electron Devices, **55**(1), pp. 220–232.
[7] Escobar, R., and Amon, C. H., 2007, "Influence of Phonon Dispersion on Transient Thermal Response of Silicon-on-Insulator Transistors Under Self-Heating Conditions," ASME J. Heat Transfer, **129**(7), pp. 790–797.
[8] Mazumder, S., 2001, "Monte Carlo Study of Phonon Transport in Solid Thin Films Including Dispersion and Polarization," ASME J. Heat Transfer, **123**(4), pp. 749–759.
[9] Narumanchi, S. V. J., Murthy, J. Y., and Amon, C. H., 2005, "Comparison of Different Phonon Transport Models for Predicting Heat Conduction in Silicon-on-Insulator Transistors," ASME J. Heat Transfer, **127**(7), pp. 713–723.
[10] Narumanchi, S. V. J., Murthy, J. Y., and Amon, C. H., 2004, "Submicron Heat Transport Model in Silicon Accounting for Phonon Dispersion and Polarization," ASME J. Heat Transfer, **126**(6), pp. 946–955.
[11] Kazan, M., Pereira, S., Coutinho, J., Correia, M. R., and Masri, P., 2008, "Role of Optical Phonon in Ge Thermal Conductivity," Appl. Phys. Lett., **92**(21), p. 211903.
[12] Holland, M. G., 1964, "Phonon Scattering in Semiconductors From Thermal Conductivity Studies," Phys. Rev., **134**(2A), pp. A471–A480.
[13] Chung, J. D., McGaughey, A. J. H., and Kaviany, M., 2004, "Role of Phonon Dispersion in Lattice Thermal Conductivity Modeling," ASME J. Heat Transfer, **126**(3), pp. 376–380.
[14] Broido, D. A., Malorny, M., Birner, G., Mingo, N., and Stewart, D. A., 2007, "Intrinsic Lattice Thermal Conductivity of Semiconductors From First Principles," Appl. Phys. Lett., **91**(23), p. 231922.
[15] Goicochea, J. V., Madrid, M., and Amon, C. H., 2010, "Thermal Properties for Bulk Silicon Based on the Determination of Relaxation Times Using Molecular Dynamics," ASME J. Heat Transfer, **132**(1), p. 012401.
[16] Hamilton, R. A., and Parrott, J. E., 1969, "Variational Calculation of the Thermal Conductivity of Germanium," Phys. Rev., **178**(3), pp. 1284–1292.
[17] Sood, K. C., and Roy, M. K., 1993, "Longitudinal Phonons and High-Temperature Heat Conduction in Germanium," J. Phys.: Condens. Matter, **5**(3), pp. 301–312.
[18] Sinha, S., Schelling, P. K., Phillpot, S. R., and Goodson, K. E., 2005, "Scattering of G-Process Longitudinal Optical Phonons at Hotspots in Silicon," J. Appl. Phys., **97**(2), p. 023702.
[19] Narumanchi, S. V. J., Murthy, J. Y., and Amon, C. H., 2006, "Boltzmann

Transport Equation-Based Thermal Modeling Approaches for Hotspots in Microelectronics," Heat Mass Transfer, **42**(6), pp. 478–491.
[20] Pop, E., Banerjee, K., Sverdrup, P., Dutton, R., and Goodson, K., 2001, "Localized Heating Effects and Scaling of Sub-0.18 Micron CMOS Devices," IEEE Int. Electron Dev. Meet., pp. 677–680.
[21] Pop, E., Dutton, R. W., and Goodson, K. E., 2005, "Monte Carlo Simulation of Joule Heating in Bulk and Strained Silicon," Appl. Phys. Lett., **86**(8), p. 082101.
[22] Pop, E., Sinha, S., and Goodson, K., 2006, "Heat Generation and Transport in Nanometer-Scale Transistors," Proc. IEEE, **94**(8), pp. 1587–1601.
[23] Reissland, J. A., 1973, *The Physics of Phonons*, Wiley-Interscience, New York.
[24] McGaughey, A. J., and Kaviany, M., 2004, "Quantitative Validation of the Boltzmann Transport Equation Phonon Thermal Conductivity Model Under the Single-Mode Relaxation Time Approximation," Phys. Rev. B, **69**(9), p. 094303.
[25] Ladd, A., Moran, B., and Hoover, W. G., 1986, "Lattice Thermal Conductivity: A Comparison of Molecular Dynamics and Anharmonic Lattice Dynamics," Phys. Rev. B, **34**(8), pp. 5058–5064.
[26] Sun, L., and Murthy, J. Y., 2005, "Molecular Dynamics Simulation of Phonon Transport in EDIP Silicon," ASME Paper No. HT2005-72200.
[27] Henry, A. S., and Chen, G., 2008, "Spectral Phonon Transport Properties of Silicon Based on Molecular Dynamics Simulations and Lattice Dynamics," J. Comput. Theor. Nanosci., **5**(2), pp. 141–152.
[28] Turney, J. E., Landry, E. S., McGaughey, A. J. H., and Amon, C. H., 2009, "Predicting Phonon Properties and Thermal Conductivity From Anharmonic Lattice Dynamics Calculations and Molecular Dynamics Simulations," Phys. Rev. B, **79**(6), p. 064301.
[29] Dove, M. T., 1993, *Introduction to Lattice Dynamics*, Cambridge University Press, New York.
[30] Pearson, E. M., Halicioglu, T., and Tiller, W. A., 1985, "Laplace-Transform Technique for Deriving Thermodynamics Equations From the Classical Microcanonical Ensemble," Phys. Rev. A, **32**(5), pp. 3030–3039.
[31] Porter, L. J., Yip, S., Yamaguchi, M., Kaburaki, H., and Tang, M., 1997, "Empirical Bond-Order Potential Description of Thermodynamic Properties of Crystalline Silicon," J. Appl. Phys., **81**(1), pp. 96–106.
[32] Tiwari, M. D., and Agrawal, B. K., 1971, "Analysis of the Lattice Thermal Conductivity of Germanium," Phys. Rev. B, **4**(10), pp. 3527–3532.
[33] Volz, S. G., and Chen, G., 1999, "Molecular Dynamics Simulation of Thermal Conductivity of Silicon Nanowires," Appl. Phys. Lett., **75**(14), pp. 2056–2058.
[34] Gomes, C., Madrid, M., Goicochea, J. V., and Amon, C. H., 2006, "In-Plane and Out-of-Plane Thermal Conductivity of Silicon Thin Films Predicted by Molecular Dynamics," ASME J. Heat Transfer, **128**(11), pp. 1114–1121.
[35] Lee, Y. H., Biswas, R., Soukoulis, C. M., Wang, C. Z., Chan, C. T., and Ho, K. M., 1991, "Molecular-Dynamics Simulation of Thermal Conductivity in Amorphous Silicon," Phys. Rev. B, **43**(8), pp. 6573–6580.
[36] Volz, S. G., and Chen, G., 2000, "Molecular-Dynamics Simulation of Thermal Conductivity of Silicon Crystals," Phys. Rev. B, **61**(4), pp. 2651–2656.
[37] Kremer, R. K., Graf, K., Cardona, M., Devyatykh, G. G., Gusev, A. V., Gibsin, A. M., Inyushkin, A. V., Taldenkov, A. N., and Pohl, H., 2004, "Thermal Conductivity of Isotopically Enriched 28Si: Revisited," Solid State Commun., **131**(8), pp. 499–503.
[38] Murakawa, A., Ishii, H., and Kakimoto, K., 2004, "An Investigation of Thermal Conductivity of Silicon as a Function of Isotope Concentration by Molecular Dynamics," J. Cryst. Growth, **267**(3–4), pp. 452–457.
[39] Carruthers, P., 1961, "Theory of Thermal Conductivity of Solids at Low Temperatures," Rev. Mod. Phys., **33**(1), pp. 92–138.
[40] Goicochea, J. V., Madrid, M., and Amon, C. H., 2009, "Effects of Quantum Corrections and Isotope Scattering on Silicon Thermal Properties," Thermal Investigations of ICs and Systems, THERMINIC, Leuven, Belgium, pp. 197–202.
[41] Goicochea, J. V., 2008, "Hierarchical Modeling of Heat Transfer in Silicon-Based Electronic Devices," Ph.D. thesis, Carnegie Mellon University, Pittsburgh, PA.
[42] Goicochea, J. V., and Michel, B., 2010, "Phonon Relaxation Times of Germanium Determined by Molecular Dynamics at 1000 K," Semiconductor Thermal Measurement, Modeling and Management Symposium (SEMITHERM), Santa Clara, CA.
[43] Desai, P. D., 1986, "Thermodynamic Properties of Iron and Silicon," J. Phys. Chem. Ref. Data, **15**(3), pp. 967–083.
[44] Ho, C. Y., Powell, R. W., and Liley, P. E., 1974, "Thermal Conductivity of the Elements," J. Phys. Chem. Ref. Data, **3**(1), pp. 1–796.
[45] Escobar, R., Smith, B., and Amon, C. H., 2006, "Lattice Boltzmann Modeling of Subcontinuum Energy Transport in Crystalline and Amorphous Microelectronic Devices," ASME J. Electron. Packag., **128**(2), pp. 115–124.
[46] Escobar, R. A., Ghai, S. S., Jhon, M. S., and Amon, C. H., 2006, "Multi-Length and Time Scale Thermal Transport Using the Lattice Boltzmann Method With Applications to Electronics Cooling," Int. J. Heat Mass Transfer, **49**(1–2), pp. 97–107.
[47] Han, Y., and Klemens, P. G., 1993, "Anharmonic Thermal Resistivity of Dielectric Crystals at Low Temperatures," Phys. Rev. B, **48**(9), pp. 6033–6042.
[48] Escobar, R. A., and Amon, C. H., 2008, "Thin Film Phonon Heat Conduction by the Dispersion Lattice Boltzmann Method," ASME J. Heat Transfer, **130**(9), p. 092402.
[49] Succi, S., 2001, *The Lattice Boltzmann Equation for Fluid Mechanics and Beyond*, Clarendon, Oxford, UK.
[50] Qian, Y. H., d'Humieres, D., and Lallemand, P., 1992, "Lattice BGK for Navier-Stokes Equation," Europhys. Lett., **17**(6), pp. 479–484.

Jacob Eapen
Department of Nuclear Engineering,
North Carolina State University,
Raleigh, NC 27695
e-mail: jacob.eapen@ncsu.edu

Roberto Rusconi
School of Engineering and Applied Sciences,
Harvard University,
Cambridge, MA 02138

Roberto Piazza
Dipartimento di Ingegneria Nucleare,
Politecnico di Milano,
Milano 20133, Italy

Sidney Yip
Department of Nuclear Science and Engineering
and Department of Material Science and
Engineering,
Massachusetts Institute of Technology,
Cambridge, MA 02139

The Classical Nature of Thermal Conduction in Nanofluids

We show that a large set of nanofluid thermal conductivity data falls within the upper and lower Maxwell bounds for homogeneous systems. This indicates that the thermal conductivity of nanofluids is largely dependent on whether the nanoparticles stay dispersed in the base fluid, form large aggregates, or assume a percolating fractal configuration. The experimental data, which are strikingly analogous to those in most solid composites and liquid mixtures, provide strong evidence for the classical nature of thermal conduction in nanofluids. [DOI: 10.1115/1.4001304]

1 Introduction

A nanofluid is a colloid with complex thermo-chemical properties. Typical colloids, even in dilute concentrations, form aggregates that are dependent on the solution chemistry, surface charges, and thermal (Brownian) motion of the nanoparticles [1–3]. External fields such as gravity and temperature can support or disrupt the formation of aggregates. Thus in most experimentally tested nanofluids, there is a competition between the growth of fractal-like structures, coalescence into large clumps, sedimentation, and fragmentation [4]. The transport properties such as viscosity and thermal conductivity, in general, are sensitive to the geometrical configuration and the connectivity of the aggregated structures.

The study of thermal transport in colloidal dispersions is relatively recent. The thermophysical and thermal transport properties of magnetic colloids *(ferrofluids)* with nanoparticles as small as 4 nm were reported in the 1980s [5–7]. In the last decade, there has been a renewed interest with nonmagnetic metallic and oxide colloids. The early experiments on dilute nanofluids have shown a fascinating increase in the thermal conductivity [8–12] as well as other interesting effects of nanoparticle size and temperature [13,14]. The initial promise of nanofluids as an advanced, nanoengineered coolant, however, has been tempered in recent years by a lack of consensus on the thermal conduction mechanism. While several experiments with well-dispersed nanoparticles have shown modest conductivity enhancements consistent with the classical Maxwell theory for noninteracting spheres [15–24], more instances of larger enhancements have also been reported in recent years [25–45]. In a recent International Benchmark Exercise [46], different experimental techniques (such as transient hotwire and forced Rayleigh scattering) are shown to be comparable in accuracy and precision. Several outliers in the experimental data, however, highlight the difficulties of accurate thermal measurements in complex colloidal systems. Against this backdrop, it is essential to have a fundamental understanding of the heat conduction mechanism in nanofluids.

Contributed by the Heat Transfer Division of ASME for publication in the JOURNAL OF HEAT TRANSFER. Manuscript received December 30, 2008; final manuscript received December 18, 2009; published online July 23, 2010. Assoc. Editor: W. Q. Tao

The effective medium or mean-field theory of Maxwell [47,48] is most often used to analyze the thermal conductivity results of nanofluid experiments. For a nanofluid with *noninteracting* spherical nanoparticles, the theory predicts

$$\frac{\kappa}{\kappa_f} = \frac{1 + 2\beta\phi}{1 - \beta\phi} \tag{1}$$

where ϕ is the nanoparticle volume fraction, $\beta = (\kappa_p - \kappa_f)/(\kappa_p + 2\kappa_f)$, and $(\kappa_p - \kappa_f)$ is the difference between the thermal conductivities of the nanoparticle and the base fluid. If a finite temperature discontinuity exists at the nanoparticle-fluid interface, the Maxwell theory would still apply, provided that one makes the substitution $\kappa_f \rightarrow \kappa_f + \alpha\kappa_p$ (on the right-hand side), where $\alpha = 2R_b\kappa_f/d$, wherein R_b is the interfacial thermal resistance and d is the nanoparticle diameter [49,50].

The thermal conductivity enhancements beyond those predicted by Eq. (1) are often reported to be anomalous or unusual. In addition to larger thermal conductivities, experiments have also revealed other disagreements with the Maxwell theory. The thermal conductivity is observed to have an inverse dependence on the nanoparticle size [25,32,51,52] and a quasi-linear dependence on the temperature [14,36,53,54]. Interestingly, there appears to be a fundamental difference between the thermal conduction behavior of solid composites and nanofluids. In the former, smaller dispersed (or filler) particles, especially those in the nanometer size range, reduce the matrix thermal conductivity significantly. In some cases the thermal conductivity is reduced well-below that of the base medium [55] at all volume fractions, while in others, the enhancement is severely suppressed [56]. The solid composite behavior is easily explained through the interfacial thermal resistance R_b, which has an inverse dependence on the particle diameter [49,57,58]. Thus, decreasing the filler particle size will dramatically reduce the effective thermal conductivity of the solid composites and *vice versa*. For the case of nanofluids some of the experimental data indicate that the thermal conductivity increases with decreasing nanoparticle size—a behavior which is clearly at odds with the Maxwell theory [25,32,51,52]. Some experiments have also shown that the nanofluid thermal conductivity is not correlated in a simple manner to that of the nanoparticle as predicted by the Maxwell model [26,34]. A limiting behavior at higher volume fractions is also observed in nanofluids, which is

qualitatively different from that in solid composites. While the thermal conductivity displays a quadratic or power law behavior at higher volume fractions for solid composites [59,60], it is known to rise rapidly at lower volume fractions and then saturate at higher volume fractions for several nanofluids [26,28,34].

Several mechanisms have been recently proposed to account for the excess thermal conductivity and other departures from the Maxwell theory (such as temperature and size dependence). These include the Brownian motion of the nanoparticles [61,62], fluid convection at microscales [63–69], liquid layering at the particle-fluid interface [70–75], nanoparticle shape [46,76,77], cluster agglomeration [78,79], or a combination of the aforesaid mechanisms [80–85]. A disconcerting aspect of having several theories is compounded by the ability of each postulated mechanism to match (a subset) of the experimental data accurately.

In this paper, we start by asking an elementary question—Is there an anomalous thermal conduction behavior in nanofluids? First we show that the classical Maxwell theory has two limiting bounds, which correspond to two geometrical configurations of the nanoparticles. These limits are also formally known as the Hashin and Shtrikman (H-S) mean-field bounds for homogeneous composite media [48]. In the first configuration, the nanoparticles constitute the *dispersed* phase with the fluid medium acting as the continuous phase. Most investigations have thus far reported this lower limiting bound given by Eq. (1). In the second configuration, the nanoparticles can form the *continuous* phase with the base fluid constituting the dispersed phase. It is easy to visualize the second configuration for high volume fractions of nanoparticles, but for small volume fractions, the nanoparticles *will necessarily need to* form linear, fractal-like or percolating structures, separating large pockets of the fluid medium. In both configurations, the effective thermal conductivity is *maximally biased* toward the continuous phase. However, if the nanoparticles have a higher thermal conductivity in relation to the base fluid, the additional conduction paths in the second configuration will lead to an effective nanofluid thermal conductivity that is larger than what is given by the lower Maxwell limit (Eq. (1)).

Next, by analyzing a large body of data including those from our own experiments, we show that most of the reported thermal conductivity data are enveloped by the upper and lower Maxwell (H-S) mean-field bounds. This observation strongly indicates that the nanoparticles can exist in several configurations ranging from a well-dispersed mode to a linear chainlike arrangement in the colloidal state. Indeed, a number of electron microscopy experiments at low volume fractions support (but does not prove conclusively) the presence of both configurations. A comparison to the conduction behavior of solid-solid composites and liquid-liquid mixtures reveal that the Maxwell bounds, to a large extent, have a universal applicability. While this is recognized for solid-composites, it is not so well-known for liquid mixtures. We further show that the conduction behavior in binary solid composites differs from that of nanofluids in one important aspect, which is its susceptibility to interfacial thermal resistance for nanometer sized filler particles. The apparent anomalous behavior of nanofluids is thus shown to stem from the assumption of well-dispersed nanoparticles. If this restriction is removed the classical theoretical models can predict much higher thermal conductivities [86]. We further stress that the differences in aggregation structures, which arise from colloidal chemistry, thermodynamic conditions and external fields, have a profound influence on the nanofluid thermal conduction behavior. While a linear or fractal configuration provides additional conduction paths that promote the effective thermal conductivity, large aggregates or clumps (which are formed, for example, by sedimentation) are detrimental to thermal conductivity enhancements. In conclusion we show that the classical theory of thermal conduction is applicable to nanofluids – the phenomena being consistent with what is known for binary solid composites and liquid mixtures.

2 The Theoretical Framework for Thermal Conduction in Nanofluids

For a single component material, thermal conduction is described uniquely with the Fourier constitutive law $\dot{q}'' = -\kappa \nabla T$, where κ is the thermal conductivity and T is the temperature. In a mixture heat can flow from multiple gradients in addition to the temperature gradient such as those resulting from concentrations and external fields. The theoretical framework for describing multicomponent transport is provided by the linear phenomenological theory, which postulates that the fluxes are linear homogeneous functions of the corresponding gradients. While an intrinsic thermal conductivity exists for the nanofluids, the measured thermal conductivity can include effects of diffusion, chemical reactions, and other external fields. Since diffusion, directly and indirectly, is considered to be a key mechanism for the nanofluid thermal conductivity in several new theories [61–69], the theoretical framework is elaborated here to make a quantitative assessment of diffusion and chemical reactions on nanofluid thermal conductivity. The formalism is well-known, and in this paper, it is adopted from de Groot and Mazur [87].

For a n component system, the linearity between the fluxes and gradients is expressed as

$$\mathbf{J} \equiv \mathbf{L}\hat{\mathbf{x}} = \sum_{k=1}^{n} L_{ik}\hat{X}_k \quad (i = 1,2, \ldots, n) \tag{2}$$

where $\mathbf{J}$ and $\hat{\mathbf{x}}$ are the generalized flux and gradient vectors, respectively. $\mathbf{L}$ is a matrix containing the phenomenological coefficients. The cross coefficients L_{ik} and L_{ki} are equal, following Onsager's reciprocity hypothesis. The heat flux in a multicomponent system is not defined uniquely, and hence, the thermal conductivity. A commonly accepted definition follows from the second law of thermodynamics which is given by [87]

$$\mathbf{J}_q = \hat{\mathbf{J}}_q - \sum_{k=1}^{n} h^k \mathbf{J}^k \tag{3}$$

where $\hat{\mathbf{J}}_q$ is the heat flux, which is usually measured in an experiment, $\mathbf{J}_q$ is the reduced (or conductive) heat flux, $\mathbf{J}$ is the mass flux, and h is the partial specific enthalpy. The difference between $\mathbf{J}_q$ and $\hat{\mathbf{J}}_q$ represents the heat transfer due to diffusion. Typically, dilute nanofluid experiments are dominated by the gradients in temperature and concentration (to a lesser extent). For components (s,l), abbreviated for solid nanoparticles and base liquid, respectively, the phenomenological relationships reduce to the following form [87]:

$$\mathbf{J}_q = -L_{qq}\frac{\nabla T}{T^2} - L_{qs}\frac{1}{T}\nabla(\mu^s - \mu^l)_T \tag{4}$$

$$\mathbf{J}^s = -L_{sq}\frac{\nabla T}{T^2} - L_{ss}\frac{1}{T}\nabla(\mu^s - \mu^l)_T \tag{5}$$

where μ is the chemical potential. Note that for a binary nanofluid system, $\mathbf{J}^s = -\mathbf{J}^l$. In experiments, diffusion is associated with a concentration gradient (c) rather than the chemical potential. The above equations can be recast in terms of the experimental coefficients in the following form [87]

$$\mathbf{J}_q = -\kappa \nabla T - \rho_s \left(\frac{\partial \mu^s}{\partial c^s}\right)_{T,p} TD'' \nabla c^s \tag{6}$$

$$\mathbf{J}^s = -\rho c^s c^l D_T \nabla T - \rho D^{sl} \nabla c^s \tag{7}$$

The phenomenological coefficients (L_{ik}) are related to the experimental coefficients in the following way:

$$\kappa = \frac{L_{qq}}{T^2} \tag{8}$$

$$D'' = \frac{L_{qs}}{\rho c^s c^l T^2} \tag{9}$$

$$D_T = \frac{L_{sq}}{\rho c^s c^l T^2} \tag{10}$$

$$D^{sl} = \frac{L_{ss}}{\rho c^l T}\left(\frac{\partial \mu^s}{\partial c^s}\right)_{T,p} \tag{11}$$

In Eqs. (6) and (7), D_T, D'', and D^{sl} stand for the thermal diffusion coefficient, the Dufour coefficient, and the mutual (binary) diffusion coefficient, respectively, while the density of the system is given by ρ. Thermal diffusion coefficient (D_T) accounts for the flow of matter with a temperature gradient, while the Dufour coefficient (D'') is a measure of the inverse effect, which is the flow of heat due to a concentration gradient. κ is the thermal conductivity of the nanofluid system, and it is clear that it is a native or intrinsic property of the nanofluid without any contribution from diffusion. The ratio of D_T to D^{sl} is defined as the Soret coefficient and is given by

$$s_T \equiv \frac{D_T}{D^{sl}} \tag{12}$$

In an experiment, measurements can be made before the diffusion transients begin ($\nabla c^s = 0$) or at steady-state conditions ($\mathbf{J}^s = \mathbf{J}^l = 0$). Therefore, multiple definitions for thermal conductivities can be defined as shown below for these limiting conditions [87].

$$\mathbf{J}_q = -\zeta \nabla T, \quad \hat{\mathbf{J}}_q = -\hat{\zeta} \nabla T \quad (\nabla c^s = 0) \tag{13}$$

$$\mathbf{J}_q = -\lambda \nabla T, \quad \hat{\mathbf{J}}_q = -\hat{\lambda} \nabla T \quad (\mathbf{J}^s = \mathbf{J}^l = 0) \tag{14}$$

The heat fluxes $\mathbf{J}_q$ and $\hat{\mathbf{J}}_q$ are associated with the thermal conductivities (ζ, λ) and $(\hat{\zeta}, \hat{\lambda})$, respectively. As mentioned before, the difference between these heat fluxes (Eq. (3)) is solely due to the heat carried by the diffusing nanoparticles. It can be shown that [87]

$$\zeta = \kappa$$

$$\hat{\zeta} = \kappa + D_T (h^s - h^l) \rho c^s c^l \tag{15}$$

$$\lambda = \kappa - \frac{(D_T)^2}{D^{sl}}\left(\frac{\partial \mu^s}{\partial c^s}\right)\rho (c^s)^2 c^l T$$

$$\hat{\lambda} = \lambda \tag{16}$$

where h denotes the partial specific enthalpy. Equations (15) and (16) correspond to the conditions $\nabla c^s = 0$ and $\mathbf{J}^s = \mathbf{J}^l = 0$, respectively. Thus for a measurement when the mass fluxes are zero, the effective thermal conductivity (λ) is always less than the intrinsic thermal conductivity (κ). At the beginning of the experiment when there are no concentration gradients, the effective thermal conductivity (ζ), as expected, is equal to that of the intrinsic value. A steady-state experiment corresponds to $\mathbf{J}^s = \mathbf{J}^l = 0$ while a transient hot wire measurement is closer to the condition $\nabla c^s = 0$. Equations (15) and (16) show the effect of diffusion on the thermal conductivity of a nanofluid, assuming that there are only two gradients, namely, temperature and concentration. The formalism can be extended to include other fields such as pressure gradient and external fields as long as the assumed linearity given in Eq. (2) is satisfied. In Sec. 3, we will give an estimate of the effective thermal conductivities with simple diffusion and with chemical reactions (since nanosized particles are known to be highly reactive).

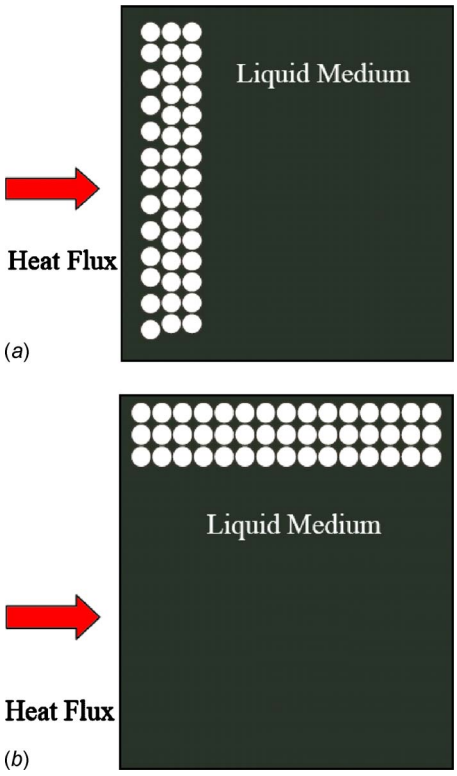

Fig. 1 A two-dimensional representation of (*a*) a series mode and (*b*) a parallel mode of thermal conduction in a binary nanofluid. Note that a typical nanofluid system is not inhomogeneous, as shown.

3 Postulated Mechanisms for Nanofluid Thermal Conduction

3.1 Classical Theories. The simplest and perhaps the most intuitive models correspond to the series and parallel modes of thermal conduction. In the former, the conducting paths, namely, those through the base fluid and the nanoparticles, are assumed to be in series, and in the latter, they are regarded to be in parallel (see Fig. 1). The effective thermal conductivities are given by [88,89]

$$\frac{1}{\kappa^{=}} = \frac{(1-\phi)}{\kappa_f} + \frac{\phi}{\kappa_p} \tag{17}$$

$$\kappa^{\parallel} = (1-\phi)\kappa_f + \phi \kappa_p \tag{18}$$

where $\kappa^{=}$ and $\kappa^{\parallel}$ are the series and parallel mode thermal conductivities, respectively.

In the dilute limit, as shown below, $\kappa^{=}/\kappa_f$ is a function of the volume fraction alone, while $\kappa^{\parallel}/\kappa_f$ is a function of the constituent thermal conductivities and volume fraction

$$\left(\frac{\kappa^{=}}{\kappa_f}\right)_{\phi \to 0} = 1 + \phi \tag{19}$$

$$\left(\frac{\kappa^{\parallel}}{\kappa_f}\right)_{\phi \to 0} = 1 + \phi \frac{\kappa_p}{\kappa_f} \tag{20}$$

From Eq. (20) it is clear that the enhancement in the parallel mode can be much larger than that in the series mode if $\kappa_p \gg \kappa_f$. As can be inferred from electron microscopy experiments, neither series nor parallel configuration is strictly applicable to most nanofluids even though the intertwined fibers allow nanotube suspensions to be approximated by the parallel mode. Since the parallel mode corresponds to a geometric configuration that allows the most ef-

ficient way of heat propagation, it represents the absolute upper limit for the effective thermal conductivity regardless of the phase of the constituents. For example, the experiments by Griesinger et al. have shown [90] an increase of 5000% in the thermal diffusivity of low density polyethylene when the polymer fiber fillers were configured *parallel* to the direction of the heat flow. Not surprisingly, numerous experiments have shown that the upper bound is rarely, if not ever, violated in binary solid composites or liquid mixtures.

The series and parallel bounds are not the narrowest that can be estimated with the classical approach. An analysis of the Maxwell's original work reveals that the theory predicts two bounds—*an upper and a lower bound*—also derived by Hashin and Shtrikman [48] using variational principles. In the first configuration, the nanoparticles constitute the dispersed phase with the fluid medium acting as the continuous phase. In the second configuration, the nanoparticles form the continuous phase with the base fluid constituting the dispersed phase. In both configurations, the effective thermal conductivity is maximally biased toward the continuous phase. The Maxwell (H-S) bounds for nanofluid thermal conductivity are given by [48,91]

$$\kappa_f\left(1+\frac{3\phi(\kappa_p-\kappa_f)}{3\kappa_f+(1+\phi)(\kappa_p-\kappa_f)}\right)\leq\kappa\leq\kappa_p\left(1-\frac{3(1-\phi)(\kappa_p-\kappa_f)}{3\kappa_p-\phi(\kappa_p-\kappa_f)}\right) \tag{21}$$

It is assumed that $\kappa_p>\kappa_f$ or otherwise, the upper and lower bounds would simply reverse. Notice that the lower Maxwell bound, which is identical to Eq. (1), is rigorously exact to the first order in the volume fraction. For a homogeneous system, the Maxwell theory predicts the above set of bounds, which is most restrictive on the basis of the volume fraction alone [48]. Any improvement on these bounds would require additional knowledge on the statistical variations in the dispersed medium. In addition to thermal conductivity, the above bounds are also applicable to other composite properties such as thermal diffusivity, electrical conductivity, and magnetic permeability.

While the lower bound has been extensively quoted in the nanofluid literature, the upper bound has not received much attention. For the lower Maxwell bound the nanoparticles are always well-dispersed, and therefore, the effective conductivity is biased toward the conduction paths through the surrounding fluid (see Fig. 2(*a*)). Theoretically, the upper bound should correspond to a configuration where continuous conduction paths emerge along the nanoparticles. It is straightforward to visualize this configuration for high volume fractions of nanoparticles, but for dilute nanofluids, the nanoparticles have to form a linear or chainlike configuration, separating large, noninteracting regions of base fluid. The correspondence between the mathematical idealization and physical realization is shown in Fig. 3.

If the nanoparticle thermal conductivity is higher than that of the base fluid, the effective thermal conductivity can be significantly enhanced by a chainlike or fractal configuration. All experimentally tested nanofluids have some form of aggregation, and thus, most of the enhancements beyond the Maxwell lower bound come from *limited* percolating effects (which can also manifest as nonspherical composite particles [46]). It is now easy to visualize that large nanoparticle clumps will *not* provide additional thermal conduction paths. Thus it is important to differentiate the difference between arbitrary coalescence (that occurs, for example, from settling of nanoparticles following ultrasonification), and stable, chainlike, percolating nanoparticle configurations.

With the two described configurations, it is easy to note that the lower Maxwell bound ($\kappa^{\mathrm{MX-}}$) lies closer to the series mode of conduction, while the upper bound ($\kappa^{\mathrm{MX+}}$) approaches the parallel mode. Also note that the variational formulation of Hashin and Shtrikman on Maxwell bounds does not place any restrictions on the volume fraction. If the configuration is neutral, i.e., neither favoring the series nor the parallel mode, then the effective thermal conductivity (κ^0) would lie between the lower and upper Maxwell bounds. This approach, attributed to Bruggeman and also sometimes known as the effective medium theory (EMT) [89], predicts the thermal conductivity in the implicit form given by

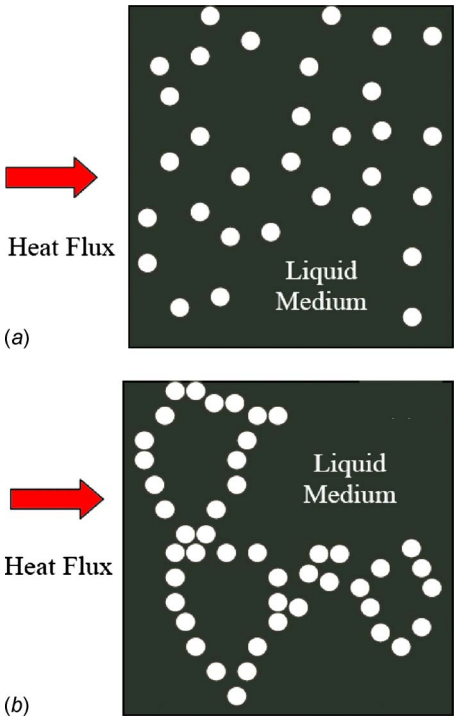

Fig. 2 A two-dimensional representation of the nanofluid configuration for the (*a*) lower and (*b*) upper Maxwell bounds

$$(1-\phi)\left(\frac{\kappa_f-\kappa}{\kappa_f+2\kappa}\right)+\phi\left(\frac{\kappa_p-\kappa}{\kappa_p+2\kappa}\right)=0 \tag{22}$$

In a nanofluid, the unbiased configuration would be a mix of well-dispersed nanoparticles and linear aggregation. All the classical models thus correspond to different configurations of the dispersed and continuous media. It can be shown for $\kappa_p>\kappa_f$

$$\kappa^{=}<\kappa^{\mathrm{MX-}}<\kappa^{0}<\kappa^{\mathrm{MX+}}<\kappa^{\parallel} \tag{23}$$

In the dilute limit with $\kappa_p>\kappa_f$, the lower Maxwell bound reduces to the well-known expression

$$\left(\frac{\kappa^{\mathrm{MX-}}}{\kappa_f}\right)_{\substack{\phi\to 0\\ \kappa_p\gg\kappa_f}}=1+3\phi \tag{24}$$

The recent model of Prasher et al. [78] assumes a linear chainlike cluster configuration for the nanoparticles, which is very similar to that for the upper Maxwell bound. The dilute limits are given by

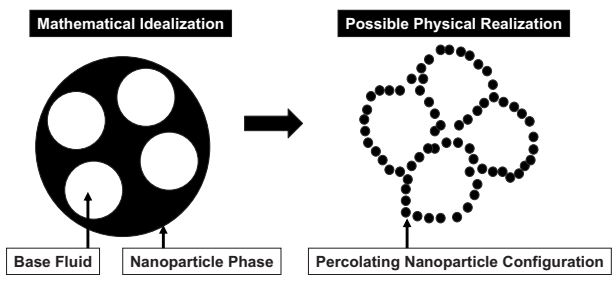

Fig. 3 Mathematical abstraction and physical realization for the Maxwell upper bound for dilute nanofluids

$$\left(\frac{\kappa^{\mathrm{MX+}}}{\kappa_f}\right)_{\phi\kappa_p/\kappa_f\to 0} = 1 + \frac{2\phi}{3}\left(\frac{\kappa_p}{\kappa_f}\right) \tag{25}$$

$$\left(\frac{\kappa^{\mathrm{Pr}}}{\kappa_f}\right)_{\phi\kappa_p/\kappa_f\to 0} = 1 + \frac{\phi}{3}\left(\frac{\kappa_p}{\kappa_f}\right) \tag{26}$$

where κ^{Pr} is the thermal conductivity predicted by the model of Prasher et al. [78]. The above limits and the parallel mode dilute limit [Eq. (20)] are identical except for the prefactor. It is thus evident that *linear*, *percolating* clustering effects can dramatically broaden the thermal conductivity range for the classical thermal conduction models. Interfacial thermal resistance has not been taken into account in any of these models yet, and if applicable, it is easily incorporated [49]. The interfacial resistance *always* reduces the effective thermal conductivity, and hence, the bounds presented here are the *highest* for the appropriate configurations [92].

In this paper, we will systematically explore the four classical bounds—series, lower and upper Maxwell, and parallel—for the reported data on nanofluids and make a critical comparison with those observed in solid-solid composites and liquid mixtures. Analogous behavior will imply classical conduction mechanisms in all three binary systems, while persistent or conspicuous violations of the upper Maxwell or parallel bounds will give credence to the anomalous thermal conduction behavior in nanofluids.

3.2 Interfacial Layer Models. The interfacial layer models can be considered under the classical models with the structure provided not by the clustering of nanoparticles but through an ordered fluid configuration around the nanoparticles [70–75]. As such, the predictions of interfacial layer models are enveloped by the classical bounds discussed before. Interestingly, the interfacial layer models are far more popular than those assuming nanoparticle clustering (even though experiments suggest otherwise) and thus, are treated as a separate mechanism in this paper.

We will analyze the current state of knowledge to make a reasonable assessment on the role of interfacial layers in nanofluids. The motivation for proposing this model stems from both theoretical and experiment evidences of ordered layering near a solid surface. For example, molecular dynamics simulations predict three ordered layers of water on the Pt (111) surface [93]. In the first layer, water molecules form icelike structures with the oxygen atoms bound to the Pt surface, while in the second and the third layers, water molecules that are hydrogen-bonded to the first and second layers, respectively, are observed. This ordering, even with a strong perturbation induced on the surface, persists over a distance of $O(1\ \mathrm{nm})$ from the Pt surface. Very similar behavior has been experimentally reported on a crystal-water interface [94]. Close to the interface, two layers of icelike structures strongly bonded to the crystal surface have been observed, followed by two diffuse layers with less pronounced lateral and perpendicular ordering. Direct experimental evidences are also available for thin layering with liquid squalane [95] and nonpolar liquids [96] adjacent to a solid surface.

In a recent molecular dynamics (MD) simulation it has been shown that atomic-sized clusters of the order of 10 atoms, which interact strongly with the host fluid, produce an amorphouslike fluid structure [97] near the cluster. This interfacial structure, which has a dimension of $O(1\ \mathrm{nm})$, provides a network of percolating conduction paths through the liquid medium [97]. The effective thermal conductivity is much higher than that of the lower Maxwell bound (50% enhancement for a volume fraction of 5%, approximately) but is enveloped by the upper Maxwell bound. However, when the clusters grow in size to hundreds of atoms, the percolation of interfacial structures gets impeded dramatically and the relatively large enhancements reduce to more modest values consistent with the lower Maxwell bound. These results are in agreement with an earlier molecular dynamics (MD) study [98], which showed no discernible increase in the interface thermal conductivity even while observing four ordered fluid layers near a surface. Similar results are also reported for water, which showed no dependence of the molecular orientation on the thermal conductivity [99].

A theoretical estimate for the interface thickness around a nanoparticle can be made from the Yan model [83], which is given by

$$h = \frac{1}{\sqrt{3}}\left(\frac{4M_f}{\rho_f N_a}\right)^{1/3} \tag{27}$$

where M_f and ρ_f are the molecular weight and density of the surrounding fluid medium around a nanocluster, respectively, and N_a is the Avogadro's number. For water-based nanofluids the Yan model gives an interfacial thickness of 0.284 nm, which is smaller than what is observed in the experiments or MD simulations, but agreeing on the order of magnitude.

Almost all the interfacial layer models, which have been proposed in the past, share the idea of a complex nanoparticle made of a bare nanoparticle and a postulated interfacial fluid nanolayer with an arbitrary thickness and thermal conductivity. Most models focus on nanoparticles that are of the order of 10 nm in size or smaller, and assume an interface thickness from 2 nm to 5 nm to provide evidence for a nanolayer-influenced thermal conduction mechanism. However, such assumptions are at variance with the theoretical and experimental evidences [94–96,100], which indicate that the interfacial layers are limited to a few molecular dimensions.

It is easy to show that an $O(1)$ nm layering is of no consequence to nanofluids that have been experimentally tested as the nanoparticle diameters (d) are mostly of the order of 10 nm and above [101]. Since the volume fraction scales as d^3, a 1 nm interfacial thickness for a 10 nm nanoparticle would correspond to a relative volume change of 10^{-3}, which is too small to account for any effect on the effective thermal conductivity. The experiments by Putnam et al. [20] show no unexpected increase in thermal conductivity for well-dispersed gold particles that are as small as 4 nm. These results are consistent with our experiments on dilute gold and platinum colloids (unpublished) and provide tangible evidence to the absence of ordered liquid structures that influence the thermal conductivity in nanofluids.

3.3 Brownian and Micro-convection Models. The recent Brownian and microconvection models attempt to rationalize the thermal conductivity enhancements as well as the temperature and size dependencies by postulating a diffusion dependent thermal conductivity, albeit, different from that given by Eqs. (15) and (16). The Brownian models [61,84] assume that that the nanofluid thermal conductivity is directly dependent on the self diffusion coefficient of the nanoparticle, which is given by the well-known Stokes–Einstein relationship $D = k_B T/(3\pi\mu d_p)$, where μ is the dynamic viscosity, d_p is the nanoparticle diameter, T is the absolute temperature, and k_B stands for the Boltzmann constant. While experimental trends for temperature and nanoparticle size are captured, this approach is criticized for several theoretical reasons, especially for the large mean free path of the liquid molecules with a magnitude of $O(1)$ cm [102,103]. In a Brownian dynamics (BD) simulation [62], the effect of diffusion is quantitatively estimated without resorting to explicit modeling. Many reported BD simulations, however, do not satisfy the momentum or energy conservation principles and hence, are incapable of predicting the thermal conductivity of colloidal systems. In classical BD simulations, the only quantity that is conserved is mass, and hence, the sole transport property that can be computed is the diffusion coefficient. When both momentum and energy conservation laws are enforced (in addition to mass conservation), BD (or dissipative particle dynamics) simulations have shown no tangible effect of Brownian motion on nanofluid thermal conductivity [104].

As discussed in Sec. 2, diffusion can enhance the thermal conductivity due to Soret effect and also through chemical reactions that can occur between the nanoparticles and the base fluid. In the

simple diffusion case, the enhancement in the thermal conductivity due to diffusion is $|\Delta\kappa| = D_T[(h^s - h^l)]\rho c^s c^l$ [87]. Typical values for nanofluid Soret coefficients are less than 0.1 K^{-1} [20,105,106]. This gives an upper bound on the thermal diffusion coefficient D_T of $O(10^{-10})$ $m^2\ s^{-1}\ K^{-1}$ with a diffusion coefficient D^{sl} of $O(10^{-11})$ m^2/s that corresponds to 10 nm sized nanoparticles. Note that the mutual and the self-diffusion coefficients are nearly the same for small volume fractions. Since the difference in the specific enthalpy (h) between the nanoparticles and the base fluid is typically of the order of 10^4 J/kg, it is relatively easy to see that the excess thermal conductivity $\Delta\kappa$ is several orders less than that of the base fluid. This conclusion is in agreement with several published reports [24,43,107,108].

At nanoscales, the nanoparticles can be exothermally reactive and diffusion accompanied by chemical reactions can also enhance the thermal conductivity [87]. If chemical equilibrium is reached quickly, the effective thermal conductivity can increase by [87]

$$\Delta\kappa = \frac{\rho_f D^{sl}(\Delta\hat{h})^2}{T\left(\frac{\partial\mu^s}{\partial c^s}\right)} \tag{28}$$

where $\Delta\hat{h}$ is the reaction heat (at constant temperature and pressure), which is of the order of the gradient in the chemical potential for the nanoparticles [87]. With a $\Delta\hat{h} = O(10^5)$ J/kg for reaction rates for nanoparticles in solutions (for example, the adsorption energy of water at the alumina surface is ~ 140 kJ/mol [109]), $\Delta\kappa$ is again several orders less than that of the base fluid. Thus, there are sufficient theoretical reasons to believe that the diffusional motion of the nanoparticles does not *directly* influence the nanofluid thermal conductivity. Since thermodiffusion, mutual diffusion, and Brownian self-diffusion of the nanoparticles govern the aggregation processes, they will *indirectly* influence the transport properties of nanofluid systems [1,110–113]. Thus mechanisms of slow diffusional processes are extremely important to understand the effect of clustering on the nanofluid thermal conductivity [43,78,85,86].

In a related, but more intriguing hypothesis, the thermal conductivity is regarded to increase from convective transport of large volume of base fluid, which is dragged by diffusing nanoparticles [63–69]. In this "microconvection" picture, it is hypothesized that convection currents set up by the Brownian motion of the nanoparticles can enhance the heat transfer between the nanoparticles and the base fluid, and hence, the nanofluid thermal conductivity. In this paper, we will focus on two microconvection models that have received recognition in recent years. In the model of Jang and Choi [64,65], a new, but somewhat heuristic, heat transfer correlation is introduced to account for the randomly moving nanoparticles. It is given by

$$\mathrm{Nu} \equiv \frac{hd}{\kappa_f} = O(\mathrm{Re}^2\ \mathrm{Pr}^2) \tag{29}$$

The effective thermal conductivity can then be written as [65]

$$\frac{\kappa}{\kappa_f} = (1-\phi) + \frac{1}{(1+\hat{\alpha})}\left(\frac{\kappa_p}{\kappa_f}\right)\phi + C\left(\frac{d_f}{d_p}\right)\mathrm{Re}_d^2\ \mathrm{Pr}\phi \tag{30}$$

where $\hat{\alpha} \equiv R_b\kappa_p/d$ stands for a nondimensional interfacial thermal resistance, and Re_d and Pr denote the Reynolds number for the nanoparticle and the Prandlt number for the base fluid, respectively. With negligible microconvection and interfacial thermal resistance, the model of Jang and Choi coincides with the parallel mode of thermal conduction. A strong microconvection effect will, however, result in a thermal conductivity much higher than that of the parallel mode.

In the model of Prasher et al. [66,67], the traditional heat transfer correlation of flow over a sphere is adopted. Assuming that the Nusselt number on the scale of particle radius is $O(1)$, the Brownian motion of a single nanoparticle is regarded to increase the effective thermal conductivity of the base fluid by a factor of $[1 + (1/4)\mathrm{Re}\ \mathrm{Pr}]$, A chief argument for microconvection hypotheses of Prasher et al. (and Jang and Choi) comes from the presumed presence of interfacial thermal resistance for the nanoparticles. Indeed, for nanosized filler particles in a solid composite, the effect of interfacial resistance can be very pronounced. Thus to account for the interfacial thermal resistance and the mixing of convection currents from multiple nanoparticles, the thermal conductivity of the nanofluid is fitted to experimental data using the expression [66]

$$\frac{\kappa}{\kappa_f} = (1 + A\ \mathrm{Re}^{\gamma}\ \mathrm{Pr}^{0.333}\ \phi)\left(\frac{1+2\beta\phi}{1-\beta\phi}\right) \tag{31}$$

where γ is a system-specific exponent, which, for aqueous suspensions, is found to have an optimal value of 2.5, and A is a constant attaining values as large as 4×10^4. For negligible microconvection effects and interfacial thermal resistance, the model of Prasher et al. reduces to the Maxwell expression for well-dispersed nanoparticles (lower bound).

We will now examine the characteristics of the microconvection models in more details. The hypothesized microconvection effects appear through $\mathrm{Re}_d = Vd/\nu$, where V and ν are the convection velocity and the base fluid kinematic viscosity, respectively. In both the microconvection models, the convection velocities are represented by a "Brownian velocity" to account for the rapidly oscillating nature of nanoparticle motion. In the Jang and Choi model, V is given by [64]

$$V = \frac{D^{ss}}{l_f} = \frac{k_B T}{3\pi\mu d_p l_f} \tag{32}$$

where l_f is the mean-free path of a base fluid molecule and D^{ss} is the self-diffusion coefficient of the nanoparticle. As noted by the authors, it is not clear whether the above ratio actually represents a random velocity of the nanoparticle. In the model of Prasher et al. (as also in Ref. [63]), the conventional thermal velocity of the nanoparticle is taken as the convection velocity, which is given by [66]

$$V = \sqrt{\frac{3k_B T}{m}} = \sqrt{\frac{18k_B T}{\pi\rho {d_p}^3}} \tag{33}$$

where m and ρ are the mass and density of the nanoparticle, respectively. Interestingly, a different form is adopted in the Patel microconvection model [69], which is given by

$$V = \frac{2k_B T}{\pi\mu {d_p}^2} \tag{34}$$

The latitude in choosing several forms, and therefore, differing physical characteristics, stems from the nonrigorous concept of a Brownian velocity. In the formal theory of Langevin dynamics, a fluctuating thermal velocity is uniquely defined, while velocities constructed based on diffusion characteristics are not.

Two peculiar consequences of Eq. (33) are that, for a given base fluid, temperature, and nanoparticle size, the enhancement in the thermal conductivity increases with decreasing nanoparticle density ρ, and for nanoparticles with low density, the thermal conductivity can be largely positive even if $\kappa_p < \kappa_f$. In our recent work [91], we had explicitly tested this prediction with the transient hot-wire (THW) technique on nanofluids with silica and MFA (a copolymer of tetrafluoroethylene and perfluoro-methylvinylether) nanoparticles that are lighter than the commonly tested alumina and copper oxide nanoparticles. We will report the main results briefly. Equation (1) predicts κ_p/κ_f to be a universal function of $\beta\phi$ while the microconvection model does not. In Fig. 4, we plot two sets of data for Ludox and MFA as a function of $\beta\phi$ along with the reported experimental data in the literature for alumina and copper oxide, which have higher densities, as previously men-

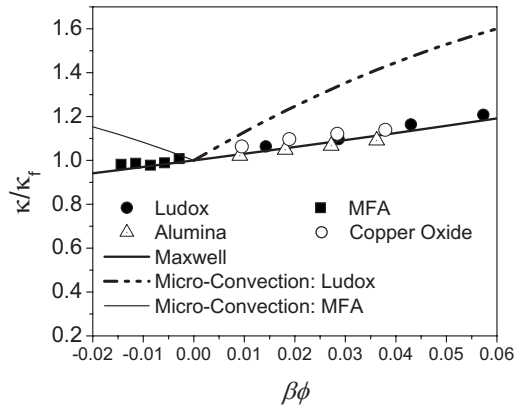

Fig. 4 THW data for Ludox ($\rho\sim2200$ kg/m^3, $d=32$ nm), MFA ($\rho\sim2140$ kg/m^3, $d=44$ nm), Al_2O_3 ($\rho\sim4000$ kg/m^3, $d=38$ nm), and CuO ($\rho\sim6300$ kg/m^3, $d=29$ nm) suspensions, plotted as a function of $\beta\phi$. The deviation of microconvection model from the Maxwell lower bound for Al_2O_3 and CuO are comparable to the experimental uncertainty.

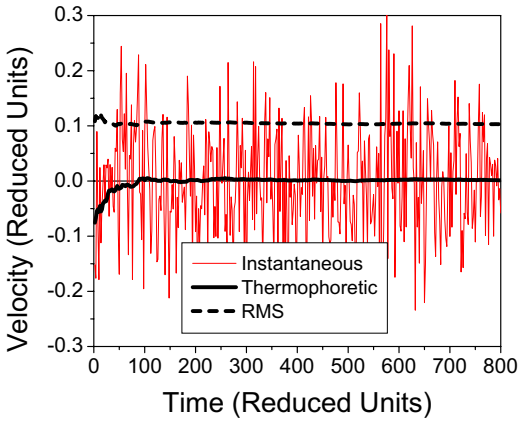

Fig. 5 Typical instantaneous and thermophoretic drift velocities in the *z*-direction of a 100 atom solid nanoparticle in a generic LJ fluid with NEMD simulations [97]. The rms velocity of the nanoparticle (0.1) is very close to $V=\sqrt{k_BT/m}$.

tioned. Quite remarkably, all the experimental data collapse on to a single line predicted by the Maxwell theory for noninteracting spheres (lower bound) without any interfacial thermal resistance and regardless of the nanoparticle density (or size). However, assuming microconvection contributions lead to system-dependent predictions, which are strongly conflicting with the experiments.

We have attributed the overprediction of the microconvection model from ascribing the nanoparticle thermal velocities as the convection velocities in place of the significantly lower thermophoretic drift velocities [91]. As explained in Sec. 2, an introduction of a thermal gradient, nonequilibrium coupling between mass and heat transport takes place due to the Soret effect. Thus, a colloidal particle acquires a thermophoretic drift velocity given by $u_T=D_T\nabla T$ [106]. For nanoparticles, which are sufficiently larger than the molecular dimensions, the small Knudsen number makes the no-slip interface conditions a reasonable approximation [114]. Thus in typical thermal conduction experiments, the microconvection velocities can only be of the order of the thermophoretic velocities.

Compared with the magnitude of the strongly fluctuating thermal speed, the thermophoretic velocities are insignificant in a nanofluid as they are characteristic of the collective motion of fluid motion around several diffusing nanoparticles. Our optical thermal lensing measurements have yielded a value of $D_T\sim10^{-12}$ m^2 s^{-1} K^{-1} for both Ludox and MFA colloids, which with typical THW temperature gradients correspond to thermophoretic velocities as low as 1 nm/s, while the assumed convection velocities in the models of Prasher et al. and Jang and Choi are $O(1)$ m/s and $O(0.1)$ m/s, respectively. Theoretical estimates of the colloidal drift speeds are also in the range of $O(10^{-8})$ m/s [105], which is consistent with our experimental values. To show that the thermophoretic velocities are insignificant even for very small nanoparticles, we have performed nonequilibrium molecular dynamics (NEMD) simulations on a model system. The details of the simulation method are given in Ref. [97]. Figure 5 shows the relative magnitudes of the typical instantaneous nanoparticle velocity and the corresponding thermophoretic drift velocity. At steady state the magnitude of the thermophoretic drift velocity is two orders smaller than that of the root-mean-square (rms) value.

The fact that the particle thermal velocity is not the relevant velocity scale for heat transport is seen from a simple argument. One should indeed compare the distance a particle moves within a Brownian relaxation time $\tau=m/f$, where f is the particle friction coefficient corresponding to the typical spatial scales of the macroscopic thermal gradients. For particles in the few tens of the nanometer size range, $\tau\sim O(10^{-10})$ s—a time scale which corresponds to a particle displacement of a few thousands of its diameter. The relaxation time τ, which also sets the time decay of correlations between the particle momentum and energy density flux in the liquid [115], is negligible on the time scales probed by THW measurements. The difference of several orders of magnitude in the convection velocities thus precludes a significant contribution to the thermal conductivity from *any* conceivable microconvection mechanism.

4 Classical Bounds

In Sec. 3, we have provided experimental and theoretical evidences to show that the interfacial layers, Brownian motion and microconvection do not influence the thermal conductivity of the commonly tested nanofluids. In this section, we show that the classical theories are capable of explaining the rather large thermal conductivity enhancements reported so far. In addition, we also show that nanofluid thermal conduction behavior is strikingly similar to that observed in solid-composites and liquid mixtures by examining the theoretical bounds discussed in Sec. 3. However, we find that the interfacial thermal resistance, which is inferred from a large body of experimental data, is negligible for most nanofluids, but can become significant for solid-composites.

4.1 Classical Bounds for Solid Composites. We will start by discussing the classical bounds for solid-composites. As discussed before the upper and lower Maxwell bounds (H-S) are the narrowest bounds that can be constructed on the basis of volume fraction alone. The Maxwell bounds, in turn, are enveloped by those from the series and parallel mode of conduction. The spread of the bounds depend on the relative thermal conductivities of the media. Most experiments with binary solid composites have a large difference in the thermal conductivities, and thus a relatively large spread ranging several orders can be expected.

In Fig. 6, we have delineated the thermal conductivity enhancements for a large number of solid composite materials. The classical bounds are calculated based on the thermal conductivity data given in the Appendix. At larger volume fractions ($\phi>10\%$), the experimental data largely lie between the lower and upper Maxwell bounds. At lower volume fractions ($\phi\leq10\%$), the thermal conductivity falls below the lower Maxwell bound for a few composites, and for polyethylene–Cu, polyethylene–Zn, and ZnS–diamond, it becomes lower than the series mode prediction. Additionally, as the size increases, the thermal conductivity increases significantly (polypropylene–Al, polyvinylidene–AlN, and ZnS–diamond). All these observations can be reconciled within the

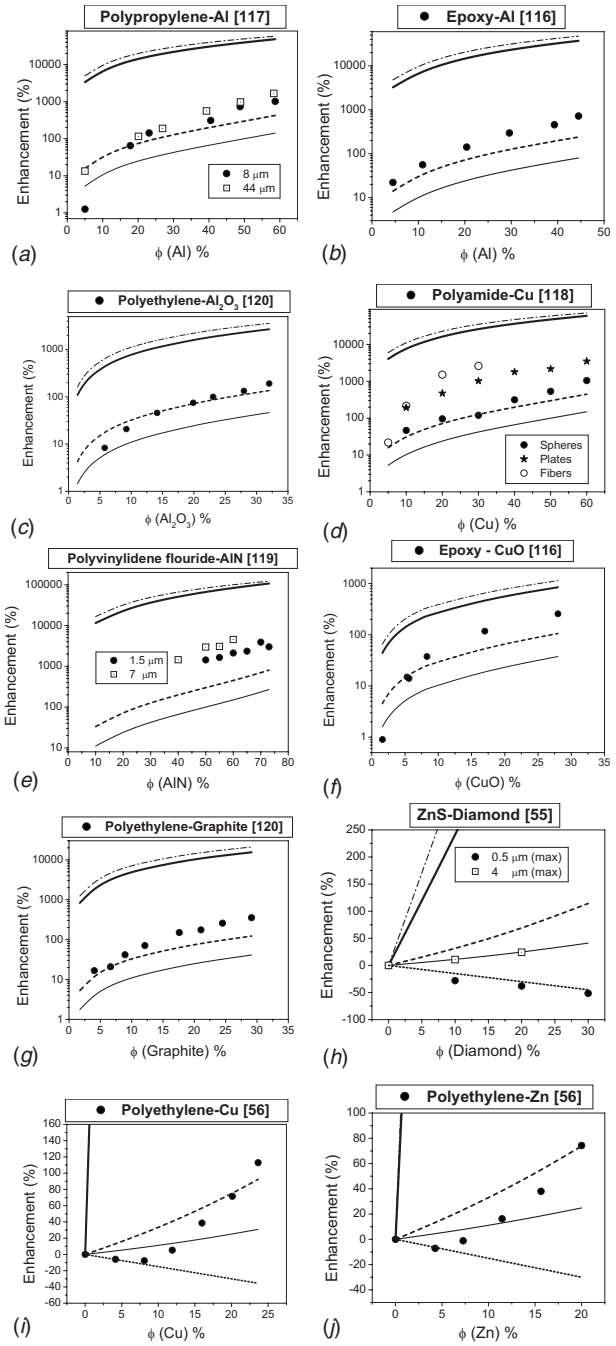

Fig. 6 Classical bounds for thermal conductivity in solid composites. The thin solid and thin dashed-dotted lines denote enhancements in thermal conductivity (or diffusivity) with the series and parallel modes, respectively. The upper Maxwell bound is delineated by the thick solid line while the lower Maxwell bound is given by the thick dashed line. The experimental data are represented by symbols. A fifth bound given by $(1-3\phi/2)$ for polyethylene–Cu, polyethylene–Zn, and ZnS–diamond (dotted line) denotes the limiting condition $\alpha\to\infty$. Table 1 in the Appendix gives the numerical values used in the calculation of classical bounds. Experimental data are taken from [55], [56], and [116–120].

framework of classical theories. The nondimensional interfacial resistance parameter $\alpha \equiv 2R_b\kappa_f/d$ determines the temperature discontinuity at the filler particle (p)-base medium (m) interface. In the limit $\kappa_p \gg \kappa_m$, the Maxwell lower bound can be expressed as

$$\frac{\kappa}{\kappa_m} = \frac{(1+2\alpha)+2\phi(1-\alpha)}{(1+2\alpha)-\phi(1-\alpha)} \tag{35}$$

Since α increases for decreasing filler particle size the effective thermal conductivity also decreases, which is consistent with the experimental data on polypropylene–Al, ZnS–diamond, and polyvinylidene fluoride–AlN. In the limit of $\alpha\to\infty$, κ/κ_m reduces to $(1-3\phi/2)$. Thus, the effective thermal conductivity can become smaller than that of the base medium for all volume fractions, as attested by the data for ZnS–diamond with 0.5 μm particles. Furthermore, the data for polyethylene–Cu and polyethylene–Zn are also bounded by $(1-3\phi/2)$.

Well-dispersed large spheres largely follow the lower Maxwell limit except at higher volume fractions. As the volume fraction increases the filler particles tend to form chainlike configurations, which promote a better heat transfer, and hence, the thermal conductivity. This formation of interconnected or percolating filler particles explains the rapid nonlinear increases in the thermal conductivity at higher volume fractions (see polyethylene–Cu and polyethylene–Zn in linear scale). The filler materials in the form of fibers, as observed with polyamide–Cu, are also very efficient for heat transfer. In a more dramatic observation, polyethylene polymer, a material having a low κ of 1 W/m K, increases its thermal conductivity to 50 W/m K, close to that of steel, when the polymer chain orientation is made parallel to the heat flow [90]. We emphasize here that the upper Maxwell bound is never violated for any of the experimental data.

4.2 Classical Bounds for Liquid Mixtures. Unlike those in solid composites, the classical bounds in liquid mixtures are not well-recognized. In the Sutherland–Wassiljewa theory, the thermal conductivity of a liquid mixture is given by [121]

$$\kappa = \kappa_1\left(\frac{n_1}{n_1+A_{12}n_2}\right)+\kappa_2\left(\frac{n_2}{n_2+A_{21}n_1}\right) \tag{36}$$

where n denotes the mole fraction and 1 and 2 stand for the two components. The coefficient A, also known as the Wassiljewa coefficient, is given by the following semi-empirical form [122]:

$$A_{ij} = \frac{1}{4}\left[1+\left(\frac{\kappa_i}{\kappa_j}\right)^{1/2}\left(\frac{M_j}{M_i}\right)^{1/4}\right]^2\left[\frac{2M_j}{M_i+M_j}\right]^{1/2} \tag{37}$$

where M denotes the molecular weight. We can observe that for equimolar liquids and $A_{12}=A_{21}=1$, Eq. (36) is identical to that of the parallel mode of thermal conduction.

In Fig. 7 we show the four bounds for a few representative liquid mixtures along with the unbiased or Bruggeman effective medium estimate given by Eq. (22). Most the data are nestled between the upper and lower Maxwell bounds. Due to a smaller difference between the thermal conductivities of the two media, the bounds are relatively narrower. While liquids, in general, do not have identifiable structures, networked bonds such as in water can facilitate liquid molecules to form loosely formed dynamic structures with characteristics of both interconnected chains and isolated blocks of molecules. Such an arrangement will be consistent with that of the unbiased Bruggeman effective medium model. Indeed, we find that most of the data on liquid mixtures are best predicted by the Brugemman model.

4.3 Classical Bounds for Nanofluids. For both solid composites with negligible interfacial thermal resistance and liquid mixtures, Maxwell bounds are respected to a large degree. However, these bounds have not been tested so far for nanofluids.

The first test of the theoretical bounds is conducted by analyzing the test data of magnetic (Fe_3O_4) nanofluids [39,45] (or ferrofluids). Strong magnetic fields induce magnetic nanoparticles to form chainlike configurations, and when the magnetic field is applied parallel to the heat flux (or ∇T), a strong thermal conductivity enhancement is observed, as shown in Fig. 8. An increasing magnetic field correlates to an enhanced chainlike formation of

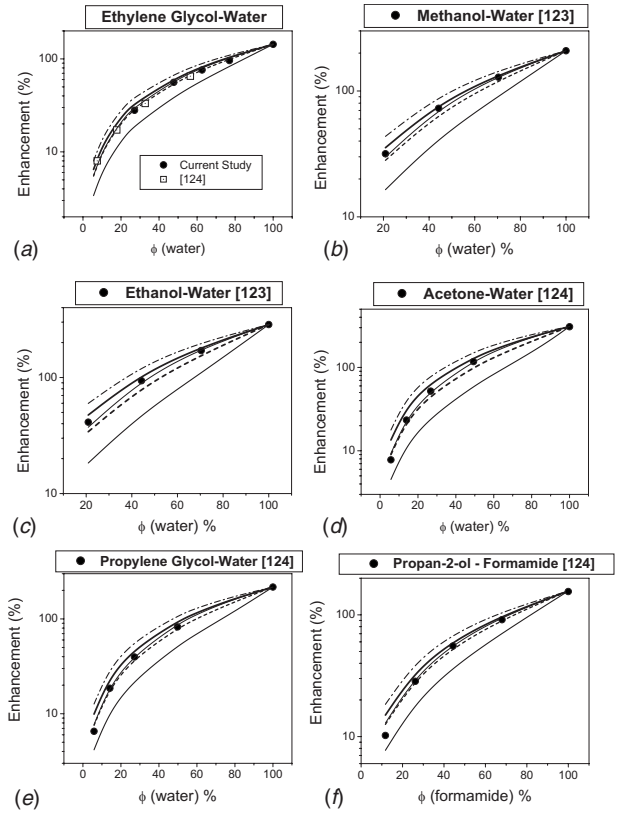

Fig. 7 Classical bounds for thermal conductivity in liquid mixtures. The line and symbol codes are the same as in Fig. 6 with the addition of a thin solid line between the Maxwell bounds, denoting the unbiased or Bruggeman model. Table 2 in the Appendix gives the numerical values used in the calculation of classical bounds. Experimental data are taken from [123], [124], and the current study.

the nanoparticles in the direction of the heat flux. This allows the nanofluid thermal conductivity to increase from the lower Maxwell bound to almost the parallel mode limit. Similar enhancements (of smaller proportions) are also observed for magnetic Fe-water nanofluids [125]. If, however, the magnetic field is applied *perpendicular* to the heat flux, the nanoparticles will stay

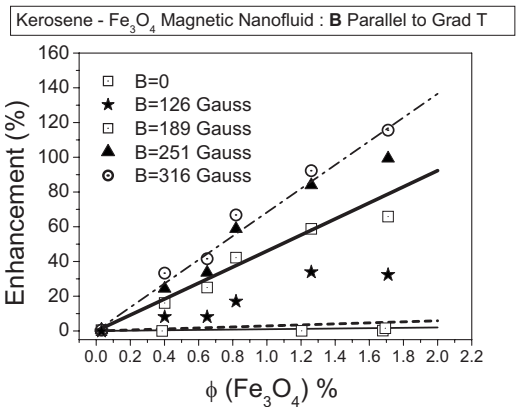

Fig. 8 Thermal conductivity of Kerosene–Fe_3O_4 magnetic nanofluid, as a function of the external magnetic field (B) in the direction of the heat flux (data from Ref. [45]). The configuration of the nanoparticles range from dispersed arrangement (at low B) to the chainlike formation in the direction of the heat flux (at high B). The line and symbol codes are the same as in Fig. 6. The classical bounds are calculated based on the data listed in Table 3 of the Appendix.

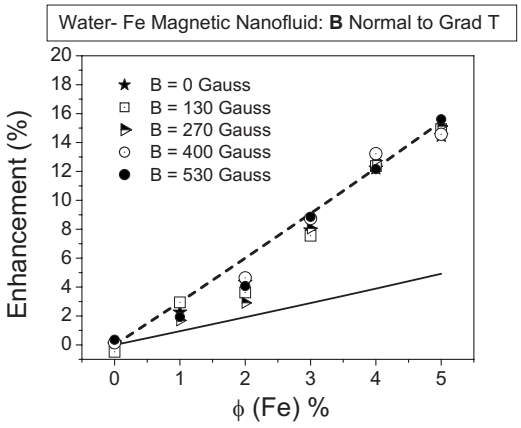

Fig. 9 Thermal conductivity of water–Fe magnetic nanofluid as a function of the external magnetic field (B) perpendicular to the direction of the heat flow (data from Ref. [125]). The nanoparticles are dispersed or form clusters perpendicular to the heat flux. The dashed and solid lines correspond to the lower Maxwell and series bounds, respectively. The classical bounds are calculated based on the data listed in Table 3 of the Appendix.

dispersed or clustered in a direction normal to the heat flux. In this case, the classical theory predicts that the enhancement will be bounded by the series mode limit and the *lower* Maxwell bound. Indeed, the experimental observation of Li et al. [125] conforms to this prediction, as shown in Fig. 9. The experiments performed with magnetic nanofluids (in magnetic fields) provide the most direct and unambiguous evidence for the effect of linear or fractal-like clustering on the nanofluid thermal conductivity.

Next, in Fig. 10, we delineate the classical bounds for a large set of nanofluids including those which have been described as unusual or anomalous. The data sets include oxide nanoparticles with relatively low κ (silica and zirconia), moderate κ (alumina and copper oxide), and high κ (copper, aluminum, and carbon nanotubes). They also include different base media including water (polar), ethylene glycol, and oil, and nanoparticles with a lower thermal conductivity relative to the base media (C-60/70 and MFA in water). Quite remarkably, all the data, except for a few sets, lie between the upper and lower Maxwell bounds, affirming the same mechanism for thermal conduction for nanofluids as that for solid composites and liquid mixtures, namely, through molecular or electronic interactions. By examining the main features of the nanofluid data, we can derive useful insights into the finer details of the conduction mechanism.

The most striking feature is that only a small set of nanofluid data falls significantly below the lower Maxwell bound even at very low volume fractions and with nanoparticle diameters that are in the tens of nanometers. This behavior is very unlike that in solid composites, where at low volume fractions and with nanometer sized filler particles, the effective thermal conductivity drop well below the series conduction bound. When the thermal conductivity of the dispersed media becomes closer to that of the base media, the Maxwell bounds becomes narrower, as can be noted with silica, zirconia, and Fe_3O_4. This also implies that uncertainties in nanoparticle thermal conductivity can cause discernible changes in the Maxwell bounds when $\kappa_p - \kappa_f$ is small. For most nanofluids, however, the difference is large. The lower Maxwell bound represents the maximum thermal conductivity that is possible with well-dispersed nanoparticles, and it can be inferred that the interfacial thermal resistance for most nanofluids is negligible (exceptions are noted, for example, in Ref. [24]). Even if the nanoparticle thermal conductivity is smaller than that of the bulk value (as observed in nanosized thin films [126]), all the experimental data, except for fullerenes (C-60/70) and to some extent,

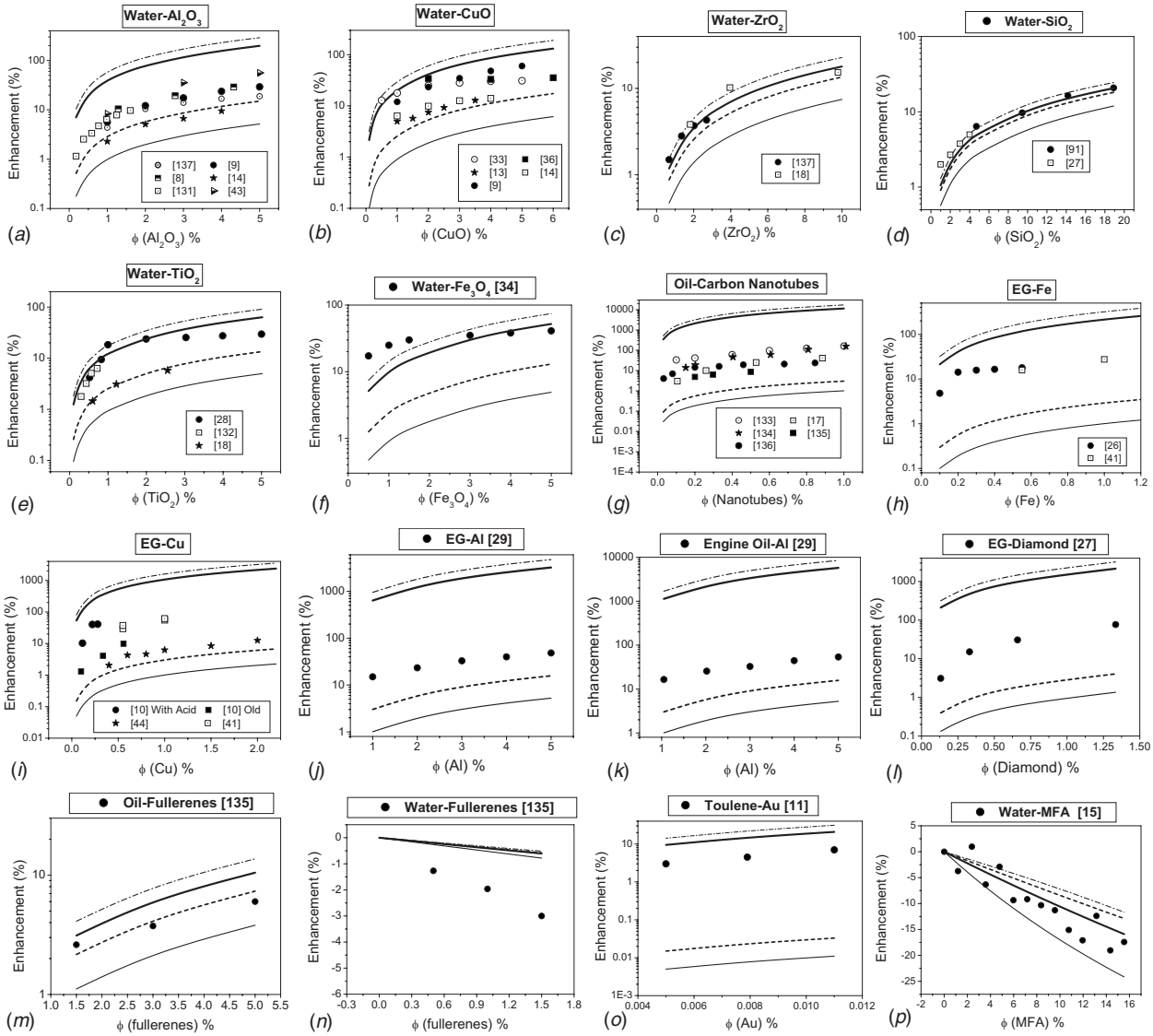

Fig. 10 The classical bounds for thermal conductivity/diffusivity in nanofluids. The line and symbol codes are the same as in Fig. 6. Since thermal conductivities of the dispersed media (nanoparticles) are generally not measured or reported, representative values listed in Table 3 of the Appendix are used to compute for the classical bounds. It is observed that $\kappa_p \gg \kappa_f$ for most nanofluids. The bounds shown are for a given temperature, while the experimental data shown may not correspond to the same temperature. This is largely of no consequence, given the rather small deviation in base fluid thermal conductivity in the range of experimentation. The assessment that most nanofluids respect the classical bounds, therefore, remains unchanged even after factoring in different experimental temperatures, and uncertainties in the experimental methods [46] and thermal conductivities. Experimental data are taken from [8–11], [13–15], [17], [18], [26–29], [33], [34], [36], [41], [43], [44], [91], and [131–137].

MFA, remain bounded by the lower Maxwell bound with $R_b = 0$.

The occurrence of an interfacial thermal (Kapitza) resistance at a liquid-solid interface has been experimentally evaluated by Ge et al. [127], who observed a bounding R_b of 0.67×10^{-8} $\mathrm{Km^2W^{-1}}$ and 2×10^{-8} $\mathrm{Km^2W^{-1}}$ for hydrophilic and hydrophobic interfaces, respectively. With nanofluids with carbon nanotubes, a large variation in R_b, ranging from a low 0.24×10^{-8} $\mathrm{Km^2W^{-1}}$ [128] to a high 8.3×10^{-8} $\mathrm{Km^2W^{-1}}$ [129,130] is also reported. The high values are comparable to those in a solid matrix, such as in diamond-silicon composite with a R_b of 27×10^{-8} $\mathrm{Km^2W^{-1}}$ [126]. The large span in the R_b data for carbon nanotube suspensions, and the near zero R_b for most other nanofluids indicate the role of solid-fluid interactions on the interfacial thermal resistance. Theoretical studies show that R_b attains relatively large values only when the liquid does not wet the solid surface. In our context, complete wetting may be a reasonable assumption for dispersions of hydrophylic colloids such as Ludox, and possibly for charged MFA colloids, where particle solvation is ensured by electrostatic forces. We also point out that terms such as "hydrophobic" and "hydrophilic" are rather subtle, and the macroscopic concepts such as the contact angle may be a bit misleading. The rate of energy transfer would be indeed weaker if the liquid does not wet the solid, since in this case the liquid density in the interfacial layer would be depleted. Yet, from a microscopic point of view, what one may need to consider is the free energy of insertion of the particle in the fluid. For a stable, nonaggregating colloidal dispersion, the latter is certainly negative (meaning, the particles are well-solvated). This means that even particles made of a hydrophobic material such as MFA can behave as hydrophilic. The reason for this apparent paradox is related to the presence of the charged double-layer, which leads to the formation of a solvation layer made of hydrated counterions, hindering solvent

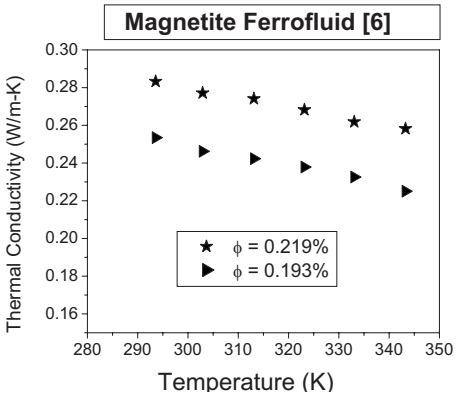

Fig. 11 Temperature dependence of magnetite nanofluid thermal conductivity [6]. While no strong correlation is generally observed to the thermal motion of the nanoparticles, there appears to be a dependence on the thermal conductivity variation of the base fluid. The base fluid (transformer oil) thermal conductivity decreases slightly with temperature for the range of temperatures shown [6].

depletion in the interfacial layer. This is partially evident by the very different behavior for fullerenes (C-60/70) suspensions in surfactant-stabilized water, and oil without the use of a surfactant. While for fullerenes in water, a small, but identifiable reduction in thermal conductivity below the Maxwell prediction is recorded, possibly due to the interactions of surfactant molecules with surrounding liquid, fullerenes in oil is consistent with Maxwell prediction with $R_b = 0$.

Several of the reported anomalous characteristics such as the lack of correlation to particle thermal conductivity and size effects can be resolved by weighing in the ability of nanoparticles into forming linear chainlike aggregates. Not all aggregates are equally efficient in increasing the thermal conductivity as experiments show that the larger clusters without the linear chain-forming configurations lead to a limiting behavior in the enhancement [52]. The temperature dependence is also not as striking as it was earlier believed with the recent experiments [137,138] showing a similar variation for both nanofluids and the base fluid. This implies that the mechanism for the increase in the thermal conductivity of water (for example, the temperature dependent slow modes [139]) is responsible for the thermal conductivity increase in the colloidal state as well. Conversely, it is reasonable to expect a *decrease* in the nanofluid thermal conductivity for a base fluid that has a negative change in thermal conductivity with increasing temperature. Early experiments on ferrofluids [6], indeed, have demonstrated this behavior, as shown in Fig. 11.

5 Concluding Remarks

The classical Maxwell theory has two limiting bounds that correspond to two geometrical nanoparticle configurations in the colloidal state. For the first bound, nanoparticles form the dispersed phase and the fluid medium acts as the continuous phase, while for the second the roles are reversed with the nanoparticles and the fluid medium constituting the continuous and dispersed phases, respectively. For the latter, the nanoparticles *must* form linear or fractal configurations, which separate the large regions of fluid pockets.

By analyzing a large body of data including those from our own experiments, we show that almost all the reported thermal conductivity data are enveloped by the upper and lower Maxwell bounds. For a homogeneous nanofluid system, these bounds set the limits for thermal conductivity enhancements. The thermal conductivity for the upper bound is maximally biased toward the thermal conductivity of the nanoparticles and *vice versa* for the lower bound. Experimental data on nanofluids, solid composites, and liquid mixtures indicate that the upper and lower Maxwell bounds are universally respected by most binary composites, regardless of the physical state and the thermal conductivity of the phases. The striking similarity of the nanofluid data to those of solid composites and liquid mixtures strongly indicate that the mechanism of nanofluid thermal conductivity is classical in nature, namely, through molecular and electronic interactions.

The earlier reports of anomalously high thermal conductivity can be traced back to an exclusive comparison of the test data to models, which are applicable only to well-dispersed nanoparticles. Once this constraint is relaxed, and a linear chain or fractal configuration is allowed for the nanoparticles, the classical models can predict a thermal conductivity range that easily accommodates almost all the experimental data. A key difference between the thermal conduction behavior in nanofluids and solid composites appears to be the interfacial thermal resistance. A large body of nanofluid experimental data suggests that the interfacial thermal resistance is negligible for most nanofluids.

On the basis of the experimental evidences provided in this paper, the key to having an enhanced thermal conductivity lies on the aggregation state and connectivity of the nanoparticles With the current experimental techniques such as neutron scattering, it is possible to characterize the aggregation state in the colloidal state. Once these geometrical details are available, a more precise comparison can be made between several samples (of the same constituents), which show appreciable differences in the thermal conductivity. While the science of making well-dispersed colloids has reached a fair amount of maturity, the techniques for developing targeted nanoparticle configurations are still in an evolving phase. It is expected that future studies can systematically address the configurational constraints necessary for enhanced thermal transport in nanofluids.

Acknowledgment

J.E. wishes to thank John Philip, Jacopo Buongiorno, Wesley Williams, Pawel Keblinski, and Ravi Prasher for their insightful discussions on nanofluids.

Appendix

Tables 1–3 show the thermal conductivity data for solid composites, liquid mixtures and nanofluids.

Table 1 Thermal conductivity data for solid composites

Material	κ (W/m -K)	Reference
Aluminum	237	[117]
Alumina	33.095	[120]
Graphite	209.2	[120]
Cupric oxide	9.21	[116]
Copper	384	[56,118]
Aluminum nitride	200	[140]
Diamond (polycrystal)	600	[55]
Zn	116	[56]
Polypropylene	0.239	[117]
Polyethylene	0.505/0.291	[56,120]
Epoxy	0.221	[116]
Polyamide	0.32	[118]
Polyvinylidene fluoride	0.12	[119]
Zinc sulphide	17.4	[55]

Table 2 Thermal conductivity data for liquid mixtures

Material	κ (W/m -K)	Reference
Water	0.61	25°C, [141]
Ethanol	0.161	32.6°C, [123]
Acetone	0.154	40°C, [124]
Methanol	0.198	28.1°C, [123]
Propylene glycol	0.199	40°C, [124]
Ethylene glycol	0.252	40°C, [124]
Propan-2-ol	0.137	40°C, [124]
Formamide	0.352	40°C, [124]

Table 3 Thermal conductivity data for nanofluids

Material	κ (W/m -K)	Reference
Water	0.61	25°C, [141]
Ethylene glycol (EG)	0.26	25°C, Measured value [142]
Oil	0.11–0.15	Representative range [133–135]
Al_2O_3	35	Representative value, [120,143]
CuO	20	Representative value, [144]
ZrO_2	2	Representative value, [145]
TiO_2	11.7	Representative value, [145]
SiO_2	1.4	Representative value, [91,135]
Fe_3O_4	9.7	[146,147]
Au	317	[143]
Ag	429	[143]
Al	237	[143]
Fe	80.2	[143]
Carbon nanotubes (CNT)	2000	Representative value, [134]
Diamond	600	Polycrystalline, [55]
Fullerenes (C_{60})	0.4	[148]
MFA	0.2	[91]

References

[1] Weitz, D. A., Huang, J. S., Lin, M. Y., and Sung, J., 1984, "Dynamics of Diffusion-Limited Kinetic Aggregation," Phys. Rev. Lett., **53**, pp. 1657–1660.

[2] Weitz, D. A., Huang, J. S., Lin, M. Y., and Sung, J., 1985, "Limits of the Fractal Dimension for Irreversible Kinetic Aggregation of Gold Colloids," Phys. Rev. Lett., **54**, pp. 1416–1419.

[3] Weitz, D. A., and Oliveria, M., 1984, "Fractal Structures Formed by Kinetic Aggregation of Aqueous Gold Colloids," Phys. Rev. Lett., **52**, pp. 1433–1436.

[4] Meakin, P., 1992, "Aggregation Kinetics," Phys. Scr., **46**, pp. 295–331.

[5] Fertman, V. E., 1987, "Thermal and Physical Properties of Magnetic Fluids," J. Eng. Phys. Thermophys., **53**, pp. 1097–1105.

[6] Fertman, V. E., Golovicher, L. E., and Matusevich, N. P., 1987, "Thermal Conductivity of Magnetite Magnetic Fluids," J. Magn. Magn. Mater., **65**, pp. 211–214.

[7] Popplewell, J., Al-Qenaie, A., Charles, S. W., Moskowitz, R., and Raj, K., 1982, "Thermal Conductivity Measurements on Ferrofluids," Colloid Polym. Sci., **260**, pp. 333–338.

[8] Masuda, H., Ebata, A., Teramae, K., and Hishinuma, N., 1993, "Alteration of Thermal Conductivity and Viscosity of Liquid by Dispersing Ultra-Fine Particles (Dispersion of γ-Al_2O_3, SiO_2, and TiO_2 Ultra-Fine Particles)," Netsu Bussei, **7**, pp. 227–233.

[9] Eastman, J. A., Choi, S. U. S., Li, S., Thompson, L. J., and Lee, S., 1997, "Enhanced Thermal Conductivity Through the Development of Nanofluids," Mater. Res. Soc. Symp. Proc., **457**, pp. 3–11.

[10] Eastman, J. A., Choi, S. U. S., Li, S., Yu, W., and Thompson, L. J., 2001, "Anomalously Increased Effective Thermal Conductivities of Ethylene Glycol-Based Nanofluids Containing Copper Nanoparticles," Appl. Phys. Lett., **78**, pp. 718–720.

[11] Patel, H. E., Das, S. K., Sundararajan, T., Nair, A. S., George, B., and Pradeep, T., 2003, "Thermal Conductivities of Naked and Monolayer Protected Metal Nanoparticle Based Nanofluids: Manifestation of Anomalous Enhancement and Chemical Effects," Appl. Phys. Lett., **83**, pp. 2931–2933.

[12] Wang, X., Xu, X., and Choi, S. U. S., 1999, "Thermal Conductivity of Nanoparticle-Fluid Mixture," J. Thermophys. Heat Transfer, **13**, pp. 474–480.

[13] Lee, S., Choi, S. U. S., Li, S., and Eastman, J. A., 1999, "Measuring Thermal Conductivity of Fluids Containing Oxide Nanoparticles," ASME J. Heat Transfer, **121**, pp. 280–289.

[14] Das, S. K., Putra, N., Thiesen, P., and Roetzel, W., 2003, "Temperature Dependence of Thermal Conductivity Enhancement for Nanofluids," ASME J. Heat Transfer, **125**, pp. 567–574.

[15] Rusconi, R., Rodari, E., and Piazza, R., 2006, "Optical Measurements of the Thermal Properties of Nanofluids," Appl. Phys. Lett., **89**, p. 261916.

[16] Venerus, D. C., Kabadi, M. S., Lee, S., and Perez-Luna, V., 2006, "Study of Thermal Transport in Nanoparticle Suspensions Using Forced Rayleigh Scattering," J. Appl. Phys., **100**, p. 094310.

[17] Zhang, X., Gu, H., and Fujii, M., 2006, "Effective Thermal Conductivity and Thermal Diffusivity of Nanofluids Containing Spherical and Cylindrical Nanoparticles," J. Appl. Phys., **100**, p. 044325.

[18] Zhang, X., Gu, H., and Fujii, M., 2006, "Experimental Study on the Effective Thermal Conductivity and Thermal Diffusivity of Nanofluids," Int. J. Thermophys., **27**, pp. 569–580.

[19] Xie, H., Wang, J., Xi, T., and Liu, Y., 2002, "Thermal Conductivity of Suspensions Containing Nanosized SiC Particles," Int. J. Thermophys., **23**, pp. 571–580.

[20] Putnam, S. A., Cahill, D. G., Braun, P. V., Ge, Z., and Shimmin, R. G., 2006, "Thermal Conductivity of Nanoparticle Suspensions," J. Appl. Phys., **99**, p. 084308.

[21] Keblinski, P., Eastman, J. A., and Cahill, D. G., 2005, "Nanofluids for Thermal Transport," Mater. Today, **8**, pp. 36–44.

[22] Singh, D., Timofeeva, E., Yu, W., Routbort, J., France, D., Smith, D., and Lopez-Cepero, J. M., 2009, "An Investigation of Silicon Carbide-Water Nanofluid for Heat Transfer Applications," J. Appl. Phys., **105**, p. 064306.

[23] Ju, Y. S., Kim, J., and Hung, M.-T., 2008, "Experimental Study of Heat Conduction in Aqueous Suspensions of Aluminum Oxide Nanoparticles," ASME J. Heat Transfer, **130**, p. 092403.

[24] Timofeeva, E. V., Gavrilov, A. N., McCloskey, J. M., Tolmachev, Y. V., Sprunt, S., Lopatina, L. M., and Selinger, J. V., 2007, "Thermal Conductivity and Particle Agglomeration in Alumina Nanofluids: Experiment and Theory," Phys. Rev. E, **76**, p. 061203.

[25] Chon, C. H., Kihm, K. D., Lee, S. P., and Choi, S. U. S., 2005, "Empirical Correlation Finding the Role of Temperature and Particle Size for Nanofluid (Al_2O_3) Thermal Conductivity Enhancement," Appl. Phys. Lett., **87**, p. 153107.

[26] Hong, T. K., Yang, H. S., and Choi, C. J., 2005, "Study of the Enhanced Thermal Conductivity of Fe Nanofluids," J. Appl. Phys., **97**, p. 064311.

[27] Kang, H. U., Kim, S. H., and Oh, J. M., 2006, "Estimation of Thermal Conductivity of Nanofluid Using Experimental Effective Particle Volume," Exp. Heat Transfer, **19**, pp. 181–191.

[28] Murshed, S. M. S., Leong, K. C., and Yang, C., 2005, "Enhanced Thermal Conductivity of TiO_2-Water Based Nanofluids," Int. J. Therm. Sci., **44**, pp. 367–373.

[29] Murshed, S. M. S., Leong, K. C., and Yang, C., 2006, "Determination of the Effective Thermal Diffusivity of Nanofluids by the Double Hot-Wire Technique," J. Phys. D, **39**, pp. 5316–5322.

[30] Chopkar, M., Das, P. K., and Manna, I., 2006, "Synthesis and Characterization of Nanofluid for Advanced Heat Transfer Applications," Scr. Mater., **55**, pp. 549–552.

[31] Chopkar, M., Kumar, S., Bhandari, D. R., Das, P. K., and Manna, I., 2007, "Development and Characterization of Al_2Cu and Ag_2Al Nanoparticle Dispersed Water and Ethylene Glycol Based Nanofluid," Mater. Sci. Eng., B, **139**, pp. 141–148.

[32] Li, C. H., and Peterson, G. P., 2007, "The Effect of Particle Size on the Effective Thermal Conductivity of Al_2O_3-Water Nanofluids," J. Appl. Phys., **101**, p. 044312.

[33] Zhu, H. T., Zhang, C. Y., Tang, Y. M., and Wang, J. X., 2007, "Novel Synthesis and Thermal Conductivity of CuO Nanofluid," J. Phys. Chem. C, **111**, pp. 1646–1650.

[34] Zhu, H., Zhang, C., Liu, S., Tang, Y., and Yin, Y., 2006, "Effects of Nanoparticle Clustering and Alignment on Thermal Conductivities of Fe_3O_4 Aqueous Nanofluids," Appl. Phys. Lett., **89**, pp. 023123.

[35] Li, Q., and Xuan, Y., 2006, "Enhanced Heat Transfer Behaviors of New Heat Carrier for Spacecraft Thermal Management," J. Spacecr. Rockets, **43**, pp. 687–689.

[36] Li, C. H., and Peterson, G. P., 2006, "Experimental Investigation of Temperature and Volume Fraction Variations on the Effective Thermal Conductivity of Nanoparticle Suspensions (Nanofluids)," J. Appl. Phys., **99**, p. 084314.

[37] Yoo, D.-H., Hong, K. S., and Yang, H.-S., 2007,"Study of Thermal Conductivity of Nanofluids for the Application of Heat Transfer Fluids," Thermochim. Acta, **455**, pp. 66–69.

[38] Vázquez Peñas, J. R., Ortiz de Zárate, J. M., and Khayet, M., 2008, "Measurement of the Thermal Conductivity of Nanofluids by the Multicurrent Hot-Wire Method," J. Appl. Phys., **104**, p. 044314.

[39] Philip, J., Shima, P. D., and Raj, B., 2008, "Nanofluid With Tunable Thermal Properties," Appl. Phys. Lett., **92**, p. 043108.

[40] Schmidt, A. J., Chiesa, M., Torchinsky, D. H., Johnson, J. A., Nelson, K. A., and Chen, G., 2008, "Thermal Conductivity of Nanoparticle Suspensions in Insulating Media Measured With a Transient Optical Grating and a Hotwire," J. Appl. Phys., **103**, p. 083529.

[41] Sinha, K., Kavlicoglu, B., Liu, Y., Gordaninejad, F., and Graeve, O. A., 2009, "A Comparative Study of Thermal Behavior of Iron and Copper Nanofluids," J. Appl. Phys., **106**, p. 064307.

[42] Shima, P. D., Philip, J., and Raj, B., 2009, "Role of Microconvection Induced by Brownian Motion of Nanoparticles in the Enhanced Thermal Conductivity of Stable Nanofluids," Appl. Phys. Lett., **94**, p. 223101.

[43] Gharagozloo, P. E., Eaton, J. K., and Goodson, K. E., 2008, "Diffusion, Aggregation, and the Thermal Conductivity of Nanofluids," Appl. Phys. Lett., **93**, p. 103110.

[44] Garg, J., Poudel, B., Chiesa, M., Gordon, J. B., Ma, J. J., Wang, J. B., Ren, Z. F., Kang, Y. T., Ohtani, H., Nanda, J., McKinley, G. H., and Chen, G., 2008, "Enhanced Thermal Conductivity and Viscosity of Copper Nanoparticles in Ethylene Glycol Nanofluid," J. Appl. Phys., **103**, p. 074301.
[45] Philip, J., Shima, P. D., and Raj, B., 2007, "Enhancement of Thermal Conductivity in Magnetite Based Nanofluid due to Chainlike Structures," Appl. Phys. Lett., **91**, p. 203108.
[46] Buongiorno, J., Venerus, D. C., Prabhat, N., McKrell, T., Townsend, J., Christianson, R., Tolmachev, Y. V., Keblinski, P., Hu, L.-W., Alvarado, J. L., Bang, I. C., Bishnoi, S. W., Bonetti, M., Botz, F., Cecere, A., Chang, Y., Chen, G., Chung, S. J., Chyu, M. K., Das, S. K., Di Paola, R., Ding, Y., Dubois, F., Dzido, G., Eapen, J., Escher, W., Funfschilling, D., Galand, Q., Gao, J., Gharagozloo, P. E., Goodson, K. E., Gutierrez, J. G., Hong, H., Horton, M., Hwang, K. S., Iorio, C. S., Jang, S. P., Jarzebski, A. B., Jiang, Y., Jin, L., Kabelac, S., Kamath, A., Kedzierski, M. A., Kieng, L. G., Kim, C., Kim, J.-H., Kim, S., Lee, S. H., Leong, K. C., Manna, I., Michel, B., Ni, R., Patel, H. E., Philip, J., Poulikakos, D., Reynaud, C., Savino, R., Savino, R., Singh, P. K., Song, P., Sundararajan, T., Timofeeva, E., Tritcak, T., Turanov, A. N., Van Vaerenbergh, S., Wen, D., Witharana, S., Yang, C., Yeh, W.-H., Zhao, X.-Z., and Zhou, S.-Q., 2009, "A Benchmark Study on the Thermal Conductivity of Nanofluids," J. Appl. Phys., **106**, p. 094312.
[47] Maxwell, J. C., 1881, *A Treatise on Electricity and Magnetism*, Vol. 1, 2nd ed., Claredon, Oxford.
[48] Hashin, Z., and Shtrikman, S., 1962, "A Variational Approach to the Theory of the Effective Magnetic Permeability of Multiphase Materials," J. Appl. Phys., **33**, pp. 3125–3131.
[49] Nan, C.-W., Birringer, R., Clarke, D. R., and Gleiter, H., 1997, "Effective Thermal Conductivity of Particulate Composites With Interfacial Thermal Resistance," J. Appl. Phys., **81**, pp. 6692–6699.
[50] Benveniste, Y., 1987, "Effective Thermal Conductivity of Composites With a Thermal Contact Resistance Between the Constituents: Nondilute Case," J. Appl. Phys., **61**, pp. 2840.
[51] Kim, S. H., Choi, S. R., and Kim, D., 2007, "Thermal Conductivity of Metal-Oxide Nanofluids: Particle Size Dependence and Effect of Laser Irradiation," ASME J. Heat Transfer, **129**, pp. 298–307.
[52] Hong, K. S., Hong, T.-K., and Yang, H.-S., 2006, "Thermal Conductivity of Fe Nanofluids Depending on the Cluster Size of Nanoparticles," Appl. Phys. Lett., **88**, p. 031901.
[53] Li, C. H., Williams, W., Buongiorno, J., Hu, L.-W., and Peterson, G. P., 2008, "Transient and Steady-State Experimental Comparison Study of Effective Thermal Conductivity of Al_2O_3/Water Nanofluids," ASME J. Heat Transfer, **130**, p. 042407.
[54] Jha, N., and Ramaprabhu, S., 2009, "Thermal Conductivity Studies of Metal Dispersed Multiwalled Carbon Nanotubes in Water and Ethylene Glycol Based Nanofluids," J. Appl. Phys., **106**, p. 084317.
[55] Every, A. G., Tzou, Y., Hasselman, D. P. H., and Raj, R., 1992, "The Effect of Particle Size on the Thermal Conductivity of ZnS/Diamond Composites," Acta Metall. Mater., **40**, pp. 123–129.
[56] Sofian, N. M., Rusu, M., Neagu, R., and Neagu, E., 2001, "Metal Powder-Filled Polyethylene Composites. V. Thermal Properties," J. Thermoplastic Composite Materials, **14**, pp. 20–33.
[57] Hasselman, D. P. H., and Donaldson, K. Y., 2000, "Role of Size in the Effective Thermal Conductivity of Composites With an Interfacial Thermal Barrier," J. Wide Bandgap Mater., **7**, pp. 306–318.
[58] Geiger, A. L., Hasselman, D. P. H., and Donaldson, K. Y., 1993, "Effect of Reinforcement Particle Size on the Thermal Conductivity of a Particulate Silicon-Carbide Reinforced Aluminum-Matrix Composite," J. Mater. Sci. Lett., **12**, pp. 420–423.
[59] Pal, R., 2007, "New Models for Thermal Conductivity of Particulate Composites," J. Reinf. Plast. Compos., **26**, pp. 643–651.
[60] Zhang, H., Ge, X., and Ye, H., 2005, "Effectiveness of the Heat Conduction Reinforcement of Particle Filled Composites," Modell. Simul. Mater. Sci. Eng., **13**, pp. 401–412.
[61] Kumar, D. H., Patel, H. E., Kumar, V. R. R., Sundararajan, T., Pradeep, T., and Das, S. K., 2004, "Model for Heat Conduction in Nanofluids," Phys. Rev. Lett., **93**, p. 144301.
[62] Bhattacharya, P., Saha, S. K., Yadav, A., Phelan, P. E., and Prasher, R. S., 2004, "Brownian Dynamics Simulation to Determine the Effective Thermal Conductivity of Nanofluids," J. Appl. Phys., **95**, pp. 6492–6494.
[63] Koo, J., and Kleinstreuer, C., 2004, "A New Thermal Conductivity Model for Nanofluids," J. Nanopart. Res., **6**, pp. 577–588.
[64] Jang, S. P., and Choi, S. U. S., 2004, "Role of Brownian Motion in the Enhanced Thermal Conductivity of Nanofluids," Appl. Phys. Lett., **84**, pp. 4316–4318.
[65] Jang, S. P., and Choi, S. U. S., 2007, "Effects of Various Parameters on Nanofluid Thermal Conductivity," ASME J. Heat Transfer, **129**, pp. 617–623.
[66] Prasher, R., Bhattacharya, P., and Phelan, P. E., 2005, "Thermal Conductivity of Nanoscale Colloidal Solutions (Nanofluids)," Phys. Rev. Lett., **94**, p. 025901.
[67] Prasher, R., Bhattacharya, P., and Phelan, P. E., 2006, "Brownian-Motion-Based Convective-Conductive Model for the Effective Thermal Conductivity of Nanofluids," ASME J. Heat Transfer, **128**, pp. 588–595.
[68] Li, C. H., and Peterson, G. P., 2007, "Mixing Effect on the Enhancement of the Effective Thermal Conductivity of Nanoparticle Suspensions (Nanofluids)," Int. J. Heat Mass Transfer, **50**, pp. 4668–4677.
[69] Patel, H. E., Sundararajan, T., Pradeep, T., Dasgupta, A., Dasgupta, N., and Das, S. K., 2005, "A Micro-Convection Model for Thermal Conductivity of Nanofluids," Pramana, J. Phys., **65**, pp. 863–869.
[70] Yu, W., and Choi, S. U. S., 2003, "The Role of Interfacial Layers in the Enhanced Thermal Conductivity of Nanofluids: A Renovated Maxwell Model," J. Nanopart. Res., **5**, pp. 167–171.
[71] Xue, Q.-Z., 2003, "Model for Effective Thermal Conductivity of Nanofluids," Phys. Lett. A, **307**, pp. 313–317.
[72] Xie, H., Fujii, M., and Zhang, X., 2005, "Effect of Interfacial Nanolayer on the Effective Thermal Conductivity of Nanoparticle-Fluid Mixture," Int. J. Heat Mass Transfer, **48**, pp. 2926–2932.
[73] Xue, Q., and Xu, W.-M., 2005, "A Model of Thermal Conductivity of Nanofluids With Interfacial Shells," Mater. Chem. Phys., **90**, pp. 298–301.
[74] Tillman, P., and Hill, J. M., 2007, "Determination of Nanolayer Thickness for a Nanofluid," Int. Commun. Heat Mass Transfer, **34**, pp. 399–407.
[75] Avsec, J., and Oblak, M., 2007, "The Calculation of Thermal Conductivity, Viscosity and Thermodynamic Properties for Nanofluids on the Basis of Statistical Nanomechanics," Int. J. Heat Mass Transfer, **50**, pp. 4331–4341.
[76] Gao, L., and Zhou, X. F., 2006, "Differential Effective Medium Theory for Thermal Conductivity in Nanofluids," Phys. Lett. A, **348**, pp. 355–360.
[77] Zhou, X. F., and Gao, L., 2006, "Effective Thermal Conductivity in Nanofluids of Nonsperical Particles With Interfacial Thermal Resistance: Differential Effective Medium Theory," J. Appl. Phys., **100**, p. 024913.
[78] Prasher, R., Evans, W., Meakin, P., Fish, J., Phelan, P., and Keblinski, P., 2006, "Effect of Aggregation on Thermal Conduction in Colloidal Nanofluids," Appl. Phys. Lett., **89**, p. 143119.
[79] Jie, X., Yu, B.-M., and Yun, M.-J., 2006, "Effect of Clusters on Thermal Conductivity in Nanofluids," Chin. Phys. Lett., **23**, pp. 2819–2822.
[80] Feng, Y., Yu, B., Xu, P., and Zou, M., 2007, "The Effective Thermal Conductivity of Nanofluids Based on the Nanolayer and the Aggregation of Nanopartciles," J. Phys. D: Appl. Phys., **40**, pp. 3164–3171.
[81] Xu, J., Yu, B., Zou, M., and Xu, P., 2006, "A New Model for Heat Conduction of Nanofluids Based on Fractal Distributions of Nanoparticles," J. Phys. D, **39**, pp. 4486–4490.
[82] Ren, Y., Xie, H., and Cai, A., 2005, "Effective Thermal Conductivity of Nanofluids Containing Spherical Nanoparticles," J. Phys. D, **38**, pp. 3958–3961.
[83] Wang, B.-X., Zhou, L.-P., and Peng, Z.-F., 2003, "A Fractal Model for Predicting the Effective Thermal Conductivity of Liquid With Suspension of Nanoparticles," Int. J. Heat Mass Transfer, **46**, pp. 2665–2672.
[84] Xuan, Y., Li, Q., and Hu, W., 2004, "Aggregation Structure and Thermal Conductivity of Nanofluids," AIChE J., **49**, pp. 1038–1043.
[85] Prasher, R., Phelan, P. E., and Bhattacharya, P., 2006, "Effect of Aggregation Kinetics on the Thermal Conductivity of Nanoscale Colloidal Solutions (Nanofluid)," Nano Lett., **6**, pp. 1529–1534.
[86] Keblinski, P., Prasher, R., and Eapen, J., 2008, "Thermal Conductance of Nanofluids: Is the Controversy Over?," J. Nanopart. Res., **10**, pp. 1089–1097.
[87] deGroot, S. R., and Mazur, P., 1984, *Nonequilibrium Thermodynamics*, Dover, New York.
[88] DeVera, A. L., and Strieder, W., 1977, "Upper and Lower Bounds on the Thermal Conductivity of a Random, Two-Phase Material," J. Phys. Chem., **81**, pp. 1783.
[89] Carson, J. K., Lovatt, S. J., Tanner, D. J., and Cleland, A. C., 2005, "Thermal Conductivity Bounds for Isotropic Porous Materials," Int. J. Heat Mass Transfer, **48**, pp. 2150–2158.
[90] Griesinger, A., Hurler, W., and Pietralla, M., 1997, "A Photothermal Method With Step Heating for Measuring the Thermal Diffusivity of Anisotropic Solids," Int. J. Heat Mass Transfer, **40**, pp. 3049–3058.
[91] Eapen, J., Williams, W. C., Buongiorno, J., Hu, L.-W., Yip, S., Rusconi, R., and Piazza, R., 2007, "Mean-Field Versus Microconvection Effects in Nanofluid Thermal Conduction," Phys. Rev. Lett., **99**, p. 095901.
[92] Torquato, S., and Rintoul, M. D., 1995, "Effect of Interface on the Properties of Composite Media," Phys. Rev. Lett., **75**, pp. 4067–4070.
[93] Raghavan, K., Foster, K., Motakabbir, K., and Berkowitz, M., 1991, "Structure and Dynamics of Water at the Pt(111) Interface: Molecular Dynamics Study," J. Chem. Phys., **94**, pp. 2110–2117.
[94] Reedijk, M. F., Arsic, J., Hollander, F. F. A., de Vries, S. A., and Vlieg, E., 2003, "Liquid Order at the Interface of KDP Crystals With Water: Evidence for Icelike Layers," Phys. Rev. Lett., **90**, p. 066103.
[95] Mo, H., Evmenenko, G., and Dutta, P., 2005, "Ordering of Liquid Squalane Near a Solid Surface," Chem. Phys. Lett., **415**, pp. 106–109.
[96] Yu, C.-J., Richter, A. G., Kmetko, J., Dugan, S. W., Datta, A., and Dutta, P., 2001, "Structure of Interfacial Liquids: X-Ray Scattering Studies," Phys. Rev. E, **63**, p. 021205.
[97] Eapen, J., Li, J., and Yip, S., 2007, "Beyond the Maxwell Limit: Thermal Conduction in Nanofluids With Percolating Fluid Structures," Phys. Rev. E, **76**, p. 062501.
[98] Xue, L., Keblinski, P., Phillpot, S. R., Choi, S. U. S., and Eastman, J. A., 2004, "Effect of Liquid Layering at the Liquid-Solid Interface on Thermal Transport," Int. J. Heat Mass Transfer, **47**, pp. 4277–4284.
[99] Evans, W., Fish, J., and Keblinski, P., 2007, "Thermal Conductivity of Ordered Molecular Water," J. Chem. Phys., **126**, p. 154504.
[100] Mo, H., Evmenenko, G., Kewalramani, S., Kim, K., Ehrlich, S. N., and Dutta, P., 2006, "Observation of Surface Layering in a Nonmetallic Liquid," Phys. Rev. Lett., **96**, p. 096107.
[101] Wang, X.-Q., and Mujumdar, A. S., 2007, "Heat Transfer Characteristics of Nanofluids: A Review," Int. J. Therm. Sci., **46**, pp. 1–19.
[102] Keblinski, P., and Cahill, D. G., 2005, "Comment on "Model for Heat Conduction in Nanofluids"," Phys. Rev. Lett., **95**, p. 209401.
[103] Bastea, S., 2005, "Comment on "Model for Heat Conduction in Nano-

fluids",," Phys. Rev. Lett., **95**, p. 019401.
[104] He, P., and Qiao, R., 2008, "Self-Consistent Fluctuating Hydrodynamics Simulations of Thermal Transport in Nanoparticle Suspensions," J. Appl. Phys., **103**, p. 094305.
[105] Morozov, K. I., 2002, *On the Theory of the Soret Effect in Colloids*, W. Köhler and S. Wiegand, eds., Springer-Verlag, Berlin.
[106] Piazza, R., 2004, "'Thermal Forces': Colloids in Temperature Gradients," J. Phys.: Condens. Matter, **16**, pp. S4195–S4211.
[107] Keblinski, P., Phillpot, S. R., Choi, S. U. S., and Eastman, J. A., 2002, "Mechanisms of Heat Flow in Suspensions of Nano-Sized Particles (Nanofluids)," Int. J. Heat Mass Transfer, **45**, pp. 855–863.
[108] Nie, C., Marlow, W. H., and Hassan, Y. A., 2008, "Discussion of Proposed Mechanisms of Thermal Conductivity Enhancement in Nanofluids," Int. J. Heat Mass Transfer, **51**, pp. 1342–1348.
[109] Hass, K. C., Schneider, W. F., Curioni, A., and Andreoni, W., 1998, "The Chemistry of Water on Alumina Surfaces: Reaction Dynamics From First Principles,"," Science, **282**, pp. 265–268.
[110] Gmachowski, L., 2002, "Aggregate Restructuring and Its Effect on the Aggregate Size Distribution," Colloids Surf., A, **207**, pp. 271–277.
[111] Kim, J., and Kramer, T. A., 2006, "Improved Orthokinetic Coagulation Model for Fractal Colloids: Aggregation and Breakup," Chem. Eng. Sci., **61**, pp. 45–53.
[112] Wiltzius, P., 1987, "Hydrodynamic Behavior of Fractal Aggregates," Phys. Rev. Lett., **58**, pp. 710–713.
[113] Hess, W., Frisch, H. L., and Klein, R., 1986, "On the Hydrodynamic Behavior of Colloidal Aggregates," Z. Phys. B: Condens. Matter, **64**, pp. 65–67.
[114] Buongiorno, J., 2006, "Convective Transport in Nanofluids," ASME J. Heat Transfer, **128**, pp. 240–250.
[115] Goldhirsch, I., and Ronis, D., 1983, "Theory of Thermophoresis. I. General Considerations and Mode-Coupling Analysis," Phys. Rev. A, **27**, pp. 1616–1634.
[116] Lin, F., Bhatia, G. S., and Ford, J. D., 1993, "Thermal Conductivities of Powder-Filled Epoxy Resins," J. Appl. Polym. Sci., **49**, pp. 1901–1908.
[117] Boudenne, A., Ibos, L., Fois, M., Gehin, E., and Majeste, J.-C., 2004, "Thermophysical Properties of Polypropylene/Aluminum Composites," J. Polym. Sci., Part B: Polym. Phys., **42**, pp. 722–732.
[118] Tekce, H. S., Kumlutas, D., and Tavman, I. H., 2007, "Effect of Particle Shape on Thermal Conductivity of Copper Reinforced Polymer Composites," J. Reinf. Plast. Compos., **26**, pp. 113–121.
[119] Xu, Y., Chung, D. D. L., and Mroz, C., 2001, "Thermally Conducting Aluminum Nitride Polymer-Matrix Composites," Composites, Part A, **32**, pp. 1749–1757.
[120] Agari, Y., and Uno, T., 1986, "Estimation of Thermal Conductivities of Filled Polymers," J. Appl. Polym. Sci., **32**, pp. 5705–5712.
[121] Cowling, T. G., Gray, P., and Wright, P. G., 1963, "The Physical Significance of Formulae for the Thermal Conductivity and Viscosity of Gaseous Mixtures," Proc. R. Soc. London, Ser. A, **276**, pp. 69–82.
[122] Pandey, J. D., and Mishra, R. K., 2005, "Theoretical Evaluation of Thermal Conductivity and Diffusion Coefficient of Binary Liquid Mixtures," Phys. Chem. Liq., **43**, pp. 49–57.
[123] Assael, M. J., Charitidou, E., and Wakeham, W. A., 1989, "Absolute Measurements of the Thermal Conductivity of Mixtures of Alcohols With Water," Int. J. Thermophys., **10**, pp. 793–803.
[124] Li, C. C., 1976, "Thermal Conductivity of Liquid Mixtures," AIChE J., **22**, pp. 927–930.
[125] Li, Q., Xuan, Y., and Wang, J., 2005, "Experimental Investigations on Transport Properties of Magnetic Fluids," Exp. Therm. Fluid Sci., **30**, pp. 109–116.
[126] Jagannadham, K., and Wang, H., 2002, "Thermal Resistance of Interfaces in AlN-Diamond Thin Film Composites," J. Appl. Phys., **91**, pp. 1224–1235.
[127] Ge, Z., Cahill, D. G., and Braun, P. V., 2006, "Thermal Conductance of Hydrophilic and Hydrophobic Interfaces," Phys. Rev. Lett., **96**, p. 186101.
[128] Bryning, M. B., Milkie, D. E., Islam, M. F., Kikkawa, J. M., and Yodh, A. G., 2005, "Thermal Conductivity and Interfacial Resistance in Single-Wall Carbon Nanotube Epoxy Composites," Appl. Phys. Lett., **87**, p. 161909.
[129] Huxtable, S. T., Cahill, D. G., Shenogin, S., Xue, L., Ozisik, R., Barone, P., Usrey, M., Strano, M. S., Siddons, G., Shim, M., and Keblinski, P., 2003, "Interfacial Heat Flow in Carbon Nanotube Suspension," Nature Mater., **2**, pp. 731–734.
[130] Nan, C.-W., Liu, G., Lin, Y., and Li, M., 2004, "Interface Effect on Thermal Conductivity of Carbon Nanotube Composites," Appl. Phys. Lett., **85**, pp. 3549–3551.
[131] Wen, D., and Ding, Y., 2004, "Experimental Investigation Into Convective Heat Transfer of Nanofluids at the Entrance Region Under Laminar Flow Conditions," Int. J. Heat Mass Transfer, **47**, pp. 5181–5188.
[132] Wen, D., and Ding, Y., 2006, "Natural Convective Heat Transfer of Suspensions of Titanium Dioxide Nanoparticles (Nanofluids)," IEEE Trans. Nanotechnol., **5**, pp. 220–227.
[133] Shaikh, S., Lafdi, K., and Ponnappan, R., 2007, "Thermal Conductivity Improvement in Carbon Nanoparticle Doped PAO Oil: An Experimental Study," J. Appl. Phys., **101**, p. 064302.
[134] Choi, S. U. S., Zhang, Z. G., Yu, W., Lockwood, F. E., and Grulke, E. A., 2001, "Anomalous Thermal Conductivity Enhancement in Nanotube Suspensions," Appl. Phys. Lett., **79**, pp. 2252–2254.
[135] Hwang, Y., Lee, J. K., Lee, C. H., Jung, Y. M., Cheong, S. I., Lee, C. G., Ku, B. C., and Jang, S. P., 2007, "Stability and Thermal Conductivity Characteristics of Nanofluids," Thermochim. Acta, **455**, pp. 70–74.
[136] Wen, D., and Ding, Y., 2004, "Effective Thermal Conductivity of Aqueous Suspensions of Carbon Nanotubes (Carbon Nanotube Nanofluids)," J. Thermophys. Heat Transfer, **18**, pp. 481–485.
[137] Williams, W., Buongiorno, J., and Hu, L.-W., 2008, "Experimental Investigation of Turbulent Convective Heat Transfer and Pressure Loss of Alumina/Water and Zirconia/Water Nanoparticle Colloids (Nanofluids) in Horizontal Tubes," ASME J. Heat Transfer, **130**, p. 042412.
[138] Williams, W. C., 2006, "Experimental and Theoretical Investigations of Transport Phenomena in Nanoparticle Colloids (Nanofluids)," Ph.D. thesis, Department of Nuclear Science and Engineering, Massachusetts Institute of Technology, Cambridge, MA.
[139] Bertolini, D., and Tani, A., 1997, "Thermal Conductivity of Water: Molecular Dynamics and Generalized Hydrodynamics Results," Phys. Rev. E, **56**, pp. 4135–4151.
[140] Li, L., and Chung, D. D. L., 1994, "Thermally Conducting Polymer-Matrix Composites Containing Both AIN Particles and SIC Whiskers," J. Electron. Mater., **23**, pp. 557–564.
[141] National Institute of Standards and Technology (NIST), "Fluid Properties," http://webbook.nist.gov/chemistry/fluid/
[142] Rusconi, R., Williams, W., Buongiorno, J., Piazza, R., and Hu, L.-W., 2007, "Numerical Analysis of Convective Instabilities in a Transient Short-Hot-Wire Setup for Measurement of Liquid Thermal Conductivity," Int. J. Thermophys., **28**, pp. 1131–1146.
[143] 2007, "CRC Handbook of Chemistry and Physics," http://www.hbcpnetbase.com
[144] Kwak, K., and Kim, C., 2005, "Viscosity and Thermal Conductivity of Copper Oxide Nanofluid Dispersed in Ethylene Glycol," Korea-Aust. Rheol. J., **17**, pp. 35–40.
[145] "The A-Z of Materials," http://www.azom.com
[146] Weidenfeller, B., Höfer, M., and Schilling, F., 2002, "Thermal and Electrical Properties of Magnetite Filled Polymers," Composites, Part A, **33**, pp. 1041–1053.
[147] Bozorth, R. M., 1978, *Ferromagnetism*, IEEE, New York.
[148] Yu, R. C., Tea, N., Salamon, M. B., Lorents, D., and Malhotra, R., 1992, "Thermal Conductivity of Single Crystal C60," Phys. Rev. Lett., **68**, pp. 2050–2053.

Molecular Dynamics Simulation of Phonon Scattering at Silicon/Germanium Interfaces

Lin Sun
Rosen Center for Advanced Computing,
Purdue University,
West Lafayette, IN 47906
e-mail: sun33@purdue.edu

Jayathi Y. Murthy
School of Mechanical Engineering,
Purdue University,
West Lafayette, IN 47906
e-mail: jmurthy@purdue.edu

Detailed phonon transport at Si/Ge interfaces is studied using the molecular dynamics wave-packet method. Three types of interfaces are investigated: A smooth interface, an interface with random roughness, and an interface with a regularly patterned roughness. The phonon transmissivity for each case is calculated as a function of phonon frequency, roughness characteristic length, and atomic structure. For a smooth interface, the transmissivities predicted by the MD simulations agree well with the acoustic mismatch model based on the continuum assumption. The rough interface simulation results indicate that random roughness is the source of incoherent phonon scattering and decreases the phonon transmission. Periodic structures such as the regularly patterned roughness employed in this paper cause strong phonon wave interference and may restore phonon transmission as the layer thickness increases. [DOI: 10.1115/1.4001912]

Keywords: molecular dynamics, phonon transport, interface, wave packet

1 Introduction

As heat flows across the interface between two different materials, a temperature drop is found at the interface, which may be represented by a thermal resistance. This is called thermal boundary resistance (TBR). The resistance to interface thermal transport has been a poorly understood but critically important phenomenon. Since surface-to-volume ratios increase as domain length scales fall, interface physics begin to dominate at submicron scales. Phonon transport across Si/SiO_2 interfaces controls self-heating in emerging silicon-on-insulator (SOI) field effect transistors (FETs) [1], for example. Here, the channel region of the transistor is fabricated on top of a silicon dioxide insulator. Heat generated due to electron-phonon scattering in the channel must be transported through the oxide into the bulk silicon and thence to the heat sink. The transmissivity of the Si/SiO_2 interface is critical for determining the effective resistance to heat transfer in the device layer, and consequently, how hot the transistor gets. Similarly, emerging carbon nanotube (CNT) FETs [2] fabricated in SiO_2 also requires a good understanding of the thermal transport of the CNT-SiO_2 interface. In the Si/Ge superlattice studies, it is found the overall thermal conductivity is significantly dependent on the combination of period thickness and the number of periods [3]. Within each layer of the superlattice, phonons are constrained by the layer boundaries and behave as in thin films. Between layers, however, wave interference and particle scattering effects may both determine phonon transmission. Surface roughness may play a critical role in determining transmissivity when multiple interfaces are present. In other applications, such as carbon nanotubes and silicon nanowire thin-film composites [4], thermal resistance at wire/substrate interfaces may limit the thermal conductivity of the composite. Similar issues arise in the fabrication of thermal interface materials for heat spreading in microelectronics [5].

However, TBR is not a newly discovered phenomenon. As early as in 1940s, Kapitza [6] found this effect in studies of heat conduction between a solid surface and liquid helium. Consequently, TBR is also referred to as the Kapitza conductance. Khalatnikov and Adamenko [7] developed the first theoretical model to explain this phenomenon, known as the acoustic mismatch (AM) model. In this model, phonons behave like plane waves so that the transmission and reflection coefficients can be calculated from plane-wave dynamics. Moreover, the interface is assumed perfect and no scattering takes place. The thermal impedance is caused by the difference of mass density and speed of sound on the two sides of the interface and is analogous to the propagation of light across the interface between two optically different materials. These assumptions are generally true when the temperature is extremely low and the interface is perfect. In 1987, Swartz and Pohl [8] proposed the diffuse mismatch (DM) model to account for phonon scattering at the interface. This model assumes that the incident phonons encounter elastic diffuse scattering at the interface and emit to both sides. The probability of being scattered to either side of the interface is proportional the phonon density of states of that region. Furthermore, the elastic scattering assumption does not allow phonon frequency change, i.e., phonons cannot convert from mode to mode. Generally, this assumption is not true. For instance, if two materials A and B have a large mismatch in their phonon dispersion relations, a certain range of phonons cannot be transmitted across the interface unless some mode conversion occurs at the interface. Thus, some inelastic scattering must occur in order to change the phonon frequency. This phenomenon has been proven by molecular dynamics (MD) simulation [9].

Neither the AM nor the DM model addresses the interface structure itself. Both theories neglect the fact that the interface atomic structure and roughness can greatly modify phonon behavior. For example, disorder and defects at the atomic level, which always exist at the interface during synthesis, can greatly scatter phonons and complicate the transport mechanism. Recently, with the growth in interest in solid-solid interfaces in nanoscale applications, there have been a series of efforts on the modeling of TBR at high temperatures by modifying the AM and DM models [10]. Experiments indicate that the DM model is not sufficient to describe heat transport at interfaces at room temperature [11].

More recently, a lattice dynamics method has been used to compute the phonon transport at the interface between two semi-infinite FCC lattices [12] and has been extended to the study of phonon scattering at ideal Si–Ge interfaces [13]. Using this technique, frequency-dependent reflection and transmission coefficients were obtained. However, it is difficult to implement this method for complex atomic interface structures. An alternative

Contributed by the Heat Transfer Division of ASME for publication in the JOURNAL OF HEAT TRANSFER. Manuscript received June 2, 2009; final manuscript received April 16, 2010; published online July 27, 2010. Assoc. Editor: Kenneth Goodson.

approach using atomistic Green's functions has been proposed to characterize the interface phonon transport [14,15]. This approach is based on a dynamical equation and the quantum mechanical description of the phonon energy distribution and is suitable for low temperatures when phonons are ballistic. The benefit of this approach is that only the equilibrium locations of atoms and the interatomic potential are needed as inputs, and many thermal properties, such as phonon dispersion curves, density of states, thermal conductivity, and transmission function, can be obtained in a straightforward way. Furthermore, it is capable of dealing with complex atomic configurations. This approach has been applied to the study of phonon transport in nanowires coated with an amorphous material [14] and extended to handle Si–Ge heterostructures [15]. More recently, it is used to study the elastic phonon scattering at an atomically rough interface that separates two FCC lattice leads [16]. Results are compared with specular and diffuse phonon scattering models.

Another important tool that has emerged in recent years for the study of interface transport is MD simulation. MD simulation provides an attractive way to help explain experimental data and in understanding the details of scattering mechanisms at the interface. In addition to its intrinsic benefits, MD is able to build well-controlled interfaces at the atomic level. Dislocations, defects, stressed boundaries, and the like, which are difficult to control in experiments, can be mimicked easily. The Lennard-Jones potential has been used for MD simulation in FCC crystals due to its simplicity. Two different virtual materials may be created by adjusting mass, lattice or potential parameters, and thus form a layered interface structure between them [16–18]. Some materials with a more complicated structure and potential such as silicon grain boundaries have also been investigated [18,19]. To gain insight into the heat transfer in detail, Schelling et al. [20] used the wave-packet method, described below to calculate the transmission coefficients for different phonon modes. Twu and Ho [21] investigated the impact of interface disorder on TBR. More recently, nonequilibrium molecular dynamics was used to study the effects of temperature and disorder on thermal boundary conductance at solid-solid interfaces and a range of mismatched interfaces were investigated and compared with the diffusive mismatch model [22]. Furthermore, the interfacial thermal conductance between single crystal silicon and amorphous polyethylene was studied and the interfacial thermal conductance at room temperature was obtained [23]. These investigations have shown that MD has enormous potential in helping to understand the fundamental mechanisms of phonon interaction with interfaces.

In this paper, we apply molecular dynamics simulation and the wave packet method to study the detailed phonon transport at a rough semiconductor interface. An interface between silicon and germanium is chosen. The Si/Ge interface is of interest in a number emerging nanotechnology applications. Furthermore, there exist mature three-body potentials to describe these atom interactions. In this paper, the interface between the two semiconductors is manipulated to create a thin layer of roughness by staggering the two types of atoms at the interface. The roughness is characterized by the interval space between these two different types of atoms on the interface plane and also by the thickness of the interface layer. A phonon wave packet is initialized with a predefined frequency and polarization and allowed to propagate through the interface. The interaction of the phonon wave packet with the interface is monitored by analyzing the simulation data in phonon wave space. The phonon transmissivity is calculated by measuring the phonon energy change before and after interface scattering. Smooth interfaces, regularly patterned interfaces, and randomly rough interfaces are studied, and the influence of interface geometry on phonon transmission is investigated for different phonon wave numbers.

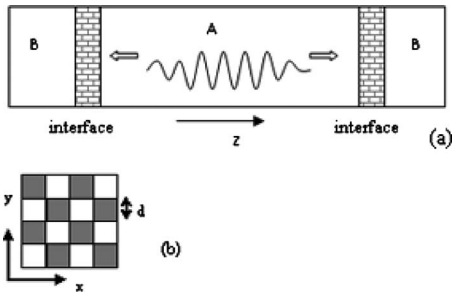

Fig. 1 (*a*) Simulation domain with two materials, A and B, and a rough interface inserted in between. A phonon wave is created at the center of material A and propagates to B by crossing interfaces. (*b*) A regularly patterned roughness structure at the interface, shown in cross-section. The white and gray squares refer to materials A and B, respectively.

2 System Setup and Simulation Parameters

The MD simulation domain is shown in Fig. 1(*a*). Here, two different materials, A and B, share a common interface. Material A is chosen to be silicon and material B to be germanium. The initial configuration of atoms employs their lattice structure at equilibrium. When phonons travel from one material to another, transmission and reflection occur at the interface because of the different acoustic properties of A and B. Lattice mismatch also affects transmissivity and reflectivity. However, in many cases, such as for the Si/Ge interface, the influence of lattice mismatch on phonon transmission is far smaller than that caused by mass difference [15]. Therefore, in this paper, we only consider the mass difference between two materials and assume that the lattice structure to be the same for both materials. An atomic mass for A (silicon) is taken to be $m_A = 4.66 \times 10^{-26}$ kg, and that for B (germanium) is taken to be $m_B = 12.05 \times 10^{-26}$ kg. The lattice constant for both A and B is $a = 5.431 \times 10^{-10}$ m.

A thin layer of roughness is inserted between material A and material B, and its atomic structure and thickness are manipulated as needed. Figure 1(*b*) shows the typical roughness structure used; here materials A and B are mixed in a regular pattern with the interval distance d as well thickness of the layer in the z-direction being varied. Classical molecular dynamics is used to compute the evolution of an N-atom system with time using Newton's second law. An empirical potential for silicon and germanium called the environment dependent interatomic potential [24] is used. The domain boundaries in all three directions are assumed periodic so that the atoms leaving a bounding surface re-enter the domain through the corresponding periodic face on the opposite side. A time step $\Delta t = 1$ fs is used. The entire simulation domain involves up to 1×10^6 atoms. In order to the keep the simulation time tractable, parallel processing using a domain decomposition paradigm is used [25]. The simulations run at zero temperature, i.e., the atoms stay stationary initially. A small amount of energy is introduced into the system merely by the excited phonon waves, disturbing the system from its equilibrium.

3 Phonon Wave Packet Method

MD simulation yields information in the real position and momentum space. However, in order to observe phonon behavior, it is most convenient to analyze the data in phonon or wave-vector space. This requires a technique to transfer MD results, obtained in physical space and time to phonon space so that phonon properties may be obtained. These post-processing techniques are described below.

The wave packet technique is used in conjunction with MD simulation to investigate phonon transmission at interfaces. Treating phonons as a particle system, a wave packet with well-defined frequency and polarization may be defined. It is then possible to

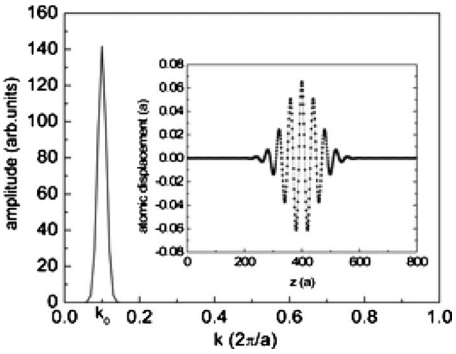

Fig. 2 Illustration of an LA wave packet example centered at $k_0=0.1(2\pi/a)$ and $z=400a$

observe how this phonon (wave packet) propagates through the system, in a manner similar to that of Schelling et al. [20], who investigated how such a wave packet interacts with a coherent semiconductor interface. The phonon transmissivities are then obtained as a function of frequency for phonons with specific polarization.

The phonon wave packet is formed by a linear combination of system vibration eigenstates, which can be obtained by diagonalizing the dynamical matrix of a perfect bulk crystal.

$$u_{in\,\mu} = A\varepsilon_{i\mu\lambda}(k_0)\exp[ik_0(z_n - z_0)]\exp[-(z_n - z_0)^2/\xi^2] \quad (1)$$

Here, $u_{in\,\mu}$ is the μth component of the displacement for atom i in the unit cell labeled by n. The phonon branch is labeled by λ and the wave amplitude is A, k_0 is wave vector and ε is the polarization vector and is calculated from lattice dynamics, z_n is the z coordinate of the unit cell n, and the factor ξ is used to define the spatial width of the wave packet. Using this equation, a Gaussian wave packet is generated centered in real space around z_0 and in phonon space around k_0. Equation (1) defines the shape of the wave packet in real space. In order to observe how the wave packet spans k space, an inverse transformation must be performed. Since the wave packet is a linear combination of a series of wave functions, the contribution of different k values may be obtained by

$$\psi(k) = \sum_i (\vec{\varepsilon}^*(k) \cdot \vec{u}_i)\exp[-ik(z_i - z_0)] \quad (2)$$

The representation of the wave packet in the k and physical spaces is shown in Fig. 2.

In order to generate the initial velocity of atoms, time-dependence is added to the normal modes using

$$u_{in\,\mu} = A\varepsilon_{i\mu\lambda}(k_0)\exp\{i[k_0(z_n - z_0) - \omega t]\} \times \exp[-(z_n - z_0)^2/\xi^2] \quad (3)$$

Differentiating this equation with respect to time yields the initial velocity.

This set of initial conditions perturbs the lattice from its equilibrium state, similar to pulling a string away from its equilibrium position. Once released, the generated wave is allowed to propagate. As the wave packet encounter the interface, part of it is reflected and the rest is transmitted. The proportion of energy being transmitted through the interface can be obtained by calculating the energy change in one of the subregions before and after the interface interaction. By repeating this process for all possible phonons, the transmissivity dependence on frequency and polarization can be determined. One may also investigate the conversion of phonon modes across the interface using Fourier transforms, as in Ref. [26].

It should be pointed out that a large domain is generally required to localize the generated wave. The wave itself must have a sufficient width in physical space to ensure that the spread in k space is as small as possible. In addition, to treat phonons as particles, the wave packet size should be larger than the wavelength of the phonon of interest. Furthermore, for wave packets to have distinct interactions with each other, the distance they travel between collisions must be much greater than the size of wave packet. All these criteria lead to a large length scale for the system. Typically, the wave packet size is 100–200 unit cells wide, and the entire domain length is typically 1000 unit cells long. One limitation of this method is that it only treats modes in isolation. It has the possibility to handle multiple phonon modes with an assumption that they are linearly superposed. However, such an approach would not account for the nonlinear coupling between modes.

4 Results

In this section, the wave packet method is applied to the investigation of phonon dynamics at different interfaces. The first step is to create a wave packet according to Eq. (1), corresponding to a specific phonon branch with a narrow frequency range and well-defined polarization. This wave packet is spatially centered at z_0 in real space and at k_0 in k space. Figure 2 shows a wave packet example centered at $k_0=0.1(2\pi/a)$ in phonon space and $z_0=400a$ in real space where a is the lattice constant. The contribution of different k values is shown. The inset shows the atomic displacement in physical space at the initial stage. Once the wave packet is created, it is allowed to propagate in both the z- and ($-z$)-directions through the simulation domain. Anharmonic scattering, which can be captured by MD simulations, may dissipate the wave packet. However, because the system background temperature is initially set to zero, anharmonic effects are negligible as long as the propagation time is relatively short. Thus, the wave packet may be assumed to encounter the interface essentially unchanged.

4.1 Smooth Interface. The first case to be considered is that of a perfectly smooth interface between material A and material B. A phonon wave packet is initialized at the center of material A (silicon) and then allowed to propagate toward material B (germanium). The lattice structure is constructed in such a way that the x, y, and z axes correspond to the [100], [010], and [001] crystal directions, respectively. The simulation domain has a dimension of $5\times5\times1000$ unit cells, resulting in a length of 543 nm in z-direction perpendicular to the interface. The cross-section has a width of 2.7 nm. Size-dependence studies were performed to identify the influence of domain cross-section size. Computations were performed for cross-sections in the range of 2×2 and 10×10 unit cells. It was found that simulation results were not sensitive to cross-section size as long as the cross section was larger than 3×3 unit cells. More discussion about the domain size effect may be found in Ref. [27]. The vibrational amplitude of the wave packet is an arbitrary (small) value and a value of 1/100 of the lattice constant is used in this paper.

Because A and B have the same potential and atomic structure and only differ in atomic mass, an identical dispersion relation is obtained for both materials, expect that the frequency in B is smaller than that in A by a factor of $\sqrt{m_A/m_B}=1.60$, as shown in Fig. 3. Therefore, a cut-off frequency exists for phonon mode conversion. For instance, the highest frequency for the longitudinal-acoustic (LA) mode in material A (Si) is $f_A=12.1$ THz while that in material B (Ge) is $f_B=7.56$ THz. So, the maximum frequency for LA-LA conversion with nonzero transmission is 7.56 THz. Likewise, the highest frequency for the longitudinal-optical (LO) mode of material A is 17.2 THz while that for material B is 10.75 THz, thus, 10.75 THz is the cut-off frequency for LO-LO mode conversion.

Figure 4 shows a series of snapshots of an LA wave packet with $k_0=0.1(2\pi/a)$ and $f=1.34$ THz propagating through interface. After encountering the interface, part of the wave is transmitted and the rest is reflected. From this figure, the group velocity of

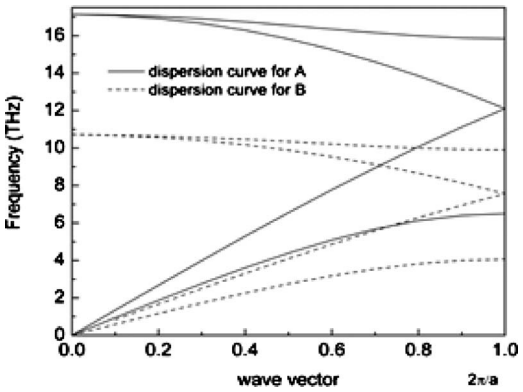

Fig. 3 Dispersion relation for materials A (silicon) and B (germanium) in the [001] direction

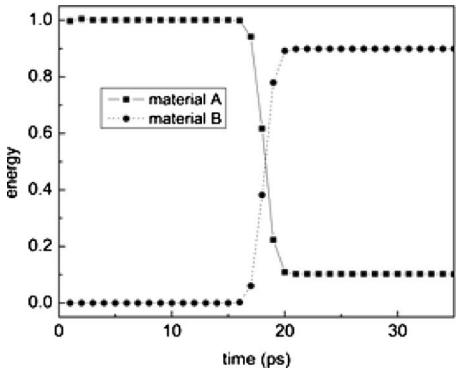

Fig. 6 Energy change with time for material A and B for the case that incident LA phonons are at $k=0.5(2\pi/a)$

incident, transmitted and reflected phonons can be calculated. Figure 5 illustrates the reflected and transmitted phonon distribution in k space assuming they are both LA branches. As shown in Fig. 5, the center of the reflected phonon packet is at $k_r=0.1(2\pi/a)$. Thus, the phonon frequency does not change before and after reflection. This indicates the reflected phonon has exactly the same character as the incident one. The transmitted phonon has a peak at $k_t=0.16(2\pi/a)$. Referring to the dispersion of material B (Fig. 3), the corresponding frequency is found to be the same as that of the incident phonon. But the group velocity of transmitted phonons is reduced roughly by half compared with that of the reflected phonons. This is reasonable because the phonon wave propagates more slowly in material B since it is composed of heavier atoms.

The total energy in material A and B can be calculated by adding the potential and kinetic energies on each side. Figure 6 shows an example that how the total energy changes with time as the wave packet propagates for a case that the incident LA phonons are at $k=0.5(2\pi/a)$. The incident wave energy is normalized to unity for clarity. Here, we define the transmissivity as the ratio of the energy transmitted to side B and the initial energy on side A.

The frequency-dependence of transmissivity for incident LA wave packets is shown in Fig. 7. In the low-frequency limit, the phonons have long wavelength and behave like classical plane waves. In this case, the AM assumption is valid and the transmissivity for phonon transport between material A and material B is given by

$$\overline{t}_{AB} = \frac{4Z_A Z_B}{(Z_A + Z_B)^2} \tag{4}$$

where $Z=\rho c$ is acoustic impedance, ρ is mass density, and c is speed of sound, respectively. This formula gives a transmissivity value of 0.95 based on the mass difference of silicon and germanium. This estimation matches the MD prediction well. As the frequency increases, the phonon wavelength becomes shorter and the transmissivity is seen to decrease smoothly with frequency. As the phonon frequency reaches the cut-off point at 10.75 THz, a nearly zero transmission is observed, as expected.

For the incident phonons with frequency smaller than 7.56 THz, both the transmitted and reflected phonons fall on the longitudinal-acoustic branch. In this regime, phonons encounter elastic scattering at the interface and the frequency of incident,

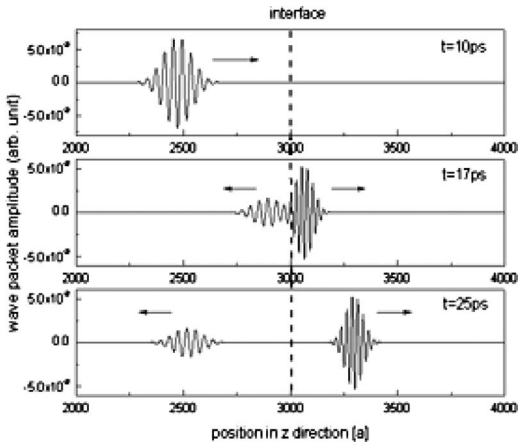

Fig. 4 Snapshots of displacement (respectively at 10 ps, 17 ps, and 25 ps) for an LA wave packet with frequency 1.34 THz

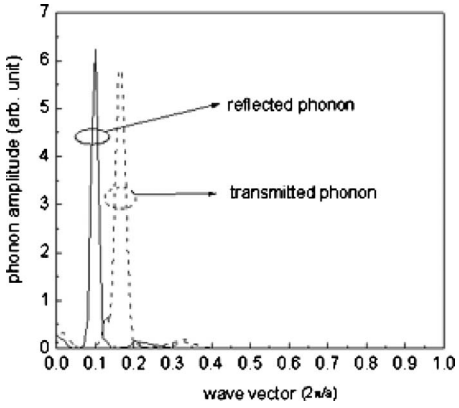

Fig. 5 Distribution of reflected and transmitted phonons in k space

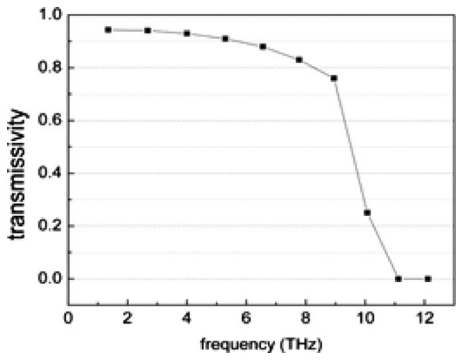

Fig. 7 Phonon transmissivity for LA wave packets at smooth Si/Ge interface

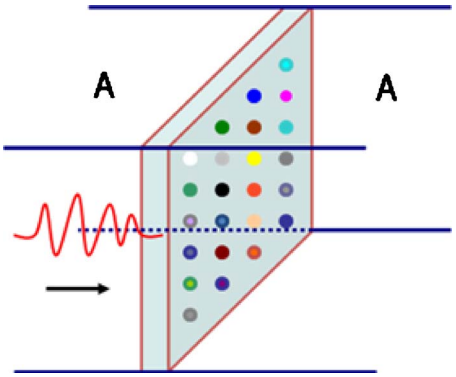

Fig. 8 Random roughness illustration: atoms at interface are endowed with mass randomly (illustrated by colors) to represent the ROUGHNESS

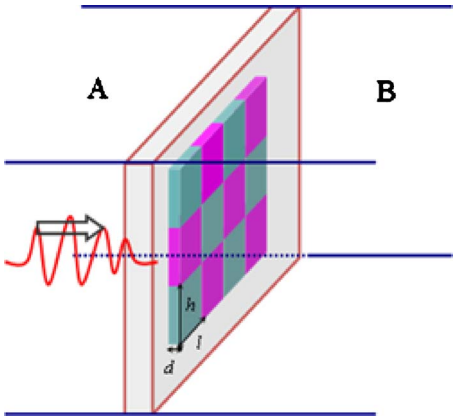

Fig. 9 Regularly patterned roughness: two materials, A and B are mixed in a regular pattern. The dimension of each unit is indicated by *h*, *l*, and *d*. This pattern is extruded in *z*-direction up to a prescribed thickness with successive layers being staggered with respect to each other.

transmitted and reflected phonons is the same. When the frequency of incident phonon is between 7.56 THz and 10.75 THz, the transmitted phonon falls into the optical range. Therefore, inelastic scattering must occur at the interface to modify the phonon mode from acoustic to optical. When the frequency is beyond 10.75 THz, there should be no transmission at all. However in reality there is still a very small fraction of phonons that are transmitted due to the anharmonic effects. The transmitted phonons have very long wavelengths and carry a very small amount of energy.

4.2 Interface With Random Roughness. Next, a layer of random roughness is inserted between material A and material B and its influence on transmission is investigated. In order to isolate the effect of random roughness from other factors, such as mass difference, the baseline system is set as homogeneous, which only consists of material A. A full transmission should be obtained in the absence of the rough interface. To introduce the random roughness, the atoms at the interface are endowed with different atomic masses and randomly mixed, as shown in Fig. 8. The atomic mass of each atom varies about the mass of material A within a certain range. In these studies, a cross-sectional area of 10×10 cells or larger is used to ensure that the placement of atoms is sufficiently random.

Table 1 shows the phonon transmissivity for three cases assuming the incident phonons are all on the LA branch. Here, k refers to wave vector of the incident phonon and $\overline{t}_{AB}$ is the transmissivity. In case 1, the interface thickness is $5a$ in the z-direction (a is the lattice constant) and the assigned random atomic masses range from 0.9 to 1.1 of the mass of material A. In case 2, the interface thickness is kept the same as in case 1 but the mass range is increased, causing a larger acoustic mismatch at the interface. In case 3, the interface thickness is increased while keeping the mass

Table 1 LA phonon transmission at an interface with random roughness

Case 1: Mass range 0.9–1.1; roughness thickness $5a$					
$k(2\pi/a)$	0.1	0.3	0.5	0.7	0.9
$\overline{t}_{AB}$	0.99	0.97	0.95	0.93	0.91
Case 2: Mass range 0.5–1.5; roughness thickness $5a$					
$k(2\pi/a)$	0.1	0.3	0.5	0.7	0.9
$\overline{t}_{AB}$	0.99	0.83	0.65	0.53	0.36
Case 3: Mass range 0.5–1.5; roughness thickness $10a$					
$k(2\pi/a)$	0.1	0.3	0.5	0.7	0.9
$\overline{t}_{AB}$	0.99	0.76	0.51	0.39	0.22

range the same as in case 2.

In case 1, the mass difference is too small to deter phonon transmission, and transmissivities are close to unity across the range of wave vectors. For case 2, long wavelength (low k) phonons exhibit transmissivities close to unity because the wavelength is much longer than the length scale of the rough layer $5a$. However, for higher values of k (shorter wavelengths) the modified dispersion due to the higher-mass roughness layer decreases the transmissivities. Similar behavior is seen in case 3, where again, low k (long wavelength) phonons exhibit transmissivities near unity. However, as the layer thickness increases, the layer begins to act like a bulk material with higher effective mass and the transmissivity falls further. A significant decrease is seen to occur for all but the longest wavelengths, pointing to a strategy for creating high thermal resistance interfaces.

4.3 Interface With Regularly Patterned Roughness. We now examine an interface with regularly patterned roughness in heterogeneous systems. The basic simulation domain is as shown Fig. 1(a), and a layer of roughness is inserted by staggering materials A and B in a regular pattern (illustrated by Fig. 9).

By varying the internal distance between the basic elements of the pattern, different in-plane structures may be created. By extruding the pattern in the z-direction, the rough interface thickness influence is addressed. In the simulations, domain A, set as 1000 unit cells long in z-direction, is sandwiched between two B domains, which are 500 unit cells long, respectively. Each domain has a cross-section of 5×5 cells. At the initial stage, the wave packet is located at the center of material A. After release, the wave propagates in both the z- and $(-z)$-directions and encounters both the A/B interfaces. Since the system is fully symmetric about the vertical centerline of the domain, we only focus on one of the interfaces. The reason that the system is set up in this way is to accommodate periodic boundary conditions in the z-direction.

First, the dependence of the transmissivity for LA phonons on rough layer thickness is investigated for a fixed roughness pattern. The basic roughness unit is set as a cube with the length of one silicon unit cell, i.e., $h=l=d=a$, (where a is the unit cell length). A total of N layers in the z-direction, each of thickness d, constitutes the overall roughness layer thickness. The arrangement of A and B in each layer is staggered with respect to adjacent layers. Figure 10 shows the phonon transmissivity as a function of thickness for LA phonons with wave number ($\underline{k}=0.1$, 0.3, 0.5, 0.7, and 0.9, respectively). In the figure, $\underline{k}=k/(2\pi/a)$ refers to the normalized wave vector and N represents the thickness (number of layers) of roughness. The rough layer thickness ranges from 0 to 50

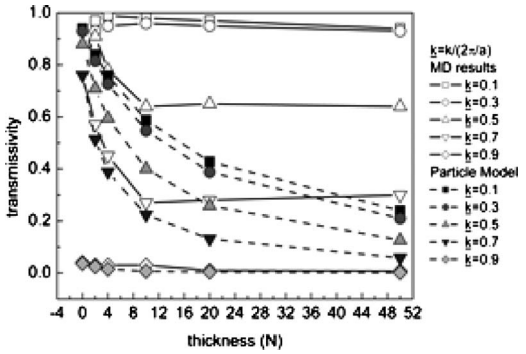

Fig. 10 Phonon transmissivity for an interface with regularly patterned roughness

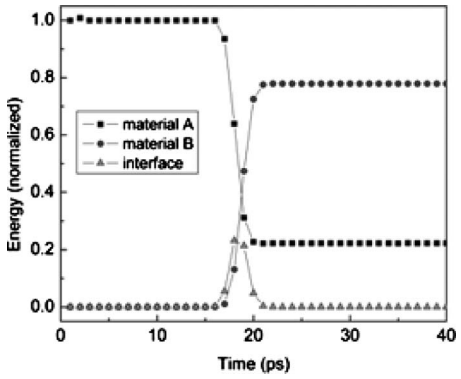

Fig. 11 Energy change with time for materials A and B and the interface region for LA phonon transport across a regularly patterned interface for $k/(2\pi/a)=0.5$ and thickness of 10*a*. Incident energy is normalized to unity.

unit cells. Zero thickness corresponds to the smooth interface case discussed earlier. Two sets of data are plotted for comparison. One is from the MD wave packet simulation and the other is calculated using a particle model. We discuss the MD results first.

Based on their behavior at interface, phonons may be categorized into three groups: long wavelength, medium wavelength and short wavelength. Group 1 ($\underline{k}=0.1,0.3$) refers to those phonons that have low frequency and long wavelength. In this range, phonons behave like harmonic plane waves and the typical wavelength is far greater than the roughness thickness. When the wave encounters the roughness, the phonon wave simply passes over the roughness and has almost no interaction with the interface. Therefore, the transmissivity is nearly unity, similar to that of the ideal interface.

For group 2 ($\underline{k}=0.5$ and 0.7), phonon transmissivity is seen to change significantly with rough layer thickness. In this range, the overall thickness of the roughness layer is comparable to the phonon wavelength and strong interactions occur. Phonon transmissivity is greatly reduced as the roughness thickness is increased. Beyond $N=10-15$, the transmissivity curve flattens out and becomes insensitive with the roughness thickness. This saturation is attributed to coherent wave interference effects due to the periodic nature of the roughness arrangement. More discussion of the detailed mode-conversion dynamics at the interface are given in the next section.

For group 3 ($\underline{k}=0.9$ or larger), the associated phonons are close to or exceed the cut-off frequency beyond which the transmissivity is expected to be zero. The phonon scattering mechanism may be changed due to the interface roughness but does not cause a significant change in the phonon transmissivity in the *z*-direction. Moreover, at room temperature, the phonon occupation number in this frequency range is relatively small, making the transmissivity in this range not crucial for most practical room-temperature applications.

Summarizing the above discussion, for long wavelength phonons, the transmissivity is nearly independent of roughness thickness. For extremely short wavelength phonons, the transmissivity is nearly zero and not of interest. The most interesting phenomena are observed for midrange phonons, where the transmissivity initially drops with increasing roughness thickness and then flattens out. This behavior is caused by the wave interference with the periodic roughness structure.

In order to illustrate this, a conventional particle model is considered in which the wave interference effects are completely absent [28]. We assume that the phonon has a probability $\overline{t}$ of transmission through a single interface. When the phonon propagates through *N* layers of the same interface, the net transmissivity is given by

$$\overline{t_N} = \frac{\overline{t}}{N+1-N\overline{t}} \tag{5}$$

Using this equation, values of transmissivity are calculated as a function of N, and plotted in Fig. 10 for comparison with the MD results; the value of the single-interface MD transmissivity is used in the computation. It is seen that the MD results, which capture wave interference effects, are generally higher than the particle model prediction. In a particle model, adding more interfaces causes transmissivity to fall. This is not seen in the MD model. Coherent wave interference effects for regularly patterned roughness structures appear to be constructive and increase the energy transmitted. In contrast, for random roughness, the transmissivity is seen to decrease with the number of layers at the interface, as shown in Table 1. It is believed that most of the phonon interference is destructive due to the randomness.

In addition to phonon interference, other phenomena also occur simultaneously at the interface, for example, mode conversion, phonon wave damping due to anharmonic effects and dispersion curve mismatch due to the presence of the heterogeneous roughness structure. These factors would tend to decrease phonon transmissivity. At zero temperature, coherent wave interference appears to be the dominant factor that influences the phonon transmissivity through regularly patterned structures.

4.4 Phonon Dynamics at Interface. We now consider the detailed phonon dynamics at the interface discussed in the previous section. A typical case of midrange LA phonons with $k/(2\pi/a)=0.5$ and a regularly patterned roughness layer thickness$=10a$ are chosen.

Figure 11 shows the change in the total energy with time for materials A and B and the interface region. The incoming phonon wave packet encounters the front interface of the roughness layer at 16 ps. The wave is then transmitted across the interface into the interface region and stays in the region for about 6 ps. During this period, phonons bounce back and forth inside the rough layer and interact with the roughness. At around 22 ps, the wave packet is released from the interface. A part of the wave packet is reflected back into material A and the rest goes into material B.

Figure 12 shows snapshots of phonon propagation. In contrast to the case of a smooth interface (Fig. 4), multiple wave packets are generated at the interface, albeit with smaller amplitudes. They are shown as the long tails of reflected and transmitted phonon packets at 25 ps in Fig. 12. These multiple packets may be separate from each other if the interface thickness is long enough to hold the energy inside for a longer time.

By analyzing the time data in phonon space, a deeper understanding of the transmission dynamics may be obtained. Figure 13 shows the evolution of the phonon distribution inside the rough interface region. In the beginning ($t<10$ ps), before the incoming phonon wave hits the interface, the phonons inside the interface region are randomly distributed and the energy is at a very low

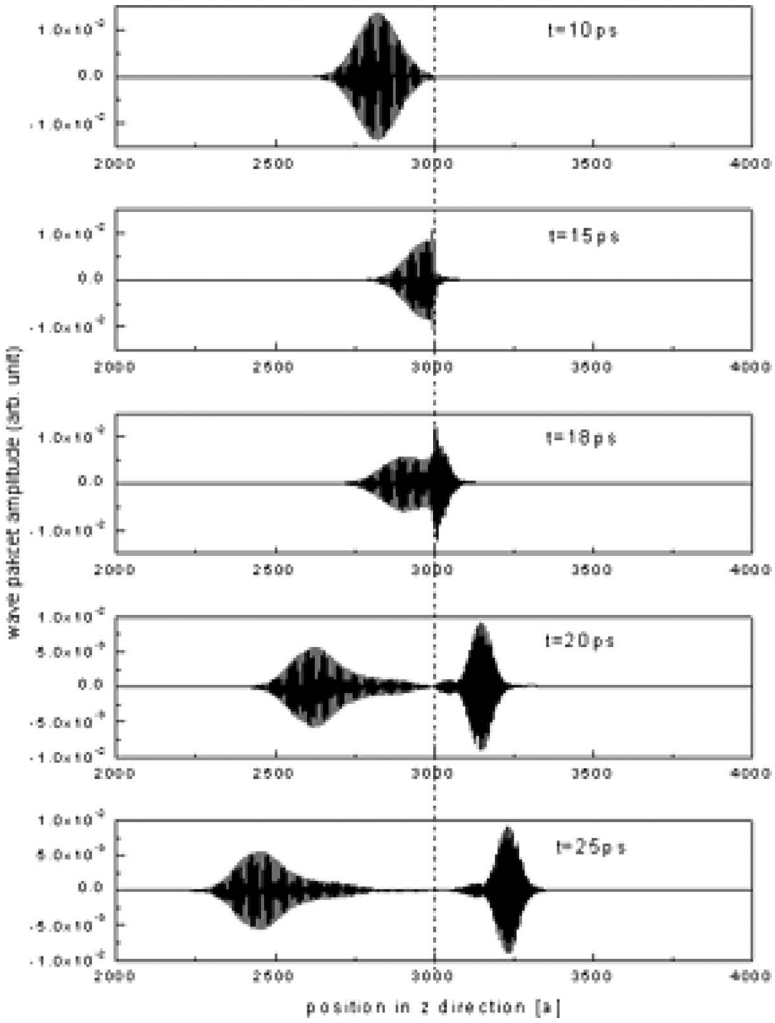

Fig. 12 Snapshots of phonon propagation at the interface with regularly patterned roughness for $k/(2\pi/a)=0.5$ and thickness=10*a*

level. When phonons begin to contact the interface, (t =15–20 ps), the phonon spectrum spans a wide range of k space and contains a number of frequencies not contained in the original incident wave. This indicates that multiple phonon modes are generated due to the contact. Furthermore, these newly developed modes interact with one another and assemble or disperse to other modes. These transient mode conversions allow extra time for energy to dissipate into material A and B and result in more resistance to phonon transport. From Fig. 14, we see that after all the phonons leave the interface (t=25 ps), the phonons of material A are concentrated at $k/(2\pi/a)=0.5$, the same as the incident phonons. The phonons of material B are concentrated at $k/(2\pi/a)=0.8$, corresponding to the incident frequency of 6.1 THz for the dispersion curve of material B.

Although it is difficult to quantify a direct the connection between these complex phonon dynamics and the trends in the transmissivity with layer thickness, we conjecture that these phonon conversions at the interface are one reason for the reduction in phonon transmissivity for midfrequency range phonons (group 2). Furthermore, the transmissivity in Fig. 10 falls with rough layer thickness up to a certain value and then flattens out or recovers to a slightly higher value as the thickness is increased further. One reason for this could be wave interference effects due to the regular periodicity of the roughness structure. Similar phenomena have been found in the superlattices structure studies [29,30]. In superlattice structures, there exists a minimum in the thermal con-

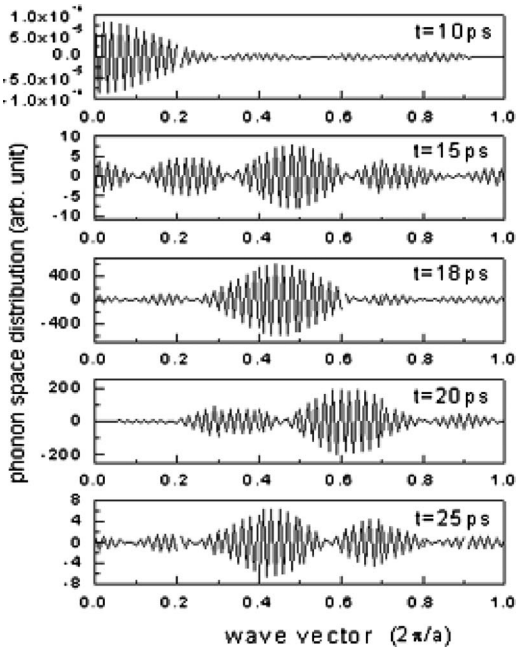

Fig. 13 Evolution of phonon distribution in *k* space with time in interface region

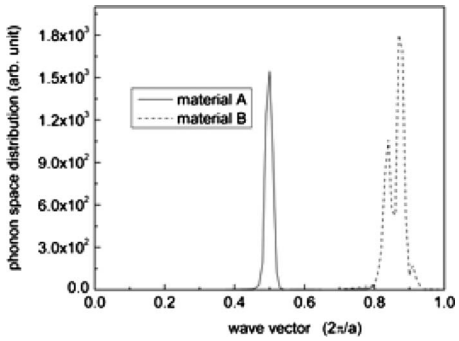

Fig. 14 Phonon distribution in *k* space for reflected phonon in material A and transmitted phonon in material B after interface interaction at 25 ps

ductivity as the period of the superlattice is increased [30]; similar physics operate in regularly patterned roughness layers as well. Constructive wave interference between multiple interfaces acts to restore the phonon transmission while particlelike scattering at interfaces impedes transmission. The interaction of these two effects determines whether the transmissivity decreases with layer thickness. If the roughness layer thickness becomes very large, the transmissivity reaches a saturation value since the interface layer is so large that it behaves like a bulk material with an equivalent effective mass [31].

4.5 Influence of In-Plane Structure. The final case explores the effect of the in-plane roughness structure on the transport of LA phonons. We consider a regularly patterned rough interface, as described in the last two sections. The interface thickness is fixed at $2a$. On a cross-sectional area of 20×20 cells, a structured roughness pattern is created, as shown in Fig. 1(b). The width (d) of each square in Fig. 1(b) is varied from $1a$ to $10a$ and LA phonons with $k/(2\pi/a)=0.5$ are considered. The simulation results, summarized in Table 2, show that the phonon transmissivity does not change significantly with in-plane atomic structure. This is because the incoming phonons are longitudinal-acoustic phonons and vibrate only along the z-direction. Some transverse modes may be activated at the interface but do not appear to be generated in large-enough numbers to alter transmissivity. The thickness of the rough layer in the z-direction is the dominant determinant of transmissivity since it is aligned with the phonon propagation direction. In order to confirm this statement, further work must be performed to study the transport of transverse acoustic phonons at interfaces. For these, the roughness structure in the x-y plane is expected to influence transmissivity to a greater extent.

5 Conclusions

Detailed phonon scattering at a rough Si/Ge interface is studied by molecular dynamics simulations. The system is set up by only considering the mass difference between two materials and neglecting the lattice mismatch. Three types of interfaces are investigated: a smooth interface, an interface with random roughness, and an interface with a regularly patterned roughness. The random roughness is created by introducing atoms with random atomic masses at the interface region. The regularly patterned roughness is addressed by staggering the two types of atoms at the interface in a regular way. The phonon transmissivities for each case are calculated as a function of phonon frequency, roughness characteristic length, and atomic structure. In order to do so, a phonon wave packet is initialized with a predefined frequency and polarization and allowed to propagate through the interface. The interaction of phonon wave packet with the interface is monitored by analyzing the resulting displacement-versus-time signal in phonon wave space. The phonon transmissivity is calculated by measuring the phonon energy change before and after the interface scattering. Phonon wave propagation along a specific direction [100] in silicon lattice has been studied and the following conclusions are drawn.

Table 2 Phonon transmissivity variation with change in in-plane roughness structure for LA phonons with $k/(2\pi/a)=0.5$

Width (a)	<1	1	2	4	8	10
Transmissivity	0.88	0.87	0.89	0.87	0.86	0.86

For an ideal (smooth) interface, the transmissivities predicted by the MD simulations agree well with the acoustic mismatch model based on the continuum assumption. The rough interface simulation results indicate that random roughness is the source of incoherent phonon scattering and decreases the phonon transmission. Periodic structures such as the regularly patterned roughness employed in this paper cause strong phonon wave interference and may restore phonon transmission as the layer thickness increases. For these structures, phonon transmissivity is a strong function of frequency and the roughness characteristic length. In the low-frequency limit, the roughness structure at interfaces is transparent to acoustic phonons and the transmissvity equals the ideal-interface results. In the midfrequency range, phonon transmission initially decreases with increasing thickness and then flattens out. Complex phonon mode conversions are observed and wave interference at this range of k is conjectured to be the reason for this behavior. At frequencies close to the cut-off frequency, the transmissivites drop rapidly to zero and the roughness influence is not evident. It is also found the transmissivity is more sensitive to the atomic structure in the propagation direction than to the structure in the transverse direction.

Acknowledgment

Support under NSF Grant Nos. CTS-0312420 and CTS-0219098 and DARPA's IMPACT Center, and the computational resources of Purdue's Network for Computational Nanotechnology (NCN) are gratefully acknowledged.

References

[1] Asheghi, M., Touzelbaev, M. N., Goodson, K. E., Leung, Y. K., and Wong, S. S., 1998, "Temperature-Dependent Thermal Conductivity of Single-Crystal Silicon Layers in SOI Substrates," ASME J. Heat Transfer, **120**, pp. 30–36.
[2] Snow, E. S., Novak, J. P., Campbell, P. M., and Park, D., 2003, "Random Networks of Carbon Nanotubes as an Electronic Material," Appl. Phys. Lett., **82**, pp. 2145–2147.
[3] Lee, S.-M., Cahill, D., and Venkatasubramanian, R., 1997, "Thermal Conductivity of Si–Ge Superlattices," Appl. Phys. Lett., **70**, pp. 2957–2959.
[4] Duan, X., Niu, C., Sahi, V., Chen, J., Parce, J. W., Empedocles, S., and Goldman, J. L., 2003, "High-Performance Thin-Film Transistors using Semiconductor Nanowires and Nanoribbons," Nature (London), **425**, pp. 274–278.
[5] Xu, J., and Fisher, T. S., 2006, "Enhancement of Thermal Interface Materials With Carbon Nanotube Arrays," Int. J. Heat Mass Transfer, **49**, pp. 1658–1666.
[6] Kapitza, P. L., 1941, "The Study of Heat Transfer in Helium II," Zh. Eksp. Teor. Fiz., **11**, pp. 1–31.
[7] Khalatnikov, I. M., and Adamenko, I. N., 1973, "Theory of the Kapitza Temperature Discontinuity at a Solid Body-Liquid Helium Boundary," Sov. Phys. JETP, **36**, pp. 391–402.
[8] Swartz, E. T., and Pohl, R. O., 1987, "Thermal Resistance at Interfaces," Appl. Phys. Lett., **51**, pp. 2200–2202.
[9] Stevens, R. J., Norris, P. M., and Zhigilei, L. V., 2004, "Molecular-Dynamics Study of Thermal Boundary Resistance: Evidence of Strong Inelastic Scattering Transport Channels," *Proceedings of IMECE*, Anaheim, CA.
[10] Burkhard, G., and Sawaoka, A. B., 1995, "The Effect of Umklapp Processes on the Heat Transport of Solids," The Symposium on Thermal Science and Engineering in Honor of Chancellor Chang-Lin Tien, University of California Berkeley, CA, pp. 145–152.
[11] Stoner, R. J., and Maris, H. J., 1993, "Kapitza Conductance and Heat Flow Between Solids at Temperatures From 50 to 300 K," Phys. Rev. B, **48**, pp. 16373–16387.
[12] Young, D. A., and Maris, H. J., 1989, "Lattice-Dynamical Calculation of the Kapitza Resistance Between FCC Lattices," Phys. Rev. B, **40**, pp. 3685–3693.
[13] Zhao, H., and Freund, J. B., 2005, "Lattice-dynamical Calculation of Phonon Scattering at Ideal Si–Ge Interfaces," J. Appl. Phys., **97**, p. 024903.
[14] Mingo, N., and Yang, L., 2003, "Phonon Transport in Nanowires Coated With

an Amorphous Material: An atomistic Green's Function Approach," Phys. Rev. B, **68**, p. 245406.
[15] Zhang, W., Fisher, T. S., and Mingo, N., 2007, "Simulation of Interfacial Phonon Transport in Si–Ge Heterostructures Using an Atomistic Green's Function Method," ASME J. Heat Transfer, **129**, pp. 483–491.
[16] Zhao, H., and Freund, J. B., 2009, "Phonon Scattering at a Rough Interface Between Two FCC Lattices," J. Appl. Phys., **105**, p. 013515.
[17] Choi, S.-H., and Maruyama, S., 2005, "Thermal Boundary Resistance at an Epitaxially Perfect Interface of Thin Films," Int. J. Therm. Sci., **44**, pp. 547–558.
[18] Maiti, A., Mahan, G. D., and Pantelides, S. T., 1997, "Dynamical Simulation of Nonequilibrium Processes—Heat Flow and the Kapitza Resistance Across Grain Boundaries," Solid State Commun., **102**, pp. 517–521.
[19] Liang, X.-G., Yue, B. J., and Maruyama, S., 2007, "Simulation of Interface Structure Influence on In-Plane Thermal Conductivity of Ar-Like Nano Films by Molecular Dynamics," J. Enhanced Heat Transfer, **14**, pp. 233–242.
[20] Schelling, P. K., Phillpot, S. R., and Keblinski, P., 2004, "Kapitza Conductance and Phonon Scattering at Grain Boundaries by Simulation," J. Appl. Phys., **95**, pp. 6082–6091.
[21] Twu, C. J., and Ho, J. R., 2003, "Molecular Dynamics Study of Energy Flow and the Kaptiza Conductance Across an Interface With Iimperfection Formed by Two Dielectric Thin Films," Phys. Rev. B, **67**, p. 205422.
[22] Schelling, P. K., Phillpot, S. R., and Keblinski, P., 2002, "Phonon Wave-Packet Dynamics at Semiconductor Interfaces by Molecular_Dynamics Simulation," Appl. Phys. Lett., **80**, pp. 2484–2486.
[23] Stevens, R. J., Zhigilei, L. V., and Norris, P. M., 2007, "Effects of Temperature and Disorder on Thermal Boundary Conductance at Solid-Solid Interfaces: Non-Equilibrium Molecular Dynamics Simulations," Int. J. Heat Mass Transfer, **50**, pp. 3977–3989.
[24] Hu, M., Shenogin, S., and Keblinski, P., 2007, "Molecular Dynamics Simulation of Interfacial Thermal Conductance between Silicon and Amorphous Polyethylene," Appl. Phys. Lett., **91**, p. 241910.
[25] Bazant, M. Z., Kaxiras, E., and Justo, J. F., 1997, "Environment Dependent Interatomic Potential for Bulk Silicon," Phys. Rev. B, **56**, pp. 8542–8552.
[26] Sun, L., Le, C., Faisal, S., and Murthy, J. Y., 2007, "Performance of a Parallel Molecular Dynamics Program for Computation of Thermal Properties," Numer. Heat Transfer, Part B, **51**, pp. 315–331.
[27] McGaughey, A. J. H., and Kaviany, M., 2005, "Observation and Description of Phonon Interaction in Molecular Dynamics Simulations," Phys. Rev. B, **71**, p. 184305.
[28] Sun, L., and Murthy, J. Y., 2006, "Domain Size Effects in Molecular Dynamics Simulation of Phonon Transport in Silicon," Appl. Phys. Lett., **89**, p. 171919.
[29] Simkin, M. V., and Mahan, G. D., 2000, "Minimum Thermal Conductivity of Super-Lattices," Phys. Rev. Lett., **84**, pp. 927–930.
[30] Daly, B. C., and Maris, H. J., 2002, "Calculation of the Thermal Conductivity of Superlattices by Molecular Dynamics Simulation," Physica B, **316–317**, pp. 247–249.
[31] Schelling, P. K., and Phillpot, S. R., 2003, "Multiscale Simulation of Phonon Transport in Superlattices," J. Appl. Phys., **93**, pp. 5377–5387.

Critical Heat Flux (CHF) of Subcooled Flow Boiling of Alumina Nanofluids in a Horizontal Microchannel

Saeid Vafaei

Dongsheng Wen
e-mail: d.wen@qmul.ac.uk

School of Engineering and Materials Science,
Queen Mary University of London,
E1 4NS, London, UK

This work investigates subcooled flow boiling of aqueous based alumina nanofluids in 510 μm single microchannels with a focus on the effect of nanoparticles on the critical heat flux. The surface temperature distribution along the pipe, the inlet and outlet pressures and temperatures are measured simultaneously for different concentrations of alumina nanofluids and de-ionized water. To minimize the effect of nanoparticle depositions, all nanofluid experiments are performed on fresh microchannels. The experiment shows an increase of ~51% in the critical heat flux under very low nanoparticle concentrations (0.1 vol %). Different burnout characteristics are observed between water and nanofluids, as well as different pressure and temperature fluctuations and flow pattern development during the stable boiling period. Detailed observations of the boiling surface show that nanoparticle deposition and a subsequent modification of the boiling surface are common features associated with nanofluids, which should be responsible for the different boiling behaviors of nanofluids. [DOI: 10.1115/1.4001629]

Keywords: flow boiling, microchannel, nanofluids, critical heat flux, burnout

1 Introduction

Microchannel cooling systems have been widely investigated and explored in recent years due to their potential wide applications in many fields, including space communication, microprocessors, and electronic devices. For instance, for the cooling of high power and density computer chips, the cooling system needs to keep the chip temperature below 85°C despite a high power density. Liquid cooling with or without phase change is proposed to meet such a requirement. Compared with single-phase liquid cooling, cooling using phase change (flow boiling) can achieve a much higher heat-removal rate under a similar flow rate while maintaining a relatively constant surface temperature determined by the saturation properties of the cooling fluid.

Flow boiling in conventional-sized channels has been widely investigated in the past few decades. Downscaling and development of a microchannel cooling system require detailed understanding of the effects of dominant phenomena in a single microchannel, such as interfacial interaction and surface condition [1], channel geometry and size [1,2], temperature and pressure fluctuations [3,4], mass flow rate and critical heat flux (CHF) [5–7], heat transfer coefficient and pressure drop [5,8–13], bubble generation frequency and flow pattern development [2,3,8,9,11,14], onset of nucleate boiling (ONB), and onset of flow instability (OFI) [13]. Compared with what happens in large channels, the effects and relation between some of these phenomena are different as the channel size decreases, which consequently causes different flow and heat transfer behaviors [15]. As can be seen from literature, downscaling of the channel size and employing new heat transfer fluids make flow boiling more complicated.

Recent advances in nanotechnology have promoted a rapid development in nanofluids, i.e., liquid suspensions of nanoparticle solids including particles, nanofibers, and nanotubes. Such materials were first brought into attention approximately a decade ago when their enhanced thermal conductivity was reported. While the original idea of using thermal nanofluids was to enhance thermal conductivities of some typical heat transfer fluids, including water, mineral oil, and ethylene glycol, the inclusion of nanoparticles for boiling heat transfer has been found more profound than that of mean thermal conductivity [16] and single-phase convective heat transfer [17–19].

For cooling systems based on phase change mechanisms, the safe operation of the system is limited by the critical heat flux, which is the upper limit of heat removal without incurring a serious surface temperature jump. Beyond that, a vapor blanket or local dryout will occur on the surface, which will prevent further direct contact of liquid. As a result, sudden temperature rise will occur due to the poor thermal conductivity of vapor. This phenomenon could happen in subcooled as well as in saturated boiling conditions. It is of vital importance to predict the critical heat flux in small channels.

The effects of nanoparticles on a critical heat flux of pool boiling have been investigated in the past few years [20–24]. Many of these experiments reported that small concentrations of nanoparticles can significantly increase the value of CHF, which was generally ascribed to the effect of heating surface modification due to the sedimentation of nanoparticles. For instance, Kim et al. [25] observed a layer of nanoparticles building up on the heating surface under pool boiling conditions, likely formed during the evaporation of microlayers beneath vapor bubbles at the solid surface. Consequently, the wettability of the heating surface was improved, as shown by a reduction of the contact angle of stationary droplets. By using Young's equation, they suggested that the enhancement in surface wettability was caused by the increase in adhesion tension and surface roughness. Kim et al. [25] also suggested that the reduction in the contact angle was responsible for a decrease in nucleate boiling heat transfer due to a possible reduction in nucleation site density based on the Wang and Dhir correlation [26]; however, this reason can be weakened by a potential increase in the number of microcavities per unit surface due to nanoparticle depositions.

Contributed by the Heat Transfer Division of ASME for publication in the JOURNAL OF HEAT TRANSFER. Manuscript received October 11, 2009; final manuscript received April 1, 2010; published online July 29, 2010. Assoc. Editor: Louis C. Chow.

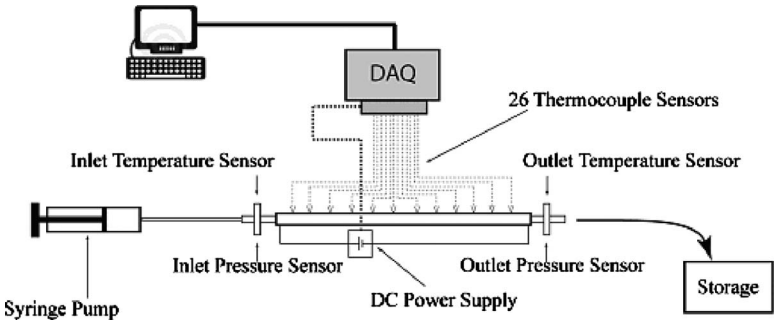

Fig. 1 Schematic of experimental setup

For the critical heat flux of flow boiling of nanofluids, only very limited studies have been conducted, which are all in conventional-sized channels. Kim et al. [27] studied nanofluid flow boiling in a stainless steel tube with an internal diameter of 8.7 mm. The flow boiling critical heat flux was found to increase up to 30% at a 0.01% volume concentration of alumina nanoparticles. The observation showed that various parameters relevant to the two phase flow and heat transfer of alumina nanofluids, such as boiling point, surface tension, thermal conductivity, and viscosity, were found virtually identical to those of pure water. Surface roughness and surface wettability are the two most important parameters that might be affected by the presence of nanoparticles on the surface. Kim et al. [28] measured the droplet contact angle and surface roughness inside the stainless steel pipe after testing with water and different concentrations of alumina nanofluids and observed that the droplet contact angle was reduced from 83 deg to 20 deg, and the average surface roughness, R_a, was changed from 2.15 μm to 1.72 μm after nanofluids experiments. It appeared that the variation in surface roughness and, consequently, nucleate site density was not much affected. The main reason for the CHF enhancement was the improvement of surface wettability. It was also claimed by the authors that the use of nanofluids mitigated the propagation of hot spots that could explain why burnout was more localized compared with water, which might be caused by high surface wettability as a result of the deposition of nanoparticles on the heating surface [27].

Aiming to apply nanofluids to microelectronic and mechanical systems (MEMS) to meet the increasing demands for advanced cooling, this work investigated the critical heat flux of subcooled flow boiling of aqueous alumina nanofluids in single microchannels. Our initial tests showed that the morphology of the boiling surface changed each time after boiling with nanofluids, which should be a major reason for the inconsistence of boiling heat transfer data reported in the literature. To avoid such boiling surface contamination by nanofluids, a number of microchannels were then constructed. Fresh microchannels were used for each concentration of nanofluids in order to establish a solid comparison with that of pure liquid. A detailed characterization of particles and the solid surface was conducted to reveal mechanisms, as detailed below.

2 Experimental Setup

The microchannel experimental system constructed for this work is an open loop, which consisted of a syringe pump, a microchannel, a heating and insulation unit, a storage tank, and a data acquisition (DAQ) system for power, pressure, and temperature measurements. The microchannels were made of stainless steel with internal diameter of 510 μm, wall thickness of 160 μm, and length of 306 mm. For each nanofluid concentration, a different stainless steel microchannel was used. The microchannel was insulated by a thick layer of Armaflex insulator and heated electrically through a variable DC power source, which provided a uniform heat flux over the test section. Twenty-six K-type thermocouples with tip diameter of 0.2 mm were installed evenly along the surface of the microchannel to obtain the surface temperature distribution. Two thermocouples were used to measure the inlet and outlet fluid temperatures. Two cross unions were connected to the inlet and the outlet of the microchannel to supply the liquid passage and spaces for temperature and pressure sensors (see Fig. 1). Pressure sensors were four active piezoresistive bridge devices in the range of 0–100 psi. Simultaneous temperature and pressure signals were recorded by the DAQ system through and controlled by a LABVIEW program. A low pass filter was installed to eliminate noises from the surroundings and power supply.

Subcooled fluids were supplied by a constant flow rate syringe pump and collected by the storage tank with a vent to the atmosphere. For flow boiling in the normal boiling regime, the surface temperature is normally a few degrees higher than the saturation temperature. However, when critical heat flux occurs, the surface temperature jumps rapidly to reach a very high temperature that leads to burnout. In literature, peak surface temperature values of 150–200°C are generally used. In our experiments, 150°C was set as the maximum surface temperature value that we chose to define the critical heat flux. The power system was designed to stop the heating when the maximum temperature along the channel was higher than 150°C to protect the tube and insulation. Heat loss is defined as the difference in the input power and the enthalpy increase in the fluids under a single-phase flow condition just before boiling as

$$Q_{\mathrm{HL}}\% = \frac{VI - \dot{m}c_p(T_{\mathrm{out}} - T_{\mathrm{in}})}{VI} \times 100 \tag{1}$$

The measured heat loss under current working conditions was less than 10%.

De-ionized water and alumina-water-based nanofluid were used as working fluids. Nanofluids were formulated by a two-step method by dispersing commercial alumina nanoparticles of average particle size of 25 nm (see Fig. 2) into the base liquid, deionized water, with the aid of an ultrasonic bath at three concentrations of 0.001 vol %, 0.01 vol %, and 0.1 vol %. To avoid other impurity influences, no surfactant or dispersants were introduced into the nanofluids. The formulated nanofluids exhibit relatively good stability without visual sedimentation for a couple of hours, which is sufficiently long for the experiments. To mitigate particle agglomerations, nanofluids were homogenized before each experiment. The experiments were conducted under low mass flow rates at a range of 600–1650 $\mathrm{kg/m^2\,s}$ and with low exit vapor quality, i.e., in the range of -0.20 and 0.18 within the experimental range.

During the experiments, the input heat flux was increased steadily until the maximum surface temperature of the microchannel reached the preset value, where the input power was protectively cut off. This is always accompanied by a sudden rapid increase in surface temperature. The input power that induces this sudden surface temperature is defined as the critical heat flux in this work.

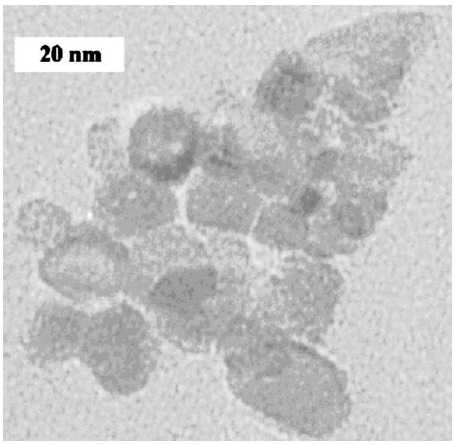

Fig. 2 Transmission electron microscopy (TEM) picture of alumina nanoparticles

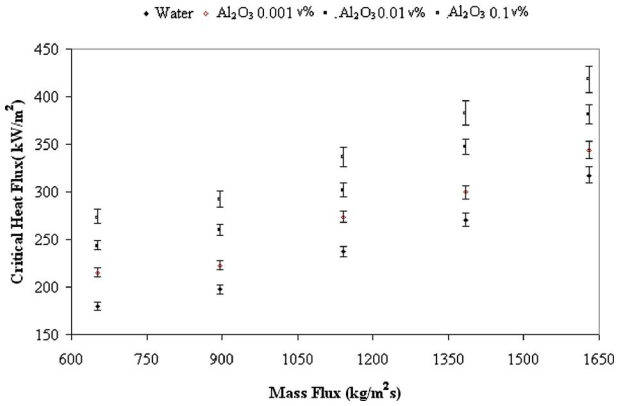

Fig. 3 Variation in the critical heat flux with mass flux for deionized water and 0.001–0.1 vol % alumina nanofluids

3 Results and Discussions

A large number of experiments were performed in this study. Some initial results revealed that the repeatability of the flow boiling experiments with nanofluids was difficult to establish. The results varied, typically within the range of 10%, each time when performing experiments in the same microchannel using identical nanofluids, whereas for water the experimental results are very repeatable. Further analysis by scanning electron microscopy (SEM) showed that the morphology of the boiling surface changed each time after boiling with nanofluids, which was caused by the trapping of nanoparticles onto the boiling surface. The degree of surface modification is affected by the relative size of nanoparticles, the boiling surface roughness, the stability of nanofluids, the surface properties, and the interactions of nanoparticles with the boiling surface, as well as the duration of nanofluid usage. Due to the sensitivity of boiling heat transfer to boiling surface characteristics, it is unsurprising that different experimental values were observed in the experiments even for the same nanofluid boiling in the same channel. Consequently, it makes the comparison of the effect of nanoparticles difficult to establish. Our other tests show that even for very stable nanofluids, boiling surface modification was also still observed.

Such an observation is important in guiding us to minimize the influence of surface morphology change and to design a number of microchannels to achieve a reliable comparison. More importantly, it may also help us understand the inconsistence reported for boiling heat transfer with nanofluids in literature. For instance, it has been widely reported that many different results were observed for nanofluids under boiling conditions, and the results were very inconsistent even for the same nanoparticles under similar experimental conditions [21,22,29–31]. Our initial experiments suggested that for experiments with nanofluids, the boiling surface would be affected by the number and frequency of the usage of the boiling surface. Consequently, different experimental results may be obtained each time, which might be one of the main reasons for the inconsistence reported in boiling heat transfer in literature.

To establish a reliable comparison of a critical heat flux of different fluids, a number of microchannels were constructed in this work in order to reduce the effect of boiling surface contamination by nanofluids. Fresh microchannels were used for each concentration of nanofluids, and the duration of nanofluid usage was kept the same in the comparison. Through such a way, the effect of boiling surface modification was reduced to the minimum. These results are presented below.

Figure 3 shows the variation in critical heat flux with mass flow rate and nanoparticle concentrations. It clearly shows a nearly linear increase in CHF with the increase in mass flow rate. Under the same mass flux, the critical heat flux increases as the nanofluid concentration increases. In addition, the maximum critical heat flux enhancement due to the increase in concentration happens at the lowest mass flux (651.84 kg/m^2 s). The same happens in conventional-sized channels [27,28]. The experiments reveal that a remarkable critical heat flux increase can be achieved for very dilute alumina nanofluids in a single microchannel. For instance, the average CHF increases of 10.73%, 28.25%, and 40.94% are obtained for particle volume concentrations of 0.001 vol %, 0.01 vol %, and 0.1 vol %, respectively, at a mass flow rate of 1385.18 kg/m^2 s. Within the whole experimental range, the increase in critical heat flux falls within a band of 8–51%. Figure 3 also shows that the enhancement of the critical heat flux is nonlinear with the particle concentration.

As shortly reviewed in Sec. 1, many studies have been conducted on the critical heat flux in the past a few decades, with a focus on the conventional-sized channels under high mass flow rates, i.e., $>10^4$ kg/m^2 s, aiming for different applications. The critical heat flux behavior for small channels under low mass flow rates is relatively little reported, and the results are still inconclusive regarding the influence of the channel size, the subcooling, and the mass flow rate. The scenario becomes more complicated when considering the effects of nanoparticles. Under very similar conditions of the current work, Roday et al. [7] investigated the critical heat flux of pure water in a single stainless steel tube with an internal diameter of 427 μm. They found that critical heat flux values increased with increasing mass flow rates with typical values of 100–300 kW/m^2 for mass flow rates smaller than 1600 kg/m^2 s. They also studied the effect of the inlet subcooling on the critical heat flux and observed that for a higher inlet subcooling, the critical heat flux slightly decreased as the inlet subcooling decreases; however, a reverse trend was observed for boiling at lower subcoolings. A comparison of different correlations for the critical heat flux for small channels under subcooled conditions was studied by Hall and Mudawar [32], and similar values were reported. These results are consistent with the critical heat flux behavior of pure water of the current work. The general trend of the effect of nanofluids on the critical heat flux enhancement of the current work is similar to that of Kim et al. [27,28] for large channels with diameters of 8.7 mm and 5.45 mm.

In all experiments, steady state boiling scenarios were established just before the occurrence of the critical heat flux. Similar to what happens in a microchannel for pure liquid, nanofluids show a regular pattern of pressure and temperature variations. Figures 4 and 5 show the variation in pressure and temperature at the channel inlet and outlet and the temperature of the hottest point of the channel, with heat power and time, for a nanoparticle concentration of 0.01 vol %, where the mass flux is 1629.62 kg/m^2 s and the average heat flux is 247 kW/m^2. In the

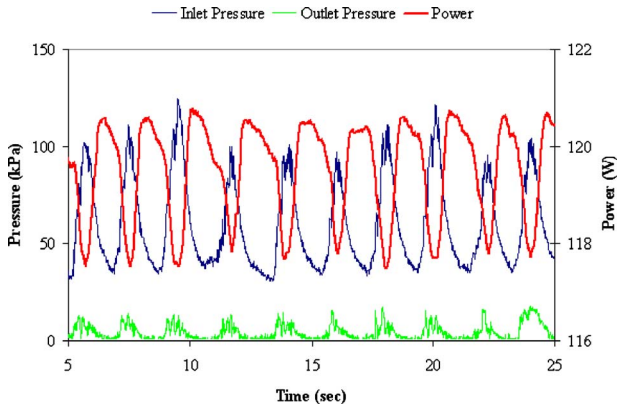

Fig. 4 Variation in pressure and heat power with time at a mass flux of 1629.62 kg/m^2 s for 0.01 vol % alumina nanofluid

experiments, the heat flux was supplied by a DC power supply under a constant voltage mode. The variation in input power was assumed to be the result of resistance variation caused by the temperature effect. These figures show that pressure and temperature fluctuations are in phase, but there is a phase shift between power and pressure. A previous detailed investigation of flow boiling in 2×1 mm^2 vertical channels [9] revealed that rapid growth of a confined bubble was triggered when a macroscopic nucleus was pressed against the heated wall of the channel. Such growth pushed a slug of liquid along the channel, causing a pressure pulse that propagated the full length of the channel, peaking as the slug left the channel. The pulse was accompanied by a traveling fluctuation in wall temperature. The current experiments also shows regular patterns of pressure and temperature signals caused by nanofluids, which may reveal cyclic boiling events (nucleation, confinement, confined bubble growth, liquid slug, etc) occurring inside the microchannel. The direct visual observation by eye at the channel outlet shows an intermittent flow of vapor and liquid, suggesting a similar confined bubble flow pattern inside the channel. However, a quantitative analysis of the flow regime at the outlet was not conducted in the experiments. Figures 4 and 5 also show that the magnitude of the pressure variation is large, reaching a peak value of ~120 kPa, which is larger than the pressure drop along the tube. Such a large pressure variation would induce a large variation in saturation temperature, which interplays with flow regime variations that affect boiling mechanisms. A detailed visualization study at the tube outlet, synchronized with pressure and temperature signals, is being conducted toward a better understanding of CHF mechanisms by nanofluids.

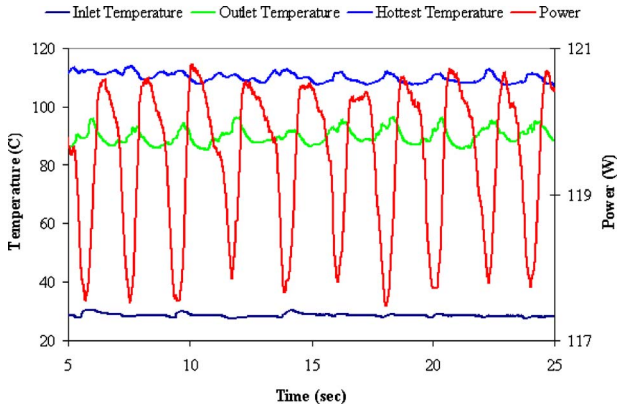

Fig. 5 Variation in temperature and heat power with time at a mass flux of 1629.62 kg/m^2 s for 0.01 vol % alumina nanofluid

Figure 6 shows the variation in inlet and outlet pressures with time for water and different concentrations of nanofluids at a mass flux of 1629.62 kg/m^2 s. The introduction of nanoparticles changes the pressure signals significantly, but the influence is not monotonic. For pure water flow, the peak pressure pulse is maintained at a regular value of ~150 kPa, similar to that of the lowest particle concentration of 0.001 vol %. However, a large reduction in pressure pulse (with peak values about 100 kPa) is observed at a particle concentration of 0.01 vol %, while some pressure peak values are found to exceed 200 kPa for a particle concentration of 0.1 vol %. The variation in pressure peak values is also the largest for the highest concentration, 0.1 vol %. A reverse trend of the effect of nanoparticle concentration is observed for the frequency of pressure pulses. Our previous study shows that pressure pulses are related to the growth of vapor bubbles inside the channel and are affected by the duration and frequency of the confined bubble growth [9,33]. In Fig. 6, it is apparent that

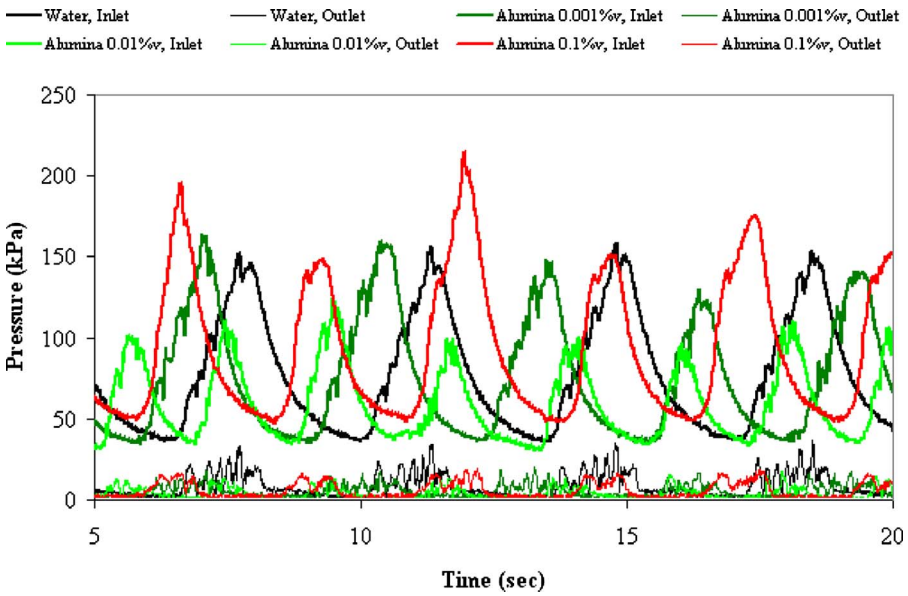

Fig. 6 Variation in pressure with time for pure water and different concentrations of alumina nanofluids at a mass flow rate of 1629.62 kg/m^2 s and an average heat flux of 246.14 kW/m^2

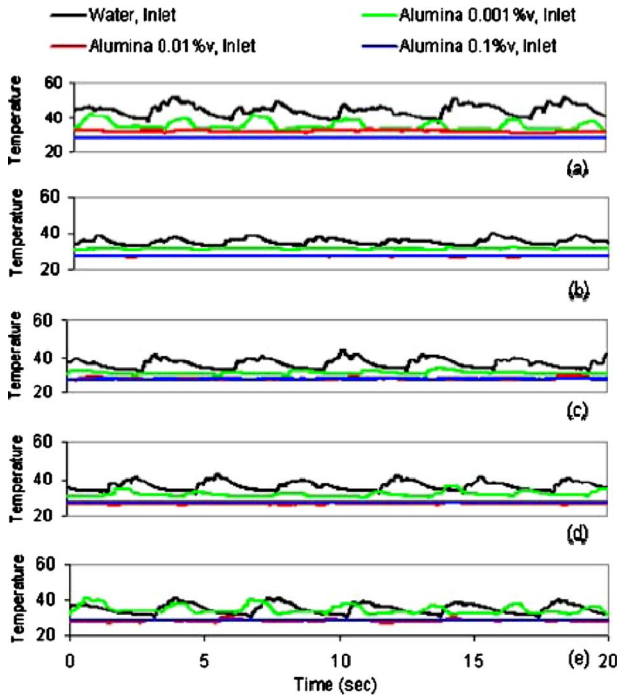

Fig. 7 Variation in inlet temperature of water and different concentrations of nanofluids at average heat flux of 246.14 kW/m^2 and mass fluxes of (*a*) 651.84 kg/m^2 s, (*b*) 896.29 kg/m^2 s, (*c*) 1140.73 kg/m^2 s, (*d*) 1385.18 kg/m^2 s, and (*e*) 1629.62 kg/m^2 s

the introduction of nanoparticles changes the bubble dynamics significantly. In general, more bubbles with shorter bubble lifetimes are observed for boiling in nanofluids. As for flow boiling in microchannels, CHF is usually associated with local dryout underneath a confined bubble; the reduced bubble growth time in nanofluids thus reduces the possibility of local dryout, which may contribute to an increase in CHF. The causes of this change in bubble dynamics are still unclear but are likely through the modification of the boiling surface, especially the interfacial and wetting properties, or a self-organization of nanoparticles at the triple line regime [34]. Compared with the influence of particles on the thermal conductivity, its influence on the interfacial surface tension and wettability is more pronounced at low particle concentrations.

Figure 7 shows the variation in inlet temperature with time and alumina concentrations before the occurrence of CHF. It shows a general trend of reduction in the temperature fluctuations at the inlet of the microchannel with the increase in mass flow rates. Under all mass flow rate conditions, the inclusion of nanoparticle reduces the value and magnitude of inlet temperature fluctuations; nearly constant inlet temperatures are observed for nanofluids at the concentrations of 0.01 vol % and 0.1 vol %. The slight modification of thermophysical properties such as thermal conductivity, specific heat, and density by nanofluids should not be responsible for such a large difference. The cyclic variations in the inlet temperature of pure water are believed to be associated with the reverse flow of liquid. Such a behavior is common for flow boiling in microchannels, especially for fluids defined as having "high compressibility" [9,10,15], i.e., usual fluids without the degassing process. The visual observation of flow boiling in a vertical 2×1 mm^2 rectangular channel clearly showed that the liquid at the entrance regime was pushed back by growing confined bubbles in both directions under high compressibility conditions, accompanied by a traveling pressure and temperature pulses. However, for fluids with "low compressibility," i.e., fluids with a proper degassing process, little reverse flow was observed [9,15]. If similar events occur in nanofluids, it may imply that the inclusion of

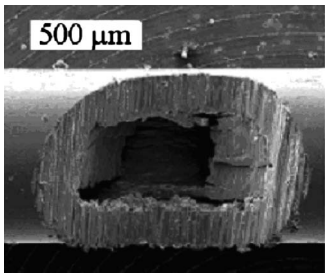

Fig. 8 Test section of the stainless steel microchannel

nanoparticles not only changes the bubble formation and frequency, as suggested by Fig. 6, but may also affect the compressibility of the fluid, as evidenced by relatively smooth inlet temperature profiles, i.e., little reverse flow occurring there. Such a modification of compressibility toward the inlet could be caused by the nanofluid preparation process, where an ultrasonification process is applied to nanofluids prior to experiments to mitigate nanoparticle agglomerations, which may modify the level of impurity gas in the liquid. Such a modification of bubble dynamics by nanoparticles would affect the flow regime development, and the pressure and temperature fluctuations, together with the modification of the boiling surface by particle-surface interactions, would influence the boiling mechanism significantly.

To investigate the effect of nanoparticle deposition on the heating surface, the stainless steel microchannel is grooved (see Fig. 8) after running with de-ionized water and nanofluids. The outlet and the inlet of the heating tube substrate were examined by SEM (see Figs. 9 and 10). Figure 9 shows the variation in heating surface in the vicinity of the outlet after running with de-ionized water and nanofluids with 0.1 vol %, 0.01 vol %, and 0.001 vol % of alumina. It clearly shows that as the nanofluid concentration increases, more particles appeared onto the surface, forming lay-

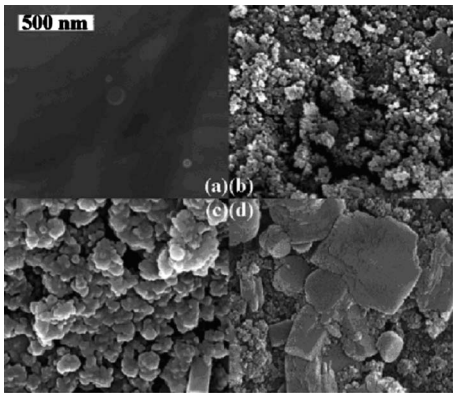

Fig. 9 SEM pictures of the test section of stainless steel microchannel close to the outlet after experiments with (*a*) de-ionized water, (*b*) 0.001 vol % alumina, (*c*) 0.01 vol % alumina, and (*d*) 0.1 vol % alumina

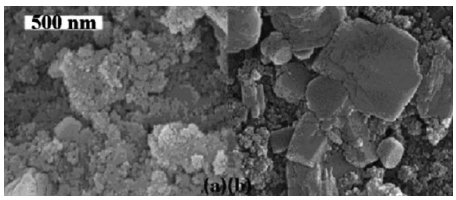

Fig. 10 SEM pictures of the test section of stainless steel microchannel after experiment with 0.1 vol % alumina at the (*a*) inlet and (*b*) outlet of the microchannel

ers of porous structures, being thicker and more condensed for higher concentrations. As a result, the surface wettability, homogeneity, and roughness of the boiling surface are changed. In large channels, the variation in surface roughness is reported to be not much compared with the variation in surface wettability [28]. Figure 10 demonstrates the difference between deposited nanoparticles at the inlet and the outlet of the heating surface after running with 0.1 vol % alumina nanofluids. The figure shows that deposited nanoparticles at the outlet are thicker with larger agglomerations since the temperature of the heating surface at the outlet is higher. For the same reason, the deposition rate at the outlet of the tube might be high. It is of note that the current method of nanofluid formulation is similar to many others [16,27,28]; such an observation may be extended to their situations and be contributed to the explanation of different results. It is worthwhile to mention that although the deposition occurs in the channel, the thickness of such deposition is still small, only a few hundred nanometers. Compared with an inner diameter of 510 μm tube, the modification of the mass flow rate is negligible, which rules out its possibility as a possible reason responsible for the observed CHF increase.

The thin porous layer of deposited nanoparticles on the heating surface would change not only the affinity of the working fluid for the substrate, but also the burnout characteristics. It was observed in the experiment that the consequences of the burnout of the heating surface, running with water and nanofluids, are different. Similar to the observation by Kim et al. [27], a complete azimuthal failure may occur for water, while a pinhole type of pipe failure is usually observed for nanofluid runs. It suggests that the deposition of nanoparticles may generate some hot spots, or prevent the spreading of the dryout underneath growing bubbles, which would consequently cause a pinhole type of failure.

4 Conclusion

The CHF of subcooled flow boiling of aqueous based nanofluids in a 510 μm single microchannel was investigated in this work under low mass flow rate conditions (600–1650 kg/m^2 s). The effect of nanoparticles was revealed by conducting all experiments on fresh microchannels to minimize the effect of particle depositions. It was found that the critical heat flux of both de-ionized water and alumina nanofluids increased with increasing mass flow rates under the condition of this work. Compared with the critical heat flux value of de-ionized water, a large increase in critical heat flux was obtained under very low particle concentrations, i.e., ~51% for 0.1% nanoparticle in volume. Different burnout characteristics were observed between water and nanofluids, as well as different pressure and temperature fluctuations and flow pattern development during the stable boiling period. The regular pressure and temperature fluctuations suggested a confined bubble flow occurring inside the microchannel for both water and nanofluids. A detailed observation of the boiling surface shows that nanoparticle deposition and a subsequent modification of the boiling surface are common features associated with nanofluids, which should be responsible for the increase in CHF in this work, as well as other different boiling behaviors of nanofluids in literature.

Acknowledgment

The authors would like to extend their thanks to EPSRC for the financial support under Grant No. EP/E065449/1, and Dr. Z. Luklinska of the Nanovision Center of Queen Mary University of London for nanoparticle characterization.

Nomenclature

c_p = specific heat (J/kg K)
I = applied ampere (A)
$\dot{m}$ = mass flow rate (kg/s)
Q_{HL} = heat loss power (W)
T = temperature (K)
V = applied voltage (V)

References

[1] Zhang, L., Wang, E. N., Goodson, K. E., and Kenny, T. W., 2005, "Phase Change Phenomena in Silicon Microchannels," Int. J. Heat Mass Transfer, **48**, pp. 1572–1582.
[2] Lee, P. C., and Pan, C., 2008, "Boiling Heat Transfer and Two-Phase Flow of Water in a Single Shallow Microchannel With a Uniform or Diverging Cross Section," J. Micromech. Microeng., **18**, p. 025005.
[3] Huh, C., Kim, J., and Kim, M. H., 2007, "Flow Pattern Transition Instability During Flow Boiling in a Single Microchannel," Int. J. Heat Mass Transfer, **50**(5–6), pp. 1049–1060.
[4] Wang, G., and Cheng, P., 2008, "An Experimental Study of Flow Boiling Instability in a Single Microchannel," Int. Commun. Heat Mass Transfer, **35**, pp. 1229–1234.
[5] Huh, C., and Kim, M. H., 2006, "An Experimental Investigation of Flow Boiling in an Asymmetrically Heated Rectangular Microchannel," Exp. Therm. Fluid Sci., **30**, pp. 775–784.
[6] Wojtan, L., Revellin, R., and Thome, J. R., 2006, "Investigation of Saturated Critical Heat Flux in a Single, Uniformly Heated Microchannel," Exp. Therm. Fluid Sci., **30**, pp. 765–774.
[7] Roday, A. P., Borca-Tasçiuc, T., and Jensen, M. K., 2008, "The Critical Heat Flux Condition With Water in a Uniformly Heated Microtube," ASME J. Heat Transfer, **130**, p. 012901.
[8] Shiferaw, D., Karayiannis, T. G., and Kenning, D. B. R., 2009, "Flow Boiling in a 1.1 mm Tube With R134a: Experimental Results and Comparison With Model," Int. J. Therm. Sci., **48**, pp. 331–341.
[9] Wen, D. S., Yan, Y., and Kenning, D. B. R., 2004, "Saturated Flow Boiling of Water in a Narrow Channel: Time-Averaged Heat Transfer Coefficients and Correlations," Appl. Therm. Eng., **24**, pp. 1207–1223.
[10] Wen, D. S., and Kenning, D. B. R., 2004, "Two-Phase Pressure Drop of Water During Flow Boiling in a Vertical Narrow Channel," Exp. Therm. Fluid Sci., **28**, pp. 131–138.
[11] Sobierska, E., Kulenovic, R., and Mertz, R., 2007, "Heat Transfer Mechanism and Flow Pattern During Flow Boiling of Water in a Vertical Narrow Channel Experimental Results," Int. J. Therm. Sci., **46**, pp. 1172–1181.
[12] Sobierska, E., Kulenovic, R., Mertz, R., and Groll, M., 2006, "Experimental Results of Flow Boiling of Water in a Vertical Microchannel," Exp. Therm. Fluid Sci., **31**, pp. 111–119.
[13] Martin-Callizo, C., Palm, B., and Owhaib, W., 2007, "Subcooled Flow Boiling of R-134a in Vertical Channels of Small Diameter," Int. J. Multiphase Flow, **33**, pp. 822–832.
[14] Brutin, D., Topin, F., and Tadrist, L., 2003, "Experimental Study of Unsteady Convective Boiling in Heated Minichannels," Int. J. Heat Mass Transfer, **46**, pp. 2957–2965.
[15] Kenning, D. B. R., and Yan, Y., 2001, "Saturated Flow Boiling of Water in a Narrow Channel: Experimental Investigation of Local Phenomena," Chem. Eng. Res. Des., **79**(4), pp. 425–436.
[16] Wen, D. S., Lin, G., Vafaei, S., and Zhang, K., 2009, "Review of Nanofluids for Heat Transfer Applications," Particuology, **7**(2), pp. 141–150.
[17] Wen, D. S., Zhang, D. S., and He, Y. R., 2009, "Flow and Migration of Nanoparticles Through a Single Channel," Heat and Mass Transfer, **45**(8), pp. 1061–1067.
[18] Daungthongsuk, W., and Wongwises, S., 2007, "A Critical Review of Convective Heat Transfer of Nanofluids," Renewable Sustainable Energy Rev., **11**, pp. 797–817.
[19] Lee, J., and Mudawar, I., 2007, "Assessment of the Effectiveness of Nanofluids for Single-Phase and Two-Phase Heat Transfer in Micro-Channels," Int. J. Heat Mass Transfer, **50**, pp. 452–463.
[20] You, S. M., Kim, J., and Kim, K. H., 2003, "Effect of Nanoparticles on Critical Heat Flux of Water in Pool Boiling Heat Transfer," Appl. Phys. Lett., **83**(16), pp. 3374–3376.
[21] Das, S. K., Putra, N., and Roetzel, W., 2003, "Pool Boiling Characteristics of Nanofluids," Int. J. Heat Mass Transfer, **46**, pp. 851–862.
[22] Bang, I. C., and Chang, S. H., 2005, "Boiling Heat Transfer Performance and Phenomena of Al_2O_3 Water Nano-Fluids From a Plain Surface in a Pool," Int. J. Heat Mass Transfer, **48**, pp. 2407–2419.
[23] Kim, H. D., Kim, J., and Kim, M. H., 2007, "Experimental Studies on CHF Characteristics of Nanofluids at Pool Boiling," Int. J. Multiphase Flow, **33**, pp. 691–706.
[24] Kim, S. J., Bang, I. C., and Buongiorno, J., 2006, "Effects of Nanoparticle Deposition on Surface Wettability Influencing Boiling Heat Transfer in Nanofluids," Appl. Phys. Lett., **89**, p. 153107.
[25] Kim, S. J., Bang, I. C., Buongiorno, J., and Hu, L. W., 2007, "Surface Wettability Change During Pool Boiling of Nanofluids and Its Effect on Critical Heat Flux," Int. J. Heat Mass Transfer, **50**, pp. 4105–4116.
[26] Wang, C. H., and Dhir, V. K., 1993, "Effect of Surface Wettability on Active Nucleation Site Density During Pool Boiling of Water on a Vertical Surface," ASME J. Heat Transfer, **115**, pp. 659–669.
[27] Kim, S. J., Buongiorno, J., and Hu, L. W., 2008, "Alumina Nanoparticles Enhance the Flow Boiling Critical Heat Flux of Water at Low Pressure," ASME J. Heat Transfer, **130**(4), p. 044501.
[28] Kim, S. J., McKrell, T., Buongiorno, J., and Hu, L. W., 2009, "Experimental Study of Flow Critical Heat Flux in Alumina-Water, Zinc-Oxide-Water, and

Diamond-Water Nanofluids," ASME J. Heat Transfer, **131**, p. 043204.
[29] Vassallo, P., Kumar, R., and D'Amico, S., 2004, "Pool Boiling Heat Transfer Experiments in Silica–Water Nano-Fluids," Int. J. Heat Mass Transfer, **47**, pp. 407–411.
[30] Wen, D. S., 2008, "On the Role of Structural Disjoining Pressure to Boiling Heat Transfer With Thermal Nanofluids," Journal of Nanoparticle Research, **10**, pp. 1129–1140.
[31] Wen, D. S., Ding, Y., and Williams, R., 2006, "Pool Boiling Heat Transfer of Aqueous Based TiO_2 Nanofluids," J. Enhanced Heat Transfer, **13**, pp. 231–244.
[32] Hall, D., and Mudawar, I., 2000, "Critical Heat Flux CHF for Water Flow in Tubes—II. Subcooled CHF Correlations," Int. J. Heat Mass Transfer, **43**, pp. 2605–2640.
[33] Kenning, D. B. R., Wen, D. S., Das, K. S., and Wilson, K. S., 2006, "Confined Growth of a Vapour Bubble in a Capillary Tube at Initially Uniform Superheat," Int. J. Heat Mass Transfer, **49**, pp. 4653–4671.
[34] Wen, D. S., 2008, "Mechanisms of Thermal Nanofluids on Enhanced Critical Heat Flux (CHF)," Int. J. Heat Mass Transfer, **51**, pp. 4958–4965.

D. Jaya Krishna
Research Scholar
Heat Transfer and Thermal Power Laboratory,
Department of Mechanical Engineering,
Indian Institute of Technology Madras,
Chennai-600 036, India

M. R. Thansekhar
Associate Professor
SSN College of Engineering,
Chennai-603110, India

S. P. Venkateshan
Professor
Heat Transfer and Thermal Power Laboratory,
Department of Mechanical Engineering,
Indian Institute of Technology Madras,
Chennai-600 036, India

Tanmay Basak
Assistant Professor
Department of Chemical Engineering,
Indian Institute of Technology Madras,
Chennai-600 036, India

Sarit K. Das[1]
Professor
Heat Transfer and Thermal Power Laboratory,
Department of Mechanical Engineering,
Indian Institute of Technology Madras,
Chennai-600 036, India
e-mail: skdas@iitm.ac.in

Natural Convection in a Partially Heat Generating Rod Bundle Inside an Enclosure

Buoyancy induced flows in a partially heat generating rod bundle enclosed inside a tall cavity are investigated. First, a detailed experimental study is carried out, and the thermal hydraulics is analyzed at different power inputs and boundary cooling rates of the enclosure. Later, a generalized non-Darcy simulation is developed using a heat generating orthotropic porous media approach and is compared with the experimental results. The results of a numerical simulation for natural convection in enclosed partially heat generating rod bundles satisfactorily predict the temperature distribution within the rod bundle. Finally, a parametric study is carried out by varying the porosity (pitch to diameter ratio of the rod bundle) of the considered enclosure for the understanding of flow physics and heat transfer in such applications. [DOI: 10.1115/1.4001610]

Keywords: natural convection, non-Darcy porous medium, heat generating rod bundle, partially heat generating enclosure

1 Introduction

The study of natural convection in heat generating rod bundles finds applications such as heat exchanger tubes, storage, or disposal of spent fuel rod bundles from nuclear power reactors encapsulated in air or helium filled canisters or storage of fibrous food grains. In order to improve the performance of energy transfer and storage, it is important to understand the thermal-hydraulic phenomena in these complex geometrical configurations.

There have been a number of studies on natural convection in rod bundles. Davis and Perona [1] carried out numerical and experimental studies for natural convection in open-ended heat generating rod bundles. A numerical study was based on one-dimensional flow through an infinite array of rods. Koenig and Buchanan [2] measured maximum temperatures in an electrically heated rod bundle for free convection associated with radial conduction and thermal radiation. Experiments were conducted with air and argon as working fluids with either open or closed ends. Driesen et al. [3] conducted a series of tests on an actual fuel rod bundle in a canister. McCann [4] developed a computer code, HYDRA–I, to treat transient three-dimensional coupled conduction, convection, and radiation in an enclosed rod bundle. The equation of motion was based on a generalization of flow through porous media, where viscous terms were retained. Gruszcynski and Viskanta [5] carried out experimental and numerical investigations for natural convection in a vertical open-ended rod bundle. The isothermal rods were arranged in a triangular fashion and were enclosed in an adiabatic cylindrical container. Keyhani et al. [6] and Arya and Keyhani [7] performed an experimental study of natural convection heat transfer in a scaled model of a sealed storage cask. Keyhani and Dalton [8] investigated experimentally natural convection in an enclosed horizontal array of electrically heated rods. The rods in the top row showed a substantial temperature increase. Haldar et al. [9] carried out experiments in two different test sections of a seven-rod bundle. The rods were arranged in a circular array with pitch to diameter ratios of 1.31 and 1.266. The one-dimensional porous medium model was developed to predict the flow rate of air. Later, Haldar [10] simulated these experiments numerically. Suresh et al. [11,12] carried out experimental and numerical studies of natural convection in a blocked subassembly of a fast breeder reactor by using liquid sodium as the heat transfer fluid. A 3D analysis was carried out by employing Darcy formulation with suitable tortuosity factors.

As the rod bundle may be approximated as an orthotropic porous medium, the literature related to anisotropic porous media is of importance for analyzing the present problem. Several comprehensive details pertaining to anisotropy, heterogeneity, and dispersion effects for porous media can be found in Nield and Bejan [13], Quintard and Whitaker [14], and Quintard et al. [15]. Royer and Flores [16] examined natural convection numerically in a rectangular enclosure filled with a heat generating, anisotropic, and heterogeneous porous medium. Parthiban and Patil [17] studied the effect of anisotropy on the onset of convection in a horizontal layer of a heat generating anisotropic porous medium. Dhanasekaran et al. [18] investigated the effects of permeability ratio and thermal conductivity ratio numerically for natural convection in a heat generating cylindrical porous enclosure. Jaya Krishna et al. [19] studied the influence of anisotropic properties on the flow behavior and heat transfer. In their numerical study, the heat gen-

[1]Corresponding author.

Contributed by the Heat Transfer Division of ASME for publication in the JOURNAL OF HEAT TRANSFER. Manuscript received May 19, 2009; final manuscript received December 29, 2009; published online July 27, 2010. Assoc. Editor: Yutaka Asako.

erating anisotropic porous media were considered, with its principal axes oriented with respect to the gravity vector.

The studies on the experimental investigation of natural convection in partially heat generating enclosed rod bundles are limited (except few studies [16–19]). Scarcer are the studies that numerically investigate the partially heat generating rod bundle by approximating as a porous model. The available numerical modeling with a porous model is limited to either Darcy formulation or by the implementation of adjustable tortuosity parameter for comparison with experimental results. To date, the numerical formulation based on the generalized non-Darcy model, which is valid for a wide range of rod packing (tightly to coarsely packed with varying pitch to diameter ratio) without any adjustable parameter, is yet to appear in the literature. These aspects are of particular importance because often the packing of the rods is too less to be approximated as a Darcy porous medium, and adjustable parameters smoke the flow physics and theoretical predictability. The present study is an attempt to address these issues and to understand the thermal hydraulics for natural convection of partially heat generating rod bundles. The study presents experimental and numerical investigations of natural convection for a system consisting of vertical enclosed partially heat generating rod bundles. For numerical modeling, the rod bundle geometry has been viewed as a partially heat generating anisotropic (orthotropic) porous medium under the generalized non-Darcy formulation without any adjustable parameter.

2 Experimental Details

The schematics of the experimental setup with a rod bundle and an air circuit test section are shown in Figs. 1(*a*) and 1(*b*), respectively. Each rod is a cartridge type cylindrical electrical heater of an 8 mm diameter, made of 316 stainless steel tube of 1 mm wall thickness, and the detailed illustration is shown in Fig. 2. Each heater rod consists of three sections: a 370 mm long heated section of at the middle and two unheated sections of 195 mm and 385 mm long at the top and bottom ends, respectively. The rod bundle consists of 19 such heater rods. On each heater rod, a stainless steel sheathed chromel-alumel (type K) thermocouple is helically wound to sense the temperature. The thermocouple is silver brazed on the rod surface at a pitch of 150 mm along the length of the rod for firm positioning of the thermocouple. The overall diameter of the thermocouple is 1.5 mm. In addition to measurement of temperatures, the thermocouples act as spacer wires to maintain the pitch between the heated rods.

The heater rods are arranged with a triangular pitch of 10.212 mm and are enclosed by a hexagonal tube of 47.8 mm inner width across flats. It is made of 316 stainless steel sheet of 1 mm thickness. The enclosed rod bundle is supported at the bottom by a 15 mm thick stainless steel plate. The test section (the stainless steel hexagonal tube containing the rod bundle) is filled with water. Water is the primary heat transfer fluid in the present work. The heat generated by the heater rods is transferred to the wall of the enclosing hexagonal tube through the water, filling the gaps between the heater rods. Finally, the heat is taken away from the outer surface of the hexagonal tube by sending compressed air around it.

The schematic of the air circuit for the rod bundle test section is shown in Fig. 1. The test section is enclosed concentrically by an outer hexagonal tube made of 3 mm thick mild steel to form a hexagonal annulus. The width across flats of the outer hexagon is 130 mm. The air supply is given to the hexagonal annulus, thus formed, by a screw compressor. The hexagonal annulus is filled with spherical ceramic beads of 5 mm diameter to form a packed bed for enhanced heat transfer. In order to support the ceramic beads, a specially designed distributor plate made of a 3 mm thick stainless steel sheet is placed at the bottom of the test section. The distributor plate allows the compressed air to flow uniformly through the packed bed.

Temperatures inside the rod bundle assembly are measured by 19 chromel-alumel (K-type) thermocouples (one on each heater). Temperature measurements are made within the rod bundle at five planes, as shown in Fig. 2, along the height of the test section at 80, 230, 380, 530, and 680 mm, respectively, from the top of the test section, out of which three planes are located within the heated zone. Bigger circles represent the heater rods and smaller circles represent the thermocouples. The thermocouples, which had their hot junctions in a particular plane, are shown as darkened circles in that plane. On the outer surface of the stainless steel hexagonal tube, 26 Teflon coated thermocouples were affixed at 14 axial locations. The temperatures measured by these thermocouples determine the temperature of the inner surface after taking into account the heat conduction in the wall. The inner surface temperatures, thus obtained, are directly used as thermal boundary conditions for the computer code for simulating the experimental results, which will be dealt with in the numerical section.

An orifice plate is used to measure the flow rate of air through the hexagonal annulus, which is designed and fabricated according to ASME specifications. A U-tube differential manometer is used to measure the differential pressure across the orifice plate. During experiments, the temperature is continuously recorded until a steady state is reached by a 60 channel Hewlett Packard Data Acquisition Unit (Serial No. 34970A). It may be noted that the maximum temperature of water is limited to 95°C to avoid boiling of water.

The uncertainty analysis for the derived quantities is carried out following the procedure given in Coleman and Steele Jr. [20]. All the thermocouples are calibrated over the range of interest, using a precision thermometer and a constant temperature bath. The uncertainty in temperature measurement is within ± 0.04°C. The energy dissipated in the heated section is determined from the electric power measurements. In all the experiments, the heater power input is measured with the help of a precision wattmeter within $\pm 2\%$ of the true value. The static pressure drop across the orifice plate is required for the calculation of mass flow rate of air flowing through the hexagonal annulus. The uncertainty in the measurement of pressure is within $\pm 2\%$. The uncertainty of airflow rate measurement is found to be $\pm 1.13\%$.

3 Mathematical Formulation and Numerical Procedure

The arrangement of the rod bundle assembly is shown in Fig. 2. To overcome computational difficulties, the analysis has been carried out by assuming a hexagonal cavity as a cylindrical enclosure. It may be noted that the present problem domain has a very high aspect ratio of $A = H/r_o = 39.75$. Deviation of a circular cross section is very marginal from the present hexagonal geometry due to fact that at a high aspect ratio, the flow is predominantly in the axial direction, and hence the small deviation of geometry in the radial direction will not affect the results significantly. Also, a perfect symmetric boundary condition was maintained on each face of the hexagon during the experimental study.

3.1 The Governing Equations. The heater rods and fluid (water) in between are together considered as a porous medium. It is assumed that the heat is generated by a uniformly heated energy source within the enclosure though the heaters only generate the heat. It is assumed that the rod bundle of the porous medium does not undergo deformation. The fluid is considered to be in local thermal equilibrium with the solid matrix. Density variation of the fluid follows Boussinesq's assumption. A generalized non-Darcy approach has been considered, and the governing equations given below are solved using a pseudotransient approach,

$$\frac{\partial u}{\partial r} + \frac{\partial v}{\partial z} + \frac{u}{r} = 0 \tag{1}$$

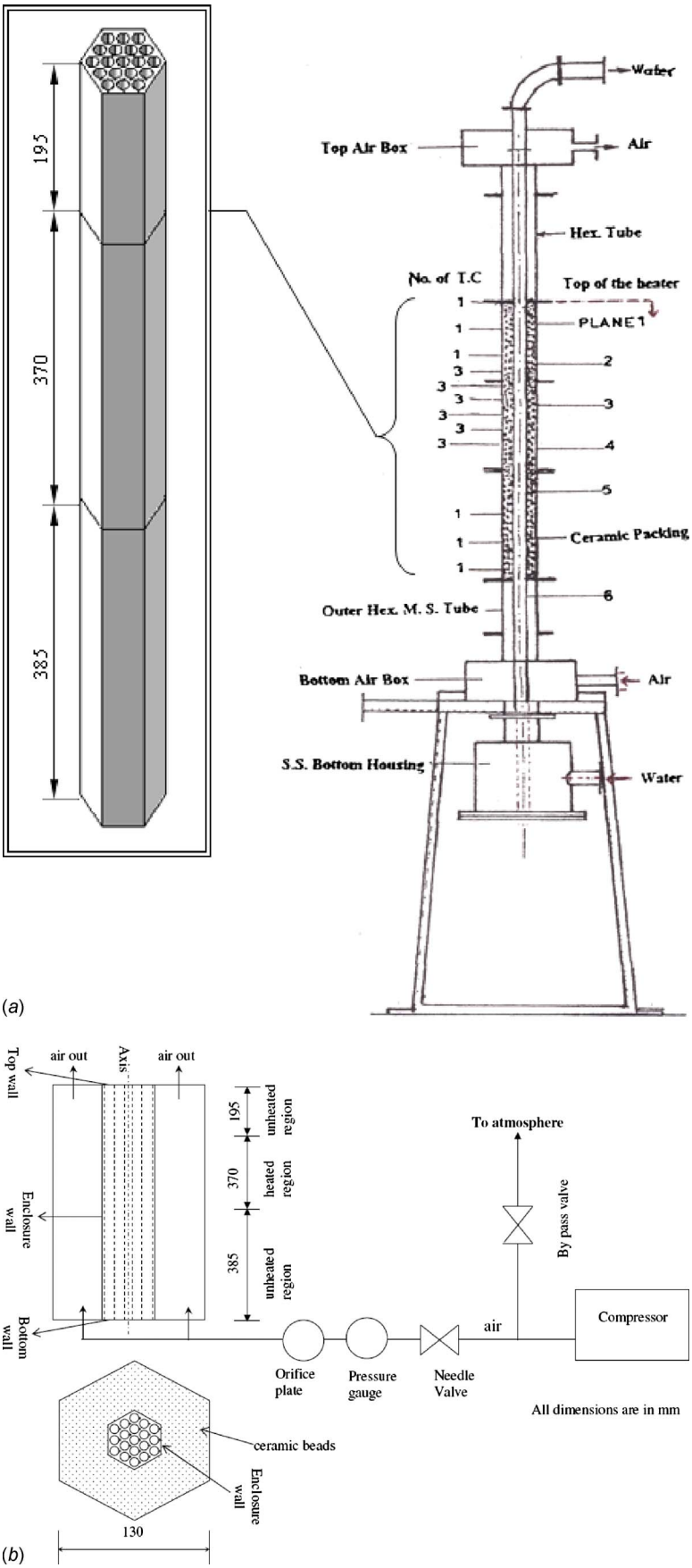

Fig. 1 (*a*) **Rod bundle test section.** (*b*) **Air circuit for rod bundle test section.**

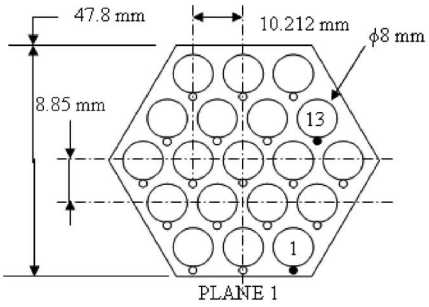

Plane	Thermocouple Location	Distance from top of the heater, mm
1	1,13	80
2	3,8,9,15,17	230
3	4,6,10,14,16	380
4	2,11,7,18,19	530
5	5	680

Fig. 2 Rod bundle arrangement

$$\rho_f\left[\frac{1}{\varepsilon}\frac{\partial u}{\partial t}+\frac{u}{\varepsilon^2}\frac{\partial u}{\partial r}+\frac{v}{\varepsilon^2}\frac{\partial u}{\partial z}\right]=\frac{1}{\varepsilon}\left[\frac{1}{r}\frac{\partial(r\sigma_{rr})}{\partial r}+\frac{\partial\sigma_{zr}}{\partial z}-\frac{\sigma_{\theta\theta}}{r}\right]-\frac{\mu_f}{K_r}u - \frac{\rho_f F_r}{\sqrt{K_r}}u\sqrt{u^2+v^2} \tag{2}$$

$$\rho_f\left[\frac{1}{\varepsilon}\frac{\partial v}{\partial t}+\frac{u}{\varepsilon^2}\frac{\partial v}{\partial r}+\frac{v}{\varepsilon^2}\frac{\partial v}{\partial z}\right]=\frac{1}{\varepsilon}\left[\frac{1}{r}\frac{\partial(r\sigma_{zr})}{\partial r}+\frac{\partial\sigma_{zz}}{\partial z}\right]-\frac{\mu_f}{K_z}v - \frac{\rho_f F_z}{\sqrt{K_z}}v\sqrt{u^2+v^2}+\rho_f g\beta(T-T_{\mathrm{ref}}) \tag{3}$$

where

$$\sigma_{rr}=-\varepsilon P+2\mu_f\frac{\partial u}{\partial r},\quad \sigma_{zz}=-\varepsilon P+2\mu_f\frac{\partial v}{\partial z},$$

$$\sigma_{rz}=\sigma_{zr}=\mu_f\left(\frac{\partial u}{\partial z}+\frac{\partial v}{\partial r}\right),\quad \sigma_{\theta\theta}=-\varepsilon P+2\mu_f\left(\frac{u}{r}\right)$$

$$(\rho Cp)_f\left(\frac{\partial(\sigma T)}{\partial t}+u\frac{\partial T}{\partial r}+v\frac{\partial T}{\partial z}\right)=\left(\frac{k_r}{r}\frac{\partial}{\partial r}\left(r\frac{\partial T}{\partial r}\right)+k_z\left(\frac{\partial^2 T}{\partial z^2}\right)\right)+q''' \tag{4}$$

where $\sigma=[\varepsilon\rho_f Cp_f+(1-\varepsilon)\rho_s Cp_s]/\rho_f Cp_f$.

In the governing equations, K_r and K_z are the permeabilities, F_r and F_z are the Forchheimer constants, k_r and k_z are the thermal conductivities of the porous medium along the radial (r) and axial (z) directions, respectively, and q''' is the volumetric heat generation.

The following dimensionless variables are used:

$$r'=\frac{r}{r_o},\quad z'=\frac{z}{H},\quad A=\frac{H}{r_o},\quad \alpha_r=\frac{k_r}{(\rho Cp)_f},\quad u'=\frac{ur_o}{\alpha_r},$$

$$v'=\frac{vr_o^2}{H\alpha_r},\quad t'=\frac{t\alpha_r}{r_o^2},\quad \mathrm{Pr}=\frac{\nu_f}{\alpha_r}$$

$$\mathrm{Da}=\frac{K_r}{r_o^2},\quad \mathrm{Ra}=\frac{g\beta\left(\frac{q'''r_o^2}{2k_r}\right)r_o^3}{\nu_f\alpha_r},\quad P'=\frac{\mathrm{Pr}_o^2}{\rho_f\alpha_r^2},\quad T'=\frac{T-T_{\mathrm{ref}}}{\left(\frac{q'''r_o^2}{2k_r}\right)},$$

$$K^*=\frac{K_r}{K_z},\quad k^*=\frac{k_r}{k_z} \tag{5}$$

Note that the prime symbol has been ignored for the sake of convenience, and the governing equations in nondimensional form are obtained as follows:

$$\frac{\partial u}{\partial r}+\frac{\partial v}{\partial z}+\frac{u}{r}=0 \tag{6}$$

$$\frac{1}{\varepsilon}\frac{\partial u}{\partial t}+\frac{u}{\varepsilon^2}\frac{\partial u}{\partial r}+\frac{v}{\varepsilon^2}\frac{\partial u}{\partial z}=\frac{1}{\varepsilon}\left[\frac{1}{r}\frac{\partial(r\sigma_{rr}^{\#})}{\partial r}+\frac{1}{A}\frac{\partial\sigma_{zr}^{\#}}{\partial z}-\frac{\sigma_{\theta\theta}^{\#}}{r}\right]-\frac{\mathrm{Pr}}{\mathrm{Da}}u - \frac{F_r}{\sqrt{\mathrm{Da}}}u\sqrt{u^2+A^2v^2} \tag{7}$$

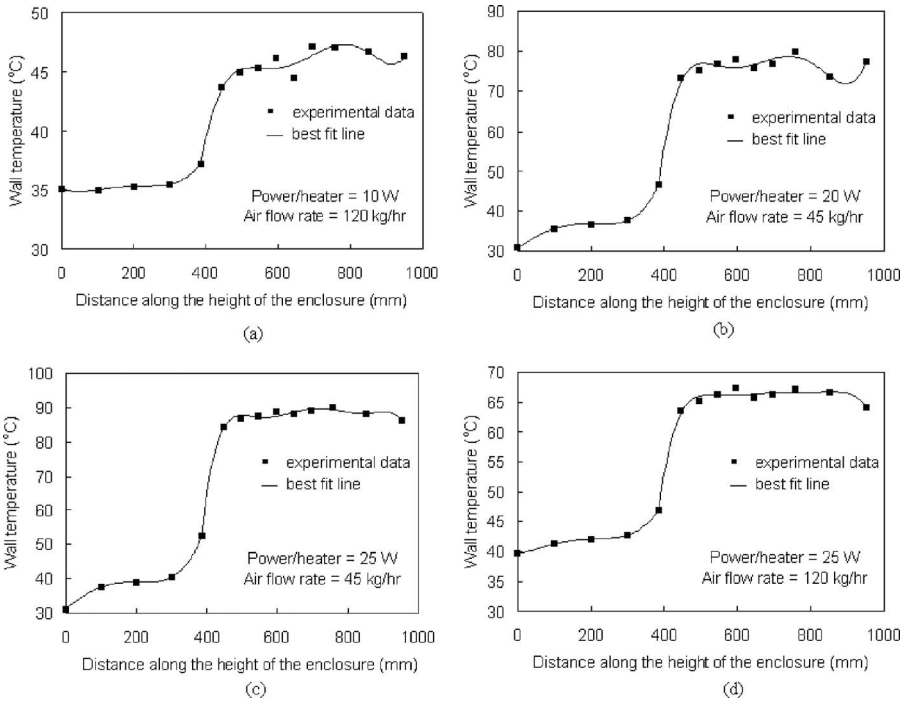

Fig. 3 Variation in temperature on the outer surface of the rod bundle enclosure for different power per heater and airflow rate: (*a*) 10 W and 120 kg/h, (*b*) 20 W and 45 kg/h, (*c*) 25 W and 45 kg/h, and (*d*) 25 W and 120 kg/h

$$\frac{1}{\varepsilon}\frac{\partial v}{\partial t}+\frac{u}{\varepsilon^2}\frac{\partial v}{\partial x}+\frac{v}{\varepsilon^2}\frac{\partial v}{\partial y}=\frac{1}{\varepsilon}\left[\left(\frac{1}{A}\right)\frac{1}{r}\frac{\partial(r\sigma_{rz}^{\#})}{\partial r}+\left(\frac{1}{A^2}\right)\frac{\partial\sigma_{zz}^{\#}}{\partial z}\right]-K^{*}\frac{\mathrm{Pr}}{\mathrm{Da}}v - \frac{F_z}{\sqrt{\mathrm{Da}}}\sqrt{K^{*}}(v\sqrt{u^2+A^2v^2})+\frac{\mathrm{Ra}\cdot\mathrm{Pr}\cdot T}{A} \quad (8)$$

where

$$\sigma_{rr}^{\#}=-\varepsilon P+2\mathrm{Pr}\frac{\partial u}{\partial r},\quad \sigma_{zz}^{\#}=\left[-\varepsilon P+2\mathrm{Pr}\frac{\partial v}{\partial z}\right],$$

$$\sigma_{rz}^{\#}=\sigma_{zr}^{\#}=\frac{\mathrm{Pr}}{A}\left[\frac{\partial u}{\partial z}+A^2\frac{\partial v}{\partial r}\right],\quad \sigma_{\theta\theta}^{\#}=-\varepsilon P+2\mathrm{Pr}\left(\frac{u}{r}\right)$$

$$\frac{\partial(\sigma T)}{\partial t}+u\frac{\partial T}{\partial r}+v\frac{\partial T}{\partial z}=\frac{1}{r}\frac{\partial}{\partial r}\left(r\frac{\partial T}{\partial r}\right)+\left(\frac{1}{A^2}\right)\left(\frac{1}{k^{*}}\right)\frac{\partial^2 T}{\partial z^2}+q \quad (9)$$

$q=2$ for the portion of the cavity with heat generation and $q=0$ for the portion of the cavity without heat generation. In the nondimensional governing equations, u and v are volume averaged velocity components.

3.2 Initial and Boundary Conditions. The initial and boundary conditions for the problem geometry shown in Fig. 1 are as follows: $t=0$, $u,v=0$, and $T=0$ (for initialization, $T_{\mathrm{ref}}=0$),

$$\text{Top wall: } t>0,\quad u,v=0,\quad \frac{\partial T}{\partial z}=0 \quad \text{at } z=H,\quad 0\le r\le r_o$$

$$\text{Bottom wall: } t>0,\quad u,v=0,\quad \frac{\partial T}{\partial z}=0 \quad \text{at } z=0,\quad 0\le r\le r_o$$

$$\text{Axis (symmetry condition): } t>0,\quad u=0,\quad \frac{\partial v}{\partial r}=0,$$

$$\frac{\partial T}{\partial r}=0 \quad \text{at } r=0,\quad 0\le z\le H$$

$$\text{Enclosure wall: } t>0 \quad \text{at } r=r_o,\quad 0\le z\le H,\quad u,v=0 \quad (10)$$

The thermal boundary condition at the enclosure wall is taken as follows:

(a) For the comparison of the present porous model with experimental results, the actual temperature measured on the outer surface of the enclosure is given as a boundary condition for the wall. It may be noted that the reference temperature for this case is the wall temperature ($T_{\mathrm{ref}}=T_w$). Figures 3(*a*)–3(*d*) show the variation in temperature with height along the outer surface of the enclosure for various power inputs and airflow rates. The equation obtained by piecewise curve fitting is used in the computation.

(b) For a parametric study, convective condition is used at the outer side of the enclosure. The reference temperature for this case is considered as ambient temperature ($T_{\mathrm{ref}}=T_{\mathrm{amb}}$):

$$\frac{\partial T}{\partial r}=-\mathrm{Bi}T \quad (11)$$

3.3 Numerical Procedure and Grid Independence. The governing equations have been discretized using the finite volume method. Quadrilateral cells in a semistaggered arrangement introduced by Hirt et al. [21] have been employed. Velocity nodes are located at the vertices, and pressure nodes are located at the centroid of the quadrilateral cells. The first order upwind scheme is used for convective terms. Nonuniform grid (cosine grid) has been employed and is shown in Fig. 4(*a*). The present study involves heat generation in a partial section of rod bundle, and a step input of the heat generation results in instability. To overcome this problem, a Heaviside step function, as shown in Fig. 4(*b*), has been employed for smoothing the step input. The convergence of the solution requires a certain number of closely packed grids near the

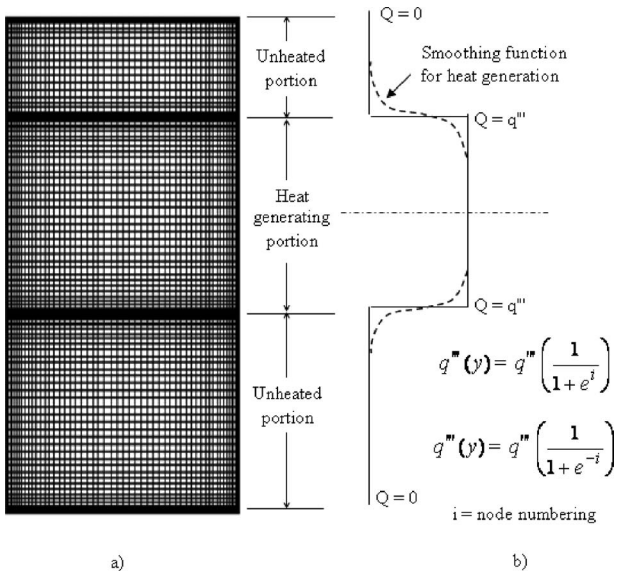

Fig. 4 (*a*) Nonuniform cosine grid. (*b*) Smoothing for the step input of the heat generation term.

isothermally cooled enclosure wall based on a grid pattern in the radial direction. A certain number of finer grids are needed near the top and bottom adiabatic walls based on a grid pattern in the axial direction. In addition, finer grids are required in the region, where heat generation starts and stops to capture the steep velocity and temperature gradients in these regions. The iteration process is continued until the following convergence criterion is achieved:

$$\frac{\sum_{i,j} |\zeta_{i,j}^{n} - \zeta_{i,j}^{n-1}|}{\sum_{i,j} |\zeta_{i,j}^{n}|} < 10^{-8} \tag{12}$$

where ζ in Eq. (12) represents u, v and T variables, and n and $n-1$ denote current and previous time iterations respectively.

To ensure that the results obtained by the numerical study are independent of the computational grid, grid independence studies are carried out using Eq. (13) between two grids for maximum temperature,

$$\%\ \text{error} = \left(\frac{\varphi^{i} - \varphi^{i-1}}{\varphi^{i}}\right) \times 100 \tag{13}$$

where φ denotes T_m, and $i-1$ and i denote successive grid sizes.

The different mesh sizes considered are 21×41, 41×81, 61×161, and 81×201. It is found that the percentage deviation between 61×161 and 81×201 is less than 1%. Therefore, a grid size of 61×161 is considered for the study. It may be noted that in the present study, as a nonuniform cosine grid is employed, a significant difference may be observed for the distance of the first node from the wall between 61×161 and 81×201 grid sizes.

To check the consistency of the current formulation and numerical procedure, comparison has been carried out with the Darcy formulation of Dhanasekaran et al. [18] for a fully heat generating cylindrical enclosure and is shown in Table 1. It may be observed from Nithiarasu et al. [22] that for $\text{Da} \leq 10^{-6}$ the porous media tends to behave as Darcy porous media. From Nithiarasu et al. [22], it may be noted that for a Darcy number of 10^{-6} the effect of porosity is not felt. As the effect of porosity is not felt, an arbitrary value of $\varepsilon = 0.999$ has been taken to compare the numerical results of Darcy porous media with the present non-Darcy formulation. It is found that the present formulation agrees well with the previous work for a wide range of modified Rayleigh numbers, aspect ratios, permeability ratios, and thermal conductivity ratios.

4 Results and Discussion

The results primarily demonstrate the influence of the heater power input, the boundary cooling of the enclosure, and the porosity (pitch to diameter ratio) of the rod bundle on the temperature distribution along different planes of the enclosure.

4.1 Results of the Experimental Study. Natural convection experiments similar to the present work have been carried out in a square arrayed nine-rod bundle by Keyhani et al. [6]. This work is based on the large pitch ($p/d = 2.25$ and 3.08) between the rods, and thus the porous medium approximation may not be appropriate for heat and fluid flow inside the rod bundle. In contrast, the present experiments, involving the rods being more closely packed, are designed to validate the numerical approach, which is developed in the present study. However, the packing of the rods in the present experiments is loose enough such that they cannot be approximated as the Darcy porous medium. This is also the typical packing used in many of the applications studied earlier. In the present work, the experiments are observed to reach a steady state typically in about 4 h, as evidenced by the temperature indicated by thermocouples.

Figures 5(*a*)–5(*c*) show the temperature distribution inside the rod bundle in the measurement planes 2, 3, and 4, respectively, for an airflow rate of 100 kg/h and various power inputs to the heaters. For planes 2 and 3, the temperature increases monotonically and reaches the maximum at the center of the rod bundle. This is due to the fact that both these planes are in the primary heated zone of the rod bundle, and hence the effect of natural convection will be felt strongly. The temperature distribution inside the rod bundle at measurement plane 4 for the same airflow rate and various power inputs indicates no appreciable variation.

Figure 6(*a*) shows the effect of power input to heaters on the temperature of the rod bundle for an airflow rate of 120.8 kg/h. It may be noted that the thermocouples chosen to bring out this effect of power input are one from each ring of heaters, and they are located in three different planes within the main heated zone. The results indicate that irrespective of the axial and radial positions, the temperature within the main heated zone varies linearly with input power. However, the temperature levels depend on the

Table 1 Comparison of present results for fully heat generating cylindrical porous enclosure ($\varepsilon = 0.999$, Pr=1, and $F_r = F_z = 0.55$)

S. No.	Ra	Da	A	K^*	k^*	Maximum temperature	
						Present	Dhanasekaran et al. [18]
1	10^8	10^{-6}	1	1	1	0.394	0.4
2	10^9	10^{-6}	5	1	1	0.289	0.294
3	5×10^8	10^{-6}	1	0.1	1	0.175	0.175
4	5×10^8	10^{-6}	3	0.1	0.1	0.157	0.158
5	5×10^8	10^{-6}	3	10	10	0.537	0.540

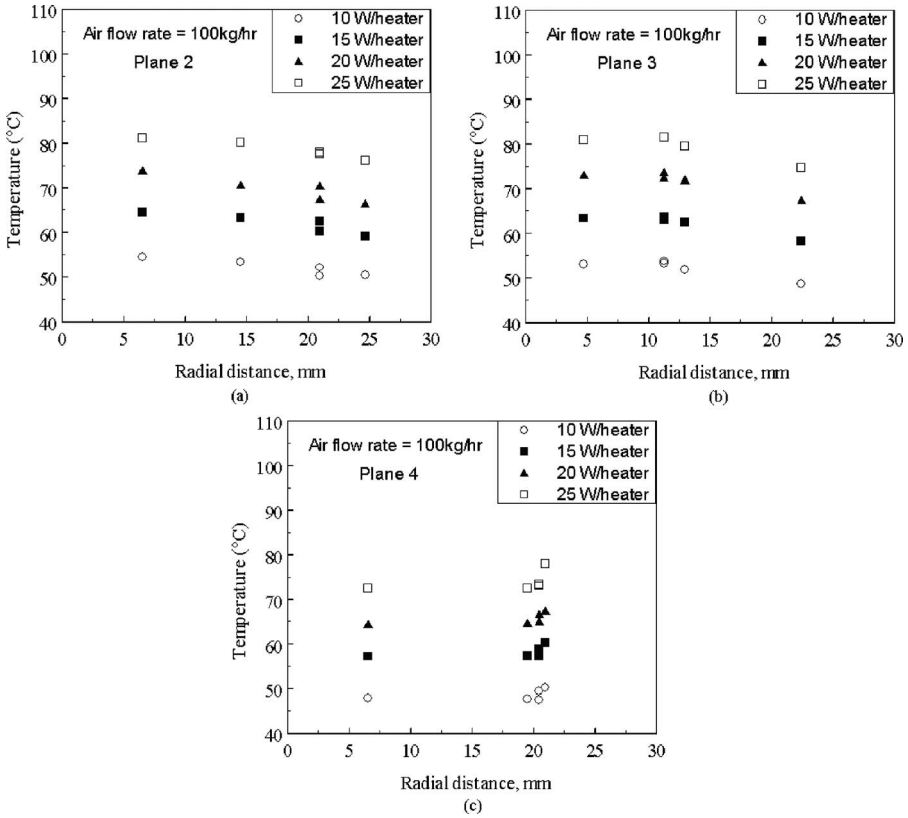

Fig. 5 Radial temperature variation in different planes for airflow rate of 100 kg/h

spatial (radial as well as axial) coordinates. Figure 6(*b*) shows the effect of the airflow rate on the temperature of the rod bundle for different power inputs. It may be noted that the central heater (heater 10) is chosen for this purpose as this heater has the maximum lateral resistance to radial heat transfer. The figure indicates that the flow in the packed bed (i.e., the boundary cooling effect) affects the temperature level strongly at different locations of the enclosed rod bundle. With an increase in airflow rate, temperature inside the bundle decreases asymptotically. It may also be observed that the decrease in temperature for higher heater power input (25 W/heater) is more compared with that for lower heater power input (10 W/heater). This can be explained by the higher degrees of convection at higher power inputs, which in turn facilitate a more efficient heat removal.

4.2 Comparison of Experimental Results With Porous Media Model. The parameters, which characterize the anisotropy of the rod bundle, are permeabilities and thermal conductivities in the radial and axial directions. The accuracy of numerical predictions depends on a proper selection of these important parameters. The comparison of present numerical results with experiments is carried out with a permeability value of $K_z = 2 \times 10^{-9}$ m^2, which is measured experimentally along the axial direction of the rod bundle assembly. The Forchheimer constant F_z measured along the axial direction is observed to be insignificant and is considered to be zero. The thermal conductivity in the radial direction is considered as $k_{\text{eff}} = k_r = 9.72$ W/m K given by Eq. (14) (also refer to Dhanasekaran [23] and Suresh [24]). The dispersion effects for the present study are considered to be negligible due to its lower values for the considered range of parameters. As there is no provision to measure the permeability and Forchheimer constant in the radial direction, the permeability (K_r/K_z) and thermal conductivity (k_r/k_z) ratios are chosen as 0.5, given by Kuwabara [25] and reported by Neale [26]. The Forchheimer constant in the radial direction is considered as $F_r = 0.28$ (Chandesris et al. [27]),

$$k_{\text{eff}} = \left(\frac{p-d}{p}\right) k_f + \frac{d}{p} k_s \tag{14}$$

The details of the parameters for the comparison of the present numerical simulation with experimental data are provided in Table 2. Figures 7(*a*)–7(*c*) show the comparison between the numerically simulated temperature distributions with that of experimental data at three different planes in the heater zone for the airflow rate of 120 kg/h with the variation in heater power input from 10 W/heater to 25 W/heater. Figure 7 illustrates that the present porous media formulation predicts the experimental data quite well for a wide range of parameters without any adjustable hydrodynamic or thermal parameters.

4.3 Parametric Study. The study is further extended by varying the porosity (pitch to diameter ratio) and convective boundary condition for the same geometry, i.e., cylindrical cavity with 370 mm as a heat generating portion and with an aspect ratio of 39.75. It may be noted that with the variation in pitch to diameter ratio, the parameters of the porous media varies according to the spacing and the arrangement of the rod bundle. Therefore, to carry out a parametric study, the correlations for effective thermal conductivity, permeability ratio, Forchheimer constant, and thermal conductivity ratio suggested by Lee and Yang [28] and Yang and Lee [29] have been used. These correlations are as follows:

$$\varepsilon = 1 - \frac{\pi}{8}\left(\frac{d}{p}\right)^2 \quad (0.2146 \le \varepsilon \le 1) \tag{15}$$

$$K_r = \frac{d^2 \varepsilon^3 (\varepsilon - 0.2146)}{31(1-\varepsilon)^{1.3}} \tag{16}$$

$$K^* = \frac{-(91.26\varepsilon^2 - 117.1\varepsilon + 8.94)(\varepsilon - 0.2146)}{31} \tag{17}$$

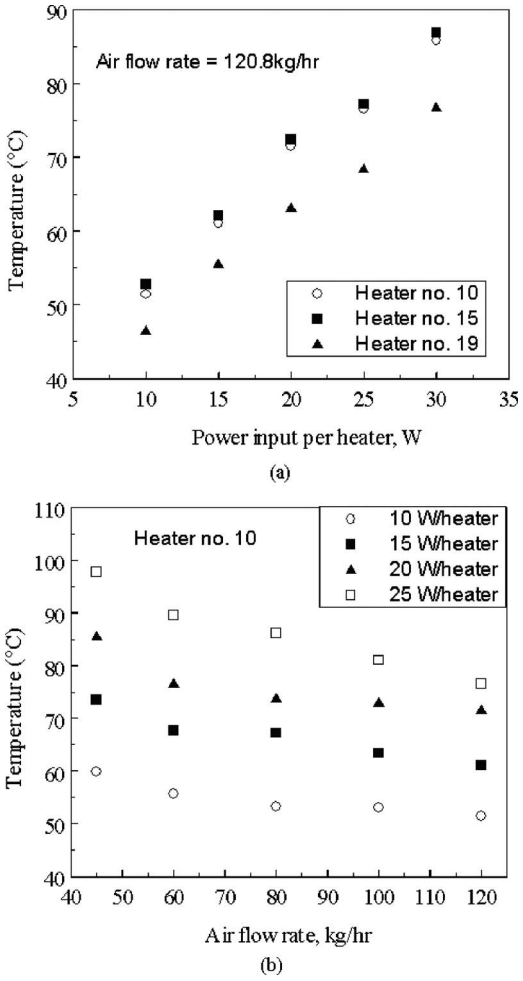

Fig. 6 Variation in maximum temperature with (*a*) heater power input for airflow rate of 120.8 kg/h and (*b*) airflow rate for different heater power inputs

$$k_r = k_{\text{ref}} f(\varepsilon, \lambda) \tag{18}$$

where

$$k_{\text{ref}} = 1 - \frac{\sqrt{2}}{2}\left(\frac{d}{p}\right) + \lambda\left(\frac{d}{p}\right)\left[(1-\lambda)\frac{d}{p} + \sqrt{2}\lambda\right]^{-1}$$

$$f(\varepsilon,\lambda) = 1 + a(1-\varepsilon)\tan^{-1}(\ln\lambda) + b(1-\varepsilon)^2\tan^{-1}(\ln\lambda)$$

$$\lambda = \frac{k_s}{k_f}, \quad \frac{d}{p} = \sqrt{\frac{8(1-\varepsilon)}{\pi}}$$

$$a = -0.01373 + 0.1552\tan^{-1}(\ln\lambda - 3.2),$$

$$b = -0.5536 - 0.3913\tan^{-1}(\ln\lambda - 2.5)$$

$$k_z = \varepsilon + (1-\varepsilon)\lambda \tag{19}$$

$$k^* = \frac{k_r}{k_z} \tag{20}$$

It may be noted that Eqs. (15)–(20) cannot be used to obtain the values listed in Table 2 as the arrangement of the rod bundle in the present study varies for experimental and parametric analysis (compare Fig. 2 and Refs. [28,29]). As the influence of heat generation has been already observed in the previous sections, the succeeding study emphasizes about the arrangement of heater rods and the aspect of boundary cooling for the cylindrical enclosure. The heater power is taken to be 50 W/heater, and the diameter of the heater rod in the cylindrical enclosure is 8 mm with the range of porosity (ε) being 0.3 ($p/d=0.749$), 0.6 ($p/d=0.99$), and 0.9 ($p/d=1.98$).

The convective boundary condition is considered with an average heat transfer coefficient (h)=1500 W/m^2 K (assumed from the studies of Suresh et al. [12])

$$\text{Biot number is defined as } \text{Bi} = \frac{hr_o}{k_r} \tag{21}$$

where h is the average heat transfer coefficient, r_o is the radius of the cylindrical enclosure, and k_r is the effective thermal conductivity in the radial direction.

The details of the parameters considered for the numerical study are shown in Table 3. To study the influence of porosity on the flow behavior and heat transfer, temperature distributions along the vertical midplane and horizontal plane 3 are shown in Fig. 8. It may be observed from Fig. 8 that with an increase in porosity, the magnitude of the nondimensional temperature decreases. The decrease in temperature with the increase in p/d ratio is due to the increase in permeability. Permeabilities (Darcy numbers) for different porosities (p/d ratio) are noted in Table 3. It is known that as the permeability increases, the resistance to flow decreases. It may also be observed from Fig. 8 that the trend for a nondimensional temperature along the vertical midplane varies with the variation in p/d ratio. The physics for this behavior can be explained by comparing isotherms and velocity vectors for the geometries with different porosities (p/d ratios). Figure 9 shows isotherms (left) and velocity vectors (right), which are marked with horizontal lines for heat generating portions for the p/d ratios of 0.749 ($\varepsilon=0.3$) and 1.98 ($\varepsilon=0.9$). The tightly packed nature and the higher heat generation rates for $\varepsilon=0.3$ lead to larger temperature gradients between the interior fluid and the externally cooled vertical wall. Due to buoyancy, the less dense heated fluid tends to move up and gets cooled by the walls. The cooled higher density fluid then circulates along the wall to the lower unheated portion of the cavity due to the higher convective strength. This phenomenon may be observed from Fig. 9(*a*) with the formation of vortex in the lower unheated portion of the cavity. The high convective strength for $p/d=0.79$ results in a steep variation in

Table 2 Details of the parameters employed for the comparison of the present numerical simulation with experimental data

S. No.	Power/heater (W/heater)	Airflow rate (kg/h)	Ra	Da	Pr	K^*	k^*	Temperature boundary condition at the sidewall
1	10	120	3.05×10^5	1.736×10^{-6}	0.258	0.5	0.5	Figure 3(*a*)
2	20	45	9.66×10^5	1.736×10^{-6}	0.201	0.5	0.5	Figure 3(*b*)
3	25	45	1.54×10^6	1.736×10^{-6}	0.174	0.5	0.5	Figure 3(*c*)
4	25	120	1.54×10^6	1.736×10^{-6}	0.174	0.5	0.5	Figure 3(*d*)

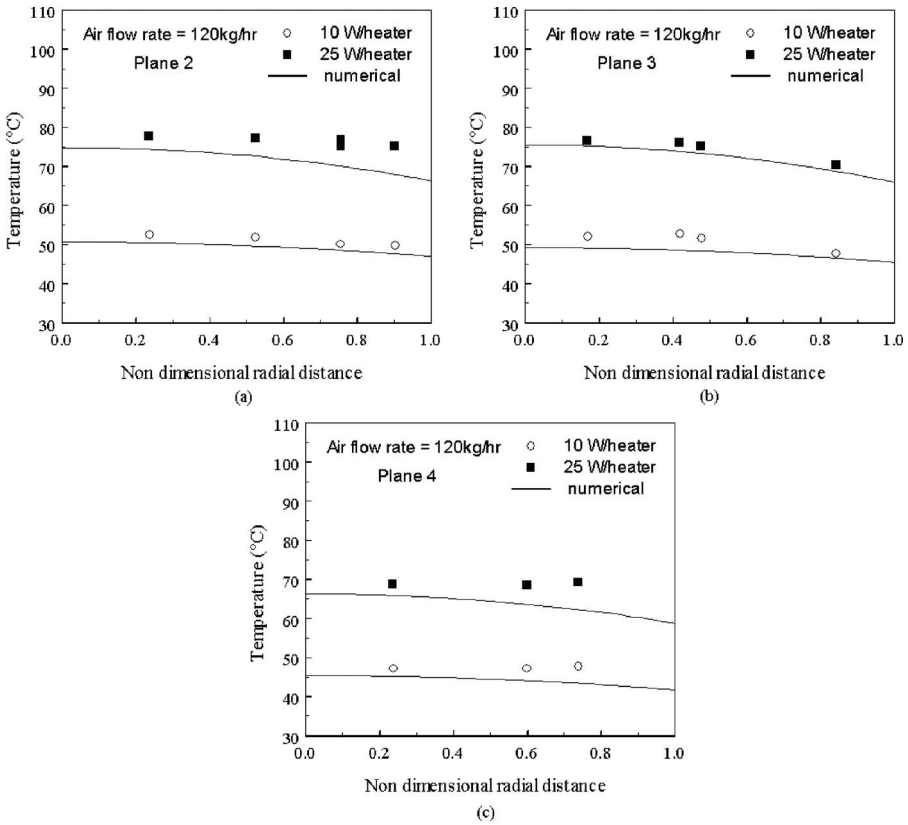

Fig. 7 Comparison of numerical simulation with experimental data for the variation in temperature in radial direction with heater power for the airflow rate of 120 kg/h

nondimensional temperature in the bottom unheated portions of the cavity. It may be observed in Fig. 9(*b*) that the lower heat generation for $\varepsilon = 0.9$ causes a lower temperature gradient between the interior fluid and the cooled walls. The lower temperature gradients result in weak convective currents, which in turn cause the fluid to circulate only in the middle heated and top unheated portions of the cavity. The trend of the nondimensional temperature, isotherms, and velocity vectors provides insight for the insignificant nature of the convection in the bottom unheated portions of the cavity. The magnitude of the nondimensional temperature is observed to be larger for plane 2 compared with that of planes 3 and 4. The hot fluid in the lower portion is driven up by buoyancy, causing the magnitude of the nondimensional temperature to be higher for upper planes.

5 Conclusions

Experimental and numerical investigations have been carried out for natural convection in a partially heat generating rod bundle inside an enclosure. An experimental setup is designed for a 19-rod bundle inside a tall hexagonal enclosure with water as the heat transfer fluid. Experiments are performed to reveal a thermal hydraulic of the enclosure when heat is generated by a part of the rods. Details of flow physics and heat transfer have been analyzed to study the influence of heater power input, boundary cooling, and porosity (pitch to diameter ratio) computationally. The overall complexity in numerical modeling of the partially heat generating rod bundle has been reduced by treating it as a porous medium. An axisymmetric numerical simulation has been developed for partially heat generating orthotropic porous media with the generalized non-Darcy formulation. The present formulation is validated with the experimental data to predict the temperature distribution within the rod bundle. A proper selection of the parameters characterizing anisotropy in radial and axial directions of the rod bundle plays the key role in the analysis of the rod bundle. The suggested formulation-parameter combination is found to be successful in bringing out the complex phenomena inside the enclosure without the need for any adjustable parameter such as tortuosity. The effect of heater power and airflow rate at the outer vertical side of the enclosure is studied by analyzing the temperature distribution along different planes of the enclosure. The boundary condition on the enclosure is also found to influence the temperature distribution within the rod bundle significantly. The decrease in magnitude of the nondimensional temperature is observed with the increase in permeability. The convective heat transfer mechanism is observed to be dominant only in the upper heated and unheated portions of the enclosure for higher porosity. The present generalized non-Darcy formulation may be a useful

Table 3 Details of the parameters considered for parametric study

S. No.	ε	p/d	k_r (W/m K)	q''' (MW/m^3)	Ra	Da	Pr_r	K^*	k^*	Bi (h=1500 W/m^2 K)
1	0.3	0.749	5.15	1.88	1.26×10^{7}	1.31×10^{-5}	0.378	0.049	0.263	7
2	0.6	0.99	2.145	1.07	4.14×10^{7}	9.82×10^{-4}	0.91	0.354	0.184	16.78
3	0.9	1.98	1.175	0.27	3.46×10^{7}	3.57×10^{-2}	1.663	0.498	0.321	30.64

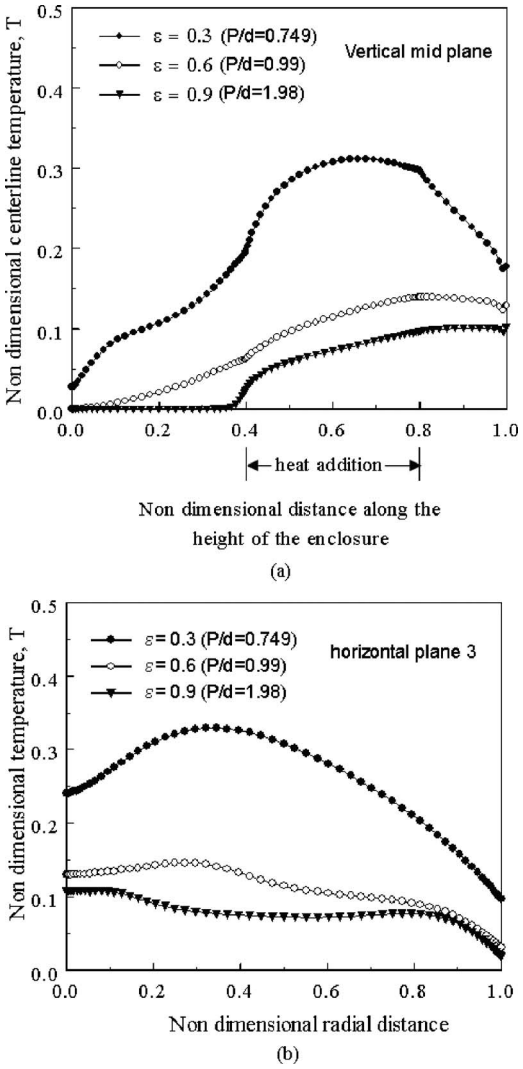

Fig. 8 Effect of porosity on variation in temperature distribution along (*a*) vertical midplane and (*b*) horizontal plane 3

tool to study the flow behavior and heat transfer for various rod bundle geometries encountered in industrial practices.

Acknowledgment

The authors would like to acknowledge the partial financial support from the Indira Gandhi Centre for Atomic Research (IGCAR), Kalpakkam (India) for carrying out this work.

Nomenclature

A = aspect ratio (H/r_o)
Bi = Biot number (hr_o/k_r)
Cp = specific heat, J kg^{-1} K^{-1}
d = diameter of the heater rod, m
Da = Darcy number (Da=K_r/r_o^2)
F = Forchheimer constant
g = acceleration due to gravity, m s^{-2}
H = height, m
h = heat transfer coefficient, W m^2 K^{-1}
K = permeability, m^2
k = thermal conductivity, W m^{-1} K^{-1}
k^* = thermal conductivity ratio (k_r/k_z)
K^* = permeability ratio (K_r/K_z)
P = pressure, N m^{-2}

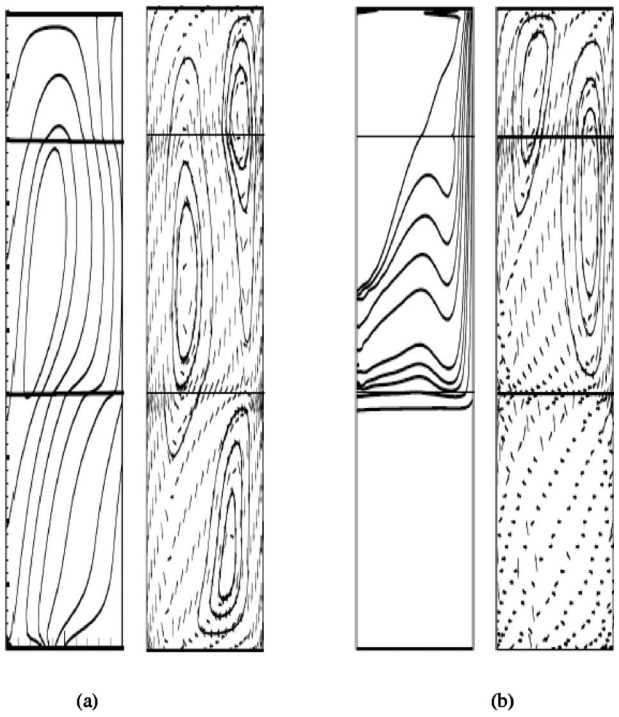

Fig. 9 Isotherms (left) and velocity vectors (right) with the variation in *p*/*d* ratios (porosities): (*a*) *p*/*d*=0.749 (ε=0.3) and (*b*) *p*/*d*=1.98 (ε=0.9)

p = transverse pitch, m
Pr = Prandtl number
q''' = volumetric heat generation, W m^{-3}
r,z = coordinates axes
Ra = Rayleigh number (Eq. (5))
r_o = radius of the cylindrical enclosure, m
T = temperature, °C/nondimensional temperature
t = time, s
u = volume averaged velocity in r-direction, m s^{-1}
v = volume averaged velocity in z-direction, m s^{-1}
$|V|$ = magnitude of velocity vector ($\sqrt{u^2+v^2}$), m s^{-1}

Greek Symbols

φ = T_m (maximum temperature)
ζ = u, v, or T variable
ρ = density, kg m^{-3}
ν = kinematic viscosity, m^2 s^{-1}
μ = viscosity of fluid, N s m^{-2}
β = coefficient of thermal expansion, K^{-1}
ε = porosity (void volume/total volume)
λ = ratio of solid to fluid conductivity (k_s/k_f)
σ = ratio of heat capacities
$\sigma_{\theta\theta}$ = hoop stress
σ_{rr} = normal stress component in radial direction
σ_{rz}, σ_{zr} = shear stress components in r-z planes
σ_{zz} = normal stress component in axial direction

Subscripts

amb = ambient
eff = effective
f = fluid
m = maximum
p = porous medium
r = for radial direction quantities
ref = reference
s = solid matrix

w = wall
z = for axial direction quantities

Superscripts

$'$ = nondimensional quantities
$\#$ = nondimensional stress components
$i, i-1$ = finer and coarser grid size
$n, n-1$ = present and previous time iteration

References

[1] Davis, L. P., and Perona, J. L., 1973, "Development of Free Convection Axial Flow Through a Tube Bundle," Int. J. Heat Mass Transfer, **16**, pp. 1425–1438.
[2] Koenig, J. F., and Buchanan, T. N., 1979, "Temperatures of EBR–II Subassemblies in Air or Argon Without Forced Cooling," ASME Paper No. 79-HT-7.
[3] Driesen, G. E., Sherba, D. F., Sherba, P. S., and Steffan, R. J., 1980, "Heat Transfer Associated With Dry Storage of Spent LWR Fuel," *Heat Transfer in Nuclear Waste Disposal*, F. A. Kulacki and R. Lyczkowski, eds., HTD Vol. 11, American Society of Mechanical Engineers, New York, pp. 9–18.
[4] McCann, R., 1980, "Thermal Hydraulic Analysis of a Spent Fuel Assembly Contained Within a Canister," *Heat Transfer in Nuclear Waste Disposal*," F. A. Kulacki and R. Lyczkowski, eds., HTD Vol. 11, American Society of Mechanical Engineers, New York.
[5] Gruszcynski, M. J., and Viskanta, R., 1983, "Heat Transfer From a Vertical Tube Bundle Under Natural Circulation Condition," *Proceedings ASME/JSME Thermal Engineering Joint Conference*, Vol. 3, pp. 403–410.
[6] Keyhani, M., Kulacki, F. A., and Christensen, R. N., 1985, "Experimental Investigation of Free Convection in a Vertical Rod Bundle—A General Correlation for Nusselt Numbers," ASME J. Heat Transfer, **107**, pp. 611–623.
[7] Arya, M. S., and Keyhani, M., 1990, "Convective Heat Transfer in a Sealed Vertical Storage Cask Containing Spent Fuel Canisters," Nucl. Sci. Eng., **105**, pp. 391–403.
[8] Keyhani, M., and Dalton, T., 1996, "Natural Convection Heat Transfer in Horizontal Rod Bundle Enclosures," ASME J. Heat Transfer, **118**, pp. 598–605.
[9] Haldar, S. C., Mohanty, A. K., and Dubey, M. R., 2000, "Laminar Free Convection in Open-Ended Vertical 7-Rod Bundles: Experiments and Porous Model," Nucl. Eng. Des., **198**, pp. 295–305.
[10] Haldar, S. C., 2000, "Laminar Free Convection in Open Ended Vertical 7 Rod Bundles," Nucl. Eng. Des., **199**, pp. 273–288.
[11] Suresh, Ch. S. Y., Sateesh, G., Das, S. K., Venkateshan, S. P., and Rajan, M., 2005, "Heat Transfer From a Totally Blocked Fuel Subassembly of a Liquid Metal Fast Breeder Reactor: Part I. Experimental Investigation," Nucl. Eng. Des., **235**, pp. 885–895.
[12] Suresh, Ch. S. Y., Sundarajan, T., Venkateshan, S. P., Das, S. K., and Thansekhar, M. R., 2005, "Heat Transfer From a Totally Blocked Fuel Subassembly of a Liquid Metal Fast Breeder Reactor: II. Numerical Simulation," Nucl. Eng. Des., **235**, pp. 897–912.
[13] Nield, D. A., and Bejan, A., 2006, *Convection in Porous Media*, 3rd ed., Springer, New York, Chaps. 5.1.9.5, 6.12, 7.3.2, and 9.1.6.
[14] Quintard, M., and Whitaker, S., 1995, "Local Thermal Equilibrium for Transient Heat Conduction: Theory and Comparison With Numerical Experiments," Int. J. Heat Mass Transfer, **38**(15), pp. 2779–2796.
[15] Quintard, M., Kaviany, M., and Whitaker, S., 1997, "Two-Medium Treatment of Heat Transfer in Porous Media: Numerical Results for Effective Properties," Adv. Water Resour., **20**(2–3), pp. 77–94.
[16] Royer, J. J., and Flores, L., 1994, "Two-Dimensional Natural Convection in an Anisotropic and Heterogeneous Porous Medium With Internal Heat Generation," Int. J. Heat Mass Transfer, **37**, pp. 1387–1399.
[17] Parthiban, C., and Patil, P. R., 1997, "Thermal Instability in an Anisotropic Porous Medium With Internal Heat Source and Inclined Temperature Gradient," Int. Commun. Heat Mass Transfer, **24**, pp. 1049–1058.
[18] Dhanasekaran, M. R., Das, S. K., and Venkateshan, S. P., 2002, "Natural Convection in a Cylindrical Enclosure Filled With Heat Generating Anisotropic Porous Medium," ASME J. Heat Transfer, **124**, pp. 203–207.
[19] Jaya Krishna, D., Basak, T., and Das, S. K., 2008, "Natural Convection in a Heat Generating Hydrodynamically and Thermally Anisotropic Non-Darcy Porous Medium," Int. J. Heat Mass Transfer, **51**, pp. 4691–4703.
[20] Coleman, H. W., and Steele, W. G., Jr., 1989, *Experimental and Uncertainty Analysis for Engineers*, Wiley, New York.
[21] Hirt, C., Amsden, A., and Cook, J., 1974, "An Arbitrary Lagrangian Eulerian Computing Method for All Flow Speeds," J. Comput. Phys., **14**, pp. 227–253.
[22] Nithiarasu, P., Seetharamu, K. N., and Sundararajan, T., 1997, "Natural Convective Heat Transfer in a Fluid Saturated Variable Porosity Medium," Int. J. Heat Mass Transfer, **40**(16), pp. 3955–3967.
[23] Dhanasekaran, M. R., 2001, "Natural Convective Inside Enclosures Filled With Plain or Porous Medium," Ph.D. thesis, Department of Mechanical Engineering, Indian Institute of Technology Madras, India.
[24] Suresh, Ch. S. Y., 2004, "Natural Convective Heat Transfer in a Blocked Subassembly of Fast Breeder Reactor," MS thesis, Department of Mechanical Engineering, Indian Institute of Technology Madras, India.
[25] Kuwabara, S., 1959, "The Forces Experienced by Randomly Distributed Parallel Circular Cylinders or Spheres in a Viscous Flow at Small Reynolds Numbers," J. Phys. Soc. Jpn., **14**, pp. 527–532.
[26] Neale, G., 1977, "Degrees of Anisotropy for Fluid Flow and Diffusion (Electrical Conduction) Through Anisotropic Porous Media," AIChE J., **23**, pp. 56–62.
[27] Chandesris, M., Serre, G., and Sagaut, P., 2006, "A Macroscopic Turbulence Model for Flow in Porous Media Suited for Channel, Pipe and Rod Bundle Flows," Int. J. Heat Mass Transfer, **49**, pp. 2739–2750.
[28] Lee, S. L., and Yang, J. H., 1997, "Modeling of Darcy-Forchheimer Drag for Fluid Flow Across a Bank of Circular Cylinders," Int. J. Heat Mass Transfer, **40**, pp. 3149–3155.
[29] Yang, J. H., and Lee, S. L., 1999, "Effect of Anisotropy on Transport Phenomena in Anisotropic Porous Media," Int. J. Heat Mass Transfer, **42**, pp. 2673–2681.

Influence of Intense Symmetric Heating and Variable Physical Properties on the Thermo-Buoyant Airflow Inside Vertical Parallel-Plate Channels

Biagio Morrone
Dipartimento di Ingegneria Aerospaziale e Meccanica (DIAM),
Seconda Università degli Studi di Napoli,
Via Roma 29,
81031 Aversa (CE), Italy

Antonio Campo[1]
Department of Mechanical Engineering,
The University of Texas at San Antonio,
San Antonio, TX 78249
e-mail: antonio.campo@utsa.edu

This paper deals with the steady, laminar, and two-dimensional natural convection inside vertical parallel-plate channels with isoflux heating. The main objective of this paper is to assess the joint influence of intense heating and variable physical properties on the flow and heat transfer characteristics of the upward air. To capture the physics of the problem, the discretized conservation equations are solved by the finite-volume technique in an aggrandized computational domain that is much larger than the physical domain. Representative numerical results based on the FLUENT *computer program are presented in terms of local quantities such as air velocity and temperature profiles, as well as global quantities such as the average heat transfer coefficients and mass flow rates, all in response to the controlling geometrical and thermal parameters. A detailed comparison of these results is made against those produced by the simple model limited to constant physical properties.* [DOI: 10.1115/1.4001932]

Keywords: natural convection, vertical parallel-plate channel, variable physical properties, elliptic conservation equations, enlarged computational domain

1 Introduction

Laminar natural convection inside vertical parallel-plate channels has been extensively investigated during the past decades due to its relevance in a multitude of technological applications. As documented in Manca et al. [1] and Bar-Cohen et al. [2], numerous researchers have studied this fluid/channel ensemble theoretically, numerically, and experimentally mostly within the framework of electronics cooling.

To maximize the packaging of electronic systems, they can be stacked in a traditional tower arrangement [2]. As the air moves up, the air temperature increases from the lower to upper shelves in the tower within the electronic system, and the heat dissipation can be drastically curtailed. In turn, this situation jeopardizes the overall integrity of the electronic system and adversely affects the reliability. When designing electronic systems, the design engineer needs to know beforehand how the interplay between the air velocities and temperatures will affect the maximum temperatures of the printed circuit boards. This information will be crucial in order to accurately determine undesirable "hot spots."

Fundamentally speaking, the heat dissipation from printed circuit boards of electronic systems is modeled as a uniform heat flux boundary condition (Kays and Crawford [3]). Experimental measurements for natural convection between vertical parallel-plate channels with symmetric, uniform flux heating are presented by Wirtz and Stutzman [4], Guo et al. [5], and Ambrosini et al. [6].

To improve the parabolic model with constant physical properties, the logical step utilizes the elliptic model with constant physical properties. The first analyst who envisioned an added region beyond the actual channel dimensions was Kettleborough [7]. A computational domain constructed by him consisted of the simple parallel-plate channel at uniform temperature plus one plenum placed upstream of the channel. Numerical simulations using the novel approach were conducted later by Nakamura et al. [8], Naylor et al. [9], and Chang and Lin [10]. Deviating from this format, an I-type shaped computational domain was employed by Morrone et al. [11] to accommodate the general elliptic conservation equations. A numerical computation was carried out by these authors to determine the optimal plate-to-plate distance in the channel. The numerical results were compared with those reported in Anand et al. [12], who employed the simple parabolic conservation equations. Besides, Marcondes and Maliska [13] developed a numerical solution for the analysis of full elliptic flows encountered in open-ended channels. The collection of the aforementioned publications [6–13] was empowered with constant physical properties with the exception of the density that was handled by the Boussinesq approximation. In this broad context, Gray and Giorgini [14] derived the prevalent conditions under which the Boussinesq approximation is valid for a Newtonian fluid.

Limited efforts have been made to investigate the variability of the physical properties on laminar natural convection in vertical parallel-plate channel flows. A complete elliptic model incorporating the variations in density, viscosity, and thermal conductivity with temperature was implemented by Hernández and Zamora [15]. An exhaustive literature review reveals that no publications involving the variability of physical properties, natural convection flows, and vertical parallel-plate channels have appeared since 2005.

Although the outcome of the above-cited works [4–15] constitutes a formidable step forward, more refined models are in unprecedented demand for an accurate estimation of the maximum plate temperature of printed boards in electronic systems. The model that complies with this requirement needs the flow and temperature solution of the full elliptic conservation equations subjected to intense heating, taking into account variable physical properties. The aim of the present paper is threefold: first, to deviate from the Boussinesqian idealization; second, to employ the full elliptic Navier–Stokes and energy equations; third, to utilize a two-sided extended computational domain consisting of the physical domain plus two appended reservoirs upstream and downstream of the channel. The system of partial differential equations was solved by means of the finite-volume technique within the platform of the FLUENT computer program. Besides, the quantification of velocity and temperature fields, including wall temperature distributions, mass flow rates, and mean convection coefficients, with and without variable physical properties have been compared in detail.

2 Model and Numerical Computation

When a still fluid in the vicinity of a vertical parallel-plate channel is heated with a symmetrical heat flux, the fluid is sucked upward between the opposing plates by the action of gravity. The general elliptic model that governs steady laminar natural convection flow implicates the 2D Navier–Stokes and energy equations

[1]Corresponding author.

Contributed by the Heat Transfer Division of ASME for publication in the JOURNAL OF HEAT TRANSFER. Manuscript received August 4, 2008; final manuscript received January 8, 2010; published online July 23, 2010. Assoc. Editor: Gautam Biswas.

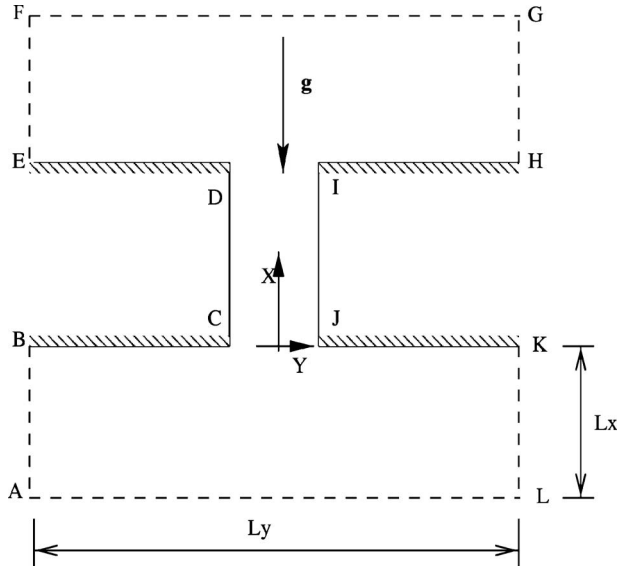

Fig. 1 Sketch of the physical domain and the two-sided enlarged computational domain

having variable physical properties. Using air as the working fluid, the system of coupled equations incorporates the temperature dependence of the four physical properties: the density $\rho(T)$, dynamic viscosity $\mu(T)$, heat capacity $c_p(T)$, and thermal conductivity k(T). The four physical properties are evaluated by the following curve-fitted polynomials found in Vargaftik [16]:

$$\log \rho = 2.55182 - 1.00331 \log T \tag{1}$$

$$\mu(T) \times 10^7 = 4.12235 + 0.72111\ T - 4.28173 \times 10^{-4}\ T^2 + 5.86408 \times 10^{-8}\ T^3 + 1.25726 \times 10^{-10}\ T^4 - 6.68760 \times 10^{-14}\ T^5 + 1.05134 \times 10^{-17}\ T^6 \tag{2}$$

$$c_p(T) = 1083.21 - 0.71465\ T + 2.08832 \times 10^{-3}\ T^2 - 2.31029 \times 10^{-6}\ T^3 + 1.35272 \times 10^{-9}\ T^4 - 4.12726 \times 10^{-13}\ T^5 + 5.27547 \times 10^{-17}\ T^6 \tag{3}$$

$$k(T) \times 10^3 = 0.81363 + 0.08083\ T + 6.13727 \times 10^{-5}\ T^2 - 2.10686 \times 10^{-7}\ T^3 + 2.06091 \times 10^{-10}\ T^4 - 8.42775 \times 10^{-14}\ T^5 + 1.27292 \times 10^{-17}\ T^6 \tag{4}$$

in the extensive temperature interval [100 K, 2500 K].

The computational domain illustrated in Fig. 1 is made of the space occupied between the two parallel plates in conjunction with two large reservoirs, one upstream and the other large downstream. The flow boundary conditions referred to in Fig. 1 are described in Refs. [9,10]. For the temperature boundary conditions, uniform heat flux q_w is applied along the opposing vertical plates, whereas the other impermeable and permeable surfaces are thermally insulated. The horizontal dimensions of the upstream and downstream reservoirs were set equal to 11 times the channel gap b, whereas the vertical dimensions of the upstream and downstream reservoirs were set equal to the channel height L.

The system of partial differential equations is solved with the finite-volume method employing the FLUENT code, version 6.2 [17]. The four physical properties $\rho(T)$, $\mu(T)$, $c_p(T)$, and k(T) are evaluated at a reference temperature $T_{ref}=T_0$.

Table 1 Dimensionless mass flow rate and average Nusselt number as affected by the grid nodes for $Ra=6.7\times10^5$ and $L/b=10$

Node number ($n_x \times n_y$)	11×21	21×21	41×41
Dimensionless mass flow rate	1903.3	1906.4	1896.6
Average Nusselt number	3.00	3.00	2.96

The global quantities of interest to be monitored are the local and average heat transfer coefficients through their corresponding Nusselt numbers:

$$\mathrm{Nu}(X) = \frac{h(X)b}{k(T)} \tag{5}$$

and

$$\mathrm{Nu} = \frac{b}{L}\int_0^{L/b} \mathrm{Nu}(X)dX$$

and the induced mass flow rate:

$$\dot{m} = \int_0^b \rho u dy \tag{6}$$

Careful checks have been flagged at all stages of the computational procedure to ensure that the results are grid independent. A sensitivity analysis of the grid is provided in Table 1, where the two global quantities, the dimensionless mass flow rate, and the average Nusselt number are reported in terms of the number of grid nodes. Further, in Fig. 2, the local Nusselt numbers Nu(X) are plotted as a function of the X-coordinate for the three preselected grid nodes. Within this perspective, errors smaller than 2% are detected for both the mass flow rate and the average heat transfer coefficient.

3 Discussion of Numerical Results

The numerical results are generated for

- working fluid, air (Pr=0.71)
- aspect ratio $L/b=10$
- ambient air temperature at 20°C
- wall heat flux varies three orders of magnitude from a low 25 W m^{-2} to a very high 2500 W m^{-2}.

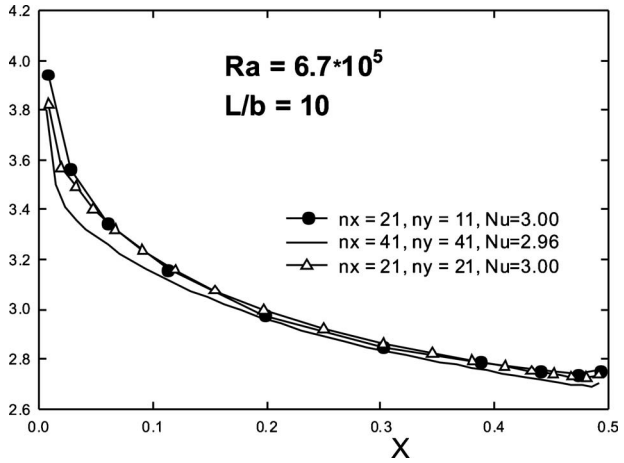

Fig. 2 Local Nusselt numbers varying with the axial coordinate X for constant physical properties. Three different grids are tested.

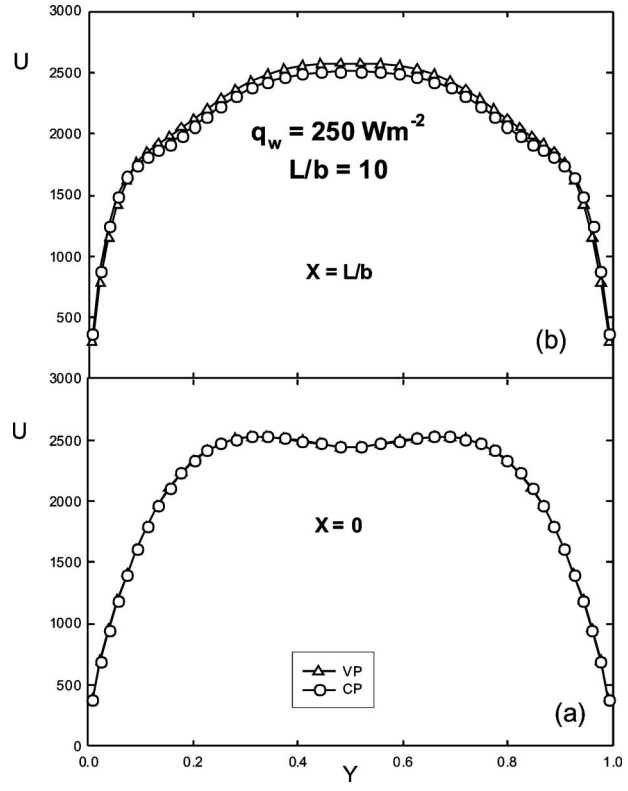

Fig. 3 Axial velocity varying with the transverse coordinate Y at (*a*) the channel inlet and (*b*) the channel exit under the influence of q_w=250 W m^{-2} and Ra=6.7×10^6

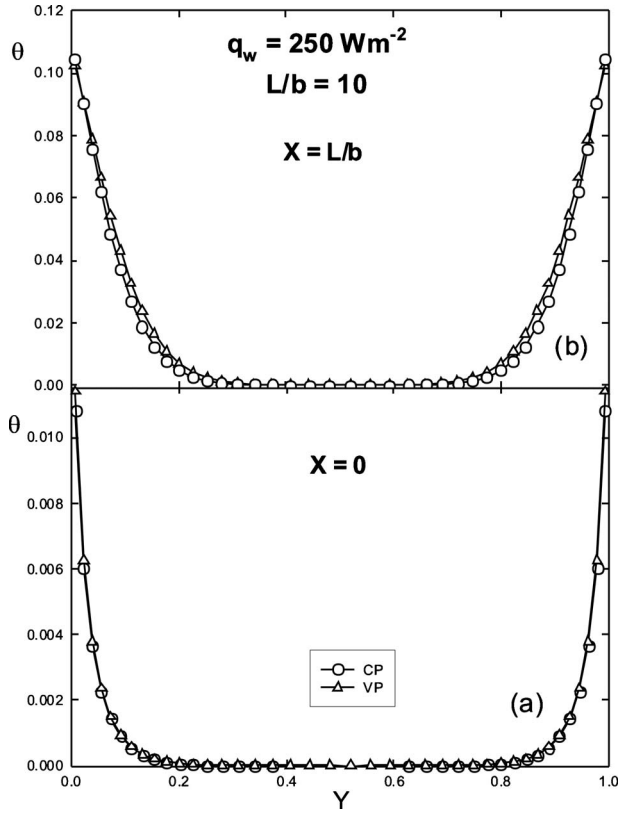

Fig. 4 Temperature varying with the transverse coordinate Y at (*a*) the channel inlet and (*b*) the channel exit under the influence of q_w=250 W m^{-2} and Ra=6.7×10^6

The combination of the above numbers gives rise to Rayleigh numbers that lie inside the large interval $6.7\times10^5 \div 6.7\times10^7$.

For purposes of identification, the flow and temperature results associated with the particular case of constant physical properties are indicated as CP, whereas those connected to the general case of variable physical properties are indicated as VP.

The pair of Figs. 3 and 4 illustrates the dimensionless velocity and temperature profiles varying with the transverse Y-coordinate at the two extreme channel stations: the inlet, X=0, and the exit, X=L/b, under the influence of a wall heat flux q_w=250 W m^{-2}. As far as the velocity along the Y-axis at the channel inlet is concerned, the two velocity profiles embracing CP and VP results appearing in Fig. 3(*a*) do not show discrepancies in terms of shape and magnitudes. The two velocity profiles present a maximum value at the critical Y=0.35 and 0.65 producing velocities of 2500 with an average of about 1800. At the channel exit (Fig. 3(*b*)), small discrepancies are detected since temperatures are higher than those at the channel inlet. This behavior is indicative of a decrement in density, which implies a subsequent increment of the velocity of about 3% for the VP case. The temperature profiles at the channel inlet and exit linked to Figs. 4(*a*) and 4(*b*) basically do not differentiate between the CP and VP cases. At any rate, the heated part of the fluid is constrained to a very thin region close to the plates since the diffusive effects are quite small for this heating condition.

When the applied heat flux is elevated by a factor of 10 to q_w =2500 W m^{-2}, as a consequence Ra ascends to 6.7×10^7. This alters the flow and temperature patterns. In fact, the velocity profiles at the channel inlet plotted in Fig. 5(*a*) are slightly different. The VP case shows moderately smaller velocities than the CP case because the mass flow rate is lower and the two velocity profiles display a similar shape motivated by the low momentum diffusion downward. At the channel exit in Fig. 5(*b*), the two velocity profiles display very sharp peaks close to the plates. These patterns occur because the two boundary layers are very thin and do not merge before reaching the channel exit. The VP case presents higher velocity values because the density is lower in the CP case. In the central part of the channel occupied by the coordinate interval $0.3<Y<0.7$, the two velocity profiles merge.

In Fig. 6(*b*) associated with the temperature profiles as a function of the traverse Y-coordinate at the channel exit, the VP case displays higher temperature values, which in turn brings lower density values.

The magnitudes for the three relevant quantities, (1) the average Nusselt number, (2) the maximum plate temperatures, and (3) the induced mass flow rates, are listed in Table 2 for the CP and VP cases. Those cases with a low q_w=25 W m^{-2} seem to be invariant with temperature-dependent properties, whereas at a high q_w =2500 W m^{-2} definitive mismatches exist. The maximum plate temperatures bring along a difference of 50 K, and in terms of the average Nusselt number the percent difference is about 75% because the evaluation of the Nusselt number has been done through the effective thermal conductivity. At this heat flux value, the thermal conductivity presents massive deviation for the VP case with respect to the CP. In terms of the convective heat transfer coefficient, the two models VP and CP deliver similar values with maximum discrepancy of 10%. Analogously, the mass flow rate manifests a similar behavior. In fact, at a low heat flux q_w =25 W m^{-2}, the two models display the same flow rate values, whereas at a high q_w=2500 W m^{-2}, the percent variation is about 14%.

The dimensionless plate temperatures varying with the axial coordinate X for the two cases under study are reported in Fig. 7. First, the case with an intermediate q_w=250 W m^{-2} exhibits no discrepancies in the values along the heated plate, as witnessed in Fig. 7(*a*), since the thermal level is low and the two models share

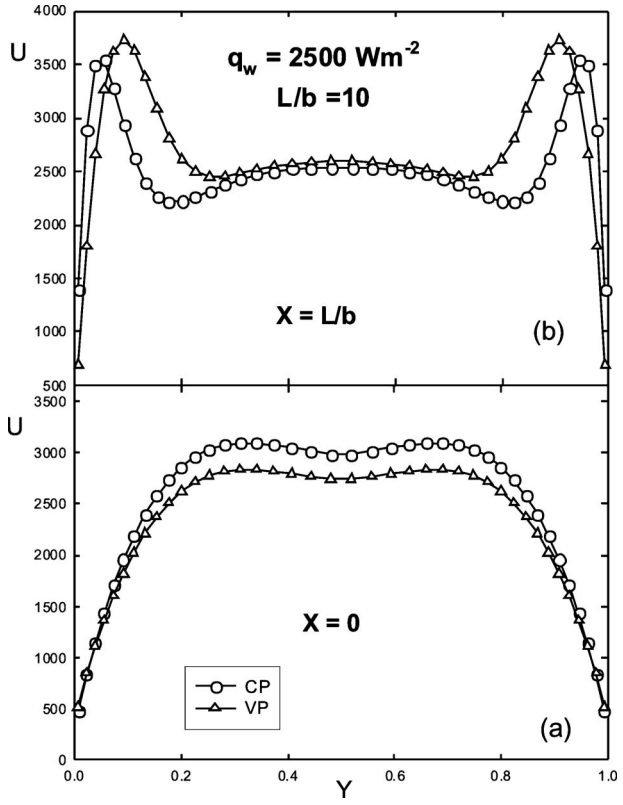

Fig. 5 Axial velocity varying with the transverse coordinate Y at (*a*) the channel inlet and (*b*) the channel exit under the influence of q_w=2500 W m^{-2} and Ra=6.7×10^6

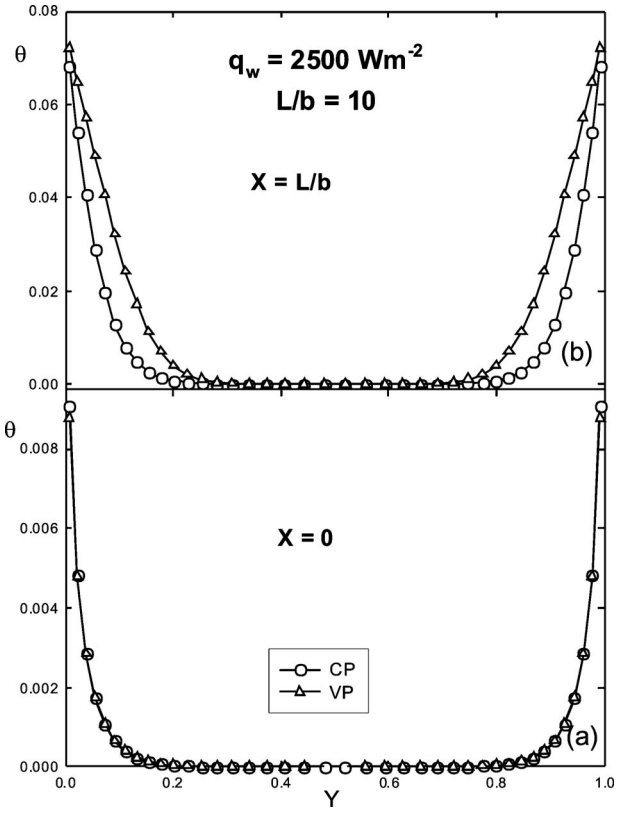

Fig. 6 Temperature varying with the transverse coordinate Y at (*a*) the channel inlet and (*b*) the channel exit under the influence of q_w=2500 W m^{-2} and Ra=6.7×10^7

the same behavior. Second, when q_w=2500 W m^{-2} this situation supplies Ra=6.7×10^7 in Fig. 7(*b*). Under these circumstances, the plate temperature differences are noticeable, exhibiting a maximum discrepancy of 6.5%.

4 Conclusions

A detailed numerical investigation has been carried out in the present paper for the characterization of natural convection between intense heated vertical parallel-plate channels by comparing the flow and temperature solutions under two scenarios: one with constant properties and the other with variable properties. Owing to the superabundance of parameters, the fluid chosen was air and the channel size was fixed at $L/b=10$, a reasonable aspect ratio. It has been demonstrated that when air is heated with very low heat fluxes there is no distinction between the flow and temperature results for constant and variable properties. On the contrary, when the air is heated with very high heat fluxes, there is a clear distinction between those sets of flow and thermal results. This issue indicates that in order to generate precise predictions for the maximum plate temperature at the trailing edge of printed circuit boards, i.e., hot spots, the incorporation of temperature-dependent physical properties to the conservation equations is indispensable.

Nomenclature

b = channel gap, m
c_p = isobaric heat capacity, kJ kg^{-1} K^{-1}
$\mathbf{g}$ = gravitational vector, m s^{-2}
Gr = Grashof number
$h(X)$ = local convective heat transfer coefficient, W m^{-2} K^{-1}
k = thermal conductivity, W m^{-1} K^{-1}
L = channel height, m
$\dot{m}$ = mass flow rate, g s^{-1}
Nu(X) = local Nusselt number
Nu = mean Nusselt number
Pr = Prandtl number
q_w = applied heat flux, W m^{-2}
Ra = Rayleigh number
T = temperature, K
U,V = dimensionless velocity components in X, Y
X,Y = dimensionless Cartesian coordinates
θ = dimensionless temperature
μ = dynamic viscosity, N s m^{-2}
ρ = density, kg m^{-3}

Subscripts

0 = ambient value
max = maximum plate
ref = reference value
w = wall

Table 2 Comparison of the average Nusselt number, maximum plate temperature, and induced mass flow rate for different wall heat fluxes. The conditions are constant properties (CP) and variable properties (VP).

Model	q_w (W m^{-2})	Nu	$T_{w,max}$ (K)	$\dot{m}$ (g/s)
CP	25	3.00	306	40.6
VP	25	2.85	306	40.3
CP	250	9.52	348	46.2
VP	250	8.26	348	45.9
CP	2500	17.36	595	56.6
VP	2500	9.96	645	48.8

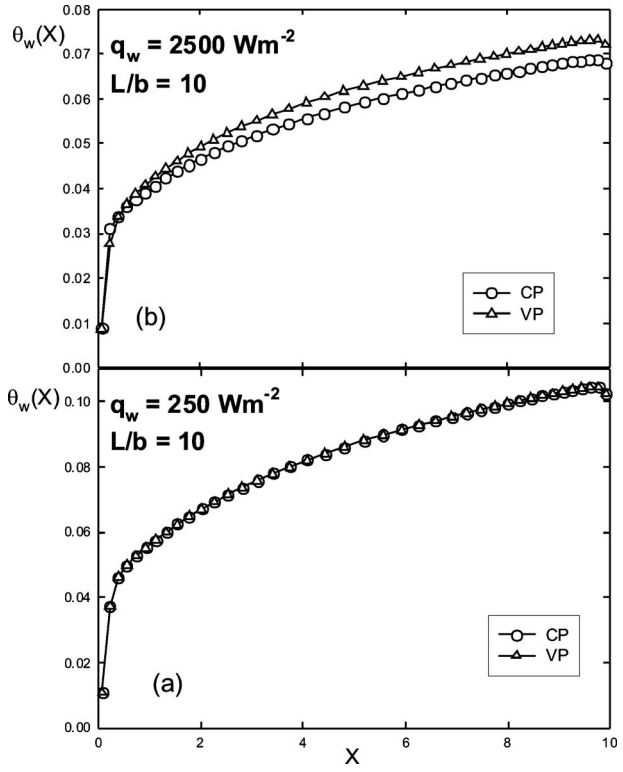

Fig. 7 Plate temperatures as a function of the axial coordinate X for (*a*) $q_w=250$ W m^{-2} and (*b*) $q_w=2500$ W m^{-2}

Acknowledgment

This research project was partially funded by a 2006 research grant awarded by Seconda Università degli Studi di Napoli in Aversa, Italy.

References

[1] Manca, O., Morrone, B., Nardini, S., and Naso, V., 2000, *Natural Convection in Open Channels, in Computational Analysis of Convection Heat Transfer*, B. Sunden and G. Comini, eds., WIT, Southampton, UK, pp. 235–278.

[2] Bar-Cohen, A., Watwe, A. A., and Prasher, R. S., 2003, "Heat Transfer in Electronic Equipment," *Heat Transfer Handbook*, A. Bejan and A. D. Kraus, eds., Wiley, New York, Chap. 13.

[3] Kays, W. M., and Crawford, M. E., 1993, *Convective Heat and Mass Transfer*, McGraw-Hill, New York.

[4] Wirtz, R. A., and Stutzman, R. J., 1982, "Experiments on Free Convection Between Vertical Plates With Symmetric Heating," ASME J. Heat Transfer, **104**, pp. 501–507.

[5] Guo, Z.-Y., Song, Y.-Z., and Zhao, X.-W., 1991, "Experimental Investigation on Natural Convection in Channel by Laser Speckle Photography," Exp. Therm. Fluid Sci., **4**, pp. 594–600.

[6] Ambrosini, D., Paoletti, D., and Tanda, G., 2004, "Investigation of Natural Convection in Vertical Channels by Schilieren and Holografic Interferometry," J. Flow Visualization Image Process., **11**(4) pp. 62–72.

[7] Kettleborough, C. F., 1972, "Transient Laminar Free Convection Between Heated Vertical Plates Including Entrance Effects," Int. J. Heat Mass Transfer, **15**, pp. 883–896.

[8] Nakamura, H., Asako, Y., and Naitou, T., 1982, "Heat Transfer by Free Convection Between Two Parallel Flat Plates," Numer. Heat Transfer, **5**, pp. 95–106.

[9] Naylor, D., Floryan, J. M., and Tarasuk, J. D., 1991, "A Numerical Study of Developing Free Convection Between Isothermal Vertical Plates," ASME J. Heat Transfer, **113**, pp. 620–626.

[10] Chang, T.-S., and Lin, T.-F., 1989, "Transient Buoyancy-Induced Flow Through a Heated, Vertical Channel of Finite Height," Numer. Heat Transfer, Part A, **16**, pp. 15–35.

[11] Morrone, B., Campo, A., and Manca, O., 1997, "Optimum Plate Separation in Vertical Parallel-Plate Channels for Natural Convective Flows: Incorporation of Large Spaces at the Channel Extremes," Int. J. Heat Mass Transfer, **40**, pp. 993–1000.

[12] Anand, N. K., Kim, S. H., and Fletcher, L. S., 1992, "The Effect of Plate Spacing of Vertical, Natural Convection Between Heated Parallel Plates," ASME J. Heat Transfer, **114**, pp. 515–518.

[13] Marcondes, F., and Maliska, C. R., 1999, "Treatment of the Inlet Boundary Conditions in Natural-Convection Flows in Open-Ended Channels," Numer. Heat Transfer, Part B, **35**, pp. 317–345.

[14] Gray, D. D., and Giorgini, A., 1976, "The Validity of the Boussinesq Approximation for Liquids and Gases," Int. J. Heat Mass Transfer, **19**, pp. 545–551.

[15] Hernández, J., and Zamora, B., 2005, "Effects of Variable Properties and Non-Uniform Heating on Natural Convection Flows in Vertical Channels," Int. J. Heat Mass Transfer, **48**, pp. 793–807.

[16] Vargaftik, N. B., 1975, *Tables of Thermophysical Properties of Liquids and Gases*, 2nd ed., Wiley, New York.

[17] FLUENT 6.2 User's Manual, Fluent Inc., 2006.

Performance of a Convectively Heated Rectangular Fin With a Step Change in Cross-Sectional Area and Losing Heat by Simultaneous Convection and Radiation (Step Fins Under Radiation Environment)

B. Kundu[1]
Department of Mechanical Engineering,
Jadavpur University,
Kolkata 700 032, India
e-mail: bkundu123@rediffmail.com

A. Aziz
Department of Mechanical Engineering,
School of Engineering,
Gonzaga University,
Spokane, WA 99258

A numerical procedure has been used to study the thermal performance of a step convective-radiative fin with temperature dependent thermal conductivity and convective base heating. An analytical solution has been developed for a pure convective fin with constant thermal conductivity, with its base exposed to a hot fluid. The effects of geometrical and thermophysical parameters on the temperature profiles in the fin, the fin efficiency, and the fin effectiveness are illustrated. The step fin is found to deliver a superior thermal performance compared with the uniformly thick fin.
[DOI: 10.1115/1.4001928]

Keywords: base convection, convection-radiation, step rectangular fin, temperature dependent thermal conductivity

1 Introduction

Longitudinal fins of rectangular profile are used to enhance heat transfer in applications ranging from heat sinks to space radiators. The rectangular geometry is widely used because it is easy and inexpensive to manufacture. The triangular and trapezoidal profiles offer lighter fins, but this advantage is often offset by the higher manufacturing costs and safety issue due to their sharp tips. Their use is consequently restricted to applications where the weight of the fins must absolutely be kept at a minimum. The concave parabolic profile has been shown to be the ideal choice because it uses the least amount of fin material for a specified heat transfer duty, but its curved surfaces make it very difficult and expensive to manufacture. The number of papers on fin heat transfer runs into thousands. The subject of extended surface heat transfer is covered in heat transfer textbooks, handbook chapters, and a treatise exclusively devoted to the subject [1–5].

The weight disadvantage of the rectangular fin compared with other profile shapes can be remedied by a design in which a rectangular fin with a step reduction in its thickness is used. This design, called here a step fin for brevity, cuts down on the amount of material with only a small increase in the manufacturing cost. Such a design was originally proposed by Hollands and Stedman [6] for a solar absorber plate. The focus of their study was to determine the efficiency of a step fin and the reduction in weight achieved compared with a uniformly thick fin design. Aziz [7] used the method of Lagrange multipliers to establish the optimum design of a step fin. He found that for specified heat dissipation, the saving in material with a step design can be as much as 23% compared with the uniform thickness fin. More recently, Kundu [8] reported a detailed performance analysis and optimum design features of a step fin. He considered three fin geometries—a step fin, a uniformly thick fin, and a trapezoidal fin—and assigned the same volume of material to each and compared their efficiencies and the maximum heat dissipation rates. Based on this comparative study, he concluded that the step fin gave better performance than the other two geometries. The step fin has also been found to give superior performance under dehumidifying conditions [9] and when it is used as an absorber plate in a solar assisted water-lithium bromide (H_20/LiBr) absorption cooler [10]. The performance and optimization of a step radial or annular fin have also been studied by Kundu and Das [11]. This study also established that the step design resulted in a superior thermal performance compared with the customary uniform thickness fin. The conclusion of Kundu and Das [11] has been corroborated by Kim and Moon [12], who studied the performance of a step circular pin-fin array and found it to be superior in performance to that of a pin-fin array consisting of pins of uniform thickness.

It is well known that a fin is most effective when it operates in a natural convection environment where the heat transfer coefficients are low [3]. In this circumstance, the radiative heat loss from the fin is comparable to the natural convection loss and cannot be neglected. Furthermore, if the temperature variation from the base of the fin to its tip is large, then the analysis must also include a temperature dependent thermal conductivity model rather than a constant thermal conductivity assumption. With the exception of a few [13–19], most fin studies assume a constant temperature at the base of the fin. However, in many circumstances the base of the fin receives heat by convection from a hot fluid and the base temperature is not known a priori. Malekzadeh and Rahideh [17,18] applied a differential quadrature method to study two-dimensional nonlinear transient heat transfer in annular and pin fins of variable sectional areas. The same method was used by Malekzadeh et al. [19] to optimize nonsymmetric convective-radiative annular fins.

In view of the considerations in the preceding paragraph, it was felt that the step fin model used in Refs. [6–8] should be modified to incorporate (a) radiative surface heat loss in addition to convective heat loss, (b) a temperature dependent thermal conductivity, and (c) a convective boundary condition at the base of the fin. The present paper develops such a model and investigates the effect of these modifications on the thermal performance of a step fin. The results presented should provide more accurate predictions for the thermal performance of a step fin operating under physically realistic conditions.

2 Step Fin With Simultaneous Convection and Radiation With Temperature Dependent Thermal Conductivity

A rectangular fin with a step change in cross-sectional area is shown in Fig. 1. The thick portion of the fin is heated by convection from a hot fluid at temperature T_L providing a heat transfer coefficient h_L. The thickness and the length of the thick portion are t_1 and L_1, respectively. The thickness of the thin portion and the total length of the fin are t_2 and L, respectively. Both sections have the same surface emissivity ε_m. The heat exchange through the tip of the thin section is assumed to be negligible in accordance with the standard practice. When a step fin design is used in a solar collector, the fin illustrated in Fig. 1 represents the left half of the absorber plate [6], and in that circumstance, the adiabatic condition at the tip of the fin is the result of thermal symmetry. The convective heat transfer coefficient over both sections of the

[1]Corresponding author.
Contributed by the Heat Transfer Division of ASME for publication in the JOURNAL OF HEAT TRANSFER. Manuscript received November 15, 2009; final manuscript received May 4, 2010; published online July 27, 2010. Assoc. Editor: W. Q. Tao.

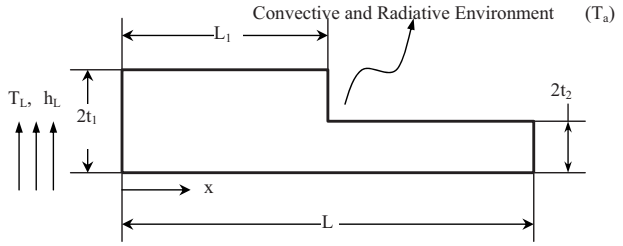

Fig. 1 Schematic of a typical step fin

fin is uniform and is denoted by h. The sink temperature for both convection and radiation is the same and is denoted by T_a. Because the thermal conductivity of most fin materials varies linearly with temperature, the following thermal conductivity-temperature relationship is assumed:

$$k = k_a[1 + \alpha(T_i - T_a)] \tag{1}$$

where k_a is the thermal conductivity at temperature T_a and α is a measure of the thermal conductivity variation with temperature T_i. Since the transverse Biot number has to be small for the fin to be effective [2], heat conduction in the fin is assumed to be one dimensional and in the longitudinal direction. Based on the above conditions, the steady state fin equations, one for the thick section and another one for the thin section, can be written as follows:

$$\left[\frac{d}{dx}\left\{[1 + \alpha(T_i - T_a)]\frac{dT_i}{dx}\right\} - \frac{h}{k_a t_i}\left\{T_i - T_a + \frac{\sigma\varepsilon_m(T_i^4 - T_a^4)}{h}\right\}\right] = [0] \tag{2}$$

where $0 \le x \le L_1$ for $i=1$, $L_1 \le x \le L_2$ for $i=2$, and σ is the Stefan–Boltzmann constant.

Convective heat transfer takes place at the base of the fin. The continuity of temperature and energy balance must be ensured at the interface between the thick and thin fins. Thus, Eq. (2) must satisfy the following boundary conditions:

$$x = 0, \quad k_a\{1 + \alpha(T_1 - T_a)\}\frac{dT_1}{dx} = -h_L(T_L - T_1) \tag{3a}$$

$$x = L, \quad \frac{dT_2}{dx} = 0 \tag{3b}$$

At the interface between the two fin sections, that is, at $x=L_1$, the following conditions apply:

$$T_1 = T_2 \tag{3c}$$

$$-t_1 k_a\{1 + \alpha(T_1 - T_a)\}\frac{dT_1}{dx} = -t_2 k_a\{1 + \alpha(T_2 - T_a)\}\frac{dT_2}{dx} + h(t_1 - t_2) \times\left[T_1 - T_a + \frac{\sigma\varepsilon_m}{h}(T_1^4 - T_a^4)\right] \tag{3d}$$

Equations (1), (2), and (3*a*)–(3*d*) can be written in dimensionless forms as

$$\frac{d^2\theta}{dX^2} + \beta\theta\frac{d^2\theta}{dX^2} + \beta\left(\frac{d\theta}{dX}\right)^2 - Z_0^2\theta\{1 + 4\delta^3 R_p + 6\delta^2 R_p\theta + 4\delta R_p\theta^2 + R_p\theta^3\} = 0 \quad (0 \le X \le L_R) \tag{4a}$$

$$R\left\{\frac{d^2\phi}{dX^2} + \beta\phi\frac{d^2\phi}{dX^2} + \beta\left(\frac{d\phi}{dX}\right)^2\right\} - Z_0^2\phi\{1 + 4\delta^3 R_p + 6\delta^2 R_p\phi + 4\delta R_p\phi^2 + R_p\phi^3\} = 0 \quad (L_R \le X \le 1) \tag{4b}$$

$$X = 0, \quad (1 + \beta\theta)\frac{d\theta}{dX} = -\mathrm{Bi}_L(1 - \theta) \tag{4c}$$

$$X = 1, \quad \frac{d\phi}{dX} = 0 \tag{4d}$$

$$X = L_R, \quad \theta = \phi \tag{4e}$$

$$X = L_R, \quad \frac{d\theta}{dX} = R\frac{d\phi}{dX} - \frac{\psi Z_0^2(1 - R)\phi}{1 + \beta\phi}[1 + R_p(4\delta^3 + 6\delta^2\phi + 4\delta\phi^2 + \phi^3)] \tag{4f}$$

where

$$\theta = \frac{(T_1 - T_a)}{(T_L - T_a)}, \quad \phi = \frac{(T_2 - T_a)}{(T_L - T_a)}, \quad \beta = \alpha(T_L - T_a),$$

$$R_p = \frac{\sigma\varepsilon_m(T_L - T_a)^3}{h}, \quad \mathrm{Bi} = \frac{ht_1}{k_a}, \quad \psi = \frac{t_1}{L}, \quad Z_0 = \frac{\mathrm{Bi}^{1/2}}{\psi},$$

$$\delta = \frac{T_a}{(T_L - T_a)}, \quad R = \frac{t_2}{t_1}, \quad \mathrm{Bi}_L = \frac{h_L L}{k_a}, \text{ and } L_R = \frac{L_1}{L} \tag{5}$$

As Eqs. (4*a*) and (4*b*) and the boundary conditions (4*c*), (4*e*), and (4*f*) are nonlinear, it cannot be solved analytically. A finite difference numerical scheme was adopted to solve these equations. The finite difference equations for both the governing equations and the boundary conditions were obtained by the Taylor series discretization with the second order accuracy, and then these equations were solved simultaneously by using the Gauss–Seidel iterative scheme. The final results were obtained after satisfying the necessary and sufficient convergence criteria. Every solution obtained was tested for grid independency.

Once the temperature distributions were calculated, the data were utilized to compute the efficiency and effectiveness of the step fin. These quantities were determined by calculating the actual heat transfer rate, the ideal heat transfer rate, and the heat transfer rate in the absence of fin. The ideal heat transfer rate was computed by assuming the entire fin surface to be its base temperature. In this analysis, the temperature of the hot fluid at the base of the fin is a known parameter. The temperature at the base is determined from the numerical solution.

Before discussing the results, an analytical solution is derived when the thermal conductivity is a constant and the surface radiation is absent. The analytical solution serves as a benchmark to test the validity and accuracy of the numerical procedure.

3 Step Fin With Pure Convection and Constant Thermal Conductivity

It is possible to derive an analytical solution of Eqs. (4*a*)–(4*f*) by putting $R_p=0$ (no radiation) and $\beta=0$ (constant thermal conductivity). Omitting the details of derivation, which are elementary, the analytical solution obtained is

$$\theta = \frac{\theta_{L_R}\{Z_0\cosh(Z_0X) + \mathrm{Bi}_L\sinh(Z_0X) + \mathrm{Bi}_L\sinh[Z_0(L_R - X)]\}}{Z_0\cosh(Z_0L_R) + \mathrm{Bi}_L\sinh(Z_0L_R)} \tag{6}$$

and

$$\phi = \frac{\theta_{L_R}\cosh[Z_1(1 - X)]}{\cosh[Z_1(1 - L_R)]} \tag{7}$$

where

$$Z_1 = \frac{Z_0}{\sqrt{R}} \tag{8}$$

and

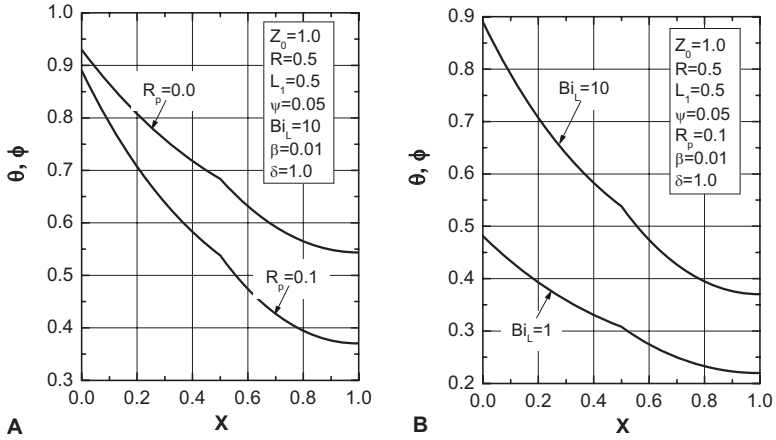

Fig. 2 Effect of radiation parameter R_p and Biot number Bi_L on the temperature distribution: (*a*) variation in R_p and (*b*) variation in Bi_L

$$\theta_{L_R} = \frac{Z_0 \mathrm{Bi}_L \{Z_0[Z_0 \sinh(Z_0 L_R) + \mathrm{Bi}_L \cosh(Z_0 L_R)]\}^{-1}}{1 + \dfrac{\{Z_0 \cosh(Z_0 L_R) + \mathrm{Bi}_L \sinh(Z_0 L_R)\}\{\psi Z_0^2 (1-R) + R Z_1 \tanh[Z_1(1-L_R)]\}}{Z_0\{Z_0 \sinh(Z_0 L_R) + \mathrm{Bi}_L \cosh(Z_0 L_R)\}}} \tag{9}$$

The expressions for the fin efficiency and the fin effectiveness are found to be

$$\eta = \frac{\mathrm{Bi}_L[\cosh(Z_0 L_R) - \theta_{L_R}]}{Z_0[1 + (1-R)\psi][\theta_{L_R} Z_0 + \mathrm{Bi}_L \sinh(Z_0 L_R)]} \tag{10}$$

and

$$\varepsilon = \frac{\mathrm{Bi}_L[\cosh(Z_0 L_R) - \theta_{L_R}]}{Z_0 \psi[\theta_{L_R} Z_0 + \mathrm{Bi}_L \sinh(Z_0 L_R)]} \tag{11}$$

4 Results and Discussion

4.1 Temperature Distribution. The numerical method was applied to a constant thermal step fin losing heat by convection alone. To illustrate the effect of surface radiation on the temperature in the fin, the temperature profile for zero radiation (pure convection) is compared with the profile for the radiation parameter $R_p = 0.1$ in Fig. 2(*a*). As expected, the radiative heat loss complements the convective heat loss, resulting in a lowering of temperature throughout the fin. The effect of radiation is smallest at the base of the fin and increases along the length of the fin. The largest difference between the two curves occurs at the tip of the thin section. The base heat flow increases due to the additional heat withdrawal induced by radiation. The increase in heat flow is manifested by the comparatively larger slope (magnitude) of the curve marked $R_p = 0.1$. Figure 2(*b*) illustrates how the temperature profiles in the two sections of the fin are affected by the strength of the convective heating at the base of the fin. Two curves are shown, one for $\mathrm{Bi}_L = 1$ and the other for $\mathrm{Bi}_L = 10$. The base temperature depends on the convection resistance, which is inversely related to the Biot number. A higher Biot number indicates smaller convection resistance. Thus, there is a smaller temperature drop across the thermal boundary layer between the mainstream fluid and the fin base. This is clearly seen in the curve for $\mathrm{Bi}_L = 10$, where the dimensionless temperature between the fluid and the fin base is $1.00 - 0.89 = 0.11$. When the Biot number is lowered to $\mathrm{Bi}_L = 1$, the convection resistance increases by a factor of 10, and the dimensionless temperature drop between the fluid and the fin base increases to $1.00 - 0.48 = 0.52$. It is also evident from a comparison of the initial slopes of two curves that the larger the Biot number Bi_L, that is, the stronger the convection process, the larger the heat dissipation from the fin.

4.2 Fin Efficiency and Fin Effectiveness. The fin efficiency, defined as the actual heat transfer from the base of the fin to the ideal heat transfer that would occur if the entire surface temperature of the fin was at its base, can be expressed in terms of the dimensionless quantities as follows:

$$\eta = \frac{\mathrm{Bi}_L(1 - \theta_b)}{\theta_b Z_0^2[1 - \psi(R-1)]} \tag{12}$$

The fin effectiveness, defined as the actual heat transfer from the base of the fin to the heat transfer without the fin, can be expressed as

$$\varepsilon = \frac{\mathrm{Bi}_L(1 - \theta_b)}{\psi Z_0^2 \theta_b} \tag{13}$$

Equations (12) and (13) may be combined to express ε in terms of η as

$$\varepsilon = \eta[1 + (1/\psi) - R] \tag{14}$$

The efficiency of a convective-radiative fin is compared with that of a pure convection fin in Fig. 3(*a*). The abscissa $Z_0 = \mathrm{Bi}^{1/2}/\psi$ is a measure of the strength of the surface convective transport. As the surface convection gets stronger, the efficiency of the fin decreases. This result for a step fin follows the trend seen with the uniformly thick fins [1,2]. The efficiency of a convective-radiative is lower than that for a pure convective fin. This behavior of a step fin mirrors the behavior of uniformly thick convective-radiative fins observed in many studies cited in Ref. [5]. The significant difference between the curves for pure convection ($R_p = 0$) and convection-radiation ($R_p = 0.1$) clearly demonstrates that the neglect of radiation can introduce large errors in the values of fin performances. The effect of the Biot number at the base of the fin on the efficiency of the fin can be studied from Fig. 3(*b*). As the Biot number increases, the fin performance decreases. Figure 3(*c*) compares the fin efficiency as a function of the thickness ratio R. For both convective and convective-

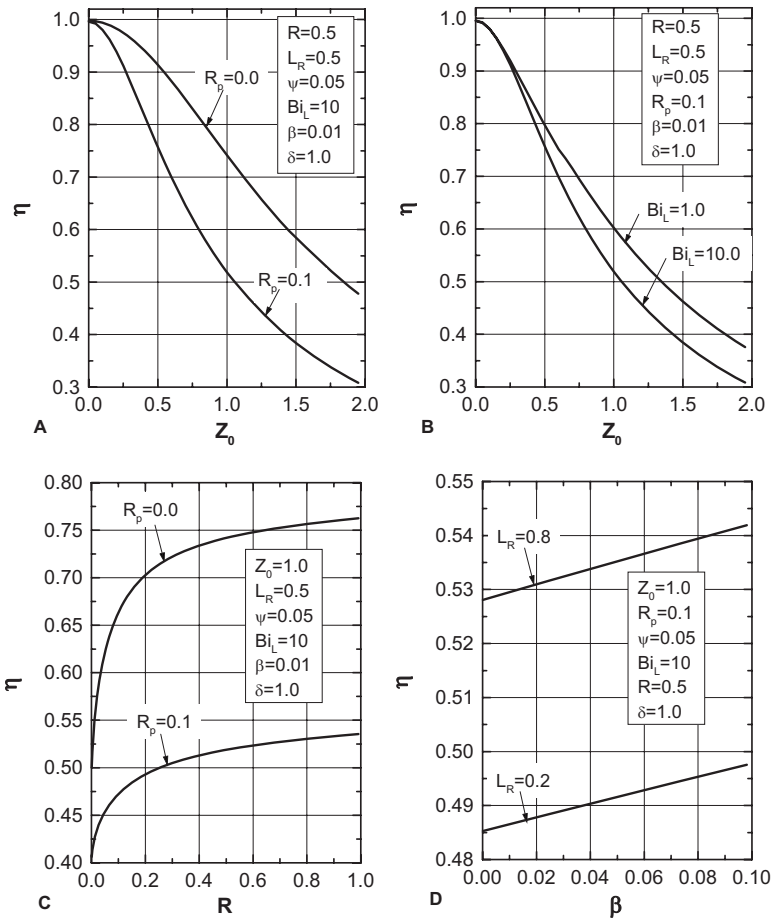

Fig. 3 Influence of Z_0, Bi_L, R_p, R, L_R, and β on the fin efficiency: (*a*) η versus Z_0 for different R_p, (*b*) η versus Z_0 for different Bi_L, (*c*) η versus R for different R_p, and (*d*) η versus β for different L_R

radiative fins, the fin efficiency increases as R increases, reaching a maximum value for a uniformly thick fin ($R=1$). The effect of radiation parameter, R_p, is to lower the efficiency at all values of R, the effect being most pronounced for a uniformly thick fin. It is interesting to note that the performance plateaus at $R=0.6$ for the convective fin as well as the convective-radiative fin. The ratio of the profile areas for a step fin and a uniformly thick fin is $R+(1-R)L_R$. With $L_R=0.5$, the ratio is 0.8. Thus, a step fin of $R=0.6$ is as effective as a uniformly thick fin ($R=1$) but provides a 20% saving in material. This conclusion is valid for both convective and convective-radiative fins. Figure 3(*d*) demonstrates how the variation in thermal conductivity with temperature affects the fin efficiency. For both a step fin with a short thick section ($L_R=0.2$) and a step fin with a long thick section ($L_R=0.8$), the fin efficiency increases as the thermal conductivity parameter is increased. In other words, the greater the sensitivity of the thermal conductivity to temperature, the higher the fin performance. This is under stable in view of the fact that as β increases, the average thermal conductivity of the fin increases. Considering the effectiveness of an infinitely long convective fin, which is given by [1]

$$\varepsilon = \sqrt{kP/hA_c} \tag{15}$$

It can be seen that the higher thermal conductivity results in higher effectiveness. Since the efficiency is directly proportional to effectiveness according to Eq. (14), it also follows the trend exhibited by the effectiveness. It is also noted from Fig. 3(*d*) that a step fin with a longer thick section ($L_R=0.8$) has a higher performance than a step fin with a shorter thick section ($L_R=0.2$). In Fig. 4(*a*), the efficiency of the fin are plotted as a function of the aspect ratio $\psi=t_1/L$ for two values of temperature parameter δ. As the thickness t_1 increases relative to the overall length of the fin, the efficiency gradually decreases. This holds true for both values of δ. Because of the relationship, $T_L-T_a=T_a/\delta$, the fin operates with a larger overall temperature difference T_L-T_a when $\delta=1$ than when $\delta=2$. Consequently, a higher efficiency is seen for $\delta=1$ than for $\delta=2$. The final set of results is presented in Figs. 4(*b*) and 4(*c*), where the efficiency and effectiveness per unit profile area of the fin are presented. Figures 4(*b*) and 4(*c*) show that the peak values occur in the neighborhood of $R=0.1$, that is, when $t_2=0.1t_1$. If the thick and the thin sections of the fin have equal lengths ($L_R=0.5$), then for the optimum design, the thickness of the thin section should be one-tenth the thickness of the thick section.

Nomenclature

a = profile area of a step fin
A = dimensionless profile area, $a/(2t_1L)$
A_c = cross-sectional area, m^2
Bi = Biot number based on the fin surface heat transfer coefficient, ht_1/k_0
Bi_L = Biot number, h_LL/k_0
h = convective heat transfer coefficient on the fin side, $W\ m^{-2}\ K^{-1}$
h_L = convective heat transfer coefficient on the hot fluid side, $W\ m^{-2}\ K^{-1}$

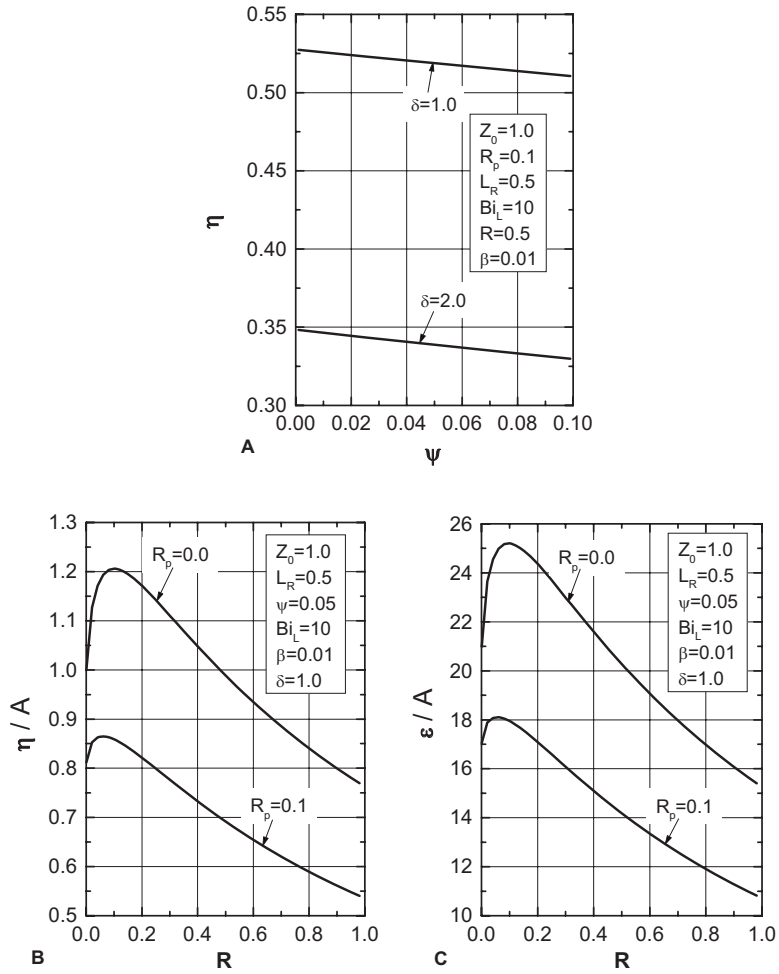

Fig. 4 A geometric variation of a step fin on the fin performance: (*a*) η versus ψ, (*b*) η/A versus R, and (*c*) ε/A versus R

k_0 = thermal conductivity of the fin material corresponding to ambient temperature, W m^{-1} K^{-1}
L = length of the fin, m
L_1 = length of the common section of the fin measured from the fin base, m
L_R = length ratio, L_1/L
P = perimeter, m
R = thickness ratio, t_2/t_1
R_p = dimensionless radiation parameter, $\sigma\varepsilon_m(T_L-T_a)^3/h$
t_1 = semibase thickness, m
t_2 = semitip thickness, m
T_1 = local fin surface temperature ($0 \le x \le L_1$), K
T_2 = local fin surface temperature ($L_1 \le x \le L$), K
T_a = surrounding temperature, K
T_L = hot liquid temperature, K
x = coordinate, m
X = dimensionless coordinate, x/L
Z_0 = dimensionless fin parameter, $\sqrt{\mathrm{Bi}}/\psi$
Z_1 = dimensionless parameter, $Z_0/\sqrt{R}$

Greek Letters

α = coefficient of thermal conductivity, K^{-1}
β = dimensionless variable thermal conductivity parameter, $(T_L-T_a)\alpha$
δ = dimensionless temperature factor, $T_a/(T_L-T_a)$
ε = fin effectiveness
ε_m = emissivity of the fin material
η = fin efficiency
σ = Boltzmann constant, W m^{-2} K^{-4}
θ = dimensionless fin temperature, $(T_1-T_a)/(T_L-T_a)$
θ_{L_R} = dimensionless interface temperature
ϕ = dimensionless fin temperature, $(T_2-T_a)/(T_L-T_a)$
ψ = aspect ratio, t_1/L

References

[1] Incropera, F. P., and Dewit, D. P., 2007, *Fundamentals of Heat and Mass Transfer*, 6th ed., Wiley, New York.
[2] Bejan, A., 1993, *Heat Transfer*, Wiley, New York.
[3] Poulikakos, D., 1994, *Conduction Heat Transfer*, Prentice-Hall, Englewood Cliffs, NJ.
[4] Bejan, A. and Kraus, A. D., eds., 2003, *Handbook of Heat Transfer*, Wiley, New York, Chap. 3.
[5] Kraus, A. D., Aziz, A., and Welty, J. R., 2001, *Extended Surface Heat Transfer*, Wiley, New York.
[6] Hollands, K. G. T., and Stedman, B. A., 1992, "Optimization of an Absorber Plate Fin With a Step Change in Local Thickness," Sol. Energy, **49**, pp. 493–495.
[7] Aziz, A., 1994, "Optimum Design of a Rectangular Fin With a Step Change in Cross-Sectional Area," Int. Commun. Heat Mass Transfer, **21**, pp. 389–401.
[8] Kundu, B., 2002, "Performance Analysis and Optimization of Absorber Plates of Different Geometry for a Flat Plate Solar Collector: A Comparative Study," Appl. Therm. Eng., **22**, pp. 999–1012.
[9] Kundu, B., 2007, "Performance and Optimization Analysis of SRC Profile Fins Subject to Simultaneous Heat and Mass Transfer," Int. J. Heat Mass Transfer,

50, pp. 1545–1558.
[10] Kundu, B., 2007, "The Influence of Collector Fluid Inlet Temperature on the Performance of a Solar-Assisted Absorption System Using Stepped-Finned Flat-Plate Collector," Heat Transfer Eng., **28**, pp. 496–505.
[11] Kundu, B., and Das, P. K., 2001, "Performance Analysis and Optimization of Annular Fin With a Step Change in Thickness," ASME J. Heat Transfer, **123**, pp. 601–604.
[12] Kim, K. Y., and Moon, M. A., 2009, "Optimization of a Stepped Circular Pin-Fin Array to Enhance Heat Transfer Performance," Heat Mass Transfer, **46**, pp. 63–74.
[13] Ma, Z., and Chung, B. T. F., 1997, "Optimization of Convecting-Radiating Longitudinal Rectangular Fins With Thermal Resistance at Base Wall," *Proceedings of the 35th Heat Transfer and Fluid Mechanics Institute*, California State University, Sacramento, CA, May 29–30.
[14] Chiu, C. H., and Chen, C. K., 2003, "Application of Adomian's Decomposition Procedure to the Analysis of Convective-Radiative Fins," ASME J. Heat Transfer, **125**, pp. 312–316.
[15] Malekzadeh, P., Rahideh, H., and Karami, G., 2006, "Optimization of Convective-Radiative Fins Using a Differential Quadrature Element Method," Energy Convers. Manage., **47**, pp. 1505–1514.
[16] Aziz, A., 1985, "Optimization of Rectangular and Triangular Fins With Convective Boundary Conditions," Int. Commun. Heat Mass Transfer, **12**, pp. 479–482.
[17] Malekzadeh, P., and Rahideh, H., 2007, "IDQ Two-Dimensional Nonlinear Transient Heat Transfer Analysis of Variable Section Annular Fins," Energy Convers. Manage., **48**, pp. 269–276.
[18] Malekzadeh, P., and Rahideh, H., 2009, "Two-Dimensional Nonlinear Transient Heat Transfer Analysis of Variable Section Pin Fins," Energy Convers. Manage., **50**, pp. 916–922.
[19] Malekzadeh, P., Rahideh, H., and Setoodeh, A. R., 2007, "Optimization of Non-Symmetric Convective–Radiative Annular Fins by Differential Quadrature Method," Energy Convers. Manage., **48**, pp. 1671–1677.

Thermal Characterizations of Fin-Thin Film Systems

A.-R. A. Khaled
Department of Thermal Engineering and Desalination Technology,
King Abdulaziz University,
P.O. Box 80204,
Jeddah 21589, Saudi Arabia
e-mail: akhaled@kau.edu.sa

This work considers heat transfer in fin-thin film systems. Two types of these systems are analyzed: (A) a thin film sandwiched between two identical fin halves, and (B) a fin sandwiched between two identical thin films. The corresponding coupled energy equations are solved numerically by an implicit, iterative, finite-difference scheme. Comparisons with derived approximate closed-form solutions are performed and good agreement is obtained. A parametric study of all involved parameters is conducted and presented graphically. Useful correlations containing the various physical parameters for both types are reported. It is found that thermal efficiencies of fins can be increased significantly by introducing an internal flow inside the fin material. Moreover, factors producing more internal convections are found to increase the fin-thin film thermal efficiency. In addition, thermal efficiencies of type A systems are found to be higher than those of type B systems. Moreover, the resulting system thermal efficiency is found to have at most one local maximum and one local minimum over the whole relative heights ratio spectrum. Finally, this work paves a way for an effective combined passive and active method for enhancing heat transfer. [DOI: 10.1115/1.4001647]

Keywords: conduction, convection, fins, enhancements, thin films

1 Introduction

Fins are widely used in the industry, especially in the heat exchanger industry [1–5]. Their role is to enhance heat transfer between the solids and the adjoining fluids. According to Bergles [1,2], they are considered as passive techniques to enhance heat transfer. In general, the literature contains many studies concerning heat transfer enhancements using fins [1–10]. One can further classify fins from these works according to the following aspects.

- Geometrical design aspects: This includes simple fin designs [1–5] (rectangular, triangular, etc.) or complicated fin designs (e.g., spiral fins [6]).
- Distribution of the fins on the solid: This includes simple fin distributions [3–5] or structured fin distributions [7,8].
- Number of different adjoining fluids: The fin may be surrounded by a single fluidic reservoir [1–8] or by at least two fluidic reservoirs [9].
- Location of the fin base surface: This surface can be on the outer solid surface [1–9] or embedded in the solid [10].

In this work, it is proposed to consider an additional classification aspect, which is "fins with internal flows". This can be achieved by introducing a fluidic thin film [11,12] inside the fin. The resulting system is named as a "fin-thin film system." The motivation behind this work is to seek new ways of enhancing the thermal efficiencies of existing fins. Two types of fin-thin film systems are considered: (A) a thin film sandwiched between two identical fin halves, and (B) a fin sandwiched between two identical thin films. Energy and momentum equations for both cases are solved numerically in order to compare their thermal efficiencies.

2 Problem Formulation

2.1 A Thin Film Sandwiched Between Two Identical Fin Halves (Type A). Consider a rectangular fin of thickness $2(H-H_o)$, width W, and length L, as shown in Fig. 1. The sandwiched fluidic thin film has height $2H_o$ and width W. Assuming the one-dimensional heat transfer inside the two fin halves, the energy equation for each half [13] is

$$\frac{d^2T_f}{dx^2} - \frac{h_o}{k_f\{H-H_o\}}(T_f - T_\infty) - \frac{h_i}{k_f\{H-H_o\}}(T_f - T_m) = 0 \quad (1)$$

where T_f, T_∞, T_m, h_o, h_i, and k_f are the fin temperature, outer free stream temperature, inner fluid mean bulk temperature, outer convection heat transfer coefficient, inner convection heat transfer coefficient, and the fin thermal conductivity, respectively. The two-dimensional energy equation applicable for the inner fluid is

$$\rho c_p\left(u\frac{\partial T}{\partial x}\right) = k\frac{\partial^2 T}{\partial y^2} \quad (2)$$

where ρ, c_p, u, k, and T are the inner fluid density, specific heat, axial velocity, thermal conductivity, and the temperature field of the inner fluid, respectively. The boundary conditions applicable for Eqs. (1) and (2) are

$$T(x=0,y) = T_b \quad (3a)$$

$$\left.\frac{\partial T}{\partial y}\right|_{x,y=0} = 0 \quad (3b)$$

$$T(x,y=H_o) = T_f(x) \quad (3c)$$

$$T_f(x=0) = T_b \quad (3d)$$

$$\left.\frac{dT_f}{dx}\right|_{x=L} = 0 \quad (3e)$$

In dimensionless forms, Eqs. (1) and (2) can be constructed as

$$\frac{d^2\theta_f}{dX^2} - \Pi_1\theta_f - \Pi_2\,\mathrm{Pe}\frac{d\theta_m}{dX} = 0 \quad (4)$$

$$U\frac{\partial\theta}{\partial X} = \frac{1}{\mathrm{Pe}}\frac{\partial^2\theta}{\partial Y^2} \quad (5)$$

when the following dimensionless variables and parameters are utilized:

$$X = \frac{x}{H_o} \quad Y = \frac{y}{H_o} \quad \theta_f = \frac{T_f - T_\infty}{T_i - T_\infty}$$

$$\theta_m = \frac{T_m - T_\infty}{T_i - T_\infty} \quad \Pi_1 = \left(\frac{\beta^2}{1-\beta}\right)\mathrm{Bi} \quad \Pi_2 = \left(\frac{\beta}{1-\beta}\right)\left(\frac{k}{k_f}\right)$$

$$\mathrm{Bi} = \frac{h_o H}{k_f} \quad \beta = \frac{H_o}{H} \quad a = \frac{H_o}{L} \quad a_H = \frac{H}{L} \quad (6)$$

$$\mathrm{Pe} = \frac{\bar{u}H_o}{\alpha} = \mathrm{Pe}_H\beta^3 \quad \mathrm{Pe}_H = \frac{1}{3(\mu\alpha)}\frac{dP}{dx}H^3$$

where Pe, P, μ, and α are the Peclet number, inner fluid pressure, inner fluid dynamic viscosity, and the inner fluid thermal diffusivity, respectively. Hdrodynamically fully developed internal flow is considered with dimensionless velocity U given by

Contributed by the Heat Transfer Division of ASME for publication in the JOURNAL OF HEAT TRANSFER. Manuscript received February 7, 2010; final manuscript received April 16, 2010; published online July 28, 2010. Assoc. Editor: Sujoy Kumar Saha.

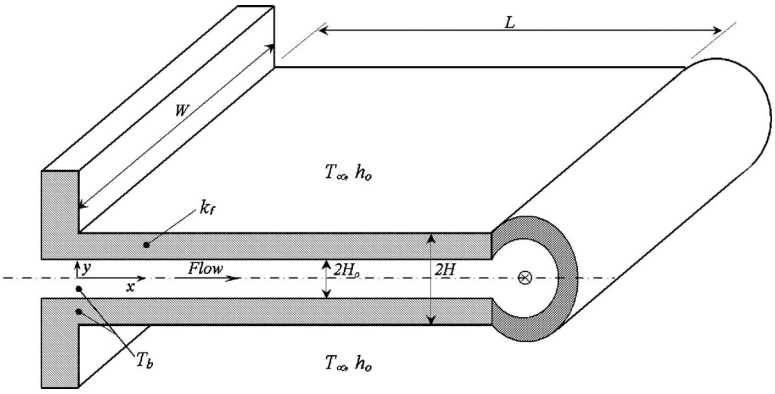

Fig. 1 Schematic diagram for type A fin-thin film systems and the corresponding coordinates system

$$U(Y) \equiv \frac{u}{\bar{u}} = \frac{3}{2}(1 - Y^2) \tag{7}$$

where $\bar{u}$ is the average velocity $\bar{u} = (H_o^2/3\mu)(dP/dx)$. It should be mentioned that Eq. (4) is derived based on the integral form of Eq. (5), which can be constructed in the form

$$\frac{d\theta_m}{dX} = \frac{\mathrm{Nu}}{\mathrm{Pe}}(\theta_f - \theta_m) \tag{8}$$

where $\mathrm{Nu} = h_i H_o/k$. The quantity η represents the thermal efficiency of the fin-thin film system. It is equal to

$$\eta \equiv \frac{q_f + q_{tf}}{q_{\max}} = \frac{-k_f 2W(H - H_o)dT_f/dx|_{x=0} + \rho c_p \bar{u} 2H_o W[T_m(x=0) - T_m(x=L)]}{2WLh_o(T_b - T_\infty)} \tag{9}$$

where q_f and q_{tf} are the fin heat transfer rate and the rate of heat transfer by the thin film, respectively. In terms of dimensionless parameters, it is equal to

$$\eta_A = \left(\frac{a}{\Pi_1}\right)\left\{\Pi_2\,\mathrm{Pe}[1 - \theta_m(X = 1/a)] - \left.\frac{d\theta_f}{dX}\right|_{X=0}\right\} \tag{10}$$

2.1.1 Approximate Solution. For conditions resulting in $d\theta_m/dx \cong d\theta_f/dx$, as when $a\,\mathrm{Pe}/\mathrm{Nu} \ll 1.0$, the solution of Eq. (4) is

$$\theta_f(X) = \frac{\exp(s_1 X) - \left(\frac{s_1}{s_2}\right)\exp\left(\frac{s_1 - s_2}{a}\right)\exp(s_2 X)}{1 - \left(\frac{s_1}{s_2}\right)\exp\left(\frac{s_1 - s_2}{a}\right)}$$

$$s_1 = \left(\frac{\Pi_2\,\mathrm{Pe}}{2}\right)\left\{1 - \sqrt{1 + \frac{4\Pi_1}{(\Pi_2\,\mathrm{Pe})^2}}\right\}$$

$$s_2 = \left(\frac{\Pi_2\,\mathrm{Pe}}{2}\right)\left\{1 + \sqrt{1 + \frac{4\Pi_1}{(\Pi_2\,\mathrm{Pe})^2}}\right\} \tag{11}$$

As such, η for type A systems become

$$\eta_A = \left(\frac{a}{s_1}\right)\left\{\frac{[1 - \exp(-s_1/a)] - \left(\frac{s_1}{s_2}\right)^2[1 - \exp(-s_2/a)]}{\exp(-s_1/a) - \left(\frac{s_1}{s_2}\right)\exp(-s_2/a)}\right\}$$

$$\frac{a\,\mathrm{Pe}}{\mathrm{Nu}} \ll 1.0 \tag{12}$$

2.2 A Fin Sandwiched Between Two Identical Thin Films (Type B). Let a rectangular fin of thickness $2(H - H_o)$, width W, and length L be sandwiched between two identical thin films of height H_o and width W, as shown in Fig. 2. The dimensionless energy equation applied to the to the thin film is given by Eq. (5). The application of conservation of energy on the fin yields, in dimensionless form, the following:

$$\frac{d^2\theta_f}{dX^2} - \Pi_2 \mathrm{Nu}_L(\theta_f - \theta_m) = 0 \tag{13}$$

where $\mathrm{Nu}_L = h_L H_o/k$. The quantity h_L is the convection heat transfer coefficient between the fin and the inner fluid flow. For type B systems, the Peclet number and the U field are given by

$$\mathrm{Pe} = \frac{\bar{u}H_o}{\alpha} = \mathrm{Pe}_H \beta^3; \quad \mathrm{Pe}_H = \frac{1}{12(\mu\alpha)}\frac{dP}{dx}H^3$$

$$U(Y) = 6Y(1 - Y) \tag{14}$$

The boundary conditions for this case are

$$\theta(X = 0, Y) = 1.0 \tag{15a}$$

$$\theta(X, Y = 0.0) = \theta_f(X) \tag{15b}$$

$$-\left.\frac{\partial\theta}{\partial Y}\right|_{X,Y=1.0} = \left(\frac{\Pi_1}{\Pi_2}\right)\theta(X, Y = 1.0) \tag{15c}$$

$$\theta_f(X = 0) = 1.0 \tag{15d}$$

$$\left.\frac{d\theta_f}{dX}\right|_{X=1.0/a} = 0.0 \tag{15e}$$

The integral form of Eq. (5), based on Eq. (15), takes the form

$$\mathrm{Nu}_L(\theta_f - \theta_m) = \mathrm{Pe}\frac{d\theta_m}{dX} + \frac{\Pi_1}{\Pi_2}\theta(X, Y = 1.0) \tag{16}$$

Substituting Eq. (16) in Eq. (13) yields

$$\frac{d^2\theta_f}{dX^2} - \Pi_1\theta(X, Y = 1.0) - \Pi_2\,\mathrm{Pe}\frac{d\theta_m}{dX} = 0 \tag{17}$$

There is an important parameter that should be mentioned in order to completely characterize this type of systems. It is Nu_L, which is given by

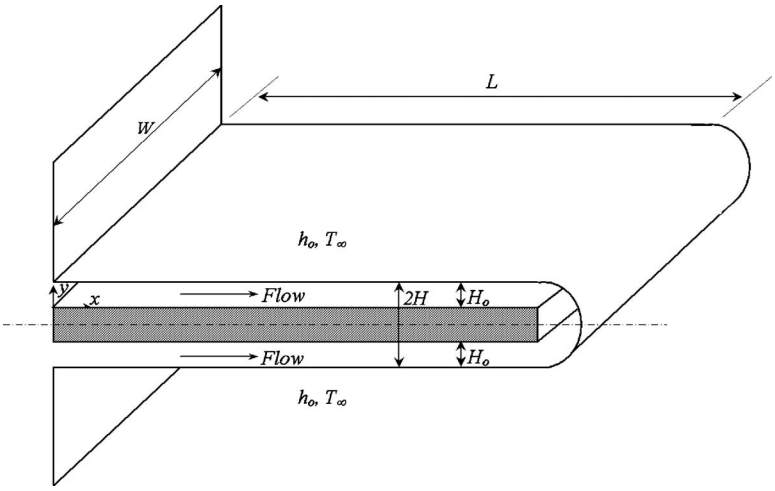

Fig. 2 Schematic diagram for type B fin-thin film systems and the corresponding coordinates system

$$\mathrm{Nu}_L \equiv \frac{h_L H_o}{k} = \frac{q_L''}{(T_f - T_m)}\left(\frac{H_o}{k}\right) = \left\{\frac{-1}{\theta_f(X) - \theta_m(X)}\right\}\left\{\left.\frac{\partial\theta}{\partial Y}\right|_{X,Y=0}\right\} \tag{18}$$

where q_L'' is the transverse heat fluxes at the fin boundary. The fin efficiency for this case η_B can be calculated from Eq. (9).

2.2.1 Approximate Solution When a $\mathrm{Pe} \ll 1.0$. When the flow is thermally developed inside the thin film, the θ field can be approximated by

$$\frac{\theta_U(X) - \theta(X,Y)}{\theta_U(X) - \theta_m(X)} \cong \left\{\frac{\theta_U(X) - \theta_f(X)}{\theta_U(X) - \theta_m(X)}\right\}(1 - 3.5Y + 2.5Y^2) + 5Y(1 - Y) \tag{19}$$

where $\theta_U(X) = \theta(X, Y = 1.0)$. Two relationships can be obtained between $\theta_f(X)$, $\theta_m(X)$, and $\theta_U(X)$. First, when Nu_L given by Eq. (18) is evaluated and substituted in Eq. (16), considering that $a\,\mathrm{Pe} \ll 1.0$. The second one is obtainable when Eq. (19) is applied on the boundary condition (15*c*). Further reductions change Eq. (17) to

$$\frac{d^2\theta_U}{dX^2} - (\Pi_2\,\mathrm{Pe})\left\{\frac{0.425\Pi_1 + \Pi_2}{0.75\Pi_1 + \Pi_2}\right\}\frac{d\theta_U}{dX} - \left\{\frac{\Pi_1\Pi_2}{0.75\Pi_1 + \Pi_2}\right\}\theta_U = 0 \tag{20}$$

with boundary conditions equal to

$$\theta_U(X = 0) = \frac{\Pi_2}{0.75\Pi_1 + \Pi_2} \tag{21a}$$

$$\left.\frac{d\theta_U}{dX}\right|_{X=1/a} = 0 \tag{21b}$$

By solving Eq. (20), η_B becomes

$$\eta_B = \left(\frac{a}{p_1}\right)\left\{\frac{\Pi_2}{0.75\Pi_1 + \Pi_2}\right\} \times \left\{\frac{[1 - \exp(-p_1/a)] - \left(\frac{p_1}{p_2}\right)^2[1 - \exp(-p_2/a)]}{\exp(-p_1/a) - \left(\frac{p_1}{p_2}\right)\exp(-p_2/a)}\right\}$$

$$p_{1,2} = \left(\frac{\Pi_2\,\mathrm{Pe}}{2}\right)\left\{\frac{0.425\Pi_1 + \Pi_2}{0.75\Pi_1 + \Pi_2}\right\} \times \left\{1 \mp \sqrt{1 + \frac{4\Pi_1\Pi_2(0.75\Pi_1 + \Pi_2)}{[\Pi_2\,\mathrm{Pe}(0.425\Pi_1 + \Pi_2)]^2}}\right\} \tag{22}$$

3 Numerical Methodology

Equations (4) and (5) or Eqs. (17) and (5) are coupled and must be solved numerically with iterations. The implicit finite-difference method discussed by Blottner [14] proved to produce accurate results for this problem. The previous equations were discretized using three-point central different quotients for the second derivative terms. The resulting tridiagonal system of algebraic equations was then solved using the Thomas algorithm [14]. The solution of Eq. (5) marches from $X = 0$ to $X = 1/a$ using a two-point backward difference formula in the X-direction. Constant step sizes of $0.001/a$ and 0.0025 are used in the X and Y directions, respectively. The convergence criterion for this problem required that the maximum difference between the current fin temperatures and the previous solution be 10^{-8}. A fin-thin film system with $H_o = 7.0$ mm, $H = 10$ mm, and $L = 56$ mm made from Nickel ($k_f = 60$ W/m K) with $h_o = 200$ W/m^2 K results in $\mathrm{Pe} = 4.0$ when $u_o = 0.021$ m/s, $\beta = 0.7$, $\Pi_1 = 0.054$, $\Pi_2 = 1.36$, and $a = 0.125$ with NaK solution ($\rho = 892$ kg/m^3, $c_p = 1058$ J/kg K, $k = 35$ W/m K). The numerical method results are in good agreement with the results of Eqs. (11) and (22), as shown in Figs. 3 and 4. As such, these validations led to more confidence in the obtained results. Also, it should be mentioned here that the one-dimensional fin problem assumption is fairly valid for the used range of Bi, $\mathrm{Bi} \leq 0.2$ according to Ref. [8].

4 Discussion of the Results

Figures 3 and 4 illustrate the behavior of the system thermal efficiencies η_A and η_B as functions of Π_1 and Π_2 for type A and type B systems, respectively. As expected, increasing the value of Π_2 while fixing the other parameters produces a larger inner fluid thermal capacity. As such, the system heat transfer rate increases. This causes the system thermal efficiencies to increase, as evident from Figs. 3 and 4. However, an increase in the value of Π_1 produces additional increases in the maximum system heat transfer rate relative to that of the system heat transfer rate. This causes decreases in the system thermal efficiencies, as shown in the figures. It is interesting to notice that increases in the system thermal

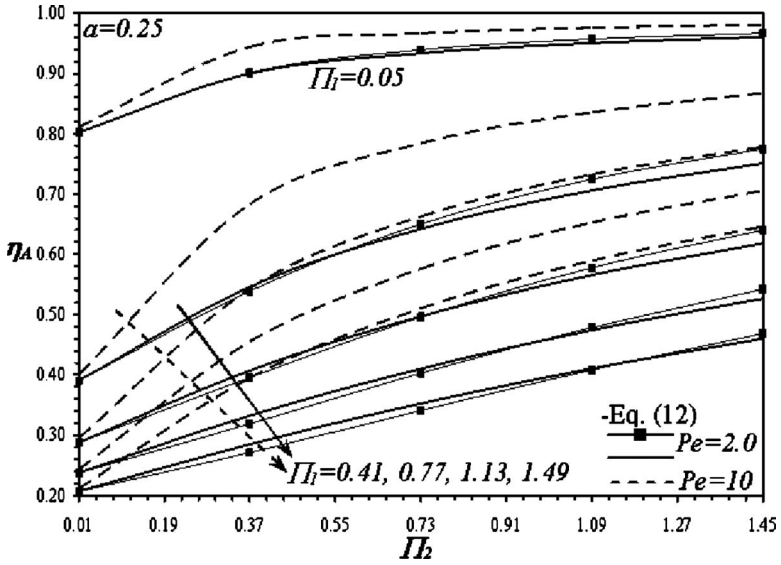

Fig. 3 Effects of Π_2 and Π_1 on η_A

efficiencies are significant at smaller values of Π_1 and Π_2 and at larger Peclet numbers. Moreover, η_B-values obtained numerically are slightly larger than those obtained from Eq. (22) because the latter values were obtained by ignoring the thermal entry region [13].

Figures 5 and 6 show the effects of the relative heights ratio and the Biot number on the thermal efficiencies η_A and η_B, respectively. Increasing β between $\beta=0.5$ and $\beta=1.0$ causes increases in the average inner convection coefficient as a result of the increase in the thermal entry region effects [13]. On the other hand, the fin cross-sectional area decreases as β increases, causing reduction in the fin heat transfer rate. As such, the system thermal efficiencies are noticed to have local maxima when $k/k_f=0.16$. When $\beta<0.5$, the inner average convection coefficient decreases as β increases due to decreases in transverse temperature gradients, and then it starts to increase as β increases when the flow starts to be dominant by the thermal entry region effects. As such, the system thermal efficiencies are noticed to have local minima values when $\beta<0.5$.

5 Conclusions

The problem of heat transfer inside fin-thin film systems was considered. Two fin-thin film systems were analyzed: (A) a thin film sandwiched between two identical fin halves, and (B) a fin sandwiched between two identical thin films. Appropriate forms of the coupled energy equations were solved using an implicit, iterative, and finite-difference scheme. The numerical results for the thermal efficiencies were validated against closed-form approximate solutions. Useful correlations were reported in the Appendix. It was found that the fin's thermal efficiencies can be increased significantly by introducing an internal flow within the fin material. Also, thermal efficiencies of type A systems were found to be higher than those of type B systems. Factors producing more internal convections such as increasing the Peclet number were found to increase the system thermal efficiency. The system thermal efficiency was found to have, at most, one local maximum and one local minimum over the whole relative heights

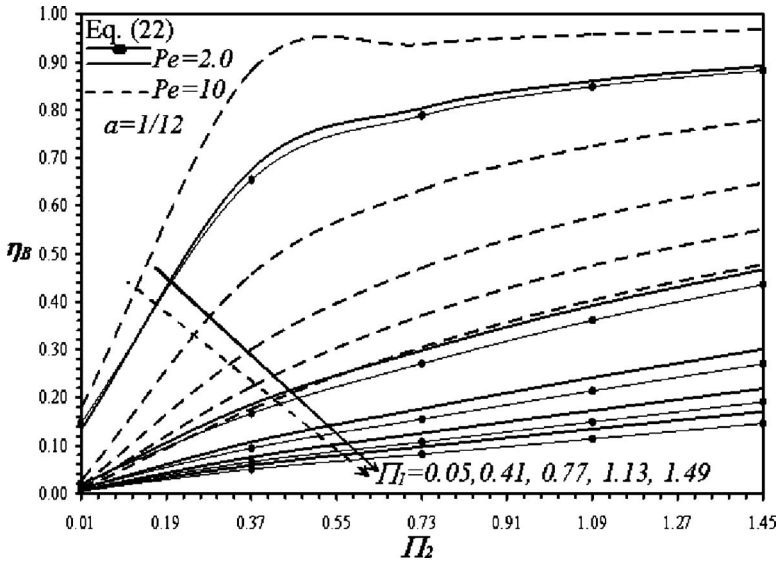

Fig. 4 Effects of Π_2 and Π_1 on η_B

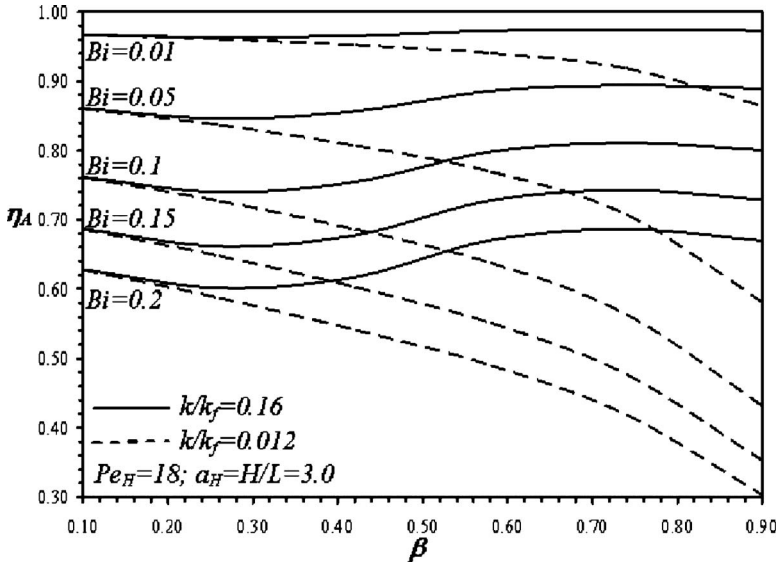

Fig. 5 Effects of β and Bi on η_A

ratio spectrum. Finally, fin-thin film systems are recommended to be part of the main channel in order to provide relatively large heat transfer enhancement ratios.

Nomenclature

a, a_H = aspect ratios
Bi = Biot number
c_p = fluid specific heat
H = half total height of the fin-thin film system
H_o = half total height of the thin film
h_o = outer convection heat transfer coefficient
h_i = inner convection heat transfer coefficient for type A
h_L = inner lower side convection heat transfer coefficient for type B
k = thermal conductivity of the inner fluid
k_f = fin thermal conductivity
L = fin and thin film length
Nu = Nusselt number for type A system
Nu_L = inner lower side Nusselt number for type B system
P = pressure
Pe, Pe_H = Peclet numbers
T = inner fluid temperature field
T_b = fin base temperature
T_f = fin temperature
T_m = mean bulk temperature
T_∞ = free temperature of the external fluid
u = inner fluid velocity field
$\overline{u}$ = fluid mean velocity
U = fluid dimensionless velocity
W = fin-thin film system width
x = coordinate axis along the fin-thin film system center line
X = dimensionless x-coordinate
y = transverse coordinate axis

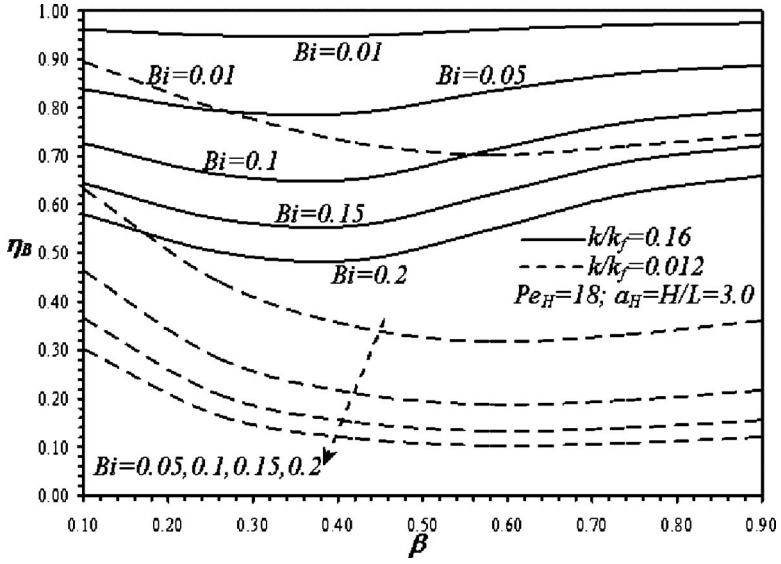

Fig. 6 Effects of β and Bi on η_B

Y = dimensionless y-coordinate

Greek Symbols

α = inner fluid thermal diffusivity
β = relative heights ratio
η_A, η_B = fin-thin film system efficiencies for types A and B
μ = inner fluid dynamic viscosity
θ = inner fluid dimensionless temperature
θ_f = fin dimensionless temperature
θ_m = mean bulk dimensionless temperature
Π_1, Π_2 = first and second fin-thin film system dimensionless parameters
ρ = inner fluid density

Appendix

The following correlations for η_A and η_B are proposed:

$$\eta_A = \left\{\frac{a\phi_1\phi_2}{\phi_3\Pi_1}\right\} \times \frac{\sinh(c_1\,\mathrm{Pe}^{0.28} + c_2[a\Pi_2\,\mathrm{Pe}]^{c_3})\exp(-\Pi_1 a^{-0.76}/\mathrm{Pe}^{4.05})}{\cosh(c_4[\Pi_1^{0.75}/a]^{c_5} + c_6[a\Pi_2\,\mathrm{Pe}]^{c_7+c_8[a\,\mathrm{Pe}/\Pi_1]^{c_9}})} \tag{A1}$$

$$\eta_B = \left\{\frac{a\varphi_1\varphi_2\varphi_3}{\Pi_1}\right\}\left\{\frac{a\,\mathrm{Pe}}{\Pi_1}\right\}^{d_1}\exp\left(d_2\left[\frac{a\,\mathrm{Pe}}{\Pi_1}\right]^{d_1}\right) \tag{A2}$$

when $0.05 \le \Pi_1 \le 1.50$, $0.01 \le \Pi_2 \le 1.45$, $2.0 \le \mathrm{Pe} \le 18$, and $0.08 \le a \le 0.25$. The functions ϕ_1, ϕ_2, ϕ_3, φ_1, φ_2, and φ_3 are

$$\phi_1 = c_{10} + c_{11}\left[\frac{\Pi_2}{\Pi_1}\right]^{1.2} + c_{12}\left[\frac{\Pi_2}{\Pi_1}\right]^{2.25} + \sum_{i=13}^{i=15} c_i\left[\frac{\Pi_2}{\Pi_1}\right]^{i-10} \tag{A3}$$

$$\phi_2 = c_{16}[a\Pi_2\,\mathrm{Pe}] + \sum_{i=17}^{i=19} c_i[a\Pi_2\,\mathrm{Pe}]^{i-15} + c_{20}[a\Pi_2\,\mathrm{Pe}]^6 \tag{A4}$$

$$\phi_3 = \left\{1 + 7\left[\frac{\Pi_1}{a^{0.229}\,\mathrm{Pe}}\right]^3 + 4\left[\frac{\Pi_1}{a^{0.229}\,\mathrm{Pe}}\right]^4 + \left[\frac{\Pi_2}{a}\right]^2\right\}^{c_{21}}\left\{\frac{\mathrm{Pe}^{2.18}}{304}\right\}^{c_{21}} \tag{A5}$$

$$\varphi_1 = d_3[\Pi_2\,\mathrm{Pe}]^{0.68} + d_4[a\Pi_2\,\mathrm{Pe}]^{2.39} + d_5[a\Pi_2\,\mathrm{Pe}]^{2.56} + d_6[a\Pi_2\,\mathrm{Pe}]^{2.73} \tag{A6}$$

$$\varphi_2 = d_7[a^2\,\mathrm{Pe}]^{d_8} + d_9[a^2\Pi_2\,\mathrm{Pe}]^{d_{10}} + d_{11}[a^2\Pi_1]^{d_{12}} + d_{13}\left[\frac{\mathrm{Pe}}{a}\right]^{d_{14}} \tag{A7}$$

$$\varphi_3 = \left\{1 - 108.66\left[\frac{a^{0.125}\Pi_1}{\mathrm{Pe}}\right]^{d_{15}} + 107.056\left[\frac{a^{0.125}\Pi_1}{\mathrm{Pe}}\right]^{d_{16}} + \left[\frac{\Pi_2}{a}\right]^{1.75}\right\}^{d_{17}}\mathrm{Pe}^{d_{18}} \tag{A8}$$

The constants $c_1 - c_{24}$ and $d_1 - d_{16}$ are equal to

$$c_1 = 0.623463 \quad c_2 = 0.314291 \quad c_3 = -0.253155$$

$$c_4 = 3.98448 \quad c_5 = 0.113461 \quad c_6 = 18.6847$$

$$c_7 = 0.0410807 \quad c_8 = 13.5668 \quad c_9 = 0.0587985$$

$$c_{10} = -12042777.9842 \quad c_{11} = 2370619.8306$$

$$c_{12} = -550334.1563 \quad c_{13} = 90538.5148 \quad c_{14} = -2815.1614$$

$$c_{15} = 35.637 \quad c_{16} = -862094324.2251$$

$$c_{17} = 104971828.2443 \quad c_{18} = -22036071.8785$$

$$c_{19} = 2183238.3364 \quad c_{20} = -9523.8054 \quad c_{21} = 0.262812 \tag{A9}$$

$$d_1 = -0.721531 \quad d_2 = -0.462346 \quad d_3 = -45483.8396$$

$$d_4 = 79126.0565 \quad d_5 = -107102.158 \quad d_6 = 36705.6174$$

$$d_7 = 5.02581 \times 10^{-5} \quad d_8 = -0.0313466 \quad d_9 = -7.12432 \times 10^{-5}$$

$$d_{10} = -0.0695067 \quad d_{11} = 0.506432 \quad d_{12} = -9.84908 \times 10^{-6} \tag{A10}$$

$$d_{13} = -0.506434 \quad d_{14} = 6.59839 \times 10^{-6} \quad d_{15} = -1.27524$$

$$d_{16} = -1.28347 \quad d_{17} = 0.100659 \quad d_{18} = 0.014696214$$

The correlations are preferred to be used when $\eta_{A,B} \ge 0.40$. This corresponds to the maximum error $<10\%$.

References

[1] Bergles, A. E., 1998, *Handbook of Heat Transfer*, 3rd ed., McGraw-Hill, New York, Chapter 11, pp. 1–76.
[2] Bergles, A. E., 2001, "The Implications and Challenges of Enhanced Heat Transfer for the Chemical Process Industries," Chem. Eng. Res. Des., **79**, pp. 437–444.
[3] Kays, W. M., 1955, "Pin-Fin Heat-Exchanger Surfaces," ASME J. Heat Transfer, **77**, pp. 471–483.
[4] Kern, D. O., and Kraus, A. D., 1972, *Extended Surface Heat Transfer*, McGraw-Hill, New York.
[5] Kraus, A. D., Aziz, A., and Welty, J. R., 2001, *Extended Surface Heat Transfer*, Wiley, New York.
[6] Nuntaphan, A., Kiatsiriroat, T., and Wang, C. C., 2005, "Air Side Performance at Low Reynolds Number of Cross-Flow Heat Exchanger Using Crimped Spiral Fins," Int. Commun. Heat Mass Transfer, **32**, pp. 151–165.
[7] Almogbel, M., and Bejan, A., 2000, "Cylindrical Trees of Pin Fin," Int. J. Heat Mass Transfer, **43**, pp. 4285–4297.
[8] Khaled, A.-R. A., 2007, "Heat Transfer Enhancement in Hairy Fin Systems," Appl. Therm. Eng., **27**, pp. 250–257.
[9] Khaled, A.-R. A., 2009, "Analysis of Heat Transfer Through Bi-Convection Fins," Int. J. Therm. Sci., **48**, pp. 122–132.
[10] Khaled, A.-R. A., 2008, "Heat Transfer Analysis Through Solar and Rooted Fins," ASME J. Heat Transfer, **130**, pp. 074503.
[11] Kleiner, M. B., Kuhn, S. A., and Haberger, K., 1995, "High Performance Forced Air Cooling Scheme Employing Micro-Channel Heat Exchangers," IEEE Trans. Compon., Packag. Manuf. Technol., Part A, **18**, pp. 795–804.
[12] Vafai, K., and Zhu, L., 1999, "Analysis of a Two-Layered Micro Channel Heat Sink Concept in Electronic Cooling," Int. J. Heat Mass Transfer, **42**, pp. 2287–2297.
[13] Incropera, F. P., Dewitt, D., Bergman, T. L., and Lavine, A. S., 2006, *Fundamentals of Heat and Mass Transfer*, Wiley, New York.
[14] Blottner, F. G., 1970, "Finite-Difference Methods of Solution of the Boundary-Layer Equations," AIAA J., **8**, pp. 193–205.